

Development and Demonstration of Ultra High Concentrator Photovoltaic System Beyond 3000x

Submitted by **Mussad Mohammed S Alzahrani** to the University of Exeter

as a thesis for a degree of

Doctor of Philosophy in Renewable Energy

In May 2022

This thesis is available for Library use on the understanding that it is copyright material and that no quotation from the thesis may be published without proper acknowledgement.

I certify that all material in this thesis which is not my own work has been identified and that no material has previously been submitted and approved for the award of a degree by this or any other University.

Signature :

Dedicated to

Father & mother

Saeed, Salman, Zayed

Brothers & Sisters

Wife

ABSTRACT

Concentrating photovoltaic technology harnesses solar energy by increasing the solar density upon solar cells using optical concentrators. Ongoing research on concentrating photovoltaic systems aim to improve the achievable energy harnessing and utilisation potential. Increasing the concentration ratio for high energy generation raises many advances and limitations in the concentrating photovoltaic design. However, the field of concentrating photovoltaic research is still in progress where new configurations, methods and materials are fabricated to reach a competitive cost by enhancing the efficiencies of the system to standard silicon photovoltaic systems.

The work presented in this thesis focuses on developing and demonstrating an ultrahigh concentrated photovoltaic system beyond 3000 ×. This system is based on a Silicon-on-Glass Fresnel lens resulting in a geometrical design of 5831 ×. The Fresnel lens as a primary optical interface was investigated theoretically, numerically, and experimentally to understand the operating limits in terms of power output, optical performance (optical efficiency and concentration ratio), and working temperature. The discrepancy between a Fresnel lens's theoretical and experimental optical characterisation results was studied. All the equations were elaborated for single- and multi-junction solar cells, emphasising the performance when the focal spot area is larger or lesser than the solar cell area. The prediction approach of optical characterisation has shown a strong agreement between the theoretical and experimental results of the multi-junction solar cells with a discrepancy of 2% at 7.7 W (77 suns) and 6% on the average cross a solar irradiance on the cell from 3.1 W – 7.7 W corresponding to 31 suns – 77 suns in concentration ratio. The numerical model using COMSOL Multiphysics software was established to study the Fresnel lens optically and

thermally. The developed optical model was validated theoretically and experimentally to show a firm agreement with a discrepancy of $\leq 1\%$. Also, the developed thermal model was validated experimentally to show a difference of only 2.18%. Further, optical and electrical characterisations of the flawed glass have been conducted. The optical characterisation has shown a drop of 3.2% in optical efficiency. I-V and power curves of cracked and non-cracked Fresnel lenses were also compared to show a drop of 3.2% in short circuit current and power.

A theoretical analysis of the optical performance for a $\frac{1}{4}$ of the ultrahigh concentrated photovoltaic system design grouping three optical interfaces is performed to estimate the optical loss and its influence on the optical efficiency and concentration ratio. Also, a numerical model was established using COMSOL Multiphysics software to simultaneously evaluate the thermal and optical performance of a $\frac{1}{4}$ of the ultrahigh concentrated photovoltaic system. The system was analysed under direct normal irradiance ranging from $400 \frac{W}{m^2}$ to $1000 \frac{W}{m^2}$ in an interval of $100 \frac{W}{m^2}$, showing a simulative optical efficiency of $\sim 93\%$ and a simulative concentration ratio of 1361 *suns* at $1000 \frac{W}{m^2}$. The thermal model was interlinked with the optical model to generate the results accordingly. The final stage receiver shows a maximum temperature ranging between 157.4 °C and 78.5 °C.

Moving toward a ultrahigh concentrated photovoltaic design raises the importance of a cooling management system due to thermal excitation. Although the thermal performance and thermal management for the ultrahigh concentrated photovoltaic system are beyond this thesis's scope, the cooling mechanism arrangement based on either pre- or post-illumination techniques was explored.

The post-cooling mechanism study was established using COMSOL Multiphysics software for numerical analysis. A flat-plate and micro fin heatsink studied the effect of concentration ratio up to 2000 *suns* to determine their limits as a passive cooling system and establish when an active cooling system is needed based on the recommended operating temperature of the solar cell of 80 °C. On the other hand, Graphene was experimentally exploited as a pre-illumination cooling technique for a solar cell with different graphene coating thicknesses. The concept of utilising graphene as a neutral density filter for focal spot concentrating photovoltaic (Fresnel lens primary optic) reduces the solar cell temperature significantly and maintains the cell temperature for a more extended period. The graphene coating orientation further influenced the temperature gradient behaviour of the focal spot and incident temperature.

The Fresnel lens working parameters (focal length and the focal spot) were defined to establish the mechanical structural design accordingly. The system was mechanically designed based on three optical interfaces, built in-house, and incorporated with a sun tracker. Different aspects were examined initially before the outdoor testing, the sun tracker alignment accuracy and payload capacity, windage load, and counterbalance weight and moments effects using SOLIDWORKS software. The ultrahigh concentrated photovoltaic system was tested outdoor with three types of secondary mirrors, resulting in an effective concentration ratio of 984 *suns*, 1220 *suns*, and 1291 *suns* and an average optical efficiency of 18.5%, 20.25%, and 22% for Aluminium reflective film, Pilkington Optimirror, and ReflecTech® Polymer secondary optic types, respectively. The fabricated ultrahigh concentrated photovoltaic system and tested experimentally outdoor is the highest in both geometrical and effective concentration ratios so far.

It would not be possible to design and perform the ultrahigh concentrated photovoltaic system without fully characterising its primary optic, which helps set the performance basis and associated losses. Although the experimented system showed the highest value in terms of both geometrical and effective concentration ratios, the subsequent optics to the Fresnel lens were standard optics. The attained outcomes are practical in progressing concentrating photovoltaic technologies to a higher concentration ratio.

Acknowledgement

"In the name of Allah, The Most Gracious and The Most Merciful."

All praise to Allah the Most Beneficent and Magnificent who provided me courage and perseverance to complete this work sincerely. I thank Almighty for allowing me to do my PhD studies at the University of Exeter-Penryn Campus. I want to express my deep gratitude to the respected university and its knowledgeable faculty members for conveying quality learning with their valuable support and guidance, which has guided me through this point of undertaking my thesis work.

My most profound appreciation to my advisor **Prof. Tapas Mallick** for his constant endeavour, guidance, positive criticism, and the numerous moments of attention he devoted throughout my research and writing. His allocated time, valuable recommendation, and continuous effort brought this work into this level. His and the advice and insights from my previous second supervisor, **Dr. Senthil Sundaram** and current second supervisor **Dr. Asif Tahir**, were invaluable to my overall research progression. Also, I extend my thanks to all my colleagues for their constructive support and encouragement.

I would also acknowledge all the co-authors involved in my publications, especial thanks to **Dr. Katie Shanks** for her continuous support and valuable insights throughout my PhD study. Dr Katie Shanks' knowledge and experience led me to secure this degree professionally, and not to forget **Dr. Hasan Baig, Dr. Anurag Roy, and Dr. Yusuf Chanchangi**. Also, I owe thanks and recognition to my fellow PhD mates.

My appreciations go to **James Yule**, who assisted me in understanding the mechanical difficulties in designing/building the UHCPV prototype, for the long discussions on material selection, system design, SOLIDWORKS training,

assembling structures, and outdoor experimental setup and for giving me his precious time and effort.

Thanks are due to my wife and three sons (Saeed, Salman, and Zayed). I do not believe this journey would not be enjoyable and full of excitement without them.

Last and most important of all is the acknowledgement, encouragement, and unlimited support from my family at home. I am grateful for my lifetime, especially to my parents, brothers, and sisters, for their prayers, support and confidence that made me achieve this ambition in my life.

Table of Contents

| | |
|---|-----------|
| ABSTRACT | 3 |
| Acknowledgement | 7 |
| List of Figures | 12 |
| Abbreviations, Symbols, and Nomenclature..... | 15 |
| CHAPTER 1: Introduction | 20 |
| 1.1 Aims and Objectives of Research..... | 21 |
| 1.2 Research Methodology..... | 22 |
| 1.2.1 Reviewing Literature | 22 |
| 1.2.2 Numerical Model Development CPV | 22 |
| 1.2.3 Primary Optic Assessment for CPV..... | 22 |
| 1.2.4 Pre-illumination Cooling Approach for Fresnel Lens Based CPV | 23 |
| 1.2.5 UHCPV Theoretical and Simulative Assessment..... | 24 |
| 1.2.6 UHCPV Prototype Manufacturing and Experimental Testing | 24 |
| 1.3 Contribution of the Papers to the Research Field | 25 |
| 1.4 Outline of the Thesis | 25 |
| CHAPTER 2: Advances and Limitations of the CPVT System – Literature Review | 28 |
| 2.1 Introduction..... | 28 |
| 2.2 The State of Arts and Challenges of CPV systems..... | 31 |
| 2.3 Electrical and Thermal Considerations for CPVT System | 33 |
| 2.4 CPVT System: Cells, Optics, and Receivers | 38 |
| 2.4.1 Semiconductor Materials: Temperature and Efficiencies..... | 38 |
| 2.4.2 Concentrators: Temperature and Efficiencies..... | 41 |
| 2.4.3 Thermal Receiver Design and Materials..... | 44 |
| 2.4.4 Linear Concentrators: The Reflective Trough of Low-Medium Concentration | 46 |
| 2.4.5 High Concentration Point-Source Concentrators and Their Secondary Optics’ Performance..... | 53 |
| 2.4.6 Summary of Photovoltaic Cell Efficiencies and Design..... | 57 |
| 2.5 Economic Aspects for High CPVTs with High Concentration Ratio | 59 |
| 2.6 Conclusion | 65 |
| CHAPTER 3: Modelling a Concentrator Solar Cell Coupled with a Passive Heat Sink..... | 66 |
| 3.1 CPV Design Considerations | 66 |
| 3.2 Passive cooling with fin design..... | 67 |
| 3.3 Heat Spreader Selection and Thermo-Physics Properties | 69 |
| 3.4 Numerical Model..... | 70 |
| 3.5 Boundary Conditions..... | 73 |

| | | |
|--|---|------------|
| 3.6 | Meshing..... | 75 |
| 3.7 | Performance Characteristics of CPV with Flat-Plate and Micro-Fin Heat Sinks 76 | |
| 3.8 | Conclusion..... | 79 |
| CHAPTER 4: Primary Optical System for UHCPV..... | | 80 |
| 4.1 | Introduction..... | 80 |
| 4.2 | Theoretical Optical Characterisations | 80 |
| 4.3 | Experimental Optical Characterisation..... | 82 |
| 4.4 | Optical-Thermal Numerical Modelling for Fresnel Lens | 85 |
| 4.4.1 | Numerical Model..... | 85 |
| 4.4.1.1 | Optical Model | 85 |
| 4.4.2 | Boundary Conditions..... | 86 |
| 4.4.3 | Theoretical/Experimental Optical Validation..... | 88 |
| 4.4.4 | Experimental Validation for the Thermal Model..... | 89 |
| 4.5 | Optical Losses of SOG Fresnel Lens | 90 |
| 4.6 | Conclusion..... | 92 |
| CHAPTER 5: Alternative Cooling Mechanism for Concentrated Photovoltaics ... | | 94 |
| 5.1 | Introduction..... | 94 |
| 5.2 | Preparation of Graphene Coating and Characterisations | 96 |
| 5.3 | Overall Characterisation Results..... | 97 |
| 5.3.1 | Graphene Layer Validation and Cost Analysis | 100 |
| 5.4 | Orientation Effect for Graphene ND Filter..... | 101 |
| 5.5 | Conclusion..... | 104 |
| CHAPTER 6: Theoretical/Numerical Assessment for UHCPV System | | 106 |
| 6.1 | Perspective of UHCPV System | 106 |
| 6.2 | Theoretical Overview – Different Secondary Mirror Coatings | 107 |
| 6.3 | Numerical Evaluation for ¼ UHCPV – Three Optical Stages..... | 111 |
| 6.3.1 | Optical Boundary Condition | 112 |
| 6.3.2 | Thermal Boundary Condition | 113 |
| 6.3.3 | Simulative Optical Performance..... | 114 |
| 6.3.4 | Simulative Thermal Performance..... | 115 |
| 6.4 | Conclusion..... | 117 |
| CHAPTER 7: UHCPV Fabrication and Experimentation | | 119 |
| 7.1 | Mechanical Design Condition and Overview..... | 119 |
| 7.1.1 | Beam Analysis | 121 |
| 7.1.2 | Wind Load Effect | 122 |
| 7.2 | Outdoor Testing | 123 |

| | | |
|--|--------------------------------------|------------|
| 7.3 | Conclusion..... | 128 |
| CHAPTER 8: Conclusions and Future Work..... | | 130 |
| 8.1 | Conclusion..... | 130 |
| 8.2 | Important Findings of the Study..... | 133 |
| 8.3 | Recommendations for Future Work..... | 134 |
| References | | 135 |

List of Figures

| | |
|---|----|
| Figure 1 Working flow of CPVT system with summarized limitations | 29 |
| Figure 2.(a) A basic Fresnel lens and (b) a basic Cassegrain CPVT system configuration for the three components of primary /secondary optics, single-/multi-junction solar cell, and thermal receiver. | 31 |
| Figure 3 Effect of (a) solar irradiance and (b) cell temperature on I-V curve of a single-junction PV cell [18]..... | 35 |
| Figure 4. Different semiconductor materials (thin-film and wafer-based) bandgap energy, maximum efficiency, all under 1 sun concentration ratio. The theoretical maximum cell efficiency is measured for terrestrial application under AM 1.5. | 37 |
| Figure 5. The limiting efficiency for ideal bandgap energy under no concentration for solar cell use. The solar cells' efficiencies were calculated based on an ideal blackbody spectrum (black line) and the AM 1.5D spectrum (red line) for various semiconductor material configurations. | 38 |
| Figure 6. Semiconductor materials and their concentration ratio in theoretical and experimental studies considered by this review with interval bars which show the range of concentration ratios tested in the literature [12,35]..... | 40 |
| Figure 7. Factor considerations in the selection of the solar cell materials in a CPVT system..... | 41 |
| Figure 8. Summary of advances and limitations in the optical concept for increasing the concentration ratio..... | 42 |
| Figure 9. Optical efficiency vs incidence angle: (a) optical efficiency in CPC for low concentration ratio in building application; (b) optical efficiency in high concentration photovoltaic design based on Fresnel lens [37,38]..... | 43 |
| Figure 10. CPVT systems with the concentration ratio ranges and working fluid temperature ranges as reported in [11,13]..... | 44 |
| Figure 11. The water output temperature/cell temperature impact on (a) the electrical efficiency and (b) the thermal efficiency of the system in different studies [56–59]..... | 47 |
| Figure 12. MaReCo (maximum reflector collector) PV-thermal hybrid has the same focal line for both parabolic reflectors. The glass cover is tilted at a 30° angle between the absorber and the horizontal. Also shown is the transverse projected angle of incidence [63]..... | 50 |
| Figure 13. I-V curve for uniform illumination over the whole cell area (30 <i>suns</i>) and non-uniform illumination on the middle third of the cell (90 <i>suns</i>) [58]. | 51 |
| Figure 14. Thermal and electrical efficiencies for the reported CPVT studies and classified based on their level of concentration ratio. | 59 |
| Figure 15. System cost as a function of concentration ratio [50,92]. | 60 |
| Figure 16. Installation cost per unit of overall system [93]..... | 61 |
| Figure 17. Comparison of the performance of the best MJPV concentrator solar cells with concentration ratio [88]. | 62 |
| Figure 18 The levelized cost of electricity (\$/kWh) for concentrated photovoltaic (CPV), Concentrated Solar Power (CSP), and Solar PV plants for completed projects [109,110]. | 64 |
| Figure 19 Performance characteristics of an Azur space 3C44C solar cell. The four lines are efficiency versus solar concentration ratio for version MC/air & glass and version HC/Air & glass where the solar cell is optimized. Measurement conditions is 1.5 AM D – 1000 W/m ² (ASTM G 173-03), $T = 25\text{ }^{\circ}\text{C}$, designated measurement area = 100.51 mm ² [91]. | 66 |
| Figure 20 Asymmetric, side-view, and cross-section view for the micro-finned heatsink with typical dimensions of the fins. | 68 |

| | |
|--|-----|
| Figure 21 Geometric model of the CPV receivers, material and thickness layers for the DBC [35], IMS [33], and Si wafer [36]. | 70 |
| Figure 22 Thermal Boundary Conditions | 75 |
| Figure 23 Tetrahedral mesh applied to the thin layer. | 76 |
| Figure 24 Temperature field distribution for a) Direct Bonded Copper (DBC), b) Insulated Metal Substrates (IMS), and c) Silicon Wafer Substrate (Si Wafer). | 78 |
| Figure 25 a schematic diagram of a. fractional concentration loss (solar cell to focal spot area) ($10 \times 10 \text{ mm}^2$), and b. solar cell area larger than the focal spot area ($5.1 \times 5.1 \text{ cm}^2$). | 83 |
| Figure 26 The asymmetric view for only the primary optic with the copper plate as a receiver where a. is the detailed geometry and b. is the optical and thermal boundary conditions. | 87 |
| Figure 27 Shows the discrepancy between the simulative and theoretical optical concentration ratio with DNI arranging from 400 W/m^2 to 1000 W/m^2 in accordance with the input power to the Fresnel lens. | 88 |
| Figure 28 Validation for the predicted maximum temperature to the measured maximum temperature. | 89 |
| Figure 29 The flawed/ unflawed Fresnel lens. | 90 |
| Figure 30 a) optical efficiency and optical concentration ratio (calculated using MJSC (Azur Space 3C44A $10 \times 10 \text{ mm}^2$) as a final optical stage) lines for the flawed/unflawed Fresnel lens. b) I-V & power curves for the flawed/unflawed Fresnel lens. | 91 |
| Figure 31 The positioning of a graphene ND filter in the CPV unit and its working principle. | 96 |
| Figure 32 The cell efficiency versus the effective solar irradiance on the focal spot. | 101 |
| Figure 33 Schematic representation for the entire experimental set-up summarising the experimental approach in which (a) GC faces the source of the concentrated solar irradiance (SOG Fresnel lens), and (b) GC faces the solar cell. | 102 |
| Figure 34 The cell efficiency of the single-junction (polycrystalline Si) solar cell for the GC facing the source of solar irradiance and GC facing the solar cell. | 103 |
| Figure 35 Illustration for the ray path and optical setup: primary optic, secondary optic, and tertiary optic. | 108 |
| Figure 36 Theoretical optical efficiency with wavelength ($400 - 2000 \text{ nm}$) for four different reflective mirrors as a secondary optical stage associated with both the Fresnel lens and the SK-700. The optical concentration ratio computed relying on a solar cell area of $10 \times 10 \text{ mm}^2$, $5.5 \times 5.5 \text{ mm}^2$, and $3 \times 3 \text{ mm}^2$ as a final stage and no fractional losses. This is only for $\frac{1}{4}$ of the UHCPV. | 109 |
| Figure 37 Optical concentration ratio plotted for three sizes of the final receiver (solar cell) and for four types of metallic coatings associated with the tertiary optic (SK-700) and the Fresnel lens, highlighting the consideration of optical fractional loss. | 110 |
| Figure 38 Asymmetric view of $\frac{1}{4}$ of UHCPV system with geometrical illustration and optimum position for the highest optical performance. | 112 |
| Figure 39 The optical boundary condition as in COMSOL Multiphysics software for a $\frac{1}{4}$ UHCPV system. | 113 |
| Figure 40 The thermal boundary condition as in COMSOL Multiphysics software for a $\frac{1}{4}$ UHCPV system | 114 |
| Figure 41 Irradiance distribution at 1000 W/m^2 a. on the optical interfaces and b. on the receiver magnified. | 115 |
| Figure 42 Shows the linear correlation between the concentration ratio and the temperature at an ambient temperature in a range between $50 \text{ }^\circ\text{C}$ and $20 \text{ }^\circ\text{C}$ and convective heat transfer coefficient of $4 \text{ W/m}^2 \cdot \text{K}$. | 116 |

Figure 43 Shows the linear correlation between the concentration ratio and the temperature at an ambient temperature in a range between 50 °C and 20 °C and convective heat transfer coefficient of $22 \text{ Wm}^2. \text{K}$ 117

Figure 44 SOLIDWORKS screenshot for the complete designed UHCPV system a. asymmetric view and b. Top view and actual design of UHCPV system c. asymmetric view and d. top view..... 120

Figure 45 The integration of counterbalance arm, counterbalance weight, and UHCPV system to the sun tracker, where a. is the SOLIDWORKS design and b. is the full actual system outdoor ready for testing. The drawings include the extended tube but not the heavy-duty floor stand tripod, where b shows the real heavy-duty floor stand tripod.. 121

Figure 46 The beam design, where a. straight and b. reinforced. 122

Figure 47 Images for a. Tertiary Optical Element (TOE), b. TOE bonded to the cell. c. shows the reflective image for the coated Aluminium film on low-iron glass simulated on a flat surface. The imperfection of the coated film is apparent in the reflected image as a bubble surface (challenging to observe on the coated film), resulting in an optical dispersion. d. shows the reflective image of the mirror with a clear reflective image. e. shows the reflective mirror of the ReflecTech® Polymer. The reflected image of the ReflecTech® Polymer is slight less dispersion than the Aluminium film. f. shows the full outdoor experimental setup. 125

Abbreviations, Symbols, and Nomenclature

| | | |
|----------------|---|-----------------|
| $A_{receiver}$ | Receiver (solar cell) Area | m^2 |
| A | Area | m^2 |
| $A_{Fresnel}$ | Fresnel Lens Area | m^2 |
| AM | Atmosphere | - |
| c | Speed of Light | m/s |
| $C_{eff,exp}$ | Experimental Effective Concentration Ratio | sun |
| $C_{eff,th}$ | Theoretical Effective Concentration Ratio | sun |
| C_g | Geometrical Concentration Ratio | \times |
| $C_{opt,sim}$ | Simulative Optical Concentration Ratio | sun |
| CPC | Compound Parabolic Concentrator | - |
| CPV | Concentrated Photovoltaic | - |
| CPVT | Concentrated Photovoltaic/thermal | - |
| CR_1 | Optical Concentration Ratio | sun |
| CRRH | Conjugate Refractive-Reflective Homogenizer | - |
| CSP | Concentrated Solar Power | - |
| C_{th} | Theoretical Concentration Ratio | sun |
| DBC | Direct Bonded Copper | - |
| DNI | Direct Normal Irradiance | W/m^2 |
| FF | Fill Factor | - |
| GC | Graphene Coating | - |
| H | Hamiltonian | - |
| h | Heat Transfer Coefficient | $W/m^2 \cdot K$ |
| HTF | Heat Transfer Fluid | - |
| IMS | Insulated Metal Substrates | - |
| I_{SC} | Short Circuit Current | $Amps$ |
| I_T/I_M | Subcell Limits | - |
| k | Wave Vector | rad/m |
| K | Thermal Conductivity | $W/m \cdot K$ |
| L | Thickness | m |
| MaReCo | Maximum Reflector Collector | - |
| MJPV | Multijunction Photovoltaic | - |
| MJSC | Multijunction Solar Cell | - |
| MPP | Maximum Power Point | W |
| n | Reflective index | - |
| ND | Natural Density | - |
| NPV | Net Present Value | - |
| OD | Optical Density | - |
| PCB | Printed Circuit Boards | - |
| PMMA | Polymethyl Methacrylate | - |
| PV | Photovoltaic | - |
| PVT | Photovoltaic Thermal | - |
| q | Ray Position | m |
| Q | Heat dissipated by the solar cell | W |
| q_o | Optical Power | W/m^2 |
| Q_s | Boundary Heat Source | W/m^2 |
| R | Thermal Resistance | $m^2 \cdot K/W$ |
| SEM | Scanning Electron Microscope | - |
| Si Wafer | Silicon Wafer | - |
| SiO | Silicon Dioxide | - |

| | | |
|-----------------------------|--|------------------------|
| SOG | Silicon-on-Glass | - |
| T | Temperature | °C |
| TOE | Tertiary Optical Element | - |
| UH | Ultrahigh | - |
| UHCPV | Ultrahigh Concentrated Photovoltaic | - |
| UV | Ultra-violet | - |
| V_{oc} | Open Circuit Voltage | <i>Volts</i> |
| WCC | Worst-Case Condition | - |
| X | The Position of Fin Along the Baseplate Area | <i>cm</i> |
| η | Efficiency | % |
| η_{cell} | Cell Efficiency | % |
| η_{module} | Module Efficiency | % |
| $\eta_{opt,eff}$ | Effective optical Efficiency | % |
| $\eta_{opt,th}$ | Theoretical Optical Efficiency | % |
| $\eta_{optical}$ | Optical Efficiency | % |
| $\eta_{simulative,optical}$ | Simulative Optical Efficiency | % |
| θ_1 | Angle of Incident | <i>Degree</i> |
| θ_2 | Angle of Refraction | <i>Degree</i> |
| ω | Angular Frequency | <i>rad/s</i> |
| $\%T$ | Transmittance of the Fresnel Lens | % |
| \dot{q} | Heat Source | <i>W/m²</i> |
| ΣQ_j | The Sum of the Ray Deposition Power | <i>W</i> |

List of Accompanying Material

In the Appendix, the following published and submitted articles are given.

Journal Papers Published

Article 1. M. Alzahrani, K. Shanks, T. Mallick, "Advances and limitations of increasing solar irradiance for concentrating photovoltaics thermal system," Renewable and Sustainable Energy Reviews, 138 (2021), p. 110517, [10.1016/j.rser.2020.110517](https://doi.org/10.1016/j.rser.2020.110517).

The entire review was accomplished and written by the author under the guidance of the second author and the supervisors.

Article 2. M. Alzahrani, H. Baig, K. Shanks, T. Mallick, "Estimation of the performance limits of a concentrator solar cell coupled with a micro heatsink based on a finite element simulation," Appl. Therm. Eng., 176 (2020), p. 115315, [10.1016/j.applthermaleng.2020.115315](https://doi.org/10.1016/j.applthermaleng.2020.115315).

The second author proposed the initial idea. The first author completed the theoretical simulation, optimisation procedure, and the entire writing up under the supervision of the second, third, and fourth authors.

Article 3. M. Alzahrani, A. Ahmed, K. Shanks, S. Sundaram, T. Mallick, "Optical losses and durability of flawed Fresnel lenses for concentrated photovoltaic application." Materials Letters, 275 (2020), p. 128145, [10.1016/j.matlet.2020.128145](https://doi.org/10.1016/j.matlet.2020.128145).

The first author proposed the research idea. The first and second authors carried out the experimentation. The first author entirely conducted the analysis and writing up under the supervision of the third, fourth and fifth authors.

Article 4. M. Alzahrani, A. Roy, K. Shanks, S. Sundaram, T. Mallick, "Graphene as a pre-illumination cooling approach for a concentrator photovoltaic (CPV) system." *Solar Energy Materials and Solar Cells*, 222 (2021), p. 110922, [10.1016/j.solmat.2020.110922](https://doi.org/10.1016/j.solmat.2020.110922).

This initial idea was proposed by the first author. The second and first authors carried out the material preparation for the experimentation. The first author conducted the experimental work and paper writing up with guidance and supervision from the other authors.

Article 5. M. Alzahrani, A. Roy, S. Sundaram, T. Mallick, "Investigation of Thermal Stress Arising in a Graphene Neutral Density Filter for Concentrated Photovoltaic System." *ENERGIES* 2021, 14 (12), 3515, [org/10.3390/en14123515](https://doi.org/10.3390/en14123515).

Since this work is an extended analysis of the previous one, the exact contribution by the authors is carried out here.

Article 6. M. Alzahrani, A. Ahmed, K. Shanks, S. Sundaram, T. Mallick, "Optical component analysis for ultrahigh concentrated photovoltaic system (UHCPV)." *Solar Energy*, 227 (2021), [10.1016/j.solener.2021.09.019](https://doi.org/10.1016/j.solener.2021.09.019).

The first author suggests the theoretical idea. Both the first and second authors conducted all the required experimentation and characterization. The first author carried out complete data analysis and paper writing under the supervision of the third, fourth, and fifth authors.

Ready for Submission

Article 7. M. Alzahrani, W. Cameron, K. Shanks, S. Sundaram, T. Mallick, "Experimentally validating the thermal performance of a Fresnel lens in concentrator photovoltaic system." Prepared to be submitted for *International Journal of Energy Research*.

The theoretical idea, numerical simulation, experimentation work, and paper writing were carried out by the first author with assistance from the second author and under the supervision of the third, fourth, and fifth authors.

Article 8. M. Alzahrani, W. Cameron, K. Shanks, S. Sundaram, T. Mallick, "Optothermal numerical investigation on an ultrahigh concentrated photovoltaics system (UHCPV)." Prepared to be submitted for Solar Energy Journal.

The theoretical idea, numerical simulation, experimentation work, and paper writing were carried out by the first author with assistance from the second author and guidance and supervision by the third, fourth, and fifth author.

Article 9. M. Alzahrani, W. Cameron, K. Shanks, S. Sundaram, T. Mallick, "Mechanical design aspects for ultrahigh concentrated photovoltaics system (UHCPV)." Prepared to be submitted for Solar Energy Journal.

The first author carried out the design concept and design conduction. All the simulations were conducted as well by the first author. The building up of the system was carried out by the first author and the lab technician (James Yale). The second author carried out the proofreading and review, while the guidance and supervision were done by the third, fourth and fifth authors.

In preparation for Submission

Article 10. M. Alzahrani, K. Shanks, Y. Chanchangi, W. Cameron, S. Sundaram, T. Mallick, "Record high solar concentration for PV: experimental validation achieving > 1200 effective sun.' Prepared to be Submitted to Nature Energy Journal.

The second author proposed the theoretical design, whereas the first author carried out the actual design, experimentation, and analysis. The third author assists in conducting the outdoor experiment. The second and fourth authors carried out the proofreading and review. The second, fifth and sixth authors provided guidance and supervision.

CHAPTER 1: Introduction

Solar energy is abundant energy on earth, generating a clean and efficient energy source. The photovoltaic (PV) cell is the most common way to convert electromagnetic radiation into direct electrical energy. However, to overcome the limitation of the PV in absorbing all the incident rays on the PV cell and maintaining the quality of generated electrical power, both optical concentrators and multijunction solar cells (MJSCs) must be used to achieve high power conversions and efficiencies.

Concentrating photovoltaic (CPV) systems utilise optical concentrators to harness a large amount of energy by increasing the solar density. Optical concentrators utilise either imaging or non-imaging reflector/refractor to intensify the solar density in either one or two optical stages into either focal line or focal point where electrical and/or thermal energy capturing. Since the CPV system is still under ongoing research and improvements to achieve the highest energy, increasing the concentration ratio for high energy generation raises many advances and limitations in the CPV design.

The ultrahigh concentrated photovoltaic system (UHCPV) has a high potential to increase the power output further and minimise the solar cell size, which lowers the cell cost and upsurges the competitiveness of the CPV system. The ultrahigh (UH) concentration ratio is achieved by integrating multiple optics in one compact system design. The succession of optics in the CPV system is designed to concentrate the incoming sun rays where the quality and shape of an optical surface strongly influence the optical losses. To achieve the UH level, the sunlight divergence should be abated to intensify the solar irradiance within a relatively small acceptance angle, considering the limitation by the sun's angular size and submitting to the law of etendue conservation. The concentrator optics

performance evenly relies on the manufacturing criteria, such as optics thickness and surface smoothness. The UHCPV system required a super-accurate tracking system to ensure minimal light divergence. The weight of optics and overall system components need to be carefully evaluated and interlinked with the payload design condition of a tracking system to ensure excellent solar monitoring and avoid tracking errors and dynamic load impact. An excellent optical tolerance allows room for relatively small misalignment during the stage of manufacturing. Since UHCPV of $> 3,000 \text{ suns}$ did not get into the scope of outdoor experimental investigations for optical assessment, this work outlines the challenges and provides several solutions to overcome them.

1.1 Aims and Objectives of Research

- To review the concentrator photovoltaic thermal (hybrid) systems observing the limitations and advances in technologies with increasing concentration ratios.
- To develop a numerical model that accurately relies on a unified heat transfer model combining concentration ratios, optical and electrical efficiencies to predict overall performances of the high concentrated photovoltaic system (HCPV) system.
- To undertake optical analysis for the primary optical components (Silicon-on Glass (SOG) Fresnel Lens) theoretically and experimentally for suitable application in the UHCPV system. This includes exploring the performance of the flawed Fresnel lens and its optical losses and defining the working limits of the Fresnel lens for setting up the final design.
- To design and manufacture a UHCPV prototype suitable to incorporate multiple-stage optics and allow for a large number of degrees of freedom through every optical stage for system adjustment and alignment. This

includes the needed preparation and analyses for the associated outdoor testing items, such as sun tracker, counterbalance weight, and counterbalance mechanical arms.

- To experimentally validate and analyse the performance of a UHCPV system.

1.2 Research Methodology

1.2.1 Reviewing Literature

A review of the advances and limitations of the concentrating photovoltaic-thermal (CPVT) system was carried out to gain an understanding of the most developed technology. This review identified the impact of concentration ratio and its resultant temperature on the CPVT system's performance, operation, and reliability. Research into the potential of the optical configuration and thermal receiver was also undertaken. Suggestions are made throughout the review regarding possible improvements in system performance.

1.2.2 Numerical Model Development CPV

A post-illumination cooling mechanism was modelled using COMSOL Multiphysics software to predict the thermal performance. Flat-plate and fin-plate heatsink configurations were modelled and validated against experimental data. The initial model was developed through this work, allowing parametric study for different meteorological conditions and different types of solar cell substrates.

1.2.3 Primary Optic Assessment for CPV

Since the UHCPV design is based on a Fresnel lens as a primary optic, a clear understanding of the optical performance and its resultant electrical power through a single junction and the MJSC was conducted theoretically and

experimentally. All equations used to solve the optical concentration ratio and efficiency for both theoretical and experimental performance were elaborated.

The Orafol Fresnel Optics company manufactured the tested Fresnel lens. The Fresnel lens was reproduced in SOLIDWORKS software and then imported into COMSOL Multiphysics software to further predict the optical and thermal performance for validation. This validation helps establish an accurate optical-thermal model when subsequent optics to the Fresnel is incorporated to simulate the UHCPV system.

1.2.4 Pre-illumination Cooling Approach for Fresnel Lens Based CPV

Graphene material as an excellent thermal dissipater was deployed and characterised to build a neutral density (ND) filter working as a pre-illumination cooling mechanism in a CPV system. The low-iron glass was coated with graphene by a screen-printing method followed by a microstructural scanning electron microscope (SEM) image to determine coating thickness. The spectrophotometer was utilised to measure the optical transmissivity of the coated sample for optical characterisation. The developed ND graphene filter was compared with the IR filter, the most used filter for heat minimisation, by cutting wavelength near IR and after. Electrical and thermal performance was analysed indoors employing a solar simulator instrument and thermal data logger and IR camera. Overall, the developed ND graphene filter proved its concept as an excellent thermal dissipater by maintaining the focal spot temperature in correlation with the graphene thickness and hence better cell efficiency. Due to heat accumulation on the graphene layer, the low iron glass substrates suffer extreme thermal stress.

1.2.5 UHCPV Theoretical and Simulative Assessment

A theoretical analysis of the optical performance for $\frac{1}{4}$ of the UHCPV system grouping three optical interfaces is performed to estimate the optical loss and its influence on the optical efficiency and optical concentration ratio. A theoretical review for the secondary optical stage explored four different metallic coatings: UV aluminium mirror, enhanced aluminium mirror, silver mirror, and gold mirror to predict the optical concentration ratio and efficiency and the allowed window of optical losses in terms of concentration ratio (suns) to still achieve a concentration ratio > 3000 *suns*. Further, the previously developed optical-thermal numerical model for only the Fresnel lens was extended to include three optical interfaces to predict the performance simulatively.

1.2.6 UHCPV Prototype Manufacturing and Experimental Testing

The UHCPV system was designed using SOLIDWORKS software based on four-Fresnel lenses as the primary optical stage resulting in a geometrical concentration ratio of $5831 \times$. The system was designed with a high capability of adjustment to allow a high degree of alignments and different optic size associations. Three secondary optics were prepared, two of which are low-iron glass coated by Aluminium reflective film and ReflecTech® Polymer, and the third is ordered Pilkington Optimirror. The system design components were purchased or produced through laser cutting. The assembly of the system was completed in-house. The UHCPV system needs to be operated by a sun tracker to conduct outdoor testing. The sun tracker was selected and purchased based on its tracking accuracy and operating capacity: payload, torque, and windage impact limit. In SOLIDWORKS software, both the windage and static loads were predicated on establishing the system working limitations associated with the selected sun tracker. Afterwards, the system was performed outdoor on a clear

sunny day during the summertime of 2021. A MJSC Azur Space 3C44- $5.5 \times 5.5 \text{ mm}^2$ was examined to compromise the electrical results optically.

1.3 Contribution of the Papers to the Research Field

- A comprehensive dissemination of the solar concentrators highlighting the potentials of different system configurations with increasing concentration ratio.
- Developing a complete workflow procedure for conducting optical-thermal analysis for UHCPV system design.
- Experimentally confirmed the concept of graphene as a pre-illumination cooling mechanism in a CPV system.
- Design aspects and prototyping approach employing multiple degrees of adjustment for high accuracy UHCPV system performance.
- Understanding and demonstrating characteristics of incorporating UHCPV system into a sun tracker for outdoor performance.
- Experimentally validating the performance of the compact UHCPV and potentials of using different secondary optical materials stage and 4-domed tertiary optic.

1.4 Outline of the Thesis

Chapter 1 states the thesis introduction, the aims and objectives of the research, the research methodology, and the outline of the thesis.

Chapter 2 introduces the advances and limitations of the CPVT system with increasing the concentration ratio. The literature review highlights the influence of the temperature with an increasing concentration ratio on CPVT components in terms of single /multi-junction semiconductor materials, primary and secondary optical concentrator materials, and thermal receiver design, from article 1.

Chapter 3 adds to the previous chapter with an understanding of the resultant temperature due to the increase in the concentration ratio. To do so, an initial numerical model was developed to determine the limits of passive cooling systems and establish when an active cooling system is needed based on the recommended operating temperature of the solar cell. Flat-plate and micro-finned heatsink configurations are thermally presented, as in article 2.

Chapter 4 demonstrates the performance of the primary optical component toward the UHCPV system. SOG Fresnel assessment is presented all through theoretical and experimental characterisation, as in article 6. The flawed SOG Fresnel lens's performance is shown to highlight its durability in a CPV unit, as in article 3. The Fresnel lens is further illustrated numerically to predicate its optical-thermal performance and establish an accurate model to extend the numerical studies by incorporating the subsequent optic to form the UHCPV system, as in article 7.

Chapter 5 illustrates the ability of the graphene based pre-illumination cooling approach in a CPV system operated by an SOG Fresnel lens. Chemical, optical, electrical and thermal characterisations are detailed, as in article 4. Further, the investigation of thermal stress arising in a Graphene ND Filter for a CPV system is explained with more time and different orientations, as in article 5.

Chapter 6 shows the theoretical optical prediction for $\frac{1}{4}$ UHCPV system with different secondary optical materials and solar cell areas, as in article 6. Also, the optical and thermal performance are illustrated simulatively for $\frac{1}{4}$ UHCPV by extending the developed model in chapter 3, as in article 8.

Chapter 7 demonstrates the mechanical system design and the associated equipment and mechanical items needed for outdoor experimentation. The

simulation of the static load and windage impact is also presented. This chapter performs all the conducted designs and simulations using SOLIDWORKS software, as in article 9. The outdoor optical performance of the designed UHCPV system is shown with details, as in article 10. This chapter also represents the first UHCPV compact design tested outdoor with having the highest geometrical and effective concentration ratio in the literature to the best of the author's knowledge.

Chapter 8 concludes the chapters and gives recommendations for future work.

CHAPTER 2: Advances and Limitations of the CPVT System – Literature Review

2.1 Introduction

CPVT systems are the combination of CPV system and photovoltaic thermal (PVT) systems. A CPV system concentrates the sun's rays onto a PV cell to generate electricity. A CPVT system concentrates the sun's rays into a fluid to transfer heat either directly or indirectly and to generate electricity. CPV systems aim to replace the large number of expensive flat PV cells due to its low solar energy density, with inexpensive optical concentrators that concentrate light into fewer PV receivers. However, increasing the solar energy density raises the PV cell temperature and results in increased heat dissipation. High PV cell temperatures impact the designed operating condition of the PV and cause losses in the solar radiation absorbed. Thus, passive or active cooling is needed to maintain the temperature of the PV cell to ensure the highest efficiency. However, cooling down the PV cell temperature causes a parasitic load and this parasitic load increases with the increase of the concentration of solar radiation. PVT systems aim to extract the generated heat and then employ it in the end-use application, such as domestic hot water or space heating. However, PVT systems need to use a large number of PV receivers to produce high-quality thermal energy, which result in high investment costs. Also, the low temperature of the thermal energy limits the possible number of end-use applications.

The drawbacks of both CPV and PVT are resolved in CPVT. CPVT systems generate both electrical and thermal energies. Since the cell temperature levels are moderate, high-temperature thermal energy can be extracted and utilized in a vast number of applications. CPVTs operate by concentrating the light rays in a minimal area, which results in a smaller number of PV cells. However, the high concentration in CPVT might result in increased optical losses (e.g. chromatic

aberration for lenses), illumination and temperature non-uniformity, and PV overheating. CPVT of more than > 10 suns (medium and upwards concentration) benefits only from direct solar radiation, not diffuse radiation. The flowchart of the working concept for the CPVT system, including a summary of its limitations, is demonstrated in Figure 1.

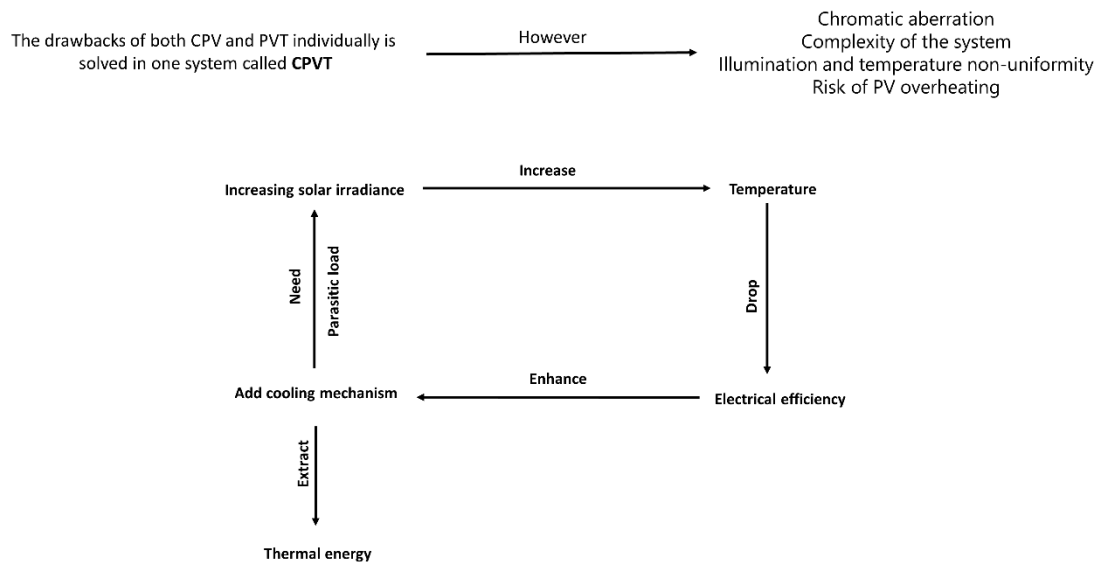


Figure 1 Working flow of CPVT system with summarized limitations

The primary component to operate the CPVT system thermally and electrically is the optical performance. Concentrators utilize either imaging or non-imaging optics to intensify the solar density in either one or multiple optical stages into either a focal line or focal point where electrical and/or thermal energy are captured. The optical performance is dependent on the amount of sunlight incident on the PV cell on the basis of suns, where 1 sun is equivalent to 1000 W/m^2 [1]. Based on the number of concentrated suns, a CPVT system is classified depending on the optical concentration ratio (CR_I), which is the irradiance ratio between the primary optical stage and the receiver. CR_I is classified as low ($CR_I < 10 \text{ sun}$), medium ($10 \text{ sun} < CR_I \leq 100 \text{ sun}$), high

($100 \text{ sun} < CR_I \leq 2000 \text{ sun}$) or UH ($CR_I > 2000 \text{ sun}$) [2]. Increasing the CR_I results in high thermal and electrical energies; however, a high level of CR_I adds to the complexity of the CPVT system, such as the tracking system (acceptance and incident angles) and irradiance non-uniformity on the PV cell.

Different review articles on PVT technology, CPV technology, and CPVT technology can already be found in the literature [3–10]. Sharaf and Orhan [11,12] have primarily focused on CPVT systems in two reviews covering the considerable number of publications on CPVTs systems. Their two publications examined and reviewed the basics and progress in CPVTs, with an exhaustive coverage of all CPVT technology. Daneshazarian et al. [13] reviewed CPVT systems with an emphasis on the fundamentals, operating concept, and system configurations, with the testing results for domestic and industrial applications. Another article by Mojiri et al. [14] provided a review of spectral beam decomposition technologies to evaluate the potential for using this mechanism for solar systems, discussing PVT/CPVT systems, whereas Ju et al. [15] reviewed particularly spectral beam splitting technologies for CPVT systems in a systematic and thorough analysis. However, to the best of the author's knowledge, there has not yet been any review dedicated mainly to assessing the influence of the temperature on the CPVT system components with increase of the concentration ratio.

As in article 1, this literature review therefore aims to investigate the effect of the temperature when increasing the concentration ratio on the CPVT components: solar cell, optics, and thermal receiver design, as shown in Figure 2(a) and (b). An explanation of the electrical considerations for single- and multi-junction semiconductor materials is given to help understand the influence of the temperature and concentration ratio. One objective of this review is to determine

the impact of the temperature in a large number of studies on the semiconductor materials and primary/secondary optics with an increasing concentration ratio in CPVT systems, as well as techniques for thermal management. Only experimental studies that gave all the system details and performance results are reported in order to gain a realistic assessment of achievable performance.

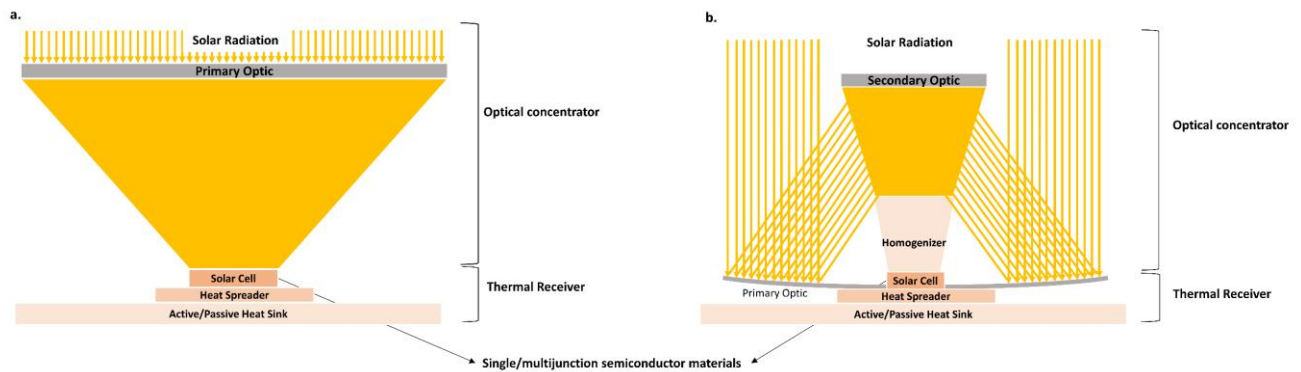


Figure 2.(a) A basic Fresnel lens and (b) a basic Cassegrain CPVT system configuration for the three components of primary /secondary optics, single-/multi-junction solar cell, and thermal receiver.

2.2 The State of Arts and Challenges of CPV systems

CPVs are in demand to progress regarding the system architecture and the optical materials in order to catch up with the efficiency achieved by multijunction solar cells. The common design approach is to build a system with a higher geometric concentration factor, allowing for more losses while still operating with a high effective concentration ratio. The CPV system advances are accomplished optically through incorporating a set of successive optics in one design toward a higher optical concentration ratio. These CPV systems intend to operate the multijunction solar cell with high cell efficiency, which has reached 47.1% experimentally [16]. The cost of multijunction solar cells is the dominant component, and the principle of CPV is to compensate for the price of PV

materials with standard inexpensive optics [17]. However, the flat silicon PV panel prices are decreasing in a race faster than in any other solar system [18].

Operating a CPV system is not just like operating a flat PV panel by just setting a PV panel on a mounting system by considering the optimal elevation and azimuth angles. CPV systems must be aligned with a high tracking accuracy to ensure the concentrated rays are directed to the receiver. While laborious for highly concentrated systems, it is vital to be aligned to the direct normal irradiance (DNI) [19]. To align the CPV system to the DNI, the CPV system needs to be incorporated with a sun tracker, where the need for an accurate sun tracker relies on the level of concentration ratio [20]. An associated mechanical component is needed to couple the CPV system with the sun tracker and a counterbalance weight to assure moment equilibrium. The overall cost to establish a CPV system is higher than having a flat PV system, and the cost associated with the systems and instruments to safely operate a CPV system increase as well the levelised cost of electricity (LCOE). The analogy of the CPV system being more area efficient than a flat PV system is a fact through less land utilisation; however, this analogy is not financially feasible for some countries where prices of renting or purchasing land are very low, which encourages the installation of flat PV panel [21].

Although optics with a better surface smoothness helps to minimise the ray scattering, the prices of state-of-art optics, which offer excellent optical efficiency, are still very high. As a succession of optics concentrates light, the heat accumulation gradually increases as light reflects/refracts in the subsequent optics to the primary stage [22–24]. Therefore, the thermal impact needs to be carefully observed and considered to ensure safe operating conditions for optics. Undoubtedly, the resultant heat out of concentrated solar irradiance confirms the

requirements of passive or active cooling arrangements at the receiver stage. However, the optics need to be functional at a relatively excellent temperature range to avoid dilation or dependency between optical performance and temperature. Similarly, the temperature of a flat PV panel is reported to reach between 55 – 65 °C, implying the need for a cooling mechanism; however, the quality of thermal energy is low because of low outlet temperature.

Although the pre-illumination cooling - spectral decomposition techniques are not experimentally mature, the employment of optical filters to either transmit or reflect one portion of the optical spectrum (wavelength range) is an excellent solution to cool down receivers [23,25]. Working out the compatibility between the optical spectrum of a filter and the solar cell spectral response would help to minimise the generated heat on the solar cell due to the maximum solar cell acceptance of input energy. The employment of optical filters in the CPV will be a game-changer for pushing further the efficiencies of the optical systems and, similarly, the solar cell conversion efficiency.

2.3 Electrical and Thermal Considerations for CPVT System

A PV cell converts electromagnetic radiation into electrical energy via the p-n junction. The electron absorbs the photon energy in the valence band (n-type semiconductor), and then the absorbed energy stimulates the electron to move to the conduction band (p-type semiconductor). This electron movement creates a hole in the valence band, allowing the free flow of the electron throughout the semiconductor. The PV cell electrical output is challenged by its bandgap energy, in which the photon energy must be greater than the energy of the bandgap to induce photogeneration of the charge carrier (electron and hole). The bandgap energy is the energy separating the valence band from the conduction band. Photon energy that is not compatible with the bandgap energy generates intrinsic

losses which can be grouped as thermalization, below bandgap, Boltzmann, Carnot, and emission losses. These intrinsic losses are associated with the limiting of the electrical performance in the form of current and voltage reductions [26]. Below bandgap and emission losses result in current reduction due to the smaller number of charge carriers. In contrast, thermalization, Carnot, and Boltzmann losses result in voltage reduction due to the smaller energy utilization of the charge carrier [27].

The I-V curve of a cell is influenced by both solar irradiance and temperature. The short-circuit current (I_{sc}) is dependent on its performance on the solar irradiance where I_{sc} and the solar irradiance have a proportional relationship, as in Figure 3(a). On the other hand, the open-circuit voltage (V_{oc}) has an inverse correlation with temperature, as in Figure 3(b). The effect of solar irradiance on V_{oc} and the temperature on I_{sc} is minimal. The excellent squareness of the I-V curve (the ratio between the maximum power point (MPP) and the product of V_{oc} and I_{sc} solar cell products) indicates a high Fill Factor (FF) which can be observed at low temperatures or relatively high temperatures but by employing the MJSC. In terms of high temperature, the squareness of the I-V curve is flattened, at which the FF value is low, reflecting a poor quality of PV cell electrical output, especially for a single-junction solar cell. As the concentration ratio is increased, the electrical parameters of the solar cell V_{oc} , I_{sc} , FF and efficiency (η) alter; thus, their sensitivity to temperature also changes.

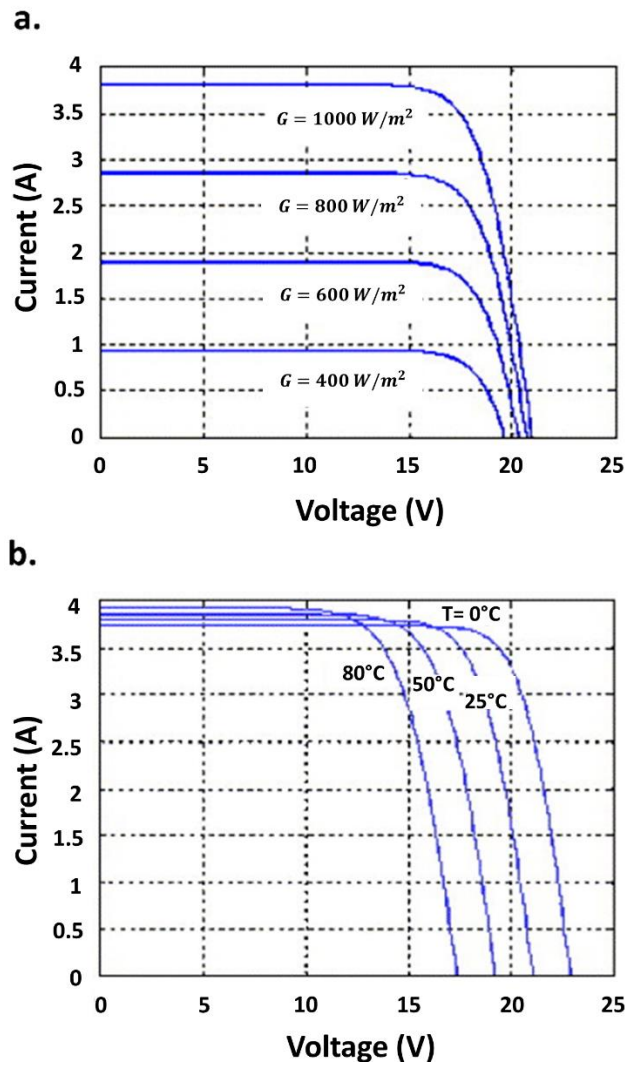


Figure 3 Effect of (a) solar irradiance and (b) cell temperature on I-V curve of a single-junction PV cell [18].

A multijunction PV (MJPV) cell allows sorting of the photon energy by adding more than one junction with different bandgap energy to maximize the efficiency of the PV cell and hence the power output [11][12]. The MJPV cell is stacked in series, where V_{oc} is the sum of all the subcells' V_{oc} . The temperature coefficient $\Delta V_{oc}/\Delta T$ of the multi-junction is also the sum of the $\Delta V_{oc}/\Delta T$ [28]. The temperature coefficient $\Delta V_{oc}/\Delta T$ of the multi-junction faces a drop in V_{oc} when the number of junctions increases due to the low bandgap energy required for the last subcell. However, increasing the solar irradiance reduces the temperature coefficient drop due to an increase in the V_{oc} . The current in the stacked series needs to be

matched to avoid losses [28]. Since the temperature coefficient is not equal from the bottom, medial, to top-subcells, the current will be different in each subcell, causing “current mismatch”. When the tandem-subcell temperature increases, the bandgap, decreases this results in the increase of the I_{sc} . The top subcell bandgap is also decreased, allowing fewer photons to reach the bottom subcell, and this minimizes the I_{sc} with temperature. Additionally, the current output at every subcell has a limitation and this influences the FF of the MJPV cell. Aiken et al. [15] conducted a temperature coefficient study of the integrated current for a triple-junction cell InGaP/InGaAs/Ge at a temperature range from 5 °C to 100 °C. The result indicated that I_{sc} has a current mismatch of only 3.3% at 100 °C. Thus, a solar cell is negligibly sensitive to temperature in terms of current mismatching. Solar cell efficiency and bandgap energy are the two main factors for solar cell selection. The maximum efficiency of single-junction solar cells is described by the Shockley–Queisser limit, where all the photons above the bandgap are absorbed, and this limits the maximum conversion efficiency to 33.7% [29]. The bandgap energy differs according to the energy-band structure of the semiconductor materials. The theoretical maximum efficiency for different single-junction solar cell materials, with their bandgap energy designed as either wafer-based or thin film, is demonstrated in Figure 4 [30,31].

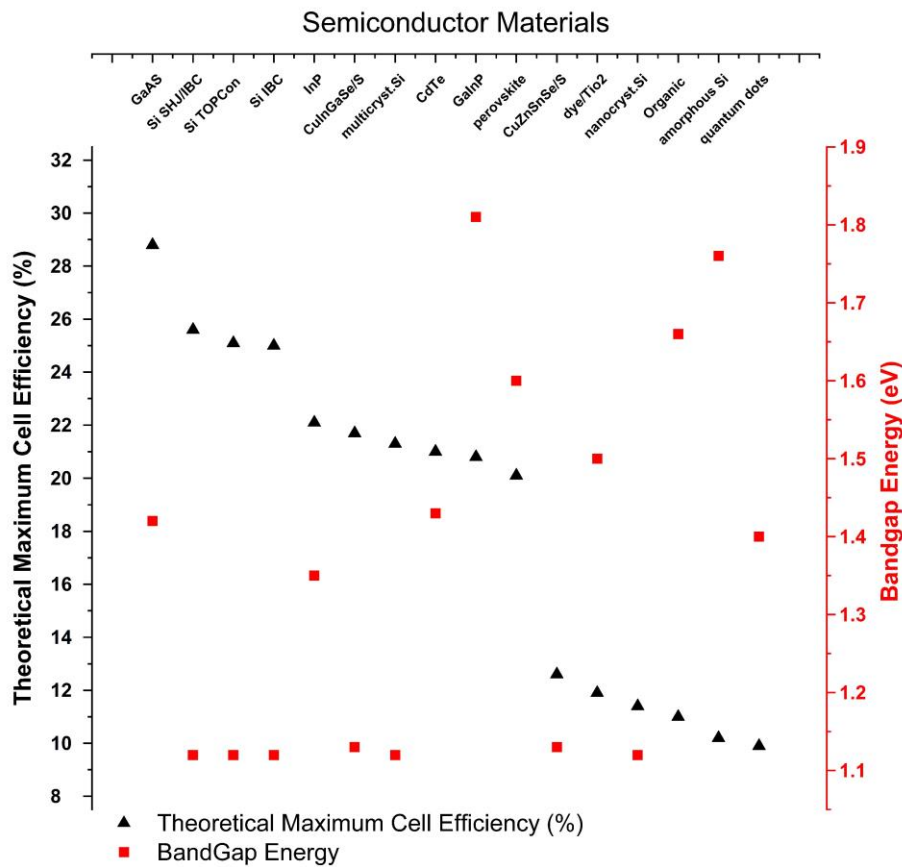


Figure 4. Different semiconductor materials (thin-film and wafer-based) bandgap energy, maximum efficiency, all under 1 sun concentration ratio. The theoretical maximum cell efficiency is measured for terrestrial application under AM 1.5.

Increasing the number of junctions reduces the thermalization to below the bandgap losses, and this increases the conversion efficiency of the solar cell [27]. A MJSC has the capability to absorb a wide range of solar wavelengths due to the different bandgap energy for the individual subcells in one monolithic junction solar cell. The limiting efficiency is illustrated in Figure 5 for several non-toxic and abundant cell materials made of 1 to 8 junctions for the ideal bandgap. The maximum efficiency of an infinite number of junctions with an optimized bandgap for a blackbody spectrum at 6000 K under concentration is 86.8% at AM 1.5 [32,33]; however, current electrical fabrication techniques have only been

optimized for up to 5 junctions. Introducing new MJPV cell architectures with different numbers of subcells should not result in any new form of loss or increase the price of electrical fabrication. However, other costs are likely to rise due to the use of rarer and more expensive materials for the multiple layers.

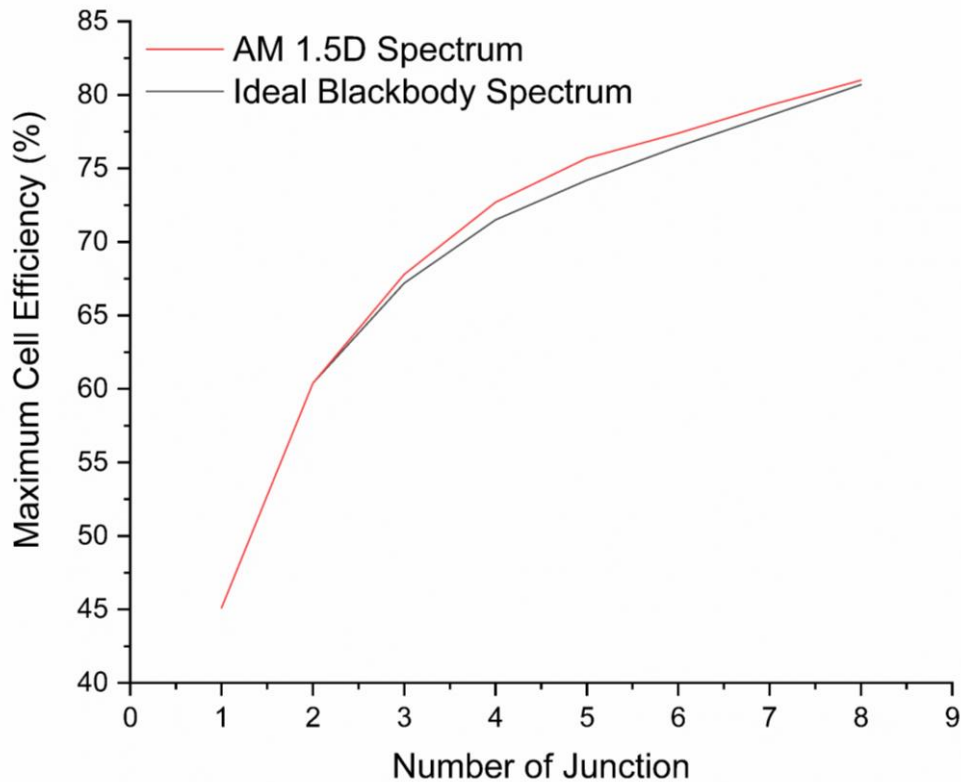


Figure 5. The limiting efficiency for ideal bandgap energy under no concentration for solar cell use. The solar cells' efficiencies were calculated based on an ideal blackbody spectrum (black line) and the AM 1.5D spectrum (red line) for various semiconductor material configurations.

2.4 CPVT System: Cells, Optics, and Receivers

2.4.1 Semiconductor Materials: Temperature and Efficiencies

Due to the bandgap energy, the unabsorbed photon energy on the solar cell surface is converted to thermal energy, increasing the cell temperature. Moreover, concentrating solar radiation onto a PV cell and solar irradiance non-uniformity also increase the cell temperature and hence reduce the cell efficiency.

Other efficiency losses also occur in the PV cell due to poor absorption of photons, such as reflectance loss in the inner and outer layers and shading loss due to the contact grid on the front side of the PV cell. Elevated cell temperatures accelerate cell degradation, thus minimizing their lifetime. To ensure the maximum possible lifetime and an adequate cell efficiency, the cell should be maintained at the typical operating temperature of 80 °C at different ranges of concentration ratio [34].

A large number of semiconductor materials used in different theoretical and experimental studies of solar concentrator systems are shown in Figure 6 with each material's respective concentration range. Clearly, gallium arsenide (GaAs) semiconductor material in one-, two- or three-junction configurations can accept a wide range of concentration ratios due to its low temperature sensitivity, high resistivity to radiation damage, and good performance under concentrated illumination.

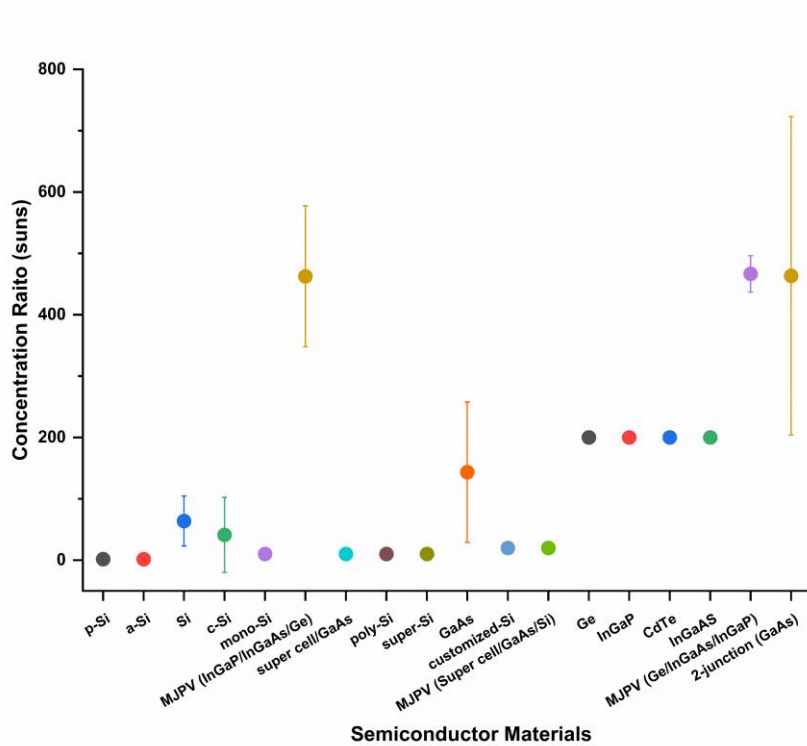


Figure 6. Semiconductor materials and their concentration ratio in theoretical and experimental studies considered by this review with interval bars which show the range of concentration ratios tested in the literature [12,35].

As outlined in Figure 7, the bandgap of the semiconductor material, the concentration ratio, and thermal properties should be taken into consideration in relation to each other in selecting the PV cell material to avoid operating at a high temperature. PV cell materials are dependent on the cell temperature under concentrated illumination. Thus, the bandgap energy of a PV cell should be selected in accordance with the concentration ratio to enhance the electrical and thermal performance.

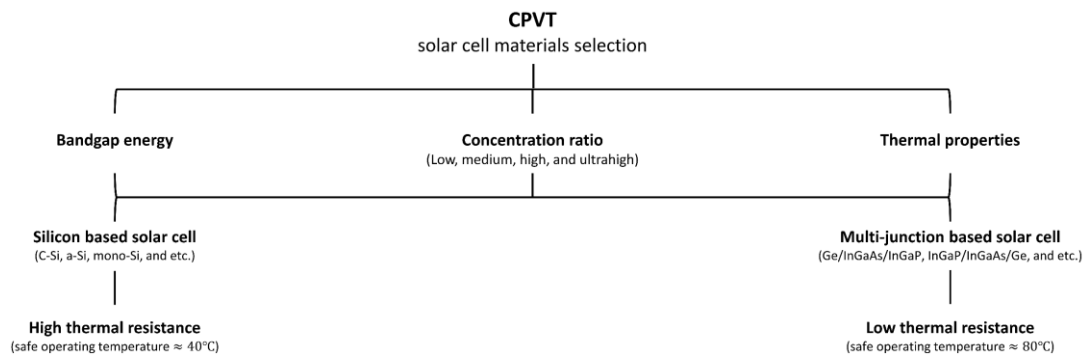


Figure 7. Factor considerations in the selection of the solar cell materials in a CPVT system.

2.4.2 Concentrators: Temperature and Efficiencies

The optical tolerance of a CPVT system is a critical factor, especially with increasing concentration ratio and taking into consideration the sunlight divergence angle of ± 0.265 . The divergence angle of the sunlight implies an equally small acceptance angle, which should be enough to capture the solar radiation emitted from the sun. However, the impact of other factors, such as tracking error, thermomechanical effects, dynamic load, and materials properties, must also be considered [36]. The acceptance angle indicates the required tracking system sensitivity, where the light divergence should be minimized to allow for a high concentration ratio. Strategies to minimise the light divergence include the use of large primary optics, secondary optics, highly accurate continuous tracking systems and highly smooth surfaces. The latter two of which are expensive and difficult to acquire. Adding a secondary optic such as a homogenizer or light funnel into the CPVT design improves the acceptance angle and uniformity of the illumination profile of the system, which reduces the demand on the system accuracy. However, the materials of the secondary optics should be carefully selected to withstand the high temperature. In addition, maximising the size of the primary optics adds to the overall cost of the initial system. The

advances and limitations of CPVT optics in terms of increasing the concentration ratio are summarised in Figure 8.

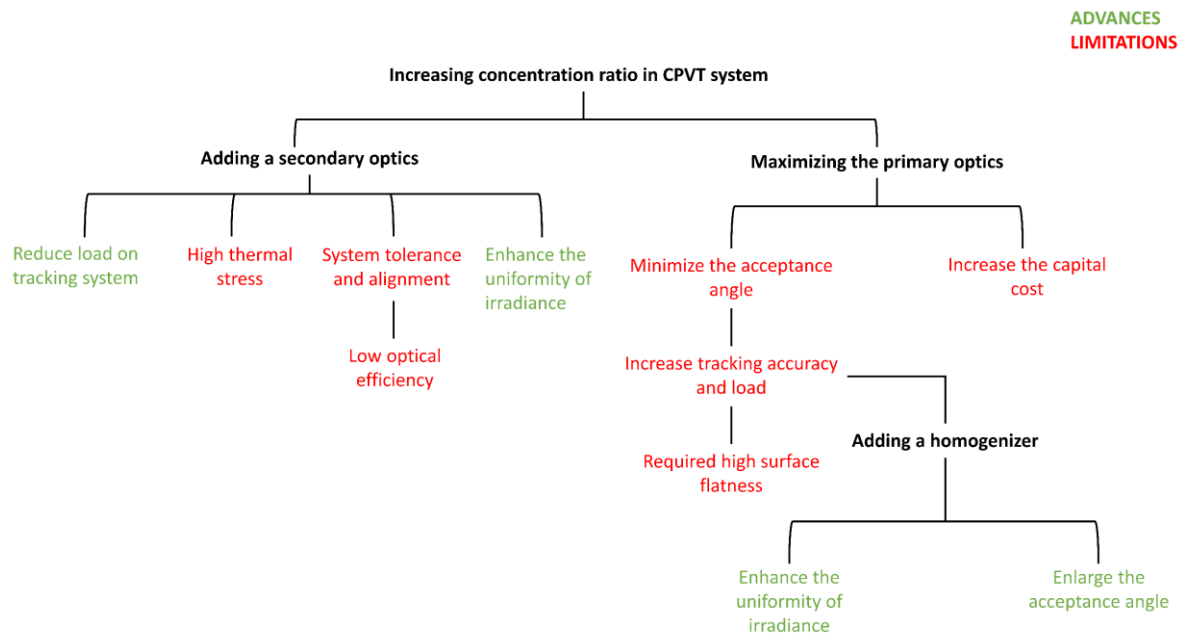


Figure 8. Summary of advances and limitations in the optical concept for increasing the concentration ratio.

The optical efficiency of a solar concentrator is dependent on the incident angle, where the maximum performance is typically achieved at normal incidence (90°) to the sun (the zenith angle is equal to the system tilt angle). This is when there is the least scattering and absorption within the system, according to the optical properties of the concentrator materials, and where the solar radiation is highly reflected/refracted from the concentrator components. The graph of a low concentration of 3.6 *suns* crossed compound parabolic concentrator shows a drastic drop in optical efficiency at a 35° incident angle (beyond the acceptance angle) [37], as shown in Figure 9(a). In contrast, the ultrahigh concentration ratio based on the Fresnel lens producing 5247 *suns* shows a drop of 90% in the optical efficiency at incidence angles of $> 0.4^\circ$, which confirms the dependency

of the optical efficiency on the incident angle and demonstrates the reduction in the required acceptance angle by increasing the concentration ratio beyond 100 suns [38,39], as in Figure 9(b).

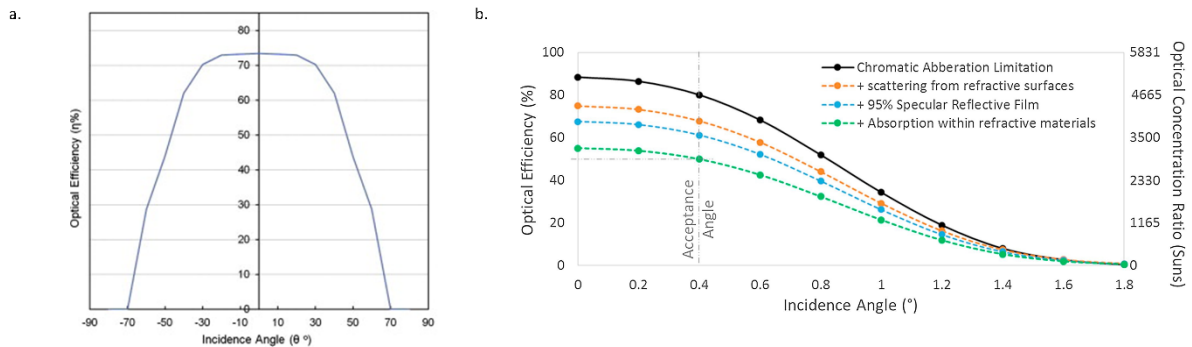


Figure 9. Optical efficiency vs incidence angle: (a) optical efficiency in CPC for low concentration ratio in building application; (b) optical efficiency in high concentration photovoltaic design based on Fresnel lens [37,38].

The mechanisms of concentrating the solar radiation are reflective, refractive, luminescent, total internal reflection, or a combination of these. Optical concentrators employ multiple stages to increase the acceptance and/or the concentration ratio. Boosting the concentration ratio is achieved at the price of different configurations of CPVT systems. The ranges of concentration ratio and working fluid temperatures for different CPVT systems theoretically and experimentally investigated are illustrated in Figure 10.

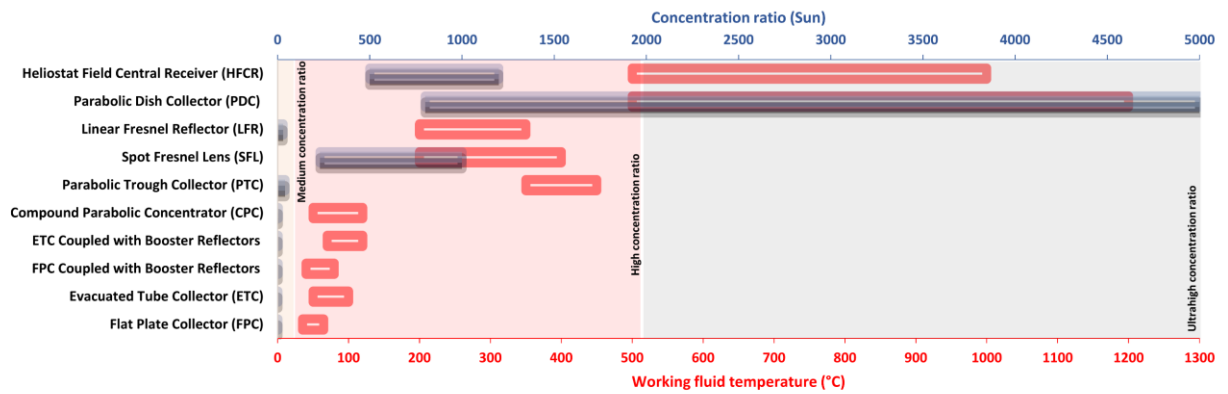


Figure 10. CPVT systems with the concentration ratio ranges and working fluid temperature ranges as reported in [11,13].

2.4.3 Thermal Receiver Design and Materials

The process of thermally managing the heat in a CPVT system relies on the concept of pre-illumination and post-illumination heat extraction utilizing a heat transfer fluid (HTF). Pre-illumination design is based on the concept of spectral decomposition, allowing a higher outlet temperature by redirecting all the unutilized spectral wavelength to a thermal receiver [14,15]. However, the difficulty of matching the optical properties with either the HTF or the filters means that pre-illumination design is less mature than post-illumination design. Post-illumination design harvests the heat after reaching the solar cell. However, the outlet HTF temperature is limited to the cell's maximum recommended operating condition in the range of 50–80 °C.

The thermal performance of the PV cell primarily relies on the heat spreader and the accompanying different layers of the materials employed. The heat spreader is located between the PV cell (heat source) and the cooling mechanism to conduct heat for thermal utilization according to the temperature range or dissipation rate. The most common heat spreaders in CPVT systems are direct bonded copper (DBC) and insulated metal substrates (IMS) due to their excellent thermophysical properties [40–42]. However, silicon wafer substrates have

shown a high potential as heat spreaders due to their thermal expansion compatibility with silicon semiconductor materials [43]. The heat spreader materials need to have a high thermal conductivity and high electrical insulation, where doubling the thermal conductivity of the heat spreader enhances the thermal efficiency by 13.5% [44]. In addition, increasing the contact factor between different layers using thermal paste results in conducting much of the heat to the thermal collector, reducing in this way the cell efficiency by just $-0.0043\%/^{\circ}\text{C}$, whereas without thermal paste the result is $-0.0094\%/^{\circ}\text{C}$ [45]. High resistance silica gel is widely used in CPVT systems as electrical insulators, having high thermal conductivity [46–48].

Cooling mechanisms (post-illumination) for the PV cell may be passive or active. Passive cooling in point focus systems has been proven to successfully manage the PV cell temperature with different heatsink geometries and for high concentration ratios for up to 2000 *suns* [45,49]. For UH concentration ratios, solar cells of 1 mm^2 or smaller can maintain the cell temperature below the maximum recommended operating temperature with a conventional flat-plate heatsink up to 10,000 *suns* [50]. In passive cooling, the heat dissipation is attributed to the cell area, where the heat is generated. Thus, maximizing the area of the heatsink by exploring different geometry configurations would maximize the heat dissipation rate. For the heatsink material, silicon has shown the lowest thermal stress and the maximum heat transfer in comparison with aluminium and copper [43]. In $> 2000\text{ suns}$, the weight of the heatsink should be considered to reduce the required dynamic load and avoid increased tracking error.

Active cooling, which ordinarily embraces forced motion for a cooling fluid, increases the overall thermal efficiency. An active cooling mechanism is widely used in systems with line focus PV cell design, where a line pipe configuration is more suitable to extract heat effectively. Pure fluid or nanofluid cooling is more suitable than air due to its high heat capacity and its potential for different end-use applications, especially with high temperature. The originality of using nanoparticles with the fluid is to enhance the thermal conductivity, in this way boosting the heat transfer between the receiver and the fluid. However, increasing the temperature of the nanoparticles has a major influence on improving the thermal conductivity [51–55]. The parasitic power for a fan or pump increases with the fluid flow rate. Naturally, this would be higher for higher concentration ratio where more heat dissipation/extraction is needed.

2.4.4 Linear Concentrators: The Reflective Trough of Low-Medium Concentration

Most CPVT designs are linear geometry systems made of reflective materials, typically in a trough shape and capable of up to 100 *suns* (medium concentration). M. Li et al. [56] studied the electrical and thermal performance of 2 m^2 and 10 m^2 configurations for an Aluminium alloy parabolic trough at 10.27 *suns* and 20 *suns*, respectively. In the 2 m^2 system, arrays of cells using four types of semiconductor materials connected in series were mounted on the receiver using a thermally conductive tape. In the 10 m^2 configuration, the width of the receiver and the width of the aperture area were increased, resulting in an increase of concentration ratio. Water was circulated as a HTF to cool down the cell temperature.

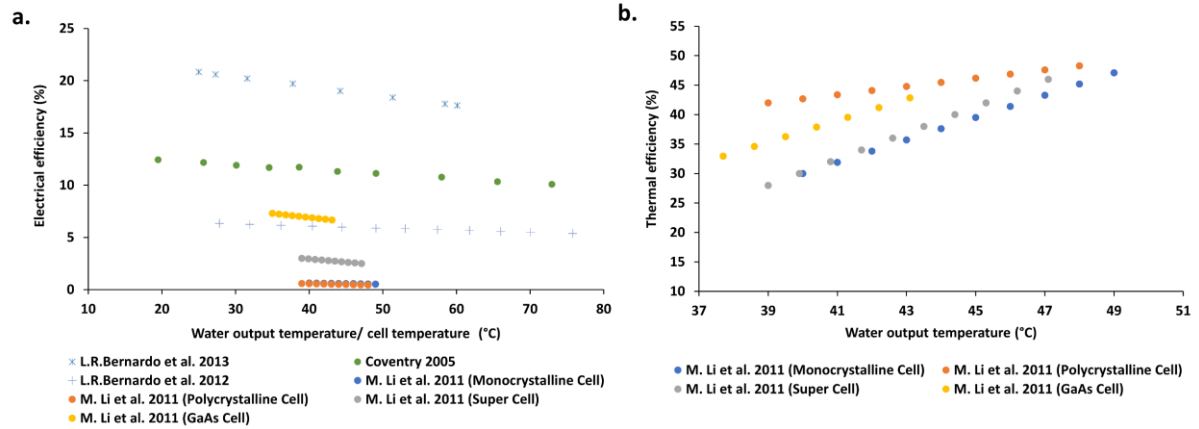


Figure 11. The water output temperature/cell temperature impact on (a) the electrical efficiency and (b) the thermal efficiency of the system in different studies [56–59].

The water output temperature can be an indication of the cell temperature, which is higher for cells with higher series resistance and hence typically reduced power outputs. The best performance of GaAs is mainly due to its lower series resistance and yet it still has a higher performance in a higher temperature environment. However, the high series resistance for mono-Si, poly-Si and super cells (made from silicon and GaAs material) indicates better thermal performance [56]. Reduction in the concentration ratio results in a decrease in the heat exchange effectiveness. Thus, the PV temperature increases due to less heat being removed, which reduces the electrical efficiency. M. Li et al. [46] demonstrate the correlation between the rise in the water output temperature and the thermal efficiency, and the reverse correlation between the water output temperature and the electrical efficiency for an aperture area of 2 m^2 , as in Figure 11(b). Kunemeyer et al. [60] investigated a V-trough concentrating model theoretically and experimentally for 1.6 suns . The concentrators were constructed from mirror-finished stainless-steel sheet to withstand the corrosive maritime

climate in New Zealand. The polished stainless-steel in [61] had a reflectivity of 0.67. However, Aluminium with 0.9 reflectivity would yield a higher solar irradiance at the absorber surface. The combined electrical and thermal efficiency peaked at 35%, even though the system was designed to achieve a peak efficiency of 70%. The drop in efficiency is due to heat loss by convection and radiation in the absence of a glazing layer, which reduced the thermal efficiency. Even with the low reflectivity, the stainless-steel sheet offered a 25% increase in the concentration ratio over a year in comparison to Aluminium. Kostic et al. [62] presented the influence of the Aluminium (Al) sheet and Aluminium foil reflectance for flat plate solar radiation concentrators. The outcomes showed that the total and diffuse reflectance of the Al sheet and Al foil concentrators are the same, whereas the specular reflectance is higher for Al foil concentrators, resulting in increasing the solar radiation intensity. The solar radiation intensity results in a daily increase of the electrical and thermal efficiency, as shown in Table 1.

Table 1 Results for solar radiation intensity, thermal energy generated, and electrical energy generated [62].

| Reflectors | Concentration ratio (<i>sun</i>) | Daily thermal energy generated (%) | Daily electrical energy generated (%) |
|-------------------|---|---|--|
| Al sheet | 1.44 | 39 | 8.6 |
| Al foil | 1.66 | 55 | 17.1 |

Although with a 10% additional cost of Al sheet and Al foil concentrators, the results demonstrated a remarkable increase in the energy efficiency of 35% and 50% for concentrators made of Al sheet and Al foil, respectively, in comparison to the system without concentrators. Nilsson et al. [63] studied the long-term performance of an asymmetric compound parabolic concentrator (CPC) built for

high altitude in Sweden. Anodized Aluminium and Aluminium-laminated steel reflectors were investigated. The Aluminium-laminated steel reflectors were the preferable option due to their improved mechanical properties which require less mechanical support. However, the steel-based reflector has a relatively low specular reflectance because its plastic coating absorbs light below 400 *nm* and silicon cells absorb from ~ 300 *nm*. The measurement of the MaReCo (Maximum Reflector Collector) in these studies showed that the front reflector collects most of the solar radiation in the summer, whereas the back reflector dominated collection in the spring and fall, as shown in Figure 12. The comparison of the electrical output results showed a 49% increase for the front collector and 23% increase for the back reflector for both materials compared with no reflector. Steel placed in the back reflector is a good option since there is no difference in the yearly output power for the two materials. For maximum utilization of the solar radiation, PV cells should be installed on both sides of the receiver. Another study showed a CPC of anodized Aluminium with 95% solar reflection resulting in 1.5 *suns*. The study demonstrated that the PV cell can still reach a high temperature even with a low concentration ratio, where the electrical efficiency was measured to be 20.9% at 25 °C [57]. The dependency of the electrical efficiency on the cell temperature is $-0.4\%/K$, as illustrated in Figure 11(a) [57]. The temperature of the outlet water was measured to show the impact of the temperature on the electrical efficiency.

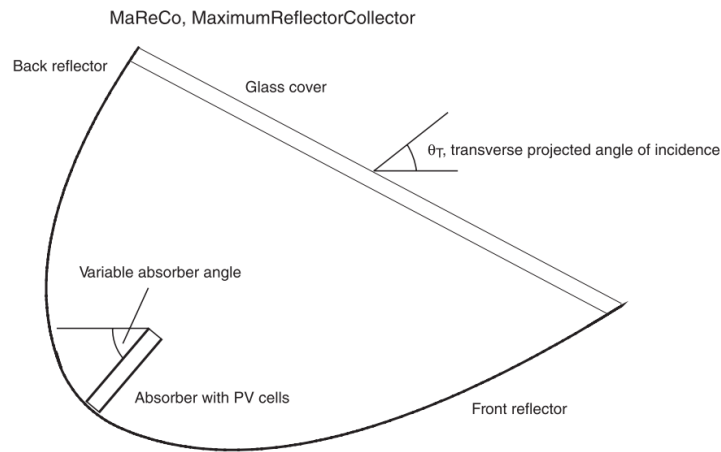


Figure 12. MaReCo (maximum reflector collector) PV-thermal hybrid has the same focal line for both parabolic reflectors. The glass cover is tilted at a 30° angle between the absorber and the horizontal. Also shown is the transverse projected angle of incidence [63].

Coventry [58] investigated a parabolic trough collector with a concentration ratio of 35 *suns*. The collector consists of a glass-on-metal mirror that focuses illumination into a mono-crystalline silicon solar cell for electricity and thermal generation. The electrical and thermal efficiency was measured to be 11% and 58% at standard operating condition (ambient temperature of 25°C and direct radiation of 1000 W/m^2), respectively. Also, the impact of non-uniform illumination on the PV cell was investigated. The illumination along the length of the trough showed a remarkable variation due to the mirror shape, the gap between mirrors, and shading by the receiver support. This investigation included measurement for the non-uniform illumination for 30 *suns* and 90 *suns* for the entire and the middle third of the cell surface. A reduction in open circuit voltage of 6.5 mV results in an electrical efficiency drop of 20.6% for uniform illumination and of 19.4% for centralized illumination, as shown in Figure 13. Consequently, non-uniform illumination causes a locally overheated spot on the PV cell area, which might result in reducing the cell lifetime, although this has still not yet been

experimentally investigated. The magnitude of the voltage drops due to the locally overheated spot is significant.

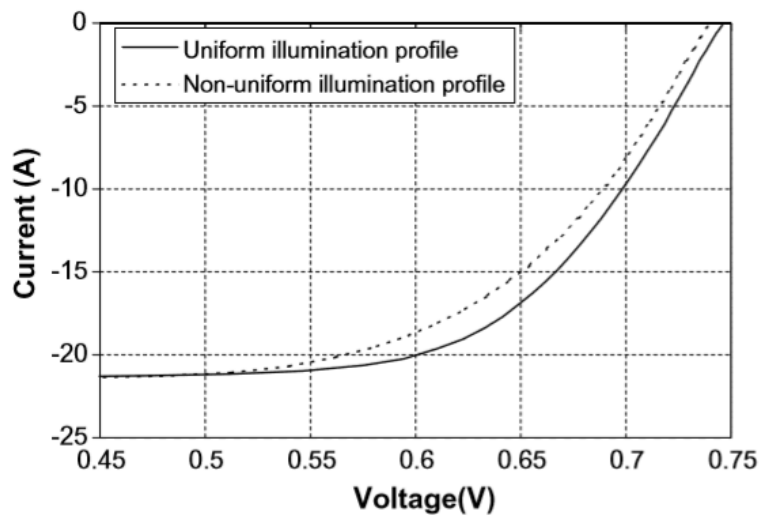


Figure 13. I-V curve for uniform illumination over the whole cell area (30 suns) and non-uniform illumination on the middle third of the cell (90 suns) [58].

The dependency of the electrical efficiency on the cell temperature is $-0.35\%/^{\circ}\text{C}$, as shown in Figure 11(a) [52]. Tripanagnostopoulos et al. [64] determined the optimum operation of the hybrid system for a pc-Si module with different scenarios of additional glazing (glass sheet), a booster reflector (Aluminium sheet), or both, aiming to maximize the total energy output with a circulating fluid (air/water). The additional glazing is intended to increase the thermal output of the system to about 30%, but this led to high optical losses, reducing the electrical efficiency by 16%. The drop in electrical efficiency is balanced by the integration of the diffuse booster reflector, increasing the electrical and thermal efficiencies by about 16% and 45%, respectively. The Aluminium sheet results in increasing the solar radiation by 50%; thus, the electrical efficiency increased from 25% to 35% at PV temperatures varying between 40–70 °C. Also, the electrical efficiency was measured for the uninsulated and insulated back surface to be 13.3% and 3.3%, respectively. With the insulated back surface, less convection and radiation

raised the cell temperature to 55 °C; however, for the uninsulated back surface, the PV cell temperature is 43 °C. Bernardo et al. [59] evaluated the performance of a parabolic trough at a low concentration ratio of 7.8 *suns*. The selected optical material was silver-coated plastic film laminated on a steel sheet with a reflectance factor of 90% and a cover glass with a transmittance of 90%. The electrical efficiency was measured to be 6.7% at 25 °C. The electrical and thermal dependency on the water outlet temperature is illustrated in Figure 11(a) [59], representing the electrical efficiency calculated as a function of working temperature at beam irradiation higher than 900 W/m^2 .

Xu et al. [65] studied a low concentrator parabolic collector of 2.44 *suns* coupled with a refrigeration cycle. The output electrical efficiency was 17.5% with mirror-finished Aluminium sheet optical concentrators whose total reflectance was 88%. The condenser was capable of raising the water temperature from 30 °C to 70 °C. Davidsson et al. [66] utilized a building-integrated multifunctional PVT solar window where the reflectors were anodized Aluminium with antireflective low-iron glazing. The antireflective material increased the transmittance by about 5% in [67] to achieve a concentration ratio of 1.33 *suns*. Anodized Aluminium [57,59,66,68–70] as an optical material is highly desirable for optical concentrators in parabolic trough systems due to its high reflectance. Aluminium reflects well for 200–400 *nm* ultraviolet and 3000–10000 *nm* infrared [71]. However, Aluminium [72] has a lower reflectance in the visible region between 700–3000 *nm* near-infrared compared to copper, gold and silver. Since Aluminium reacts with air to create an oxidization layer, anodization as a common electrochemical process is needed to grow a protective oxide film on the Aluminium metal surface to improve protection and durability.

For refractive materials, PMMA (methyl methacrylate) [48,68,73] is the dominant material used most commonly in Fresnel lens systems due to its high transparency and excellent stability in different weather conditions up to 85 °C [74]. Spectral colour dispersion in a PMMA Fresnel lens system relies on the refractive index of the lens materials in the range of 1.515 to 1.470 between blue and red light. The dependence of the refractive index on the temperature, humidity and incident angle is minimal for PMMA Fresnel lens materials. For low and medium concentration ratios, a trough-based CPVT system is commonly a linear-focal design with reflective materials, whereas refractive lenses are utilized more in the point source system and secondary optics to achieve a high concentration ratio.

2.4.5 High Concentration Point-Source Concentrators and Their Secondary Optics' Performance

In a high concentration photovoltaic system, the optical materials and optical tolerance need to be carefully investigated throughout design. Secondary optics are introduced to bring the concentration to the required value and reduce demand on the system accuracy. The integration of a homogenizer in the optical configuration allows the system to minimize the non-uniformity of the solar irradiance and increase the acceptance angle. However, thermo-mechanical stresses as a result of non-uniformity could damage the optical materials. Thus, the secondary optics and homogenizer materials need to be thermally stable and durable, with low thermal expansion coefficients and high working temperatures. Al Siyabi et al. [75] investigated the effects on one unit of a $10 \times 10 \text{ mm}^2$ concentrator prototype producing 200 *suns* of concentration ratio on K9 glass using crystal resin homogenizers which were refractive truncated pyramid designs (RTP-homogenizer). The in-house test showed that the K9 glass

homogenizer was 20% more optically efficient than the crystal resin counterpart, although this translated into only a 5% improvement in the electrical efficiency when comparing the K9 glass homogenizer to the crystal resin homogenizer. However, both improved the electrical performance of the CPV system by 27% and 23% respectively in comparison to the system without secondary optics. Also, this study reported the degradation on the top surface of the crystal resin homogenizer, which starts melting at a high concentration ratio.

An elevated temperature on the optical materials stimulates their thermal expansion and thereby decreases their reflectivity and can change the shape of the optics, which is one of the causes of illumination non-uniformity. Sarwar et al. [76] studied the effect of temperature and solar irradiance on the thermal performance and optical properties on unpolished 304/304L stainless-steel using a sun simulator. The material was tested under five different levels of uniform illumination ranging between 579.3 kW/m^2 and 917.1 kW/m^2 for 17 and 50 minutes, respectively. The results showed that the material's thermal performance decreases with increase of the solar irradiance. However, the drop in the thermal performance is dependent on the material temperature. When the material temperature dropped by 159 K the thermal performance fell to 21%, and when the material temperature dropped by 22 K the thermal performance declined to 6.7%. Also, the study highlighted the impact of temperature on the optical performance, where the reflectance of the material changed by 26% and 7% at the temperatures of 557 K and 368 K , respectively. Another study by McVey-White et al. [77] discussed the effect of the lens temperature on the illumination uniformity of three Fresnel-based configurations where the concentration ratio exceeded 500 *suns*. The three configurations were silicon-on-glass primary with no secondary, PMMA primary with truncated inverted pyramid

secondary, and a PMMA 4-quadrant Fresnel–Köhler configuration. The performance of the optical lens for the three configurations was measured at 25 to 50 °C. The silicon-on-glass primary with no secondary showed a 12.4% increase in the total amount of solar irradiance up to a temperature of 30 °C, and then a drop of 81.2% in the total irradiance as the temperature reached 50 °C. Up to 40 °C, the PMMA primary with truncated inverted pyramid secondary showed uniformity in the solar irradiance across the lens; however, a further temperature rise showed an increase in the irradiance and a drop in the uniformity. Compared with the silicon-on-glass primary with no secondary, the PMMA primary with a truncated inverted pyramid secondary showed an increase of 8.5% in the total amount of solar irradiance uniformity at 25 °C.

Shanks et al. [78] reported the temperature and solar misalignment effects on the optical materials within a 200 *suns* conjugate refractive-reflective homogenizer (CRRH) based on a Cassegrain design. The system was made up of a low-iron glass cover, a plastic substrate primary with a vapor-deposited reflective coating, and a slygard-184 refractive secondary optic supported by an ABSplus-P430 plastic casing. The full design was tested in a vacuum drying oven for 3 hours at setpoint temperatures of 60, 70, and 80 °C, where no deformation was observed. The slygard-184 homogenizer bulk had an operating temperature from –45 °C to 200 °C, but the support structure underwent heat deflection at 96 °C under 66 *psi*. Due to sun misalignment, the sun focused on the ABSplus-P430 homogenizer support structure and caused melting. The focal area of concentrated light was measured to be at a temperature of 149 °C with ventilation (no system walls) and 226.3 °C without air ventilation (with enclosure walls in place), which is far higher than its operating temperature. Also, the measured temperature of the central MJPV cell varied in the range of 43–48 °C for no walls and 54–61 °C with walls.

However, the electrical and thermal performance needs to be investigated to identify the overall efficiency with this level of concentration ratio. Vincenzi et al. [79] investigated a novel configuration of 400 *suns* based on Cassegrain optics. The optical materials were: polycarbonate coated with PVD metallization in Aluminium as a primary optic; BK-7 optical glass coated with an Aluminium layer and silicon oxide protection as a secondary optic; and highly reflective Alanod MIRO as a homogenizer. The maximum efficiency of MJPV was measured to be 29% at mid-afternoon with a corresponding cell temperature of 70 °C. Even with a high concentration ratio, the author did not report any thermoplastic defects for the optical concentrators, which indicates the robustness of the designed dual-axis solar tracking system, where its angular acceptance is $\pm 0.6^\circ$.

Colozza et al. [80] designed a small Cassegrain system of 3000 *suns* to melt lunar regolith simulant. The primary and secondary were made of Aluminium and were coated with vacuum-deposited chrome, silver, and protective silicon dioxide (SiO₂). Since Aluminium has a poor surface finish, a silver coating was proposed for both optics, and this resulted in an optical efficiency of 90%. The silver coating gave a 5% increase in the reflectivity. However, the silver coating's durability and lifetime is a major concern compared to Aluminium. Also, the mechanical surface finishing and precision of the optics is an additional cost in the overall system expense. When the mirrored surfaces operated at less than 10%, the concentrator achieved a temperature of 415 °C at the receiver. The author stated that by minimizing the solar cell to one half, the geometrical concentration ratio can reach 6000 *suns*. A unique design was proposed by Chayet et al. [81] of a dish parabolic concentrator consisting of a flat mirror placed on a plastic parabolic surface molded into a global parabolic shape. The system was designed to achieve a concentration ratio of 629 *suns* with a 21% and 50% electrical and

thermal efficiency, respectively. This system has the capacity to produce hot water in the range of 60–90 °C. Kribus et al. [82] studied the performance of a 500 – *sun* parabolic dish design. The parabolic dish is made of glass back-coated with silver to produce the reflectivity, and externally coated with a protective coating to protect the silver from environmental exposure. The system achieved electrical and thermal efficiencies of 60% and 20%, respectively. The system generated water at 58 °C, where the cell efficiency of the Azur Space MJSC was 32% and its maximum operating temperature 100 °C.

2.4.6 Summary of Photovoltaic Cell Efficiencies and Design

Many researchers have explored different semiconductor materials of single /multi-junction PV cells and demonstrated the effect on the cell temperature and thermal and electrical efficiency under a wide range of concentration ratios in CPVT systems, as reported above. The PV design is not within the scope of this literature review as it has been thoroughly researched in different articles [11,83,84]. However, a summary of the different PV performance and characteristics has been provided in Table 2 as an essential consideration in CPVT design (as discussed in section 2.4.1), specifically for the studies where the cell temperature, electrical and thermal efficiency were reported.

Table 2 Experimental CPVT studies covered in this review article.

| Reference | Method | CR_I | Thermal efficiency | Cell materials | Cell temperature (°C) | Design | Electrical efficiency |
|-----------|--------------|----------|--------------------|---|-----------------------|--|-----------------------|
| [64] | Experimental | 1.35 | 70% | pc-Si, a-Si | - | PV panel | 13% |
| [32] | | 1.5 | 15% | c-Si | 55.6 | Linear | 15% |
| [47] | | 1.5 | - | Si | - | Double-sided PV | 10% |
| [60] | | 1.6 | overall 35% | Si | - | Linear | 1% |
| [85] | | 1.86 | above 50% | c-Si | 87.7 | Linear | 9% |
| [86] | | 5.2 | 39.40% | - | - | Linear | 14.10% |
| [48] | | 5.85 | 46.6 | mono-Si | 20 | Linear | 7.63% |
| [59] | | 7.8 | 45% | mono-Si | - | Linear on two sides of triangular design | 6.40% |
| [87] | | 5.81–7.1 | 12.55% | c-Si, pc-Si | - | Linear | 12.50% |
| [69] | | 15 | 60% | c-Si | - | Linear | 20% |
| [73] | | 17 | 38.50% | c-Si | 50 | Linear | 8.50% |
| [58] | | 37 | 58% | c-Si | 65 | Linear | 11% |
| [78] | | 200 | - | 3-junction | 60 | Point | 41.5% |
| [88] | | 208.6 | - | InGaP/InGaAs/Ge | 105 | Point | 39% |
| [79] | | 400 | - | First: MJ (Ge/InGaAs/InGaP) Second: mono-Si & GaAs | 70 | Point | 30% 27% |
| [82] | | 500 | 60% | MJPV | 100 | Point | 20% |
| [89,90] | | 132–795 | 53% | 2-junction (GaAs) | - | Point | 24% |
| [81] | | 629 | 70% | MJPV | - | Point | 20% |

The cell temperature and electrical efficiency of the reported studies are ranged based on their concentration ratio and denoted with their single/multi-junction semiconductor materials, as shown in Figure 14.

Clearly, the electrical efficiency reduces with an increase in the cell temperature, especially for single-junction materials where there is a high series resistance with increasing cell temperature. These results are expected because increasing the concentration ratio raises the cell temperature, thereby increasing the heat dissipation, which results in a drop in the electrical efficiency. In addition, the electrical and thermal efficiencies have shown an inverse relationship for different CPVTs configurations, considering only the experimental studies where system details are fully reported, as in Figure 14.

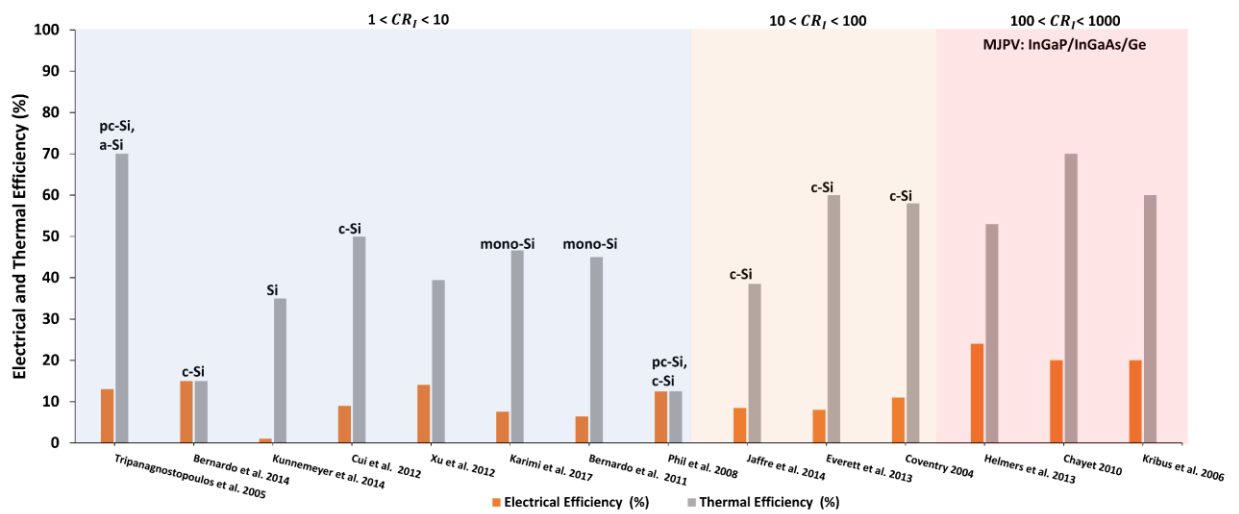


Figure 14. Thermal and electrical efficiencies for the reported CPVT studies and classified based on their level of concentration ratio.

2.5 Economic Aspects for High CPVTs with High Concentration Ratio

Novel optical configurations of CPVT systems are proposed to reach a high level of concentration ratio, at which the system cost is reduced, and the system progression is enhanced. Further, increasing the system efficiency by means of

diminishing the volume, weight, and the manufacturing cost of the system reduces the overall system cost. A CPVT system with a high concentration ratio allows the increase in the cell conversion efficiency up to a concentration factor beyond which the cell conversion efficiency reduces, while producing more power and more cost-effectively. To illustrate this, the MJPV Azur Space (Model 3C44 – $3 \times 3 \text{ mm}^2$) has a maximum cell conversion efficiency of 44% at 250 *suns*, after which the cell conversion efficiency reduces to 43.9% at 500 *suns* and 42.9% at 1000 *suns* in measurement conditions of 1.5 AM – 1000 W/m^2 , $T = 25 \text{ }^\circ\text{C}$ [91]. The relationship between the system’s initial cost as a power-related cost and the level of the concentration ratio in the range of 300–2000 *suns* for two system efficiencies is shown in Figure 15.

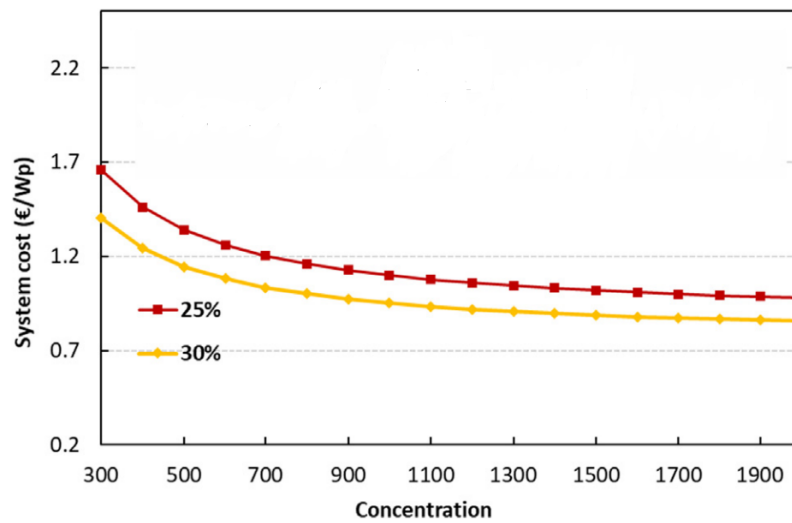


Figure 15. System cost as a function of concentration ratio [50,92].

Choosing a high-performance PV cell is not the best metric for selection. Cost-effectiveness is one key approach for developing a high concentration CPVT system. For a high concentration ratio, multi-junction and non-silicon based solar cells are preferable due to their high performance under elevated operating temperatures. In contrast, for low concentration ratios, single-junction silicon-based solar cells are preferred due to their cost-effectiveness and ready

availability. Yazawa and Shakouri [93] studied theoretically the installation cost of CPVT systems per unit area with concentration ratios up to 1000 *suns*. They found that the cost of the PV material diminishes while the cost of the optics dominates at concentration ratios above 100 *suns*, without considering the cost of the mechanical complexity, as shown in Figure 16.

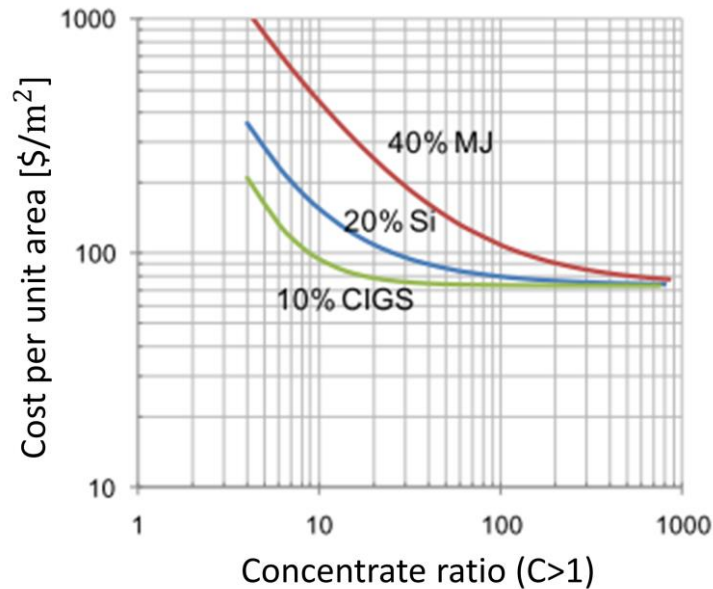


Figure 16. Installation cost per unit of overall system [93].

Although MJPV cells have the highest efficiency in respect of the solar concentration, the market demand for them is not high due to their high production cost and to MJPV constituents being less available. MJPV cells are currently economically feasible only if the concentration ratio is sufficient to minimize the cell area and offset its initial cost [94]. Research and development for MJPVs to reduce the payback period and maximize the net present value (NPV) are important for operation under high concentration ratios. Comparison of the performance of single- dual-, and triple-junction solar cells versus concentration ratios ranging from 1– 10000 *suns* is shown in Figure 17. At certain concentration ratios, the PV cells reach their highest efficiency [95]. The peak

efficiency occurs when the series resistance of the subcells dominate due to an increase in the current in accordance with the concentration ratio (as discussed in section 2.2). For selection of the MJPV type, the MJPV cell with a slight drop in efficiency after reaching the peak efficiency is more advantageous as, during real-time operation, the PV cell is not subject to a uniform concentration ratio, resulting in a localized hotspot. Moreover, the dual-junction cell has a smooth drop in efficiency, indicating that this type will have better efficiency in different concentrator modules close to 1000 *suns*.

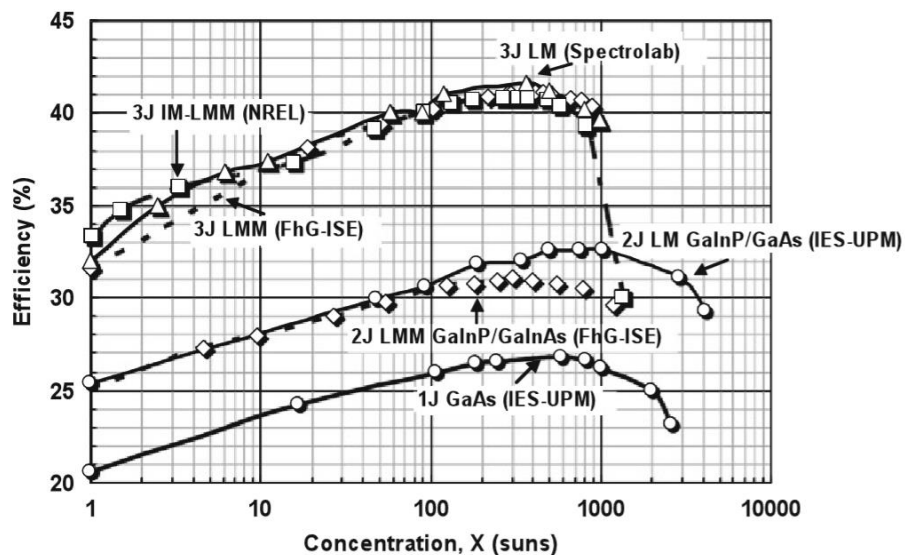


Figure 17. Comparison of the performance of the best MJPV concentrator solar cells with concentration ratio [88].

Concentrating sunrays to generate solar power is potentially more cost-effective, but it relies on the cost of the optical concentrators. The concentrators' price is still the main issue and it has been reported that the price of solar concentrators is between \$150 – \$250/ m^2 , which is about half the total cost of installing a concentrated solar power (CSP) plant [96]. This issue is worsened by incorporating multiple optical interfaces to attain a high concentration factor. Although the CPVT is area-efficient and this results in less overall system cost

(i.e., fewer PV materials), a vast number of large-scale solar PV deployments are required in a desert region, such as Saudi Arabia, Australia, and North Africa, where the value of land is dramatically low [97]. Thus, the highest efficiency CPVT does not convert into economic impact because the land cost is depressed. Because CPVT systems utilize an optical device to intensify direct solar radiation, the CPVT system's electrical and thermal output is maximized at the price of not only the optical device but also by incorporating a tracking system, MJPV cells, and an appropriate cooling mechanism. These associated components can result in an expensive CPVT system in comparison to the conventional solar PV panel. Micro-tracking technology is suggested to be subordinate to the CPVT system, but it might be cost-competitive with solar PVs. However, the progression in CPVT system design is not expedited in the same manner as solar PV, resulting in more profitability than the CPVT on the utility scale [98,99].

The cost of solar PV has not only competed with the CPV and CSP systems but also with the least fossil fuel cost, due to its ongoing technological development [100]. The use of concentrated solar technologies has expanded while their cost continues to fall [98]. For example, the cost of utility-scale solar PV has fallen from \$0.378/*kWh* to \$0.043/*kWh* with 89% of cost reduction, while CSP's price has decreased from \$0.344/*kWh* to \$0.095/*kWh* with 72% of cost reduction for the period between 2010 and 2020 [101]. The CPV system has also had a much lower cost in 2010 of \$0.13/*kWh* in comparison to both solar PV and CSP and the price kept gradually decreasing until it reached \$0.082/*kWh* with falling percent of 60% not less than the solar PV, as in Figure 18 [102]. To put this in the context of technological progression, the amount of installed CSP (5.5 *GW*) in 2018 was accomplished by solar PV in 2005. The solar PV cost reduction is set to continue beyond 2020 and it will offer cheaper electricity than the least fossil

fuel cost. In 2020, CSP electricity offers a price between \$0.06 to \$0.10/*kWh* range, while Solar PV provides a price of less than \$0.048/*kWh*. The cause of the highest cost reduction for the solar PV system in comparison to the CPV and CSP systems is the drop in the silicon module prices from \$2/*W* to just over \$0.20/*W* during the 2010s [18]. In contrast, concentrated solar technology could further reduce costs in view of developing cheaper optical materials with higher performance, and considering the induced high temperature on optics and solar cells [103].

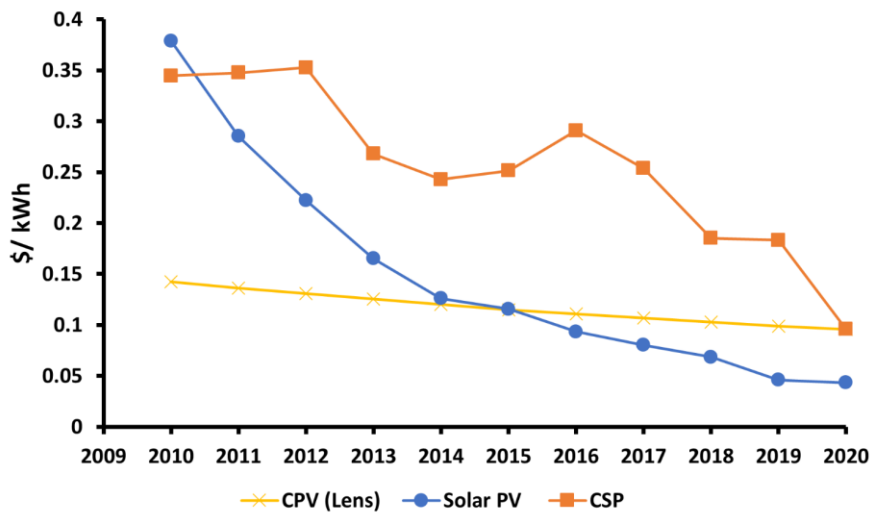


Figure 18 The levelized cost of electricity (\$/kWh) for concentrated photovoltaic (CPV), Concentrated Solar Power (CSP), and Solar PV plants for completed projects [109,110].

2.6 Conclusion

Concentrated photovoltaic technologies need to focus on some aspects of ongoing research, especially with increasing the concentration ratio. The increase in concentration ratio results in temperature growth in the solar cell and all-optical stages within the system. One of these aspects is having a proper cooling arrangement through either passive or active cooling mechanism to assure the safe operating condition of the MJSC at 80 °C. On the other hand, the working optical interfaces must be made of materials with high working temperatures and excellent optical performance. From the literature reviewed in article 1, other methods to be underlined that exhibited the CPVT system include: (1) Electrical/thermal performance and consideration within the CPVT system; (2) the CPVT system optical tolerance with rising concentration ratio; (3) thermal receiver design and materials to thermally managing the heat in a CPVT; (4) the CPVT system economic aspects with increasing concentration ratio.

In this chapter, a complete illustration of the CPVT system with emphasis on advances and limitations with regard to optical, thermal, and solar cell components with increasing the concentration ratio was conducted. In the next chapter, a 3D thermal model will be established to estimate the cell temperature under a wide range of high concentration ratios. This 3D model will enrich the understanding of solar cell thermal behaviour with increasing concentration ratio.

CHAPTER 3: Modelling a Concentrator Solar Cell Coupled with a Passive Heat Sink

3.1 CPV Design Considerations

A starting point for the design of any CPV system is to determine the type of solar cell used and its associated heat dissipation system. A clear understanding of the expected environmental conditions can help determine the solar cell operating temperatures, the amount of power to be extracted and the overall physical dimensions of the system depending on the type of heatsink deployed. The cell temperature's linear correlation with the concentration ratio is dependent on the cell area, where increasing the cell area increases the wasted heat. This chapter is fully detailed in article 2.

This study has considered a $3 \times 3 \text{ mm}^2$ MJSC (Model 3C44C) cell from Azur space, as shown in Figure 19. The cell is designed to operate within a range of 100 – 1500 *suns* and has a peak efficiency of 42%. The maximum operating temperature is reported to be 110 °C [91]; however, it is recommended to operate below 80 °C. The cell has a widely recognized H-pattern optimized to perform under non-uniform illumination conditions.

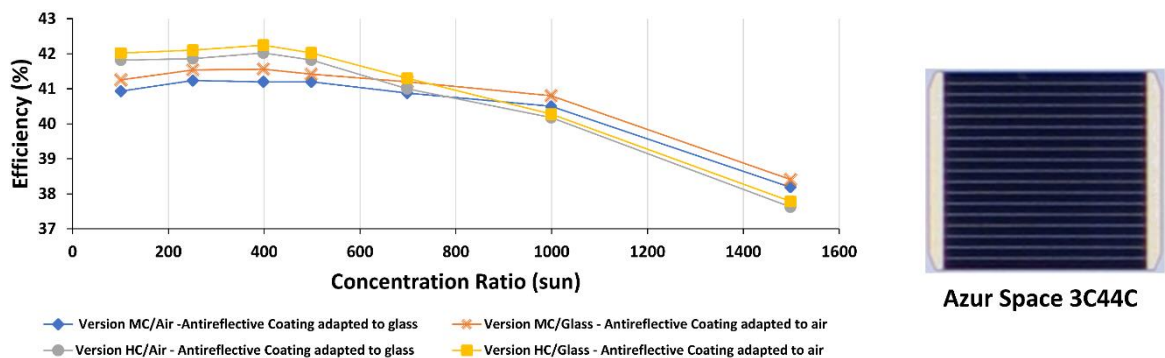


Figure 19 Performance characteristics of an Azur space 3C44C solar cell. The four lines are efficiency versus solar concentration ratio for version MC/air & glass and version HC/Air & glass where the solar cell is optimized.

Measurement conditions is 1.5 AM D – 1000 W/m^2 (ASTM G 173-03), $T = 25$ °C, designated measurement area = 100.51 mm^2 [91].

3.2 Passive cooling with fin design

In different studies, the utilisation of passive cooling mechanisms has been proven to successfully handle the thermal management for a wide range of concentration ratios. Flat-plates and finned heatsinks are used commonly in passive cooling systems. Generally, increasing the area of the heatsink baseplate easily dissipates heat but at the cost of increased module weight which ultimately increases the cost of tracking and the LCOE. So, the minimum heatsink baseplate area for Azur Space 3C44 – 3×3 mm^2 cell area is calculated, applying the same approaches in [43], by Eq.(1).

$$A_{baseplate} = \frac{Q_c}{[q_{conv} + q_{rad}]} \quad (1)$$

The CPV system exchanges heat with its surrounding through natural convection and radiation. The convective heat flux (q_{conv}) is proportional to the difference between the solar surface temperature (T_s) and the ambient fluid temperature (T_a) considering the exchange baseplate area ($A_{baseplate}$) and the convective heat transfer coefficient (h), as in Eq.(2).

$$q_{conv} = A_{baseplate} \cdot h \cdot (T_s - T_a) \quad (2)$$

Where radiation (q_{rad}) is proportional to the difference between the solar surface temperature (T_s) and the surrounding fluid temperature (T_{sur}) to the fourth power considering the radiative property (ε) of the exchange baseplate area ($Area_{baseplate}$) and the Stefan-Boltzmann constant ($\sigma = 5.67 \times 10^{-8} \frac{W}{m^2 \cdot K^4}$), as in Eq.(3).

$$q_{rad} = A_{baseplate} \cdot \varepsilon \cdot \sigma (T_s^4 - T_{Sur}^4) \quad (3)$$

Assuming that all the heat generated (Q_C) by Azur Space 3C44C – $3 \times 3 \text{ mm}^2$ cell is conducted to the bottom surface of the heat sink, considering only the flat bottom surface of the receiver, and taking into account the highest value of natural convective heat transfer coefficient of $25 \text{ W/m}^2 \cdot \text{K}$, an emissivity value of polished Aluminium surface of 0.09, a heatsink surface temperature of $60 \text{ }^\circ\text{C}$, and an ambient temperature of $25 \text{ }^\circ\text{C}$. Thus, the minimum required dissipating area of 0.0025 m^2 is needed correspondent to $5 \times 5 \text{ cm}^2$. The assumption was made considering the emissivity value of Aluminium instead of copper and silicon where they would result in the lesser dissipating area due to their higher emissivity. The fin heatsink geometry is obtained from [104], as in Figure 20. A $3 \times 3 \text{ mm}^2$ MJSC is attached to a heatsink with an area of 25 cm^2 and uses 50 micro-fins (thickness $200 \text{ }\mu\text{m}$ and pitch of $800 \text{ }\mu\text{m}$).

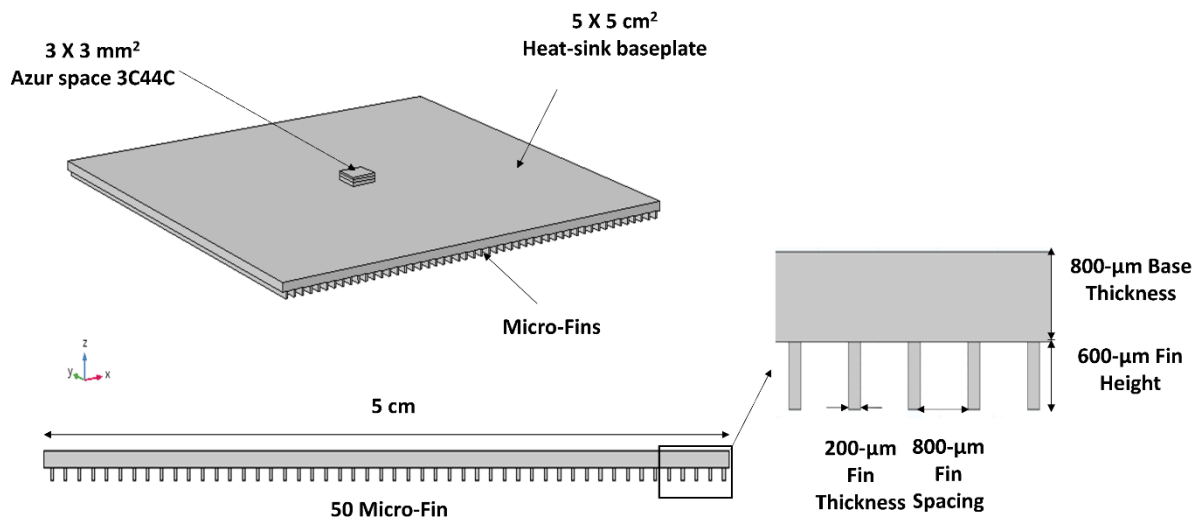


Figure 20 Asymmetric, side-view, and cross-section view for the micro-finned heatsink with typical dimensions of the fins.

3.3 Heat Spreader Selection and Thermo-Physics Properties

The selection of the CPV system's components and materials play a fundamental role in thermal management. The heat spreader between the PV cell and the heatsink needs to be highly efficient to transfer the generated heat out of the PV cell. A material with a high thermal conductivity is preferable, while electrical conductivity needs to be minimized. The most commonly used substrate in the CPV system is Direct Bonded Copper (DBC) due to its mechanical strength and excellent thermal and electrical properties [40,41,105]. Printed Circuit Boards (PCB) substrates on the other hand which is widely used in the electronic applications have a laminated fiberglass on one or both sides with copper that decreases the thermal conductivity [106] and limits its application in CPV. Replacing the laminated material with a metal improves the thermal conductivity and is referred to as Insulated Metal Substrate (IMS). IMS is an alternative for DBC due to its affordability and excellent thermal performance [42]. Also, a silicon wafer (Si wafer) is an excellent material for the substrate because the Si wafer has a similar thermal expansion rate to the MJSC semiconductor material that can improve its reliability [43]. Silicon manufacturability is simple, but silicon is an expensive material compared to other substrates and mechanically fragile [107].

The substrate layer thickness and materials have been selected according to the cell area, as shown in Figure 21.

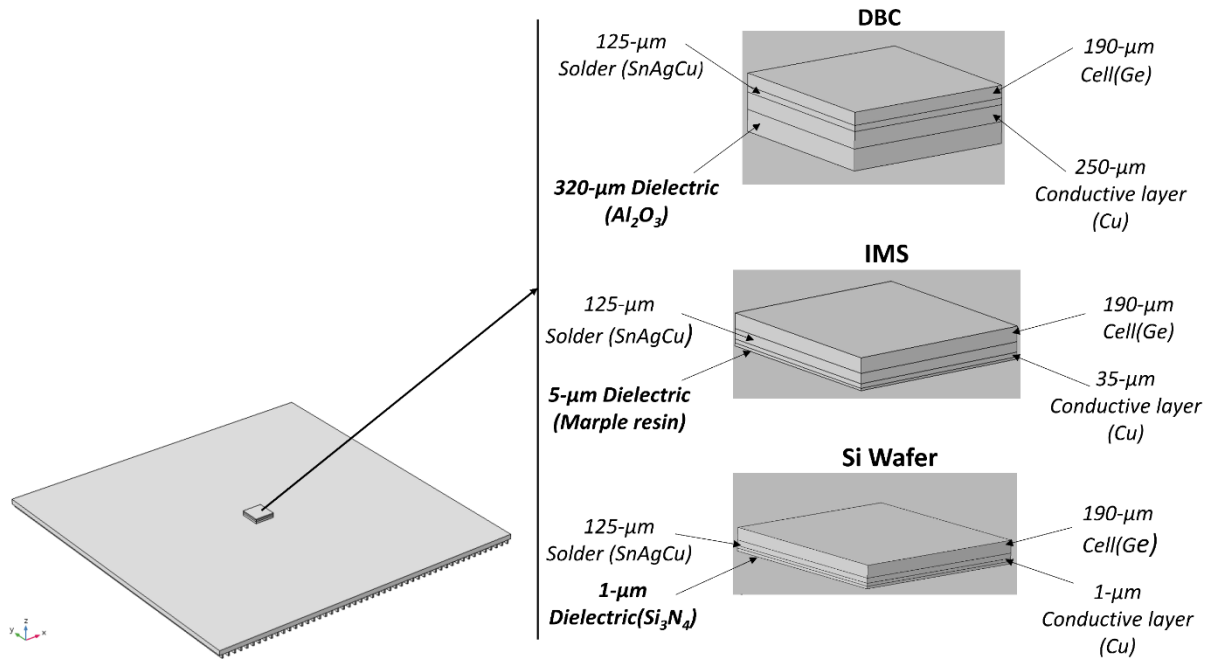


Figure 21 Geometric model of the CPV receivers, material and thickness layers for the DBC [35], IMS [33], and Si wafer [36].

Three different substrates with three different heatsink materials have been researched in COMSOL Multiphysics software to evaluate the thermal performance with a fixed heatsink geometry, as in Table 3.

Table 3 Thermo-physical properties used in COMSOL

| Material | Density [kg/m^3] | Heat Capacity [$J/kg \cdot K$] | Thermal Conductivity [$W/m \cdot K$] |
|-------------------------------|-------------------------|-------------------------------------|---|
| Germanium (Ge) | 5323 | 700 | 60 |
| Copper (Cu) | 8700 | 385 | 400 |
| Aluminium (Al) | 2700 | 900 | 238 |
| Silicon (Si) | 2329 | 700 | 130 |
| Alumina (Al_2O_3) | 3900 | 900 | 27 |
| Silicon nitride (Si_3N_4) | 2370 | 673 | 10 |
| Marble Resin | - | - | 3 |

3.4 Numerical Model

We model the solar cell and the associated heat dissipation using the energy equation. The heat transfer rate in the CPV unit is governed by considering the

energy conservation law for the steady-state condition with the heat source (\dot{q}), where (q_{cond}) and (q_{conv}) indicate the conduction heat transfer and the convective heat flux, respectively, in Eq.(4).

$$q_{cond} = \dot{q} + q_{conv} \quad (4)$$

The analysis of the conduction heat transfer rate (q_{cond}) in the solid domain is obtained by Fourier's law. The conduction heat transfer equation is solved to obtain the temperature distribution between the solid layers in three dimensions (x, y, z) where it is presented as a del operator (∇) considering the solid layers thermal resistance ($R_{tr,cond}$) in Eq.(5).

$$q_{cond} = \nabla \left(-\frac{1}{R_{tr,cond}} \nabla T \right) \quad (5)$$

The thermal resistance, by different layer composition, influences the heat transfer rate because thermal resistance and thermal conductivity are inversely correlated as in Eq.(6).

$$R_{tr,cond} = \frac{L_L}{k_L} \quad (6)$$

The thermal resistance is basically the reciprocal of the thermal conductivity (K_L) through a plain layer of a thickness (L_L).

The convective heat flux (q_{conv}) on the external boundaries is obtained by Newton's law of cooling considering $R_{tr,conv}$ using Eq.(7). However, the adiabatic condition has been applied for the baseplate periphery of the heatsink taking into consideration the real condition where the receiver is contiguous with other receivers.

$$q_{conv} = \nabla \left(\frac{1}{R_{tr,conv}} \cdot \nabla T \right) \quad (7)$$

The thermal resistance is also associated with convective heat transfer where it is the reciprocal of the convective heat transfer coefficient (h) in Eq.(8).

$$R_{tr,conv} = \frac{1}{h} \quad (8)$$

The CPV system was mounted in a horizontal position, where buoyancy force is normal to the layer, to allow the natural convection flow and to avoid the temperature gradient on the layer.

Considering the energy conservation law with a heat source for a steady-state condition in Eq.(4), the conduction heat transfer equation for estimating the temperature distribution in the solids can be solved by Eq.(9).

$$\nabla \left(\frac{1}{R_{tr,cond}} \nabla T \right) = \dot{q} \quad (9)$$

The heat source can be modelled as shown in Eq.(10) below. Where (q_o) indicates the optical power output in (W/m^2) after solar concentration and ($\eta_{electrical}$) indicates the electrical efficiency of the solar cell.

$$\dot{q} = q_o \cdot (1 - \eta_{electrical}) \quad (10)$$

The arrangement of the solar cell as a heat source is to model the portion of solar irradiance that converts to wasted heat. The optical power after concentration can simply be expressed as the product of DNI available, the geometric concentration factor and the optical efficiency. For a worst-case condition, we consider that the solar cell generates no electrical energy and assume that all the available optical

power is to be dissipated by the heat sink. The optical efficiency ($\eta_{optical}$), the DNI, and the geometrical concentration ratio was assumed to be 85%, $1000 W/m^2$ and between 100 – 1000 *suns*, respectively.

3.5 Boundary Conditions

The Azur Space 3C44 - $3 \times 3 mm^2$ cell was modelled as one block of germanium (Ge), as is standard practice by authors of previous investigations [45,50,106,108,109]. The thermal boundary conditions applied to the system can be seen in Figure 22. Substrates and finned heatsink was modelled using material of different layers and thicknesses (Figure 21) and using the thermophysics properties of each layer (Table 1). Density and thermal conductivity had been set to be independent, no variation with temperature. Solder material was considered as thin thermal resistive layers. All the analyzed inputs and boundary conditions in the simulations are summarized in Table 4 and Figure 22.

Table 4 Input parameters for the simulations and thermal boundary conditions for Figure 22.

| Components | Symbols | Value | Units |
|------------------------------------|---|----------------------------------|-------------|
| Solar Cell | A_c | 3×3 | mm^2 |
| | DNI | 1000 | W/m^2 |
| | $\eta_{electric}$ | 42.5 | % |
| | $\eta_{optical}$ | 85 | % |
| | Concentration ratio | 100 - 1000 | Sun |
| Substrates | Area | 3×3 | mm^2 |
| | Type | Direct Bonded Copper (DBC) | |
| | | Insulated Metal Substrates (IMS) | |
| Silicon Wafer (Si Wafer) | | | |
| Fin heatsink | Baseplate thickness | 0.8 | μm^2 |
| | Baseplate Width | 5 | cm |
| | Baseplate Length | 5 | cm |
| | Materials | Aluminium | |
| | | Copper | |
| Silicon | | | |
| CPV system | h | 3 - 25 | $W/m^2.K$ |
| | T_a | 20 - 56 | $^{\circ}C$ |
| Thermal Boundary conditions | | | |
| Number | Region | Boundary Condition | |
| 1 | Solar Cell | Boundary heat Source | |
| 2 | All free surfaces and micro-fin heat-sin | Natural Convection | |
| 3 | | | |
| 4 | All Side surfaces of the heatsink baseplate | Adiabatic $q = 0$ | |
| 5 | Surrounding | Ambient Temperature | |

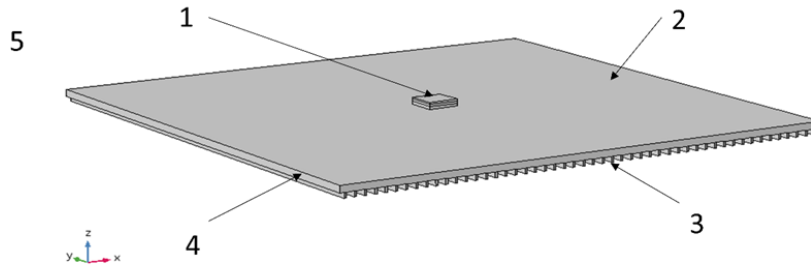


Figure 22 Thermal Boundary Conditions

3.6 Meshing

Meshing is a key process when using the finite element method. The accuracy and the time it takes to solve the model is strongly related to the mesh set-up. In this study, different sizes of meshing were applied to ensure the optimal meshing size in every domain. The thickness of the thin layers in the substrates was smaller than the smallest element size for the predefined value in COMSOL's extremely fine mesh setting. The tetrahedral mesh was introduced to customize the maximum and the minimum element size to be within the thickness of the thin layer by taking into consideration the required computational time, as in Figure 23. The normal mesh size was selected to give a temperature of 156.42 °C. The normal mesh size results in a relative error of 0.03% to the asymptotic value at extremely fine meshing.

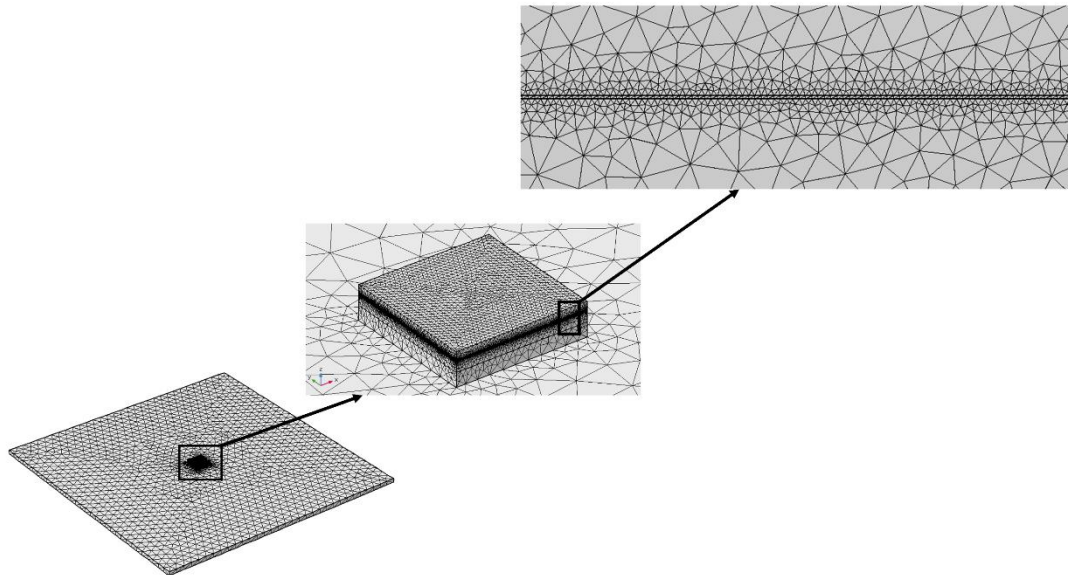


Figure 23 Tetrahedral mesh applied to the thin layer.

3.7 Performance Characteristics of CPV with Flat-Plate and Micro-Fin Heat Sinks

The HCPV was subjected to operate in the worst-case conditions (WCCs) wherein the cell is not capable of producing any electrical power ($\eta_{electrical} = 0$). Thus, all the sunlight incident on the solar cell is to be dissipated as heat. In this condition, the cell temperature rapidly elevates. For safe operation, the solar cell must not exceed 110 °C, which is the maximum operating temperature of the 3C44C Azur Space solar cell.

Utilizing the COMSOL Multiphysics numerical simulation model, we can predict the maximum cell temperature for a $3 \times 3 \text{ mm}^2$ solar cell mounted on DBC, IMS, and Si wafer attached with a flat-plate and micro-finned heatsink under concentration ratios ranging from 100 to 1000 *suns*. Figure 24 shows the temperature contours of the solar cell when using different substrate materials and using micro fin heat sinks. In the worst-case conditions, the developed model was able to determine the concentration ratio limits based on the solar cell maximum recommended temperature of 80 °C for different values of natural

convective heat transfer coefficient, ambient temperature, and the number of fins, as detailed in article 2. Based on the predicted results, we reached the following discoveries:

- 1- The micro-finned heatsink showed a drop-in temperature of 57.31 °C, 55.43 °C, and 56.07 °C at 1000 *suns* in comparison with the flat plate heatsink for the DBC, IMS, and Si wafer, respectively.
- 2- Increasing the convective heat transfer coefficient from 4–22 $W/m^2.K$ allows the concentration limits to rise to 401.3 *suns*, 507.5 *suns*, and 431.2 *suns* for the DBC, IMS, and Si wafer, respectively.
- 3- Increasing the ambient temperature from 20 to 56 °C reduces the concentration ratio limits by 265.4 *suns*, 267.2 *suns*, and 249.6 *suns* for the DBC, IMS, Si wafer, respectively
- 4- Increasing the number of fins from 20 to 120 fins result in allowing the concentration ratio limit to increase by 233.7 *suns*, 250 *suns*, and 216.9 *suns* for the DBC, IMS, and Si wafer, respectively.

Clearly, the thermal resistance of Al_2O_3 in DBC, Marble resin in IMS, and Si_3N_4 in Si wafer generate a temperature gradient between the cell and the heat-sink material. However, the low thermal resistance of the IMS substrate results in the best thermal performance in terms of maintaining the cell temperature below 80 °C and allowing a wider range of concentration ratio.

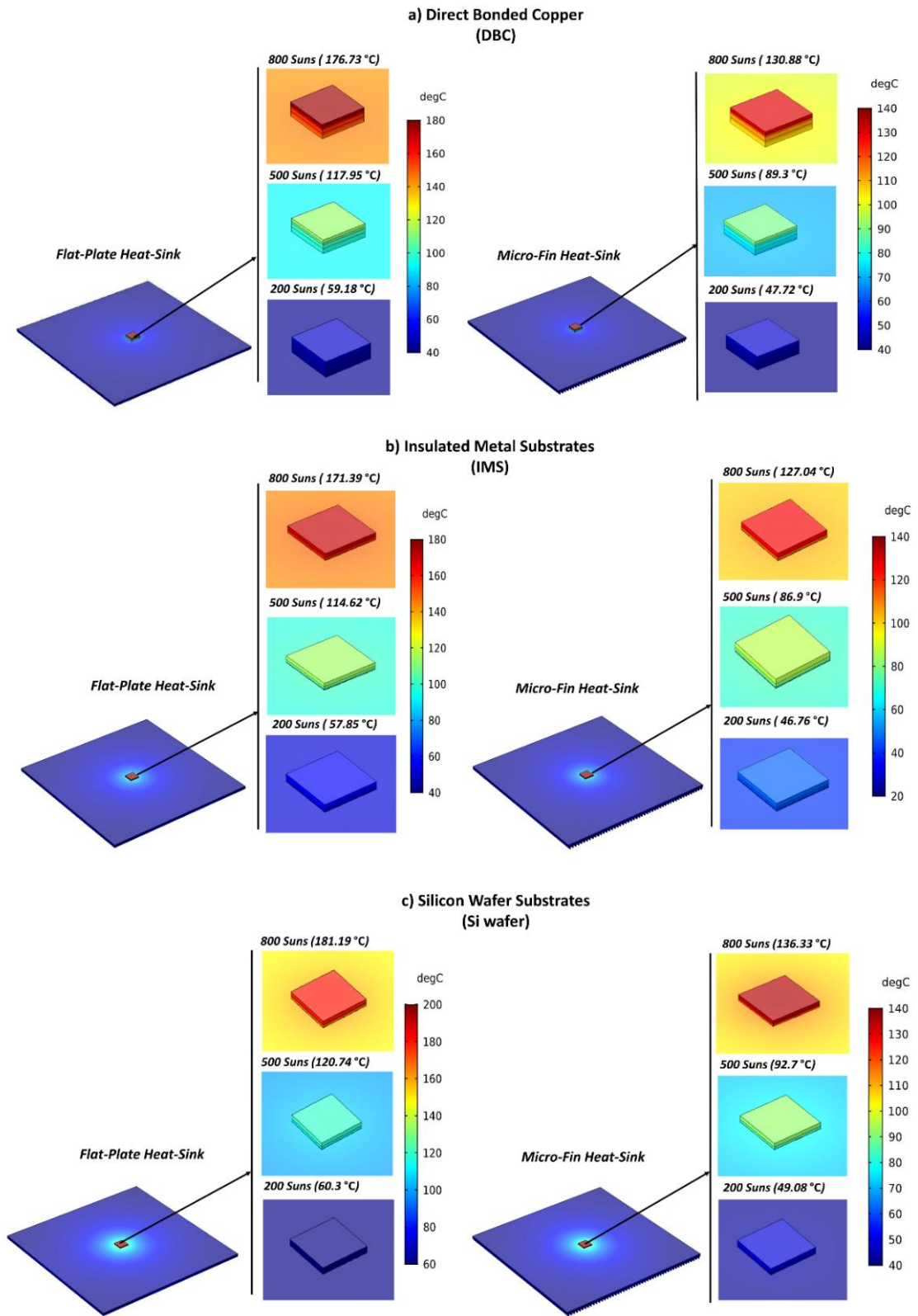


Figure 24 Temperature field distribution for a) Direct Bonded Copper (DBC), b) Insulated Metal Substrates (IMS), and c) Silicon Wafer Substrate (Si Wafer).

3.8 Conclusion

A 3D numerical model has been developed to predict the maximum temperature of a PV cell paired with a finned heat-sink under various concentration ratios for three different substrates materials using COMSOL Multiphysics software. In the worst-case conditions, the developed model was able to determine the concentration ratio limits based on the solar cell maximum temperature various throughout for different values of natural convective heat transfer coefficient, ambient temperature, and the number of fins.

The established 3D model in this chapter helped enrich the understanding of a thermal model in correlation with increasing the concentration ratio. This thermal model will be extended in the next chapter to account for an optical model. The coupling process between the optical and thermal models will be detailed only for the SOG Fresnel lens primary optical component.

CHAPTER 4: Primary Optical System for UHCPV

4.1 Introduction

A Fresnel lens is a refractive optical component that converges input solar rays into a focal spot. The focal length is idealised based on the intercept radius by readjusting the Fresnel lens position for its optimum energy output. Fresnel lens is one of the most common primary concentrators in CPV systems for its cost-effective, lightweight, relatively high acceptance angle and optical efficiency. However, the standard Fresnel lens is limited in concentration ratio to about 1000 *suns* due to the alteration of its refractive index materials with temperature (chromatic aberration). Thus, achromatic Fresnel doublets show a minimised chromatic aberration, increasing the concentration factor [17,110]. Experimentally, a flat achromatic Fresnel doublet showed a concentration factor of up to 2000 × but is still not commercially available [111]. SOG - Fresnel lens is manufactured by applying a thin layer of liquid silicon into a glass. The stamping and curing process is performed to form the Fresnel structure. However, the thin silicon layer leads to a strong dependence between the ambient temperature and optical efficiency at which the thermal expansion coefficient of the silicon to glass magnitude is different. Thus, the temperature effect hinders the optical efficiency for the Fresnel lens and the solar cell efficiency due to different focal lengths and focal spot sizes [112]. This chapter is fully detailed in articles 3, 6, and 7.

4.2 Theoretical Optical Characterisations

To theoretically characterise the optical efficiency ($\eta_{opt,th}$) and the concentration ratio (C_{th}), we incorporate the average total transmittance of the Fresnel lens ($\%T$), the geometrical concentration ratio (C_g), and the fractional concentration loss ($\%C$) with radiant flux (J) on the receiver area ($A_{receiver}$), and then divided

with the radiant flux on the concentrator area ($A_{Fresnel}$), as in Eq.(11). The radiant flux here expresses the amount of radiant energy emitted per unit area ($\frac{W}{m^2}$).

$$\eta_{opt,th} = \frac{(J \times A_{receiver}) \times \%T \times C_g \times \%C}{(J \times A_{Fresnel})} \times \frac{I_T}{I_M} \quad (11)$$

Hence, the theoretical concentration ratio can be given in Eq.(12).

$$C_{th} = \eta_{opt,th} \times C_g \quad (12)$$

In anticipation of the optical concentration ratio, the geometrical concentration ratio could be approached either by considering only the Fresnel lens area to the focal spot area ($A_{focal\ spot}$) or by considering the area of the Fresnel to the area of the solar cell and then apply the fractional concentration loss of 16.24%, as in Eq.(13). The fractional concentration ratio only requires to be accounted for when the focal spot area is bigger than the solar cell, whilst the focal spot area matches the solar cell (usually due to another funnel optic receiver) or is smaller than the solar cell, there is no fractional concentration loss.

$$C_g = \frac{A_{Fresnel}}{A_{focal\ spot}} = \frac{A_{Fresnel}}{A_{receiver}} \times \%C \quad (13)$$

The adjustment of the Fresnel lens under the solar simulator at $1000\ W/m^2$ shows an optimum focal length and a focal spot diameter of $\sim 42\ cm$ and $2.8\ cm$, respectively.

The theoretical concentration ratio considering the fractional loss was found to be $77\ suns$ on average. Fractional loss stands for the actual portion of light falling on the cell (16.24%) and that does to generated focal spot bigger than the solar cell. The theoretical effective concentration ratio ($C_{eff,th}$) is calculated as the actual solar irradiance on the solar cell surface area after transmitting and concentrating

through the Fresnel lens at different solar irradiance in the range of 400 – 1000 W/m^2 given the theoretical optical efficiency, as in Eq.(14).

$$C_{eff,th} = \frac{J \times C_g \times \eta_{opt,th}}{1000} = \frac{J \times A_{Fresnel} \times \%T}{A_{receiver} \times 1000} \quad (14)$$

4.3 Experimental Optical Characterisation

The optical characterisation of the Fresnel lens is experimentally achievable through the electrical characterisation of a solar cell. Indoor, we can control the solar intensity of the lamp (helicon value) at which electrical characterisation for different solar irradiance (concentration ratio after the Fresnel lens) is realistic. We simulate the solar irradiance from 400 – 1000 W/m^2 in the interval of 100 W/m^2 to measure the solar cell electrical products (I_{sc} , V_{oc} , FF). The I-V and power curves for the MJSC (Azur Space 3C44A $10 \times 10 \text{ mm}^2$), for Si polycrystalline single-junction ($10 \times 10 \text{ mm}^2$), and Si polycrystalline single-junction ($5.1 \times 5.1 \text{ cm}^2$) are measured to determine the electrical limits with and without the Fresnel lens. The optimum arrangement of the Fresnel lens results in focal spot utilisation by the solar cell of $10 \times 10 \text{ mm}^2$ of only 16.24%, which is the actual portion of light falling on the cell, resulting in optical efficiency of 14.6% (Fractional concentration efficiency of 16.24% \times average Fresnel lens transmittance of 89.6%) and concentration ratio of 77 *suns*, as illustrated in Figure 25.a. The optical efficiency of 14.6% is due to the indoor solar simulator divergence angle, and certainly, the optical efficiency would be different under outdoor conditions. In a solar cell of $5.1 \times 5.1 \text{ cm}^2$, the solar cell area is more significant than the focal spot area; hence the geometrical concentration ratio (the Fresnel lens area divided by the solar cell area) is not quite appropriate and instead the Fresnel input aperture area divided by the illuminated cell area would give a more useful indication of concentration ratio. In Figure 25.b, the theoretical

optical efficiency was found to be 91.1% (simply the Fresnel transmittance), resulting in a theoretical concentration ratio of 18 *suns*.

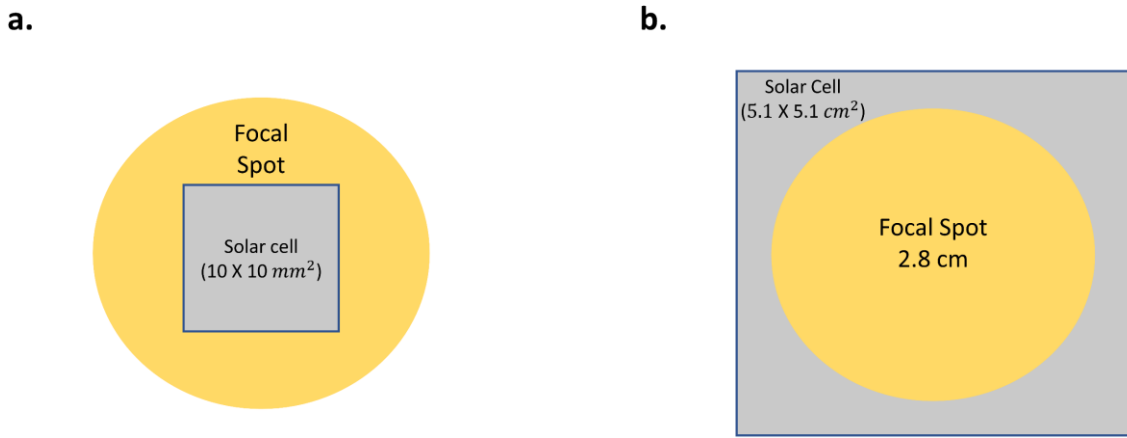


Figure 25 a schematic diagram of a. fractional concentration loss (solar cell to focal spot area) ($10 \times 10 \text{ mm}^2$), and b. solar cell area larger than the focal spot area ($5.1 \times 5.1 \text{ cm}^2$).

Experimentally, the effective concentration ratio ($C_{eff,exp}$) can be characterized considering the measured I_{sc} with/without the Fresnel, as in Eq.(15).

$$C_{eff,exp} = \frac{I_{sc,concentrated}}{I_{sc,not\ concentrated}} \quad (15)$$

To find out the effective optical efficiency ($\eta_{opt,eff}$), the electrical characterisation of the solar cell at different solar irradiance has been incorporated in Eq.(16) to predict the effective optical efficiency considering the Fresnel lens efficiency (Module efficiency - η_{module}) concerning solar cell efficiency (η_{cell}). I_T/I_M terms in both Eq.(11) and Eq.(16) is only to express the subcell limits for the MJSC.

$$\eta_{opt,eff} = \frac{\eta_{module}}{\eta_{cell}} \times \frac{I_T}{I_M} \quad (16)$$

The module efficiency is the maximum electrical power output from the solar cell to the power input for the Fresnel lens, as in Eq.(17).

$$\eta_{module} = \frac{Power_{max(V_{oc}, I_{sc}, F.F), concentrated}}{J \times A_{Fresnel}} \quad (17)$$

The cell efficiency is the electrical output to the power input of the cell with concentration, which is driven from Eq.(18).

$$\eta_{cell} = \frac{Power_{max(V_{oc}, I_{sc}, F.F), concentrated}}{Radiant\ flux\ on\ the\ target\ area\ (J \times A_{Fresnel}) \times \%T \times \%C} \quad (18)$$

All the results from both the theoretical and experimental characterisation relying on the detailed equation above are summarized in Table 5 and detailed in Article 6. This prediction approach of optical characterisation has shown a strong agreement between the theoretical and experimental results of the MJSC, with a discrepancy of 2% at $1000 \frac{W}{m^2}$.

Table 5 Summarise the geometric concentration, theoretical/experimental optical concentration ratio, and the optical efficiency in every testing scenario at $1000 W/m^2$.

| Solar Cells | Geometrical concentration Ratio (x)(Cg) | Theoretical Optical Concentration Ratio (suns) (C_{th} and $C_{eff,th}$) | Experimental Optical Concentration Ratio (suns) ($C_{eff,exp}$) | Theoretical Optical Efficiency (%) ($\eta_{opt,th}$) | Effective Optical Efficiency (%) ($\eta_{opt,eff}$) |
|----------------------------|---|--|---|--|---|
| $1 \times 1 cm^2$ (1J) | 529 | 77 | 33 | 14.6 | 14.6 |
| $5.1 \times 5.1 cm^2$ (1J) | 20 | 18 | 7 | 91.1 | 91.1 |
| $1 \times 1 cm^2$ (MJ) | 529 | 77 | 79 | 14.6 | 14.6 |

Although the concentration ratio value is far from the UH concentration limits, these results are an important step towards carrying out the full UHCPV experiment. These results here are focused on evaluating the Fresnel lens individually and the performance of the concentrator MJSC in these poorer conditions to have a concrete reference performance for the whole UHCPV system.

4.4 Optical-Thermal Numerical Modelling for Fresnel Lens

An optical and thermal numerical model is established using COMSOL Multiphysics software and carried out using a bidirectional coupled ray-tracing study approach. The optical model was established to operate a CPV system based on a Fresnel lens as primary optical components toward multiple optics in one CPV system to achieve a UH concentration ratio [38]. Then, the generated heat on the receiver area as an output from the optical model will be interlinked with the heat transfer in the solid model as a heat boundary source term.

4.4.1 Numerical Model

4.4.1.1 Optical Model

The optical model is calculated by the analogous to the Hamiltonian formulation in classical mechanics [113], which is a set of ordinary equations describing the trajectories of rays in terms of ray position $q(t)(m)$ and wave vector $k(t)(\frac{rad}{m})$. The angular frequency $(\omega)(\frac{rad}{s})$ substitute a place usually taken by the Hamiltonian (H) in the right-hand side of the Eq.(19) and (20), which is the gradient of the angular frequency with respect to the vectors $q(t)$ and $k(t)$.

$$\frac{dq}{dt} = \frac{\partial \omega}{\partial k} \quad (19)$$

$$\frac{dk}{dt} = - \frac{\partial \omega}{\partial q} \quad (20)$$

In the isotropic medium, when the refractive index is homogenous, the H formulation as in Eq.(19) and (20) is rewritten to only account for the constant speed and ray direction of light as in Eq.(21) and (22).

$$\frac{dq}{dt} = \frac{c k}{n |k|} \quad (21)$$

$$\frac{dk}{dt} = 0 \quad (22)$$

where c is the speed of light ($c = 2.99792458 \times 10^8 \frac{m}{s}$), and n (dimensionless) is the refractive index.

When the inhomogeneous refractive index at the optical interface is accounted for, the direction of the refracted ray is calculated relying on Snell's law, as in Eq.(23).

$$n_1 \sin (\theta_1) = n_2 \sin (\theta_2) \quad (23)$$

Where θ_1 and θ_2 denotes the angle of incidence and refraction, respectively.

The optical model performed Snell's law and the law of reflection between different optical interfaces based on the deterministic ray splitting approach.

The deposited ray power sub-node calculates the energy of concentrated rays that arrives on a surface relying on the incident ray's power based on Eq.(24).

$$Q_s = \frac{1}{A_i} \sum Q_j \quad (24)$$

Where Q_s is the boundary heat flux ($\frac{W}{m^2}$), A_i is the receiver surface area (m^2), $\sum Q_j$ is the sum of rays depositing power into the receiver (W). The thermal model governing equation is described in section 3.4.

4.4.2 Boundary Conditions

The numerical model was carried out using the "Geometrical Optic" and the "Heat Transfer in Solid" physics packages to compute the system optically and then thermally based on the "bidirectional coupled ray tracing". Optically, the top of the Fresnel lens was applied as an illuminated surface with a transmittance of 90%,

and the copper plate was set up as a freezing surface with a "Ray Deposited Power" sub-node. The optical dispersion of the system surrounding domain held constant at 20 °C. The Fresnel lens is designed in SOLIDWORKS software to produce a focal length of 42 cm as in [22]. Thermally, all domains are subjected to a convective heat transfer coefficient of $10 \frac{W}{m^2.K}$ and ambient temperature of 20 °C. The thermal emissivity considered as 0.9 for the copper plate. The copper plate was also assigned as a boundary heat source relying on the "Ray Deposited Power" sub-node, which is calculated in the "Geometrical Optic" physics module. In the optical model, the optical dispersion for the SOG Fresnel lens and the chromatic aberration assumed to be negligible. The defined position for the Fresnel and the copper sheet with its geometry is shown in Figure 26a, where the optical and thermal boundary conditions are illustrated in Figure 26b.

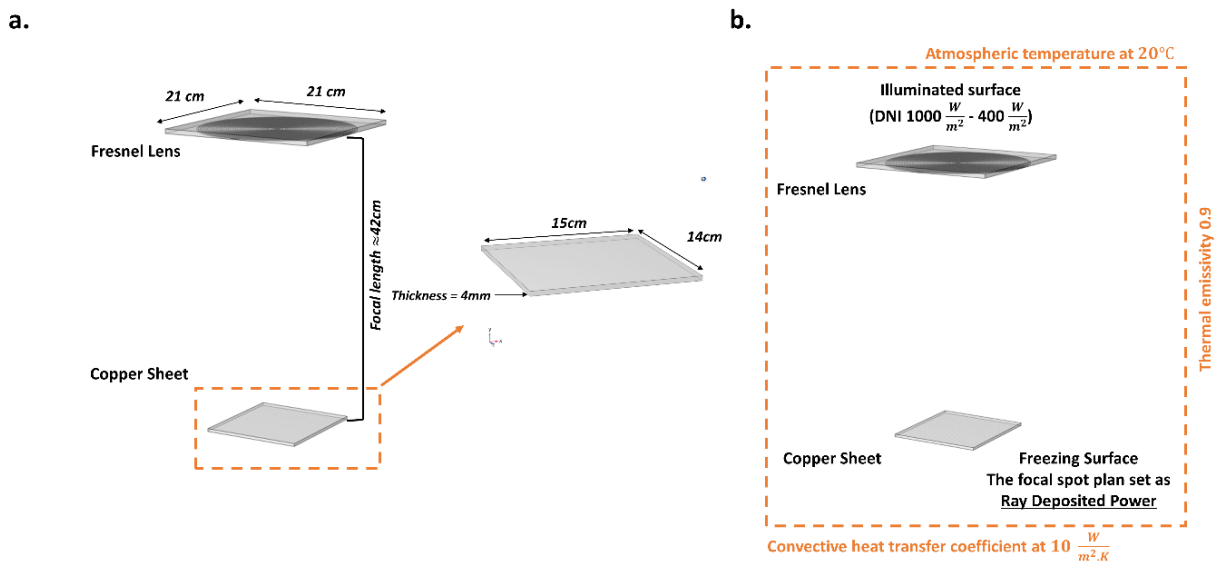


Figure 26 The asymmetric view for only the primary optic with the copper plate as a receiver where a. is the detailed geometry and b. is the optical and thermal boundary conditions.

4.4.3 Theoretical/Experimental Optical Validation

Theoretically optical characterisation in section 4.2 was carried out here conducting the same approach to validate the simulative optical concentration ratio ($C_{opt,sim}$) with $C_{opt,eff}$. To validate experimentally, the simulation results must consider the collimating angle of irradiance for the WACOM solar simulator, which is 1.43° , and then account for the measured η_{cell} under the concentrated sun rays, which is found to be 33.5% on average.

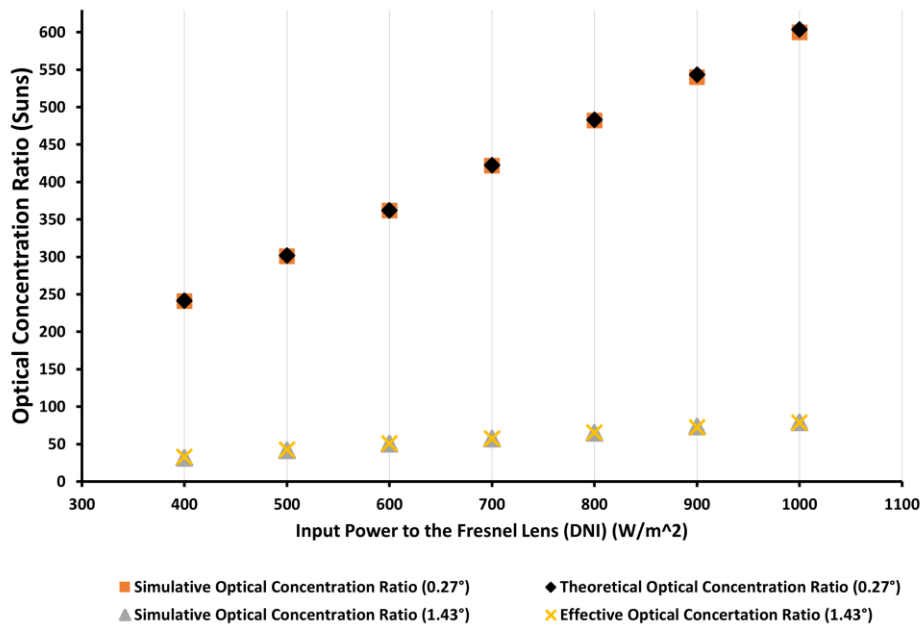


Figure 27 Shows the discrepancy between the simulative and theoretical optical concentration ratio with DNI arranging from 400 W/m^2 to 1000 W/m^2 in accordance with the input power to the Fresnel lens.

In Figure 27, the divergence of optical concentration between $C_{opt,eff}$ and $C_{opt,sim}$ is found to be 1.1% on average at 1.43° convergence angle, indicating a stable matching between the simulation and the experimental measurements. However, we can observe a drop in the optical concentration ratio at a convergence angle of 1.43° in comparison to the one at 0.27° because the large collimating angle

results in a wider focal spot than the solar cell area where some light rays are diverted away from the cell.

4.4.4 Experimental Validation for the Thermal Model

To measure the maximum temperature, the solar simulator illuminates the Fresnel lens, which concentrates solar irradiance to produce a focal spot on a copper plate. The simulated maximum temperature using COMSOL Multiphysics software and measured maximum temperature are in good agreement with an average discrepancy of 2.18%, as in Figure 28.

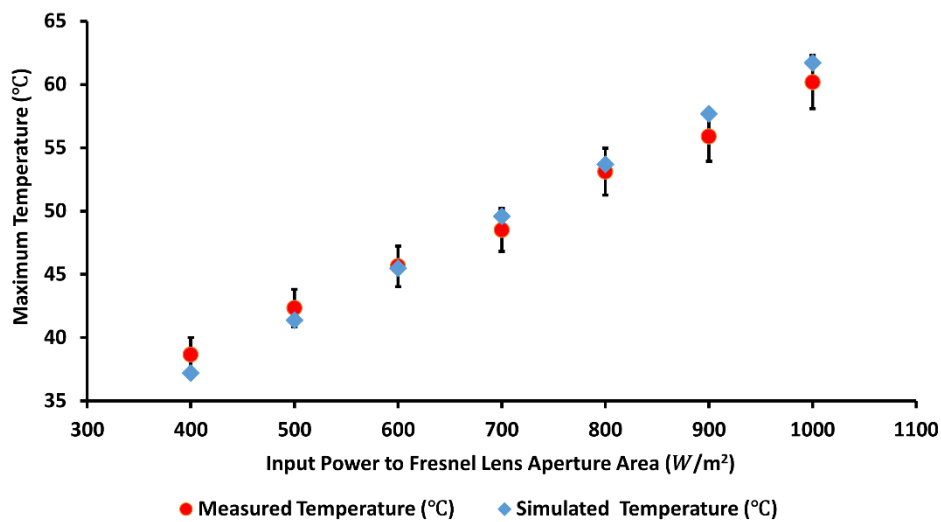


Figure 28 Validation for the predicted maximum temperature to the measured maximum temperature.

It has been ascertained that the conducted approach to validate the optical-thermal model is reliable, and we can extend its geometry to investigate the full UHCPV system design [38], which requires significant optical and thermal understanding before full-scale experimental testing can begin. Further details are in article 7.

4.5 Optical Losses of SOG Fresnel Lens

The durability of a cracked SOG Fresnel lens incorporated as the primary optical component in a CPV application must be considered to confirm if a cracked SOG Fresnel lens are more or less still fully functional or worthy of recycling. As highlighted in section 4.2, the utilisation of the focal spot is merely 16% which can be considered as a focal spot loss that will compromise the optical and electrical performance of both lenses equally. As in Figure 29, the percentage of the crack size to the full Fresnel lens area is estimated to be 2.7%.

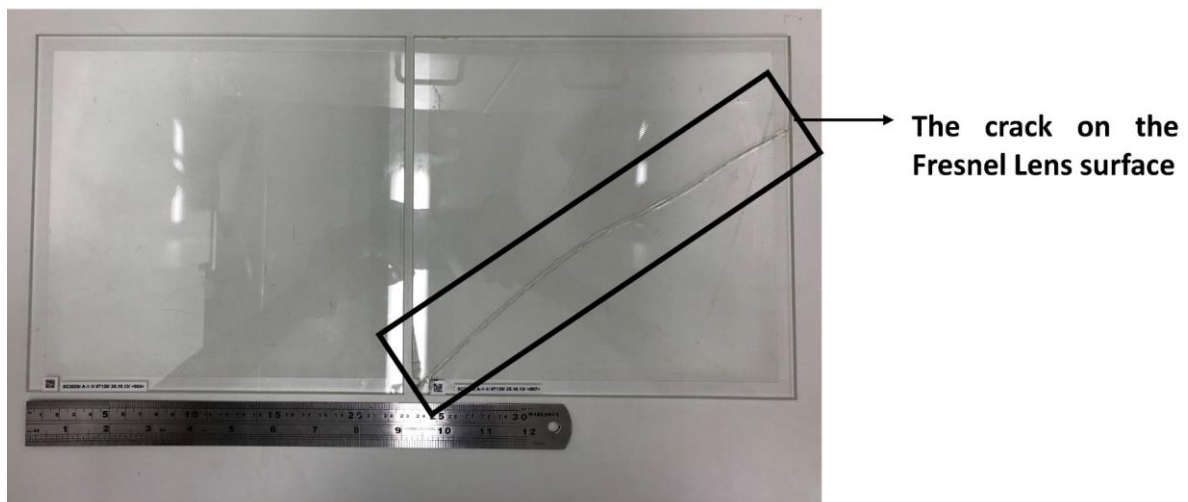


Figure 29 The flawed/ unflawed Fresnel lens.

Optical and electrical characterisations of the flawed glass have been conducted to show the effect on the performance using MJSC (Azur Space 3C44A $10 \times 10 \text{ mm}^2$). The lens optical efficiency was found to be an average of 91% and 88% and hence the concentration ratio after the Fresnel lens would be 480 *suns* and 463 *suns* for the non-cracked and cracked Fresnel lenses, respectively. The consideration of the fractional concentration loss as described previously results in system optical efficiencies of 15% and 14% and optical concentration ratios of 78 *suns* and 75 *suns* for the non-cracked and cracked Fresnel lenses, respectively. The optical characterisation has shown a drop of 3.2% in optical

efficiency. I-V and power curves of cracked and non-cracked Fresnel lens were compared and also show a drop of 3.2% in I_{sc} and power, Figure 30a and b. All successive optics performance in the singular CPV unit will be dependent on the performance of the primary flawed/unflawed Fresnel lens.

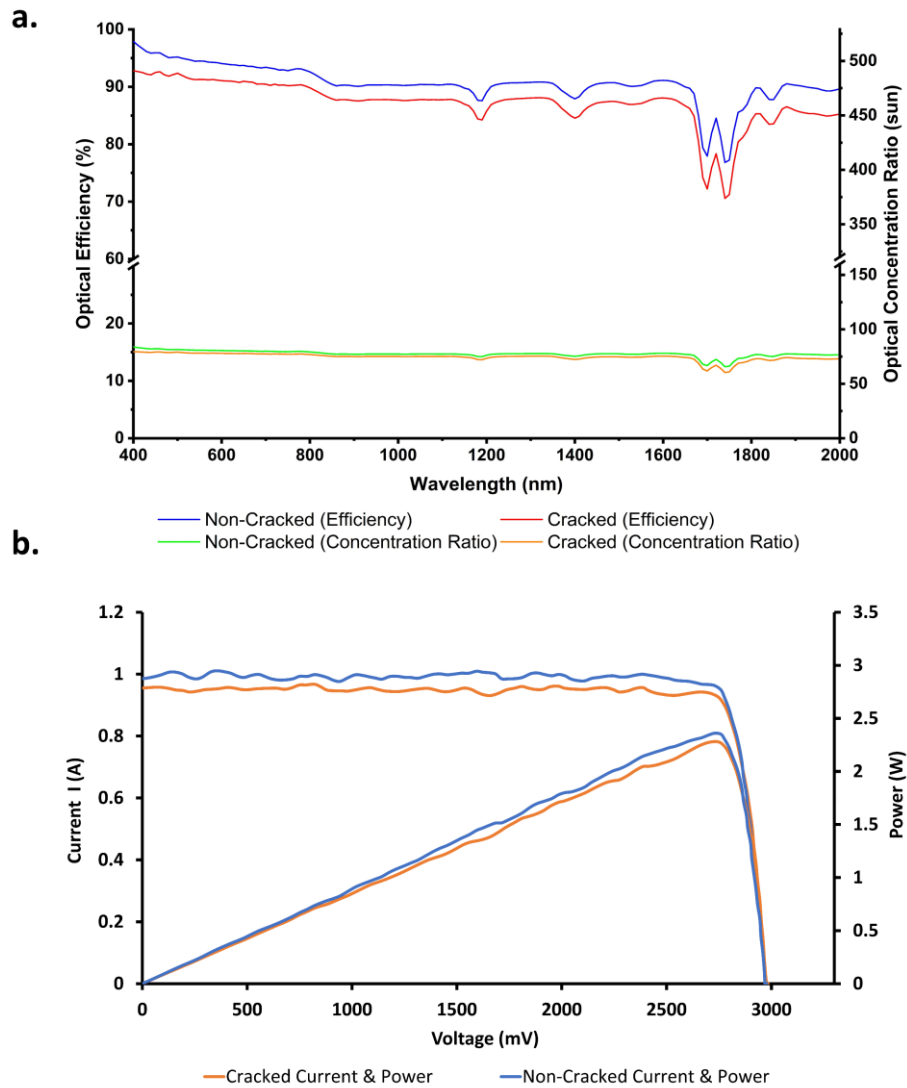


Figure 30 a) optical efficiency and optical concentration ratio (calculated using MJSC (Azur Space 3C44A $10 \times 10 \text{ mm}^2$) as a final optical stage) lines for the flawed/unflawed Fresnel lens. b) I-V & power curves for the flawed/unflawed Fresnel lens.

4.6 Conclusion

The optical performance of the primary optical component of the UHCPV (SOG Fresnel lens) has been evaluated theoretically and experimentally. The approach used simple indoor measurements to estimate the effective optical efficiency and concentration ratio, especially in a CPV. This optical characterisation shows that the optical performance decay is significantly due to the fractional concentration loss and the design conditions of single-junction solar cells. Also, the MJSC has shown minimal inconsistency in the experimental optical characterisation resulting in a discrepancy of 2% at 7.7 W. A concentrated solar irradiance on the cell from 3.1 to 7.7 W correspondent to input power in terms of DNI ranging from $400 \frac{W}{m^2}$ - $1000 \frac{W}{m^2}$, as fully scripted in article 6.

Further, a numerical model was built to investigate the SOG - Fresnel Lens optically and thermally. The model resulted in optical efficiency of 89.08%, an optical concentration ratio ranging from 600 *suns* to 240 *suns* and a maximum focal spot temperature ranging from 61.7 °C and 37.2 °C, corresponding to DNI ranging from $1000 \frac{W}{m^2}$ to $400 \frac{W}{m^2}$. This modelling result was validated experimentally in both the optical and the thermal models. Theoretically, the optical analysis showed an effective concentration ratio ranging from 604 to 242 *suns*, whereas experimentally, an effective concentration ratio ranged between 79 *suns* to 32 *suns*. Thermally, the experimental results showed a maximum temperature in the focal spot ranging from 60.2 °C and 38.67 °C corresponding to DNI ranging from $1000 \frac{W}{m^2}$ to $400 \frac{W}{m^2}$. The validation shows a strong agreement in the modelling results. The reliability of COMSOL Multiphysics software to numerically investigate a complicated UHCPV with

multiple optical stages has been ascertained. Full study and results are illustrated in article 7.

In addition, the durability of an SOG Fresnel lens was characterised optically and electrically and compared to a flawed SOG Fresnel lens. This approach allows estimating the percentage of the crack size to the overall Fresnel lens area, then estimating the optical performance (optical efficiency and optical concentration ratio) and investigating its influence on the electrical performance. A loss of 3.2% optically and electrically should be low enough for similarly flawed and damaged optics to still be used or recycled for low demand projects and installations. The durability of such systems however, requires further study. This characterisation in full written in article 3.

In this chapter, the entire investigation of the SOG Fresnel lens helped us understand the operative limits before proceeding with the complete system modelling and fabrication. The next chapter will focus on finding a cooling solution based on a pre-illumination technique to control the resultant heat from the SOG Fresnel lens's primary optical components on the solar cell.

CHAPTER 5: Alternative Cooling Mechanism for Concentrated Photovoltaics

5.1 Introduction

High electrical power outputs require maximising the geometrical concentration ratio, this can only occur for CPV systems with high optical efficiencies. However, the optical efficiency is practically compromised electrically depending on the solar cell's electrical performance. Attention needs to be paid to the amount of concentrated light and resultant generated heat on the solar cell's surface to minimise the solar cell's electrical series resistance increase. It is a possible solution to reduce the temperature elevation by reducing the geometrical concentration ratio, but this approach does not fit with the trend of increasing the electrical power output within CPV research [17]. Alternatively, this trend can be followed by increasing the concentration ratio and combatting the negative effects of the generated temperature using a cooling mechanism. Post-illumination or pre-illumination cooling techniques are essential for maintaining solar cell performance and reliability for safe operation, especially toward high and UH concentration ratios. Post-illumination is the conventional solar cell cooling mechanism, including passive cooling and active cooling, which are mainly based on the engineering design concepts and heat transfer components: conduction, convection, and radiation [114]. In a passive cooling approach, a variety of heatsink dimensional configurations [4] are used in an attempt to maintain the solar cell at safe operating conditions for MJSCs [40,115–118] which can be more vulnerable to such high temperatures when compared to single-junction silicon-based cells. On the contrary, active cooling has proven its competence in solar cell thermal management at the cost of a parasitic load, especially with increasing the concentration ratio adding to the required load, the system complexity, and the overall system cost [110,119–122]. In pre-illumination, spectral

decomposition [14,70] -including ultraviolet (UV), visible (VIS), and near-infrared (NIR) - for the solar spectrum allows bandpass and bandstop. These pre-illuminations mechanisms can lead to high cell conversion efficiencies bypassing the compatible photon energy to the PV cell and redirecting the photon energy with energy more than the bandgap energy to reduce the cell temperature. Unique configurations including spectral beam splitting (SBS) [15], hot or cold mirrors [123], holographic optics [124], and luminescent concentrator beams [125], have been mainly focused on improving the cell efficiency by reducing the heat generation. This spatial pre-illumination approach represents high efficiency in low concentration ratio applications, but it becomes a very complex approach with a high concentration ratio due to the tracking system.

Although the increase of concentration ratio on the MJSC would produce more power despite their low efficiency beyond 1000 *suns*, the expensive low internal resistance MJSC cannot overrun a temperature of 110 °C [91]. Indeed, this temperature influence will be excessive for single-junction solar cells without cooling mechanisms. In order to address this issue, ND filter is fabricated utilizing a graphene material to attenuate the transmittance of solar irradiance over a wide spectral band. The optical density (*OD*) of graphene material, from colourless to dark in appearance, regulates the amount of energy incident on the cell at which heat generated on the solar cell is controllable in inverse correlation with optical density. Although using graphene as a ND filter causes an optical loss across the wavelength range evenly, the excellent opto-thermal properties of graphene improve the system by reducing the focal spot temperature at which a higher cell efficiency is achieved. Since the temperature influence will be excessive for single-junction solar cells designed to cope with 1 sun, the validation of the developed graphene ND filter is performed with polycrystalline Si solar cell.

Figure 31 shows a graphical abstract for positioning a graphene ND filter in the CPV unit and thermal processes. This chapter is thoroughly detailed in both articles 4 and 5.

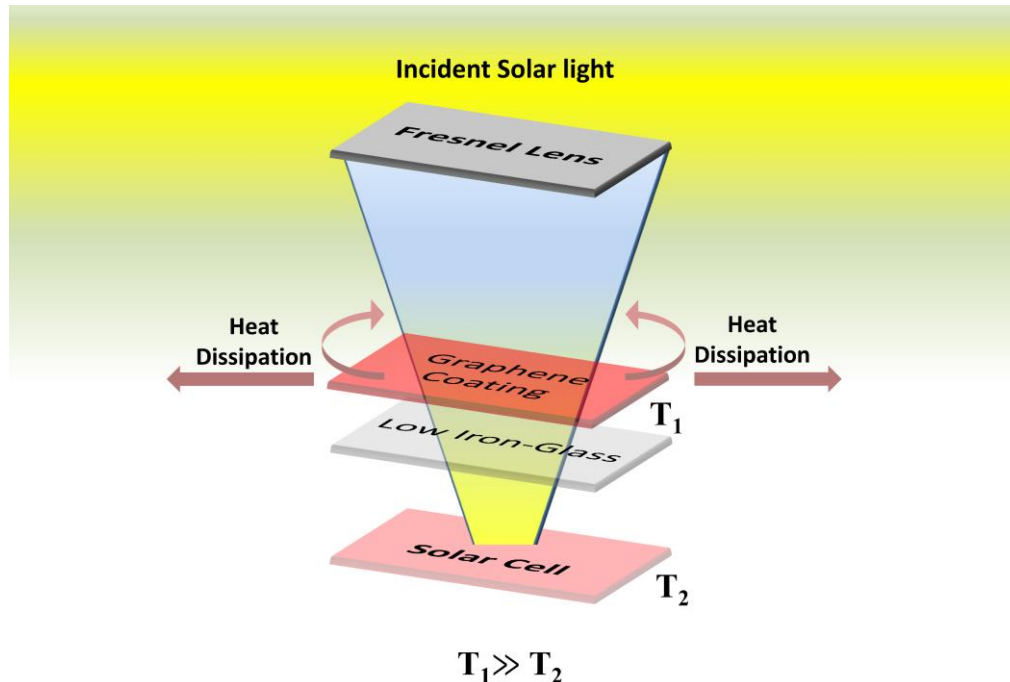


Figure 31 The positioning of a graphene ND filter in the CPV unit and its working principle.

5.2 Preparation of Graphene Coating and Characterisations

The graphene coating (GC) is executed using graphene ink without further purification. A layer of graphene ink is applied to develop the coating on a $5 \times 5 \text{ cm}^2$ low iron-glass (4 mm thick) by a screen-printing (120T mesh/inch, Mascoprint, UK) method. The low-iron glass-coated samples were characterised based on graphene quantity: thick, medium, and thin coatings. Using one layer of graphene screen printing coating resulted in an average thickness of $2.2 \pm 0.2 \mu\text{m}$, which is termed a thin coating (GC_{2.2}). Two and three layers of graphene ink are used to fabricate an average thickness of 6.3 ± 0.1 and $9.1 \pm 0.05 \mu\text{m}$ of

coating and termed as medium (GC_{6.3}) and thick coating (GC_{9.1}). These three thickness-based GCs are determined using SEM.

Further, the prepared samples' optical characterisation was conducted using a PerkinElmer LAMBDA 1050+ UV/Vis/NIR spectrophotometer in a spectral range of 300 – 2000 *nm*. Both the electrical and thermal performance were conducted under a WACOM AAA rating solar simulator. The adjustment of an SOG Fresnel lens and resultant focal length and focal spot is highlighted in section 4.2. The thermal characterisation relied on both the thermal camera and the thermocouple to assess the temperature levels on the graphene ND filter itself and the generated focal spot temperature on the solar cell. With the developed graphene ND filter, the IR filter was characterised and utilised to compare the performance as it is the most used filter for heat reduction in solar systems.

5.3 Overall Characterisation Results

Table 6 shows the results for the four different characterisation approaches (chemical, optical, thermal, and electrical). As highlighted, the results confirmed that graphene is an appropriate material for an ND filter with optimum performance for the GC_{6.3}. Although the IR filter with a cooling mount base showed the lowest focal spot temperature of 55 °C and a relatively similar *FF* value with GC_{6.3}; however, that is at the price of system weight, cost, and parasitic load. For the case of the IR filter associated with the cooling mount base, the focal spot temperature is given by considering the equilibrium temperature of 25 °C for the cooling mount base and 117.28 °C for the focal spot temperature after the IR filter, which results in a focal spot temperature of 55 °C. Also, the IR filter has shown a lower power output than GC_{6.3} because GC_{6.3} attenuates the intensity of solar irradiance across the wavelength range where the IR filter blocks

all wavelengths beyond visible light with less control on the focal spot temperature. The optimisation for the graphene thickness coating still has the potential to improve the overall performance further. It has been ascertained that the introduction of graphene as the ND filter component improved the solar cell efficiency instead of just reducing the optical concentration ratio by not using any filter. Details of both characterisation and results are fully illustrated in article 4.

Table 6 The summary of the characterisation results for the graphene ND filter.

| Graphene Neutral density (ND) filter | Chemical Characterization | Optical Characterisation | | | | Thermal Characterisation | Electrical Characterisation | |
|--|--------------------------------|--------------------------|-------|------------------------|---|--|-----------------------------|------------------|
| | Graphene thickness (μm) | Total transmittance (%T) | OD | Optical Efficiency (%) | Optical Concentration ratio (<i>suns</i>) | Focal Spot Temperature ($^{\circ}C$) | Power output (W) | Fill Factor (FF) |
| Fresnel Lens | - | 90 | 0.045 | 90 | 18 | 219 | 1.5 | 0.32 |
| IR filter + cooling Mount @ 25 $^{\circ}C$ | - | 19 | 0.72 | 18 | 4 | 55 | 1.13 | 0.442 |
| Glass No Coating | - | 89 | 0.05 | 80 | 16 | 196 | 1.49 | 0.329 |
| Thick Coating (GC _{9.1}) | 9.1 \pm 0.05 | 2 | 1.69 | 2 | 1 | 24.6 | 0.11 | 0.746 |
| Medium Coating (GC _{6.3}) | 6.3 \pm 0.1 | 43 | 0.36 | 42 | 8 | 66.4 | 1.34 | 0.446 |
| Thin Coating (GC _{2.2}) | 2.2 \pm 0.2 | 64 | 0.19 | 58 | 12 | 132.7 | 1.49 | 0.376 |

5.3.1 Graphene Layer Validation and Cost Analysis

To validate that the improvement in power output is predominantly due to the graphene layer, we have attenuated the solar simulator (WACOM) lamp intensity (helicon value) to examine the polycrystalline silicon (Si) solar cells at different solar irradiance values in the range of $400 - 1000 \text{ W/m}^2$ in an interval of 100 W/m^2 without GCs. This attenuation of input solar irradiance to the concentrator optic (Fresnel lens) results in a lower concentration ratio in the focal spot area, which could increase the FF and hence the cell efficiency without GCs. Figure 32 shows the downward slope of the cell efficiency from 5.96% to 2.44%, increasing the effective solar irradiance on the focal spot area for solar irradiance from 400 W/m^2 to 1000 W/m^2 , corresponding to an optical concentration ratio range from 7 *suns* to 18 *suns*. The GC_{6.3} and GC_{2.2} show a cell efficiency of 6.57% at 8 *suns* and 4.91% at 13 *suns* with effective solar irradiance on the focal spot at 1000 W/m^2 . The relatively low cell efficiency to the maximum cell efficiency of 17% [23] as reported by the manufacturer is simply due to using the single-junction solar cell beyond its design concentration range (1 *sun*). Still, this utilization was essential to see the temperature and concentration ratio reduction effects. The closest optical concentration ratio for the GC_{6.3} at 8 *suns* is the base case at 400 W/m^2 with an optical concentration ratio of 7 *suns* but with less efficiency by 12%, whereas the closest optical concentration ratio for the GC_{2.2} is the base case at 700 W/m^2 with an optical concentration ratio of 12.8 *suns* but with less efficiency by 28%. This comparison has certainly confirmed that the cell efficiency has been improved due to the integration of graphene as an ND filter instead of lowering the concentration ratio. Thus, in theory, the same benefits should be replicable for a MJSC under UH concentration ratios. The GC_{6.3} represent the highest cell efficiency.

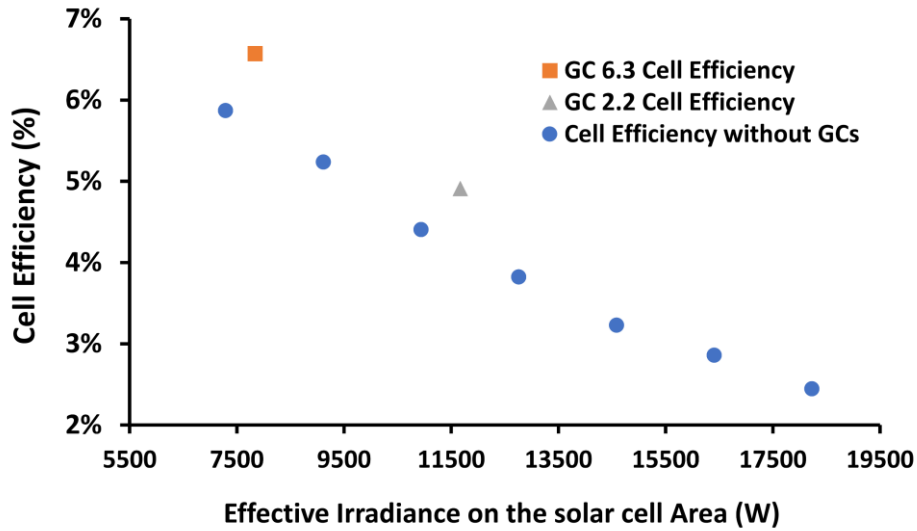


Figure 32 The cell efficiency versus the effective solar irradiance on the focal spot.

5.4 Orientation Effect for Graphene ND Filter

The impact of graphene orientation, whether normal to the solar cell area or the Fresnel lens area, is analysed further electrically and thermally, considering its effects on the polycrystalline Si solar cell efficiency. Schematic is given to illustrate the overall experimental set-up configuration highlighting the graphene layer orientation. It faces the source of solar irradiance and the solar cell, as in Figure 33a and b, respectively.

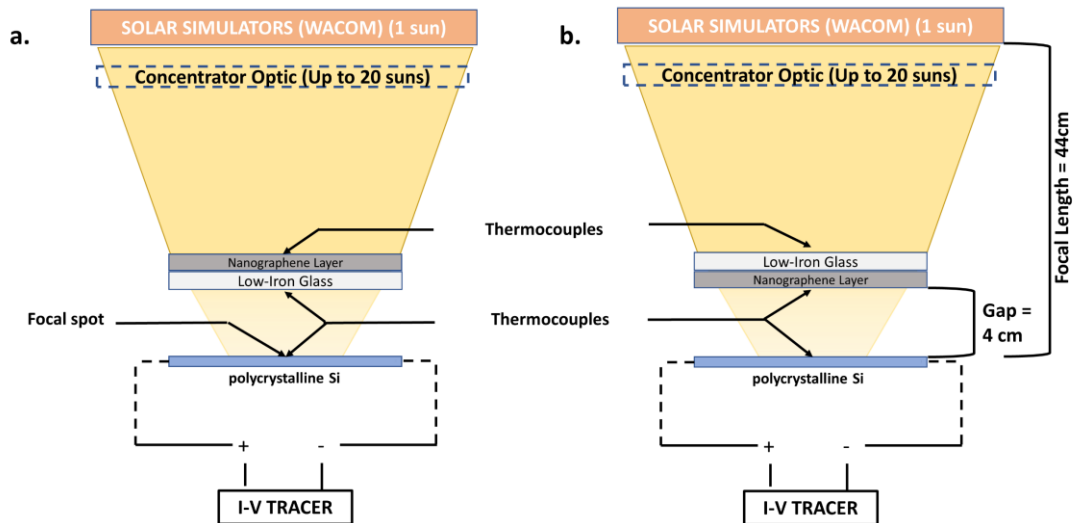


Figure 33 Schematic representation for the entire experimental set-up summarising the experimental approach in which (a) GC faces the source of the concentrated solar irradiance (SOG Fresnel lens), and (b) GC faces the solar cell.

The cell efficiency for the GC_{9.1} was the highest. This is because the solar cell was subjected to the lowest concentrated solar irradiance and hence heat, in comparison to the samples, as its transmissivity was only 2%, representing the lowest power output of 0.25 W and 0.18 W for GC facing the source of the solar irradiance and GC facing the solar cell, respectively. The difference in cell efficiency for GC_{9.1} between GC facing the solar irradiance and the GC source facing the solar cell was 26.4%. GC_{6.3} and GC_{2.2} demonstrated 6.6% and 4.9% efficiency for the GC facing the solar irradiance source and 5.9% and 4% for the GC facing the solar cell. The GC orientation, either facing the solar cell or the solar irradiance source, resulted in a solar cell efficiency discrepancy of 11% and 17% for GC_{6.3} and GC_{2.2}, as in Figure 34.

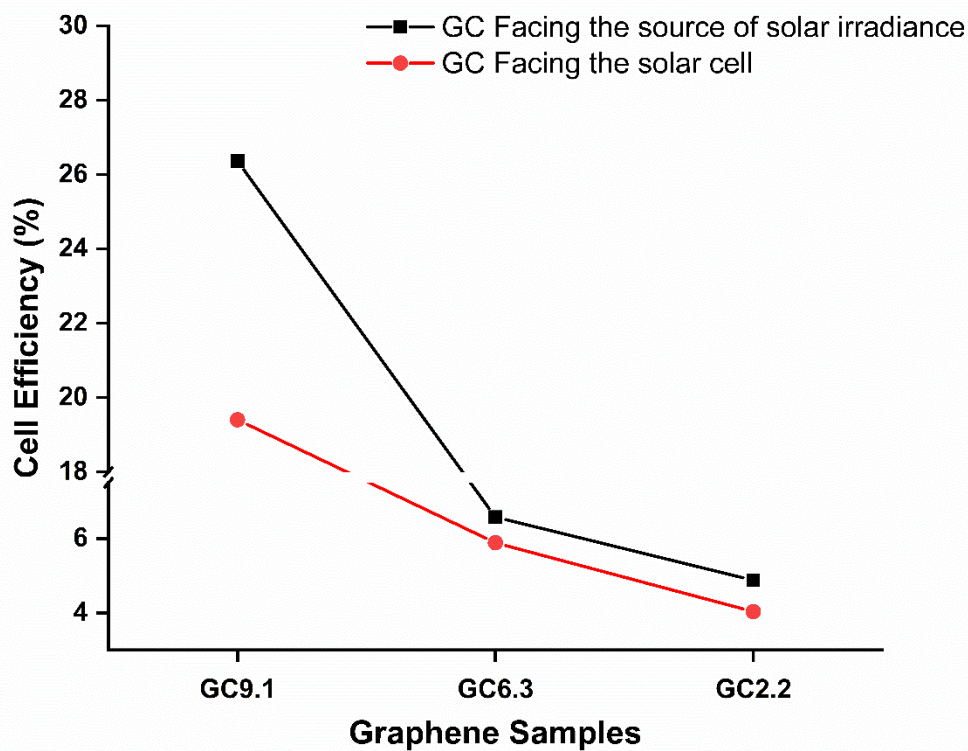


Figure 34 The cell efficiency of the single-junction (polycrystalline Si) solar cell for the GC facing the source of solar irradiance and GC facing the solar cell.

The thermal characterisation was further extended to analyse the thermal behaviour due to GC orientation. The temperature on the GC_{9.1} surface was found to be less than on the surface glass for the GC_{9.1} facing the source of the solar irradiance by 50%. In contrast, the temperature on the GC_{9.1} surface was found to be less than the surface glass for the GC_{9.1} facing the solar cell by 7%. The temperature on the GC_{6.3} surface was lower than on the surface glass for the GC_{6.3} facing the source of the solar irradiance by 17%. On the other hand, the temperature on the GC_{6.3} surface was lower than the surface glass for the GC_{6.3} facing the solar cell by 15%. Also, the temperature on the GC_{2.2} surface was higher than the surface glass for the GC_{2.2} facing the source of the solar irradiance by 15%.

On the contrary, the temperature on the GC_{2.2} surface was lower than the surface glass for the GC_{2.2} facing the solar cell by only 2.2%. Using a low-iron glass as a base for graphene material to form the ND filter suffered excessive thermal stress.

5.5 Conclusion

Three graphene ND filters were developed to attenuate the concentration of solar rays for a CPV system. To fabricate and characterize the ND filter, four different approaches: chemical, optical, thermal and electrical characterizations have been adopted for a comprehensive understanding of the filter. All four characterisation approaches have confirmed that the performance is dependent on the graphene thickness. The indoor experiment has been conducted for a polycrystalline Si solar cell, which is vulnerable to the observed level of temperature generated by an SOG Fresnel lens (with a geometrical concentration ratio of ≈ 20 suns). The results have indicated graphene can be brought into play as an ND filter component for a pre-illumination passive cooling mechanism. The simplistic employment of GC as an ND filter component can eliminate the traditional and strenuous cooling techniques such as active water cooling and combined heat pipe cooling for CPV. Although, the optimization of the GC thickness still has the potential to improve the overall performance further. Detailed are fully scripted in article 4.

An extended thermal analysis has shown various aspects of the GC and its influences on the temperature gradient of the glass sample and its corresponding electrical output through the cell efficiency. Using low-iron glass as a base for graphene material to form the ND filter is not a durable solution. We have concluded that low-iron glass is not suitable for integrating with the GC through

thermal analysis. This is confirmed through the breakage of glass samples under extended solar concentration exposure, further details are given in article 5.

For the SOG Fresnel lens as a primary optical component for the UHCPV system, the findings here showed the graphene ND filters as a tangible cooling solution with the potential to be incorporated in the UHCPV system to maintain the temperature on the solar cell surface area. The next chapter will theoretically and numerically investigate the $\frac{1}{4}$ of the UHCPV system. The numerical investigation accounts for the optical and thermal models to estimate the optical performance and temperature limits on every optical stage after the primary one.

CHAPTER 6: Theoretical/Numerical Assessment for UHCPV System

6.1 Perspective of UHCPV System

The SOG Fresnel lens is 1 of 4 identical primary optics, which would make up the entry aperture for the UHCPV system of concentration ratio > 3000 suns. The subsequent optics, which are flat reflective mirrors and tertiary optics on the top of the solar cell, are theoretically discussed, accounting only for three optical stages starting with the Fresnel lens to the flat plain reflective optical mirror ending with the tertiary optic. There is a potential for the UHCPV to include 2 flat mirrors accounting four optical stages. Due to the fractional concentration loss, significant optical losses occur when compromised electrically, as is explained systematically in section 4.2. Incorporating more than one optic in the CPV system results in increasing the concentration ratio through minimised sunray divergence. There will likely still be some loss and hence the optical efficiency of 14.6% due to the fractional loss is considered as the worst-case scenario through which the UHCPV system will be theoretically analysed and discussed. Certainly, the fractional loss would increase with increasing the concentration ratio. Checking the irradiance distribution of the Fresnel lens would reflect an increase in the fractional loss. If the short-circuit current shows an effective concentration value significantly higher than the fractional loss indicated then the majority of the irradiance was actually focused on the inner area of the focal spot – where the solar cell are placed, which would be important to know for the UH system. Still, the UH system is strongly influenced by alignment, manufactured optical materials, the temperature of optics and divergence angle of light source.

In the design of the UHCPV system, four or three optical interfaces will be incorporated to examine the possibility of accomplishing an UH level configuration. In the case of four optical stages, the sunrays will be refracted from

the Fresnel lens into the flat reflective secondary mirror, which reflects concentrated sun rays into the tertiary flat central mirror. Afterwards, the tertiary flat central mirror will reflect the concentrated rays into the low refractive tertiary optic as a final optical stage. Although this amount of optics in one system will add to the complexity of the fabrication and challenge the accuracy and alignment of the system, the subsequent optical stages are a flat mirrors which should have minimal light divergence effects if of high quality. These optical stages will aid the system at which the convergence angle is minimised (less fractional concentration loss), resulting in increased concentration ratio. Inherently, a minimum light divergence (the maximum angle from the furthest incident rays from the normal axis to arrive at the focal spot) has a smaller acceptance angle, adding to the tracking system load and accuracy requirement. In the UHCPV system, the concentrated rays would still not converge enough into the solar cell area, resulting in a reduction in the optical efficiency and hence in the optical concentration ratio. Although the UHCPV system aims to incorporate smaller MJSC for higher geometrical concentration ratio, less heat generation, and higher cell efficiency, the CPV system is challenged in design and alignment accuracy. Refractive optics are suggested and implemented on the top surface of the solar cell. Although tertiary optics would decrease the optical efficiency also, tertiary optics improve the acceptance angle and the uniformity of irradiance distribution and that would potentially improve effective concentration. This chapter is detailed in both articles 6 and 8.

6.2 Theoretical Overview – Different Secondary Mirror Coatings

The UHCPV system consists of Fresnel lenses, as primary refractive optics, reflective mirror, as secondary optics, and a tertiary centre optic, as final refractive optic attached on the solar cell, as shown in Figure 35.

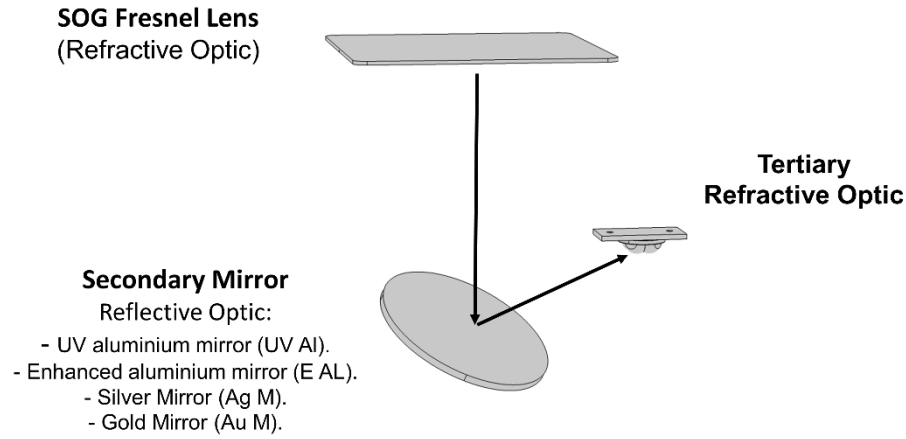


Figure 35 Illustration for the ray path and optical setup: primary optic, secondary optic, and tertiary optic.

The secondary reflective mirror will be interpolated for four different metallic coatings (MCs): UV aluminium mirror (UV Al), enhanced aluminium mirror (E Al), silver mirror (Ag M), and gold mirror (Au M). These secondary mirrors' optical efficiencies (Reflectance %) are retrieved from the NEWPORT Corporation [126]. The optical efficiency is showing the losses for three optical stages, first the SOG Fresnel lens material absorption and scattering, second the mirror's coatings reflectivity, and third the tertiary optics absorption and scattering, solved for as in Eq.(25).

$$\eta_{opt,th} = \eta_{Fresnel\ lens} \times \eta_{MC (UV\ Al, E\ Al, Ag\ M, and\ Au\ M)} \times \eta_{SK-700} \quad (25)$$

Hence, the three stages' performance would produce the final optical efficiency and concentration ratio for only $\frac{1}{4}$ of the system, when all 4 lenses and mirrors are in place the concentration would be $\times 4$ (as all focal spots from each of the 4 Fresnel lenses are redirected via flat mirrors towards the centre [38]. To consider different geometrical concentration ratios, the utilization of three different receivers was theoretically analysed, as in Figure 36.

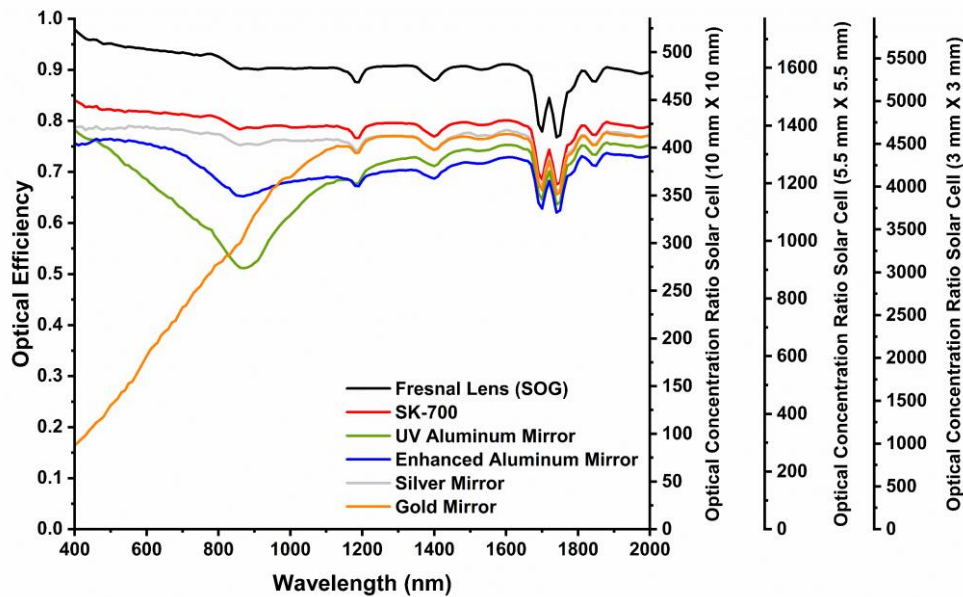


Figure 36 Theoretical optical efficiency with wavelength (400 – 2000 nm) for four different reflective mirrors as a secondary optical stage associated with both the Fresnel lens and the SK-700. The optical concentration ratio computed relying on a solar cell area of $10 \times 10 \text{ mm}^2$, $5.5 \times 5.5 \text{ mm}^2$, and $3 \times 3 \text{ mm}^2$ as a final stage and no fractional losses. This is only for $\frac{1}{4}$ of the UHCPV.

Achieving high optical efficiency for $3 \times 3 \text{ mm}^2$ cell and optics setup as its maximum geometrical concentration ratio would become $23,511 \times$, which it seems unlikely to be reached in real-life testing conditions within the current available optics and manufacturing. Given the fractional loss optical efficiency of 14.6%, the system optical concentration ratio would be 3433 suns , which is still within the target of the design of $> 3000 \text{ suns}$. However, such an analysis is given to illustrate how substantial the effect of the final receiver size on the concentration ratio. On average, the theoretical optical concentration ratio has been computed for a spectral band from 400 – 2000 nm, as plotted in Figure 37.

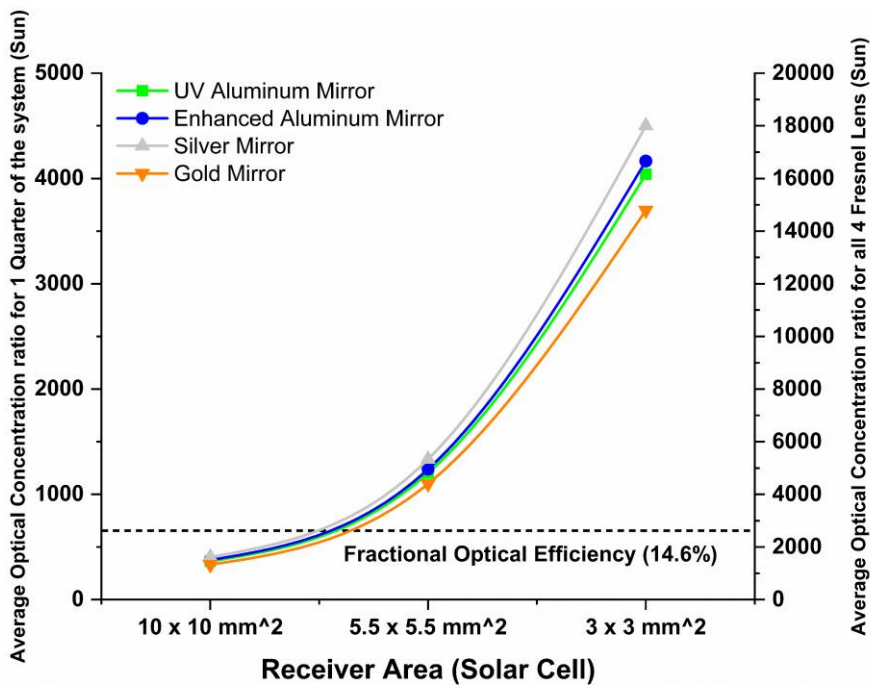


Figure 37 Optical concentration ratio plotted for three sizes of the final receiver (solar cell) and for four types of metallic coatings associated with the tertiary optic (SK-700) and the Fresnel lens, highlighting the consideration of optical fractional loss.

The optical losses are more likely to occur due to further transmittance and reflectiveness loss. Also, the amount of the accumulated heat at the focal spot due to the UH concentration ratio might induce other losses when compromising the optical performance electrically as the electrical performance deteriorates if no suitable cooling mechanism is in place. The secondary reflective mirror's function is to minimise the light divergence, and the tertiary optics role is to funnel as much of the focal point light and concentrate it further to the cell active area, hence minimising the geometrical fractional loss. The tertiary optic only reduces fractional loss but adds some absorption/scattering to the concentrated light. So, the added dashed line in Figure 37 gives a theoretical estimate of the minimum concentration ratio for the system. The aim is to build a prototype that falls within the solid lines and the dashed lines. Given the limits of UH concentration ratio of

> 3000 *suns* and the calculated theoretical concentration ratio based on the selected optical mirror, the range of optical losses differ depending on the optical stages and their optical performance for solar cell area of $5.5 \times 5.5 \text{ mm}^2$ and $3 \times 3 \text{ mm}^2$ wherein our case is based on the selected optics. The detailed losses based on the performance of the coated reflective mirror have been listed in Table 7.

Table 7 The range of optical concentration ratio loss based on the selected optics and the metallic coating type for the secondary reflective mirror and solar cell area of $5.5 \times 5.5 \text{ mm}^2$ and $3 \times 3 \text{ mm}^2$

| Solar cell Area (mm) | The range of optical concentration ratio losses (%) | | | |
|----------------------|---|---------------------------|---------------|-------------|
| | UV Aluminium Mirror | Enhanced Aluminium Mirror | Silver Mirror | Gold Mirror |
| 5.5 × 5.5 | 37.6% | 39.4% | 43.8% | 31.8% |
| 3 × 3 | 81.4% | 81.9% | 83.3% | 79.7% |

6.3 Numerical Evaluation for ¼ UHCPV – Three Optical Stages

To follow up the theoretical assessment, an optical-thermal numerical investigation is performed to evaluate the system's performance and anticipate the temperature limits in correlation with optical input power and concentration ratio under different levels of DNI ranging from 400 W/m^2 to 1000 W/m^2 in an interval of 100 W/m^2 . In the thermal model, wind effect is included by varying the natural convective heat transfer coefficient between $4 \left[\frac{\text{W}}{\text{m}^2 \cdot \text{K}} \right]$ and $22 \left[\frac{\text{W}}{\text{m}^2 \cdot \text{K}} \right]$ and the outdoor temperature between $20 \text{ }^\circ\text{C}$ and $50 \text{ }^\circ\text{C}$ is also investigated. All the governing equations are previously illustrated in sections 3.4 and 4.4.1. The identification of the focal spot experimentally under the solar simulator for the SOG Fresnel lens helped primarily to set-up the model. Afterward, adjustments were made to determine the distance between optics. Moving optics by a

millimetre or an angle of a degree has considerable influence on the results. Repeated alignment adjustments were carried out until the model revealed the maximum optical simulative concentration ratio at which the distances between optics were ascertained. It should be noted that alignment such as this, for UH concentration levels, is very time consuming especially since this was only $\frac{1}{4}$ of the system and future manufacturing will need to incorporate accurate placement and testing technology. The optimum distances among optics were found and illustrated along with the optical geometries, as in Figure 38.

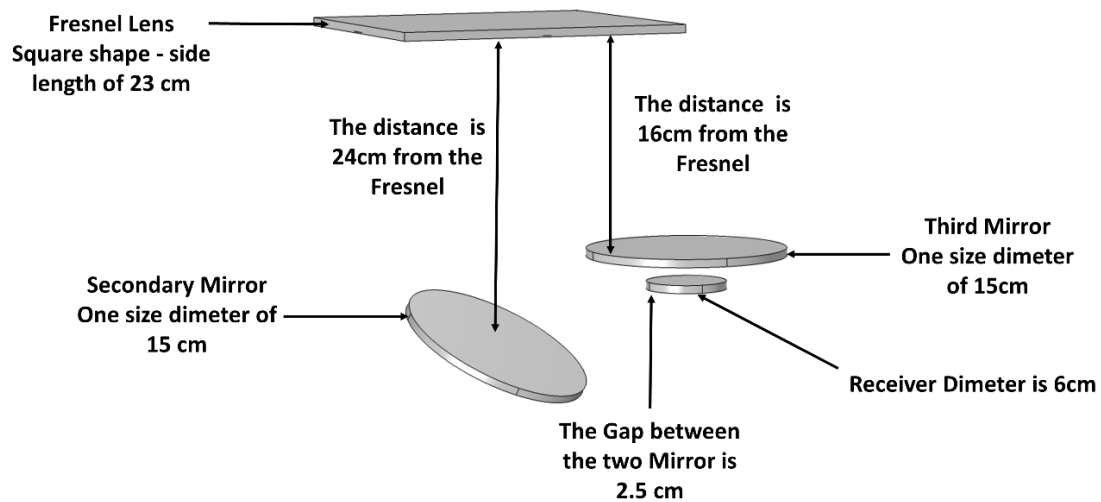


Figure 38 Asymmetric view of $\frac{1}{4}$ of UHCPV system with geometrical illustration and optimum position for the highest optical performance.

6.3.1 Optical Boundary Condition

The top surface of the Fresnel lens domain is selected as an illuminated surface under DNI, assuming that the released rays are refracted from an exterior radiation source and the external domain has refractive index of 1 like air. The Fresnel lens established with a transmissivity of 90% and illuminated with 30,000 rays. Both secondary and tertiary reflective optics are established as specular reflection wall of 95%. The model was set up to compute both the intensity and power of the concentrated rays on the optics interfering with the concentrated

rays. The heat source calculation is carried out in the secondary and tertiary reflective optical stage and the receiver using the ray deposited power function. The receiver is established as a freezing domain. The optical dispersion for the external domain is kept at the initial temperature of 20 °C. The optical model assumes that there is no chromatic aberration effect and the optical dispersion of the SOG Fresnel lens is negligible. Figure 39 details the boundary condition for the optical model.

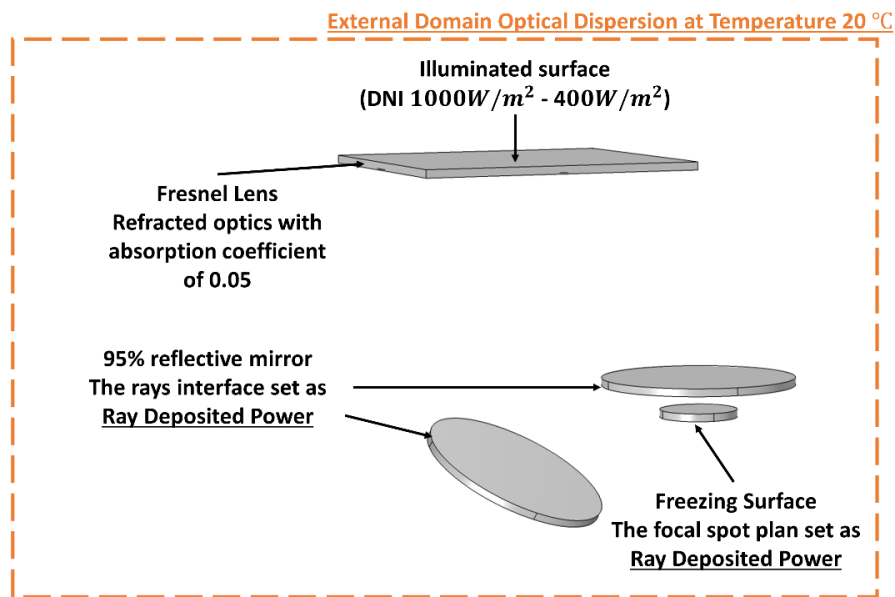


Figure 39 The optical boundary condition as in COMSOL Multiphysics software for a ¼ UHCPV system.

6.3.2 Thermal Boundary Condition

To establish the boundary condition for the heat transfer in the solid model, all optics were assigned $Q_{conv.}$ and surface-to-ambient radiation $Q_{rad.}$. Within heat flux, the model was investigated with a parametric sweep for the ambient temperature at 20 °C and 50 °C and convective heat transfer coefficient at $4 \frac{W}{m^2.K}$ and $22 \frac{W}{m^2.K}$. This parametric sweep study aimed to observe the thermal model in relatively excellent weather conditions (safe operating condition) for the

combination of ($20\text{ }^{\circ}\text{C}$ and $22\frac{\text{W}}{\text{m}^2\cdot\text{K}}$) and for extreme weather conditions (worst operating condition) for the combination of ($50\text{ }^{\circ}\text{C}$ and $4\frac{\text{W}}{\text{m}^2\cdot\text{K}}$). The radiation heat transfer model has an emissivity product of 0.82 for the aluminium surfaces [127]. Boundary heat source nodes were selected for all optics successive to the Fresnel lens. Through these nodes, the calculated ray deposited power in the optical model was interlinked with the boundary heat source in the thermal model to find a solution. The thermal model has no thermal insulation selections. Figure 40 illustrates the boundary condition for the thermal model.

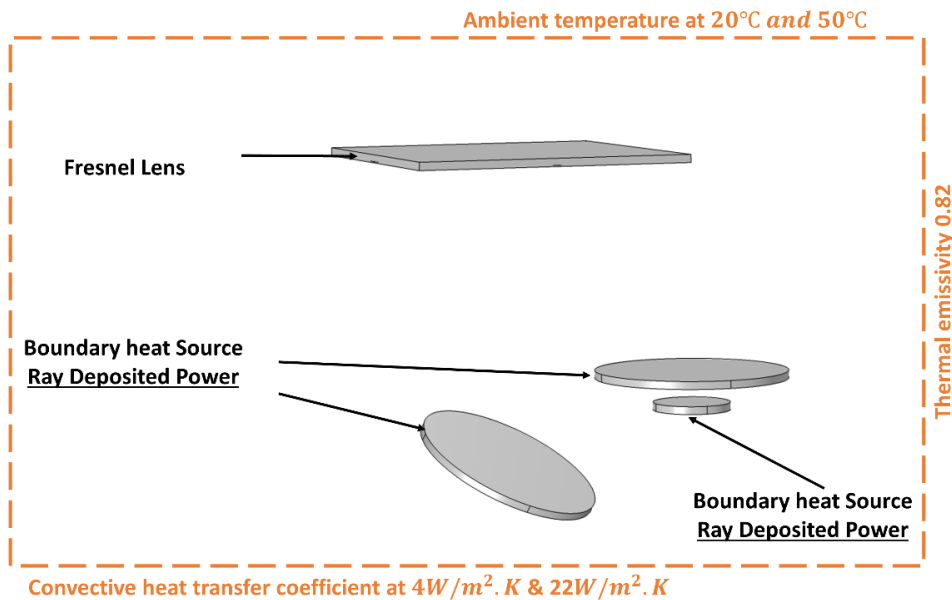


Figure 40 The thermal boundary condition as in COMSOL Multiphysics software for a $\frac{1}{4}$ UHCPV system

6.3.3 Simulative Optical Performance

The deposited ray power was assessed on every optical stage subsequent to the Fresnel lens. Knowing the boundary heat source on the optics prior to the receiver illustrates the losses in the boundary source power of concentrated rays. At DNI of $1000\frac{\text{W}}{\text{m}^2}$, the boundary heat source on the optical interfaces was found to be $1.28 \times 10^3\frac{\text{W}}{\text{m}^2}$ (1 sun), $10 \times 10^3\frac{\text{W}}{\text{m}^2}$ (10 suns), and $1.361 \times 10^6\frac{\text{W}}{\text{m}^2}$ (1361 suns)

on the surface of the secondary mirror, tertiary mirror, and the receiver, respectively. The boundary heat source on the final receiver resulted in simulative optical efficiency ($\eta_{simulative\ optical} = 93\%$). The irradiance distribution on the optics influenced by the angular reflection of concentrated rays is given in Figure 41a and the magnified irradiance distribution on the receiver is given in Figure 41b.

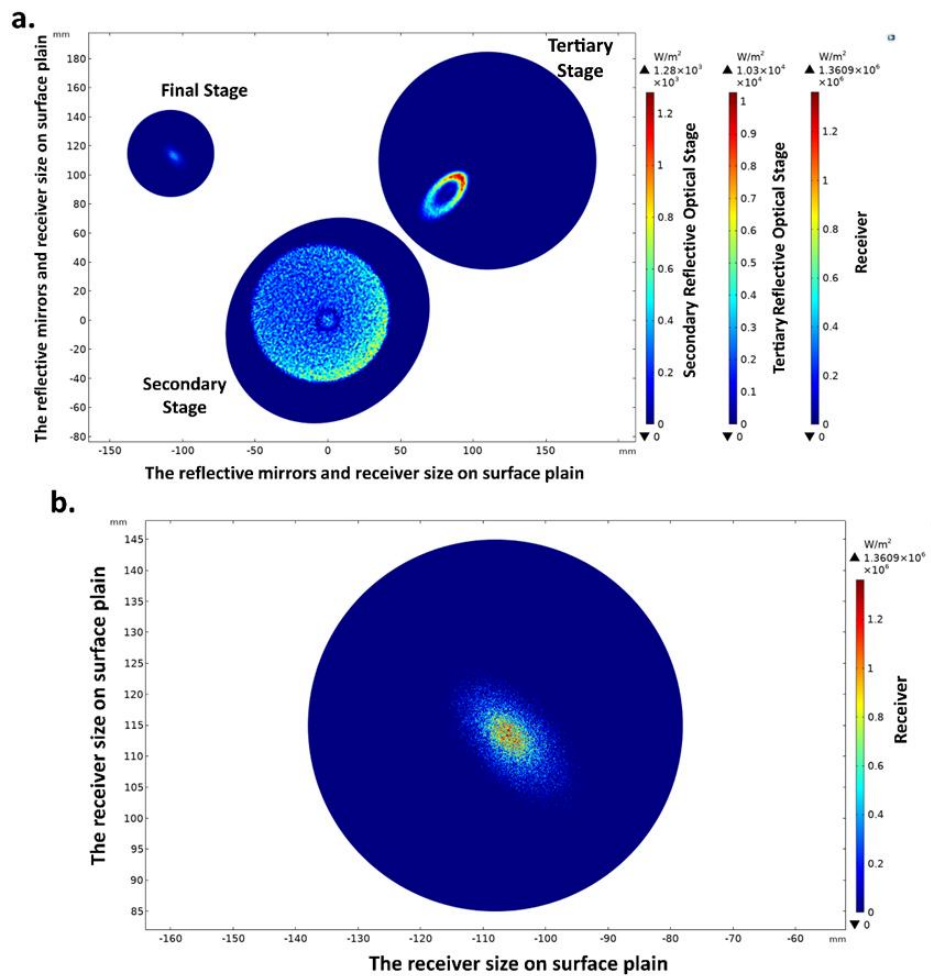


Figure 41 Irradiance distribution at $1000 \frac{W}{m^2}$ a. on the optical interfaces and b.

on the receiver magnified.

6.3.4 Simulative Thermal Performance

The deposited power density in the optical model was coupled to solve the heat transfer equations in the solid model. The receiver maximum temperature was

observed at worst operating and safe operating conditions to be 157.4 °C and 74.9 °C, respectively. Figure 42 and Figure 43 show the temperature operating range on the subsequent stage to the SOG Fresnel lens. In Figure 42, the receiver temperature linear increase tends to have a logarithmic growth with increasing the DNI, and that is due to the proportional increase in radiative heat transfer with the increase in the receiver temperature.

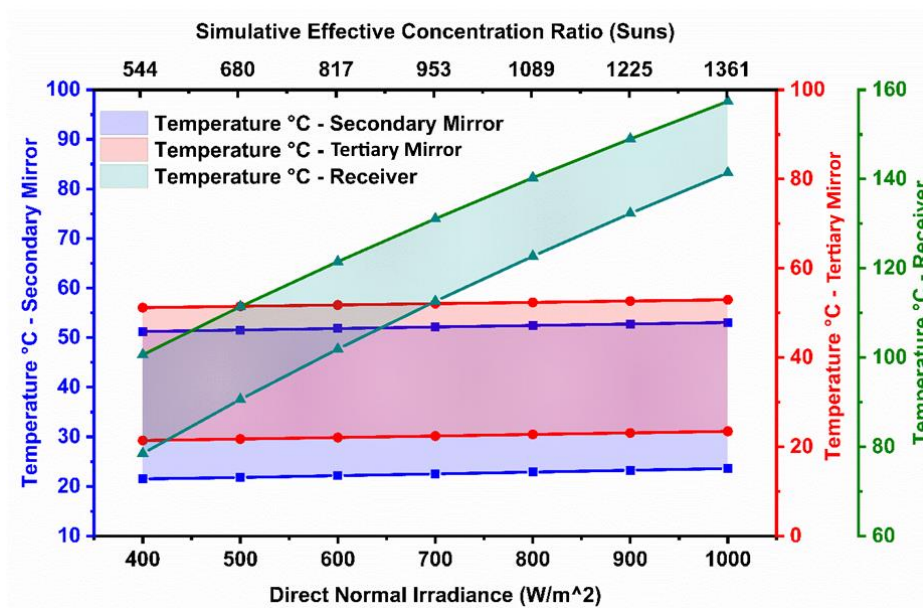


Figure 42 Shows the linear correlation between the concentration ratio and the temperature at an ambient temperature in a range between 50 °C and 20 °C

and convective heat transfer coefficient of $4 \frac{W}{m^2.K}$.

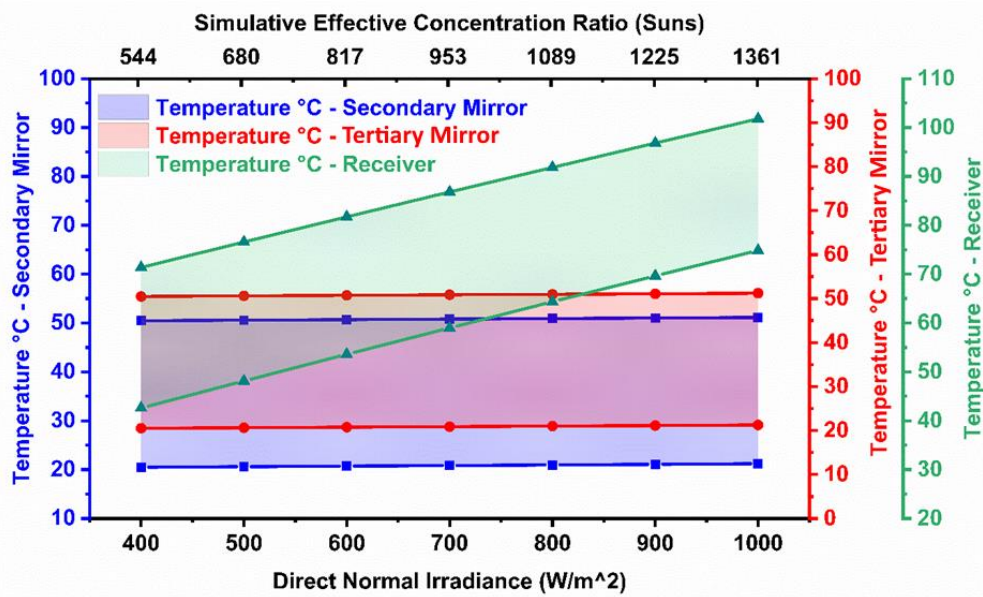


Figure 43 Shows the linear correlation between the concentration ratio and the temperature at an ambient temperature in a range between 50 °C and 20 °C and

$$\text{convective heat transfer coefficient of } 22 \frac{W}{m^2.K}.$$

6.4 Conclusion

The results of the theoretical analysis of the overall optical components in the UHCPV emphasised the optical losses and aspects that challenge the system to reach a concentration ratio > 3000 *suns*. Four different metallic coatings for the reflective secondary mirror have been analysed considering the range of optical losses to still achieve the UH concentration ratio and balance that with the correlation between the solar cell size and the primary optic size (geometrical concentration ratio). The full study is in article 6.

To follow up the theoretical investigations, analysing the UHCPV system is very demanding simulatively for full system coherence. The COMSOL Multiphysics software was utilized to evaluate the UHCPV system optically and thermally. DNI was investigated in a range between $1000 \frac{W}{m^2}$ – $400 \frac{W}{m^2}$ assuming different geographical locations, which helps to evaluate the optical performance in terms

of simulative optical concentration ratio. In addition, a range of ambient temperatures and convective heat transfer coefficients was studied assuming a wide range of meteorological conditions considering both the worst-case scenario and the best-case scenario in order to realize the maximum achievable temperature on the optics and finally on the receiver. This informs the design for a suitable cooling mechanism arrangement. The temperature range on the secondary and tertiary reflective optics are safe enough to not cause substantial thermal stress whereas the receiver subjected to the maximum working temperature operating between 157 °C and 74.8 °C in accordance with the DNI. It is ascertained that a heat extraction mechanism is a necessity at the receiver stage to ensure a safe operating condition when a solar cell is integrated. The detailed numerical study is illustrated in article 8.

In this chapter, the findings showed the estimated optical performance, optical losses, and the resultant heat on every optical stage due to the optical concentration ratio. The UHCPV system will benefit from these findings by selecting a proper optical material that can operate optically well and with a wide working temperature range. Also, the UHCPV system will benefit from the optimum distances among optics during the system alignment stage. The next stage will be the UHCPV mechanical system design and the outdoor experimentation, which will be presented in the next chapter.

CHAPTER 7: UHCPV Fabrication and Experimentation

7.1 Mechanical Design Condition and Overview

The UHCPV design is based on a rigorous principle and carefully considers the interlink among the main system components: UHCPV mechanical structure, sun tracker, and interlinking mechanical structure. Boundary design conditions were assigned first to guide the mechanical structure and facilitate components' employability within the design. The following conditions were given:

1. The system is based on four Fresnel lenses– Silicon on Glass (SOG).
2. Fresnel lenses are fixed in place.
3. The system is based on one central third stage and/or receiver.
4. The system can operate either with three and/or four optical interfaces.
5. The rest of the optical interfaces are adjustable with a large degree of freedom.
6. The system is designed to host a reflective mirror in secondary and tertiary for different diameter sizes ranging from 10, 15, and 20 *cm* with thickness ranging between 4 – 6 *mm*.
7. The designed UHCPV system can be experimented with by utilising a sun tracker with excellent weight compatibility to host the UHCPV system.

The system has been established first as a diamond shape in the middle with four triangles attached to the side of the diamond. The idea of the central diamond is to clear the centre from any mechanical obstacle that will interfere with the concentrated light path. The complete UHCPV system is shown in asymmetric view and plane view, where Figure 44a and b shows the SOLIDWORKS screenshot and Figure 44c and d show the actual system photo, respectively.

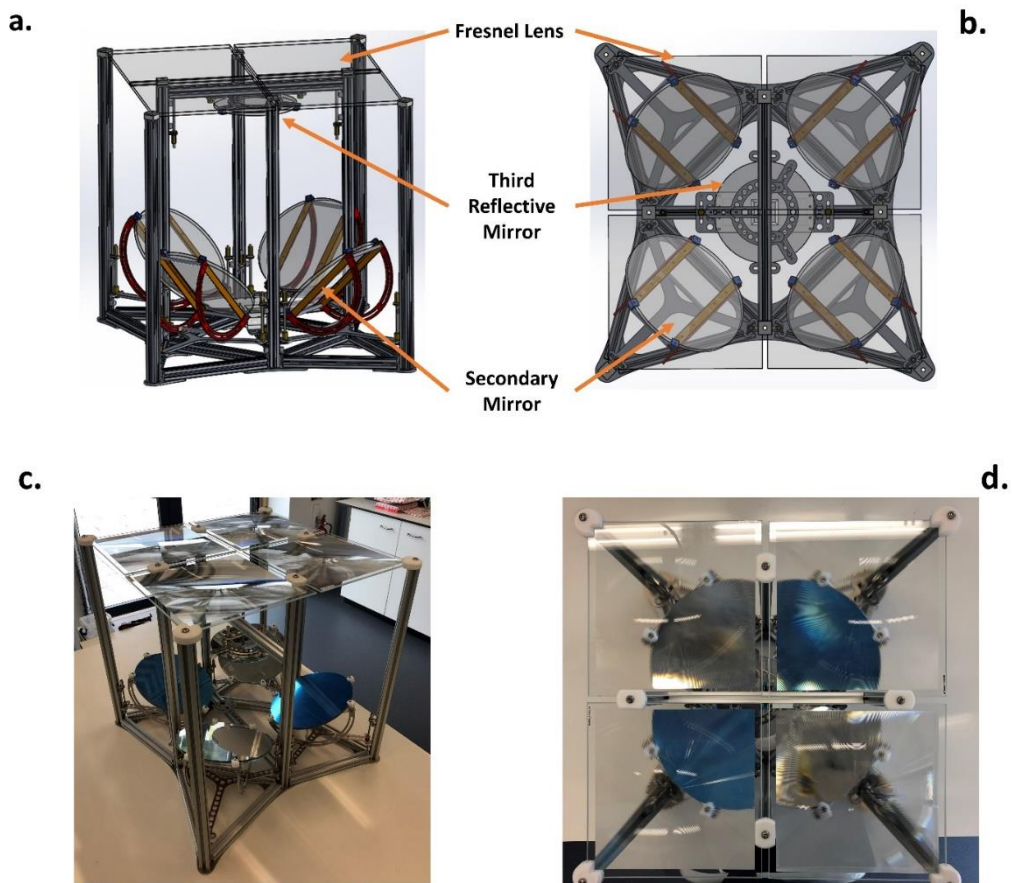
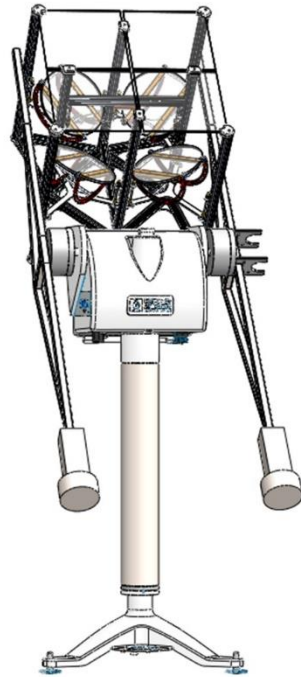


Figure 44 SOLIDWORKS screenshot for the complete designed UHCPV system a. asymmetric view and b. Top view and actual design of UHCPV system c. asymmetric view and d. top view.

The UHCPV system, counterbalance arm, and weight were integrated with the sun tracker and plotted in SOLIDWORKS. This integration is meant to perform system spatial analysis for the minimum required operating area, wind load impact, and have an excellent visualisation for the overall system considering both azimuth angle and sun elevation, as in Figure 45a and b. This chapter is briefing the findings in both article 9 and 10.

a.



b.



Figure 45 The integration of counterbalance arm, counterbalance weight, and UHCPV system to the sun tracker, where a. is the SOLIDWORKS design and b. is the full actual system outdoor ready for testing. The drawings include the extended tube but not the heavy-duty floor stand tripod, where b shows the real heavy-duty floor stand tripod.

7.1.1 Beam Analysis

To link the UHCPV design to the sun tracker, two tube beams are needed to carry weights on both sides. Those weights are the UHCPV system and the counterbalance. The selected arms are a hollow square tube of $20\text{ mm} \times 20\text{ mm} \times 1.5\text{ mm}$ made of stainless-steel grade 316. Two design was simulated using SOLIDWORKS software for static load. The static load study is meant to make sure the resultant stress distribution after applying the system weight, and the counterbalance weight is below the yielding value. Most importantly, the resulting deformation must be below 0.01 mm for alignment and system

accuracy. The two designs were straight tube beam and reinforced tube beam, as in Figure 46 a and b.

a.



b.

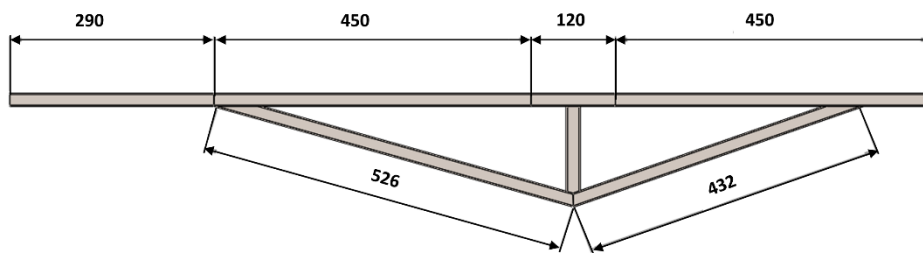


Figure 46 The beam design, where a. straight and b. reinforced.

The simulated results are presented for force, stress, and deformation, as in Table 8. Both maximum stress and deformation are evaluated for an applied mass of 6.5 kg on both sides.

Table 8 The simulated results for two interlinks geometry design.

| Geometry | Force (N) | Stress (MN/m ²) | Deformation (mm) |
|------------------------|-----------|-----------------------------|------------------|
| Straight Beam | 65 | 47.81 | 3.181 |
| Reinforced Tube | 65 | 3.279 | 0.065 |

7.1.2 Wind Load Effect

The impact of wind load is an essential factor in ensuring no extra loads occur on the system. The associated loads will affect the sun tracker by either turning over the entire setup or applying an excessive torque higher than the system torque capacity of 60 N.m. The setup is mechanically fixed, and the infrastructure is made to assure system stability. As a result, turning over is not a concern. On the

other hand, the torque needs to be investigated in all directions (x, y, z) under various setup angles ($100^\circ, 145^\circ, 185^\circ$). According to the World Weather Online database [128], the maximum recorded wind speed at the Penryn campus was 54 kmph (15 m/s) in December 2015. Thus, we will analyse the torque results at all dimensions and comply with the one reached first as an operating limit, either the sun tracker torque limit or the maximum wind speed. In this section, the UHCPV system was built as a solid block to worsen the impact of wind, at which safe operating conditions will always be in place. Table 9 summarized the wind simulation results in terms of resultant torque and force due to applied wind speed of 15 m/s as the worst condition. The illustrated results are given in article 9.

Table 9 Force and torque results for three sun elevation angles at maximum wind speed of 15 m/s .

| System Orientation Angle -Sun Elevation Angle | Force (X) (N) | Force (Y) (N) | Force (Z) (N) | Torque (X – Z) (N. m) | Torque (Y – Z) (N. m) | Torque (Z – X) (N. m) |
|--|----------------------|----------------------|----------------------|------------------------------|------------------------------|------------------------------|
| 100° | 60.097 | 76.654 | 60.514 | 56.291 | 64.055 | 12.759 |
| 145° | 56.098 | 72.315 | 50.364 | 47.135 | 38.999 | 29.598 |
| 185° | 63.882 | 71.512 | 44.489 | 41.56 | 22.488 | 26.427 |

7.2 Outdoor Testing

The UHCPV one-cell model is designed and fabricated to result in a geometrical concentration ratio of $5831 \times$. To consistently target concentration ratios above 3000 suns a high tolerance design is required. The UHCPV design is meant to be simplified for viability and hence employs a wide degree of freedom at every optical stage.

Enhanced Fresnel Assembly -EFA (3C44A) - MJSC Azur Space 3C44 - $5.5 \times 5.5 \text{ mm}^2$ is incorporated in the system for evaluating the optical performance

electrically. A 4-domed optic was manufactured using Silygard-184 material (Figure 47a) in-house and directly attached to the cell (Figure 47b). Three types of reflective optic were implemented in the secondary optical stage. Two of which is applying high reflective films, and the another is just a flat mirror. The reflective films are Aluminium Reflective film (Figure 47c) and ReflecTech® Polymer [129] (Figure 47e), where the mirror is Pilkington Optimirror (Figure 47d). Associated mechanical components were built for complete systems outdoor testing, such as counterbalance weight and arms. High pointing accuracy sun tracker ($< 0.02^\circ$) by KIPP & ZONEN manufacturer – SOLYES GEAR DRIVE (GD) model hosted the system for continuous tracking, Figure 47f.

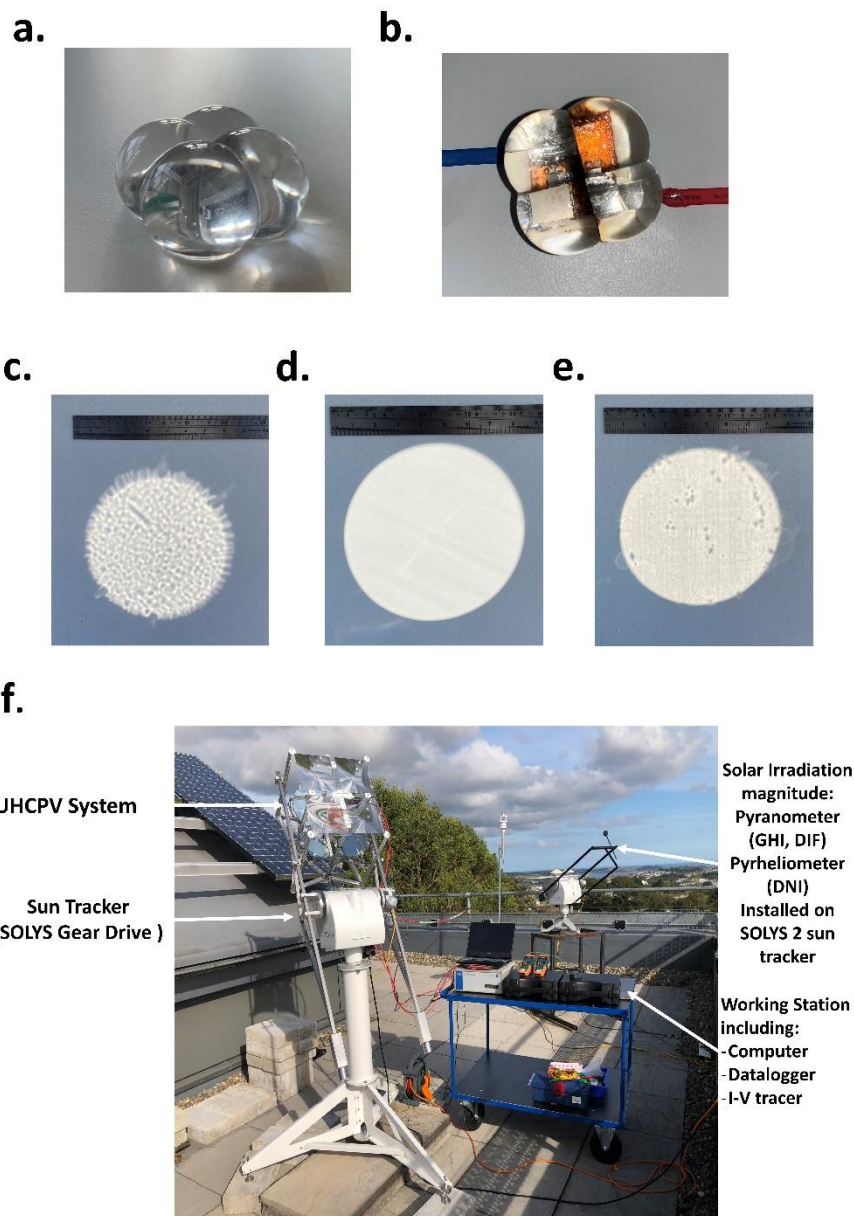


Figure 47 Images for a. Tertiary Optical Element (TOE), b. TOE bonded to the cell. c. shows the reflective image for the coated Aluminium film on low-iron glass simulated on a flat surface. The imperfection of the coated film is apparent in the reflected image as a bubble surface (challenging to observe on the coated film), resulting in an optical dispersion. d. shows the reflective image of the mirror with a clear reflective image. e. shows the reflective mirror of the ReflecTech® Polymer. The reflected image of the ReflecTech® Polymer is

slight less dispersion than the Aluminium film. f. shows the full outdoor experimental setup.

The UHCPV system was assessed on $\frac{1}{4}$ base ($\frac{1}{4}$ of the aperture area - 1 Fresnel lens), $\frac{2}{4}$ (2 Fresnel lenses), $\frac{3}{4}$ (3 Fresnel lenses), and $\frac{4}{4}$ (complete system - 4 Fresnel lenses) to observe the solar cell electrical performance. The aperture area is kept covered to ensure a focal spot capable of burning out system components is not produced. Therefore, the Fresnel lens was exposed for only 3 seconds with instantaneous measurements on a $\frac{1}{4}$ basis, relying on the I-V tracer instrument to evaluate electrical components. The electrical components help to complete the optical performance of the UHCPV system. To establish the effective concentration correlation, the solar cell electrical performance was measured under the illumination of 1 *sun* resulting in an I_{sc} of 4.4 mA. Therefore, the effective concentration (C_{eff}) is solved based on the fraction of $I_{sc,conc}$ under concentration to the I_{sc} , with no concentration, as in Eq.(26).

$$C_{eff} = I_{sc,conc} / I_{sc} \quad (26)$$

The optical efficiency is related to C_{eff} to the geometrical concentration (C_{geo}), as in Eq.(27).

$$\eta_{opt,eff} = C_{eff} / C_{geo} \quad (27)$$

All the measurements in this section were conducted on the 23rd of August 2021 and summarized in Table 10 for full system electrical measurements and optical outcomes (complete system - 4 Fresnel lenses).

Table 10 The electrical and optical results for full system testing outdoor using three types of secondary optics.

| Electrical Measurements | | | | Optical Results | |
|---------------------------|--------------|-------|---------------|------------------|----------------------|
| Aluminium Reflective film | | | | | |
| I_{sc} (A) | V_{oc} (V) | FF(-) | P_{max} (W) | C_{eff} (suns) | $\eta_{opt,eff}$ (%) |
| 4.3 | 2.2 | 0.68 | 6.75 | 984 | 18.5 |
| Pilkington Optimirror | | | | | |
| I_{sc} (A) | V_{oc} (V) | FF(-) | P_{max} (W) | C_{eff} (suns) | $\eta_{opt,eff}$ (%) |
| 5.4 | 2.8 | 0.53 | 7.87 | 1220 | 20.25 |
| ReflecTech® Polymer | | | | | |
| I_{sc} (A) | V_{oc} (V) | FF(-) | P_{max} (W) | C_{eff} (suns) | $\eta_{opt,eff}$ (%) |
| 5.6 | 2.1 | 0.58 | 7.09 | 1291 | 22 |

The built 4-domed TOE is bonded into the solar cell and then used in the system. The Sylgard-184 offers a reflective index of ~ 1.5 . The outdoor experimentation was conducted here only for $\frac{1}{4}$ UHCPV system for Aluminium film, Pilkington Optimirror, and ReflecTech® Polymer secondary optics. The amount of generated heat is excessive and reaches 155°C within the instantaneous measurements of 3 seconds for $\frac{1}{4}$ UHCPV system with TOE. This is obviously not the maximum temperature of the cell. The absence of a proper cooling mechanism scaled up with the resulting effective concentration ratio limited the ability to examine the whole system with TOE. Therefore, we relied on the typical temperature coefficient to predict the electrical product utilising the initial measurements of the MJSC Azur Space 3C44 - $5.5 \times 5.5 \text{ mm}^2$ with $\frac{1}{4}$ of the UHCPV and TOE. The typical temperature coefficients with temperature ranging ($25 - 80^\circ\text{C}$), assuming the availability of an excellent cooling mechanism, are $(\frac{\Delta I_{sc}}{I_{sc(25^\circ\text{C})}})/\Delta T = 0.080\%/K$, $(\frac{\Delta V_{oc}}{V_{oc(25^\circ\text{C})}})/\Delta T = -0.135\%/K$, $(\frac{\Delta P_{mpp}}{P_{mpp(25^\circ\text{C})}})/\Delta T = -0.106\%/K$, and $(\Delta\eta/\eta_{(25^\circ\text{C})})/\Delta T = -0.106\%/K$. The optical results for both $\frac{1}{4}$ UHCPV and full system are summarized in Table 11.

Table 11 TOE ¼ UHCPV and full system optical results.

| ¼ optical Results | | Full Optical Results | |
|---------------------------|----------------------|----------------------|----------------------|
| Aluminium Reflective film | | | |
| C_{eff} (suns) | $\eta_{opt,eff}$ (%) | C_{eff} (suns) | $\eta_{opt,eff}$ (%) |
| 440 | 30 | 1705 | 29 |
| Pilkington Optimirror | | | |
| C_{eff} (suns) | $\eta_{opt,eff}$ (%) | C_{eff} (suns) | $\eta_{opt,eff}$ (%) |
| 448 | 31 | 1740 | 30 |
| ReflecTech® Polymer | | | |
| C_{eff} (suns) | $\eta_{opt,eff}$ (%) | C_{eff} (suns) | $\eta_{opt,eff}$ (%) |
| 485 | 33 | 1879 | 32 |

The TOE has improved the optical efficiency by offering a wider acceptance angle, compensating for any slight misalignment in the system. TOE utilisation improves optical efficiency and enhances effective concentration ratio by 32% in all secondary optic types. Full and detailed results are illustrated in article 10.

7.3 Conclusion

As in article 9, this mechanical study showed the boundary condition for the design through which the system was built. All the system design and numerical analysis were performed using SOLIDWORKS software. The main mechanical items were detailed in the manuscript and further illustrated in photographs based on the optical stage order. Most of the design items was outsourced and assembled in the workshop of the Solar Energy Research Group in Penryn Campus - University of Exeter. The selected sun tracker to host the UHCPV system were discussed, pointing out its specification and capacity. Two interlinking mechanical beam structure designs were presented to exhibit both the stress and deformation distribution. The entire setup integration for spatial and windage analyses was performed. The outdoor experimental validation for the UHCPV compact design was carried out for three different optical materials for the secondary stage: Aluminium reflective film, Pilkington Optimirror, and

ReflecTech® Polymer. Due to the lack of proper active heatsink design, just ¼ UHCPV system was tested with 4-domed TOE and in one-hour continuous measurement. Still, losses regarding the FF and V_{oc} are present due to the existing heat, which can be avoided by scaling up an appropriate cooling mechanism not only for better electrical performance but also to evaluate the waste heat recovery capabilities of the system. The outdoor study results are shown comprehensively in article 10.

In this chapter, the UHCPV system was fabricated and experimented outdoor to validate the system performance. The findings showed the highest geometrical concentration ratio that has been experimented outdoor resulting in the highest effective concentration ratio.

CHAPTER 8: Conclusions and Future Work

8.1 Conclusion

The optical concentrator is the key element in amplifying solar irradiance and concentrating irradiance onto relatively small cells. Increasing the concentration ratio comes at the price of revealing many advances and limitations in the CPVT systems. Therefore, concentrated photovoltaic systems have been investigated through a comprehensive literature review. Only experimental studies have been considered in order to gain a realistic assessment of achievable performance. This literature helped to build a clear understanding that aligned with the research aim of demonstrating and performing a UHCPV system based on the SOG Fresnel lens.

To follow up on the literature review and expand the understanding of increasing concentration ratio on a thermal receiver, a simulation method has been presented using COMSOL Multiphysics software to predict the maximum cell temperature of flat-plate and micro-finned heat-sink in Fresnel based CPV under different concentration ratios for three different substrates materials. The developed model determined the concentration ratio limits based on the solar cell's maximum recommended temperature of 80 °C for different values of natural convective heat transfer coefficient, ambient temperature, and the number of fins.

As a primary component in the UHCPV system, the SOG Fresnel lens was thoroughly investigated to establish the working limits through optical and electrical outcomes. The indoor optical characterisation is adopted to analyse the optical performance of the Fresnel lens theoretically and experimentally. This approach allowed simple measurements to estimate the effective optical efficiency and concentration ratio, especially in a CPV system. This optical characterisation shows that the optical performance decay is significantly due to

the fractional concentration loss and the designing conditions of single-junction solar cells. Also, the MJSC has shown minimal inconsistency in the experimental optical characterisation compared to the single-junction solar cells, simply due to its design condition of 1 sun. In addition, a numerical model was built to investigate a CPV system based on a Fresnel lens design optically and hence thermally. The model resulted in optical efficiency of 89.08%, an optical concentration ratio ranging from 600 *suns* to 240 *suns* and a maximum focal spot temperature ranging from 61.7 °C and 37.2 °C, corresponding to DNI ranging from $1000 \frac{W}{m^2}$ to $400 \frac{W}{m^2}$. This modelling result was validated experimentally both optically and thermally and shows excellent agreement.

This work also provides a new solution to cool down a CPV system based on SOG Fresnel lenses, relying on the pre-illumination cooling mechanism. Three graphene ND filters were developed to attenuate the concentration of solar rays. To fabricate and characterise the ND filter, four different approaches, such as chemical, optical, thermal and electrical characterisations, have been adopted for a comprehensive understanding of the filter. All four characterisation approaches have confirmed that the performance is dependent on the graphene thickness. The indoor experiment was conducted for a polycrystalline Si solar cell, which is vulnerable to the observed temperature level generated by SOG Fresnel lens. The results have shown graphene can be brought into play as an ND filter component for a pre-illumination passive cooling mechanism.

Before developing and performing experiments upon a UHCPV system, a full theoretical and numerical analysis of all optical components in the UHCPV is conducted. This must emphasise the optical losses and aspects that challenge the system to reach a concentration ratio $> 3000 \text{ suns}$. Theoretically, $\frac{1}{4}$ UHCPV

system based on three optical stages considering different metallic coatings for the reflective secondary mirror have been analysed. A range of optical losses which allow the UH concentration ratio to be achievable have been balanced with the correlation between the solar cell size and the primary optic size (geometrical concentration ratio). Further, COMSOL Multiphysics software was utilised to evaluate the UHCPV system optically and thermally. DNI was varied in a range between $400 \frac{W}{m^2} - 1000 \frac{W}{m^2}$, assuming different geographical locations, which helps evaluate the optical performance. In addition, a range of ambient temperatures and convective heat transfer coefficients was studied, assuming a wide range of meteorological conditions considering both worst and best-case scenario. This allows the realisation of the maximum achievable temperature on the optics and finally the receiver. This informs the design for a suitable cooling mechanism arrangement.

To bring the UHCPV system into the experimental stage, mechanical design for the UHCPV system has been established based on SOLIDWORKS software detailing the UHCPV design aspect and the design boundary conditions. This design results in a geometrical concentration ratio of $5831 \times$. The system required an accurate 3-dimensional sun track with the associated mechanical arms. An examination on the static load on the tracker and the windage of the whole system was conducted theoretically. The outdoor experimental validation was conducted with MJSC Azur Space 3C44 - $5.5 \times 5.5 \text{ mm}^2$ and three different types of secondary optics. The system accomplished an effective concentration ratio of 984 suns , 1220 suns , and 1291 suns and an average optical efficiency of 18.5%, 20.25%, and 22% for Aluminium reflective film, Pilkington Optimirror, and ReflecTech® Polymer, respectively. However, testing the system with 4-domed TOE resulted in an effective concentration ratio of 1705 suns , 1740 suns , and

1879 *suns* and an optical efficiency of 29%, 30%, and 32% for Aluminium film, mirror, and ReflecTech® Polymer, respectively. Testing the UHCPV system resulted in the highest effective concentration ratio in the literature for both testing approaches, namely, with the bare cell and the cell with a TOE.

8.2 Important Findings of the Study

This work, its findings and the attached articles contribute to the research field of CPV systems toward UH concentrations in the following ways:

1. The literature review is proving the importance of the concentration ratio for CPV system advances.
2. Pioneering work with using graphene material to develop an ND filter as a pre-illumination cooling technique for CPV systems.
3. A detailed characterisation of the primary optical components toward the UHCPV system to fully understand the optical performance: theoretically, experimentally, and numerically.
4. Optical performance losses due to flawed SOG Fresnel lens and/or fractional concentration.
5. Investigation of multi-interface UHCPV systems with highly accurate optical and thermal modelling in COMSOL Multiphysics software.
6. Similarly, to the previous point, the UHCPV system compiling multiple interfaces was analysed theoretically and numerically before fabricating the system to ensure its viability.
7. Thorough detailing for UHCPV mechanical design and its associated aspects through compiling UHCPV system with a sun tracker and other mechanical elements.
8. First UHCPV compact design experimented outdoors, with still being the highest in geometrical concentration ratio.

9. The optical characterisation for UHCPV of one central solar cell resulted in the highest effective concentration ratio.

8.3 Recommendations for Future Work

1. Outdoor investigation for the UHCPV system considering optical performance with the optical angle variance.
2. Correlate the wind load impact on the sun tracker accuracy by examining the electrical performance outputs.
3. Designing and scaling up a post-illumination cooling mechanism to ensure good performance at high effective concentration ratios.
4. Investigating the waste heat recovery potential of the UHCPV system.
5. Re-evaluate the optical performance with bare cell and TOE continuously outdoors with scaled-up cooling arrangements to overcome any loss due to build up heat.
6. Evaluating the optical system by considering state-of-the-art-optics.
7. Develop a numerical model to predict the electrical performance associated with the optical and thermal models for the full system predication.

References

- [1] H. Baig, N. Sarmah, K.C. Heasman, T.K. Mallick, Numerical modelling and experimental validation of a low concentrating photovoltaic system, *Solar Energy Materials and Solar Cells*. (2013). doi:10.1016/j.solmat.2013.01.035.
- [2] D. Chemisana, T.K. Mallick, Building integrated concentrating solar systems, *Solar Energy Sciences and Engineering Applications*. (2013) 545–587. doi:10.1201/b15507.
- [3] A. Zahedi, Review of modelling details in relation to low-concentration solar concentrating photovoltaic, *Renewable and Sustainable Energy Reviews*. 15 (2011) 1609–1614. doi:10.1016/j.rser.2010.11.051.
- [4] L. Micheli, N. Sarmah, X. Luo, K.S. Reddy, T.K. Mallick, Opportunities and challenges in micro- and nano-technologies for concentrating photovoltaic cooling : A review, *Renewable and Sustainable Energy Reviews*. 20 (2013) 595–610. doi:10.1016/j.rser.2012.11.051.
- [5] G. Almonacid, P.G. Vidal, E. Mu, High Concentrator PhotoVoltaics efficiencies : Present status and forecast, *Renewable and Sustainable Energy Reviews*. 15 (2015) 1810–1815. doi:https://doi.org/10.1016/j.rser.2010.11.046.
- [6] W.T. Xie, Y.J. Dai, R.Z. Wang, K. Sumathy, Concentrated solar energy applications using Fresnel lenses : A review, *Renewable and Sustainable Energy Reviews*. 15 (2011) 2588–2606. doi:10.1016/j.rser.2011.03.031.
- [7] D. Chemisana, Building Integrated Concentrating Photovoltaics : A review, *Renewable and Sustainable Energy Reviews*. 15 (2011) 603–611. doi:10.1016/j.rser.2010.07.017.
- [8] A. Makki, S. Omer, H. Sabir, Advancements in hybrid photovoltaic systems for enhanced solar cells performance, *Renewable and Sustainable Energy Reviews*. 41 (2015) 658–684. doi:10.1016/j.rser.2014.08.069.
- [9] R.R. Avezov, J.S. Akhatov, N.R. Avezova, A Review on Photovoltaic-Thermal (PV–T) Air and Water Collectors¹, *Applied Solar Energy*. 47 (2011) 169–183. doi:10.3103/S0003701X11030042.
- [10] B. Singh, M.Y. Othman, A review on photovoltaic thermal collectors, *Journal of Renewable and Sustainable Energy*. 062702 (2009). doi:10.1063/1.3266963.
- [11] O.Z. Sharaf, M.F. Orhan, Concentrated photovoltaic thermal (CPVT) solar collector systems: Part I - Fundamentals, design considerations and current technologies, *Renewable and Sustainable Energy Reviews*. 50 (2015) 1500–1565. doi:10.1016/j.rser.2015.05.036.
- [12] O.Z. Sharaf, M.F. Orhann, Concentrated photovoltaic thermal (CPVT) solar collector systems: Part II - Implemented systems, performance assessment, and future directions, *Renewable and Sustainable Energy Reviews*. 50 (2015) 1566–1633. doi:10.1016/j.rser.2014.07.215.
- [13] R. Daneshazarian, E. Cuce, P.M. Cuce, F. Sher, Concentrating

- photovoltaic thermal (CPVT) collectors and systems: Theory, performance assessment and applications, *Renewable and Sustainable Energy Reviews*. 81 (2018) 473–492. doi:10.1016/j.rser.2017.08.013.
- [14] A. Mojiri, R. Taylor, E. Thomsen, G. Rosengarten, Spectral beam splitting for efficient conversion of solar energy — A review, *Renewable and Sustainable Energy Reviews*. 28 (2013) 654–663. doi:10.1016/j.rser.2013.08.026.
- [15] X. Ju, C. Xu, X. Han, X. Du, G. Wei, Y. Yang, A review of the concentrated photovoltaic/thermal (CPVT) hybrid solar systems based on the spectral beam splitting technology, *Applied Energy*. 187 (2017) 534–563. doi:10.1016/j.apenergy.2016.11.087.
- [16] J.F. Geisz, R.M. France, K.L. Schulte, M.A. Steiner, A.G. Norman, H.L. Guthrey, M.R. Young, T. Song, T. Moriarty, Six-junction III–V solar cells with 47.1% conversion efficiency under 143 Suns concentration, *Nature Energy*. 5 (2020) 326–335. doi:10.1038/s41560-020-0598-5.
- [17] K. Shanks, S. Senthilarasu, T.K. Mallick, Optics for concentrating photovoltaics: Trends, limits and opportunities for materials and design, *Renewable and Sustainable Energy Reviews*. 60 (2016) 394–407. doi:10.1016/j.rser.2016.01.089.
- [18] D. Feldman, E. O’Shaughnessy, R. Margolis, Solar Industry Update Q3/Q4 2019, NREL Presentation. (2020) 1–83. <https://www.nrel.gov/docs/fy20osti/76158.pdf>.
- [19] M. Alzahrani, A. Ahmed, K. Shanks, S. Sundaram, T. Mallick, Optical component analysis for ultrahigh concentrated photovoltaic system (UHCPV), *Solar Energy*. 227 (2021) 321–333. doi:10.1016/j.solener.2021.09.019.
- [20] Kipp & Zonen, Instruction Manual SOLYS2 Sun Tracker SOLYS Gear Drive Sun Tracker, Instruction Manual. 001 (2017) 1–112. <http://www.kippzonen.com/Product/20/SOLYS2-Sun-Tracker#.WyzN1vIKjcs>.
- [21] M. Alzahrani, K. Shanks, T.K. Mallick, Advances and limitations of increasing solar irradiance for concentrating photovoltaics thermal system, *Renewable and Sustainable Energy Reviews*. 138 (2021) 110517. doi:10.1016/j.rser.2020.110517.
- [22] M. Alzahrani, A. Ahmed, K. Shanks, S. Sundaram, T. Mallick, Optical losses and durability of flawed Fresnel lenses for concentrated photovoltaic application, *Materials Letters*. 275 (2020) 128145. doi:10.1016/j.matlet.2020.128145.
- [23] A. Ahmed, M. Alzahrani, K. Shanks, S. Sundaram, T.K. Mallick, Effect of using an infrared filter on the performance of a silicon solar cell for an ultra-high concentrator photovoltaic system, *Materials Letters*. 277 (2020) 128332. doi:10.1016/j.matlet.2020.128332.
- [24] M. Alzahrani, H. Baig, K. Shanks, T. Mallick, Estimation of the performance limits of a concentrator solar cell coupled with a micro heat sink based on a finite element simulation, *Applied Thermal Engineering*. 176 (2020) 115315. doi:10.1016/j.applthermaleng.2020.115315.

- [25] M. Alzahrani, A. Roy, K. Shanks, S. Sundaram, T.K. Mallick, Graphene as a pre-illumination cooling approach for a concentrator photovoltaic (CPV) system, *Solar Energy Materials and Solar Cells*. 222 (2021) 110922. doi:10.1016/j.solmat.2020.110922.
- [26] N.L.A. Chan, N.J. Ekins-Daukes, J.G.J. Adams, M.P. Lumb, M. Gonzalez, P.P. Jenkins, I. Vurgaftman, J.R. Meyer, R.J. Walters, Optimal bandgap combinations-does material quality matter, *IEEE Journal of Photovoltaics*. 2 (2012) 202–208. doi:10.1109/JPHOTOV.2011.2180513.
- [27] L.C. Herst, N. Ekins-Daukes, Fundamental losses in solar cells, *Progress in Photovoltaics: Research and Applications*. 19 (2010) 286–293. doi:10.1002/pip.
- [28] S.P. Philipps, F. Dimroth, A.W. Bett, High-Efficiency III–V Multijunction Solar Cells, in: *McEvoy's Handbook of Photovoltaics*, Elsevier, 2018: pp. 439–472. doi:10.1016/B978-0-12-809921-6.00012-4.
- [29] M. Bercx, R. Saniz, B. Partoens, D. Lamoen, Exceeding the Shockley–Queisser Limit Within the Detailed Balance Framework, in: *Many-Body Approaches at Different Scales*, Springer International Publishing, Cham, 2018: pp. 177–184. doi:10.1007/978-3-319-72374-7_15.
- [30] A. Polman, M. Knight, E.C. Garnett, B. Ehrler, W.C. Sinke, Photovoltaic materials: Present efficiencies and future challenges, *Science*. 352 (2016) 10–12. doi:10.1126/science.aad4424.
- [31] M.A. Green, K. Emery, Y. Hishikawa, W. Warta, E.D. Dunlop, Solar cell efficiency tables (version 41), *Progress in Photovoltaics: Research and Applications*. 21 (2013) 1–11. doi:10.1002/pip.2352.
- [32] A. Martí, G.L. Araújo, Limiting efficiencies for photovoltaic energy conversion in multigap systems, *Solar Energy Materials and Solar Cells*. 43 (1996) 203–222. doi:10.1016/0927-0248(96)00015-3.
- [33] Hugo Doleman, Limiting and realistic efficiencies of multi-junction solar cells, FOM Institute AMOLF, 2012. doi:https://pdfs.semanticscholar.org/b083/753c6d04cd2af20379de785e7a71f2e885b6.pdf?_ga=2.85718480.83315905.1592515641-107842748.1553173981.
- [34] W. Hu, Y. Harada, A. Hasegawa, T. Inoue, O. Kojima, T. Kita, Intermediate band photovoltaics based on interband-intraband transitions using In_{0.53}Ga_{0.47}As/InP superlattice, *Progress in Photovoltaics: Research and Applications*. 20 (2011) n/a-n/a. doi:10.1002/pip.1208.
- [35] O.Z. Sharaf, M.F. Orhan, Concentrated photovoltaic thermal (CPVT) solar collector systems: Part I – Fundamentals, design considerations and current technologies, *Renewable and Sustainable Energy Reviews*. 50 (2015) 1500–1565. doi:10.1016/j.rser.2015.05.036.
- [36] A. Luque, S. Hegedus, *Handbook of Photovoltaic Science*, Springer, 2003. [https://scholar.google.com/scholar_lookup?title=Concentrator photovoltaics&author=A.L. Luque&publication_year=2007](https://scholar.google.com/scholar_lookup?title=Concentrator+photovoltaics&author=A.L.+Luque&publication_year=2007).
- [37] H. Baig, N. Sellami, D. Chemisana, J. Rosell, T.K. Mallick, Performance analysis of a dielectric based 3D building integrated concentrating

- photovoltaic system, *Solar Energy*. 103 (2014) 525–540.
doi:10.1016/j.solener.2014.03.002.
- [38] K. Shanks, J.P. Ferrer-rodriguez, E.F. Fernández, F. Almonacid, A > 3000 suns high concentrator photovoltaic design based on multiple Fresnel lens primaries focusing to one central solar cell, *Solar Energy*. 169 (2018) 457–467. doi:10.1016/j.solener.2018.05.016.
- [39] A. Yavrian, S. Tremblay, M. Levesque, R. Gilbert, How to increase the efficiency of a high concentrating PV (HCPV) by increasing the acceptance angle to $\pm 3.2^\circ$, in: *AIP Conference Proceedings*, 2013: pp. 197–200. doi:10.1063/1.4822230.
- [40] L. Micheli, N. Sarmah, E.F. Fernandez, K.S. Reddy, T.K. Mallick, Technical issues and challenges in the fabrication of a 144-Cell 500x Concentrating Photovoltaic receiver, 2014 IEEE 40th Photovoltaic Specialist Conference, PVSC 2014. (2014) 2921–2925.
doi:10.1109/PVSC.2014.6925543.
- [41] Azur Space Solar Power GMBH, Enhanced Fresnel Assembly - EFA Type: 3C42A – with 5.5x5.5 mm² CPV TJ Solar Cell Application: Concentrating Photovoltaic (CPV) Modules, (2014) 0–4.
http://www.azurspace.com/images/products/DB_3987-00-00_3C42_AzurDesign_EFA_10x10_2014-03-27.pdf.
- [42] L. Mabile, C. Mangeant, M. Baudrit, Development of CPV solar receiver based on insulated metal substrate (IMS): Comparison with receiver based on the direct bonded copper substrate (DBC) - A reliability study, *AIP Conference Proceedings*. 1477 (2012) 289–293.
doi:10.1063/1.4753888.
- [43] L. Micheli, S. Senthilarasu, K.S. Reddy, T.K. Mallick, Applicability of silicon micro-finned heat sinks for 500x concentrating photovoltaics systems, *Journal of Materials Science*. 50 (2015) 5378–5388.
doi:10.1007/s10853-015-9065-2.
- [44] M. Iba, J.I. Rosell, X. Vallverdu, Design and simulation of a low concentrating photovoltaic / thermal system, 46 (2005) 3034–3046.
doi:10.1016/j.enconman.2005.01.012.
- [45] S. Chow, C.E. Valdivia, J.F. Wheeldon, R. Ares, O.J. Arenas, V. Aimez, D. McMeekin, S. Fafard, K. Hinzer, Thermal test and simulation of alumina receiver with high efficiency multi-junction solar cell for concentrator systems, *Photonics North 2010*. 7750 (2010) 775035.
doi:10.1117/12.872894.
- [46] J. Gomes, L. Diwan, R. Bernardo, B. Karlsson, Minimizing the Impact of Shading at Oblique Solar Angles in a Fully Enclosed Asymmetric Concentrating PVT Collector, *Energy Procedia*. 57 (2014) 2176–2185.
doi:10.1016/j.egypro.2014.10.184.
- [47] L. Guiqiang, P. Gang, Y. Su, Z. Xi, J. Jie, Preliminary study based on building-integrated compound parabolic concentrators (CPC) PV / thermal technology, (2012). doi:10.1016/j.egypro.2011.12.887.
- [48] F. Karimi, H. Xu, Z. Wang, J. Chen, M. Yang, Experimental study of a concentrated PV/T system using linear Fresnel lens, *Energy*. 123 (2017)

- 402–412. doi:10.1016/j.energy.2017.02.028.
- [49] F. Gualdi, O. Arenas, A. Vossier, A. Dollet, V. Aimez, R. Arès, Determining passive cooling limits in CPV using an analytical thermal model, *AIP Conference Proceedings*. 1556 (2013) 10–13. doi:10.1063/1.4822187.
- [50] A. Valera, E.F. Fernández, P.M. Rodrigo, F. Almonacid, Feasibility of flat-plate heat-sinks using microscale solar cells up to 10,000 suns concentrations, *Solar Energy*. 181 (2019) 361–371. doi:10.1016/j.solener.2019.02.013.
- [51] A.H.A. Al-Waeli, K. Sopian, M.T. Chaichan, H.A. Kazem, H.A. Hasan, A.N. Al-Shamani, An experimental investigation of SiC nanofluid as a base-fluid for a photovoltaic thermal PV/T system, *Energy Conversion and Management*. 142 (2017) 547–558. doi:10.1016/j.enconman.2017.03.076.
- [52] E. Bellos, C. Tzivanidis, Investigation of a nanofluid-based concentrating thermal photovoltaic with a parabolic reflector, *Energy Conversion and Management*. 180 (2019) 171–182. doi:10.1016/j.enconman.2018.11.008.
- [53] S.K. Verma, A.K. Tiwari, S. Tiwari, D.S. Chauhan, Performance analysis of hybrid nanofluids in flat plate solar collector as an advanced working fluid, *Solar Energy*. 167 (2018) 231–241. doi:10.1016/j.solener.2018.04.017.
- [54] S. Iranmanesh, H.C. Ong, B.C. Ang, E. Sadeghinezhad, A. Esmaeilzadeh, M. Mehrali, Thermal performance enhancement of an evacuated tube solar collector using graphene nanoplatelets nanofluid, *Journal of Cleaner Production*. 162 (2017) 121–129. doi:10.1016/j.jclepro.2017.05.175.
- [55] S. Lee, S.U.-S. Choi, S. Li, J.A. Eastman, Measuring Thermal Conductivity of Fluids Containing Oxide Nanoparticles, *Journal of Heat Transfer*. 121 (1999) 280–289. doi:10.1115/1.2825978.
- [56] L. Xu, X. Ji, F. Yin, M. Li, G.L. Li, The performance analysis of the Trough Concentrating Solar Photovoltaic/Thermal system, *Energy Conversion and Management*. 52 (2011) 2378–2383. doi:10.1016/j.enconman.2010.12.039.
- [57] B. Ricardo, H. Davidsson, G. Niko, J. Gomes, G. Christian, C. Luis, M. Chabu, B. Karlsson, Measurements of the Electrical Incidence Angle Modifiers of an Asymmetrical Photovoltaic/Thermal Compound Parabolic Concentrating-Collector, *Engineering*. 05 (2013) 37–43. doi:10.4236/eng.2013.51B007.
- [58] J.S. Coventry, Performance of a concentrating photovoltaic/thermal solar collector, *Solar Energy*. 78 (2005) 211–222. doi:10.1016/j.solener.2004.03.014.
- [59] L.R. Bernardo, B. Perers, H. Håkansson, B. Karlsson, Performance evaluation of low concentrating photovoltaic/thermal systems: A case study from Sweden, *Solar Energy*. 85 (2011) 1499–1510. doi:10.1016/j.solener.2011.04.006.

- [60] R. Künnemeyer, T.N. Anderson, M. Duke, J.K. Carson, Performance of a V-trough photovoltaic/thermal concentrator, *Solar Energy*. 101 (2014) 19–27. doi:10.1016/j.solener.2013.11.024.
- [61] M. Chaabane, W. Charfi, H. Mhiri, P. Bournot, Performance evaluation of concentrating solar photovoltaic and photovoltaic/thermal systems, *Solar Energy*. 98 (2013) 315–321. doi:10.1016/j.solener.2013.09.029.
- [62] L.T. Kostic, T.M. Pavlovic, Z.T. Pavlovic, Influence of reflectance from flat aluminum concentrators on energy efficiency of PV/Thermal collector, *Applied Energy*. 87 (2010) 410–416. doi:10.1016/j.apenergy.2009.05.038.
- [63] J. Nilsson, H. Håkansson, B. Karlsson, Electrical and thermal characterization of a PV-CPC hybrid, *Solar Energy*. 81 (2007) 917–928. doi:10.1016/j.solener.2006.11.005.
- [64] Y. Tripanagnostopoulos, T. Nousia, M. Souliotis, P. Yianoulis, Hybrid photovoltaic/thermal solar systems, *Solar Energy*. 72 (2002) 217–234. doi:10.1016/S0038-092X(01)00096-2.
- [65] G. Xu, X. Zhang, S. Deng, Experimental study on the operating characteristics of a novel low-concentrating solar photovoltaic/thermal integrated heat pump water heating system, *Applied Thermal Engineering*. 31 (2011) 3689–3695. doi:10.1016/j.applthermaleng.2011.01.030.
- [66] H. Davidsson, B. Perers, B. Karlsson, Performance of a multifunctional PV/T hybrid solar window, *Solar Energy*. 84 (2010) 365–372. doi:10.1016/j.solener.2009.11.006.
- [67] G.K. Chinyama, A. Roos, B. Karlsson, Stability of antireflection coatings for large area glazing, *Solar Energy*. 50 (1993) 105–111. doi:10.1016/0038-092X(93)90081-X.
- [68] P.J. Sonneveld, G.L.A.M. Swinkels, J. Campen, B.A.J. van Tuijl, H.J.J. Janssen, G.P.A. Bot, Performance results of a solar greenhouse combining electrical and thermal energy production, *Biosystems Engineering*. 106 (2010) 48–57. doi:10.1016/j.biosystemseng.2010.02.003.
- [69] V. Everett, J. Harvey, S. Surve, E. Thomsen, D. Walter, M. Vivar, A. Blakers, A. Tanner, M. Greaves, P. Le Leivre, Evaluation of electrical and thermal performance of a linear hybrid CPV-T micro-concentrator system, *AIP Conference Proceedings*. 1407 (2011) 262–265. doi:10.1063/1.3658340.
- [70] S.-L. Jiang, P. Hu, S.-P. Mo, Z.-S. Chen, Modeling for Two-Stage Dish Concentrating Spectral Beam Splitting Photovoltaic/Thermal System, in: *2009 Asia-Pacific Power and Energy Engineering Conference*, IEEE, 2009: pp. 1–4. doi:10.1109/APPEEC.2009.4918499.
- [71] R. Liu, *An Overview of Aluminum Protective Coating Properties and Treatments*, OPTI, The University of ARIZONA. (2009).
- [72] B.M. Ziapour, V. Palideh, F. Mokhtari, Performance improvement of the finned passive PVT system using reflectors like removable insulation covers, *Applied Thermal Engineering*. 94 (2016) 341–349.

doi:10.1016/j.applthermaleng.2015.10.143.

- [73] D. Jaffré, F. Gualdi, M. Sicre, R. El Ouamari, A. Dollet, G. Baud, D. Martin, Design and characterization of a curved linear fresnel lens concentrating photovoltaic and thermal system, AIP Conference Proceedings. 1616 (2014) 173–176. doi:10.1063/1.4897054.
- [74] G. Soni, S. Srivastava, P. Soni, P. Kalotra, Y.K. Vijay, Optical, mechanical and structural properties of PMMA/SiO₂ nanocomposite thin films, Materials Research Express. 5 (2018) 015302. doi:10.1088/2053-1591/aaa0f7.
- [75] I. Al Siyabi, K. Shanks, S. Khanna, T.K. Mallick, S. Sundaram, Evaluation of concentrating photovoltaic performance under different homogeniser materials, Materials Letters. 241 (2019) 219–222. doi:10.1016/j.matlet.2019.01.129.
- [76] J. Sarwar, T. Shrouf, K.E. Kakosimos, Characterization of thermal performance and optical properties of a material under concentrated radiation using a high flux solar simulator, in: AIP Conference Proceedings, 2017: p. 160025. doi:10.1063/1.4984559.
- [77] P. McVey-White, P. Besson, M. Baudrit, H.P. Schriemer, K. Hinzer, Effects of lens temperature on irradiance profile and chromatic aberration for CPV optics, in: AIP Conference Proceedings, 2016: p. 040004. doi:10.1063/1.4962081.
- [78] K. Shanks, H. Baig, N.P. Singh, S. Senthilarasu, K.S. Reddy, T.K. Mallick, Prototype fabrication and experimental investigation of a conjugate refractive reflective homogeniser in a cassegrain concentrator, Solar Energy. 142 (2017) 97–108. doi:10.1016/j.solener.2016.11.038.
- [79] D. Vincenzi, S. Baricordi, S. Calabrese, M. Musio, A. Damiano, A cassegrain concentrator photovoltaic system: Comparison between dichroic and multijunction photovoltaic configurations, IECON Proceedings (Industrial Electronics Conference). (2014) 1900–1905. doi:10.1109/IECON.2014.7048761.
- [80] A. Colozza, R. Macosko, C. Castle, K. Sacksteder, N. Suzuki, J. Mulherin, Cassigranian Solar Concentrator for ISRU Material Processing, in: 50th AIAA Aerospace Sciences Meeting Including the New Horizons Forum and Aerospace Exposition, American Institute of Aeronautics and Astronautics, Reston, Virginia, 2012: pp. 1–15. doi:10.2514/6.2012-637.
- [81] H. Chayet, I. Lozovsky, O. Kost, R. Loeckenhoff, K.-D. Rasch, A.W. Bett, R.D. McConnell, G. Sala, F. Dimroth, HIGH EFFICIENCY, LOW COST PARABOLIC DISH SYSTEM FOR COGENERATION OF ELECTRICITY AND HEAT, in: AIP Conference Proceedings, 2010: pp. 175–178. doi:10.1063/1.3509183.
- [82] A. Kribus, D. Kaftori, G. Mittelman, A. Hirshfeld, Y. Flitsanov, A. Dayan, A miniature concentrating photovoltaic and thermal system, Energy Conversion and Management. 47 (2006) 3582–3590. doi:10.1016/j.enconman.2006.01.013.
- [83] N. Rathore, N.L. Panwar, F. Yettou, A Comprehensive review on different types of solar photovoltaic cells and their applications, International

Journal of Ambient Energy. 0 (2019) 1–48.
doi:10.1080/01430750.2019.1592774.

- [84] M. Kouhnavard, S. Ikeda, N.A. Ludin, N.B. Ahmad Khairudin, B.V. Ghaffari, M.A. Mat-Teridi, M.A. Ibrahim, S. Sepeai, K. Sopian, A review of semiconductor materials as sensitizers for quantum dot-sensitized solar cells, *Renewable and Sustainable Energy Reviews*. 37 (2014) 397–407. doi:10.1016/j.rser.2014.05.023.
- [85] W. Cui, L. Zhao, W. Wu, K. Wang, T.C. Jen, Energy efficiency of a quasi cpc concentrating solar PV/T system, in: *ASME International Mechanical Engineering Congress and Exposition, Proceedings (IMECE)*, 2010: pp. 1071–1076. doi:10.1115/IMECE2010-38341.
- [86] Y. Xu, C.Y. Wang, Y.M. Hua, Y.M. Zhang, Studies on a Low Concentration Photovoltaic/Thermal System with Constant Volume Refrigeration, *Key Engineering Materials*. 517 (2012) 776–783. doi:10.4028/www.scientific.net/KEM.517.776.
- [87] E. Pihl, C. Thapper, H.J. Nilsson, Evaluation of the concentrating PVT systems MaReCo and Solar8, 2006. <http://lup.lub.lu.se/record/1027919>.
- [88] C. Renno, F. Petito, Experimental and theoretical model of a concentrating photovoltaic and thermal system, *Energy Conversion and Management*. 126 (2016) 516–525. doi:10.1016/j.enconman.2016.08.027.
- [89] H. Helmers, A.W. Bett, J. Parisi, C. Agert, Modeling of concentrating photovoltaic and thermal systems, *Progress in Photovoltaics: Research and Applications*. 22 (2014) 427–439. doi:10.1002/pip.2287.
- [90] H. Helmers, A. Boos, F. Jetter, A. Heimsath, M. Wiesenfarth, A.W. Bett, F. Dimroth, S. Kurtz, G. Sala, A.W. Bett, Outdoor Test Setup for Concentrating Photovoltaic and Thermal (CPVT) Systems, in: *AIP Conference Proceedings*, 2011: pp. 175–179. doi:10.1063/1.3658320.
- [91] Concentrator Triple Junction Solar Cell Cell Type : 3C44C- 3 × 3 mm² Azur Space, 2012. http://www.azurspace.com/images/products/0004357-00-01_3C44_AzurDesign_3x3.pdf.
- [92] P. Fernández, E.F., Almonacid, F., Rodrigo, P.M., Pérez-Higueras, CPV Systems., in: *McEvoy's Handbook Photovoltaic*, 2017: pp. 931–985.
- [93] K. Yazawa, A. Shakouri, Material Optimization for Concentrated Solar Photovoltaic and Thermal Co-Generation, in: *ASME 2011 Pacific Rim Technical Conference and Exhibition on Packaging and Integration of Electronic and Photonic Systems, MEMS and NEMS: Volume 1*, ASMEDC, 2011: pp. 733–739. doi:10.1115/IPACK2011-52190.
- [94] A. Lopez, A. Vega, A. Lopez, *Next Generation of Photovoltaics*, Springer Berlin Heidelberg, Berlin, Heidelberg, 2012. doi:10.1007/978-3-642-23369-2.
- [95] C. Algora, I. Rey-Stolle, Chapter 2 The Interest and Potential of Ultra-High Concentration. *Next Generation of Photovoltaics: New Concept*, Springer Berlin Heidelberg, Berlin, Heidelberg, 2012. doi:10.1007/978-3-642-23369-2.

- [96] Low-Cost, Lightweight Solar Concentrator (Fact Sheet), Golden, CO (United States), 2012. doi:10.2172/1053327.
- [97] D.J. Wright, S. Badruddin, C. Robertson-Gillis, Micro-Tracked CPV Can Be Cost Competitive With PV in Behind-The-Meter Applications With Demand Charges, *Frontiers in Energy Research*. 6 (2018). doi:10.3389/fenrg.2018.00097.
- [98] J.E. Haysom, O. Jafarieh, H. Anis, K. Hinzer, D. Wright, Learning curve analysis of concentrated photovoltaic systems, *Progress in Photovoltaics: Research and Applications*. 23 (2015) 1678–1686. doi:10.1002/pip.2567.
- [99] E. Gil, M. Martinez, O. de la Rubia, Operation and maintenance results from ISFOC CPV plants, in: 2017: p. 020006. doi:10.1063/1.5001405.
- [100] A. Kalair, N. Abas, M.S. Saleem, A.R. Kalair, N. Khan, Role of energy storage systems in energy transition from fossil fuels to renewables, *Energy Storage*. (2020). doi:10.1002/est2.135.
- [101] I.R.E. Agency, Renewable Power Generation Costs in 2018, 2018. https://www.irena.org/-/media/Files/IRENA/Agency/Publication/2018/Jan/IRENA_2017_Power_Costs_2018.pdf.
- [102] Chapter 5 Energy. Optics and Photonics, National Academies Press, Washington, D.C., 2013. doi:10.17226/13491.
- [103] Overview and Summary of America’s Energy Future: Technology and Transformation, National Academies Press, Washington, D.C., 2010. doi:10.17226/12943.
- [104] L. Micheli, K.S. Reddy, T.K. Mallick, Plate micro-fins in natural convection: An opportunity for passive concentrating photovoltaic cooling, *Energy Procedia*. 82 (2015) 301–308. doi:10.1016/j.egypro.2015.12.037.
- [105] E.F.A.-E. Azur Space Solar Power GMBH, Enhanced Fresnel Assembly - EFA Type: 3C42A – with 10x10mm² CPV TJ Solar Cell Application: Concentrating Photovoltaic (CPV) Modules, 2014. http://www.azurspace.com/images/products/DB_3987-00-00_3C42_AzurDesign_EFA_10x10_2014-03-27.pdf.
- [106] L. Micheli, N. Sarmah, X. Luo, K.S. Reddy, T.K. Mallick, Design of a 16-cell densely-packed receiver for high concentrating photovoltaic applications, *Energy Procedia*. 54 (2014) 185–198. doi:10.1016/j.egypro.2014.07.262.
- [107] L. Micheli, K. Reddy, T.K. Mallick, Plate Micro-Fins in Natural Convection: Experimental Study on Thermal Effectiveness and Mass Usage, *International Conference on Polyaeneration*. (2013). doi:00.0000/PhysRevLett.000.000000.
- [108] G. Peharz, J.P. Ferrer Rodríguez, G. Siefer, A.W. Bett, A method for using CPV modules as temperature sensors and its application to rating procedures, *Solar Energy Materials and Solar Cells*. 95 (2011) 2734–2744. doi:10.1016/j.solmat.2011.03.030.
- [109] M. Theristis, T.S. O’Donovan, Electrical-thermal analysis of III-V triple-

- junction solar cells under variable spectra and ambient temperatures, *Solar Energy*. 118 (2015) 533–546. doi:10.1016/j.solener.2015.06.003.
- [110] Y.L. He, K. Wang, Y. Qiu, B.C. Du, Q. Liang, S. Du, Review of the solar flux distribution in concentrated solar power: Non-uniform features, challenges, and solutions, *Applied Thermal Engineering*. 149 (2019) 448–474. doi:10.1016/j.applthermaleng.2018.12.006.
- [111] F. Languy, C. Lenaerts, J. Loicq, T. Thibert, S. Habraken, Performance of solar concentrator made of an achromatic Fresnel doublet measured with a continuous solar simulator and comparison with a singlet, *Solar Energy Materials and Solar Cells*. 109 (2013) 70–76. doi:10.1016/j.solmat.2012.10.008.
- [112] T. Hornung, M. Steiner, P. Nitz, Estimation of the influence of Fresnel lens temperature on energy generation of a concentrator photovoltaic system, *AIP Conference Proceedings*. 1407 (2011) 97–100. doi:10.1063/1.3658303.
- [113] M. Tawalbeh, A. Al-Othman, F. Kafiah, E. Abdelsalam, F. Almomani, M. Alkasrawi, Environmental impacts of solar photovoltaic systems: A critical review of recent progress and future outlook, *Science of The Total Environment*. 759 (2021) 143528. doi:10.1016/j.scitotenv.2020.143528.
- [114] A. Royne, C.J. Dey, D.R. Mills, Cooling of photovoltaic cells under concentrated illumination: A critical review, *Solar Energy Materials and Solar Cells*. 86 (2005) 451–483. doi:10.1016/j.solmat.2004.09.003.
- [115] L. Micheli, K.S. Reddy, T.K. Mallick, General correlations among geometry, orientation and thermal performance of natural convective micro-finned heat sinks, *International Journal of Heat and Mass Transfer*. 91 (2015) 711–724. doi:10.1016/j.ijheatmasstransfer.2015.08.015.
- [116] E.M. Abo-Zahhad, S. Ookawara, A. Radwan, A.H. El-Shazly, M.F. Elkady, Numerical analyses of hybrid jet impingement/microchannel cooling device for thermal management of high concentrator triple-junction solar cell, *Applied Energy*. 253 (2019) 113538. doi:10.1016/j.apenergy.2019.113538.
- [117] E.M. Abo-Zahhad, S. Ookawara, A. Radwan, A.H. El-Shazly, M.F. El-Kady, M.F.C. Esmail, Performance, limits, and thermal stress analysis of high concentrator multijunction solar cell under passive cooling conditions, *Applied Thermal Engineering*. 164 (2020) 114497. doi:10.1016/j.applthermaleng.2019.114497.
- [118] M. Alzahrani, H. Baig, K. Shanks, T. Mallick, Estimation of the performance limits of a concentrator solar cell coupled with a micro heat sink based on a finite element simulation, *Applied Thermal Engineering*. (2020) 115315. doi:10.1016/j.applthermaleng.2020.115315.
- [119] A. Aldossary, S. Mahmoud, R. Al-dadah, Technical feasibility study of passive and active cooling for concentrator PV in harsh environment, *Applied Thermal Engineering*. 100 (2016) 490–500. doi:10.1016/j.applthermaleng.2016.02.023.
- [120] Y.L. He, K. Wang, Y. Qiu, B.C. Du, Q. Liang, S. Du, Review of the solar flux distribution in concentrated solar power: Non-uniform features,

- challenges, and solutions, Elsevier Ltd, 2019.
doi:10.1016/j.applthermaleng.2018.12.006.
- [121] S. Wang, J. Shi, H.H. Chen, S.R. Schafer, M. Munir, G. Stecker, W. Pan, J.J. Lee, C.L. Chen, Cooling design and evaluation for photovoltaic cells within constrained space in a CPV/CSP hybrid solar system, *Applied Thermal Engineering*. 110 (2017) 369–381.
doi:10.1016/j.applthermaleng.2016.08.196.
- [122] M. Renzi, L. Egidi, G. Comodi, Performance analysis of two 3.5 kWp CPV systems under real operating conditions, *Applied Energy*. 160 (2015) 687–696. doi:10.1016/j.apenergy.2015.08.096.
- [123] C. Kandilli, Performance analysis of a novel concentrating photovoltaic combined system, *Energy Conversion and Management*. 67 (2013) 186–196. doi:10.1016/j.enconman.2012.11.020.
- [124] A. Kumar, N. Deo, H.L. Yadav, Analysis of design parameters for wavelength selective holographic solar concentrators, *Conference Record of the IEEE Photovoltaic Specialists Conference*. (2008) 8–11.
doi:10.1109/PVSC.2008.4922898.
- [125] W.G.J.H.M. van Sark, Luminescent solar concentrators - A low cost photovoltaics alternative, *Renewable Energy*. 49 (2013) 207–210.
doi:10.1016/j.renene.2012.01.030.
- [126] Newport Corporation, Neutral Density Filter Selection Guide, (n.d.).
<https://www.newport.com/g/neutral-density-filter-selection-guide>
(accessed March 1, 2020).
- [127] R.C. Shurtz, Total Hemispherical Emissivity of Metals Applicable to Radiant Heat Testing, (n.d.).
- [128] World Weather Online, (n.d.). <https://www.worldweatheronline.com>
(accessed February 2, 2022).
- [129] M. Digrazia, G. Jorgensen, REFLECTECH MIRROR FILM : DESIGN FLEXIBILITY AND DURABILITY IN REFLECTING SOLAR APPLICATIONS, (n.d.).

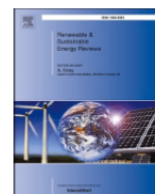
Appendix

Article 1. M. Alzahrani, K. Shanks, T. Mallick, "Advances and limitations of increasing solar irradiance for concentrating photovoltaics thermal system," Renewable and Sustainable Energy Reviews, 138 (2021), p. 110517, [10.1016/j.rser.2020.110517](https://doi.org/10.1016/j.rser.2020.110517).



Contents lists available at ScienceDirect

Renewable and Sustainable Energy Reviews

journal homepage: <http://www.elsevier.com/locate/rser>

Advances and limitations of increasing solar irradiance for concentrating photovoltaics thermal system

Mussad Alzahrani^{a,b,*}, Katie Shanks^a, Tapas K. Mallick^a^a Environment and Sustainability Institute, University of Exeter, Penryn Campus, Cornwall, TR10 9FE, UK^b Mechanical and Energy Engineering Department, Imam Abdulrahman Bin Faisal University, Dammam, 34212, Saudi Arabia

ARTICLE INFO

Keywords:

Concentrated photovoltaic thermal (CPVT)
Semiconductor materials
Bandgap energy
Thermal receiver
Optical concentrator and concentration ratio

ABSTRACT

Concentrating photovoltaic-thermal (CPVT) technology harnesses solar energy by increasing the solar density upon cells using optical concentrators. CPVT systems are the focus of ongoing research and improvements to achieve the highest potential for energy harnessing and utilization. Increasing the concentration ratio for high energy generation raises many advances and limitations in the CPVT design. This article highlights the influence of the temperature with an increasing concentration ratio on CPVT components in terms of single-/multi-junction semiconductor materials, primary and secondary optical concentrator materials, and thermal receiver design. To achieve this, the theory of single- and multi-junction solar cell electrical characteristics (V_{oc} , I_{sc} , FF and η) is first explained to understand their dependence on the temperature and concentration ratio. An extensive literature review discussing the advantages, disadvantages, and potential of current CPVT research is given. This includes graphical and tabular summaries of many of the various CPVT design performances.

In this review, it has been ascertained that higher concentration ratios raise the temperature at which the performance, operation and reliability of CPVT system are affected. Also, this review indicates that the temperature elevation of the CPVT components is significantly impacted by the optical configuration and their material types and reflectance. A thermal receiver is illustrated as three components: solar cell (heat source), heat spreader (substrates) and its different types, and cooling mechanism. In addition, the article addresses the thermomechanical stress created with intensified illumination, especially with secondary optics, where the optical materials and optical tolerance need to be carefully explored. The economic implications of a high concentration ratio level are briefly considered, addressing the reduction in system cost by enhancing the system efficiency. Suggestions are made throughout the review as to possible improvements in system performance.

1. Introduction

Concentrator photovoltaic thermal (CPVT) systems are the combination of concentrator photovoltaics (CPV) and photovoltaic thermal (PVT) systems. A CPV system concentrates the sun's rays onto a PV cell to generate electricity. A CPVT system concentrates the sun's rays into a fluid to transfer heat either directly or indirectly and to generate electricity. CPV aims to replace the large number of expensive flat PV cells due to its low solar energy density, with inexpensive optical concentrators that concentrate light into fewer PV receivers. However, increasing the solar energy density raises the PV cell temperature and results in increased heat dissipation. High PV cell temperatures impact the designed operating condition of the PV and cause losses in the solar radiation absorbed. Thus, passive or active cooling is needed to maintain

the temperature of the PV cell to ensure the highest efficiency. However, cooling down the PV cell temperature causes a parasitic load and this parasitic load increases with increase of the concentration of solar radiation. PVT aims to extract the generated heat and then employ it in the end-use application, such as domestic hot water or direct heating. However, PVT needs to use a large number of PV receivers to produce high-quality thermal energy, and that results in high investment costs. Also, the low temperature of the thermal energy limits the possible number of end-use applications.

The drawbacks of both CPV and PVT are resolved in CPVT. CPVT generates both electrical and thermal energies at moderate cell temperatures. Since the cell temperature levels are moderate, high-temperature thermal energy can be extracted and utilized in a vast number of applications. CPVT operates by concentrating the ray optics

* Corresponding author. Environment and Sustainability Institute, University of Exeter, Penryn Campus, Cornwall, TR10 9FE, UK.
E-mail addresses: ma778@exeter.ac.uk, mmsalzahrani@iau.edu.sa (M. Alzahrani).

in a minimal area, which results in a smaller number of PV cells. However, the high concentration in CPVT might result in increased optical losses (e.g. chromatic aberration for lenses), illumination and temperature non-uniformity, and PV overheating. CPVT of more than >10 suns (medium and upwards concentration) benefits only from direct solar radiation, not diffuse radiation. The flowchart of the working concept for the CPVT system, including a summary of its limitations, is demonstrated in Fig. 1.

The primary component to operate the CPVT system thermally and electrically is the optical performance. Concentrators utilize either imaging or non-imaging optics to intensify the solar density in either one or two optical stages into either a focal line or focal point where electrical and/or thermal energy are captured. The optical performance is dependent on the amount of sunlight incident on the PV cell on the basis of suns, where 1 sun is equivalent to 1000 W/m^2 [1]. Based on the number of concentrated suns, a CPVT system is classified depending on the optical concentration ratio (CR_T), which is the irradiance ratio between the primary optical stage and the receiver. CR_T is classified as low ($CR_T < 10 \text{ sun}$), medium ($10 \text{ sun} < CR_T \leq 100 \text{ sun}$), high ($100 \text{ sun} < CR_T \leq 2000 \text{ sun}$) or ultrahigh ($CR_T > 2000 \text{ sun}$) [2]. Increasing the CR_T results in high thermal and electrical energies; however, a high level of CR_T adds to the complexity of the CPVT system, such as the tracking system (acceptance and incident angles) and irradiance non-uniformity on the PV cell.

Different review articles on PVT technology, CPV technology, and CPVT technology can already be found in the literature [3–10]. Sharaf and Orhan [11,12] have primarily focused on CPVT systems in two reviews covering the considerable number of publications on CPVT. Their two publications examined and reviewed the basics and progress in CPVTs, with an exhaustive coverage of all CPVT technology. Daneshazarian et al. [13] reviewed CPVT systems with an emphasis on the fundamentals, operating concept, and system configurations, with the testing results for domestic and industrial applications. Another article by Mojiri et al. [14] provided a review of spectral beam decomposition technologies to evaluate the potential for using this mechanism for solar systems, discussing PVT/CPVT systems, whereas Ju et al. [15] reviewed particularly spectral beam splitting technologies for CPVT systems in a systematic and thorough analysis. However, to the best of the author's knowledge, there has not yet been any review dedicated mainly to assessing the influence of the temperature on the CPVT system components with increase of the concentration ratio.

This literature review therefore aims to investigate the effect of the temperature when increasing the concentration ratio on the CPVT components: solar cell, optics, and thermal receiver design, as shown in Fig. 2 (a) and (b). An explanation of the electrical considerations for single- and multi-junction semiconductor materials is given to help

understand the influence of the temperature and concentration ratio. One objective of this review is to determine the impact of the temperature in a large number of studies on the semiconductor materials and primary/secondary optics with an increasing concentration ratio in CPVT systems, as well as techniques for thermal management. Only experimental studies that gave all the system details and performance results are reported in order to gain a realistic assessment of achievable performance.

2. Electrical and thermal considerations for CPVT system

A photovoltaic (PV) cell converts electromagnetic radiation into electrical energy via the p-n junction. The electron absorbs the photon energy in the valence band (n-type semiconductor), and then the absorbed energy stimulates the electron to move to the conduction band (p-type semiconductor). This electron movement creates a hole in the valence band, allowing the free flow of the electron throughout the semiconductor. The PV cell electrical output is challenged by its bandgap energy, in which the photon energy must be greater than the energy of the bandgap to induce photogeneration of the charge carrier (electron and hole). The bandgap energy is the energy separating the valence band from the conduction band. Photon energy that is not compatible with the bandgap energy generates intrinsic losses which can be grouped as thermalization, below bandgap, Boltzmann, Carnot, and emission losses. These intrinsic losses are associated with the limiting of the electrical performance in the form of current and voltage reductions [16]. Below bandgap and emission losses result in current reduction due to the smaller number of charge carriers. In contrast, thermalization, Carnot, and Boltzmann losses result in voltage reduction due to the smaller energy utilization of the charge carrier [17].

The I-V curve of a cell is influenced by both solar irradiance and temperature. The short-circuit current (I_{sc}) is dependent on its performance on the solar irradiance where I_{sc} and the solar irradiance have a proportional relationship, as in Fig. 3 (a). On the other hand, the open-circuit voltage (V_{oc}) has an inverse correlation with temperature, as in Fig. 3 (b). The effect of solar irradiance on V_{oc} and the temperature on I_{sc} is minimal. The excellent squareness of the I-V curve (the ratio between the maximum power point (MPP) and V_{oc} and I_{sc} solar cell products) indicates a high Fill Factor (FF) which can be observed at low temperatures or relatively high temperatures (concentrated solar irradiance) but by employing the multi-junction solar cell. In terms of high temperature, the squareness of the I-V curve is flattened, at which the FF value is low, reflecting a poor quality of PV cell electrical output, especially for a single-junction solar cell. As the concentration ratio is increased, the electrical parameters of the solar cell V_{oc} , I_{sc} , FF and efficiency (η) alter; thus, their sensitivity to temperature also changes.

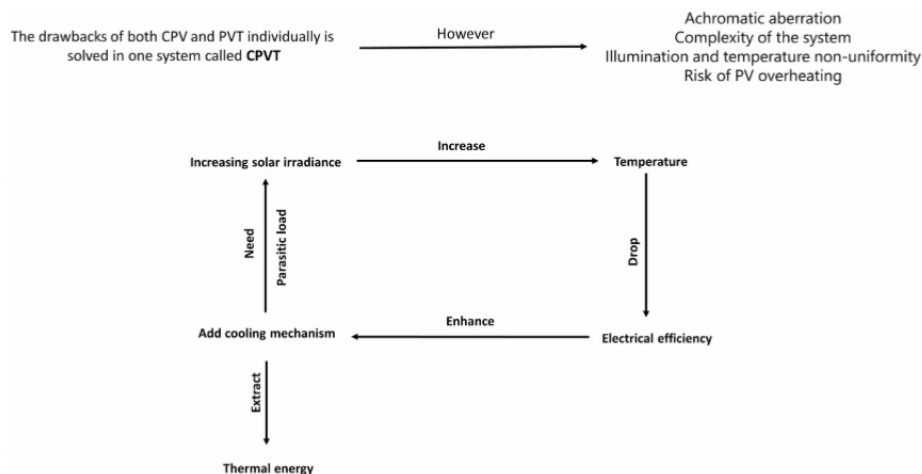


Fig. 1. Working flow of CPVT system with summarized limitations for CPVT system.

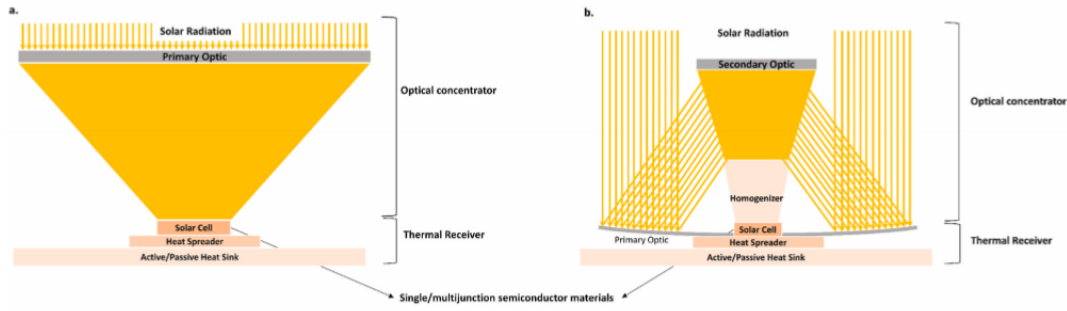


Fig. 2. (a) A basic Fresnel lens and (b) a basic Cassegrain CPVT system configuration for the three components of primary/secondary optics, single-/multi-junction solar cell, and thermal receiver.

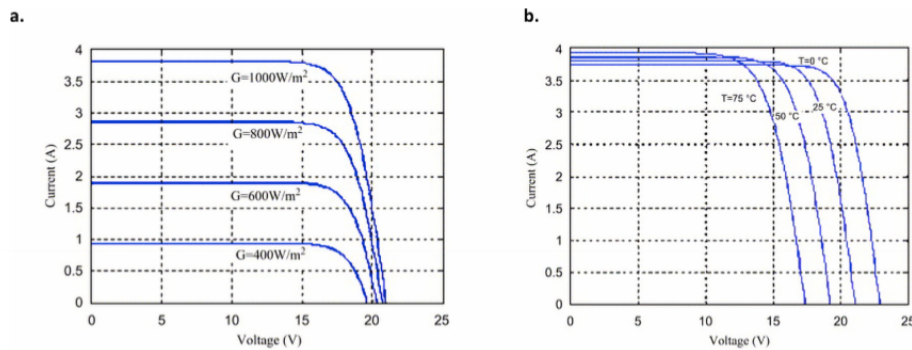


Fig. 3. Effect of (a) solar irradiance and (b) cell temperature on I-V curve of a single-junction PV cell [18].

A multi-junction PV (MJPV) cell allows sorting of the photon energy by adding more than one junction with different bandgap energy to maximize the efficiency of the PV cell and hence the power output [11, 12]. The MJPV cell is stacked in series, where V_{oc} is the sum of all the subcells' V_{oc} . The temperature coefficient $\Delta V_{oc}/\Delta T$ of the multi-junction is also the sum of the $\Delta V_{oc}/\Delta T$ [19]. The temperature coefficient $\Delta V_{oc}/\Delta T$ of the multi-junction faces a drop in V_{oc} when the number of junctions increases due to the low bandgap energy required for the last subcell. However, increasing the solar irradiance reduces the temperature coefficient drop due to an increase in the V_{oc} . The current in the stacked series needs to be matched to avoid losses [19]. Since the temperature coefficient is not equal from the bottom, medial, to top-subcells, the current will be different in each subcell, causing “current mismatch”. When the tandem-subcell temperature increases, the bandgap decreases and this results in the increase of the I_{sc} . The top subcell bandgap is also decreased, allowing fewer photons to reach the bottom subcell, and this minimizes the I_{sc} with temperature. Additionally, the current output at every subcell has a limitation and this influences the FF of the MJPV cell. Aiken et al. [15] conducted a temperature coefficient study of the integrated current for a triple junction cell InGaP/InGaAs/Ge at a temperature range from 5 °C to 100 °C. The result indicated that I_{sc} has a current mismatch of only 3.3% at 100 °C. Thus, a solar cell is negligibly sensitive to temperature in terms of current mismatching.

Solar cell efficiency and bandgap energy are the two main factors for solar cell selection. The maximum efficiency of single-junction solar cells is described by the Shockley–Queisser limit, where all the photons above the bandgap are absorbed, and this limits the maximum conversion efficiency to 33.7% [20]. The bandgap energy differs according to the energy-band structure of the semiconductor materials. The theoretical maximum efficiency for different single-junction solar cell materials, with their bandgap energy designed as either wafer-based or thin film, is measured in different companies and demonstrated in Fig. 4 [21, 22].

Increasing the number of junctions reduces the thermalization to

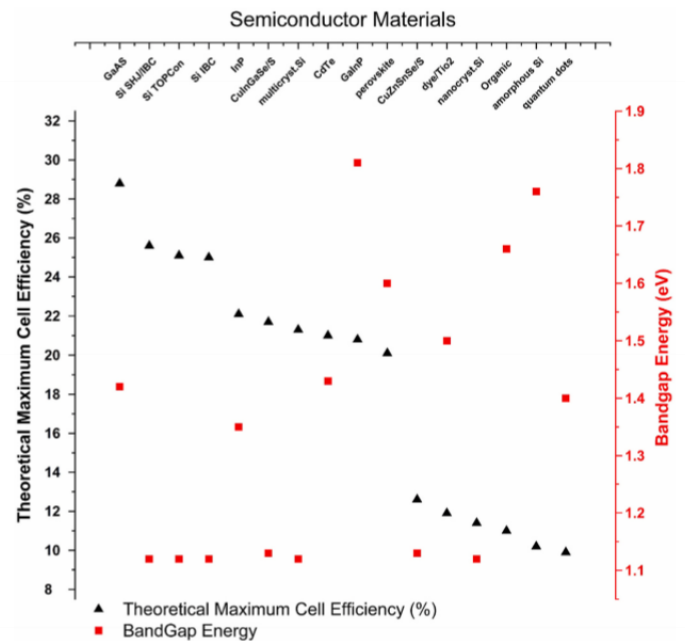


Fig. 4. Different semiconductor materials (thin-film and wafer-based) bandgap energy, maximum efficiency, all under 1 sun concentration ratio. The theoretical maximum cell efficiency is measured for terrestrial application under AM 1.5.

below the bandgap losses, and this increases the conversion efficiency of the solar cell [17]. A multi-junction solar cell has the capability to absorb a wide range of solar wavelengths due to the different bandgap energy for the individual subcells in one monolithic junction solar cell. The limiting efficiency is illustrated in Fig. 5 for several non-toxic and abundant cell materials made of 1–8 junctions for the ideal bandgap.

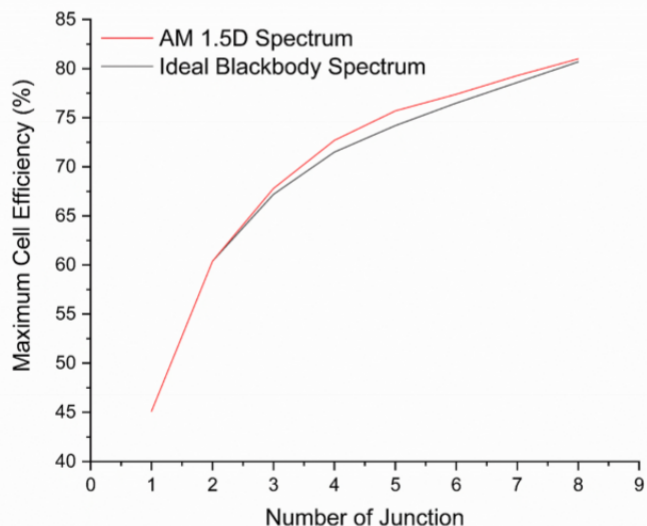


Fig. 5. The limiting efficiency for ideal bandgap energy under no concentration for solar cell use. The solar cells' efficiencies were calculated based on an ideal blackbody spectrum (black line) and the AM 1.5D spectrum (red line) for various semiconductor material configurations. (For interpretation of the references to color in this figure legend, the reader is referred to the Web version of this article.)

The maximum efficiency of an infinite number of junctions with an optimized bandgap for a blackbody spectrum at 6000 K under concentration is 86.8% at AM 1.5 [23,24]; however, current electrical fabrication techniques have only been optimized for up to 5 junctions. Introducing new MJPV cell architectures with different numbers of subcells should not result in any new form of loss or increase the price of electrical fabrication. However, other costs are likely to rise due to the use of rarer and more expensive materials for the multiple layers.

3. CPVT system: cells, optics, and receivers

3.1. Semiconductor materials: temperature and efficiencies

Due to the bandgap energy, the unabsorbed photon energy on the solar cell surface is converted to thermal energy, increasing the cell temperature. Moreover, concentrating solar radiation onto a PV cell and solar irradiance non-uniformity also increase the cell temperature and hence reduce the cell efficiency. Other efficiency losses also occur in the PV cell due to poor absorption of photons, such as reflectance loss in the inner and outer layers and shading loss due to the contact grid on the front side of the PV cell. Elevated cell temperatures accelerate cell degradation, thus minimizing their lifetime. To ensure the maximum possible lifetime and an adequate cell efficiency, the cell should be maintained at the typical operating temperature at different ranges of concentration ratio [25].

A large number of semiconductor materials used in different theoretical and experimental studies of solar concentrator systems with their concentration ratio range are collectively shown in Fig. 6. Clearly, gallium arsenide (GaAs) semiconductor material in one-, two- or three-junction configurations can accept a wide range of concentration ratios due to its low temperature sensitivity, high resistivity to radiation damage, and good performance under concentrated illumination.

As outlined in Fig. 7, the bandgap of the semiconductor material, the concentration ratio, and thermal properties should be taken into consideration in relation to each other in selecting the PV cell material to avoid operating at a high temperature. PV cell materials are dependent on the cell temperature under concentrated illumination. Thus, the bandgap energy of a PV cell should be selected in accordance with the concentration ratio to enhance the electrical and thermal performance.

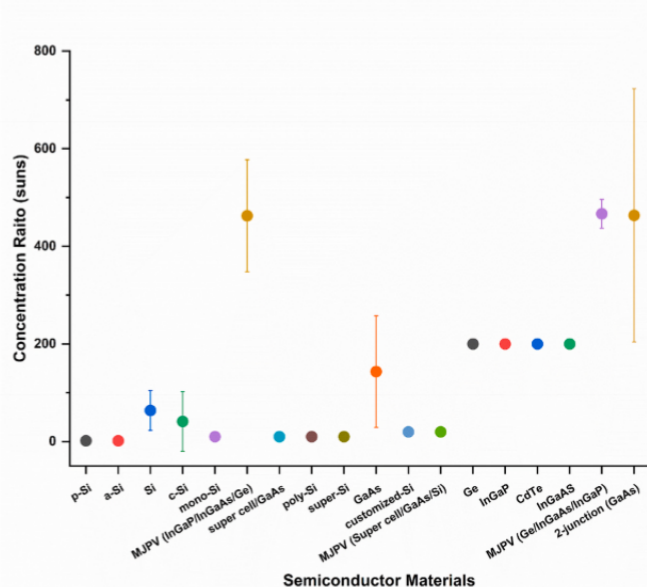


Fig. 6. Semiconductor materials and their concentration ratio in theoretical and experimental studies considered by this review with interval bars which show the range of concentration ratios tested in the literature.

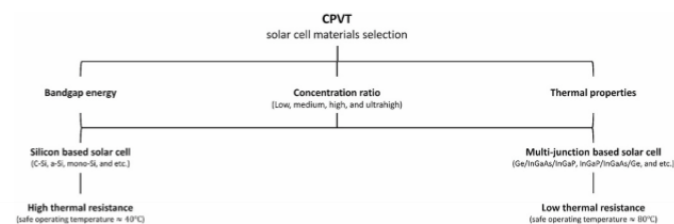


Fig. 7. Factor considerations in the selection of the solar cell materials in a CPVT system.

3.2. Concentrators: temperature and efficiencies

The optical tolerance of a CPVT system is a critical factor, especially with increasing concentration ratio and taking into consideration the sunlight divergence angle of ± 0.265 . The divergence angle of the sunlight implies an equally small acceptance angle, which should be enough to capture the solar radiation emitted from the sun. However, the impact of other factors, such as tracking error, thermomechanical effects, dynamic load, and materials properties, must also be considered [26]. The acceptance angle indicates the required tracking system sensitivity, where the light divergence should be minimized to allow for a high concentration ratio. Minimized light divergence is achieved by either a large size primary optic or a secondary optic. To ensure the lowest light divergence, a highly accurate continuous tracking system and a highly smooth surface are required, which are expensive and difficult to acquire. Adding a secondary optic such as a homogenizer or light funnel into the CPVT design improves the acceptance angle and uniformity of the illumination profile of the system, which reduces the demand on the system accuracy. However, the materials of the secondary optics should be carefully selected to withstand the high temperature. In addition, maximizing the size of the primary optics adds to the overall cost of the initial system. The advances and limitations of CPVT optics in terms of increasing the concentration ratio are summarized in Fig. 8.

The optical efficiency of a solar concentrator is dependent on the incident angle, where the maximum performance is typically achieved at normal incidence (90°) to the sun (the zenith angle is equal to the system tilt angle). This is when there is the least scattering and

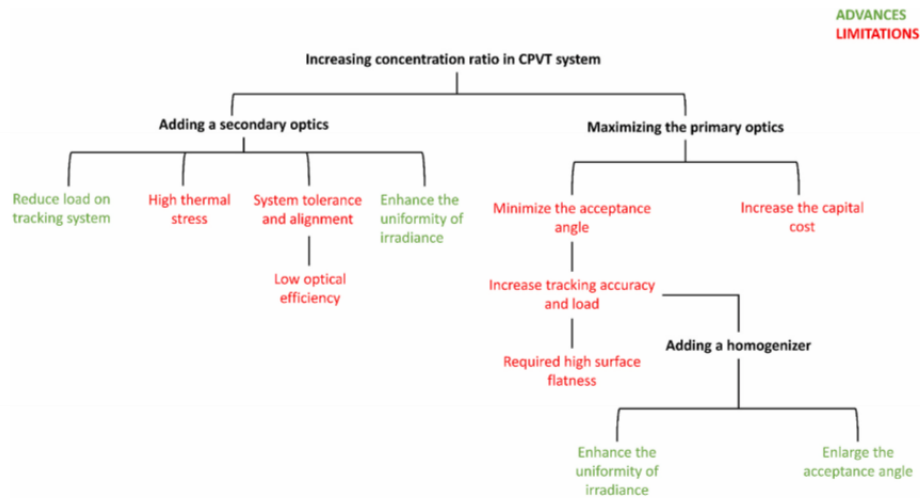


Fig. 8. Summary of advances and limitations in the optical concept for increasing the concentration ratio.

absorption within the system, according to the optical properties of the concentrator materials, and where the solar radiation is highly reflected/refracted from the concentrator components. The graph of a low concentration of 3.6 suns crossed compound parabolic concentrator shows a drastic drop in optical efficiency at a 35° incident angle (the acceptance angle) [27], as shown in Fig. 9 (a). In contrast, the ultrahigh concentration ratio based on the Fresnel lens producing 5247 suns shows a drop of 90% in the optical efficiency at incidence angles of 0.4°, which confirms the dependency of the optical efficiency on the incident angle and demonstrates the reduction in the required acceptance angle by increasing the concentration ratio beyond 100 suns [28,29], as in Fig. 9 (b).

The mechanisms of concentrating the solar radiation are reflective, refractive, luminescent, total internal reflection, or a combination of these. Optical concentrators employ multiple stages to increase the acceptance and/or the concentration ratio. Boosting the concentration ratio is achieved at the price of different configurations of CPVT systems. The ranges of concentration ratio and working fluid temperatures for different CPVT systems theoretically and experimentally investigated are illustrated in Fig. 10.

3.3. Thermal receiver design and materials

The process of thermally managing the heat in a CPVT system relies on the concept of pre-illumination and post-illumination heat extraction utilizing a heat transfer fluid (HTF). Pre-illumination design is based on the concept of spectral decomposition, allowing a higher outlet temperature by redirecting all the unutilized spectral wavelength to a thermal receiver [14,15]. However, the difficulty of matching the optical properties with either the HTF or the filters means that pre-illumination design is less mature than post-illumination design.

Post-illumination design harvests the heat after reaching the solar cell. However, the outlet HTF temperature is limited to the cell’s maximum recommended operating condition in the range of 50–80 °C.

The thermal performance of the PV cell primarily relies on the heat spreader and the accompanying different layers of the materials employed. The heat spreader is located between the PV cell (heat source) and the cooling mechanism to conduct heat for thermal utilization according to the temperature range or dissipation rate. The most common heat spreaders in CPVT systems are direct bonded copper (DBC) and insulated metal substrates (IMS) due to their excellent thermophysical properties [30–32]. However, silicon wafer substrates have shown a high potential as heat spreaders due to their thermal expansion compatibility with silicon semiconductor materials [33]. The heat spreader materials need to have a high thermal conductivity and high electrical insulation, where doubling the thermal conductivity of the heat spreader enhances the thermal efficiency by 13.5% [34]. In addition, increasing the contact factor between different layers using thermal paste results in conducting much of the heat to the thermal collector, reducing in this way the cell efficiency by just $-0.0043\%/^{\circ}\text{C}$, whereas without thermal paste the result is $-0.0094\%/^{\circ}\text{C}$ [35]. High resistance silica gel is widely used in CPVT systems as electrical insulators, having high thermal conductivity [36–38].

Cooling mechanisms (post-illumination) for the PV cell may be passive or active. Passive cooling in point focus systems has been proven to successfully manage the PV cell temperature with different heatsink geometries and for high concentration ratios for up to 2000 suns [35, 39]. For ultrahigh concentration ratios, solar cells of 1 mm² or smaller can maintain the cell temperature below the maximum recommended operating temperature with a conventional flat-plate heatsink up to 10,000 suns [40]. In passive cooling, the heat dissipation is attributed to the cell area, where the heat is generated. Thus, maximizing the area of the

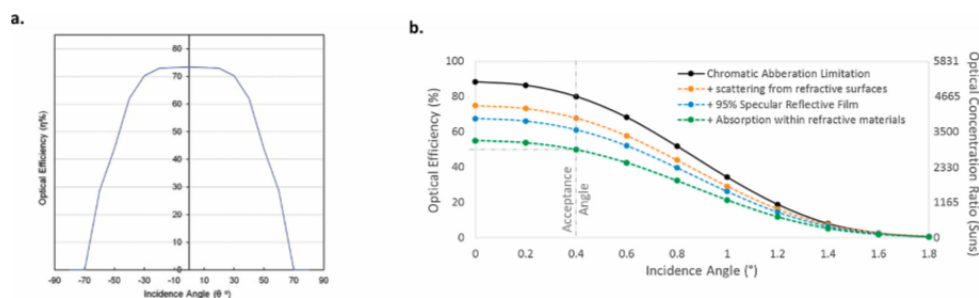


Fig. 9. Optical efficiency vs incidence angle: (a) optical efficiency in CPC for low concentration ratio in building application; (b) optical efficiency in high concentration photovoltaic design based on Fresnel lens [27,28].

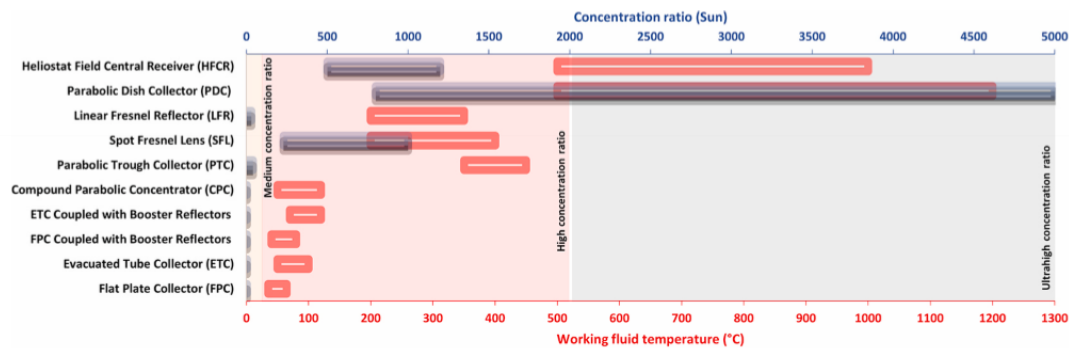


Fig. 10. CPVT systems with the concentration ratio ranges and working fluid temperature ranges as reported in Ref. [11,13].

heatsink by exploring different geometry configurations would maximize the heat dissipation rate. For the heatsink material, silicon has shown the lowest thermal stress and the maximum heat transfer in comparison with aluminum and copper [33]. In >2000 suns, the weight of the heatsink should be considered to reduce the required dynamic load and avoid increased tracking error.

Active cooling, which ordinarily embraces forced motion for a cooling fluid, increases the overall thermal efficiency. An active cooling mechanism is widely used in systems with line focus PV cell design, where a line pipe configuration is more suitable to extract heat effectively. Pure fluid or nanofluid cooling is more suitable than air due to its high heat capacity and its potential for different end-use applications, especially with high temperature. The originality of using nanoparticles with the fluid is to enhance the thermal conductivity, in this way boosting the heat transfer between the receiver and the fluid. However, increasing the temperature of the nanoparticles has a major influence on improving the thermal conductivity [41–45]. The parasitic power for a fan or pump increases with the increase in the concentration ratio, where more fluid needs to be forced onto the heat dissipation domain at an optimized rate for the maximum heat extraction.

3.4. Linear concentrators: the reflective trough of low-medium concentration

Most CPVT designs are linear geometry systems made of reflective materials, typically in a trough shape and capable of up to 100 suns (medium concentration). M. Li et al. [46] studied the electrical and thermal performance of 2 m² and 10 m² configurations for an aluminum alloy parabolic trough at 10.27 suns and 20 suns, respectively. In the 2 m² system, arrays of cells using four types of semiconductor materials connected in series were mounted on the receiver using a thermally-conductive tape. In the 10 m² configuration, the width of the receiver and the width of the aperture area were increased, resulting in an increase of the concentration ratio. Water circulated as HTF to cool down the cell temperature. The experimental results of the different semiconductor materials are listed in Table 1.

The water output temperature can be an indication of the cell temperature, which is higher for cells with higher series resistance and

hence typically reduced power outputs. The best performance of GaAs is mainly due to its lower series resistance and yet it still has a higher performance in a higher temperature environment. However, the high series resistance for mono-Si, poly-Si and super cells (made from silicon and GaAs material) indicates better thermal performance [46]. Reduction in the concentration ratio results in a decrease in the heat exchange effectiveness. Thus, the PV temperature increases due to less heat being removed, which reduces the electrical efficiency. M. Li et al. [46] demonstrate the correlation between the rise in the water output temperature and the thermal efficiency, and the reverse correlation between the water output temperature and the electrical efficiency for an aperture area of 2 m², as in Fig. 11 (b). Kunnemeyer et al. [50] investigated a V-trough concentrating model theoretically and experimentally for 1.6 suns. The concentrators were constructed from mirror-finished stainless steel sheet to withstand the corrosive maritime climate in New Zealand. The polished stainless steel in Ref. [51] had a reflectivity of 0.67. However, aluminum with 0.9 reflectivity would yield a higher solar irradiance at the absorber surface. The combined electrical and thermal efficiency peaked at 35%, even though the system was designed to achieve a peak efficiency of 70%. The drop in efficiency is due to heat loss by convection and radiation in the absence of a glazing layer, which reduced the thermal efficiency. Even with the low reflectivity, the stainless-steel sheet offered a 25% increase in the concentration ratio over a year in comparison to aluminum. Kostic et al. [52] presented the influence of the aluminum (Al) sheet and aluminum foil reflectance for flat plate solar radiation concentrators. The outcomes showed that the total and diffuse reflectance of the Al sheet and Al foil concentrators are the same, whereas the specular reflectance is higher for Al foil concentrators, resulting in increasing the solar radiation intensity. The solar radiation intensity results in a daily increase of the electrical and thermal efficiency, as shown in Table 2.

Although with a 10% additional cost of Al sheet and Al foil concentrators, the results demonstrated a remarkable increase in the energy efficiency of 35% and 50% for concentrators made of Al sheet and Al foil, respectively, in comparison to the system without concentrators. Nilsson et al. [53] studied the long-term performance of an asymmetric compound parabolic concentrator (CPC) built for high altitude in Sweden. Anodized aluminum and aluminum-laminated steel reflectors were

Table 1
The parameters of the 2 m² and 10 m² trough parabolic configuration [46].

| Semiconductor materials | Number of cells in an array | Water output temperature (°C) | Thermal efficiency (%) | Electrical efficiency (%) |
|----------------------------------|-----------------------------|-------------------------------|------------------------|---------------------------|
| Apertures area 2 m ² | | | | |
| Monocrystalline cell | 10 | 40–49 | 30–47 | 0.53–0.63 |
| Polycrystalline cell | 10 | 39–48 | 42–48 | 0.44–0.59 |
| Super cell | 16 | 39–47 | 36–46 | 2.50–3.00 |
| GaAs cell | 40 | 35–43 | 28–43 | 6.67–7.31 |
| Apertures area 10 m ² | | | | |
| Concentrating silicon cell | 96 | 29.60 | 42.41 | 7.51 |
| GaAs cell | 40 | 33.89 | 49.84 | 9.88 |

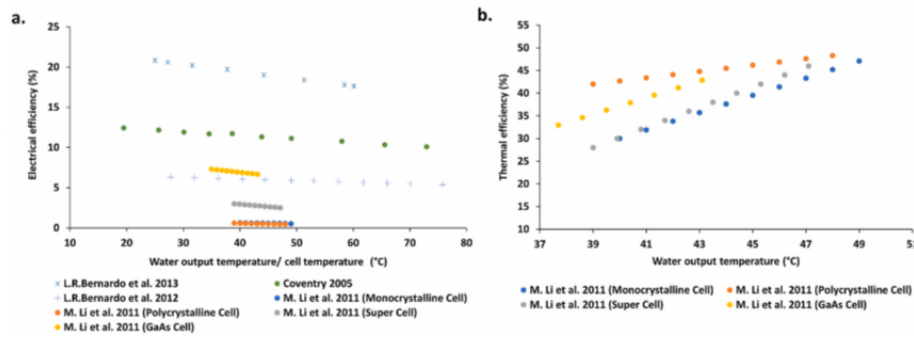


Fig. 11. The water output temperature/cell temperature impact on (a) the electrical efficiency and (b) the thermal efficiency of the system in different studies [46–49].

Table 2
Results for solar radiation intensity, thermal energy generated, and electrical energy generated.

| Reflectors | Concentration ratio (sun) | Daily thermal energy generated (%) | Daily electrical energy generated (%) |
|------------|---------------------------|------------------------------------|---------------------------------------|
| Al sheet | 1.44 | 39 | 8.6 |
| Al foil | 1.66 | 55 | 17.1 |

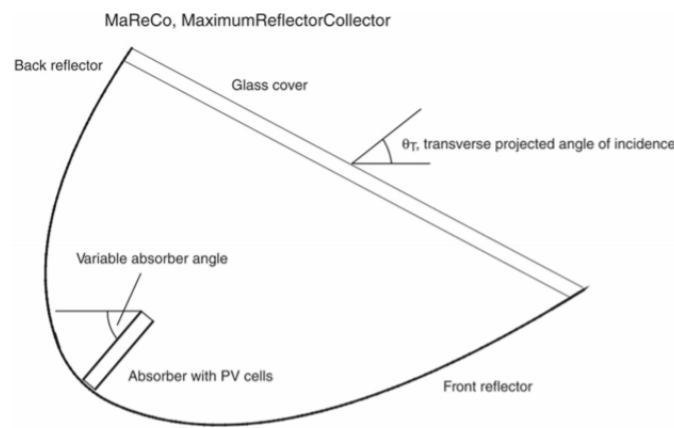


Fig. 12. MaReCo (maximum reflector collector) PV-thermal hybrid has the same focal line for both parabolic reflectors. The glass cover is tilted at a 30° angle between the absorber and the horizontal. Also shown is the transverse projected angle of incidence [53].

investigated. The aluminum-laminated steel reflectors were the preferable option due to their improved mechanical properties which require less mechanical support. However, the steel-based reflector has a relatively low specular reflectance because its plastic coating absorbs light below 400 nm and silicon cells absorb from ~300 nm. The measurement of the MaReCo (Maximum Reflector Collector) in these studies showed that the front reflector collects most of the solar radiation in the summer, whereas the back reflector dominated collection in the spring and fall, as shown in Fig. 12. The comparison of the electrical output results showed a 49% increase for the front collector and 23% increase for the back reflector for both materials compared with no reflector. Steel placed in the back reflector is a good option since there is no difference in the yearly output power for the two materials. For maximum utilization of the solar radiation, PV cells should be installed on both sides of the receiver. Another study showed a compound parabolic concentrator (CPC) of anodized aluminum with 95% solar reflection resulting in 1.5 suns. The study demonstrated that the PV cell can still reach a high temperature even with a low concentration ratio, where the electrical efficiency was measured to be 20.9% at 25 °C [47]. The dependency of

the electrical efficiency on the cell temperature is $-0.4\%/K$, as illustrated in Fig. 11 (a) [47]. The temperature of the outlet water was measured to show the impact of the temperature on the electrical efficiency.

Coventry [48] investigated a parabolic trough collector with a concentration ratio of 35 suns. The collector consists of a glass-on-metal mirror that focuses illumination into a mono-crystalline silicon solar cell for electricity and thermal generation. The electrical and thermal efficiency was measured to be 11% and 58% at standard operating condition (ambient temperature of 25 °C and direct radiation of 1000 W/m²), respectively. Also, the impact of non-uniform illumination on the PV cell was investigated. The illumination along the length of the trough showed a remarkable variation due to the mirror shape, the gap between mirrors, and shading by the receiver support. This investigation included measurement for the non-uniform illumination for 30 suns and 90 suns for the entire and the middle third of the cell surface. A reduction in open circuit voltage of 6.5 mV results in an electrical efficiency drop of 20.6% for uniform illumination and of 19.4% for centralized illumination, as shown in Fig. 13. Consequently, non-uniform illumination causes a locally overheated spot on the PV cell area, which might result in reducing the cell lifetime, although this has still not yet been experimentally investigated. The magnitude of the voltage drops due to the locally overheated spot is significant.

The dependency of the electrical efficiency on the cell temperature is $-0.35\%/^{\circ}C$, as shown in Fig. 11 (a) [52]. Tripanagnostopoulos et al. [54] determined the optimum operation of the hybrid system for a pc-Si module with different scenarios of additional glazing (glass sheet), a booster reflector (aluminum sheet), or both, aiming to maximize the total energy output with a circulating fluid (air/water). The additional glazing is intended to increase the thermal output of the system to about

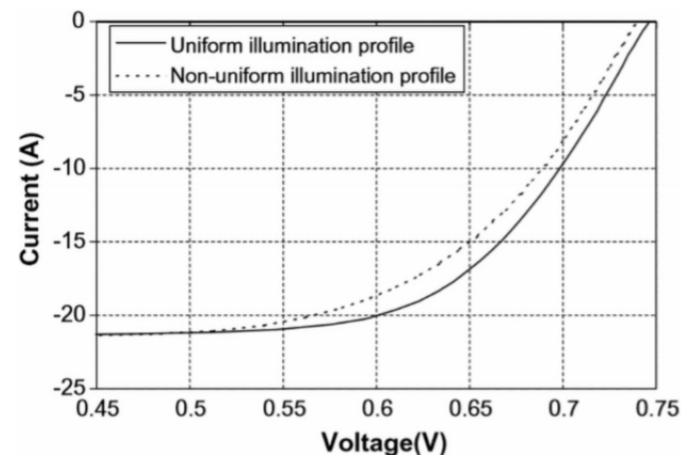


Fig. 13. I-V curve for uniform illumination over the whole cell area (30 suns) and non-uniform illumination on the middle third of the cell (90 suns) [48].

30%, but that results in high optical losses, reducing the electrical efficiency by 16%. The drop in electrical efficiency is balanced by the integration of the diffuse booster reflector, increasing the electrical and thermal efficiencies by about 16% and 45%, respectively. The aluminum sheet results in increasing the solar radiation by 50%; thus, the electrical efficiency increased from 25% to 35% at PV temperatures varying between 40 and 70 °C. Also, the electrical efficiency was measured for the uninsulated and insulated back surface to be 13.3% and 3.3%, respectively. With the insulated back surface, less convection and radiation raised the cell temperature to 55 °C; however, for the uninsulated back surface, the PV cell temperature is 43 °C. Bernardo et al. [49] evaluated the performance of a parabolic trough at a low concentration ratio of 7.8 suns. The selected optical material was silver-coated plastic film laminated on a steel sheet with a reflectance factor of 90% and a cover glass with a transmittance of 90%. The electrical efficiency was measured to be 6.7% at 25 °C. The electrical and thermal dependency on the water outlet temperature is illustrated in Fig. 11 (a) [49], representing the electrical efficiency calculated as a function of different working temperatures at beam irradiation higher than 900 W/m².

Xu et al. [55] studied a low concentrator parabolic collector of 2.44 suns coupled with a refrigeration cycle. The output electrical efficiency was 17.5% with mirror-finished aluminum sheet optical concentrators whose total reflectance was 88%. The condenser was capable of raising the water temperature from 30 °C to 70 °C. Davidsson et al. [56] utilized a building-integrated multifunctional PVT solar window where the reflectors were anodized aluminum with antireflective low-iron glazing. The antireflective material increased the transmittance by about 5% in Ref. [57] to achieve a concentration ratio of 1.33 suns. Anodized aluminum [47,49,56,58–60] as an optical material is highly desirable for optical concentrators in parabolic trough systems due to its high reflectance. Aluminum reflects well for 200–400 nm ultraviolet and 3000–10000 nm infrared [61]. However, aluminum [62] has a lower reflectance in the visible region between 700 and 3000 nm near-infrared compared to copper, gold and silver. Since aluminum reacts with air to create an oxidation layer, anodization as a common electrochemical process is needed to grow a protective oxide film on the aluminum metal surface to improve protection and durability.

For refractive materials, PMMA (methyl methacrylate) [38,58,63] is the dominant material used most commonly in Fresnel lens systems due to its high transparency and excellent stability in different weather conditions up to 85 °C [64]. Spectral color dispersion in a PMMA Fresnel lens system relies on the refractive index of the lens materials in the range of 1.515 to 1.470 between blue and red light. The dependence of the refractive index on the temperature, humidity and incident angle is minimal for PMMA Fresnel lens materials. For low and medium concentration ratios, a trough-based CPVT system is commonly a linear-focal design with reflective materials, whereas refractive lens is utilized more in the point source system and secondary optics to achieve a high concentration ratio. For the comparison and understanding of the optical materials discussed above, the optical materials with low-medium concentration ratios discussed in this section are summarized, along with their thermal properties (coefficient of thermal expansion and working temperature) and remarks for every study, in Table 3.

3.5. High concentration point source concentrators and their secondary optics performance

In a high concentration photovoltaic system, the optical materials and optical tolerance need to be carefully investigated and designed. Secondary optics are introduced to bring the concentration to the required value and relax the demand on the system accuracy. The integration of a homogenizer in the optical configuration allows the system to minimize the non-uniformity of the solar irradiance and increase the acceptance angle. However, thermo-mechanical stresses as a result of non-uniformity could damage the optical materials. Thus, the

secondary optics and homogenizer materials need to be thermally stable and durable, with low thermal expansion coefficients and high working temperatures. Al Siyabi et al. [82] investigated the effects on one unit of a 3 × 3 concentrator prototype producing 200 suns of concentration ratio on K9 glass and crystal resin homogenizers which were refractive truncated pyramid designs (RTP-homogenizer). The in-house test showed that the K9 glass homogenizer was 20% more optically efficient than the crystal resin counterpart, although this translated into only a 5% improvement in the electrical efficiency when comparing the K9 glass homogenizer to the crystal resin homogenizer. However, both improved the electrical performance of the CPV system by 27% and 23% respectively in comparison to the system without secondary optics. Also, this study reported the degradation on the top surface of the crystal resin homogenizer, which starts melting at a high concentration ratio. An elevated temperature on the optical materials stimulates their thermal expansion and thereby decreases their reflectivity and can change the shape of the optics, which is one of the causes of illumination non-uniformity. Sarwar et al. [83] studied the effect of temperature and solar irradiance on the thermal performance and optical properties on unpolished 304/304L stainless steel using a sun simulator. The material was tested under five different levels of uniform illumination ranging between 579.3 kW/m² and 917.1 kW/m² for 17 and 50 min, respectively. The results showed that the material's thermal performance decreases with increase of the solar irradiance. However, the drop in the thermal performance is dependent on the material temperature, which was tested between 557 K and 368 K. When the material temperature dropped by 159 K the thermal performance fell to 21%, and when the material temperature dropped by 22 K the thermal performance declined to 6.7%. Also, the study highlighted the impact of temperature on the optical performance, where the reflectance of the material changed by 26% and 7% at the temperatures of 557 K and 368 K, respectively. Another study by McVey-White et al. [84] discussed the effect of the lens temperature on the illumination uniformity of three Fresnel-based configurations where the concentration ratio exceeded 500 suns. The three configurations were silicon-on-glass primary with no secondary, PMMA primary with truncated inverted pyramid secondary, and a PMMA 4-quadrant Fresnel-Köhler configuration. The performance of the optical lens for the three configurations was measured at 25–50 °C. The silicon-on-glass primary with no secondary showed a 12.4% increase in the total amount of solar irradiance up to a temperature of 30 °C, and then a drop of 81.2% in the total irradiance as the temperature reached 50 °C. Up to 40 °C, the PMMA primary with truncated inverted pyramid secondary showed uniformity in the solar irradiance across the lens; however, a further temperature rise showed an increase in the irradiance and a drop in the uniformity. Compared with the silicon-on-glass primary with no secondary, the PMMA primary with truncated inverted pyramid secondary showed an increase of 8.5% in the total amount of solar irradiance uniformity at 25 °C. Shanks et al. [85] reported the temperature and solar misalignment effects on the optical materials within a 200 suns conjugate refractive-reflective homogenizer (CRRH) based on a Cassegrain design. The system was made up of a low-iron glass cover, a plastic substrate primary with a vapor-deposited reflective coating, and a Sylguard 184 refractive secondary optic supported by an ABSplus-P430 plastic casing. The full design was tested in a vacuum drying oven for 3 h at setpoint temperatures of 60, 70, and 80 °C, where no deformation was observed. The Sylguard homogenizer bulk had an operating temperature from –45 °C to 200 °C, but the support structure underwent heat deflection at 96 °C under 66 psi. Due to sun misalignment, the sun focused on the ABSplus-P430 homogenizer support structure and caused melting. The focal area of concentrated light was measured to be at a temperature of 149 °C with ventilation (no system walls) and 226.3 °C without air ventilation (with enclosure walls in place), which is far higher than its operating temperature. Also, the measured temperature of the central MJPV cell varied in the range of 43–48 °C for no walls and 54–61 °C with walls. However, the electrical and thermal performance needs to be

Table 3

Summary of optical materials for low and medium optical concentration ratio.

| Reference | Concentration Ratio (suns) | Optics Configuration | Primary Optics Material | Coefficient of Thermal Expansion (m/m °C) | Working Temperature (°C) | Remarks | |
|--|----------------------------|----------------------|---------------------------|--|--------------------------|--------------------|--|
| Low Concentration Ratio ($1 < CR < 10$) & Medium Concentration Ratio ($10 < CR < 100$) | [38] | 5.85 | Linear Fresnel lens | PMMA | 0.000077 [65] | - 40–85 [65] | <ul style="list-style-type: none"> • Experimental performance evaluation of pure thermal and integrated PV/T solar system using linear Fresnel lens. • Reduction in electrical efficiency from 10.9% to 7.63% due to solar concentration. • Power output increases by about 28%. • Theoretical and experimental performance assessment of Idhelio CPV-T module based on curved Fresnel lens. • The overall electrical and thermal efficiencies were evaluated to compare with targeted performance. • Theoretical and measured optical efficiency found to be 80% and 77%, respectively. • Experimental performance of solar greenhouse reflects near-infrared radiation (NIR) to improve the climate condition in the greenhouse. • Reflected NIR results in electrical and thermal production utilizing PV/T collector module. |
| | [63] | 17 | Domed linear Fresnel lens | PMMA | | | <ul style="list-style-type: none"> • Performance characteristics of finned passive PV/T system combining PV panel with a solar water heater for heat and electrical generation. • Two removable reflectors were integrated on the collector to increase the total solar irradiance and to save extra sensible thermal energy |
| | [58] | 25 | Linear Fresnel lens | PMMA | | | <ul style="list-style-type: none"> • Two-stage parabolic dish with spectral beam splitting technology. • Spectral beam-splitting reduced the cell temperature and increased the cell conversion efficiency. |
| | [62] | 0.8 | Flat reflector | Aluminum | 0.0000267 [66] | Up to 298–932 [66] | <ul style="list-style-type: none"> • Thermal and electrical efficiencies of PV/T collector with and without reflector have been determined in an optimal position. • Additional cost of about 10% considering reflectors made of aluminum sheet. • Aluminum reflectors resulted in energy gain in the range of 20.5%–35.7% during summer. |
| | [60] | 80 | Parabolic dish | Aluminum with protective coating | | | <ul style="list-style-type: none"> • Hybrid PV/T experimentally studied outdoors benefiting from air and water to extract heat. • Glazing is used to increase the thermal output, and a diffuse booster reflector is used to increase solar irradiance density. |
| | [67] | 1.5 | Flat reflector | Aluminum sheet | | | <ul style="list-style-type: none"> • Energy efficiency of PV/T collector is studied for aluminum foil reflector. • Energy generated by PV/T collector made of Al foil was higher than the Al sheet due to higher specular reflectance. |
| | [54] | 1.35 | Flat reflector | Diffused aluminum plate | 0.000014 [68] | 550–600 [69] | <ul style="list-style-type: none"> • The experimental performance analysis and optimization of 2 m² and 10 m² TCPV/T system is investigated for different solar cell materials. • Increasing the width of the reflector mirror and decreasing the width of the focal line resulted in increasing the energy flux on the receiver. |
| | [52] | 1.5 | Flat reflector | Aluminum foil | 0.0000257 [70] | 260–510 [71,72] | <ul style="list-style-type: none"> • Estimates the annual electrical and thermal energy from MaReCo hybrid system in Lund, Sweden. • Front-side positioning of the cell was better than back-side, but the optimum design was to have cells on both sides. |
| | [46] | 10.27 | Parabolic trough | Aluminum alloy | 0.0000248 [66] | 298–780 [66] | <ul style="list-style-type: none"> • Anodized aluminum and aluminum- laminated steel did not influence the power output. • PV/T system cooled by water in Alvkärleby, Sweden, was investigated. |
| | [53] | 3.5 | CPC | Anodized aluminum and aluminum-laminated steel | 0.000013 [73] | Up to 80 [74] | |
| | [75] | 4 | CPC | Anodized aluminum | 0.000023 [76] | 2072 [77] | |

(continued on next page)

Table 3 (continued)

| Reference | Concentration Ratio (suns) | Optics Configuration | Primary Optics Material | Coefficient of Thermal Expansion (m/m °C) | Working Temperature (°C) | Remarks |
|-----------|----------------------------|--------------------------|---|---|--------------------------|---|
| [47] | 1.5 | CPC | Anodized aluminum | | | <ul style="list-style-type: none"> Optical efficiency measurements of glazing, reflectors, and PV solar cell determined to be 71%. Anti-reflection treated glazing increased electrical power further. The electrical performance variations of an asymmetrical PV/T CPC-collector considering reflector edges, sharp acceptance angles and bypass diodes were studied over a short incidence angle. The focus was to achieve a high-resolution incident angle. Diffuse radiation to the total power was considered. |
| [56] | 1.33 | Parabolic reflector | Anodized aluminum | | | <ul style="list-style-type: none"> PV/T collector for building applications to decrease the overall cost of the PV and thermal system. Tilttable reflectors are used to direct solar irradiance into the PV cell, reducing the thermal loss through windows. |
| [59] | 15 | Linear Fresnel reflector | Anodized aluminum | | | <ul style="list-style-type: none"> Micro hybrid concentrators were developed for urban rooftop application in Australian National University. The preliminary results showed electrical power and thermal power of more than 300 W and 1500 W, respectively. One sub-module in every receiver showed non-operational mode due to not optimizing the incident angle, reducing electrical power by 10%. |
| [55] | 2.44 | CPC | Mirror-finished aluminum sheet | | | <ul style="list-style-type: none"> LCPV/T-HP system to generate both electricity and heat output. Heat output is used to run a refrigerant (R134a) cycle. The system gave an average coefficient of performance (COP) of 4.8 during summer times. |
| [51] | 14.5 | CPC | Stainless steel | 0.000008 [66] | Up to 1800 [78] | <ul style="list-style-type: none"> LCPVT systems were tested during spring time in Tunisian Sahara. Two mass flowrates were tested in the system $\dot{m} = 0.01871/s$ and $\dot{m} = 0.051/s$. $\dot{m} = 0.01871/s$ resulted in higher thermal efficiency. |
| [49] | 7.8 | Parabolic trough | Silver-coated plastic film laminated on a steel sheet | 0.0000168 [78] | 650 [78] | <ul style="list-style-type: none"> PV/T hybrid system investigated in simulation for different geographic locations. The experimental comparison was made between the hybrid and conventional design. The PV/T hybrid system showed an electrical efficiency of 6.4% at optical efficiency of 45%. The results of the hybrid system were poor in comparison with the conventional system due to the difficulties in concentrating solar irradiance. |
| [50] | 1.6 | V-trough | Mirror-finished stainless steel | 0.000496 [66] | 298–1673 [66] | <ul style="list-style-type: none"> V-trough PV/T system with active cooling improved the electrical output of the system. The durability of stainless steel is higher than the reflective aluminum concentrator. This system design needs further modifications for reducing heat losses by either enhanced cooling methodology or higher thermal efficiency. |
| [79] | 30 | Linear Fresnel reflector | 1-mm thick rear-silvered glass 1-mm thick galvanised steel | 0.0000196 [80]/0.0000123 [81] | 593 [66,80]/420 [66] | <ul style="list-style-type: none"> Initial field results of [59] for micro concentrator CPVT system. The average electrical and thermal efficiencies were 8% and 50%, respectively. For one day testing, the combined efficiency of the system was more than 70%. |

Table 4
Summary of optical materials for high optical concentration ratio.

| Reference | Concentration ratio (suns) | Optics configuration | Optics material | | | Remarks | |
|---|----------------------------|----------------------|-------------------|--|--|---|---|
| | | | Primary | Secondary | Homogenizer | | |
| High Concentration Ratio ($CR_t > 100$) | [85] | 200 | CRRH Cassegrain | Plastic with a low-iron glass cover | Plastic with a low-iron glass cover | Sylguard with support structure from ABSplus-P430 | <ul style="list-style-type: none"> • Reflective refractive homogenizer tested with Cassegrain design increased power output by 7.76% compared to theoretical. • At different incidence angle, experimental results showed 4.5% increase in power output in comparison with purely refractive homogenizer. |
| | [87] | 300 | CRRH Cassegrain | Aluminum coated with vacuum-deposited chrome, silver, and protective silicon dioxide | Aluminum coated with vacuum-deposited chrome, silver, and protective silicon dioxide | – | <ul style="list-style-type: none"> • The concentration ratio achieved was significantly lower than the target. • The deterioration of silver coating affected the reflectivity of its surface. • The focal spot was Gaussian distribution, maximum power at the center of the focal point. |
| | [90] | 550 | Spot Fresnel lens | PMMA | – | Refractive truncated pyramids | <ul style="list-style-type: none"> • Optimizing the inverter size for the maximum energy yield to attain the typical efficiency curve for low-, medium-, and high efficiency inverter. • The optimum inverter size ratio differed between 0.84 and 1.12. • The optimum inverter sizing ratio increases as DNI increases and inverter efficiency decreases. |
| | [91] | 208.6 | Spot Fresnel lens | PMMA | Kaleidoscope | – | <ul style="list-style-type: none"> • CPVT system was analyzed experimentally and theoretically to assess the electrical performance, the concentration ratio, the cell temperature in different working conditions, and working fluid temperature. • For a module of 60 cells, the daily electrical production on a sunny day and cloudy day is 686 Wh and 541 W, respectively. |
| | [86] | 400 | Cassegrain | Polycarbonate coated with PVD metallization in aluminium | BK-7 optical glass coated with an aluminum layer and silicon oxide protection | Alanod MIRO | <ul style="list-style-type: none"> • HCPV system designed to be suitable for implementing both multi-junction and spectrum-splitting configurations. • Outdoor characterization of the two receivers' configurations showed a low overall efficiency of 23% for the spectrum-splitting due to the short wavelength band (400–1200 nm) in comparison with multi-junction solar cell. |
| | [88] | 629 | Parabolic dish | Flat mirrors mounted on a plastic parabolic surface | – | – | <ul style="list-style-type: none"> • The dish design resulted in 2.3 kWp electrical and 5.5 kWp thermal power per dish. • The output temperature was dependent on the flow rate and it was high enough for domestic applications. |
| | [89] | 500 | Parabolic dish | Low-iron glass with a silver back-coating | – | – | <ul style="list-style-type: none"> • CPVT system is designed for rooftop use producing 140–180 W (20% at 58 °C) of electricity and 400–500 W (60% at 58 °C) of heat. • The wide range of temperatures allows different applications, such as cooling processes, water desalination, and industrial processes. |

Table 5
Experimental CPVT studies covered in this review article.

| Reference | Method | CRI | Thermal efficiency | Cell materials | Cell temperature (°C) | Design | Electrical efficiency |
|-----------|--------------|----------|---|----------------|-----------------------|--|-----------------------|
| [54] | Experimental | 1.35 | 70% | pc-Si, a-Si | – | PV panel | 13% |
| [32] | | 1.5 | 15% | c-Si | 55.6 | Linear | 15% |
| [47] | | 1.5 | – | Si | – | Double-sided PV | 10% |
| [50] | | 1.6 | overall 35% | Si | – | Linear | 1% |
| [94] | | 1.86 | above 50% | c-Si | 87.7 | Linear | 9% |
| [95] | | 5.2 | 39.40% | – | – | Linear | 14.10% |
| [38] | | 5.85 | 46.6 | mono-Si | 20 | Linear | 7.63% |
| [49] | | 7.8 | 45% | mono-Si | – | Linear on two sides of triangular design | 6.40% |
| [96] | | 5.81–7.1 | 12.55% | c-Si, pc-Si | – | Linear | 12.50% |
| [59] | | 15 | 60% | c-Si | – | Linear | 20% |
| [63] | 17 | 38.50% | c-Si | 50 | Linear | 8.50% | |
| [48] | 37 | 58% | c-Si | 65 | Linear | 11% | |
| [85] | 200 | – | 3-junction | 60 | Point | 41.5% | |
| [91] | 208.6 | – | InGaP/InGaAs/Ge | 105 | Point | 39% | |
| [86] | 400 | – | First: MJ (Ge/InGaAs/InGaP) Second: mono-Si & GaAs | 70 | Point | 30% | |
| [89] | 500 | 60% | MJPV | 100 | Point | 20% | |
| [97,98] | 132–795 | 53% | 2-junction (GaAs) | – | Point | 24% | |
| [88] | 629 | 70% | MJPV | – | Point | 20% | |

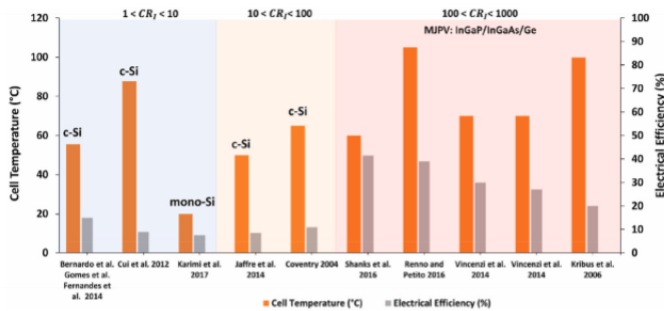


Fig. 14. The cell temperature and electrical efficiency for the reported CPVT studies and classified based on their level of concentration ratio.

investigated to identify the overall efficiency with this level of concentration ratio. Vincenzi et al. [86] investigated a novel configuration of 400 suns based on Cassegrain optics. The optical materials were: polycarbonate coated with PVD metallization in aluminum as a primary optic; BK-7 optical glass coated with an aluminum layer and silicon oxide protection as a secondary optic; and highly reflective Alanod MIRO as a homogenizer. The maximum efficiency of MJPV was measured to be 29% at mid-afternoon with a corresponding cell temperature of 70 °C. Even with a high concentration ratio, the author did not report any thermoplastic defects for the optical concentrators, which

indicates the robustness of the designed dual-axis solar tracking system, where its angular acceptance is $\pm 0.6^\circ$. Colozza et al. [87] designed a small Cassegrain system of 3000 suns to melt lunar regolith simulant. The primary and optics were made of aluminum and were coated with vacuum-deposited chrome, silver, and protective silicon dioxide (SiO). Since aluminum has a poor surface finish, a silver coating was proposed for both optics, and this resulted in an optical efficiency of 90%. The silver coating gave a 5% increase in the reflectivity. However, the silver coating’s durability and secondary lifetime is a major concern compared to aluminum. Also, the mechanical surface finishing and precision of the optics is an additional cost in the overall system expense. When the mirrored surfaces operated at less than 10%, the concentrator achieved a temperature of 415 °C at the receiver. The author stated that by minimizing the solar cell to one half, the geometrical concentration ratio can reach 6000 suns. A unique design was proposed by Chayet et al. [88] of a dish parabolic concentrator consisting of a flat mirror placed on a plastic parabolic surface molded into a global parabolic shape. The system was designed to achieve a concentration ratio of 629 suns with a 21% and 50% electrical and thermal efficiency, respectively. This system has the capacity to produce hot water in the range of 60–90 °C. Kribus et al. [89] studied the performance of a 500-sun parabolic dish design. The parabolic dish is made of glass back-coated with silver to produce the reflectivity, and externally coated with a protective coating to protect the silver from environmental exposure. The system achieved electrical and thermal efficiencies of 60% and 20%, respectively. The system generated water at 58 °C, where the cell efficiency of the Azur Space

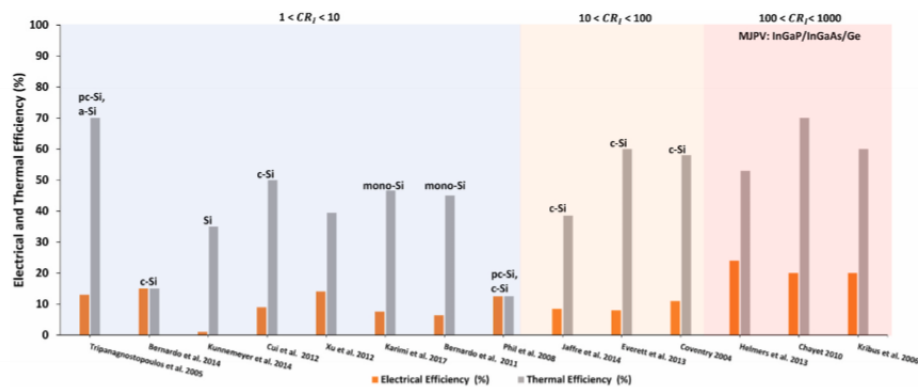


Fig. 15. Thermal and electrical efficiencies for the reported CPVT studies and classified based on their level of concentration ratio.

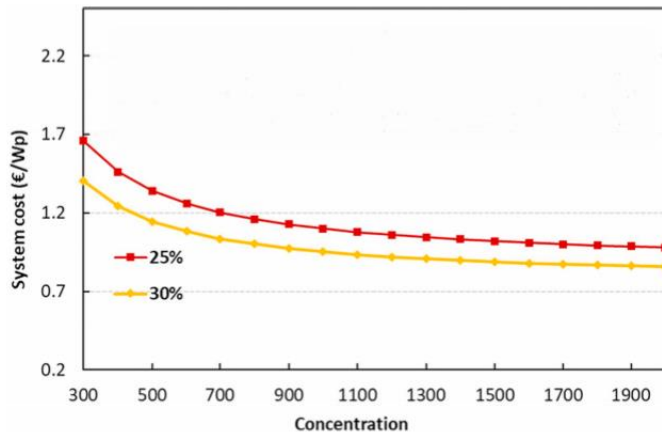


Fig. 16. System cost as a power with concentration ratio [40,100].

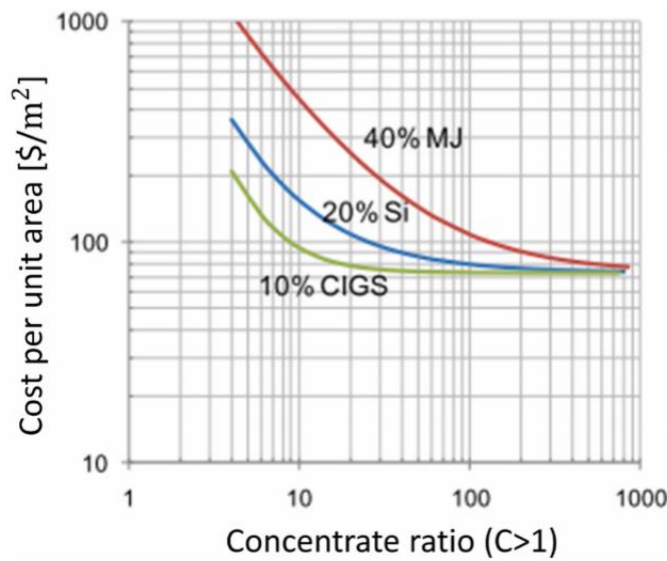


Fig. 17. Installation cost per unit of overall system [101].

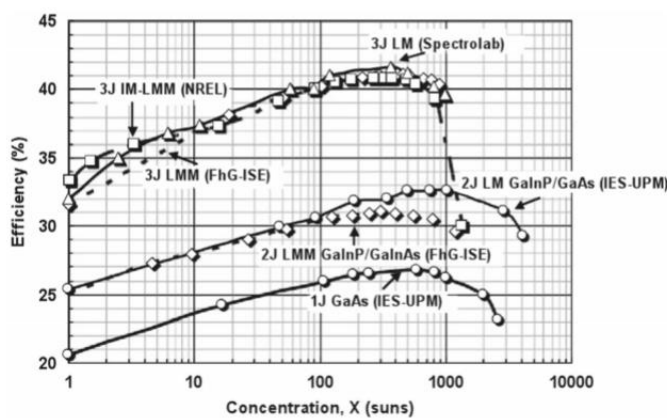


Fig. 18. Comparison of the performance of the best MJPV concentrator solar cells with the concentration ratio [88].

MJPV cell was 32% and its maximum operating temperature 100 °C. To assist with the comparison and understanding of the optical materials discussed above, the secondary optical designs and materials investigated within the literature reviewed here are summarized in Table 4.

3.6. Summary of photovoltaic cell efficiencies and design

A large number of researchers have explored different semiconductor materials of single-/multi-junction PV cells and demonstrated the effect on the cell efficiency, cell temperature and thermal and electrical efficiency under a wide range of concentration ratios in CPVT systems, as reported above. The PV design is not within the scope of this literature review as it has been thoroughly researched in different articles [11,92,93]. However, a summary of the different PV performance and characteristics has been provided in Table 5 as an essential consideration in CPVT design (as discussed in section 3.1), specifically for the studies where the cell temperature, electrical and thermal efficiency were reported.

The cell temperature and electrical efficiency of the reported studies are ranged based on their concentration ratio and denoted with their single-/multi-junction semiconductor materials, as shown in Fig. 14. Clearly, the electrical efficiency reduces with an increase in the cell temperature, especially for single-junction materials where there is a high series resistance with increasing cell temperature. These results are as expected because increasing the concentration ratio raises the cell temperature, thereby increasing the heat dissipation, which results in a drop in the electrical efficiency. In addition, the electrical and thermal efficiencies have shown an inverse relationship for different CPVTs configurations, considering only the experimental studies where system details are fully reported, as in Fig. 15.

4. Economic aspects for high concentration ratio CPVTs

Novel optical configurations of CPVT systems are proposed to reach a high level of concentration ratio, at which the system cost is reduced, and the system progression is enhanced. Further, increasing the system efficiency by means of diminishing the volume, weight, and the manufacturing cost of the system reduces the overall system cost. A CPVT system with a high concentration ratio allows the increase in the cell conversion efficiency up to a concentration factor beyond which the cell conversion efficiency reduces, while producing more power and more cost-effectively. To illustrate this, the MJPV AzurSpace (Model 3C44-3 × 3 mm²) has a maximum cell conversion efficiency of 44% at 250 suns, after which the cell conversion efficiency reduces to 43.9% at 500 suns and 42.9% at 1000 suns in measurement conditions of 1.5 AM-1000 W/m², T = 25 °C [99]. The relationship between the system's initial cost as a power-related cost and the level of the concentration ratio in the range of 300–2000 suns for two system efficiencies is shown in Fig. 16.

Choosing a high-performance PV cell is not the best metric for selection. Cost-effectiveness is one key approach for developing a high concentration CPVT system. For a high concentration ratio, multi-

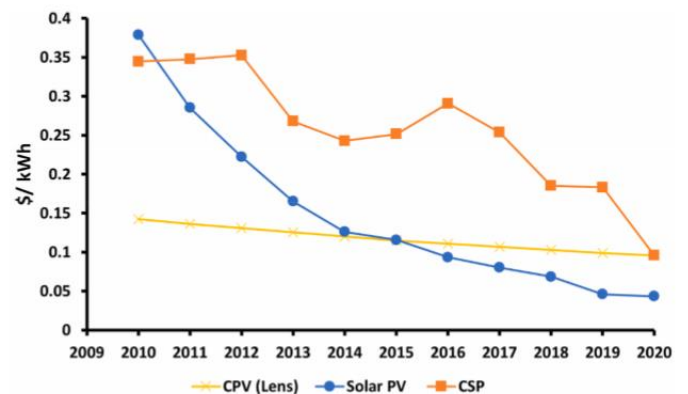


Fig. 19. The levelized cost of electricity (\$/kWh) for concentrated photovoltaic (CPV), Concentrated Solar Power (CSP), and Solar PV plants for completed projects [109,110].

junction and non-silicon based solar cells are preferable due to their high performance under elevated operating temperatures. In contrast, for low concentration ratios, single-junction silicon-based solar cells are preferred due to their cost-effectiveness and ready availability. Yazawa and Shakouri [101] studied theoretically the installation cost of CPVT systems per unit area with concentration ratios up to 1000 suns. They found that the cost of the PV material diminishes while the cost of the optics dominates at concentration ratios above 100 suns, without considering the cost of the mechanical complexity, as shown in Fig. 17.

Although MJPV cells have the highest efficiency in respect of the solar concentration, the market demand for them is not high due to their high production cost and to MJPV constituents being less available. MJPV cells are currently economically feasible only if the concentration ratio is sufficient to minimize the cell area and offset its initial cost [102]. Research and development for MJPVs to reduce the payback period and maximize the net present value (NPV) are important for operation under high concentration ratios. Comparison of the performance of single-dual-, and triple-junction solar cells versus concentration ratios ranging from 1 to 10000 suns is shown in Fig. 18. At certain concentration ratios, the PV cells reach their highest efficiency [103]. The peak efficiency occurs when the series resistance effects of the subcells dominate due to an increase in the current in accordance with the concentration ratio (as discussed in section 2). For selection of the MJPV type, the MJPV cell with a slight drop in efficiency after reaching the peak efficiency is more advantageous as, during real-time operation, the PV cell is not subject to a uniform concentration ratio, resulting in a localized hotspot. Moreover, the dual-junction cell has a smooth drop in efficiency, indicating that this type will have better efficiency in different concentrator modules close to 1000 suns.

Concentrating sunrays to generate solar power is potentially more cost-effective, but it relies on the cost of the optical concentrators. The concentrators' price is still the main issue and it has been reported that the price of solar concentrators is between \$150–\$250/m², which is about half the total cost of installing a concentrated solar power (CSP) plant [104]. This issue is exaggerated by incorporating multiple optical interfaces to attain a high concentration factor. Although the CPVT is area-efficient and this results in less overall system cost (i.e., fewer PV materials), a vast number of large-scale solar PV deployments are required in a desert region, such as Saudi Arabia, Australia, and North Africa, where the value of land is dramatically low [105]. Thus, the highest efficiency CPVT does not convert into economic impact because the land cost is depressed. Because CPVT systems utilize an optical device to intensify direct solar radiation, the CPVT system's electrical and thermal output is maximized at the price of not only the optical device but also by incorporating a tracking system, MJPV cells, and an appropriate cooling mechanism. These associated components can result in an expensive CPVT system in comparison to the conventional solar PV panel. Micro-tracking technology is suggested to be subordinate to the CPVT system but it might be cost-competitive with solar PVs. However, the progression in CPVT system is not expedited in the same manner as solar PV, resulting in more profitability than the CPVT on the utility scale [106,107].

The cost of solar PV has not only competed with the CPV and CSP systems but also with the least fossil fuel cost, due to its ongoing technological development [108]. The use of concentrated solar technologies has expanded while their cost continues to fall [106]. For example, the cost of utility-scale solar PV has fallen from \$0.378/kWh to \$0.043/kWh with 89% of cost reduction, while CSP's price has decreased from \$0.344/kWh to \$0.095/kWh with 72% of cost reduction for the period between 2010 and 2020 [109]. The CPV system has also had a much lower cost in 2010 of \$0.13/kWh in comparison to both solar PV and CSP and the price kept gradually decreasing until it reached \$0.082/kWh with falling percent of 60% not less than the solar PV, as in Fig. 19 [110]. To put this in the context of technological progression, the amount of installed CSP (5.5 GW) in 2018 was accomplished by solar PV in 2005. The solar PV cost reduction is set to continue beyond 2020 and

it will offer less expensive electricity cost than the least fossil fuel cost. In 2020, CSP electricity offers a price between \$0.06 to \$0.10/kWh range, while Solar PV provides a price of less than \$0.048/kWh. The cause of the highest cost reduction for the solar PV system in comparison to the CPV and CSP systems is the drop in the silicon module prices from \$2/W to just over \$0.20/W during the 2010s [111]. In contrast, concentrated solar technology could further reduce costs in view of developing cheaper optical materials with higher performance, and considering the induced high temperature on optics and solar cells [112].

5. Future work

Advances in CPVT research with the objective of reaching the highest concentration ratios are ongoing in order to achieve high thermal and electrical efficiencies. To do so, a range of high efficiency solar cell architectures along with novel optical configurations are needed. From this literature review, the key methods and techniques that need to be applied more consistently to improve CPVT performance and design have been identified as:

- Testing of the CPVT module's stability for accelerated aging when CPVT components are exposed to different outdoor climates and subjected to the worst-case operating conditions.
- Thermal cycling to assess the thermal deformation of all CPVT components where the thermal load varies from day to night and seasonally.

These measures will help solve the challenge of designing CPVT and PV cells with higher tolerances for elevated temperatures at high and ultrahigh concentration ratios.

6. Conclusion

In this review, a thorough analysis has been presented of the effect of temperature on CPVT solar cells and optics. The low resistance of multi-junction solar cells at 80 °C allows higher concentration ratios to be accepted in comparison to single-junction solar cells. Intermetallic and monolithic multi-junction configurations, in particular, are effective and are readily available but with limitations. An intermetallic connection for each subcell results in maximum efficiency at the price of:

- Using a different substrate for every subcell
- Using antireflective coating for every subcell
- Additional thermal losses
- Complexity in the mechanical design and electrical connection

The monolithic multi-junction is dependent on the following factors for compatibility:

- Semiconductor materials need to be structurally compatible
- Compatible materials are required for electro-optical interconnection
- Current matching, since the subcell design is in one stack

Common techniques for thermally managing the cell include spectral decomposition where only the photons in a range compatible with the cell are transmitted through the system. As is already known, the thermal receiver component needs to have a high thermal conductivity to conduct heat to the consecutive component. The thermal conductivity of the heat spreader, being centered between the PV cell and cooling mechanism, also needs to be as high as possible to ensure a high thermal utilization afterwards. Post-illumination techniques with a focal point and line have proven their capability to thermally manage the solar cell temperature within safe operating conditions under concentration ratios up to 10000 suns.

The optical concentrator is the key element to amplify the solar

irradiance and concentrate it onto small-sized cells. Increasing the concentration ratio comes at the price of large optical areas or minimizing the receiver area, resulting in high extraction and generation of both thermal and electrical energies, respectively. At low levels of concentration ratio, a CPVT system receiver absorbs both direct and diffuse solar irradiance. At higher ranges of concentration ratio, the optics are subjected to higher temperatures, where the working temperature and thermal expansion coefficient of the optics, especially the secondary/homogenizer, need to be thoroughly investigated to avoid thermomechanical stresses. It is clear that boosting the concentration ratio above 100 suns increases the efficiencies and reduces the cost per unit area of the CPVT system. Still, more research and development is

required to push performance/cost benefits at >1000 suns.

Declaration of competing interest

The authors declare that they have no known competing financial interests or personal relationships that could have appeared to influence the work reported in this paper.

Acknowledgment

Mr Mussad Alzahrani would like to duly acknowledge the financial support from the Saudi Arabia Culture Bureau in the United Kingdom.

Annex.

The data in Fig. 5 is derived from Table 6, which shows the limited efficiency for ideal bandgap energy under no concentration. Red and black lines represent two semiconductor material sets tested at the AM 1.5D spectrum and ideal blackbody spectrum, respectively.

Table 6
Number of junctions with their semiconductor materials.

| Number of junctions | Red line (AM 1.5D spectrum) | Black line (ideal blackbody spectrum) |
|---------------------|---|---|
| 1 | c-Si | c-Si |
| 2 | β -FeSi2/a-Si | β -FeSi2/a-Si |
| 3 | Ge/c-Si/a-Si | β -FeSi2/Cu2ZnSn/Cu2O |
| 4 | Ge/c-Si/a-Si/GaP | Ge/c-Si/Cu2ZnSn/ZnP2 |
| 5 | Ge/c-Si/Cu2ZnSn/a-Si/GaP | Ge/c-Si/Cu2ZnSn/a-SiC/GaP |
| 6 | CuFeS2/ β -FeSi2/c-Si/a-SiGe:H/Cu2O/3C-SiC | CuFeS2/ β -FeSi2/c-Si/a-SiGe:H/Cu2O/3C-SiC |
| 7 | Ge/ β -FeSi2/c-Si/Cu2ZnSn/a-Si/ZnP2/CuAlS2 | CuFeS2/ β -FeSi2/c-Si/Cu2ZnSn/a-Si/ZnP2/CuAlS2 |
| 8 | CuFeS2/Ge/ β -FeSi2/c-Si/Cu2ZnSn/a-Si/Cu2O/CuAlS3 | CuFeS2/Ge/ β -FeSi2/c-Si/Cu2ZnSn/a-Si/ZnP2/CuAlS2 |

The data in Fig. 6 is derived from Table 7, which shows the semiconductor materials and their concentration ratio for theoretical and experimental studies.

Table 7
semiconductor materials, study method, and their concentration ratio of theoretical and experimental CPVT studies.

| Reference | Method | Cell materials | Concentration ratio (CR) |
|-----------|----------------------------|-----------------|--------------------------|
| [54] | Experimental | p-Si a-Si | 1.35 |
| [41] | Experimental | Si | 1.41 |
| [36] | Experimental | c-Si | 1.5 |
| [47] | Experimental | Si | 1.5 |
| [52] | Theoretical & experimental | c-Si | 1.5 |
| [13] | Theoretical & experimental | Si | 1.6 |
| [94] | Experimental | c-Si | 1.86 |
| [113] | Theoretical | p-Si | 2 |
| [114] | Experimental | a-Si | 2.22 |
| [75] | Experimental | mono-Si | 4 |
| [38] | Experimental | mono-Si | 5.85 |
| [62] | Theoretical | c-Si | 1.5 |
| [53] | Experimental | mono-Si | 3 |
| [96] | Theoretical & experimental | mono-Si | 3.5 |
| [2] | Experimental | c-Si | 5.81 |
| [49] | Experimental | pc-Si | 7.1 |
| [115] | Theoretical & experimental | c-Si | 6 |
| [116] | Theoretical | c-Si | 7.8 |
| [46] | Experimental | mono-Si | 7 |
| [34] | Theoretical & experimental | c-Si | 10 |
| [117] | Theoretical | InGaP/InGaAs/Ge | 10 |
| [51] | Experimental | super cell/GaAs | 10.27 |
| [59] | Experimental | mono-Si | |
| [63] | Experimental | poly-Si | |
| [118] | Experimental | super-Si | |
| | | GaAs | |
| | | Si | 11.1 |
| | | Si | 13.5 |
| | | mono-Si | 14.5 |
| | | c-Si | 15 |
| | | c-Si | 17 |
| | | customized-Si | 20 |

(continued on next page)

Table 7 (continued)

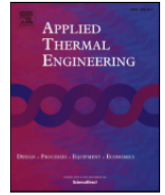
| Reference | Method | Cell materials | Concentration ratio (CR) |
|-----------|----------------------------|---------------------------|--------------------------|
| | | GaAs | |
| | | MJPV (super cell/GaAs/Si) | |
| [58] | Experimental | mono-Si | 25 |
| [119] | Theoretical | c-Si | 25 |
| [120] | Theoretical | c-Si | 28.4 |
| [79] | Experimental | c-Si | 30 |
| [121] | Experimental | Si | 30 |
| [48] | Experimental | c-Si | 37 |
| [60] | Theoretical | Si | 80 |
| [40] | Theoretical | Si | 100 |
| [122] | Theoretical | Ge | 200 |
| | | Si | |
| | | InGaP | |
| | | CdTe | |
| | | InGaAs | |
| [91] | Theoretical & experimental | MJPV (InGaP/InGaAs/Ge) | 208.6 |
| [86] | Theoretical & experimental | MJPV (Ge/InGaAs/InGaP) | 400 |
| | | mono-Si | |
| | | GaAs | |
| [97] | Theoretical | MJPV (Ge/InGaAs/InGaP) | 500 |
| [89] | Experimental | MJPV (Ge/InGaAs/InGaP) | 500 |
| [123] | Theoretical | c-Si | 500 |
| [90] | Experimental | MJPV (InGaP/InGaAs/Ge) | 550 |
| [88] | Experimental | MJPV (InGaP/InGaAs/Ge) | 629 |
| [98] | Theoretical & experimental | 2-junction (GaAs) | 795 |

References

- Baig H, Sarmah N, Heasman KC, Mallick TK. Numerical modelling and experimental validation of a low concentrating photovoltaic system, Solar Energy Materials and Solar Cells. 2013. <https://doi.org/10.1016/j.solmat.2013.01.035>.
- Chemisana D, Mallick TK. Building integrated concentrating solar systems. Solar Energy Sciences and Engineering Applications 2013;545–87. <https://doi.org/10.1201/b15507>.
- Zahedi A. Review of modelling details in relation to low-concentration solar concentrating photovoltaic. Renew Sustain Energy Rev 2011;15:1609–14. <https://doi.org/10.1016/j.rser.2010.11.051>.
- Micheli L, Sarmah N, Luo X, Reddy KS, Mallick TK. Opportunities and challenges in micro- and nano-technologies for concentrating photovoltaic cooling : a review. Renew Sustain Energy Rev 2013;20:595–610. <https://doi.org/10.1016/j.rser.2012.11.051>.
- Almonacid G, Vidal PG, Mu E. High concentrator Photovoltaics efficiencies : present status and forecast. Renew Sustain Energy Rev 2015;15:1810–5. <https://doi.org/10.1016/j.rser.2010.11.046>.
- Xie WT, Dai YJ, Wang RZ, Sumathy K. Concentrated solar energy applications using Fresnel lenses : a review. Renew Sustain Energy Rev 2011;15:2588–606. <https://doi.org/10.1016/j.rser.2011.03.031>.
- Chemisana D. Building integrated concentrating Photovoltaics : a review. Renew Sustain Energy Rev 2011;15:603–11. <https://doi.org/10.1016/j.rser.2010.07.017>.
- Makki A, Omer S, Sabir H. Advancements in hybrid photovoltaic systems for enhanced solar cells performance. Renew Sustain Energy Rev 2015;41:658–84. <https://doi.org/10.1016/j.rser.2014.08.069>.
- Avezov RR, Akhatov JS, Avezova NR. A review on photovoltaic-thermal (PV-T) air and water Collectors1. Appl Sol Energy 2011;47:169–83. <https://doi.org/10.3103/S0003701X11030042>.
- Singh B, Othman MY. A review on photovoltaic thermal collectors. J Renew Sustain Energy 2009;062702. <https://doi.org/10.1063/1.3266963>.
- Sharaf OZ, Orhan MF. Concentrated photovoltaic thermal (CPVT) solar collector systems: Part I - fundamentals, design considerations and current technologies. Renew Sustain Energy Rev 2015;50:1500–65. <https://doi.org/10.1016/j.rser.2015.05.036>.
- Sharaf OZ, Orhan MF. Concentrated photovoltaic thermal (CPVT) solar collector systems: Part II - implemented systems, performance assessment, and future directions. Renew Sustain Energy Rev 2015;50:1566–633. <https://doi.org/10.1016/j.rser.2014.07.215>.
- Daneshzarian R, Cuce E, Cuce PM, Sher F. Concentrating photovoltaic thermal (CPVT) collectors and systems: theory, performance assessment and applications. Renew Sustain Energy Rev 2018;81:473–92. <https://doi.org/10.1016/j.rser.2017.08.013>.
- Mojiri A, Taylor R, Thomsen E, Rosengarten G. Spectral beam splitting for efficient conversion of solar energy — a review. Renew Sustain Energy Rev 2013;28:654–63. <https://doi.org/10.1016/j.rser.2013.08.026>.
- Ju X, Xu C, Han X, Du X, Wei G, Yang Y. A review of the concentrated photovoltaic/thermal (CPVT) hybrid solar systems based on the spectral beam splitting technology. Appl Energy 2017;187:534–63. <https://doi.org/10.1016/j.apenergy.2016.11.087>.
- Chan NLA, Ekins-Daukes NJ, Adams JGJ, Lumb MP, Gonzalez M, Jenkins PP, Vurgaftman I, Meyer JR, Walters RJ. Optimal bandgap combinations-does material quality matter. IEEE Journal of Photovoltaics 2012;2:202–8. <https://doi.org/10.1109/JPHOTOV.2011.2180513>.
- Herst LC, Ekins-Daukes N. Fundamental losses in solar cells. Prog Photovoltaics Res Appl 2010;19:286–93. <https://doi.org/10.1002/ppp>.
- Chenni R, Makhlouf M, Kerbache T, Bouzid A. A detailed modeling method for photovoltaic cells. Energy 2007;32:1724–30. <https://doi.org/10.1016/j.energy.2006.12.006>.
- Phillips SP, Dimroth F, Bett AW. High-efficiency III–V multijunction solar cells. In: McEvoy's handbook of photovoltaics. Elsevier; 2018. p. 439–72. <https://doi.org/10.1016/B978-0-12-809921-6.00012-4>.
- Bercx M, Saniz R, Partoens B, Lamoen D. Exceeding the shockley–queisser limit within the detailed balance framework. In: Many-body approaches at different scales. Cham: Springer International Publishing; 2018. p. 177–84. https://doi.org/10.1007/978-3-319-72374-7_15.
- Polman A, Knight M, Garnett EC, Ehrler B, Sinke WC. Photovoltaic materials: present efficiencies and future challenges. Science 2016;352:10–2. <https://doi.org/10.1126/science.aad4424>.
- Green MA, Emery K, Hishikawa Y, Warta W, Dunlop ED. Solar cell efficiency tables (version 41). Prog Photovoltaics Res Appl 2013;21:1–11. <https://doi.org/10.1002/ppp.2352>.
- Martí A, Araújo GL. Limiting efficiencies for photovoltaic energy conversion in multigap systems. Sol Energy Mater Sol Cell 1996;43:203–22. [https://doi.org/10.1016/0927-0248\(96\)00015-3](https://doi.org/10.1016/0927-0248(96)00015-3).
- Doeleman Hugo. Limiting and realistic efficiencies of multi-junction solar cells. FOM Institute AMOLF; 2012. <https://pdfs.semanticscholar.org/b083/753c6d04cd2af20379de785e7a71f2e885b6.pdf?ga=2.85718480.83315905.1592515641-107842748.1553173981>.
- Hu W, Harada Y, Hasegawa A, Inoue T, Kojima O, Kita T. Intermediate band photovoltaics based on interband-intraband transitions using In_{0.53}Ga_{0.47}As/InP superlattice. Prog Photovoltaics Res Appl 2011;20. <https://doi.org/10.1002/ppp.1208>.
- Luque A, Hegedus S. Handbook of photovoltaic science. Springer; 2003. [https://scholar.google.com/scholar_lookup?title=Concentrator photovoltaics&author=A.L. Luque&publication_year=2007](https://scholar.google.com/scholar_lookup?title=Concentrator+photovoltaics&author=A.L.+Luque&publication_year=2007).
- Baig H, Sellami N, Chemisana D, Rosell J, Mallick TK. Performance analysis of a dielectric based 3D building integrated concentrating photovoltaic system. Sol Energy 2014;103:525–40. <https://doi.org/10.1016/j.solener.2014.03.002>.
- Shanks K, Ferrer-rodriguez JP, Fernández EF, Almonacid F. A > 3000 suns high concentrator photovoltaic design based on multiple Fresnel lens primaries focusing to one central solar cell. Sol Energy 2018;169:457–67. <https://doi.org/10.1016/j.solener.2018.05.016>.
- Yavrian A, Tremblay S, Levesque M, Gilbert R. How to increase the efficiency of a high concentrating PV (HCPV) by increasing the acceptance angle to ±3.2°. In: AIP conference proceedings; 2013. p. 197–200. <https://doi.org/10.1063/1.4822230>.
- Micheli L, Sarmah N, Fernandez EF, Reddy KS, Mallick TK. Technical issues and challenges in the fabrication of a 144-Cell 500× Concentrating Photovoltaic receiver. In: 2014 IEEE 40th photovoltaic specialist conference, PVSC 2014; 2014. p. 2921–5. <https://doi.org/10.1109/PVSC.2014.6925543>.
- Azur Space Solar Power GMBH. Enhanced Fresnel assembly - EFA type: 3C42A – with 10x10mm² CPV TJ solar cell application: concentrating photovoltaic (CPV)

- [84] McVey-White P, Besson P, Baudrit M, Schriemer HP, Hinz K. Effects of lens temperature on irradiance profile and chromatic aberration for CPV optics. AIP Conference Proceedings 2016;040004. <https://doi.org/10.1063/1.4962081>.
- [85] Shanks K, Baig H, Singh NP, Senthilarasu S, Reddy KS, Mallick TK. Prototype fabrication and experimental investigation of a conjugate refractive reflective homogeniser in a cassegrain concentrator. Sol Energy 2017;142:97–108. <https://doi.org/10.1016/j.solener.2016.11.038>.
- [86] Vincenzi D, Baricordi S, Calabrese S, Musio M, Damiano A. A cassegrain concentrator photovoltaic system: comparison between dichroic and multijunction photovoltaic configurations. IECON Proceedings (Industrial Electronics Conference) 2014;1900–5. <https://doi.org/10.1109/IECON.2014.7048761>.
- [87] Colozza A, Macosko R, Castle C, Sacksteder K, Suzuki N, Mulherin J. Cassigranian solar concentrator for ISRU material processing. In: 50th AIAA aerospace sciences meeting including the new horizons forum and aerospace exposition. Reston, Virginia: American Institute of Aeronautics and Astronautics; 2012. p. 1–15. <https://doi.org/10.2514/6.2012-637>.
- [88] Chayet H, Lozovsky I, Kost O, Loekenhoff R, Rasch K-D, Bett AW, McConnell RD, Sala G, Dimroth F. High efficiency, low cost parabolic dish system for cogeneration of electricity and heat. In: AIP conference proceedings; 2010. p. 175–8. <https://doi.org/10.1063/1.3509183>.
- [89] Kribus A, Kaftori D, Mittelman G, Hirshfeld A, Flitsanov Y, Dayan A. A miniature concentrating photovoltaic and thermal system. Energy Convers Manag 2006;47:3582–90. <https://doi.org/10.1016/j.enconman.2006.01.013>.
- [90] Pérez-Higueras PJ, Almonacid FM, Rodrigo PM, Fernández EF. Optimum sizing of the inverter for maximizing the energy yield in state-of-the-art high-concentrator photovoltaic systems. Sol Energy 2018;171:728–39. <https://doi.org/10.1016/j.solener.2018.07.013>.
- [91] Renno C, Petito F. Experimental and theoretical model of a concentrating photovoltaic and thermal system. Energy Convers Manag 2016;126:516–25. <https://doi.org/10.1016/j.enconman.2016.08.027>.
- [92] Rathore N, Panwar NL, Yettou F. A Comprehensive review on different types of solar photovoltaic cells and their applications. Int J Ambient Energy 2019;1–48. <https://doi.org/10.1080/01430750.2019.1592774>.
- [93] Kouhnavard M, Ikeda S, Ludin NA, Ahmad Khairudin NB, Ghaffari BV, Mat-Teridi MA, Ibrahim MA, Sepeai S, Sopian K. A review of semiconductor materials as sensitizers for quantum dot-sensitized solar cells. Renew Sustain Energy Rev 2014;37:397–407. <https://doi.org/10.1016/j.rser.2014.05.023>.
- [94] Cui W, Zhao L, Wu W, Wang K, Jen TC. Energy efficiency of a quasi cpc concentrating solar PV/T system. In: ASME international mechanical engineering congress and exposition, proceedings (IMECE); 2010. p. 1071–6. <https://doi.org/10.1115/IMECE2010-38341>.
- [95] Xu Y, Wang CY, Hua YM, Zhang YM. Studies on a low concentration photovoltaic/thermal system with constant volume refrigeration. Key Eng Mater 2012;517:776–83. <https://doi.org/10.4028/www.scientific.net/KEM.517.776>.
- [96] Pihl E, Thapper C, Nilsson HJ. Evaluation of the concentrating PVT systems MaReCo and Solar8. 2006. <http://lup.lub.lu.se/record/1027919>.
- [97] Helmers H, Bett AW, Parisi J, Agert C. Modeling of concentrating photovoltaic and thermal systems. Prog Photovoltaics Res Appl 2014;22:427–39. <https://doi.org/10.1002/pip.2287>.
- [98] Helmers H, Boos A, Jetter F, Heimsath A, Wiesenfarth M, Bett AW, Dimroth F, Kurtz S, Sala G, Bett AW. Outdoor test setup for concentrating photovoltaic and thermal (CPVT) systems. In: AIP conference proceedings; 2011. p. 175–9. <https://doi.org/10.1063/1.3658320>.
- [99] Data M, Average T, Data E. Concentrator triple junction solar cell cell Type : 3C44C- 3 × 3 mm2 Azur Space. 2012. p. 3–6. http://www.azurspace.com/images/products/0004357-00-01_3C44_AzurDesign_3x3.pdf.
- [100] Fernández P, Almonacid EF, Rodrigo F, Pérez-Higueras PM. CPV systems. In: McEvoy's handbook photovoltaic; 2017. p. 931–85.
- [101] Yazawa K, Shakouri A. Material optimization for concentrated solar photovoltaic and thermal Co-generation. In: ASME 2011 pacific rim technical conference and exhibition on packaging and integration of electronic and photonic systems, MEMS and NEMS. vol. 1. ASMEDC; 2011. p. 733–9. <https://doi.org/10.1115/IPACK2011-52190>.
- [102] Lopez A, Vega A, Lopez A. Next generation of photovoltaics. Berlin, Heidelberg: Springer Berlin Heidelberg; 2012. <https://doi.org/10.1007/978-3-642-23369-2>.
- [103] Algora C, Rey-Stolle I. Chapter 2 the interest and potential of ultra-high concentration. Next generation of photovoltaics: new concept. Berlin, Heidelberg: Springer Berlin Heidelberg; 2012. <https://doi.org/10.1007/978-3-642-23369-2>.
- [104] Low-cost, lightweight solar concentrator (fact sheet). 2012. <https://doi.org/10.2172/1053327>. Golden, CO (United States).
- [105] Wright DJ, Badruddin S, Robertson-Gillis C. Micro-tracked CPV can be cost competitive with PV in behind-the-meter applications with demand charges. Frontiers in Energy Research 2018;6. <https://doi.org/10.3389/fenrg.2018.00097>.
- [106] Haysom JE, Jafarieh O, Anis H, Hinz K, Wright D. Learning curve analysis of concentrated photovoltaic systems. Prog Photovoltaics Res Appl 2015;23:1678–86. <https://doi.org/10.1002/pip.2567>.
- [107] Gil E, Martínez M, de la Rubia O. Operation and maintenance results from ISFOC CPV plants. 2017, 020006. <https://doi.org/10.1063/1.5001405>.
- [108] Kalair A, Abas N, Saleem MS, Kalair AR, Khan N. Role of energy storage systems in energy transition from fossil fuels to renewables. Energy Storage 2020. <https://doi.org/10.1002/est2.135>.
- [109] Agency IRE. Renewable power generation costs in 2018. 2018. https://www.irena.org/-/media/Files/IRENA/Agency/Publication/2018/Jan/IRENA_2017_Power_Costs_2018.pdf.
- [110] Chapter 5 Energy. Optics and photonics. Washington, D.C.: National Academies Press; 2013. <https://doi.org/10.17226/13491>.
- [111] Feldman D, O'Shaughnessy E, Margolis R. Solar industry update Q3/Q4 2019. NREL Presentation; 2020. p. 1–83. <https://www.nrel.gov/docs/fy20osti/76158.pdf>.
- [112] Overview and summary of America's energy future: technology and transformation. Washington, D.C.: National Academies Press; 2010. <https://doi.org/10.17226/12943>.
- [113] Hedayatzadeh M, Ajabshirchi Y, Sarhaddi F, Safavinejad A, Farahat S, Chaji H. Thermal and electrical assessment of an integrated solar photovoltaic thermal (PV/T) water collector equipped with a compound parabolic concentrator (CPC). Int J Green Energy 2013;10:494–522. <https://doi.org/10.1080/15435075.2012.678524>.
- [114] Matsuoka H, Tamura T. Design and evaluation of thermal-photovoltaic hybrid power generation module for more efficient use of solar energy. NIT DOCOMO Technical Journal 2010;12:61–7. https://www.nttdocomo.co.jp/english/binary/pdf/corporate/technology/rd/technical_journal/bn/vol12_3/vol12_3_061en.pdf.
- [115] Chemisana D, Ibáñez M, Rosell JI. Characterization of a photovoltaic-thermal module for Fresnel linear concentrator. Energy Convers Manag 2011;52:3234–40. <https://doi.org/10.1016/j.enconman.2011.04.008>.
- [116] Calise F, Vanoli L. Parabolic trough photovoltaic/thermal collectors: design and simulation model. Energies 2012;5:4186–208. <https://doi.org/10.3390/en5104186>.
- [117] Ahmad N, Ijro T, Yamada N, Kawaguchi T, Maemura T, Ohashi H. Optical design of wavelength selective CPVT system with 3D/2D hybrid concentration. In: Winston R, Gordon JM, editors; 2012. 84850T. <https://doi.org/10.1117/12.929395>.
- [118] Li M, Ji X, Li G, Wei S, Li Y, Shi F. Performance study of solar cell arrays based on a Trough Concentrating Photovoltaic/Thermal system. Appl Energy 2011;88:3218–27. <https://doi.org/10.1016/j.apenergy.2011.03.030>.
- [119] Coventry JS, Franklin E, Blakers A. Thermal and electrical performance of a concentrating PV/Thermal collector: results from the ANU CHAPS collector. ANZSES Solar Energy Conference; 2004.
- [120] Hu P, Zhang Q, Liu Y, Sheng C, Cheng X, Chen Z. Optical analysis of a hybrid solar concentrating Photovoltaic/Thermal (CPV/T) system with beam splitting technique. Sci China Technol Sci 2013;56:1387–94. <https://doi.org/10.1007/s11431-013-5209-2>.
- [121] Sonneveld PJ, Swinkels GLAM, van Tuijl BAJ, Janssen HJJ, Campen J, Bot GPA. Performance of a concentrated photovoltaic energy system with static linear Fresnel lenses. Sol Energy 2011;85:432–42. <https://doi.org/10.1016/j.solener.2010.12.001>.
- [122] Otanicar TP, Taylor RA, Telang C. Photovoltaic/thermal system performance utilizing thin film and nanoparticle dispersion based optical filters. J Renew Sustain Energy 2013;5:033124. <https://doi.org/10.1063/1.4811095>.
- [123] Segal A, Epstein M, Yogev A. Hybrid concentrated photovoltaic and thermal power conversion at different spectral bands. Sol Energy 2004;76:591–601. <https://doi.org/10.1016/j.solener.2003.12.002>.

Article 2. M. Alzahrani, H. Baig, K. Shanks, T. Mallick, "Estimation of the performance limits of a concentrator solar cell coupled with a micro heatsink based on a finite element simulation," Appl. Therm. Eng., 176 (2020), p. 115315, [10.1016/j.applthermaleng.2020.115315](https://doi.org/10.1016/j.applthermaleng.2020.115315).



Estimation of the performance limits of a concentrator solar cell coupled with a micro heat sink based on a finite element simulation



Mussad Alzahrani^{a,b}, Hasan Baig^{a,*}, Katie Shanks^a, Tapas Mallick^a

^a Environment and Sustainability Institute, University of Exeter, Penryn Campus, Cornwall TR109FE, UK

^b Mechanical and Energy Engineering Department, Imam Abdulrahman Bin Faisal University, Dammam 34212, Saudi Arabia

HIGHLIGHTS

- FEM of a heat sink is developed to analyse the performance of HCPV system.
- Use of different substrates and the impact of using micro fins is studied.
- Safe operation limits for different climates and solar concentrations is studied.
- The proposed model can be applied for a variety of HCPV systems.

ARTICLE INFO

Keywords:

Concentrating Photovoltaic
Concentration Ratio
Passive cooling
Flat-plate heat-sink
Micro fin heat-sink
Finite element

ABSTRACT

Concentrated photovoltaic (CPV) technology makes use of cheap optical elements to amplify the irradiance and focus it on small-sized solar cells enabling the extraction of higher amounts of electricity. However, increasing the solar concentration raises the temperature of the PV cell which can deter its performance and can also cause its failure. To combat this issue both active and passive cooling mechanisms are utilized for different types of CPV systems. In this study, we determine the limits of passive cooling systems and establish when an active cooling system is needed based on the recommended operating temperature of the solar cell. We investigate the temperature characteristics of the solar cells bonded to three different substrate materials under different solar concentrations. Results showed that cell temperature is linearly dependent on the concentration ratio and ambient temperature independent of the substrate material. Further, the integration of a micro-finned heatsink results in higher heat dissipation by 25.32%, 23.13%, and 22.24% in comparison with a flat plate heatsink for Direct Bonded Copper (DBC), Insulated Metal Substrate (IMS), and Silicon Wafer (Si wafer) substrates respectively. The low thermal resistance of the IMS substrate compared to the DBC and the Si wafer substrates result in the best thermal performance in terms of maintaining the cell temperature < 80 °C and allowing a wider range of high concentration ratio.

1. Introduction

A concentrator photovoltaic (CPV) system replaces expensive, high-efficiency semiconductor materials with cost-efficient optical concentrators [1] with an aim to lower the Levelized Cost of electricity compared to standard solar panels. Single junction silicon solar cells although widely utilized due to their availability and affordability have performance limitations in areas with high DNI and temperature [2] and have been primarily utilized for Low Concentration Photovoltaic Systems. Multijunction solar cells, on the other hand, have better tolerance to extreme DNI and can very well operate at high temperatures and solar concentrations and are essential in any type of High

Concentrating Photovoltaic system (HCPV). Currently, multijunction solar cells have been reported to have an efficiency of 47.1% under a solar concentration of 143 suns. These cells optimize the bandgap energy to expand the absorption range of the solar spectrum resulting in less thermalization loss (low thermal performance) [3]. One of the major issues however in the HCPV systems is the dissipation of the excess heat generated due to the limited electrical conversion of the solar energy. Increasing the concentration ratio enables higher power extraction using a smaller solar cell but at the same time increases their operating temperature. The solar cell temperature's linear correlation with the concentration ratio is dependent on the cell area, where increasing the cell area increases the wasted heat [4]. The most

* Corresponding author.

E-mail address: h.baig@exeter.ac.uk (H. Baig).

| Nomenclature | | | |
|----------------------|--|--------------------------------|----------------------------|
| A | Area (m ²) | a | ambient |
| Q | Heat dissipated by the solar cell (W) | c | solar cell |
| q | heat flux (W/m ²) | Ge | germanium |
| \dot{q} | heat source (W/m ²) | Cu | copper |
| q _o | optical power (W/m ²) | Al | aluminium |
| T | Temperature (°C) | Al ₂ O ₃ | alumina |
| h | Heat transfer coefficient (W/ m ² K) | Si ₃ N ₄ | silicon nitride |
| DNI | Direct normal irradiance (W/m ²) | SnAgCu | tin-silver-copper |
| R | Thermal resistance (m ² .K/W) | cond | conduction |
| L | thickness (m) | conv | convective |
| K | thermal conductivity (W/ m K) | rad | radiation |
| X | The position of fin along the baseplate area (cm) | tr | Thermal resistance |
| | | L | plain layer |
| | | baseplate | baseplate area of heatsink |
| | | n | number of fins |
| <i>Greek Symbols</i> | | <i>Abbreviations</i> | |
| ε | Emissivity | DBC | Direct Bonded Copper |
| σ | Stefan-Boltzmann constant 5.67×10^{-8} (W/m ² . K ⁴) | IMS | Insulated Metal Substrate |
| ∇ | three dimensions (x, y, z) | Si Wafer | Silicon Wafer |
| η | Efficiency | PCB | Printed Circuit Boards |
| | | CPV | Concentrated Photovoltaic |
| | | WCC | Worst-Case Condition |
| <i>Subscript</i> | | | |
| s | solar surface | | |
| sur | surrounding | | |

commonly used solar cell sizes include $3 \times 3 \text{ mm}^2$, $5.5 \times 5.5 \text{ mm}^2$ and $10 \times 10 \text{ mm}^2$ with peak efficiencies of 42.5%, 41.6% and 40.9% respectively [5]. The performance of a CPV module is strongly influenced by the cell temperature and it is highly desirable to maintain it between 50 and 80 °C [6]. Use of optical concentrators results in localized heated spots due to the nonuniformity of solar irradiance at which mechanical failures such as cell surface deformation might occur [7].

The solar cells are typically mounted on heat spreaders made using highly thermally conductive materials which serve at the same time as contact pads for the internal electrical connection of the module. The thermal behavior of the solar cell mainly depends on the heat spreader type and the associated different layers of the materials employed in its assembly. The heat spreader is located between the PV cell and cooling

mechanism to conduct the heat and then dissipate it, as shown in Fig. 1

The heat sink which is typical of a larger area helps further dissipate the heat to the surroundings. Active and passive cooling mechanisms can be utilized within the heat sink enabling better control of the operating solar cell temperature [8]. Traditionally, passive cooling systems have shown good potential for maintaining temperatures of the PV cell at high concentrations of up to $500\times$ in severe weather conditions [9,10]. Active cooling, in particular, has been utilized for HCPV systems enabling co-generation of both heat and electricity simultaneously [11–14]. A number of studies have been reported earlier that [15–17] illustrates different cooling mechanisms which have been integrated into CPV systems to maintain the cell temperature below the cell's operational limits. Min et al. [18] developed a thermal model to study a

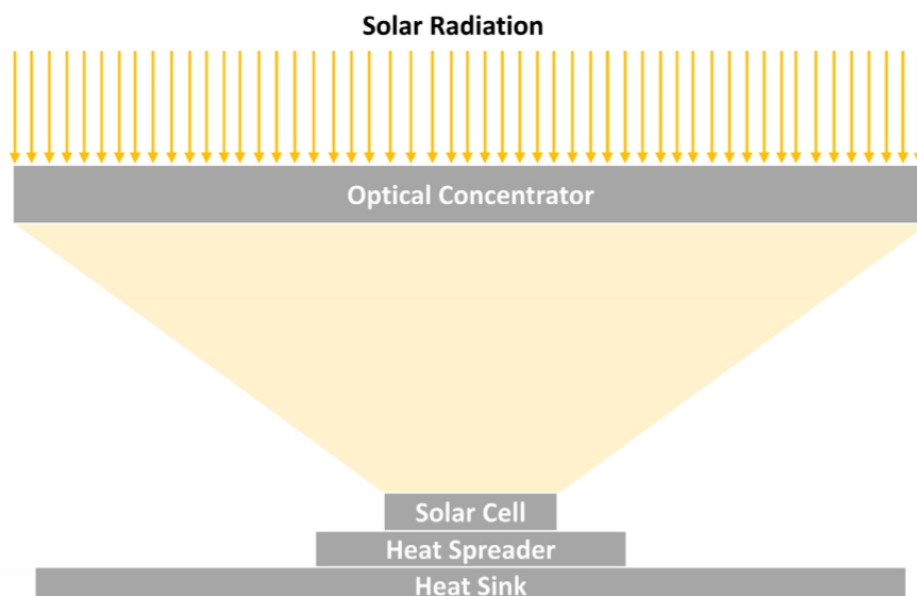


Fig. 1. Basic Configuration of a CPV Unit.

$3 \times 3 \text{ mm}^2$ triple-junction solar cell and found the cell temperature reached $1200 \text{ }^\circ\text{C}$ at 400 suns with no heatsink.

Gualdi et al. [19] identified the limits of passive cooling for concentration ratios up to 2000 suns. Results showed that a flat heat-sink could maintain the cell temperature below $80 \text{ }^\circ\text{C}$ for a cell side length between 2 and 4 mm. A thermal test and simulation of an Alumina flat heat-sink for a concentration ratio in the range from 1 sun up to 1000 suns showed that at 500 suns the cell temperature reached $80 \text{ }^\circ\text{C}$ and kept increasing to reach about $120 \text{ }^\circ\text{C}$ at 750 suns [20]. Wang et al. [8] presented a numerical investigation addressing the effect of DNI, the wind speed, the module elevation angle, and the ambient temperature. Renzi et al. [21] studied the performance of two commercial 3.5 kWp CPV systems at 476 suns. The temperature of the backside of the aluminum heatsink was measured to be in the range of 55 and $65 \text{ }^\circ\text{C}$. Chou et al. [22] developed a thermal model to assess the performance of a $6.5 \times 5.5 \text{ mm}^2$ triple-junction solar cell under a concentration ratio of 380 suns cooled with an aluminum flat-plate heatsink and reported the maximum cell temperature of $69 \text{ }^\circ\text{C}$ correspondent to the thermal resistance of $4.67 \text{ }^\circ\text{C/W}$. Theristis and Donovan [23] used finite element analysis to estimate the operating temperature of a $10 \times 10 \text{ mm}^2$ triple-junction solar cell and found that the flat plate heatsink of 1.63 K/W thermal resistance can passively maintain the solar cell in a safe operating condition up to 500 suns. A further study showed that a solar cell of $1 \times 1 \text{ mm}^2$ or below with an aluminum flat-heatsink could maintain the cell temperature below $60 \text{ }^\circ\text{C}$ [4]. Micheli et al. [24] showed that the optimized fin array improved the mass-specific power by up to 50%. Further, they explored the use of different substrate materials like DBC and, IMS [5].

Abo-Zahhad et al. [25] developed a thermal model to investigate effect of increasing the area ratio (proposed two copper areas/originally defined two copper areas). Hu et al. [26] studied the dynamic performance of a hybrid system coupled subsystems. The subsystems helped to maintain the electrical efficiency to 35.15% with a tank water mass altering range between 0.82 and 17.52 L. Abo-Zahhad et al. [27] examined novel jet impingement microchannel heatsink design and compared it with a conventional model. Maka and Donovan [28] reported that, at 1000 concentration ratio, a minimum of 2400 W/m^2 . K

of the convective heat transfer coefficient is needed to maintain the cell $< 80 \text{ }^\circ\text{C}$.

Aldossary et al. [29] studied two passive cooling designs (round pin and straight fins heatsinks) and showed that they are incapable of maintaining the cell temperature $< 80 \text{ }^\circ\text{C}$. Wang et al. [30] reported that the temperature could be maintained below $75 \text{ }^\circ\text{C}$ at the worst ambient temperature of $45 \text{ }^\circ\text{C}$ with a fan pump power of less than 2 W.

Fin heat-sinks are widely used to enhance the heat transfer between two media by the thermal exchanging surface. Parametric optimization for fin heat-sink geometry in CPV application showed that a thicker fin does not improve the heat transfer because of the surpassing convective heat transfer between fins [31,32]. A thinner fin in a heat-sink with an optimized fin number minimizes the weight. The minimized weight of the heat-sink materials reduces the load and size of the tracking system, especially with a high and ultra-high concentration ratio, where the acceptance angle is limited. The optimization of the fin number and fin spacing is strongly related to the temperature difference and inclination angle [33–35]. In a micro fin heat sink, a general correlation among geometry and orientation has been experimentally studied and showed that convective heat transfer coefficient increases by decreasing the height of the fins, increasing the fin spacing, and/or decreasing the fin thickness for upward/ downward horizontal orientation and vertical orientation, as in Fig. 2. The upward horizontal orientation showed a 12% discrepancy in the thermal resistance compared to the downward surface orientation. Kim and Micheli [36,37] carried out their experimental study at $100 - 200 \text{ }\mu\text{m}$ -height and their work showed an enhancement in the thermal exchange of up to 10%. Also, the correlation between the fin's geometry and thermal performance was investigated for a range of temperatures [38,39]. Recently, flared heatsink configurations applied in CPV module were experimentally investigated and showed a reduction in the thermal resistance of 10% in comparison to a flat-plate heat sink [40].

In this study we report the influence of different parameters that dictate the solar cell operating temperature. The concentration ratio in the range of 100–1000 suns has been investigated for the worst-case operating condition on a $3 \times 3 \text{ mm}^2$ multijunction solar cell bonded to a flat-plate and micro fin heat-sink. The use of three different substrate

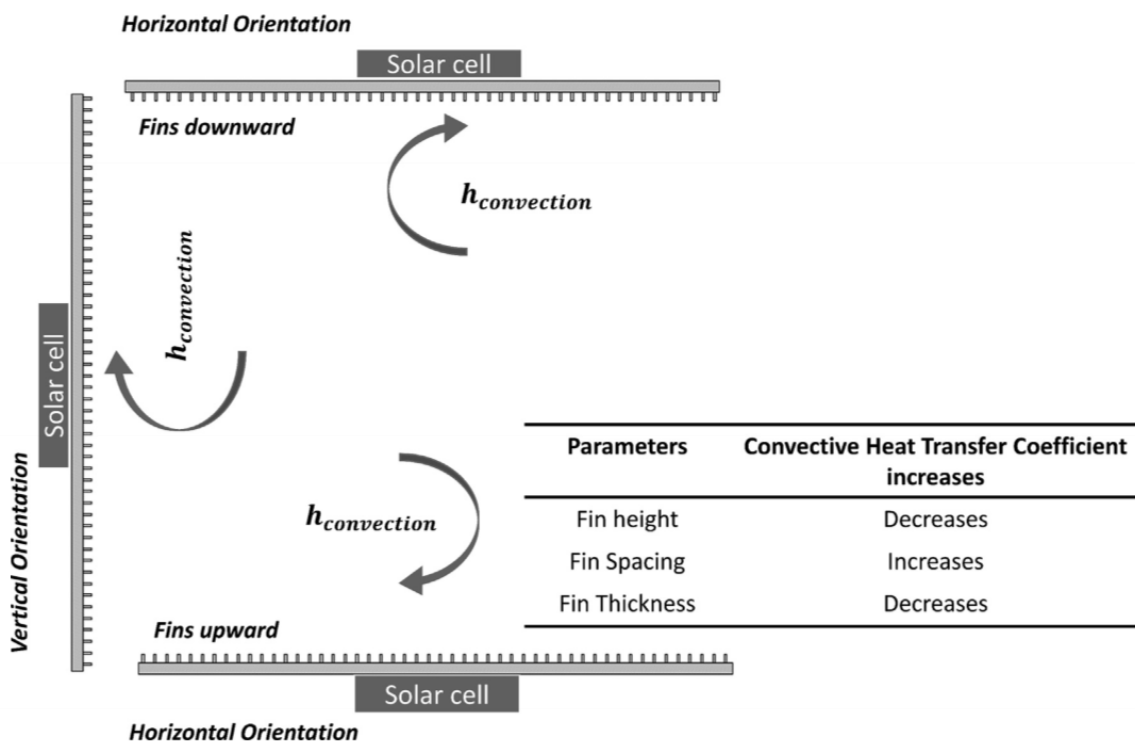


Fig. 2. General correlation between geometry and orientation for micro-fin heat-sink [33–35].

materials namely Direct Bonded Copper (DBC), Insulated Metal Substrate (IMS), and Silicon Wafer substrate (Si wafer) has been explored. For the micro-fin heat-sink, the effect of wind speed on the external boundaries has been taken into consideration by varying the convective heat transfer coefficient between $3 - 25 \left[\frac{W}{m^2 \cdot K} \right]$ [41]. The impacts of extreme weather conditions have been considered by varying the ambient temperature beyond 50 °C. Furthermore, a geometrical parametric study for heat sink fin number and fin spacing has been numerically investigated to optimize the thermal performance. The results help determine the concentration ratio limits at which passive cooling is no longer enough and active cooling is needed to thermally manage the solar cell for improved reliability.

2. CPV design considerations

A starting point for the design of any CPV system is to determine the type of solar cell used and its associated heat dissipation system. A clear understanding of the expected environmental conditions can help determine the solar cell operating temperatures, the amount of power to be extracted and the overall physical dimensions of the system depending on the type of heat sink deployed. The cell temperature's linear correlation with the concentration ratio is dependent on the cell area, where increasing the cell area increases the wasted heat.

In this study, a $3 \times 3 \text{ mm}^2$ multijunction PV (Model 3C44C) cell from Azur space has been considered as shown in Fig. 3. The cell is designed to operate within a range of 100–1500 suns and has a peak efficiency of 42%. The maximum operating temperature is reported to be 110 °C [42]. The cell has a widely recognized H-pattern optimized to perform under non-uniform illumination conditions.

2.1. Passive cooling with fin design

Utilization of passive cooling mechanisms in different studies has been proven to successfully handle the thermal management for a wide range of concentration ratio. Flat-plates and finned heat-sinks are used commonly in a passive cooling system. Generally, increasing the area of the heat-sink baseplate easily dissipates heat but at the cost of increased module weight which ultimately increases the cost of tracking and the LCOE ultimately. So, the minimum heat-sink baseplate area for Azur Space 3C44 – $3 \times 3 \text{ mm}^2$ cell area is calculated, applying the same approaches in [5], by the Eq. (1).

$$A_{\text{baseplate}} = \frac{Q_C}{[q_{\text{conv}} + q_{\text{rad}}]} \quad (1)$$

The CPV system exchanges heat with its surrounding through natural convection and radiation. The convective heat flux (q_{conv}) is proportional to the difference between the solar surface temperature (T_s) and the ambient fluid temperature (T_a) considering the exchange

baseplate area ($A_{\text{baseplate}}$) and the convective heat transfer coefficient (h), as in Eq.(2).

$$q_{\text{conv}} = A_{\text{baseplate}} \cdot h \cdot (T_s - T_a) \quad (2)$$

where radiation (q_{rad}) is proportional to the difference between the solar surface temperature (T_s) and the surrounding fluid temperature (T_{Sur}) to the fourth power considering the radiative property (ϵ) of the exchange baseplate area ($Area_{\text{baseplate}}$) and the Stefan-Boltzmann constant ($\sigma = 5.67 \times 10^{-8} \frac{W}{m^2 \cdot K^4}$), as in Eq. (3)

$$q_{\text{rad}} = A_{\text{baseplate}} \cdot \epsilon \cdot \sigma (T_s^4 - T_{\text{Sur}}^4) \quad (3)$$

Assuming that all the heat generated (Q_C) by Azur Space 3C44C – $3 \times 3 \text{ mm}^2$ cell is conducted to the bottom surface of the heat sink, considering only the flat bottom surface of the receiver, and taking into account the highest value of natural convective heat transfer coefficient of $25 \text{ W/m}^2 \cdot \text{K}$, an emissivity value of polished aluminum surface of 0.09, a heat sink surface temperature of 60 °C, and an ambient temperature of 25 °C. Thus, the minimum required dissipating area of 0.0025 m^2 is required correspondent to $5 \times 5 \text{ cm}^2$. The assumption was made considering the emissivity value of aluminum instead of copper and silicon where they would result in the lesser dissipating area due to their higher emissivity. The fin heat-sink geometry is obtained from [24], as in Fig. 4. A $3 \times 3 \text{ mm}^2$ multijunction solar cell is attached to a heat sink with an area of 25 cm^2 and uses 50 micro-fins (thickness 200 μm and pitch of 900 μm).

2.2. Heat spreader selection and thermo-physics properties

The selection of the CPV system's components and materials plays a fundamental role in thermal management. The heat spreader between the PV cell and the heat-sink needs to be highly efficient to transfer the generated heat out of the PV cell. A high thermal conductivity material for the substrate is preferable, while electrical conductivity needs to be minimized. The most commonly used substrate in the CPV system is Direct Bonded Copper (DBC) due to its mechanical strength and excellent thermal and electrical properties [43–45]. Printed Circuit Boards (PCB) substrates on the other hand which is widely used in the electronic applications have a laminated fiberglass on one or both sides with copper that decreases the thermal conductivity [46] and limits its application in CPV. Replacing the laminated material with a metal improves the thermal conductivity and is referred to as Insulated Metal Substrate (IMS). IMS is an alternative for DBC due to its affordability and excellent thermal performance [47]. Also, Silicon wafer (Si wafer) is an excellent material for the substrate because Si wafer has a similar thermal expansion rate to the multijunction PV cell semiconductor material that can improve its reliability [5]. Silicon manufacturability is simple, but silicon is an expensive material compared to other substrates and mechanically fragile [37].

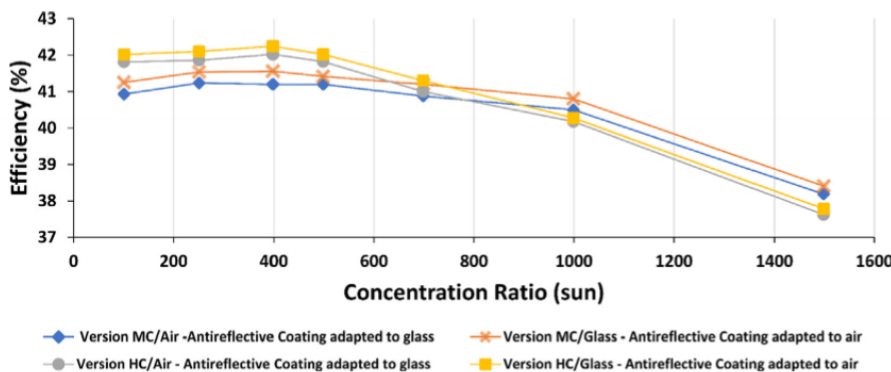


Fig. 3. Performance characteristics of an Azur space 3C44C. The four lines are efficiency versus sun concentrations for version MC/air & glass and version HC/Air & glass where the solar cell is optimized. Measurement conditions is 1.5 AM D – 1000 W/m² (ASTM G 173–03), T = 25 °C, designated measurement area = 100,51 mm² [42].

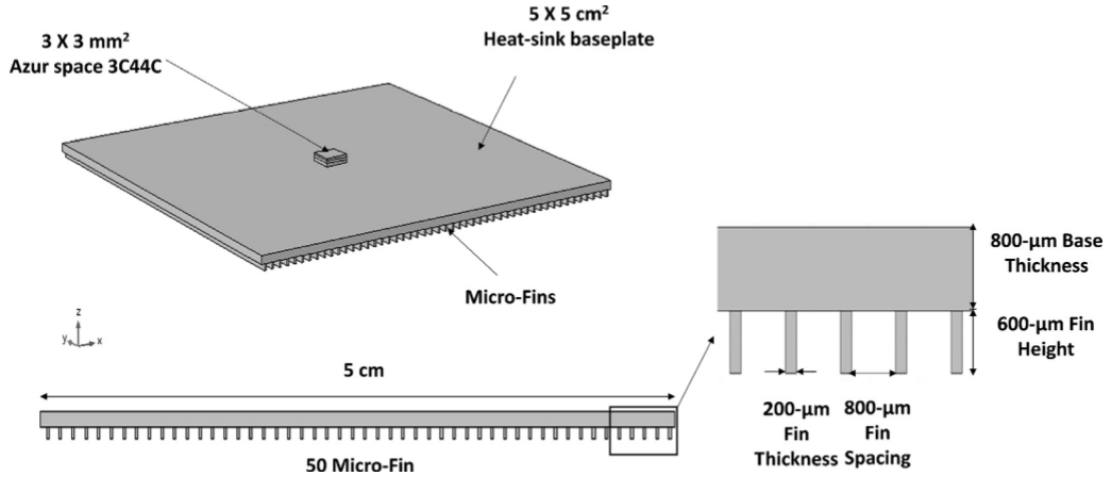


Fig. 4. Asymmetric, side-view, and cross-section view for the micro-finned heat-sink with typical dimensions of the fins.

The substrate layer thickness and materials have been selected according to the cell area, as shown in Fig. 5.

Three different substrates with three different heat-sink materials have been researched in COMSOL Multiphysics to evaluate the thermal performance at fixed heat-sink geometry, as in Table 1.

3. Numerical model

In the present study, we model the solar cell and the associated heat dissipation using the energy equation. The heat transfer rate in the CPV unit is governed by considering the energy conservation law for the steady-state condition with the heat source (\dot{q}), where (q_{cond}) and (q_{conv}) indicate the conduction heat transfer and the convective heat flux, respectively, in Eq. (4).

$$q_{cond} = \dot{q} + q_{conv} \quad (4)$$

The analysis of the conduction heat transfer rate (q_{cond}) in the solid domain is obtained by Fourier's law. The conduction heat transfer equation is solved to obtain the temperature distribution between the solid layers in three dimensions (x, y, z) where it is presented as a del operator (∇) considering the solid layers thermal resistance ($R_{tr,cond}$) in

Table 1

Thermo-physical properties used in COMSOL.

| Material | Density [kg/m ³] | Heat Capacity [J/kg. K] | Thermal Conductivity [W/m. K] |
|---|------------------------------|-------------------------|-------------------------------|
| Germanium (Ge) | 5323 | 700 | 60 |
| Copper (Cu) | 8700 | 385 | 400 |
| Aluminium (Al) | 2700 | 900 | 238 |
| Silicon (Si) | 2329 | 700 | 130 |
| Alumina (Al ₂ O ₃) | 3900 | 900 | 27 |
| Silicon nitride (Si ₃ N ₄) | 2370 | 673 | 10 |
| Marble Resin | - | - | 3 |

Eq. (5)

$$q_{cond} = \nabla \left(-\frac{1}{R_{tr,cond}} \nabla T \right) \quad (5)$$

The thermal resistance, by different layer composition, influences the heat transfer rate because thermal resistance and thermal conductivity are inversely correlated as in Eq. (6)

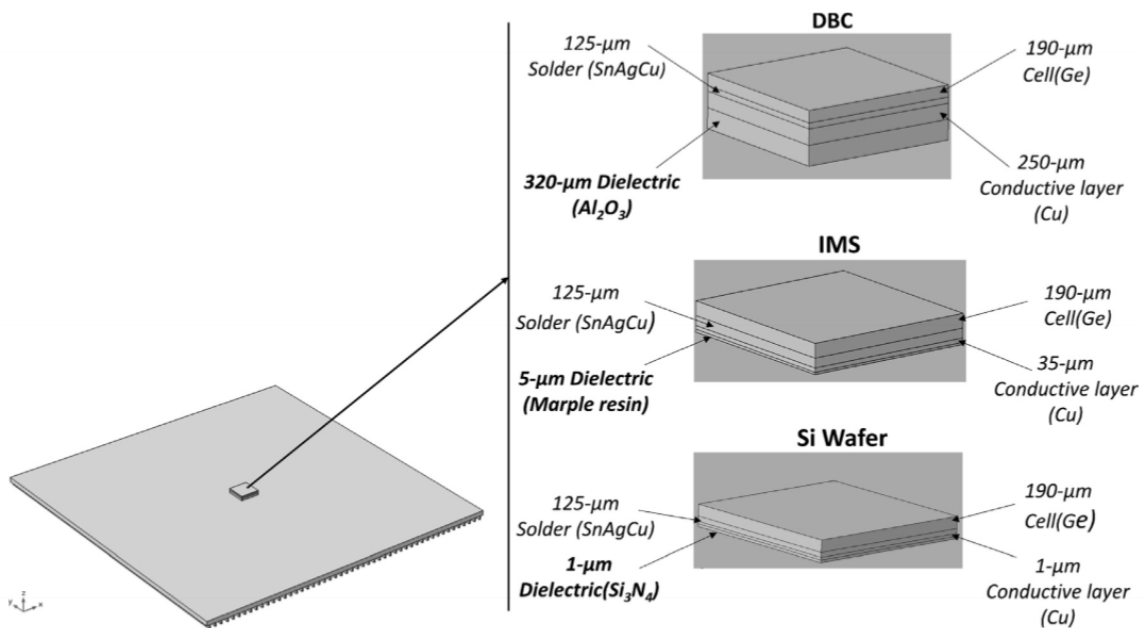


Fig. 5. Geometric model of the CPV receivers, material and thickness layers for the DBC [34], IMS [32], and Si wafer [35].

$$R_{tr,cond} = \frac{L_L}{k_L} \quad (6)$$

The thermal resistance is basically the reciprocal of the thermal conductivity (K_L) through a plain layer of a thickness (L_L)

The convective heat flux (q_{conv}) on the external boundaries is obtained by Newton's law of cooling considering $R_{tr,conv}$ using Eq. (7). However, the adiabatic condition has been applied for the baseplate periphery of the heat-sink taking into consideration the real condition where the receiver is contiguous with other receivers.

$$q_{conv} = \nabla \left(\frac{1}{R_{tr,conv}} \cdot \nabla T \right) \quad (7)$$

The thermal resistance is also associated with convective heat transfer where it is the reciprocal of the convective heat transfer coefficient (hc) in Eq. (8).

$$R_{tr,conv} = \frac{1}{h} \quad (8)$$

The CPV system was mounted in a horizontal position, where buoyancy force is normal to the layer, to allow the natural convection flow and to avoid the temperature gradient on the layer.

Considering the energy conservation law with a heat source for a steady-state condition in Eq. (4), the conduction heat transfer equation for estimating the temperature distribution in the solids can be solved by Eq. (9)

$$\nabla \left(\frac{1}{R_{tr,cond}} \nabla T \right) = \dot{q} \quad (9)$$

The heat source can be modelled as shown in Eq. (10) below. Where (q_o) indicates the optical power output in (W/m^2) after solar concentration and ($\eta_{electrical}$) indicates the electrical efficiency of the solar cell.

$$\dot{q} = q_o \cdot (1 - \eta_{electrical}) \quad (10)$$

The arrangement of the solar cell as a heat source is to model the portion of solar irradiance that converts to wasted heat. The optical power after concentration can simply be expressed as the product of the direct normal irradiance available, the geometric concentration factor and the optical efficiency. For a worst-case condition, we consider that the solar cell generates no electrical energy and assume that all the available optical power is to be dissipated by the heat sink. The optical efficiency ($\eta_{optical}$), the direct normal irradiance (DNI), and the geometrical concentration ratio was assumed to be 85%, 1000 W/m^2 and between 100 and 1000 sun, respectively.

3.1. Boundary conditions

Azur Space 3C44- 3x3 mm² cell area was modelled as one block of germanium (Ge), as considered by other authors [4,20,23,46,48]. The thermal boundary conditions applied to the system can be seen in Fig. 6. Substrates and fin heat-sink, as a consecutive component for the solar cell in building-up the CPV system, was modelled using material

Table 2
Input parameters for the simulations and thermal boundary conditions for Fig. 6.

| Components | Symbols | Value | Units |
|------------------------------------|--|--|---|
| Solar Cell | A_c | 3 × 3 | mm ² |
| | DNI | 1000 | W/m ² |
| | $\eta_{electric}$ | 42.5 | % |
| | $\eta_{optical}$ | 85 | % |
| | Concentration ratio | 100–1000 | Sun |
| Substrates | Area | 3 × 3 | mm ² |
| | Type | Direct Bonded Copper (DBC) Insulated Metal Substrates (IMS) Silicon Wafer (Si Wafer) | |
| | Fin heat-sink | Baseplate thickness Baseplate Width Baseplate Length Materials | 0.8 μm ² 5 cm 5 cm Aluminium Copper Silicon |
| CPV system | h | 3 – 25 | W/ m ² . K |
| | T_a | 20 – 56 | °C |
| <i>Thermal Boundary conditions</i> | | | |
| Number | Region | | Boundary Condition |
| 1 | Solar Cell | | Boundary heat Source |
| 2 | All free surfaces and micro-fin heat-sin | | Natural Convection |
| 3 | | | |
| 4 | All Side surfaces of the heat-sink baseplate | | Adiabatic q = 0 |
| 5 | Surrounding | | Ambient Temperature |

of different layers and thicknesses (Fig. 5) and using the thermo-physics properties of each layer Table 1. Density and thermal conductivity had been set to be independent, no variation with temperature. Solder material was considered as thin thermal resistive layers. All the analyzed inputs and boundary conditions in the simulations are summarized in Table 2 and Fig. 6.

3.2. Meshing

Meshing is a key process when using the finite element method. The accuracy and the time it takes to solve the model is strongly related to the mesh set-up. In this study, different sizes of meshing were applied to ensure the optimal meshing size in every domain. The thickness of the thin layers in the substrates was smaller than the smallest element size for the predefined value in extremely fine mesh in COMSOL. The tetrahedral mesh was introduced to customize the maximum and the minimum element size to be within the thickness of the thin layer by taking into consideration the required computational time, as in Fig. 7.

Different mesh sizes were simulated at 1000 × concentration ratio. The cell temperature obtained at every mesh size is used to consider the relative error between consecutive mesh sizes and to consider the computational time. The maximum cell temperature was simulated to be 156.39 °C and 156.47 °C for mesh size ranged from extremely coarser to extremely fine with a computational time from 4 s to 84 s,

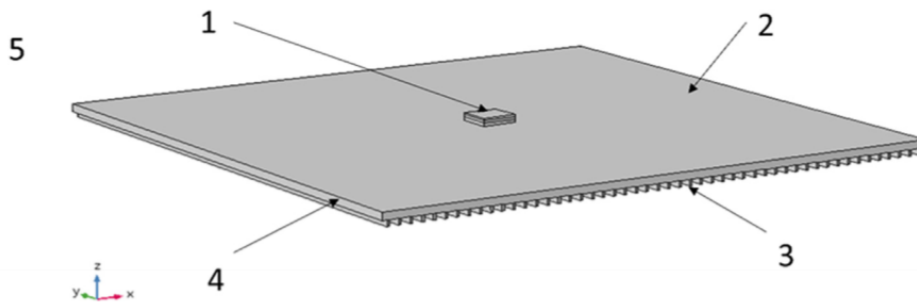


Fig. 6. Thermal Boundary Condition.

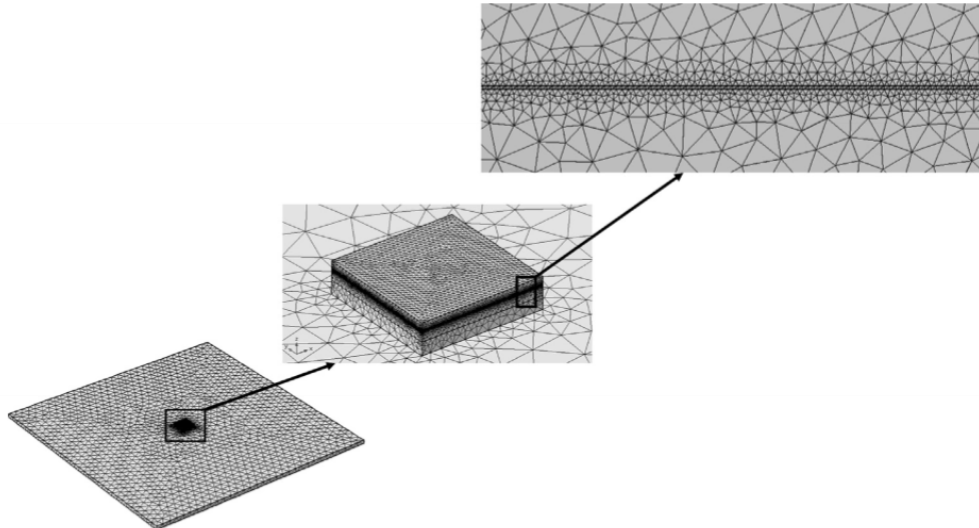


Fig. 7. Tetrahedral mesh applied to the thin layer.

respectively. Thus, the normal mesh size was selected to give a temperature of 156.42 °C. The normal mesh size results in a relative error of 0.03% to the asymptotic value at extremely fine meshing, as in Fig. 8.

4. Results

In this work, the HCPV was subjected to operate in the worst-case conditions (WCCs) wherein the cell is not capable of producing any electrical power ($\eta_{electrical} = 0$). Thus, all the sunlight incident on the solar cell is to be dissipated as heat. In this condition, the cell temperature rapidly elevates rapidly. For safe operation, the solar cell must not exceed 110 °C, which is the maximum operating temperature of 3C44C Azur Space.

We validated the model by comparison with previous studies for the same solar cell size and heatsink configuration. First, we adjusted the developed thermal model to the same conditions in [18] with no

heatsink to predicted the cell temperature under a concentration ratio in the range of 100–1000 Suns, and the results of the current study are in good agreement with [18,25] with an average error factor of 2.7%, as in Fig. 9.

Second, the thermal model was adjusted for standard operating test conditions (SOTC) allowing the cell to produce electrical power ($\eta_{electrical} = 42.5\%$) at 500 suns for a flat-plate heatsink. Table 3 shows a significant agreement between this study and [5,49]. Table 4 shows the concentration ratio limits for a range of micro-fins used in the heat sink for all the three different substrate materials.

4.1. Performance characteristics of CPV with flat-Plate and micro-fin heat sinks

Utilizing the COMSOL Multiphysics numerical simulation model, we can predict the maximum cell temperature for a 3x3 mm² solar cell

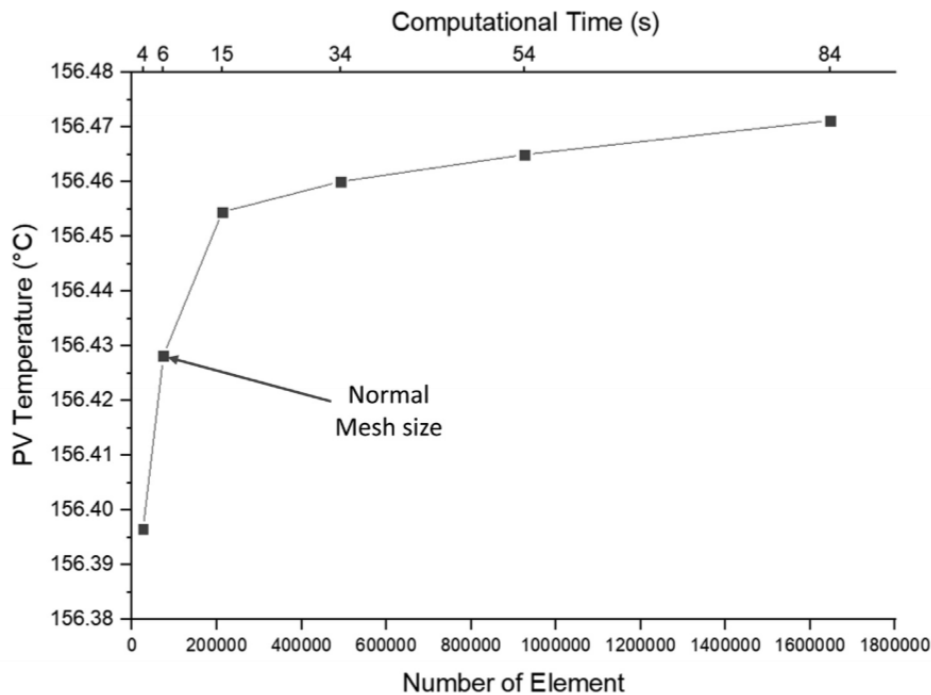


Fig. 8. Mesh selection study for cell temperature (micro-finned heat-sink with DBC substrate at 1000 suns).

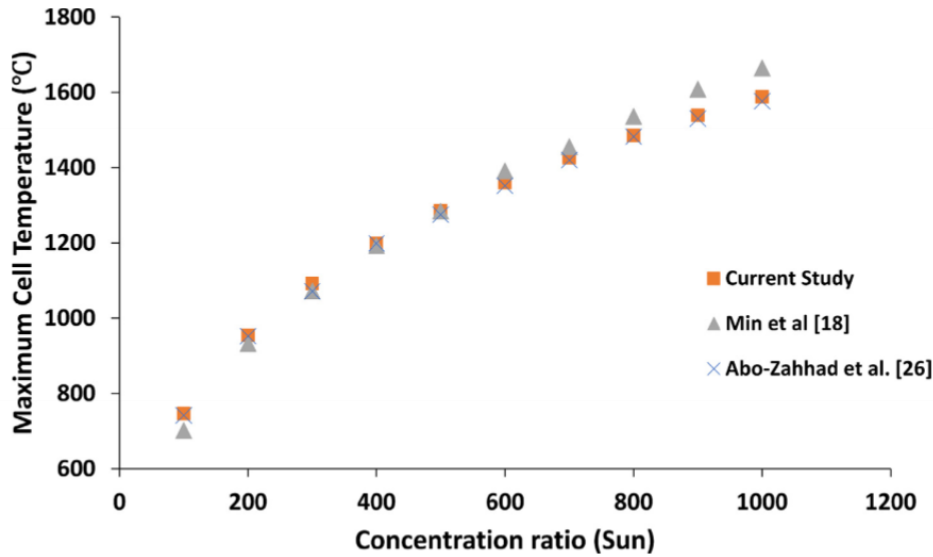


Fig. 9. Validation for the predicted maximum cell temperature with Min et al. [18] and Abo-Zahhad et al. [25] with no cooling aid for DBC substrates.

Table 3
Validation with the previous study.

| | DBC [°C] | IMS [°C] | Si wafer [°C] |
|-------------------|----------|----------|---------------|
| Current Study | 75.11 | 71.2 | 77 |
| Micheli et al [5] | 75 | 72.8 | 78.8 |
| Current Study | 74 | - | - |
| Algora et al [49] | 73 | - | - |

Table 4
The concentration ratio limits with a range of micro-fin number.

| Micro-Fin Number | Concentration ratio at 80 °C (Sun) | | |
|------------------|------------------------------------|-------|----------|
| | DBC | IMS | Si Wafer |
| 10 | 340.8 | 345.1 | 322.7 |
| 20 | 367.3 | 372.6 | 347.1 |
| 30 | 392.5 | 398.8 | 370.1 |
| 40 | 416.5 | 424.1 | 392.2 |
| 50 | 439.6 | 448.3 | 413.2 |
| 60 | 461.7 | 471.6 | 433.5 |
| 70 | 482.7 | 494.1 | 452.8 |
| 80 | 503.2 | 515.7 | 471.5 |
| 90 | 522.5 | 536.6 | 489.5 |
| 100 | 541.5 | 556.7 | 506.8 |
| 110 | 559.5 | 576.3 | 523.5 |
| 120 | 576.9 | 595.1 | 539.6 |

mounted on DBC, IMS, and Si wafer attached with a flat-plate and micro-finned heat-sink under concentration ratios ranging from 100 to 1000 suns. Copper, aluminum, and silicon were selected as the heat-sink materials for DBC, IMS, and Si wafer, respectively. Fig. 10 shows the temperature contours of the solar cell when using different substrate materials and using micro fin heat sinks.

Even as the concentration ratio increased, the cell on the micro-finned heat-sink exhibited a lower maximum cell temperature compared to the system with a flat-plate heat-sink. The difference in maximum temperature between the flat-plate heat-sink and micro-finned heat-sink increased linearly. As shown in Fig. 11, the switching values from passive to active cooling for the flat plate is 305.7, 316.6 and 296.2 suns for DBC, IMS, and Si wafer; whereas, the switching value for micro-finned are 433.7, 450 and 411.8 suns for DBC, IMS, and Si wafer, respectively. The introduction of the micro-finned heat sink results in 25.32%, 23.13%, and 22.24% as an average drop in temperature for

DBC, IMS, and Si wafer, respectively. The result shows an average increase of 0.254 °C, 0.248 °C, and 0.26 °C for every Sun in the flat-plate heat-sinks for DBC, IMS, and Si wafer; whereas, the result shows an average increase of 0.197 °C, 0.192 °C, and 0.204 °C for every Sun in the micro-finned heat-sinks for DBC, IMS, and Si wafer, respectively. At 1000 suns the micro-finned heat sink showed a much lower temperature than the flat-plate heat sinks. It can be seen in Fig. 11 that this was 57.31 °C, 55.43 °C, and 56.07 °C for the micro-finned DBC, IMS, and Si wafer heat sinks respectively.

4.2. Impact of increasing convective heat transfer coefficient

The convective heat transfer is classified according to the nature of the flow and is dependent on the wind speed and the temperature gradient. Forced convection is caused by external intervention. However, for natural convection, the temperature gradient induces the density differences causing a buoyancy force within the air to move. The CPV system is subjected to external winds which impacts the operating solar cell temperature.

The impact of the wind speed is studied by varying the convective heat transfer coefficient in the natural convection range of $3 - 25 \left[\frac{W}{m^2 \cdot K} \right]$ in an interval of $2 \left[\frac{W}{m^2 \cdot K} \right]$ at an ambient temperature of 20 °C for the micro-fin heat-sink. The results showed that the cell temperature is linearly dependent on the concentration ratio, as shown in Fig. 12.a. Also, the cell temperature dependency on the convective heat transfer has a strong effect up to $14 \left[\frac{W}{m^2 \cdot K} \right]$ and then the drop-in cell temperature begins diminishing. Clearly, the higher the convective heat transfer coefficient, the lower the cell temperature meaning high exploitation of natural air circulation. The solar cell on the DBC substrate was found to have a maximum temperature of 429.38 °C at 1000 suns under the lowest convective heat transfer coefficient of $4 \left[\frac{W}{m^2 \cdot K} \right]$ and goes down to 129.57 °C using a convective heat transfer coefficient of $22 \left[\frac{W}{m^2 \cdot K} \right]$. The solar concentration limits for safe operation also increase with the increasing heat transfer coefficient. As shown in Fig. 12.a. the solar concentration limits increase by 401.3 suns, 507.5 suns, and 431.2 suns for the DBC, IMS, and Si wafer, respectively.

Using linear interpolation, we identified the concentration ratio limits for a range of convective heat transfer coefficient whilst maintaining an 80 °C maximum recommended operating temperature. The concentration ratio limits are plotted for DBC, IMS and Si wafer in Fig. 12.b.

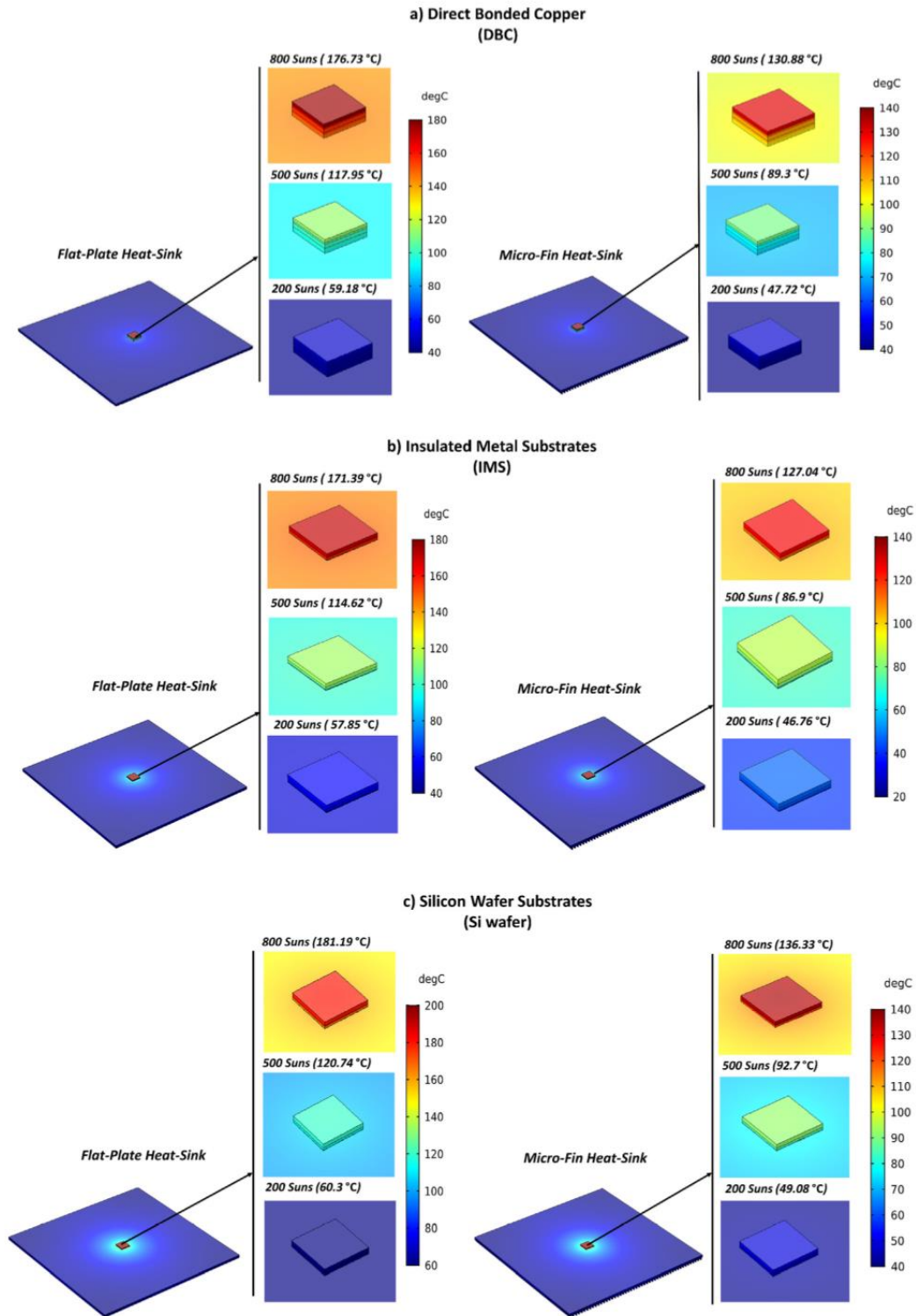


Fig. 10. Temperature field distribution for a) Direct Bonded Copper (DBC), b) Insulated Metal Substrates (IMS), and c) Silicon Wafer Substrate (Si Wafer).

4.3. Impact of ambient temperature and increasing concentration ratio

One of the important parameters that influence the PV performance is the ambient temperature. In the present study, we vary the ambient temperature taking it from a nominal value of 20 °C to extreme weather condition of 56 °C. The selection of the temperature range is made to accommodate the historical day temperatures in countries like Saudi Arabia, India and Spain where these CPV systems would be typically deployed.

Studies were carried out to evaluate the performance of the micro-fin heat-sink varying the ambient temperature, concentration ranges 100 – 1000 suns and at a fixed convective heat transfer coefficient 10 W/m². K. The incremental linear correlations between the cell temperature and ambient temperature are shown in Fig. 13.a. It was observed that for every degree increment of the ambient temperature between 100 and 1000 sun, the cell temperature for DBC, IMS, and Si wafer increased by 123.08 °C, 120.72 °C, and 130.87 °C, respectively. Obviously, a lower ambient temperature results in better heat exchange

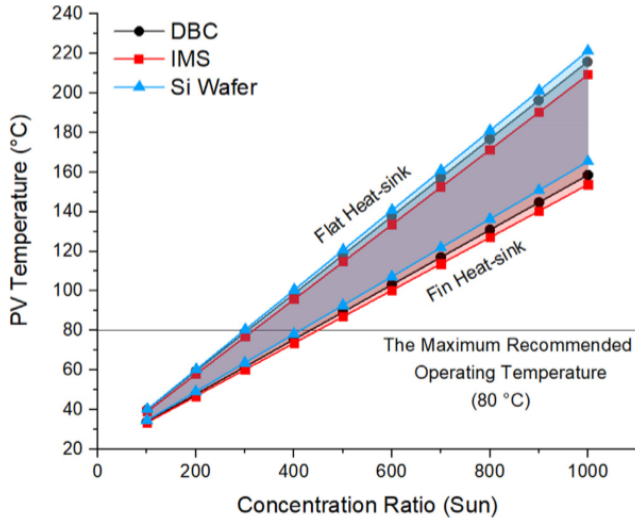


Fig. 11. Simulated maximum temperature for the solar cell mounted on DBC, IMS, and Si wafer.

with the surrounding reducing by that the cell temperature and allowing the cell to accept a higher concentration ratio. Increasing the ambient temperature from 20 to 56 °C reduces the concentration ratio limits by 265.4 suns, 267.2 suns, and 249.6 suns for the DBC, IMS, Si wafer, respectively. The results obtained were extrapolated to determine the concentration ratio limits with ambient temperature at 80 °C and plotted for DBC, IMS and Si wafer as in Fig. 13.b.

It can be seen clearly that the solar concentration needs to decrease for optimal operation at places with higher ambient temperatures. The most comfortable range to operate under any of these extreme conditions would be in the range of 100-200suns.

4.4. Impact of varying the number of micro-fins

Fins can play a crucial role in dissipating the heat from the substrate. Different types of fins with different shapes and sizes can be utilized. However, in our study we have used micro fins with a linear profile and varied them between 10 and 120 maintaining a fixed fin thickness. It is important to note that increasing the micro-fin number also reduces the pitch spacing between them. The thermal model was performed based on convective heat transfer at 10 W/ m². K and ambient temperature at 20 °C assuming, there is no effect by the reduction in the spacing between micro-fin. To configure the micro-fin on the

baseplate for spacing evenly, the following Eq (11) were conducted in the thermal model

$$\begin{aligned}
 X_1 &= \frac{\text{BaseplateWidth}}{\text{Micro} - \text{finnumber}} \quad \text{positionoffirstmicro} - \text{fin} \\
 X_2 &= X_1 + \frac{\text{BaseplateWidth}}{\text{micro} - \text{finnumber}} \quad \text{positionofsecondmicro} - \text{fin} \\
 X_n &= X_1 + X_2 + X_n + \frac{\text{BaseplateWidth}}{\text{micro} - \text{finnumber}} \quad \text{positionofconsecutivemicro} - \text{fins}
 \end{aligned}
 \tag{11}$$

Where X is the position of micro-fin localized along the baseplate width and distributed based on the micro-fin number. As in Fig. 14.a. the results show a linear dependency of cell temperature on the concentration ratio. The maximum safe operating concentration ratio range increases to up to 600 suns when using a micro finned heat sink of up to 120 fins. Increasing the number of fins helps improve the heat dissipation from the heat sink. It was found that increasing the number of fins from 20 to 120 fins results in improving the concentration ratio limits by 233.7 suns, 250 suns, and 216.9 suns for the DBC, IMS, and Si wafer, respectively.

The manufacturing techniques of micro-fins out of metals are laborious process at which the cost of machining a micro scaling fin is primarily related to the machining time. Thus, the limits of concentration ratio at 80 °C for a large number of fins clearly increases but at the price of required machining time as shown in Fig. 4 and Fig. 14b.

5. Performance metrics and outlook

CPV systems can be designed using a variety of heat sinks in order to dissipate heat and operate the solar cell at the desired operating temperature. If natural convection is the only available choice, then this would involve the use of sophisticated machining of the heat sinks in order to achieve the optimal operating conditions. Micro heat sinks have been widely used in a variety of applications including in space and the cooling of a variety of electronic equipment given their light-weight and small dimensions. In CPV applications the weight of the CPV module dictates the load for the tracker and hence makes it equally important to use lighter heat sinks.

The limitations posed by these heat sinks include their physical geometry, machining costs and the amount of heat that they can dissipate. In our study, we chose a standard design of a micro heat sink and evaluated its performance while changing its material properties, the number of fins and the operating variables. We studied a variety of substrate materials including DBC, Si wafer and IMS. The choice of the materials was based on previous research studies highlighting the advantages of different substrates. Silicon being a semiconductor has very

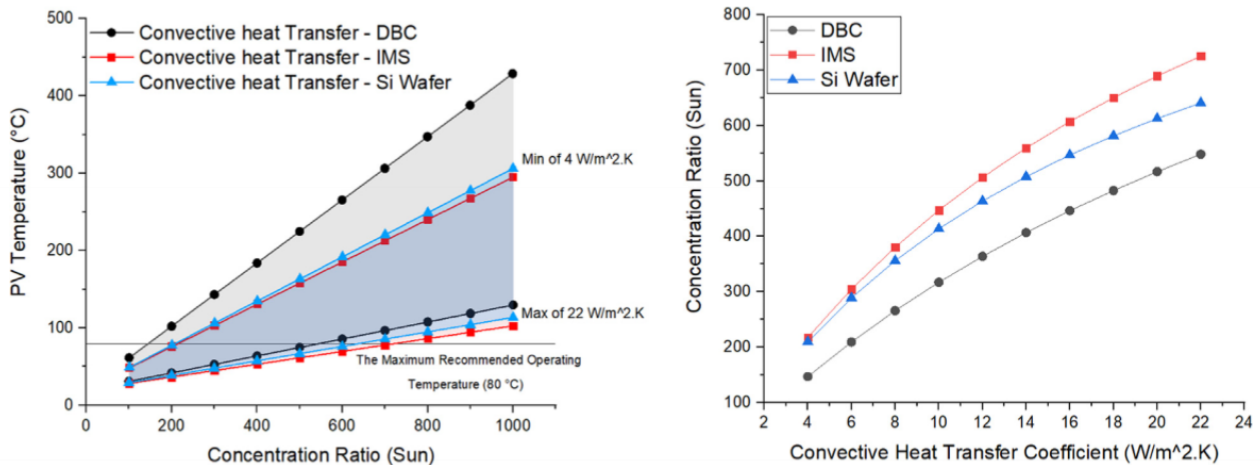


Fig. 12. a. cell temperature with concentration ratio and convective heat transfer coefficient range for DBC, IMS, and Si wafer and b. Concentration ratio limits with convective heat transfer coefficient for DBC, IMS, Si wafer.

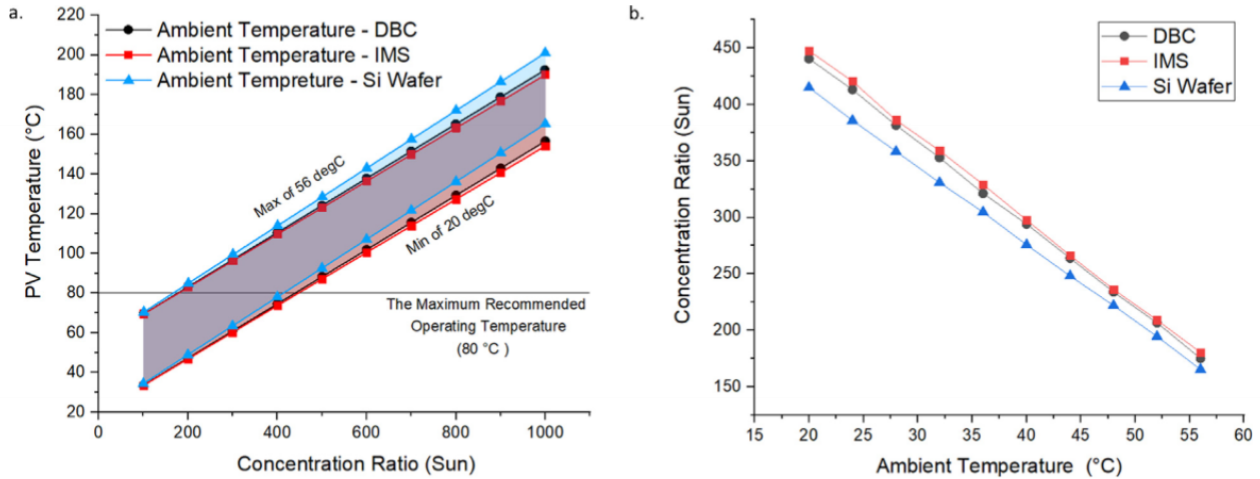


Fig. 13. a. PV temperature with concentration ratio at a range of ambient temperature value for DBC, IMS, and Si wafer and b. concentration ratio limits with ambient temperature for DBC, IMS, and Si wafer.

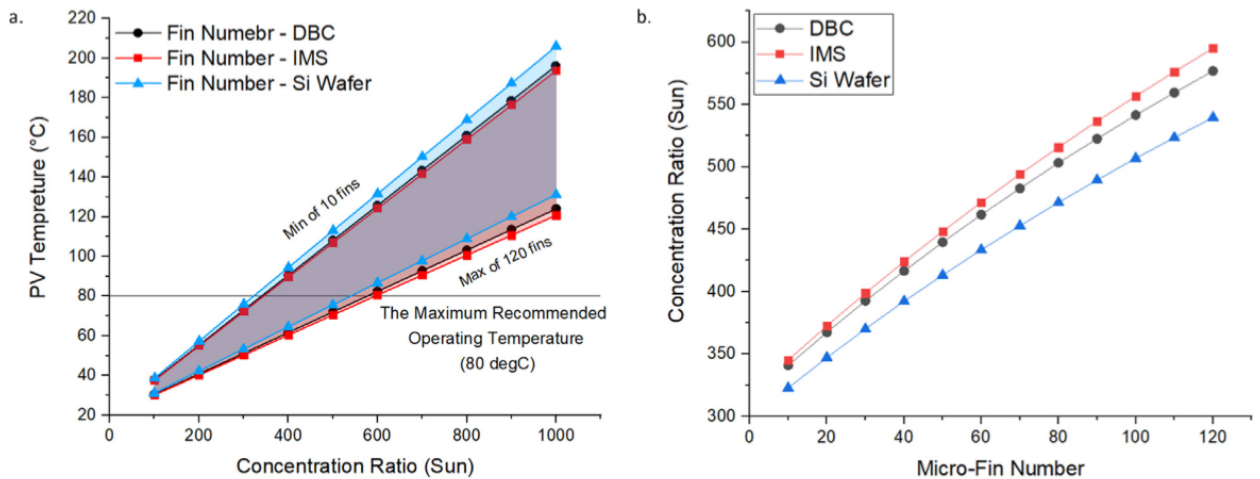


Fig. 14. a. PV temperature with concentration ratio at a range of micro-fin number for DBC, IMS, and Si wafer and b. Concentration ratio limits with micro-fin number for DBC, IMS and Si wafer.

similar thermal expansion properties to those of the solar cell and can help prevent mechanical failure due to the mechanical stresses induced via thermal loading. DBC uses multiple layers of copper sheet enabling higher conduction of heat but has a higher thermal expansion coefficient. IMS is an alternative to DBC and has been very commonly used in the PCB industry making it the cheapest heat sink currently available.

The geometrical parameters of the heat sink dictate the performance limits of the CPV solar cell attached to them. The number of fins, the pitch and their shape can determine the amount of heat dissipation from these devices and ultimately enable the optimization of the system design. In our study, we maintained a linear fin geometry and heat sink area but varied the number of the fins and the pitch. Increasing the number of fins improved the heat dissipation rate but also increases the machining costs of the heat sink. The operating range of the CPV device also increased with an increase in the number of fins. We found that heat sinks using IMS at 10 W/m². K and an ambient temperature of 20 °C were limited to its solar concentration of 595suns while using the maximum number of fins (1 2 0). Which leads us to the question of understanding the impact of the operating variables which can vary significantly in places with high DNI.

The key operating variables that influence the performance of the CPV system are the ambient temperature and the wind speed which determines the heat transfer coefficient available at the heat sinks. In our study, we have exhaustively varied the temperature range between

20 and 56 °C and the heat transfer coefficient between 4–20 W/m². K. We found that both these parameters have a huge impact. For example, the maximum solar concentration of 595suns drastically decreases the IMS performance limit to 180 suns at 56 °C and 10 W/m². K. The increase in the heat transfer coefficient can have a positive impact becomes 22 W/m². K the performance limit of solar concentration increases to 725suns.

6. Conclusion

A 3D numerical model has been developed to predict the maximum cell temperature of micro-finned heat-sink in Fresnel based CPV under different concentration ratio levels for three different substrates materials using COMSOL. In the worst-case conditions, the developed model was able to determine the concentration ratio limits based on the solar cell maximum recommended temperature of 80 °C for different values of natural convective heat transfer coefficient, ambient temperature, and the number of fins. Based on the predicted results, we reached the following:

- 1- Micro-finned heat sink showed 57.31 °C, 55.43 °C, and 56.07 °C as a drop-in temperature at 1000 suns in comparison with the flat-plate heatsink for the DBC, IMS, and Si wafer, respectively.
- 2- Increasing the convective heat transfer coefficient from 4–22 W/m².

K allows the concentration limits to rise by 401.3 suns, 507.5 suns, and 431.2 suns for the DBC, IMS, and Si wafer, respectively.

- 3- Increasing the ambient temperature from 20 to 56 °C reduces the concentration ratio limits by 265.4 suns, 267.2 suns, and 249.6 suns for the DBC, IMS, Si wafer, respectively
- 4- Increasing the number of fins from 20 to 120 fins result in improving the concentration ratio limits by 233.7 suns, 250 suns, and 216.9 suns for the DBC, IMS, and Si wafer, respectively.

Clearly, the thermal resistance of Al₂O₃ in DBC, Marble resin in IMS, and Si₃N₄ in Si wafer generate a temperature gradient between the cell and the heat-sink material. However; the low thermal resistance of the IMS substrate results in the best thermal performance in terms of maintaining the cell temperature below 80 °C and allowing a wider range of high concentration ratio.

Declaration of Competing Interest

The authors declare that they have no known competing financial interests or personal relationships that could have appeared to influence the work reported in this paper.

Acknowledgement

Mr Mussad Alzahrani would like to duly acknowledge the financial support from the Saudi Arabia Culture Bureau in the United Kingdom.

Appendix A. Supplementary material

Supplementary data to this article can be found online at <https://doi.org/10.1016/j.applthermaleng.2020.115315>.

References

- [1] H. Baig, K.C. Heasman, T.K. Mallick, Non-uniform illumination in concentrating solar cells, *Renew. Sustain. Energy Rev.* 16 (2012) 5890–5909, <https://doi.org/10.1016/j.rser.2012.06.020>.
- [2] R. Venkateswari, S. Sreejith, Factors influencing the efficiency of photovoltaic system, *Renew. Sustain. Energy Rev.* 101 (2019) 376–394, <https://doi.org/10.1016/j.rser.2018.11.012>.
- [3] N.L.A. Chan, N.J. Ekins-Daukes, J.G.J. Adams, M.P. Lumb, M. Gonzalez, P.P. Jenkins, et al., Optimal bandgap combinations-does material quality matter, *IEEE J. Photovoltaics* 2 (2012) 202–208, <https://doi.org/10.1109/JPHOTOV.2011.2180513>.
- [4] A. Valera, E.F. Fernández, P.M. Rodrigo, F. Almonacid, Feasibility of flat-plate heat-sinks using microscale solar cells up to 10,000 suns concentrations, *Sol. Energy* 181 (2019) 361–371, <https://doi.org/10.1016/j.solener.2019.02.013>.
- [5] L. Micheli, S. Senthilarasu, K.S. Reddy, T.K. Mallick, Applicability of silicon micro-finned heat sinks for 500× concentrating photovoltaics systems, *J. Mater. Sci.* 50 (2015) 5378–5388, <https://doi.org/10.1007/s10853-015-9065-2>.
- [6] E.F. Fernández, F. Almonacid, P. Rodrigo, P. Pérez-Higueras, Calculation of the cell temperature of a high concentrator photovoltaic (HCPV) module: A study and comparison of different methods, *Sol. Energy Mater. Sol. Cells* 121 (2014) 144–151, <https://doi.org/10.1016/j.solmat.2013.11.009>.
- [7] Y.L. He, K. Wang, Y. Qiu, B.C. Du, Q. Liang, S. Du, Review of the solar flux distribution in concentrated solar power: Non-uniform features, challenges, and solutions. vol. 149, Elsevier Ltd (2019), <https://doi.org/10.1016/j.applthermaleng.2018.12.006>.
- [8] Y. Wang, Q. Liu, J. Lei, F. Liu, Design and characterization of the non-uniform solar flux distribution measurement system, *Appl. Therm. Eng.* 150 (2019) 294–304, <https://doi.org/10.1016/j.applthermaleng.2018.12.150>.
- [9] K. Araki, H. Uozumi, M. Yamaguchi, A simple passive cooling structure and its heat analysis for 500× concentrator, PV module (2003) 1568–1571, <https://doi.org/10.1109/pvsc.2002.1190913>.
- [10] A. Segal, M. Epstein, A. Yogeve, Hybrid concentrated photovoltaic and thermal power conversion at different spectral bands, *Sol. Energy* 76 (2004) 591–601, <https://doi.org/10.1016/j.solener.2003.12.002>.
- [11] D. Vincenzi, S. Baricordi, S. Calabrese, M. Musio, A. Damiano, A cassegrain concentrator photovoltaic system: comparison between dichroic and multijunction photovoltaic configurations, *IECON Proceedings (Industrial Electronics Conference)* (2014) 1900–1905, <https://doi.org/10.1109/IECON.2014.7048761>.
- [12] A. Kribus, D. Kaftori, G. Mittelman, A. Hirschfeld, Y. Flitsanov, A. Dayan, A miniature concentrating photovoltaic and thermal system, *Energy Convers. Manage.* 47 (2006) 3582–3590, <https://doi.org/10.1016/j.enconman.2006.01.013>.
- [13] H. Helmers, A. Boos, F. Jetter, A. Heimsath, M. Wiesenfarth, A.W. Bett, Outdoor test setup for concentrating photovoltaic and thermal (CPVT) systems, *AIP Conf. Proc.* 1407 (2011) 175–179, <https://doi.org/10.1063/1.3658320>.
- [14] T.P. Otanicar, R.A. Taylor, C. Telang, Photovoltaic/thermal system performance utilizing thin film and nanoparticle dispersion based optical filters, *J. Renew. Sustain. Energy* 5 (2013), <https://doi.org/10.1063/1.4811095>.
- [15] S. Jakkhar, M.S. Soni, N. Gakkhar, Historical and recent development of concentrating photovoltaic cooling technologies, *Renew. Sustain. Energy Rev.* 60 (2016) 41–59, <https://doi.org/10.1016/j.rser.2016.01.083>.
- [16] A. Roynce, C.J. Dey, D.R. Mills, Cooling of photovoltaic cells under concentrated illumination: a critical review, *Sol. Energy Mater. Sol. Cells* 86 (2005) 451–483, <https://doi.org/10.1016/j.solmat.2004.09.003>.
- [17] L. Micheli, N. Sarmah, X. Luo, K.S. Reddy, T.K. Mallick, Opportunities and challenges in micro- and nano-technologies for concentrating photovoltaic cooling: a review, *Renew. Sustain. Energy Rev.* 20 (2013) 595–610, <https://doi.org/10.1016/j.rser.2012.11.051>.
- [18] M. Cui, N. Chen, X. Yang, Y. Wang, Y. Bai, X. Zhang, Thermal analysis and test for single concentrator solar cells, *J. Semicond.* 30 (2009), <https://doi.org/10.1088/1674-4926/30/4/044011>.
- [19] F. Gualdi, O. Arenas, A. Vossier, A. Dollet, V. Aimez, R. Arès, Determining passive cooling limits in CPV using an analytical thermal model, *AIP Conf. Proc.* 1556 (2013) 10–13, <https://doi.org/10.1063/1.4822187>.
- [20] S. Chow, C.E. Valdivia, J.F. Wheeldon, R. Ares, O.J. Arenas, V. Aimez, et al., Thermal test and simulation of alumina receiver with high efficiency multi-junction solar cell for concentrator systems, *Photonics North 2010 (7750)* (2010) 775035, <https://doi.org/10.1117/12.872894>.
- [21] M. Renzi, L. Egidi, G. Comodi, Performance analysis of two 3.5 kWp CPV systems under real operating conditions, *Appl. Energy* 160 (2015) 687–696, <https://doi.org/10.1016/j.apenergy.2015.08.096>.
- [22] T.L. Chou, Z.H. Shih, H.F. Hong, C.N. Han, K.N. Chiang, Thermal performance assessment and validation of high-concentration photovoltaic solar cell module, *IEEE Trans. Compon. Packag. Manuf. Technol.* 2 (2012) 578–586, <https://doi.org/10.1109/TCPMT.2011.2181165>.
- [23] M. Theristis, T.S. O'Donovan, Electrical-thermal analysis of III-V triple-junction solar cells under variable spectra and ambient temperatures, *Sol. Energy* 118 (2015) 533–546, <https://doi.org/10.1016/j.solener.2015.06.003>.
- [24] L. Micheli, K.S. Reddy, T.K. Mallick, Plate micro-fins in natural convection: An opportunity for passive concentrating photovoltaic cooling, *Energy Procedia* 82 (2015) 301–308, <https://doi.org/10.1016/j.egypro.2015.12.037>.
- [25] E.M. Abo-Zahhad, S. Ookawara, A. Radwan, A.H. El-Shazly, M.F. El-Kady, M.F.C. Esmail, Performance, limits, and thermal stress analysis of high concentrator multijunction solar cell under passive cooling conditions, *Appl. Therm. Eng.* 164 (2020) 114497, <https://doi.org/10.1016/j.applthermaleng.2019.114497>.
- [26] H. Hu, D. Yuan, T. Wang, Y. Jiang, Dynamic performance of high concentration photovoltaic/thermal system with air temperature and humidity regulation system (HCPVTH), *Appl. Therm. Eng.* 146 (2019) 577–587, <https://doi.org/10.1016/j.applthermaleng.2018.10.028>.
- [27] E.M. Abo-Zahhad, S. Ookawara, A. Radwan, A.H. El-Shazly, M.F. Elkady, Numerical analyses of hybrid jet impingement/microchannel cooling device for thermal management of high concentrator triple-junction solar cell, *Appl. Energy* 253 (2019) 113538, <https://doi.org/10.1016/j.apenergy.2019.113538>.
- [28] A.O.M. Maka, T.S. O'Donovan, Modelling of the thermal behaviour of solar high concentrating photovoltaic receiver, *Therm. Sci. Eng. Prog.* 9 (2019) 281–288, <https://doi.org/10.1016/j.tsep.2018.12.001>.
- [29] A. Aldossary, S. Mahmoud, R. Al-dadah, Technical feasibility study of passive and active cooling for concentrator PV in harsh environment, *Appl. Therm. Eng.* 100 (2016) 490–500, <https://doi.org/10.1016/j.applthermaleng.2016.02.023>.
- [30] S. Wang, J. Shi, H.H. Chen, S.R. Schafer, M. Munir, G. Stecker, et al., Cooling design and evaluation for photovoltaic cells within constrained space in a CPV/CSP hybrid solar system, *Appl. Therm. Eng.* 110 (2017) 369–381, <https://doi.org/10.1016/j.applthermaleng.2016.08.196>.
- [31] S.K. Natarajan, T.K. Mallick, M. Katz, S. Weingaertner, Numerical investigations of solar cell temperature for photovoltaic concentrator system with and without passive cooling arrangements, *Int. J. Therm. Sci.* 50 (2011) 2514–2521, <https://doi.org/10.1016/j.ijthermalsci.2011.06.014>.
- [32] N. Sendhil Kumar, K. Matty, E. Rita, W. Simon, A. Ortrun, C. Alex, et al., Experimental validation of a heat transfer model for concentrating photovoltaic system, *Appl. Therm. Eng.* 33–34 (2012) 175–182, <https://doi.org/10.1016/j.applthermaleng.2011.09.031>.
- [33] K.H. Do, T.H. Kim, Y.S. Han, Choi B Il, M.B. Kim, General correlation of a natural convective heat sink with plate-fins for high concentrating photovoltaic module cooling, *Sol. Energy* 86 (2012) 2725–2734, <https://doi.org/10.1016/j.solener.2012.06.010>.
- [34] G. Mittelman, A. Dayan, K. Dado-Turjeman, A. Ullmann, Laminar free convection underneath a downward facing inclined hot fin array, *Int. J. Heat Mass Transf.* 50 (2007) 2582–2589, <https://doi.org/10.1016/j.ijheatmasstransfer.2006.11.033>.
- [35] A. Bar-Cohen, M. Iyengar, A.D. Kraus, Design of optimum plate-fin natural convective heat sinks, *J. Electron. Packag.* 125 (2003) 208, <https://doi.org/10.1115/1.1568361>.
- [36] J.S. Kim, B.K. Park, J.S. Lee, Natural convection heat transfer around microfin arrays, *Exp. Heat Transfer* 21 (2008) 55–72, <https://doi.org/10.1080/08916150701647835>.
- [37] L. Micheli, K. Reddy, T.K. Mallick, Plate micro-fins in natural convection: experimental study on thermal effectiveness and mass usage, *Int. Conf. Polyaeneration* (2013).
- [38] L. Micheli, K.S. Reddy, T.K. Mallick, General correlations among geometry, orientation and thermal performance of natural convective micro-finned heat sinks,

- Int. J. Heat Mass Transf. 91 (2015) 711–724, <https://doi.org/10.1016/j.ijheatmasstransfer.2015.08.015>.
- [39] S. Mahmoud, R. Al-Dadah, D.K. Aspinwall, S.L. Soo, H. Hemida, Effect of micro fin geometry on natural convection heat transfer of horizontal microstructures, *Appl. Therm. Eng.* 31 (2011) 627–633, <https://doi.org/10.1016/j.applthermaleng.2010.09.017>.
- [40] Q. Luo, P. Li, L. Cai, X. Chen, H. Yan, H. Zhu, et al., Experimental investigation on the heat dissipation performance of flared-fin heat sinks for concentration photovoltaic modules, *Appl. Therm. Eng.* 157 (2019) 113666, <https://doi.org/10.1016/j.applthermaleng.2019.04.076>.
- [41] F. Incropera, T. Bergman, A. Lavine, D. DeWitt, *Fundamentals of heat and mass transfer*, Wiley, 2011.
- [42] M. Data, T. Average, E. Data, Concentrator triple junction solar cell cell type : 3C44C- 3 × 3 mm² Azur, *Space* (2012) 3–6.
- [43] Micheli L, Sarmah N, Fernandez EF, Reddy KS, Mallick TK. Technical issues and challenges in the fabrication of a 144-Cell 500 × Concentrating Photovoltaic receiver. 2014 IEEE 40th Photovoltaic Specialist Conference, PVSC 2014 2014:2921–5. <https://doi.org/10.1109/PVSC.2014.6925543>.
- [44] M.J. Concentrator, C. Assembly, *Prototype Product, Area 91342 (2010).
- [45] Azur Space Solar Power GmbH. Enhanced Fresnel Assembly - EFA Type: 3C42A – with 10x10mm² CPV TJ Solar Cell Application: Concentrating Photovoltaic (CPV) Modules 2014:0–4.
- [46] L. Micheli, N. Sarmah, X. Luo, K.S. Reddy, T.K. Mallick, Design of a 16-cell densely-packed receiver for high concentrating photovoltaic applications, *Energy Procedia* 54 (2014) 185–198, <https://doi.org/10.1016/j.egypro.2014.07.262>.
- [47] L. Mabilie, C. Mangeant, M. Baudrit, Development of CPV solar receiver based on insulated metal substrate (IMS): comparison with receiver based on the direct bonded copper substrate (DBC) - A reliability study, *AIP Conf. Proc.* 1477 (2012) 289–293, <https://doi.org/10.1063/1.4753888>.
- [48] G. Peharz, J.P. Ferrer Rodríguez, G. Siefer, A.W. Bett, A method for using CPV modules as temperature sensors and its application to rating procedures, *Sol. Energy Mater. Sol. Cells* 95 (2011) 2734–2744, <https://doi.org/10.1016/j.solmat.2011.03.030>.
- [49] Algora, Carlos Rey-Stolle I. Algora, Carlos Rey-Stolle, Ignacio. Handbook of Concentrator Photovoltaic Technology - 5.3.3.2 Solar Cell Packaging for Efficient Heat Transfer. John Wiley & Sons; 2016.

Article 3. M. Alzahrani, A. Ahmed, K. Shanks, S. Sundaram, T. Mallick, "Optical losses and durability of flawed Fresnel lenses for concentrated photovoltaic application." *Materials Letters*, 275 (2020), p. 128145, [10.1016/j.matlet.2020.128145](https://doi.org/10.1016/j.matlet.2020.128145).



Optical losses and durability of flawed Fresnel lenses for concentrated photovoltaic application



Mussad Alzahrani^{a,b}, Asmaa Ahmed^{a,c}, Katie Shanks^a, Senthilarasu Sundaram^{a,*}, Tapas Mallick^a

^aEnvironmental and Sustainability Institute, University of Exeter, Penryn TR10 9FE, UK

^bMechanical and Energy Engineering Department, Imam Abdulrahman Bin Faisal University, Dammam 34212, Saudi Arabia

^cMechanical Power Engineering Department, Port Said University, Port Said 42523, Egypt

ARTICLE INFO

Article history:

Received 8 May 2020

Received in revised form 8 June 2020

Accepted 9 June 2020

Available online 10 June 2020

Keywords:

Fresnel lens

Optical efficiency

Concentrator photovoltaics

Optical and electrical characterization

Silicon PV

ABSTRACT

Recycling optical devices and materials for solar concentrator devices is a relatively unstudied area but one which is likely to grow in importance as we progress towards an increasingly sustainable and minimum waste environment. As such, considerations into major optical flaws are required. Here, we have investigated the durability of a cracked Silicon on Glass (SOG) Fresnel lens incorporated as the primary optical component in a concentrated photovoltaic (CPV) application. Optical and electrical characterisations of the flawed glass have been conducted to show the effect on the performance. The optical characterisation has shown a drop of 3.2% in optical efficiency. As well, I-V and power curves of cracked and non-cracked Fresnel lens were compared to show a drop of 3.2% in short circuit current (I_{sc}) and power. The results have confirmed that the power loss is directly related to only the area of the primary optic flawed, which has been calculated through as a percentage of geometrical loss (a form of shadowing) which was estimated to be 2.7% of the concentrator area. From the results, we can confirm that although the performance has slightly declined for the significantly flawed Fresnel lens, there are no other detrimental optical effects. The durability of such optics still needs to be tested, but from these results, we recommend that similarly critically flawed optics can be utilised, likely in non-demanding singular CPV units where <5% loss is acceptable.

© 2020 Elsevier B.V. All rights reserved.

1. Introduction

Refractive concentrator photovoltaic (CPV) systems typically utilise Fresnel Lenses to collimate and focus solar illuminations onto a smaller solar cell which is economically advantageous by minimising the required photovoltaic (PV) cell area [1]. The Fresnel lens is commonly exploited as a primary optical interface in focal point CPV systems due to its high optical efficiency and acceptance angle in comparison to reflective paraboloid–hyperboloid optical shapes. However, mechanical fragility of glass rises its vulnerability for cracking due to external physical impact and such optics are typically abandoned/wasted. The waste expenses in the United Kingdom (UK) glass manufacturing is a minimum of £15 billion/a year which is about 4.5% of the total revenue [2]. Glass recycling practice aids both UK glass industry by applying the waste minimisation program (reduce cost by 1%) and ensure the UK countries to meet European (EU) Directive target of at least 60% of glass recovery/recycling rate [3]. Most of the studies are investigating the

glass cracks and their characteristics (length, depth, and angle) for the laser damage performance but none of which has studied glass cracks for CPV applications [4–7]. In these other studies, artificial scratches were made on Fused Silica glass to study the effect of the laser transmittance and show that the ductile scratches have less influence on the transmittance of light in comparison with brittle scratches [8]. Further, the effect of brittle scratches on transmission was carried out for a set of K9 glasses. The results indicated that the brittle scratches reduce the transmittance of light; but increasing the chemical etching time for the K9 glass improves the transmittance of light especially for high density cracked samples [9]. Even a small optical flaw or crack made leads to severe hot focal spot effects that either degrade the lifetime of the solar cell or damage it, and also this small optical flaw causes a significant loss to an arrayed CPV system as all series optics would be limited by the performance of the flawed optics. However, these mechanical concerns contain loss of physical strength of Silicon on Glass (SOG) Fresnel lens and its influence on the optical and electrical performance for CPV application are notably absent from the literature [10,11]. Thus, this article aims to investigate the power output, optical efficiency (loss of transmittance) and durability of a

* Corresponding author.

E-mail address: s.sundaram@exeter.ac.uk (S. Sundaram).

cracked Fresnel lens (SOG) in comparison with a non-cracked one to confirm if such broken optics are more or less still fully functional or worthy of recycling, perhaps for less demanding systems (local/educational projects) with singular unit systems rather than full scale power plants.

2. Experimental approach

Optical and electrical characterisation approaches were conducted for the unflawed and flawed lenses (23 × 23 cm²) (Fig. 1a) utilising both a PerkinElmer spectrophotometer and solar simulator (WACOM). Firstly, the unflawed and flawed lenses were optically characterised by measuring their total transmittance for every wavelength in the range of 400 – 2000 nm. Secondly, at 1000 W/m² solar irradiance, the lenses were adjusted in height to assure the optimum focal spot and length, as in Fig. 1b. Afterwards, a multijunction solar cell Azur space (10 × 10 mm²) (Fig. 1c) [12], was positioned in the centre of the focal spot for I-V curve measurements for each lens.

The temperature range of the solar cell is a further consideration; the solar cells requiring below 80 °C to perform electrically well [13]. A cooling mount base was hence utilised to maintain the cell at 25 °C whilst under the concentrated light. Also, a thermometer was attached to the solar cell surface and the cooling mount base to observe temperature simultaneously and to avoid any damage of the cell and assure proper electrical performance.

3. Results and discussion

The adjustment of the Fresnel lens under the solar simulator results in a focal length of ~42 cm and a focal spot of 2.8 cm, as in Fig. 1b. Since the solar cell area is 1 cm², the utilisation of the focal spot is merely 16% which can be considered as a focal spot loss that although will compromise both the optical and electrical performance, should affect both lenses equally. As in Fig. 2, the percentage of the crack size to the full Fresnel lens area is estimated to be 2.7%.

3.1. Optical characterisation

The optical efficiency was calculated with respect to the total transmittance at every wavelength unit as in Eq. (1).

$$Oppeff = \%T \times \%C \tag{1}$$

where Oppeff is the optical efficiency, %T is the measured total transmittance of the Fresnel lens, and %C is the fractional concentration loss (fraction of the cell area to the focal spot area). The fractional concentration loss is due to the limit of which the Fresnel lens geometric design cannot concentrate solar rays to a focal spot as the solar cell size.

The optical concentration ratio C_o is calculated with respect to the optical efficiency and geometrical concentration ratio C_g and can be done similarly at every wavelength unit as in Eq. (2).

$$C_o = Oppeff \times C_g \tag{2}$$

These calculations result in Fig. 3.a, where the lens optical efficiency was found to be an average of 91% and 88% and hence the concentration ratio (primary optic area/cell area) after the Fresnel lens would be 480 suns and 463 suns for the non-cracked and cracked Fresnel lenses, respectively. The consideration of the fractional concentration loss as described previously, (due to focal spot area being larger than cell area) into the previous equations results in system optical efficiencies of 15% and 14% and optical concentration ratios of 78 suns and 75 suns for the non-cracked and cracked Fresnel lenses, respectively. All displayed in Fig. 3.a. All successive optics performance in the singular CPV unit will be dependent on the performance of primary flawed/unflawed Fresnel lens.

3.2. Electrical characterisation

The solar simulator helicon lamp was adjusted to illuminate solar irradiance of 1000 W/m² for electrical characterisation. Thus, as in Fig. 3.b, I-V curves show a short circuit current (I_{sc}) of 0.985 and 0.954, and the power curve shows a maximum power of 2.35 W and 2.275 W for non-cracked and cracked Fresnel lens, respectively. The optical and electrical characterisation has shown an agreement in the performance drop of non-cracked to cracked Fresnel lens by about 3.2%. This drop of performance is slightly higher than the percentage of the crack size, which we consider as a geometrical loss % (shadow) in the focal spot. The difference

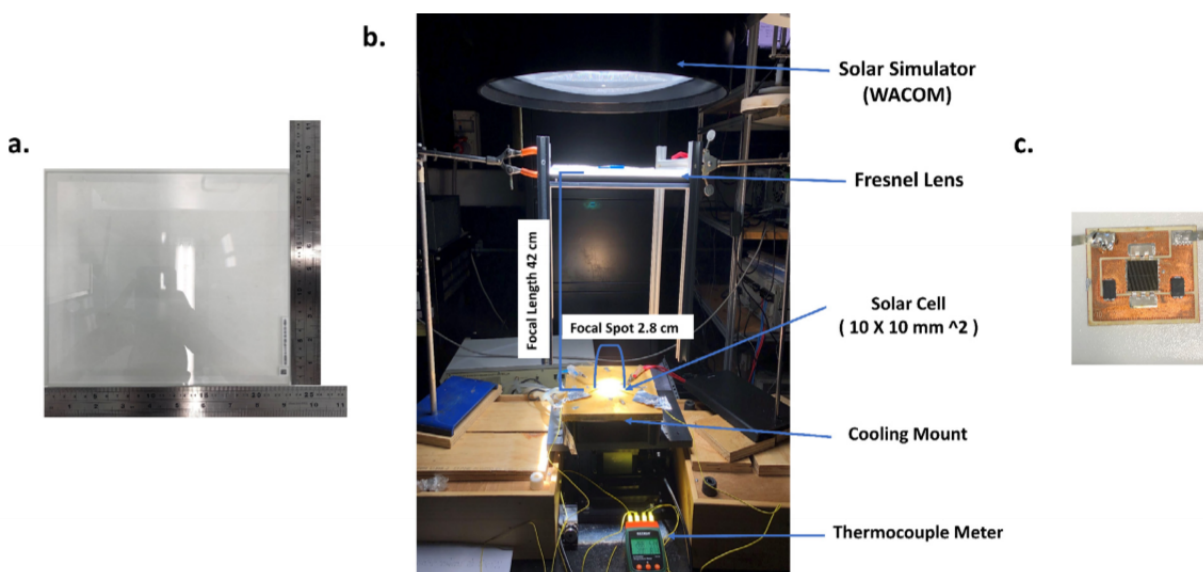


Fig. 1. a) Fresnel lens (SOG) (23 × 23 cm²). b) experiment setup under WACOM Solar Simulator. c) IIV Azur space 10 × 10 mm² solar cell.

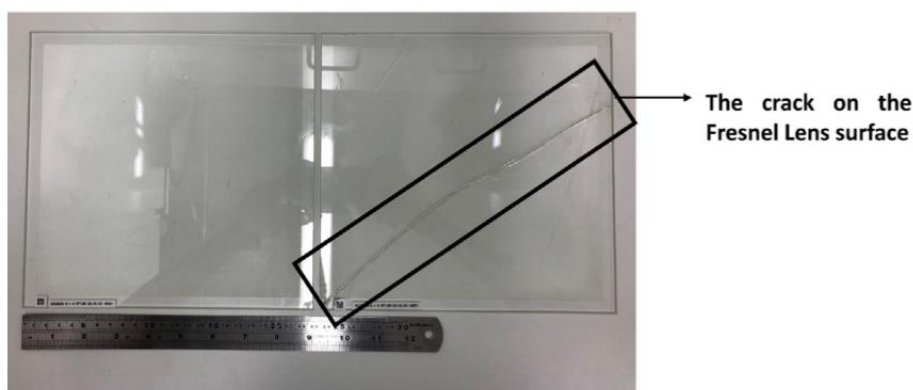


Fig. 2. The flawed/unflawed Fresnel lens.

is due to the limits with which the crack size can be estimated. The altered irradiance distribution upon the cell (due to the crack) would not add to efficiency loss since temperature profiles upon

cells are rarely as discreet as the incident light profile. As in Fig. 3.b, open-circuit voltage (V_{oc}) and fill factor (F.F.) were observed to be quite similar for both non-cracked and cracked

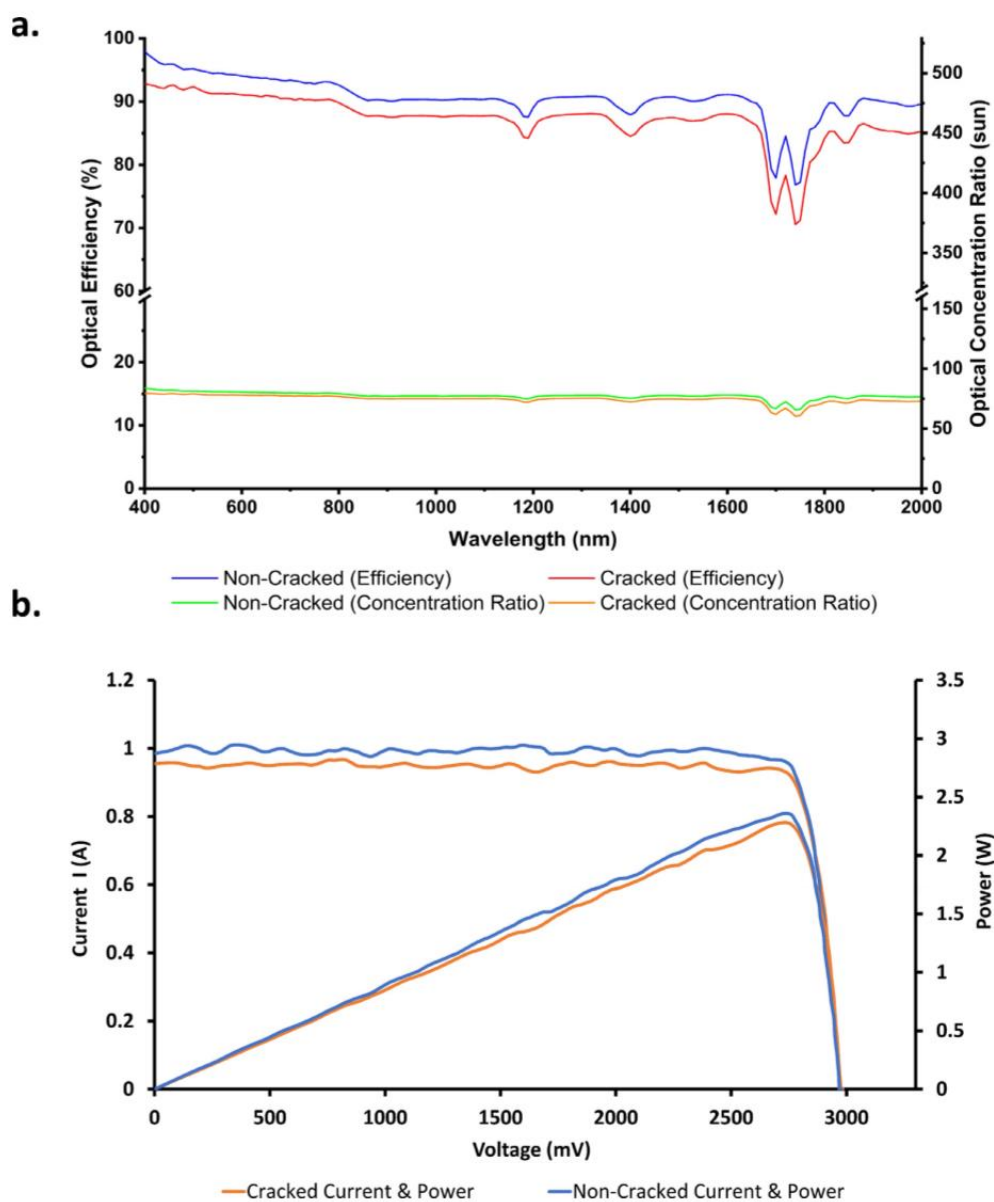


Fig. 3. a) optical efficiency and optical concentration ratio (calculated using the solar cell area as a final optical stage) lines for the flawed/unflawed Fresnel lens. b) I-V & power curves for the flawed/unflawed Fresnel lens.

Fresnel lens indicating no temperature impact because open-circuit voltage (V_{oc}) is temperature-dependent. As well, in these measurements the thermocouples attached to the cell back and top remained at 25 °C. On the other hand, the reduction in the I_{SC} , which is dominated by the solar irradiance intensity, from the non-cracked and cracked Fresnel lens is the only indicator for the drop in the power curve. Thus, all these justifications are affirmed that the drop-in performance is due to only the hinder of solar irradiance by the percentage of the geometric loss not to any other optical, thermal, and electrical factors. Although the Fresnel lens is significantly flawed, still the amount of optical losses compromised on the electrical performance is within a reasonable level of less than 5% allowing the utilisation of such an optic as a primary optical stage in non-demanding CPV unit.

4. Conclusion

The optical and electrical characterisations of flawed SOG Fresnel lens is adopted to see its durability in CPV systems. This approach allows to estimate the percentage of the crack size to the overall Fresnel lens area, and then estimate the optical performance (optical efficiency and optical concentration ratio) and investigate its influence on the electrical performance. The optical and electrical performance has shown a similarity in the percentage decay but when sizing the shadow of optical flaws, overestimation may be the safer procedure as difficult to estimate size visually. A loss of 3.2% optically and electrically should be low enough for similarly flawed and damaged optics to still be used or recycled for low demand projects and installations. The durability of such systems however requires further study.

CRedit authorship contribution statement

Mussad Alzahrani: Writing - original draft, Visualization, Investigation. **Asmaa Ahmed:** Investigation. **Katie Shanks:** Conceptualization. **Senthilarasu Sundaram:** Supervision. **Tapas Mallick:** Resources, Conceptualization, Supervision.

Declaration of Competing Interest

The authors declare that they have no known competing financial interests or personal relationships that could have appeared to influence the work reported in this paper.

Acknowledgements

Mr. Mussad Alzahrani duly acknowledges the financial support from the Saudi Arabia Culture Bureau in the United Kingdom. As well, the Ph.D. scholarship of Ms. Asmaa Ahmed funded by Newton-Mosharafa Fund (UK-Egypt partnership) is acknowledged.

References

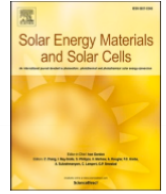
- [1] K. Shanks, J.P. Ferrer-rodriuez, E.F. Fernández, F. Almonacid, A > 3000 suns high concentrator photovoltaic design based on multiple Fresnel lens primaries focusing to one central solar cell, *Solar Energy* 169 (2018) 457–467, <https://doi.org/10.1016/j.solener.2018.05.016>.
- [2] Technology, TI-Waste_Minimisation_(Glass)-Tangram.PDF, (n.d.). [https://www.tangram.co.uk/TI-Waste_Minimisation_\(Glass\)-Tangram.PDF](https://www.tangram.co.uk/TI-Waste_Minimisation_(Glass)-Tangram.PDF).
- [3] Department for Environment Food & Rural Affairs, 2010 to 2015 government policy: waste and recycling, Open Government Licence v3.0. (n.d.). <https://www.gov.uk/government/publications/2010-to-2015-government-policy-waste-and-recycling/2010-to-2015-government-policy-waste-and-recycling>.
- [4] T. Suratwala, L. Wong, P. Miller, M.D. Feit, J. Menapace, R. Steele, P. Davis, D. Walmer, Sub-surface mechanical damage distributions during grinding of fused silica, *J. Non-Cryst. Solids* 352 (2006) 5601–5617, <https://doi.org/10.1016/j.jnoncrysol.2006.09.012>.
- [5] H. Liu, X. Ye, X. Zhou, J. Huang, F. Wang, X. Zhou, W. Wu, X. Jiang, Z. Sui, W. Zheng, Subsurface defects characterisation and laser damage performance of fused silica optics during HF-etched process, *Optical Mater.* 36 (2014) 855–860, <https://doi.org/10.1016/j.optmat.2013.11.022>.
- [6] Z. Zheng, X. Zu, X. Jiang, X. Xiang, J. Huang, X. Zhou, C. Li, W. Zheng, L. Li, Effect of HF etching on the surface quality and laser-induced damage of fused silica, *Optics Laser Technol.* 44 (2012) 1039–1042, <https://doi.org/10.1016/j.optlastec.2011.10.013>.
- [7] F.Y. Génin, A. Salleo, T.V. Pistor, L.L. Chase, Role of light intensification by cracks in optical breakdown on surfaces, *J. Optical Soc. Am. A* 18 (2001) 2607, <https://doi.org/10.1364/josaa.18.002607>.
- [8] Y. Li, H. Ye, Z. Yuan, Z. Liu, Y. Zheng, Z. Zhang, S. Zhao, J. Wang, Q. Xu, Generation of scratches and their effects on laser damage performance of silica glass, *Sci. Rep.* 6 (2016) 1–7, <https://doi.org/10.1038/srep34818>.
- [9] H. Xiao, H. Wang, Z. Chen, G. Fu, J. Wang, Effect of brittle scratches on transmission of optical glass and its induced light intensification during the chemical etching, *Optical Eng.* 56 (2017) 1, <https://doi.org/10.1117/1.oe.56.10.105101>.
- [10] D.C. Miller, S.R. Kurtz, Durability of Fresnel lenses: A review specific to the concentrating photovoltaic application, *Solar Energy Materials and Solar Cells*. DOI:10.1016/j.solmat.2011.01.031.
- [11] D.C. Miller, L.M. Gedvilas, B. To, C.E. Kennedy, S.R. Kurtz, Durability of poly (methyl methacrylate) lenses used in concentrating photovoltaic modules, Reliability of Photovoltaic Cells, Modules, Components, and Systems III. 7773 (2010) 777303. DOI:10.1117/12.861096.
- [12] M. Data, T. Average, E. Data, Concentrator Triple Junction Solar Cell Cell Type : 3C44C- 3 × 3 mm2 Azur Space, (2012) 3–6. http://www.azurspace.com/images/products/0004357-00-01_3C44_AzurDesign_3x3.pdf.
- [13] E.F. Fernández, F. Almonacid, P. Rodrigo, P. Pérez-Higueras, Calculation of the cell temperature of a high concentrator photovoltaic (HCPV) module: a study and comparison of different methods, *Solar Energy Mater. Solar Cells* 121 (2014) 144–151, <https://doi.org/10.1016/j.solmat.2013.11.009>.

Article 4. M. Alzahrani, A. Roy, K. Shanks, S. Sundaram, T. Mallick, "Graphene as a pre-illumination cooling approach for a concentrator photovoltaic (CPV) system." *Solar Energy Materials and Solar Cells*, 222 (2021), p. 110922, [10.1016/j.solmat.2020.110922](https://doi.org/10.1016/j.solmat.2020.110922).



Contents lists available at ScienceDirect

Solar Energy Materials and Solar Cells

journal homepage: <http://www.elsevier.com/locate/solmat>

Graphene as a pre-illumination cooling approach for a concentrator photovoltaic (CPV) system

Mussad Alzahrani^{a,b,*}, Anurag Roy^a, Katie Shanks^a, Senthilarasu Sundaram^a, Tapas K. Mallick^a

^a Environmental and Sustainability Institute, University of Exeter, Penryn Campus, Cornwall, TR10 9FE, UK

^b Mechanical and Energy Engineering Department, Imam Abdulrahman Bin Faisal University, Dammam, 34212, Saudi Arabia

ARTICLE INFO

Keywords:

Graphene
Single-junction solar cell
Passive cooling
Neutral density filter
Optical density
Concentrator photovoltaic

ABSTRACT

The concentrator photovoltaic (CPV) system has a high potential in increasing the power output, propelling further the concentration ratio generating excessive heat that significantly deteriorates the solar cell efficiency and reliability. To thoroughly exploit graphene as a pre-illumination cooling technique for a solar cell, we experimentally characterized screen printed graphene coating (GC) physicochemical characterizations to observe the attenuation of light across a wide wavelength range with different GC thicknesses on a low iron-glass. The thermal and electrical characterizations were further executed to observe the performance of GC on a concentrated CPV system. Based on these comprehensive experimental characterizations, the concept of utilizing graphene as a neutral density (ND) filter for focal spot CPV system is shown to reduce the device temperature significantly by 20% and 12% for GC_{6.3} (6.3 μm thickness) and GC_{2.2} (2.2 μm thickness) in comparison with the infrared filter, respectively. It has been observed that GC_{6.3} increased the cell efficiency by about 12% at 8 suns compared to the base case at 400 W/m² producing 7 suns. It has been ascertained that the introduction of graphene as the ND filter component improved the solar cell efficiency instead of just reducing the geometrical concentration ratio. Further, even the most susceptible single-junction solar cell under a concentration ratio of ≈20 suns with no cooling aid has shown an excellent cell efficiency. Therefore, our approach envisages its application for non-CPV and high and ultrahigh CPV system incorporated with a triple-junction solar cell eliminate the use of external heat sinks or other cooling arrangements.

1. Introduction

The function of the construction of a single junction solar cell is to convert radiation into direct electrical energy. The main issue with the photovoltaic (PV) cell is the energy of the bandgap, in which the photon energy must be greater than the energy of the bandgap to induce the photogeneration of charge carrier. The maximum theoretical conversion efficiency under one sun AM1.5 for a single-junction solar cell is described by Shockley and Queasier to not exceed 33.7% [1], where currently single-junction silicon-based solar cell proposes efficiency of 26.1% and 27.4% [2] for concentrated and non-concentrated solar irradiance, respectively. The limitation of a single-junction solar cell in absorbing all the incident ray on the PV cell leads to intrinsic thermalization losses which is the cause of heat generation [3]. At 1sun, the outdoor operating temperature of a single-junction solar cell is typically around 55 °C [4–6]: where increasing the concentration ratio might raise the thermal impact on the solar cell to be fatal (1200 °C) at 400

suns [7] with no cooling aid. This amount of heat harms the quality of generated electrical power and the durability of the cell [8,9]. The use of cooling techniques can offer a potential solution to avoid excessive heating of PV panels and to reduce cell temperature [10]. It can be inferred that both air and water cooling methods have been used to a large extent since they can provide additional thermal energy that can be used for different purposes.

Post-illumination or pre-illumination heat extraction techniques are essential to maintain the solar cell performance and reliability for safe operation, especially toward high and ultrahigh concentration ratio. Post-illumination is the conventional solar cell cooling mechanism, including passive cooling and active cooling, which are mainly based on the engineering design concepts and heat transfer components: conduction, convection, and radiation [11]. In a passive cooling approach, a variety of heatsink dimensional configurations [12] are attempting to maintain the solar cell at safe operating conditions for a multi-junction solar cells (MJSCs) [13–17] which can be vulnerable to such high

* Corresponding author. Environmental and Sustainability Institute, University of Exeter, Penryn Campus, Cornwall, TR10 9FE, UK.
E-mail address: ma778@exeter.ac.uk (M. Alzahrani).

<https://doi.org/10.1016/j.solmat.2020.110922>

Received 25 July 2020; Received in revised form 3 November 2020; Accepted 10 December 2020

Available online 16 December 2020

0927-0248/© 2020 Published by Elsevier B.V.

temperatures than single-junction silicon-based cells. On the contrary, active cooling has proven its competence in solar cell thermal management at the cost of a parasitic load especially by increasing the concentration ratio adding to the required load, the system complexity, and the overall system cost [18] [–] [22]. In pre-illumination, spectral decomposition [23,24] -including ultraviolet (UV), visible (VIS), and near-infrared (NIR) - for the solar spectrum tolerates bandpass and bandstop. These pre-illuminations mechanisms can lead to high cell conversion efficiencies bypassing the compatible photon energy to the PV cell and redirecting the photon energy with energy more than the bandgap energy to reduce the cell temperature. Unique configurations including spectral beam splitting (SBS) [25], hot/or cold mirrors [26], holographic optics [27], and luminescent concentrator beam [28], have been mainly focusing on improving the cell efficiency relying on the required load of generation. This spatial pre-illumination approach represents high efficiency in low concentration ratio applications, but it becomes a very complex approach with a high concentration ratio due to the tracking system.

A clear area, where further improvements can be realized, is in the use of selective absorber coatings. Currently, available coating materials are still expensive, subject to degradation and not as efficient as their potential suggests [29–32]. Therefore, the development of sunlight absorbers with rational structure designs has become a popular research topic, because it has remarkable potential to improve efficiency. With a relatively simple generation process and enhanced optical absorption, carbon-based materials have low cost, reusability, and excellent light to heat conversion properties. The combination of maximum light absorption, high specific surface area, and greater thermal stability makes the carbon an effective solar heat absorber material. Graphene exhibits distinct differences from the other carbon nanomaterials in terms of its two-dimensional (2D) features which offers a wide range of interesting properties such as high charge mobilities, superior thermal conductivity, a high degree of transparency, as well as mechanical flexibility among other carbon allotropes [33,34]. Due to its flat elaselectronic 2D band structure, it imparts an exceptional horizontal heat conductor with high thermal stability compared to conventional solar absorber coatings. This is due to the existence of the large aromatic network and extent of pi bond cloud which captures the electrons or ions during the diffusion and oxidation process; resulting in a broad Brillouin zone of band structure for the graphene [35–37]. Graphene absorbs and scatters photons at the upper band, and then a part of photons are transmitted to be incident on the solar cell, as schematically represented in Fig. 1. The high absorption capacity of graphene catalyzes strong interaction between the electronic band of the graphene and incident sunlight results in a strong releasing of heat. A larger portion of the generated heat on the graphene surface is

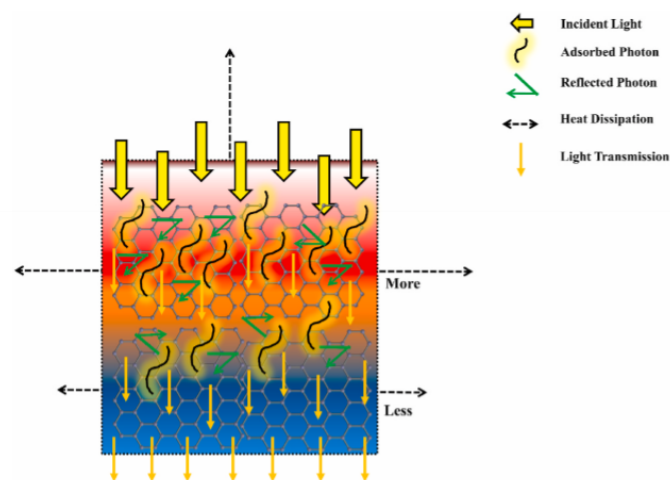


Fig. 1. Scheme of localized solar heating and light transmission of the graphene coating.

dissipated horizontally. For instance, graphene benefits from the high *in-plane* thermal conductivity, up to a certain channel length. However, weak thermal properties for the substrates implies that interfaces and contacts remain the significant dissipation bottlenecks. The heat generation mainly originates from the phonon-phonon coupling within the graphene electronic band structure [38,39].

The concentrator photovoltaic system has a high potential for encouraging power output and reducing the cell size [40–42]. The progression of concentrated photovoltaic (CPV) configuration inclines to increase the concentration ratio and upsurge the competitiveness in the CPV system. This increment in concentration ratio results in minimizing the MJSC cost contribution to the overall system cost [43]. Although the increase of concentration ratio on the MJSC would produce more power despite their low efficiency beyond 1000 suns, the expensive low internal resistance MJSC cannot overrun a temperature of 110 °C [44]. Indeed, this temperature influence will be excessive for single-junction solar cells. In order to address this issue, a neutral density (ND) filter is fabricated utilizing a graphene material to attenuate the transmittance of solar irradiance over a wide spectral band. The optical density (OD) of graphene material from colourless to dark in appearance regulates the amount of energy incident on the cell at which heat generated on the solar cell is controllable in inverse correlation with optical density. More recently, the concept of infrared (IR) filter [45,46] or heat-absorbing filters [47] has evolved into a photonic approach to perform a radiative cooling technique selectively exploiting sunlight with consideration for bandgap energy but with a reduction in cell temperature by 5.7 °C [48]. Coinage metals, such as gold, silver, copper exhibits a high reflectance at the (NIR) [49] and are commonly utilized in ND filter. The standard method to fabricate a ND filter is by coating glass with a thin layer of materials with possessing a different material, such as Co, Fe, and Cr, with precise control of the alloy composition through a vacuum procedure [50–52].

Since the electrical products for the solar cell rely on the solar irradiance intensity, solar cell temperature, and the wavelength band, the influence of diverse colour filter was found in the literature [53]. Indeed, the PV module is influenced under a selective band of wavelength, and excellent performance was found for both blue and magenta. However, the highest electrical performance was found by subjecting all the wavelength band (no filter) on the PV module, and that can be attributed to the actuality of receiving the maximum solar irradiance in the lack of any filters. Besides that, the PV module temperature with no filters was not the maximum one in comparison to all sorts of coloured filters [54]. The utilization of coloured filter has undoubtedly resulted in the cut-off of light intensity intrinsic to the tint of the filter. Thus, in this study, graphene is used as a neutral density filter to attenuate the entire incident solar irradiance by uncomplicated characterization method (no power).

The integration of graphene in the CPV system specifically at the top of the front-grid metallization of triple junction III-V solar cells is studied for one graphene monolayer or two graphene monolayers. The utilization of graphene as a transparent electrode allows the series resistance mitigation. The simple concept is that one monolayer of graphene absorbs lights, causing a reduction of 1% in the change of the short circuit current (ΔI_{sc}). However, in return, the excellent electrical conductivity of graphene provides significant gain by the change of fill factor (ΔFF) \approx 2% at a concentration ratio of 1000suns [55,56]. The incorporation of graphene one monolayer has shown a drop in the solar cell series resistance by 35% and improve the FF by 4% at 1000 suns where two monolayer reduced the series resistance but did not increase the FF due to the optical loss [56]. Further study has integrated one monolayer of graphene between the front-grid and the antireflective coating and compare its energy gain result with conventional III-V solar cell at 800 suns. The energy gain increased between 6 and 7% based on the geographical location when using the monolayer of graphene [57].

The ongoing research in fabricating and developing a CPV system is to achieve a high optical concentration ratio for higher electrical power

output, maintaining an excellent solar cell efficiency. The concept for high electrical output is through attaining as much as possible of the geometrical concentration ratio, and that only occurs when the CPV system has high optical efficiency. However, practically the optical efficiency is compromised electrically depending on the solar cell electrical performance where attention needs to be paid to the amount of concentrated light (generated temperature) on the surface of the solar cell to avert the increase in the solar cell electrical series-resistance. It is a possible solution to reduce the temperature elevation by reducing the geometrical concentration ratio, but this approach is not toward the advances in CPV technology [58]. Differently, allowing CPV system advances is through a high level of geometrical concentration ratio giving a range of optical losses at which higher power output is produced by associating a suitable cooling mechanism. Although using graphene as a neutral density filter causes an optical loss across the wavelength range evenly, the excellent opto-thermal properties of graphene compensate the system by reducing the focal spot temperature at which a higher cell efficiency is gained.

Many studies have investigated graphene based on single or multi-junction deposited on the front-grid of the solar cell but none of which has examined graphene as a pre-illumination method (ND filter) coupled in a CPV system based on Fresnel lens design and its power output potential. The fabrication of graphene as an ND filter will aid the advances and evolution of CPV systems to reach a high concentration ratio by limiting the cell temperature which allows the thermal-mechanical effect to be decreased, the electrical performance to be enhanced, the utilization of low cost and high series resistance solar cells, the employment of continuous 3-D tracking system in pre-illumination cooling techniques, and the minimization of overall system weight, cost, and parasitic load by cancelling the post-illumination cooling mechanism. To illustrate the efficacy technique, in this study four approaches have been conducted for full characterization and analysis of Graphene ND filter utilization in CPV system; chemical characterization, optical characterization, thermal characterization, and electrical characterization.

2. Experimental approach description

2.1. Preparation of graphene coating and optical characterization

The chemical characterization of the graphene coating (GC) is executed by using the graphene ink (Product No. 900960), Sigma Aldrich, and used without any further purification. A layer of graphene ink is employed to develop the coating on a $5 \times 5 \text{ cm}^2$ low iron-glass (4 mm thick) by a screen-printing (120T mesh/inch, Mascoprint, UK) method. The low iron-glass with an excellent performance in both visible and NIR wavelength range has been used for the deposition of graphene quantity and optical characterization, as in Fig. 2a. The low-iron glass-coated samples were characterized based on graphene quantity: thick, medium, and thin coatings, as in Fig. 2c. After each layer of deposition, the sample has been heated for a $120 \text{ }^\circ\text{C}$ for 10 min and allowed to cool for next layer deposition. Finally, the prepared coating is then heated on a hot plate at $300 \text{ }^\circ\text{C}$ for 30 min to remove the binders.

The total transmittance of low iron-glass, different GCs on low iron-glass and the IR filter (Fig. 2b) was measured using a PerkinElmer LAMBDA 1050+ UV/Vis/NIR spectrophotometer in a spectral range of 300–2000 nm for optical characterization and comparison among the coated samples and with the IR filter.

2.2. Thermal and electrical characterization of graphene coating

To perform the thermal and electrical characterizations, a WACOM AAA rating and 2% spatial non-uniformity was applied. Xenon short-arc lamp plus and optical filter are combined to simulate a continuous solar irradiance at AM1.5 spectrum coincidence. The provided calibration cell with the WACOM solar simulator was used to ensure the strong linear

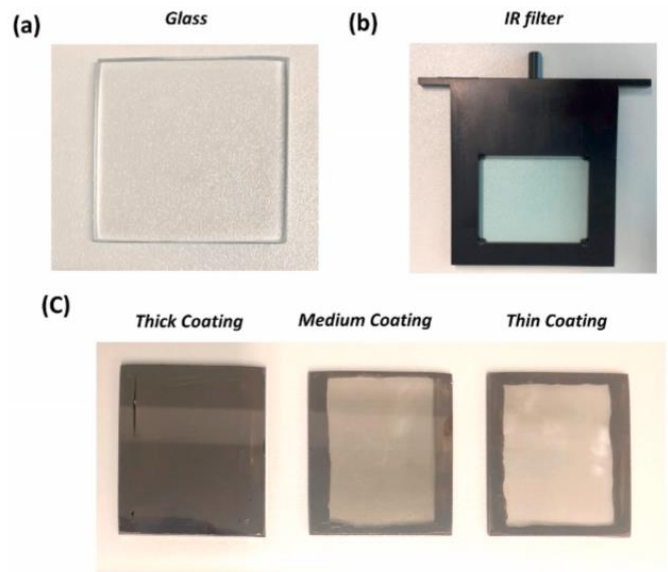


Fig. 2. (a) The digital image of the low iron-glass. (b) the photo of IR filter. (c) the digital image of different samples of GC classified based on the graphene quantity on the glass.

correlation between the I_{sc} and the helicon value (solar irradiance) with the attenuation of the Xenon lamp intensity and the consistency of the solar irradiance.

A refractive [Silicon-on-glass (SOG) - Fresnel lens] optic of 529 cm^2 ($23 \text{ cm} \times 23 \text{ cm}$) area was introduced under the solar simulator (WACOM) at a constant solar irradiance of 1000 W/m^2 and adjusted in elevation for the optimum focal spot and focal length where the highest concentration ratio was achieved. A polycrystalline Si solar cell of 26 cm^2 ($5.1 \text{ cm} \times 5.1 \text{ cm}$) area was placed within the focal spot and centred for maximum electrical output. A polycrystalline Si solar cell was soldered with a tabbing wire (electrical terminal) applying a solder flux along the cell's busbar for oxidization and soldering tip at a temperature of $350 \text{ }^\circ\text{C}$. The electrical terminals are connected to the I-V tracer device to extrapolate the electrical products with time intervals. The experimental setup to concentrate the solar irradiance using the Fresnel lens results in a geometrical concentration ratio of ≈ 20 suns at a focal spot of $\approx 3 \text{ cm}$ in diameter and a focal length of $\approx 44 \text{ cm}$. The gap between the polycrystalline Si solar cells and the low iron-glass is kept $\approx 4 \text{ cm}$ because direct contact with the polycrystalline Si solar cells, where the focal spot temperature is significantly high, induces the thermo-mechanical effects and hinders the FF, as schematically and experimentally layout in Fig. 3a and b.

For thermal characterization, the temperature is measured and collected utilizing a thermocouple meter (Datalogger SDL200 - EXTECH INSTRUMENTS). As well, the FLIR thermal camera is utilized to observe the thermal distribution across the area of the focal spot and the low

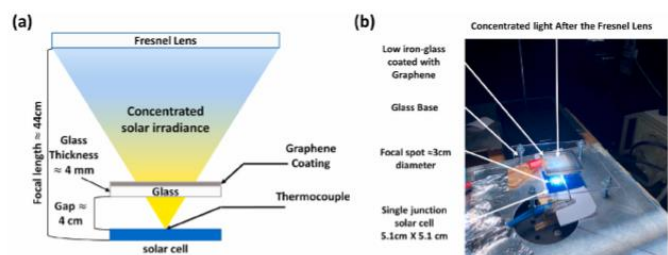


Fig. 3. (a) The schematic approach to generate concentration and measure the focal spot temperature and layout the gap between the solar cell and low iron-glass. (b) the experimental approach under the solar simulator indoor.

iron-glass coated with graphene.

3. Results and discussion

3.1. Chemical characterization

The cross-sectional microstructural scanning electron microscope (SEM) image of the GC samples were analysed on a TESCAN VEGA3 SEM. Different coating thicknesses of the graphene sample on low iron-glass is achieved by a number of screen-printed layers of graphene ink, as in Fig. 4. In this case, using one layer of graphene screen printing coating resulted in an average thickness of $2.2 \pm 0.2 \mu\text{m}$, which is termed as a thin coating (GC_{2.2}), as in Fig. 4a. Further, two and three layers of graphene ink are used to fabricate an average thickness of 6.3 ± 0.1 and $9.1 \pm 0.05 \mu\text{m}$ of coating and termed as medium (GC_{6.3}) and thick coating (GC_{9.1}), as in Fig. 4b and c, respectively. These three different thickness-based GCs are further employed for further characterizations.

3.2. Optical characterization

Graphene is optically characterized to comprehend its optical performance as an ND filter and compared with the most common photonic approach IR filter approach in a wide spectral range of 300–2000 nm. In this study, the CPV unit is based on a Fresnel lens design where the optical performance of all optics and filters integrated after is dependent on the optical behaviour of the Fresnel lens. Thus, the measurement for the total transmittance of the Fresnel lens has found to be 90%. The total transmittance of the low iron-glass has an average loss of $\approx 11\%$ after the graphene has been coated on top of it to attenuate the transmittance of the solar spectrum. The attenuation of solar irradiance has been approached by differing the thickness of graphene during the coating process resulting in GC_{9.1}, GC_{6.3}, and GC_{2.2} after the chemical characterization. The optical characterization of GC_{9.1}, GC_{6.3}, and GC_{2.2} shows an average total transmittance of 2%, 43%, and 64%, respectively. As well, the total transmittance of the IR filter has an average of 74% in a wavelength range of 300–700 nm where after all spectral wavelength is blocked to mitigate the heat. However, considering a wide spectral range of 300–2000 nm results in IR filter average transmittance of 19%. The optical measurements for the IR filter are conducted to compare its performance with GCs. The thickness of the GC has an inverse correlation with the transmittance of light.

To illustrate, the optical characterization, optical efficiency and concentration ratio need to be investigated to see the deterioration in the optical performance with the Fresnel lens at first and then with integrating the IR filter, low-iron glass, GC_{9.1}, GC_{6.3} and GC_{2.2} in one CPV unit, respectively. The incorporation of the optical efficiency of the Fresnel lens (η_{Fresnel}), IR filter ($\eta_{\text{IR Filter}}$), low-iron glass (η_{glass}), and low-iron glass with GCs (η_{GC}) results in the total theoretical optical efficiency for the CPV unit, which is a relevance between the concentrated solar irradiance passing all-optical stages with respect to the incoming solar

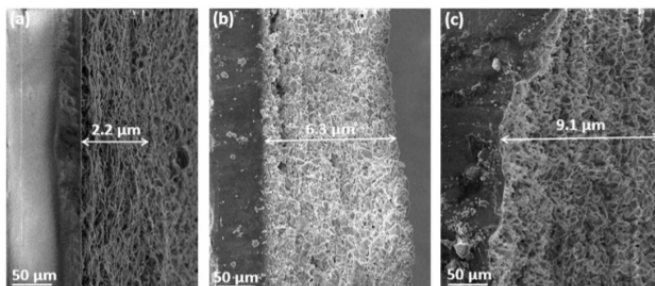


Fig. 4. Cross-sectional SEM images of (a) one (GC_{2.2}), (b) two (GC_{6.3}) and (c) three (GC_{9.1}) layer of screen-printed GC using graphene ink on glass, respectively.

irradiance at the primary optical stage surface area, as in the equation 1

$$\text{Optical Efficiency} = \eta_{\text{Fresnel}} \times \eta_{\text{IR filter, glass, GCs}} \quad (1)$$

The calculated optical efficiency is substituted in equation (2) to extrapolate the optical concentration ratio.

$$\text{Optical Concentration Ratio} = \text{Optical Efficiency} \times G_C \quad (2)$$

where G_C is the geometrical concentration ratio which is the area of the Fresnel to the area of the solar cell.

As in Fig. 5a, the optical efficiency and concentration ratio are measured for after the Fresnel lens and with every test scenario at every wavelength unit. As on average for a wavelength range of 300–2000 nm, the optical efficiency after the Fresnel lens is 90% and equivalent to the optical concentration ratio of 18suns and with integrating the low-iron glass the optical efficiency and concentration ratio dropped to 80% and 16suns, respectively. The graphene coatings dropped the optical efficiency from after the Fresnel to 2%, 42%, and 58% and the optical concentration ratio from after the Fresnel to 1 sun, 8 suns, and 12 suns for GC_{9.1}, GC_{6.3}, and GC_{2.2}, respectively. The IR filter showed a drop from after the Fresnel to 18% and 4 suns for the optical efficiency and concentration ratio, respectively. The total transmittance of GCs has shown almost no fluctuation across the measured wavelength length, indicating less dispersion of light and that is due to the high absorptivity of graphene relative to its thickness. However, Fig. 5a showed that IR filter, low iron-glass, and GCs are dependent on their performance on the primary optic Fresnel lens and that can be observed across the wavelength range.

The measurements of the total transmittance of graphene ND filter allow us to characterize the graphene in terms of optical density (OD) instead of quantity by exploiting the transmittance as the logarithm to the base ten, as in equation (3).

$$\text{Graphene Optical Density} = -\log_{10}(\%T_{\text{avg}}) \quad (3)$$

Where $\%T_{\text{avg}}$ is the average transmittance for a wavelength range between 300 and 2000 nm.

Fig. 5b shows an inverse correlation between the optical density and total transmittance. The ODs are 0.045 0.13, 0.05, 1.69, 0.36, and 0.193 for the Fresnel lens, IR filter, low-iron glass, GC_{9.1}, GC_{6.3}, and GC_{2.2},

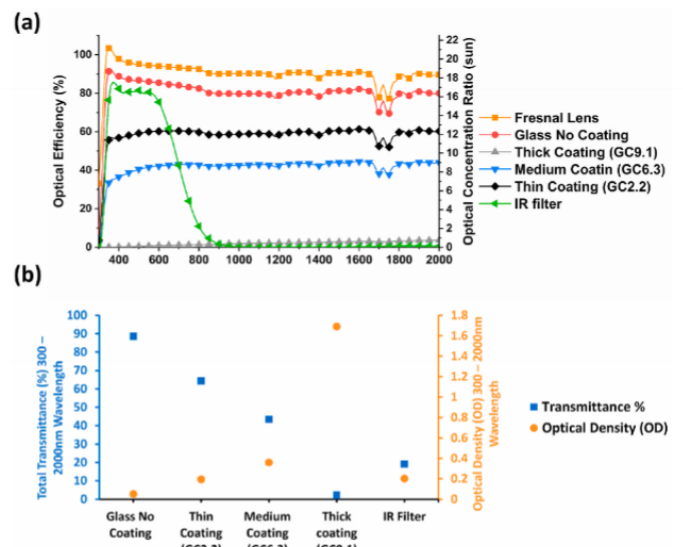


Fig. 5. (a) The correlation between the optical efficiency and the optical concentration ratio for Fresnel lens, IR filter, low iron-glass, GC_{9.1} coating, GC_{6.3} coating, and GC_{2.2} coating with a wavelength range between 300 and 2000 nm. (b) the total transmittance and the optical density (OD) for the Fresnel lens, IR filter, low iron-glass, GC_{9.1} coating, GC_{6.3} coating, and GC_{2.2} coating.

respectively. Table 1 summarizes the total transmittance on average, optical density (OD), optical efficiency, and optical concentration ratio for the optically characterized samples.

It is crucial to evaluate the current production from the polycrystalline Si solar cell when illuminated by wavelength range similar to polycrystalline Si solar cell spectral response range. In order to execute the spectral response, the external quantum efficiency (EQE) was measured for a wavelength range between 300 and 1100 nm using Bentham spectral response arrangement, as shown in Fig. S1, SI. The current density, J_{sc} (mA/cm²) is determined by uniting all the photon energy with the EQE and integrating cross all the correspondent wavelength range to be 38.26 mA/cm².

3.3. Thermal characterization

Thermal characterization is conducted to observe the fluctuation of temperature over time for the focal spot produced by the Fresnel lens and then with the introduction of uncoated low iron-glass and with the GCs, as schematically in Fig. 3a. Three thermocouples were attached at the centre of the graphene layer (top surface of the glass facing the Fresnel lens), the centre of the rear glass surface, and the centre of the focal spot. The rear surface of the glass temperature was measured to observe the temperature difference on the glass and identify any cause for thermal shock, as in Fig. 6a. The temperature was recorded in the three positions. The focal spot temperature reaches the saturation (observing no accumulation in temperature) within a short time of 10 s at which the temperature of the graphene layer was found to be 211.7 ± 4 °C for all the GCs samples. It is undoubtedly expected that high accumulation of heat on the graphene layer would occur resulting in severe temperature degrading the graphene layer with time. The back surface of the glass was found to be 107 °C, 179 °C, and 180 °C for GC_{2,2}, GC_{6,3}, and GC_{9,3}, respectively, as in Fig. 6b. As the graphene thickness decreases, the temperature gradient between the graphene layer and rear surfaces of the glass decrease as well. In order to conduct similar temperature measurements, the orientation of the glass has also been altered where the graphene layer was facing the solar cell, as in Fig. 6c. The results exhibit a minimal temperature difference between the graphene layer and the other side of the glass surface, and that is because glass is much heat conductor than air. However, the focal spot temperature, in comparison to the graphene facing the Fresnel lens, increased on average by 1.63%, 8.8%, and 2.2% for GC_{2,2}, GC_{6,3}, and GC_{9,3}, respectively, as in Fig. 6d. This rise in the focal spot temperature is related to the amount of heat accumulated in the graphene layer drives both heat radiation and convection in its surrounding (4 cm distance between the solar cell and the graphene layer). Although this temperature gradient is not significant, we kept the orientation of the graphene

layer facing the Fresnel lens. The influence of temperature on the Fresnel lens – SOG is out of the scope of this study; however, enough safe distance of 39.6 cm between the graphene layer and Fresnel lens ensures no impact for accumulated heat.

Temperature measurements are extrapolated on average after it reaches the equilibrium. Once the solar simulator lamp was on, the temperature reached its saturated level within a maximum of 10 s and relatively maintained for 70 s, and when the solar simulator lamp was turned off, the temperature released to the surrounding within 20 s to reach a room temperature of 22 °C, as in Fig. 7a. The introduction of the Fresnel lens has shown a focal spot temperature of 219 °C, which after the introduction of the uncoated low iron-glass has attenuated the light slightly reducing the focal spot temperature by 11%. However, the GCs show a significant drop in the focal spot temperature by 89%, 70%, and 39% for GC_{9,1}, GC_{6,3}, and GC_{2,2}, respectively. The focal spot temperature has an inverse correlation with the optical density due to the effectiveness of graphene as a thermal insulator depending on the graphene thickness and that is observed through the consistency of temperature with time. Thus, the introduction of the graphene ND filter shows an average focal spot temperature of 24.6 °C, 66.4 °C, and 132.7 °C for GC_{9,1}, GC_{6,3}, and GC_{2,2} coating measured with the thermocouple, respectively. Fig. 7b shows the correlation between the optical efficiency and the focal spot temperature to illustrate the optical and thermal operating conditions. Fresnel lens and glass no coating have shown the highest optical efficiency but challenged by the highest focal spot temperature. Whereas, it can be observed that the GC_{6,3} and GC_{2,2} have shown that the optical efficiency relatively low in comparison with the Fresnel lens and with uncoated glass but with much reduction in focal spot temperature where the GC_{9,1} has shown the lowest for both focal spot temperature and optical efficiency. The utilization of the IR filter in this experiment is due to its working principle of minimizing heat to the most by cutting off light near IR to ensure excellent electrical performance and to avoid any damage on the solar cell surface. The comparison between the moderate ND filter thermal performance for GC_{6,3} (300–2000 nm) and the IR filter (300–900 nm) is expected to exhibit less temperature after the IR filter due to the difference in the wavelength range in accordance to the polycrystalline Si solar cell spectral response (300–1100 nm) at which the IR filter has shown an optical efficiency lower than the optical efficiency of GC_{6,3} by 38%. However, the IR filter has shown a focal spot temperature of 117.28 °C, which is higher than the focal spot temperature of GC_{6,3} by 43%.

The thermal images were taken for GC_{6,3} to investigate the heat distribution across the top surface. Fig. 7c shows the temperature increasing causing a large area on the top surface of GC_{6,3} with a total testing time of 100 s where the left thermal image shows the thermal distribution at the initial testing time (~1 cm at the centre). The right thermal image shows the thermal distribution where the temperature scale is at least 151 °C increase from 1 cm to 3 cm at the centre. The saturation in the right thermal image is due because the temperature is chosen as a maximum of 151 °C to show how heat is conducted and distributed given the time frame of 100 s on the graphene layer. Longer test time might show a uniformed output across the total area of the GCs (greater than the focal spot size), which brings the graphene as a superior thermal conductor material for the thermal applications, and that can be simplified because as graphene holds the thermal conductivity of $\sim 3000 \text{ Wm}^{-1} \text{ K}^{-1}$ [35].

3.4. Electrical characterization

The polycrystalline Si solar cell electrical products I_{sc} , open-circuit voltage (V_{oc}), and FF, which can be determined simply from the I–V curve, are affected by the increase in the concentration ratio. The large flow of photons increases the current with inducing joule heat on the solar cell surface area. Increasing the concentration ratio (temperature) leads to a reduction in the V_{oc} with significant growth in the I_{sc} . This increase in current density due to the solar concentration inclines to

Table 1

The optical characterization for the measured total transmittance, calculated optical density, optical efficiency, and the optical concentration ratio.

| Tested Samples | Avg. Transmittance (%) | Optical Density (OD) | Optical Efficiency (%) | Optical Concentration ratio (suns) |
|-------------------------------------|------------------------|----------------------|------------------------|------------------------------------|
| Fresnel Lens | 90 | 0.045 | 90 | 18 |
| IR Filter | 19 | 0.72 | 18 | 4 |
| Glass No Coating | 89 | 0.05 | 80 | 16 |
| Thick coating (GC _{9,1}) | 2 | 1.69 | 2 | 1 |
| Medium Coating (GC _{6,3}) | 43 | 0.36 | 42 | 8 |
| Thin Coating (GC _{2,2}) | 64 | 0.193 | 58 | 12 |

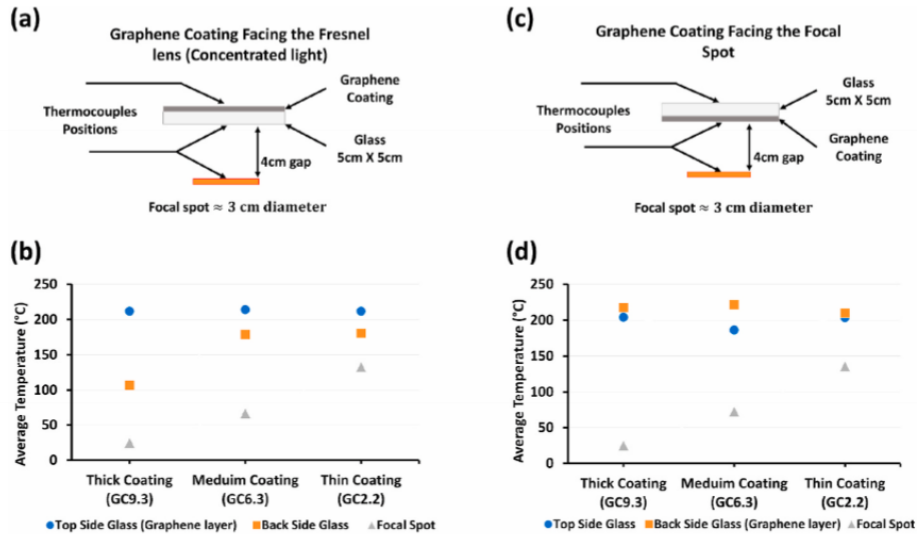


Fig. 6. Thermal investigation for (a) graphene layer facing the Fresnel lens and (c) graphene layer facing the focal spot. The average temperature at the centre for the top side of the glass, the back side of the glass, and the focal spot for (b) graphene layer facing the focal spot and (d) graphene layer facing the focal spot.

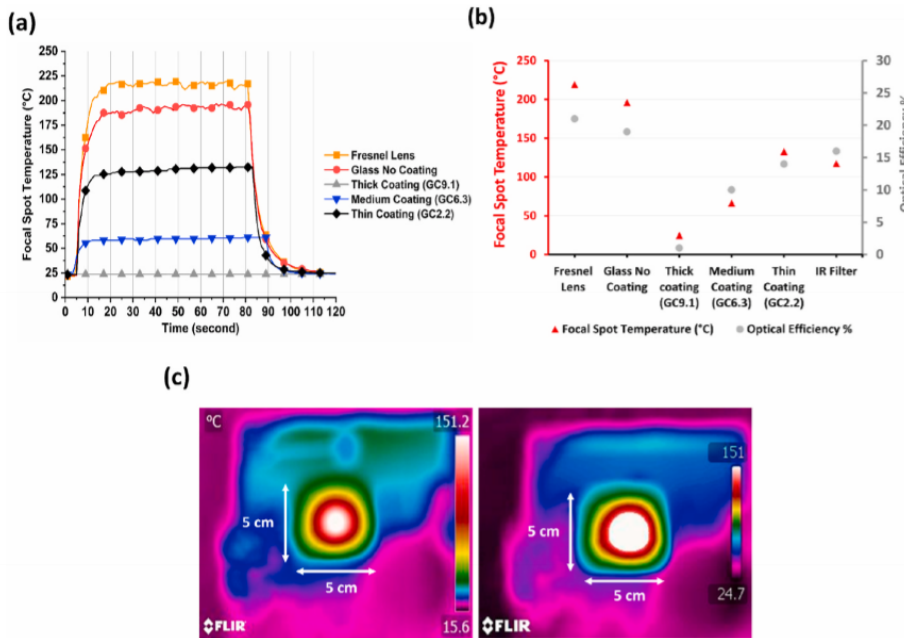


Fig. 7. (a) The focal spot temperature (thermocouple measurement) over time produced by the Fresnel lens and with glass, with GC_{9.1}, with GC_{6.3}, and with GC_{2.2}, respectively. (b) the correlation between the focal spot temperature (thermocouple measurement) and the optical efficiency for the Fresnel lens and with glass, with GC_{9.1}, with GC_{6.3}, and with GC_{2.2}, respectively. (c) the thermal camera image for the GC_{6.3} to show the thermal distribution across the 5 cm × 5 cm area based graphene layer (the temperature scale was set at 151 °C).

source additional resistive losses in the solar cell beside the losses at its standard design conditions at 1sun where the influence of the resistive loss can be detected by observing the FF (flattening in the squareness shape of the I–V characteristic curve). The impact of series resistance is producing a decrease in the FF and thereby drop in cell efficiency.

Metallization acts an essential role in both optical and electrical performance of the polycrystalline Si solar cell. Optically, where the width of the gridlines associates to shading impacting the I_{sc} . Electrically, through the series resistance of metal conductors impacting the FF. The effect of resistance on polycrystalline Si solar cell is reflected through wasting power in the resistance components. Considering one diode (solar cell) model, the impact of resistance on polycrystalline Si solar cell under no concentration is significant as the temperature increase, and therefore resistance effect exaggerates under a concentration ratio due to the imbalance of the current production to the solar cell area. The utmost common resistances in one diode model is series resistance (R_s) and shunt resistance (R_{sh}). The R_s losses rise substantially

due to having a current flow beyond the capacity of the electrical connectors on the solar cell surface area. The R_s is impacted by factors such as semiconductor material resistivity (emitter) and metal conductors (Busbar and fingers). In contrast, the R_{sh} is mainly affected by the

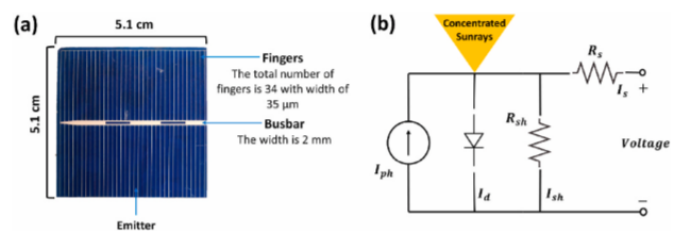


Fig. 8. Illustration of (a) dimensions and series resistance factors and (b) electrical circuit of a solar cell with one diode model, where I_{ph} is the photo-generated current, I_d is the diode current, and I_{sh} is the shunt current [59].

impurities adjacent the p-n junction, as in Fig. 8a and b.

The indoor electrical characterization examines the effectiveness of the graphene ND filter with the high series resistance $5.1 \text{ cm} \times 5.1 \text{ cm}$ polycrystalline Si solar cell (300–1300 nm). To observe the fluctuation in performance for comparison and analysis, the electrical components such as I_{sc} , V_{oc} , and FF are measured on the polycrystalline Si solar cell under only the Fresnel lens and after with glass, with $GC_{9.1}$, with $GC_{6.3}$, with $GC_{2.2}$, and with IR filter. Many cells were soldered and prepared for the testing because the polycrystalline Si solar cell is easily cracked under the concentrated solar irradiance due to its low thermal expansion (fragility). The IR filter itself was not enough to avoid the breakage of the polycrystalline Si solar cell. Thus, the IR filter was associated with a cooling mount base set at 25°C to operate the solar cell in a safe condition and also bring the IR filter to the competition with the GCs for comparison.

Although determining the J_{sc} through the EQE is advantageous being independent for the used light source spectral figure, the J_{sc} was carried out also through the I–V curve measurements by illuminating the polycrystalline Si solar cell with solar irradiance of 1000 W/m^2 (no concentration) and found to be 37.82 mA/cm^2 , as shown in Fig. S2, SI. The minimal discrepancy of 1.2% between the EQE calculation and I–V curve measurement is might be due to either the contact area of the cell being undetermined or the inaccuracy of the simulated solar irradiance.

In Fig. 9a, I–V curve shows the dependence of I_{sc} on the illumination and V_{oc} on the temperature where the attenuation of the solar intensity has shown the highest and lowest I_{sc} for the polycrystalline Si solar cell under the Fresnel and $GC_{9.1}$ to be 7510 mA and 255 mA , respectively. On the other hand, the uppermost and the lowest V_{oc} is for $GC_{6.3}$ and $GC_{9.1}$ to be 631 mV and 588.2 mV , respectively. The least I_{sc} and V_{oc} for the $GC_{9.1}$ is due to the excessive blockage of light. The apical I_{sc} value for only under the Fresnel is because the optical efficiency of 90%, where the apical V_{oc} value for the $GC_{6.3}$ relies on the accomplished focal spot temperature in comparison to other test scenarios, as in Fig. 9d. Both $GC_{6.3}$ and the IR filter with a cooling mount base has a lower I_{sc} than the $GC_{2.2}$ by 31% and 58% respectively. However, both $GC_{6.3}$ and the IR filter with a cooling mount base has a higher V_{oc} than $GC_{2.2}$ by 2.4% and

0.62%, respectively. Fig. 9b shows the highest maximum power for under the Fresnel (1.5 W), and a similar maximum power of 1.49 W for both the glass no coating and $GC_{2.2}$ where glass no coating has a higher I_{sc} than the $GC_{2.2}$ and $GC_{2.2}$ has a higher V_{oc} than glass no coating by 8.8%, respectively. Then after, $GC_{6.3}$ and IR filter with a cooling mount base come with a drop in the maximum power by 11% and 32% in comparison to $GC_{2.2}$, respectively. In case of $GC_{9.1}$, the maximum power is recorded about 0.11 W.

In addition, FF has to be investigated with both the optical efficiency and focal spot temperature because the high intensity of the current flowing via the solar cell causes a resistive loss where its primary influence can be observed through the FF. In Fig. 9c and d, the FF has an inverse correlation with the optical density of graphene and the focal spot temperature. The most influenced FF is the one for the Fresnel lens due to the highest optical efficiency and hence the focal spot temperature. It has been observed that the medium coating exhibited the optimum FF value of 0.446 as a result of the lowest series-resistance reflected on a relatively less flattening of the solar cell output characteristic with an optical efficiency of 10%, as highlighted in the box in Fig. 9c and d. The observation of the FF is needed to be considered in the consecutive section to find solar cell efficiency.

Table 2 summarizes the results for the four different characterization approaches. The results confirmed that graphene is an appropriate material for natural density filter with optimum performance for the $GC_{6.3}$ as highlighted. Although the IR filter with a cooling mount base showed the lowest focal spot temperature of 55°C and relatively similar FF value with $GC_{6.3}$; however, that is at the price of system weight, cost, and parasitic load. For the case of the IR filter associated with the cooling mount base, the focal spot temperature is given via considering the equilibrium temperature of 25°C for the cooling mount base and a 117.28°C for the focal spot temperature after the IR filter, which results in a focal spot temperature of 55°C . Also, the IR filter has shown a lower power output in comparison to $GC_{6.3}$ because $GC_{6.3}$ attenuates the intensity of solar irradiance across the wavelength range where the IR filter blocks all wavelengths beyond visible light with less control on the focal spot temperature. The optimization for the graphene thickness coating still has the potential to improve the overall performance

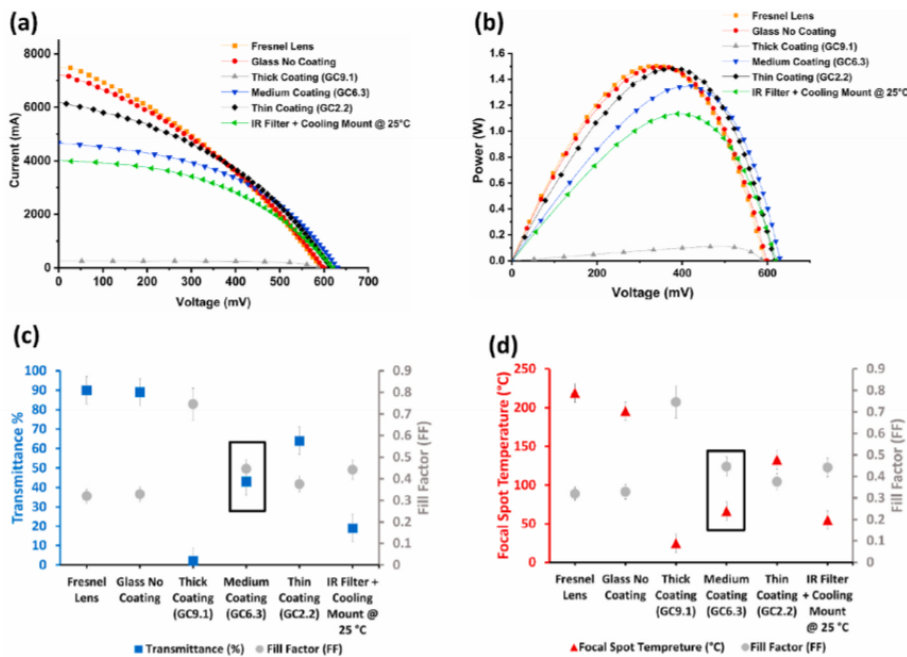


Fig. 9. (a) I–V curve and (b) power curve for polycrystalline Si solar cell, with glass, with adding different coating thickness, and with IR filter, respectively. (c) the inverse correlation between fill factor as a component of power quality and transmittance with a highlight box for the optimum performance ($GC_{6.3}$). (d) the inverse correlation between fill factor as a component of power quality and focal spot temperature with a highlight box for the optimum performance ($GC_{6.3}$).

Table 2
The summary for the characterization results for Graphene neutral density (ND) filter.

| Graphene Neutral density (ND) filter | Chemical Characterization | Optical Characterization | | | | Thermal Characterization | Electrical Characterization | |
|--------------------------------------|---------------------------|--------------------------|-------|------------------------|------------------------------------|-----------------------------|-----------------------------|------------------|
| | Graphene thickness (μm) | Total transmittance (%T) | OD | Optical Efficiency (%) | Optical Concentration ratio (suns) | Focal Spot Temperature (°C) | Power output (W) | Fill Factor (FF) |
| Fresnel Lens | – | 90 | 0.045 | 90 | 18 | 219 | 1.5 | 0.32 |
| IR filter + cooling Mount @ 25 °C | – | 19 | 0.72 | 18 | 4 | 55 | 1.13 | 0.442 |
| Glass No Coating | – | 89 | 0.05 | 80 | 16 | 196 | 1.49 | 0.329 |
| Thick Coating (GC _{9,1}) | 9.1 ± 0.05 | 2 | 1.69 | 2 | 1 | 24.6 | 0.11 | 0.746 |
| Medium Coating (GC _{6,3}) | 6.3 ± 0.1 | 43 | 0.36 | 42 | 8 | 66.4 | 1.34 | 0.446 |
| Thin Coating (GC _{2,2}) | 2.2 ± 0.2 | 64 | 0.19 | 58 | 12 | 132.7 | 1.49 | 0.376 |

further.

4. Graphene layer validation and cost analysis

To validate that the improvement in power output is predominantly due to the graphene layer, we have attenuated the solar simulator (WACOM) lamp intensity (helicon value) to examine the polycrystalline silicon (Si) solar cells at different solar irradiance value in the range of 1000–400 W/m² in an interval of 100 W/m² without GCs. This attenuation of input solar irradiance to the concentrator optic (Fresnel lens) results in a lower concentration ratio in the focal spot area which could be the reason for increasing the fill factor and hence the cell efficiency without GCs. Fig. 10a shows the downward slope of the cell efficiency from 5.96% to 2.44% with increasing the effective solar irradiance on the focal spot area for solar irradiance from 400 W/m² to 1000 W/m²

corresponding for optical concentration ratio range from 7 suns to 18 suns. The GC_{6,3} and GC_{2,2} show a cell efficiency of 6.57% at 8 suns and 4.91% at 13 suns with effective solar irradiance on the focal spot at 1000 W/m², respectively. The relatively low cell efficiency to the maximum cell efficiency of 17% [60] as reported by the manufacturer is simply due to using the single-junction solar cell beyond its design concentration range (1 sun). Still, this utilization was important to see the temperature and concentration ratio reduction effects. The closest optical concentration ratio for the GC_{6,3} at 8 suns is the base case at 400 W/m² with an optical concentration ratio of 7 suns but with less efficiency by 12%, where the closest optical concentration ratio for the GC_{2,2} is the base case at 700 W/m² with an optical concentration ratio of 12.8 suns but with less efficiency by 28%. This comparison has certainly approved that the cell efficiency has been improved due to the integration of graphene as ND filter instead of lowering the concentration ratio. Thus, the same benefits should be in theory, replicable for a multijunction solar cell under ultrahigh concentration ratios. The GC_{6,3} represent the highest cell efficiency. The GC challenges the optical efficiency of the CPV unit with improving cell efficiency in case of both GC_{6,3} and GC_{2,2}. For GC_{9,3}, the drop in the solar cell series-resistance is acquired by the highest drop in temperature resulting in FF of 0.746. However, the power output of GC_{9,3} is constrained as to counterbalance the extreme loss in optical efficiency. The cell efficiency improvements are simply due to the reduction in the high-series resistance polycrystalline Si solar cells caused by the thermo-optic absorption properties of GC.

The utilization of graphene as the ND filter has shown graphene as an excellent thermal filtering material. ND filters are commercially available by coating an absorptive material on low-iron glass, borosilicate glass, or fused silica with different thicknesses and design tolerance from one manufacturer to another to attenuate the light evenly across a spectral band. The simple concept to perform an ND filter is to have a coating thickness of not less than 2 μm, and that was the case of not having GC samples less than 2.2 μm. The ND filters are classified commercially based on their OD. According to the optical characterization, we have collected the cost for ND filters with comparable OD value to the GCs ones in this study from Newport, Edmund optics, and Knight optical. The cost of graphene coating was estimated considering only the low-iron glass and graphene ink, as in equation (4).

$$\begin{aligned}
 \text{Graphene coating} &= \left(\frac{\pounds 15}{\text{ml}} \right) \\
 &\times \left(\frac{3\text{ml}}{\text{Thick Coating}} \text{ or } \frac{2\text{ml}}{\text{Medium coating}} \text{ or } \frac{1\text{ml}}{\text{Thin Coating}} \right) \\
 &+ \frac{\pounds 5}{\text{low iron glass (5cm} \times \text{5cm)}}
 \end{aligned}
 \tag{4}$$

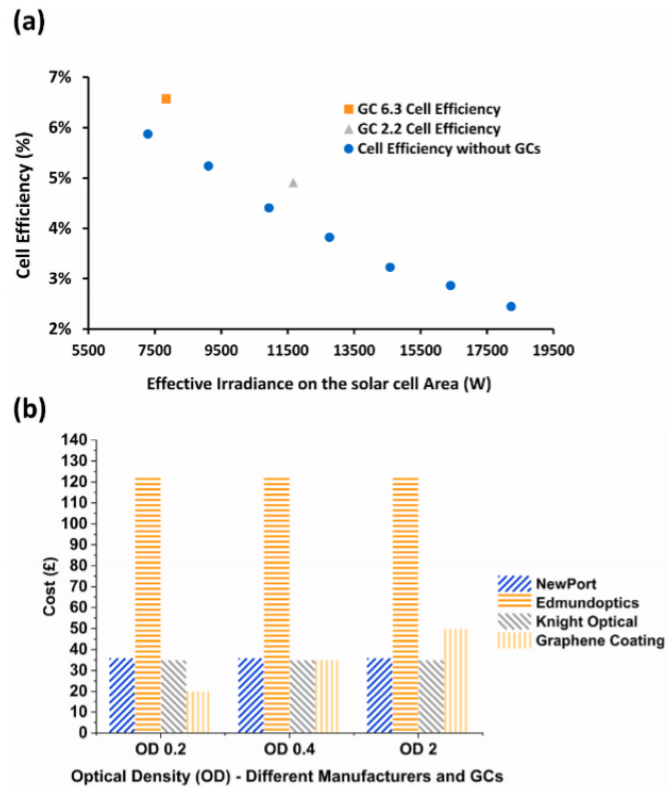


Fig. 10. (a) The cell efficiency verses the effective solar irradiance on the focal spot. (b) the cost of the developed GCs in comparison with the commercially available ND filters (Newport [50], Edmundoptics [51], and Knight optical [52]) for relatively similar optical density (OD).

where the cost of the other manufacturers is not affected by the degree of light transmittance. Indeed, the GCs are economically feasible in comparison with all ND filters manufactured by Edmundoptics and others with $OD \leq 0.4$. In this study, the economic advantage of integrating graphene as the ND filter is to improve the CPV system power output where that occurs at $OD \leq 0.4$. As highlighted previously, the medium coating ($OD 0.36$) is the optimum scenario for power output with still high potential for improvement. This improvement could be achieved by minimizing the amount of graphene by a certain percentage across the glass surface for more power output or by only coating a glass surface area comparable to the focal spot area which will result in a relative drop in the GC cost.

5. Conclusion

We have developed three graphene ND filters to attenuate the concentration of solar rays for a CPV system. To fabricate and characterize the ND filter, four different approaches such as chemical, optical, thermal and electrical characterizations have been adopted for a comprehensive understanding of the filter. All four characterization approaches have confirmed that the performance is dependent on the graphene thickness. The indoor experiment has been conducted for a polycrystalline Si solar cell, which is vulnerable to the observed level of temperature generated by SOG Fresnel lens (a geometrical concentration ratio of ≈ 20 suns). The results have manifested graphene can bring into play as an ND filter component for a pre-illumination passive cooling mechanism. The simplistic employment of GC as an ND filter component can eliminate the traditional and strenuous cooling techniques such as active water cooling and combined heat pipe and sink cooling for CPV. Although the optimization of the GC thickness still has the potential to improve the overall performance further. The future direction of GC technology can pave the way on developing facile cooling methods to maintain the solar cell temperature low and stable for a CPV system.

CRedit authorship contribution statement

Mussad Alzahrani: Writing - original draft, Visualization, Investigation, process. **Anurag Roy:** Critical review, Discussion, Conceptualization. **Katie Shanks:** Investigation, process, discussion. **Senthilarasu Sundaram:** Pre-publication review, Supervision. **Tapas K. Mallick:** Resources, Conceptualization, Supervision.

Declaration of competing interest

The authors declare that they have no known competing financial interests or personal relationships that could have appeared to influence the work reported in this paper.

Acknowledgment

M.A would like to duly acknowledge the financial support from the Saudi Arabia Culture Bureau in the U.K. A.R. and S.S. acknowledges Agri-tech Cornwall and the Isles of Scilly project (award number: 05R16P00366). The funders have no role in study design data collection, or preparation of the manuscript.

Appendix A. Supplementary data

Supplementary data related to this article can be found at <https://doi.org/10.1016/j.solmat.2020.110922>.

References

- [1] M. Berx, R. Saniz, B. Partoens, D. Lamoen, Exceeding the shockley-queisser limit within the detailed balance framework. Many-body Approaches at Different Scales, Springer International Publishing, Cham, 2018, pp. 177–184, https://doi.org/10.1007/978-3-319-72374-7_15.




- [2] National Renewable Energy Laboratory, Best Research-Cell Efficiencies, 2020, <https://www.nrel.gov/pv/cell-efficiency.html>.
- [3] L.C. Herst, N. Ekins-Daukes, Fundamental losses in solar cells, Prog. Photovoltaics Res. Appl. 19 (2010) 286–293, <https://doi.org/10.1002/pip>.
- [4] J.G. Ingersoll, Simplified calculation of solar cell temperatures in terrestrial photovoltaic arrays, Journal of Solar Energy Engineering, Transactions of the ASME. 108 (1986) 95–101, <https://doi.org/10.1115/1.3268087>.
- [5] M.W. Davis, A.H. Fanney, B.P. Dougherty, Prediction of building integrated photovoltaic cell temperatures, Journal of Solar Energy Engineering, Transactions of the ASME. 123 (2001) 200–210, <https://doi.org/10.1115/1.1385825>.
- [6] A.D. Jones, C.P. Underwood, A thermal model for photovoltaic systems, Fuel Energy Abstr. 43 (2002) 199, [https://doi.org/10.1016/S0140-6701\(02\)85831-3](https://doi.org/10.1016/S0140-6701(02)85831-3).
- [7] M. Cui, N. Chen, X. Yang, Y. Wang, Y. Bai, X. Zhang, Thermal analysis and test for single concentrator solar cells, J. Semiconduct. 30 (2009), <https://doi.org/10.1088/1674-4926/30/4/044011>.
- [8] O.Z. Sharaf, M.F. Orhann, Concentrated photovoltaic thermal (CPVT) solar collector systems: Part II - implemented systems, performance assessment, and future directions, Renew. Sustain. Energy Rev. 50 (2015) 1566–1633, <https://doi.org/10.1016/j.rser.2014.07.215>.
- [9] O.Z. Sharaf, M.F. Orhan, Concentrated photovoltaic thermal (CPVT) solar collector systems: Part I - fundamentals, design considerations and current technologies, Renew. Sustain. Energy Rev. 50 (2015) 1500–1565, <https://doi.org/10.1016/j.rser.2015.05.036>.
- [10] P. Dwivedi, K. Sudhakar, A. Soni, E. Solomin, I. Kirpichnikova, Advanced cooling techniques of P.V. modules: a state of art, Case Studies in Thermal Engineering 21 (2020) 100674, <https://doi.org/10.1016/j.csite.2020.100674>.
- [11] A. Roynce, C.J. Dey, D.R. Mills, Cooling of photovoltaic cells under concentrated illumination: a critical review, Sol. Energy Mater. Sol. Cell. 86 (2005) 451–483, <https://doi.org/10.1016/j.solmat.2004.09.003>.
- [12] L. Micheli, N. Sarmah, X. Luo, K.S. Reddy, T.K. Mallick, Opportunities and challenges in micro- and nano-technologies for concentrating photovoltaic cooling: a review, Renew. Sustain. Energy Rev. 20 (2013) 595–610, <https://doi.org/10.1016/j.rser.2012.11.051>.
- [13] L. Micheli, K.S. Reddy, T.K. Mallick, General correlations among geometry, orientation and thermal performance of natural convective micro-finned heat sinks, Int. J. Heat Mass Tran. 91 (2015) 711–724, <https://doi.org/10.1016/j.ijheatmasstransfer.2015.08.015>.
- [14] L. Micheli, N. Sarmah, E.F. Fernandez, K.S. Reddy, T.K. Mallick, Technical issues and challenges in the fabrication of a 144-cell 500× concentrating photovoltaic receiver, 2014 IEEE 40th photovoltaic specialist conference, PVSC 2014 (2014) 2921–2925, <https://doi.org/10.1109/PVSC.2014.6925543>.
- [15] E.M. Abo-Zahhad, S. Ookawara, A. Radwan, A.H. El-Shazly, M.F. Elkady, Numerical analyses of hybrid jet impingement/microchannel cooling device for thermal management of high concentrator triple-junction solar cell, Appl. Energy 253 (2019) 113538, <https://doi.org/10.1016/j.apenergy.2019.113538>.
- [16] E.M. Abo-Zahhad, S. Ookawara, A. Radwan, A.H. El-Shazly, M.F. El-Kady, M.F. C. Esmail, Performance, limits, and thermal stress analysis of high concentrator multijunction solar cell under passive cooling conditions, Appl. Therm. Eng. 164 (2020) 114497, <https://doi.org/10.1016/j.applthermaleng.2019.114497>.
- [17] M. Alzahrani, H. Baig, K. Shanks, T. Mallick, Estimation of the performance limits of a concentrator solar cell coupled with a micro heat sink based on a finite element simulation, Appl. Therm. Eng. (2020) 115315, <https://doi.org/10.1016/j.applthermaleng.2020.115315>.
- [18] A. Aldossary, S. Mahmoud, R. Al-dadah, Technical feasibility study of passive and active cooling for concentrator PV in harsh environment, Appl. Therm. Eng. 100 (2016) 490–500, <https://doi.org/10.1016/j.applthermaleng.2016.02.023>.
- [19] Y.L. He, K. Wang, Y. Qiu, B.C. Du, Q. Liang, S. Du, Review of the solar flux distribution in concentrated solar power: non-uniform features, challenges, and solutions, Appl. Therm. Eng. 149 (2019) 448–474, <https://doi.org/10.1016/j.applthermaleng.2018.12.006>.
- [20] Y.L. He, K. Wang, Y. Qiu, B.C. Du, Q. Liang, S. Du, Review of the Solar Flux Distribution in Concentrated Solar Power: Non-uniform Features, Challenges, and Solutions, Elsevier Ltd, 2019, <https://doi.org/10.1016/j.applthermaleng.2018.12.006>.
- [21] S. Wang, J. Shi, H.H. Chen, S.R. Schafer, M. Munir, G. Stecker, W. Pan, J.J. Lee, C. L. Chen, Cooling design and evaluation for photovoltaic cells within constrained space in a CPV/CSP hybrid solar system, Appl. Therm. Eng. 110 (2017) 369–381, <https://doi.org/10.1016/j.applthermaleng.2016.08.196>.
- [22] M. Renzi, L. Egidi, G. Comodi, Performance analysis of two 3.5 kWp CPV systems under real operating conditions, Appl. Energy 160 (2015) 687–696, <https://doi.org/10.1016/j.apenergy.2015.08.096>.
- [23] A. Mojiri, R. Taylor, E. Thomsen, G. Rosengarten, Spectral beam splitting for efficient conversion of solar energy — a review, Renew. Sustain. Energy Rev. 28 (2013) 654–663, <https://doi.org/10.1016/j.rser.2013.08.026>.
- [24] S.-L. Jiang, P. Hu, S.-P. Mo, Z.-S. Chen, Modeling for two-stage dish concentrating spectral beam splitting photovoltaic/thermal system. 2009 Asia-Pacific Power and Energy Engineering Conference, IEEE, 2009, pp. 1–4, <https://doi.org/10.1109/APPEEC.2009.4918499>.
- [25] X. Ju, C. Xu, X. Han, X. Du, G. Wei, Y. Yang, A review of the concentrated photovoltaic/thermal (CPVT) hybrid solar systems based on the spectral beam splitting technology, Appl. Energy 187 (2017) 534–563, <https://doi.org/10.1016/j.apenergy.2016.11.087>.

- [26] C. Kandilli, Performance analysis of a novel concentrating photovoltaic combined system, *Energy Convers. Manag.* 67 (2013) 186–196, <https://doi.org/10.1016/j.enconman.2012.11.020>.
- [27] A. Kumar, N. Deo, H.L. Yadav, Analysis of design parameters for wavelength selective holographic solar concentrators. Conference Record of the IEEE Photovoltaic Specialists Conference, 2008, pp. 8–11, <https://doi.org/10.1109/PVSC.2008.4922898>.
- [28] W.G.J.H.M. van Sark, Luminescent solar concentrators - a low cost photovoltaics alternative, *Renew. Energy* 49 (2013) 207–210, <https://doi.org/10.1016/j.renene.2012.01.030>.
- [29] D. Mattox, R. Sowell, A survey OF selective solar absorbers and their limitations, *J. Phys.* (1981), <https://doi.org/10.1051/jphyscol:1981102>.
- [30] A. Boubault, C.K. Ho, A. Hall, T.N. Lambert, A. Ambrosini, Durability of solar absorber coatings and their cost-effectiveness, *Sol. Energy Mater. Sol. Cell.* 166 (2017) 176–184, <https://doi.org/10.1016/j.solmat.2017.03.010>.
- [31] K. Xu, M. Du, L. Hao, J. Mi, Q. Yu, S. Li, A review of high-temperature selective absorbing coatings for solar thermal applications, *Journal of Materiomics* 6 (2020) 167–182, <https://doi.org/10.1016/j.jmat.2019.12.012>.
- [32] A. Roy, A. Ghosh, D. Benson, T.K. Mallick, S. Sundaram, Emplacement of screen-printed graphene oxide coating for building thermal comfort discernment, *Sci. Rep.* 10 (2020) 15578, <https://doi.org/10.1038/s41598-020-72670-8>.
- [33] V. Dhinakaran, M. Lavanya, K. Vigneswari, M. Ravichandran, M.D. Vijayakumar, Review on exploration of graphene in diverse applications and its future horizon, *Mater. Today: Proceedings* (2020), <https://doi.org/10.1016/j.matpr.2019.12.369>.
- [34] T.C. Dinadayalane, J. Leszczynski, Remarkable diversity of carbon-carbon bonds: structures and properties of fullerenes, carbon nanotubes, and graphene, *Struct. Chem.* 21 (2010) 1155–1169, <https://doi.org/10.1007/s11224-010-9670-2>.
- [35] M.J. Allen, V.C. Tung, R.B. Kaner, Honeycomb carbon: a review of graphene, *Chem. Rev.* 110 (2010) 132–145, <https://doi.org/10.1021/cr900070d>.
- [36] X. Yu, H. Cheng, M. Zhang, Y. Zhao, L. Qu, G. Shi, Graphene-based smart materials, *Nature Reviews Materials* 2 (2017) 17046, <https://doi.org/10.1038/natrevmats.2017.46>.
- [37] H.S. Ahn, J.M. Kim, T. Kim, S.C. Park, J.M. Kim, Y. Park, D.I. Yu, K.W. Hwang, H. Jo, H.S. Park, H. Kim, M.H. Kim, Enhanced heat transfer is dependent on thickness of graphene films: the heat dissipation during boiling, *Sci. Rep.* 4 (2015) 6276, <https://doi.org/10.1038/step06276>.
- [38] V.-D. Dao, H.-S. Choi, Carbon-based sunlight absorbers in solar-driven steam generation devices, *Global Challenges* 2 (2018) 1700094, <https://doi.org/10.1002/gch2.201700094>.
- [39] M. Gao, L. Zhu, C.K. Peh, G.W. Ho, Solar absorber material and system designs for photothermal water vaporization towards clean water and energy production, *Energy Environ. Sci.* 12 (2019) 841–864, <https://doi.org/10.1039/C8EE01146J>.
- [40] H. Atwater, A. Polman, E. Kosten, D. Callahan, P. Spinelli, C. Eisler, M. Escarra, E. Warmann, C. Flowers, Nanophotonic design principles for ultrahigh efficiency photovoltaics, *AIP Conference Proceedings* 1519 (2013) 17–21, <https://doi.org/10.1063/1.4794700>.
- [41] J.P. Ferrer-Rodríguez, E.F. Fernández, F. Almonacid, P. Pérez-Higuera, Optical design of a 4-off-axis-unit Cassegrain ultra-high concentrator photovoltaics module with a central receiver, *Optic Lett.* 41 (2016) 1985, <https://doi.org/10.1364/ol.41.001985>.
- [42] C. Algora, I. Rey-Stolle, Chapter 2 the interest and potential of ultra-high concentration. *Next Generation of Photovoltaics: New Concept*, Springer Berlin Heidelberg, Berlin, Heidelberg, 2012, <https://doi.org/10.1007/978-3-642-23369-2>.
- [43] K. Shanks, J.P. Ferrer-rodriguez, E.F. Fernández, F. Almonacid, A > 3000 suns high concentrator photovoltaic design based on multiple Fresnel lens primaries focusing to one central solar cell, *Sol. Energy* 169 (2018) 457–467, <https://doi.org/10.1016/j.solener.2018.05.016>.
- [44] M. Data, T. Average, E. Data, Concentrator Triple Junction Solar Cell Cell Type : 3C44C- 3 × 3 Mm2 Azur Space, 2012, pp. 3–6. http://www.azurspace.com/images/products/0004357-00-01_3C44_AzurDesign_3x3.pdf.
- [45] X. Ding, X. Yang, J. Wang, K. Guo, F. Shen, H. Zhou, R. Sun, Z. Ding, J. Gao, Z. Guo, Theoretical analysis and simulation of a tunable mid-infrared filter based on Ge₂Sb₂Te₅ (GST) metasurface, *Superlattice. Microst.* 132 (2019) 106169, <https://doi.org/10.1016/j.spmi.2019.106169>.
- [46] A. Emadi, H. Wu, G. De Graaf, R.F. Wolffenbuttel, IR microspectrometers based on linear-variable optical filters, *Procedia Engineering* 25 (2011) 1401–1404, <https://doi.org/10.1016/j.proeng.2011.12.346>.
- [47] K. Xu, M. Du, L. Hao, J. Mi, Q. Yu, S. Li, A review of high-temperature selective absorbing coatings for solar thermal applications, *Journal of Materiomics* 6 (2020) 167–182, <https://doi.org/10.1016/j.jmat.2019.12.012>.
- [48] W. Li, Y. Shi, K. Chen, L. Zhu, S. Fan, A comprehensive photonic approach for solar cell cooling, *ACS Photonics* 4 (2017) 774–782, <https://doi.org/10.1021/acsp Photonics.7b00089>.
- [49] G.K. Dalapati, S. Masudy-Panah, S.T. Chua, M. Sharma, T.I. Wong, H.R. Tan, D. Chi, Color tunable low cost transparent heat reflector using copper and titanium oxide for energy saving application, *Sci. Rep.* 6 (2016) 1–14, <https://doi.org/10.1038/srep20182>.
- [50] Newport Corporation, Neutral Density Filter Selection Guide, n.d. <https://www.newport.com/g/neutral-density-filter-selection-guide> (accessed March 1, 2020)
- [51] EO Edmund Optics Worldwide, Neutral Density (ND) Filters, n.d. <https://www.edmundoptics.com/c/neutral-density-filters/619/#> (accessed March 1, 2020)
- [52] Ko Knight Optical, Metallic Neutral Density Filters, n.d. <https://www.knightoptical.com/stock/optical-components/uvvisnir-optics/filters/neutral-density-filters/metallic-neutral-density-filters/> (accessed March 1, 2020)
- [53] H.A. Kazem, M.T. Chaichan, The impact of using solar colored filters to cover the PV panel in its outcomes, *Scholars Bulletin* 2 (2016) 464–469, <https://doi.org/10.21276/sb.2016.2.7.5>.
- [54] B. Ramkiran, C.K. Sundarabalan, K. Sudhakar, Performance evaluation of solar PV module with filters in an outdoor environment, *Case Studies in Thermal Engineering* 21 (2020) 100700, <https://doi.org/10.1016/j.csite.2020.100700>.
- [55] L. Barutia, C. Algora, I. Rey-Stolle, OPTIMIZATION PATHWAYS TO IMPROVE GaInP/GaInAs/Ge TRIPLE JUNCTION SOLAR CELLS FOR CPV APPLICATIONS, *Universidad Politécnica de Madrid*, 2017.
- [56] L. Barrutia, I. Lombardero, M. Ochoa, M. Gabás, I. García, T. Palacios, A. Johnson, I. Rey-Stolle, C. Algora, On the use of graphene to improve the performance of concentrator III-V multijunction solar cells, *Prog. Photovoltaics Res. Appl.* 28 (2020) 60–70, <https://doi.org/10.1002/ppp.3207>.
- [57] I. Rey-Stolle, L. Barrutia, I. García, C. Algora, Assessment of the energy yield gain in high CPV systems using graphene-enhanced III-V multijunction solar cells, *AIP Conference Proceedings* 2149 (2019), <https://doi.org/10.1063/1.5124173>.
- [58] K. Shanks, S. Senthilarasu, T.K. Mallick, Optics for concentrating photovoltaics: trends, limits and opportunities for materials and design, *Renew. Sustain. Energy Rev.* 60 (2016) 394–407, <https://doi.org/10.1016/j.rser.2016.01.089>.
- [59] H. Baig, N. Sellami, D. Chemisana, J. Rosell, T.K. Mallick, Performance analysis of a dielectric based 3D building integrated concentrating photovoltaic system, *Sol. Energy* 103 (2014) 525–540, <https://doi.org/10.1016/j.solener.2014.03.002>.
- [60] A. Ahmed, M. Alzahrani, K. Shanks, S. Sundaram, T.K. Mallick, Effect of using an infrared filter on the performance of a silicon solar cell for an ultra-high concentrator photovoltaic system, *Mater. Lett.* 277 (2020) 128332, <https://doi.org/10.1016/j.matlet.2020.128332>.

Article 5. M. Alzahrani, A. Roy, S. Sundaram, T. Mallick, "Investigation of Thermal Stress Arising in a Graphene Neutral Density Filter for Concentrated Photovoltaic System." ENERGIES 2021, 14 (12), 3515, [org/10.3390/en14123515](https://doi.org/10.3390/en14123515).

Article

Investigation of Thermal Stress Arising in a Graphene Neutral Density Filter for Concentrated Photovoltaic System

Mussad M. Alzahrani ^{1,2}, Anurag Roy ¹ , Senthilarasu Sundaram ¹  and Tapas K. Mallick ^{1,*} 

¹ Environmental and Sustainability Institute, Penryn Campus, University of Exeter, Cornwall TR10 9FE, UK; ma778@exeter.ac.uk (M.M.A.); a.roy30@exeter.ac.uk (A.R.); s.sundaram@exeter.ac.uk (S.S.)

² Mechanical and Energy Engineering Department, Imam Abdulrahman Bin Faisal University, Dammam 34212, Saudi Arabia

* Correspondence: t.k.mallick@exeter.ac.uk; Tel.: +44-01326-259465

Abstract: As an excellent heat spreader candidate, graphene attracts considerable interest concerning its application in concentrated photovoltaic (CPV) systems. The consequences of employing a graphene-coated neutral density (GCND) filter to mitigate concentrated light impact adequately. Hence, the temperature for a concentrated photovoltaic system is reported in this work. A systematic thermal characterisation study was carried out using three different thickness-based GCND filters. Interestingly, using the GCND filter, the focal spot temperature remained considerably lower than that of the incident temperature for a more extended period. The graphene coating orientation further influenced the temperature gradient behaviour of the focal spot and incident temperature. The thermal and electrical results depended on the GC samples' thickness and emplacement, leading to dramatic differences in their respective photovoltaic performance. As a base substrate of the GCND filter, the low-iron glass suffered extreme thermal stress under concentrated solar irradiance. This thermal stress phenomenon on the GCND filter was further analysed. This study suggests that using GCND leads to lower temperature maintenance of the CPV focal point, which minimises the PV cell thermal stress. However, the GCND filter also experienced considerable thermal stress during the CPV experiment.

Keywords: graphene coating; low-iron glass; CPV; cracking; focal spot



Citation: Alzahrani, M.M.; Roy, A.; Sundaram, S.; Mallick, T.K. Investigation of Thermal Stress Arising in a Graphene Neutral Density Filter for Concentrated Photovoltaic System. *Energies* **2021**, *14*, 3515. <https://doi.org/10.3390/en14123515>

Academic Editor: Gregorio García

Received: 29 April 2021

Accepted: 10 June 2021

Published: 13 June 2021

Publisher's Note: MDPI stays neutral with regard to jurisdictional claims in published maps and institutional affiliations.



Copyright: © 2021 by the authors. Licensee MDPI, Basel, Switzerland. This article is an open access article distributed under the terms and conditions of the Creative Commons Attribution (CC BY) license (<https://creativecommons.org/licenses/by/4.0/>).

1. Introduction

Concentrated photovoltaic (CPV) systems are designed to increase the sun concentration ratio for an ample electrical power output but require an adequate cooling mechanism [1,2]. Besides that, the involvement of expensive multi-junction solar cells (MJSCs) is necessary to limit the elevated operating temperature to 80 °C and allow higher power generation, resulting in diminishing the MJSC cost to the overall system cost [1]. However, the MJSC cannot sustain a temperature of 110 °C without one form of pre-cooling or post-cooling mechanisms [3]. Another approach to mitigate the thermal impact is through graphene coating for the front-grid metallisation of the MJSC. Although applying a graphene layer absorbs light, resulting in a reduction in the short circuit current, graphene's excellent electrical conductivity enhances the fill factor (FF) and hence the power output [4]. Indeed, the impact of temperature on the cost-effective single-junction solar cell is severe since its outdoor typical operating temperature is between 45 and 55 °C [5,6]. A high operating temperature due to >1 sun of concentration ratio induces thermal stress on the solar cell, resulting in rapid cracking of the solar cell due to the low thermal expansion coefficient of the semiconductors materials and high fragility. Under thermal stress operating conditions, metallisation can be affected by melting the electrical busbars, resulting in diffusing or forming alloys with the semiconductor materials. This impact leads to permanent damage caused by shunting of junction, increasing shunt

resistance [7]. Thus, the melting temperature point for both the soldering and electrical conductors must be higher than the operating temperature [8].

Graphene, as a form of lineament two-dimensional (2D) carbon [9–11] material, has astonished researchers with its superior thermomechanical properties, particularly with thermal conductivity of almost $\sim 5000 \text{ W}\cdot\text{m}^{-1}\text{K}^{-1}$ and a negative thermal expansion coefficient, i.e., the graphene allotrope contracts as the temperature increases [12,13]. These rare properties make graphene an excellent material for nanoelectromechanical systems (NEMS) [4]. Ye et al. [14] fabricated a graphene resonator and examined their electrothermal performance at a high-temperature operation up to 927°C . Considering the stability of graphene with a chemical vapour deposition (CVD) synthesis temperature of regularly less than 900°C , the researchers found that graphene can work at a higher temperature with excellent stability. The thermal stability of graphene is associated with its layers. It was conveyed that graphene's thermal stability strongly correlated with the interlayer interaction in atmospheric conditions. Two or more graphene layers show higher thermal stability than just one. Nan et al. [15] investigated the thermal stability of graphene in atmospheric conditions utilising Raman spectroscopy for two synthesising methods: microchemical cleavage (MC) and chemical vapour deposition. Their study attempted to observe the structural alterations in graphene under high temperature. The two synthesising methods showed that a single graphene layer starts to exhibit defects at a temperature of around 500°C . In contrast, two graphene layers are stable up to 600°C , and graphene remains intact beyond 700°C . It is clear that multiple factors play a positive role in revealing how high temperature is related to thermal stability, such as annealing time, vacuum and monitored atmospheric conditions, and synthesising and characterisation approaches. However, further investigations are still required. Although the inert atmosphere was controlled to test graphene thermal stability with diverse heat treatment temperature, the results showed that a temperature above 800°C would damage the graphene even with a controlled atmosphere and conditions [16]. Other studies investigated replacing the expensive indium–tin–oxide (ITO) with graphene in an optically transparent and flexible metallic electrode. It was identified that graphene is stable with standard test conditions (STC) and high temperature up to 600°C and relative humidity of 100% [17].

Our previous study attempted to improve a CPV module efficiency utilising a single-junction (polycrystalline Si) solar cell by introducing a graphene layer for heat control [18]. The solution incorporated neutral density (ND) filters as a subsequent optical stage to the concentrator to improve thermal performance as a pre-illumination cooling technique. Various samples of filters were characterised chemically, optically, thermally, and electrically. The results showed that graphene as an ND filter is a suitable approach to attenuate the intensity of concentrated solar irradiance as a trade-off with the graphene thickness allowing control over the operating temperature without the need for any cooling mechanism arrangements.

This work presents an extension of our previous report regarding their thermal analysis [18] and a corresponding interpretation on the focal spot and graphene-coated ND (GCND) filter. The impact of graphene orientation, whether normal to the solar cell area or the Fresnel lens area, is discussed, considering its effects on the single-junction (polycrystalline Si) solar cell efficiency. Additionally, defects and suggestions are addressed to enhance the ND filter's durability.

2. Materials and Methodology

The GC was developed by the screen-printing method, and the detailed fabrication process has been mentioned in our earlier work [18]. Therefore, we adopted similar GC samples for this study. GC samples of $2.2 \mu\text{m}$ (thin coating), $6.3 \mu\text{m}$ (medium coating), and $9.1 \mu\text{m}$ (thick coating) were thermally analysed. Hence, the GC samples consisting of different thicknesses are denoted as $\text{GC}_{2.2}$, $\text{GC}_{6.3}$, and $\text{GC}_{9.1}$ μm for thin, medium, and thick coating samples, respectively, throughout the manuscript.

The scanning electron microscopy (SEM) images of the GC samples were analysed on a TESCAN VEGA3 SEM. The prototype chamber temperature profile was measured under $1000 \text{ W}\cdot\text{m}^{-2}$ (1 SUN 1.5 AM) of light from a WACOM AAA + continuous solar simulator (model WXS-210S-20). Temperature recording was performed using the thermocouple meter (Datalogger SDL200-EXTECH INSTRUMENTS). The GC samples were optically characterised to correlate the GC thickness to transmittance using a PerkinElmer LAMBDA 1050 + UV/Vis/NIR spectrophotometer.

A refractive optical concentrator silicon-on-glass (SOG) Fresnel Lens of $23 \text{ cm} \times 23 \text{ cm}$ surface area was used to concentrate solar irradiance, an optical length and focal spot of 42 cm and 2.8 cm, respectively. In addition, a polycrystalline Si solar cell of 26 cm^2 surface area was placed in the focal spot region and shaded by the GC samples to overcome any simultaneous optical and thermal (optothermal) stresses. The used polycrystalline Si solar cell has a manufacturing cell efficiency of 17% [19].

Figure 1a,b represents the scanning electron microscopy (SEM) microstructural cross-sectional and surface images of the GC sample consisting thickness of $6.3 \mu\text{m}$, respectively. The images show that the coating was homogeneous and well distributed throughout the glass surface.

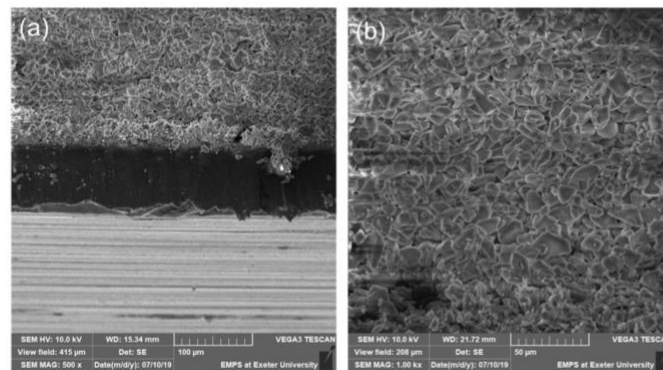


Figure 1. (a) SEM microstructural cross-sectional and (b) corresponding surface image of the developed graphene coating on the ($5 \text{ cm} \times 5 \text{ cm}$) low-iron glass.

3. Results and Discussion

The experimental approach and set-up for this study are the same as reported in our previous work [18]. A further schematic is given in this study to illustrate the overall experimental set-up configuration highlighting the graphene layer orientation. It faces the source of solar irradiance and the solar cell, as in Figure 2a,b, respectively.

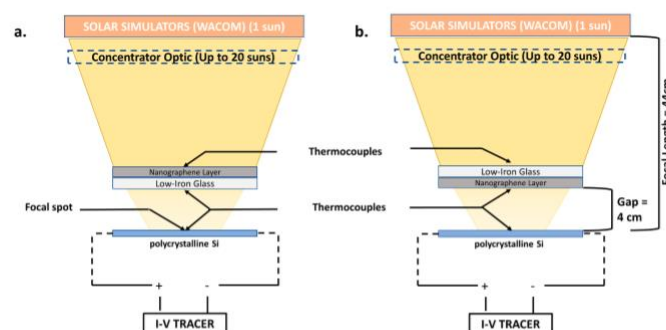


Figure 2. Schematic representation for the entire experimental set-up summarising the experimental approach in which (a) graphene coating (GC) faces the source of the concentrated solar irradiance (Fresnel lens) and (b) GC faces the solar cell.

The temperature was logged for the three developed graphene samples, GC_{9.3}, GC_{6.3}, and GC_{2.2}, and in three various positions to observe the heat-absorbing behaviour of graphene and to identify the level of temperature on the consecutive stages. First, we concentrated the light until the focal spot temperature showed a maintained temperature level within a short period to avoid the thermal stress effect. Then, we switched off the source of solar irradiance. The results showed that the temperature peaked significantly on the graphene surface and glass surface, sustained on the focal spot area. The GC_{9.3} demonstrated that the glass surface temperature was affected by the orientation of the GC surface. The temperature on the GC surface was found to be less than on the surface glass for the GC facing the source of the solar irradiance by 50%, as shown in Figure 3a. In contrast, the temperature on the GC surface was found to be less than the surface glass for the GC facing the solar cell by 7%, as in Figure 3b.

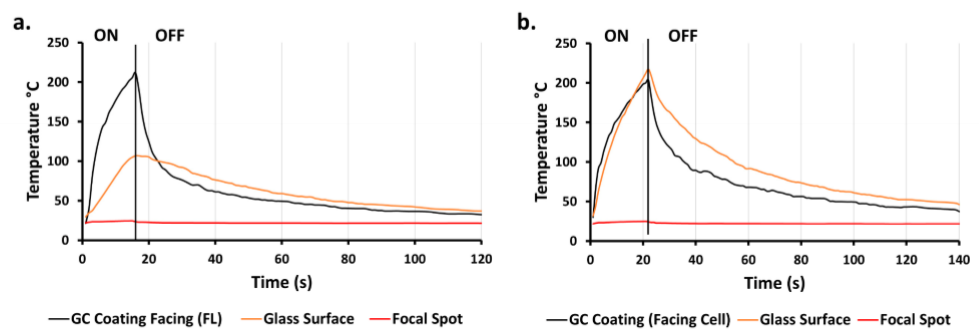


Figure 3. GC_{9.3} sample emplaced towards (a) the source of solar irradiance and (b) polycrystalline cell, respectively.

The GC_{6.3} showed a lower discrepancy in temperature than the GC_{9.3}, which is due to the thickness of graphene. As a result, the temperature on the GC surface was lower than on the surface glass for the GC facing the source of the solar irradiance by 17%, as in Figure 4a. In contrast, the temperature on the GC surface was lower than the surface glass for the GC facing the solar cell by 15%, as in Figure 4b.

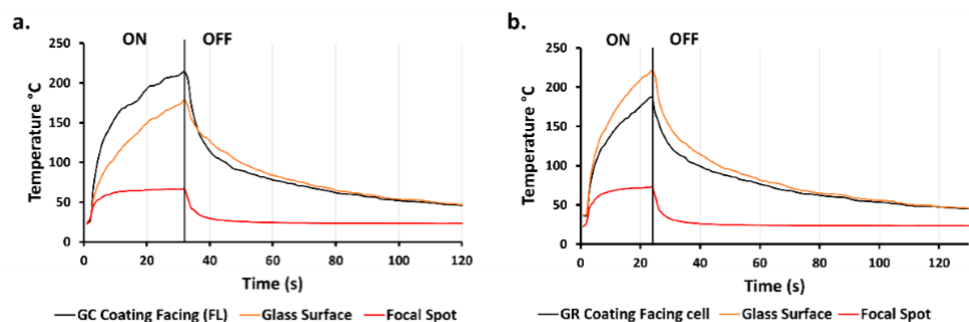


Figure 4. GC_{6.3} sample (a) facing the source of solar irradiance and (b) facing the polycrystalline cell.

The GC_{2.2} demonstrated a relatively low-temperature difference, in contrast to GC_{6.3}. The temperature on the GC surface was higher than the surface glass for the GC facing the source of the solar irradiance by 15%, as in Figure 5a. In contrast, the temperature on the GC surface was lower than the surface glass for the GC facing the solar cell by only 2.2%, as in Figure 5b.

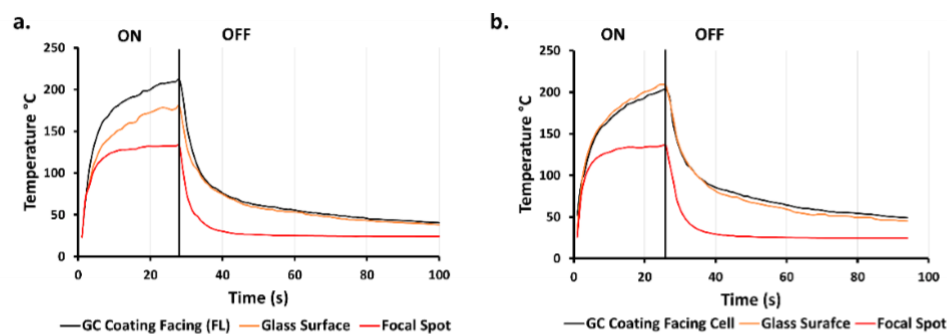


Figure 5. GC_{2.2} sample (a) facing the source of solar irradiance and (b) meeting the polycrystalline cell.

The results showed a lower thermal reduction of the GC facing the solar cell than the GC facing the light source. This is due to the accumulation of heat on GC up to a level after which the GC begins to transfer heat through the medium (air) in the form of radiation. In addition, the small gap between the GC and the focal spot causes the temperature to build up in the focal spot region. This is the reason for less heat reduction of the GC facing the solar cell. This thermal effect contributes to the polycrystalline Si solar cell efficiency.

The graphene showed excellent thermal stability in the focal spot by blocking accumulated heat and concentrated solar irradiance. For a longer time, keeping the light on led to further thermal stability in the focal spot region; however, the graphene-coated surface temperature reached an extreme level. This is discussed in the subsequent section. The GC orientation indicated a minimal temperature gradient across the coated glass sample due to unusual reversible directional thermal behaviour [20]. The GC surface for all samples showed an excellent heat absorption capacity and took a relatively long time to release heat and return to the room temperature status.

Although the single-junction (polycrystalline Si) cell efficiency for samples facing the solar irradiance source was represented in [18], the comparison for the cell efficiency according to the graphene orientation is needed to prove the optimum performance. Figure 6 shows the cell efficiency as a function of the measured solar cell power output to the effective solar irradiance on the solar cell area. The cell efficiency for the GC_{9.3} was the highest. This is because the solar cell was subjected to the lowest concentrated solar irradiance and hence heat, in comparison to the samples, as its transmissivity was only 2%, representing the lowest power output of 0.25 W and 0.18 W for GC facing the source of the solar irradiance and GC facing the solar cell, respectively. The difference in cell efficiency for GC_{9.3} between GC facing the solar irradiance and the GC source facing the solar cell was 26.4%. GC_{6.3} and GC_{2.2} demonstrated 6.6% and 4.9% efficiency for the GC facing the solar irradiance source and 5.9% and 4% for the GC facing the solar cell. The GC orientation, either facing the solar cell or the solar irradiance source, resulted in a solar cell efficiency discrepancy of 11% and 17% for GC_{6.3} and GC_{2.2}.

Many low-iron glass samples were coated with different graphene thicknesses to enable this experiment to observe the thermal performance limitation and potential. Some of those samples were kept under a concentrated light for a longer time, and unfortunately, most of those samples were cracked at a certain point. Figure 7a shows a photograph of the thick coating sample that suffered extreme thermal stress resulting in cracking. Within 30 s, the temperature of the coated surface kept rising, reaching 285.6 °C, which was higher than the temperature of the glass sample with no coatings by 66.6 °C. The temperature consistency is noticeable, considering that the focal spot temperature remained constant at only 23.9 °C, as Figure 7b.

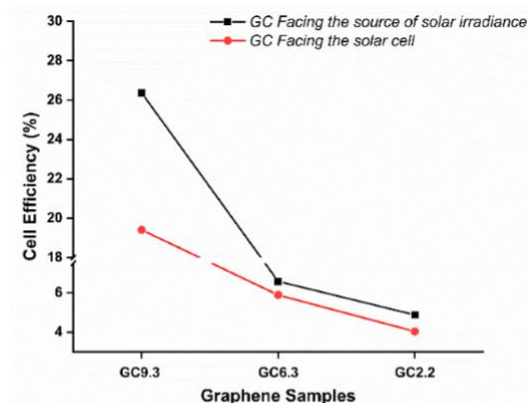


Figure 6. The cell efficiency of single-junction (polycrystalline Si) solar cell for the GC facing the source of solar irradiance and GC_{9,3} facing the solar cell.

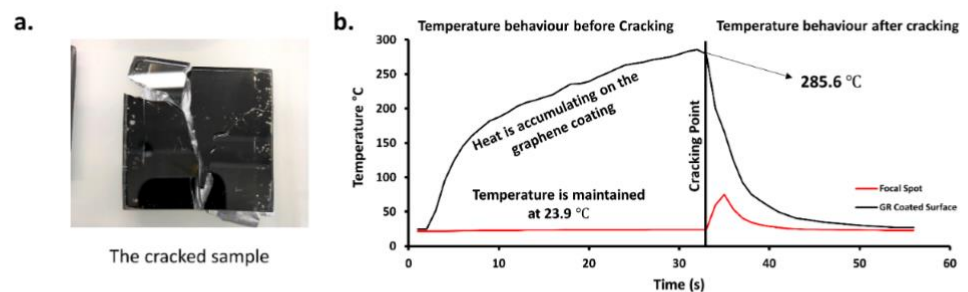


Figure 7. Thick GC sample facing the source of the solar irradiance showing (a) the breakage photograph and (b) the maximum temperature at the cracking point and the temperature behaviour.

Figure 8 shows a medium coating sample. The glass breakage here was significant, and the size of the pieces was small, as in Figure 8a. Within 118 s, the coated surface temperature kept increasing until it reached 338.1 °C, which was higher than the glass sample with no coating, by 119.1 °C. The temperature in the focal spot region remained constant at 50.4 °C, as in Figure 8b.

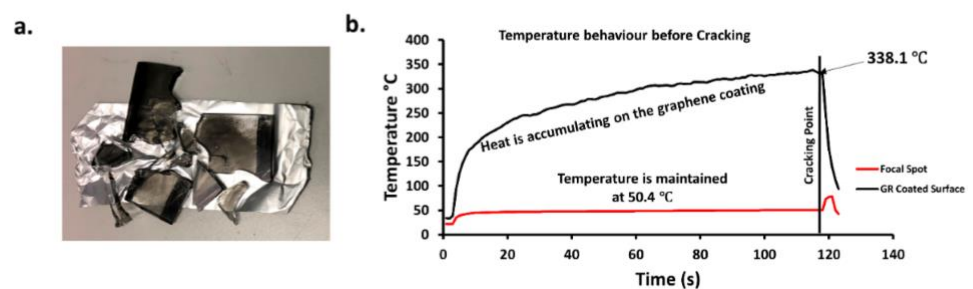


Figure 8. Medium GC sample facing the source of the solar irradiance showing (a) the breakage photograph and (b) the maximum temperature at the cracking point and the temperature behaviour.

Figure 9a shows another medium coating sample facing the solar cell in which others were remained facing the source of solar irradiance. Within 24 s, the temperature of the coated surface increased to reach only 213.7 °C, and this sample broke quicker than expected. The temperature in the focal spot region remained constant at 51.8 °C. The maximum achieved temperature without the GC was 219 °C, and this sample exhibited a low cracking point temperature of about 5.3 °C, as in Figure 9b.

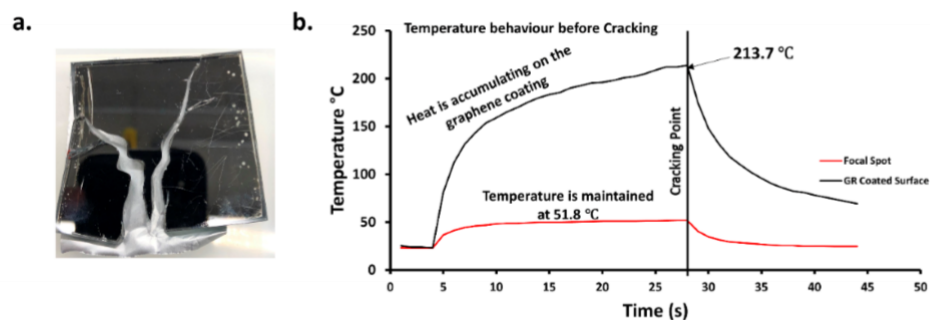


Figure 9. Medium GC sample facing the cell showing (a) the breakage photograph and (b) the maximum temperature at the cracking point and the temperature behaviour.

The low-iron glass's uniform arrangements and lower impurity, in comparison to the standard glass, provide a transmissivity of more than 91.5%, in addition to its cost affordability. However, the low-iron glass is unstable under thermal stress since it is tempered glass. All the tested samples under a long period of concentrated solar irradiance exposure have shown instability in the low-iron glass-cracking pattern, especially when coated with graphene. Low-iron glass is not an ideal candidate for concentrated solar irradiance-high temperature applications as it can only tolerate a constant temperature of up to ≈ 250 °C [21,22]. Still, the low-iron glass is an excellent selection as a safety glass. It mitigates the chances of health and safety issues through fracturing in small pieces below 250 °C. The low-iron glass, classified as tempered glass, is strengthened through thermal or chemical treatment, causing the low-iron glass to shatter into relatively small fragments under high temperature instead of a large, sharp-angle [19] cracking pattern Figure 8. The temperature and accumulated heat on the GC surface caused an extreme thermal shock on the low-iron glass. The graphene's remarkable thermal properties have a significant thermal impact on the glass.

The GC coating significantly reduces the focal spot temperature, which facilitates the polycrystalline Si solar cell performance and avoids thermal stress because of the concentrated light and heat in the focal spot using an optical concentrator. The GC coating absorbs heat proportionally to the GC thickness. This absorption stage collects heat up to a certain point at which severe thermal stress causes breakage for the substrate. Therefore, the optothermal properties of the used substrate (low-iron glass) cannot cope with the optothermal properties of graphene materials. Nevertheless, the vulnerability of the substrate did not hinder the excellent performance of the polycrystalline Si solar cell, where it was found that the cell efficiency increased by about 12% at a concentration ratio of 8 suns, in comparison to the sample with no GC [18]. The GC sample protected the solar cell from cracking and also increased the cell efficiency.

Ceramic glass should be used to avoid a range of glass cracking patterns as it has excellent thermal performance for temperatures up to 983 °C [23]. Ceramic glass is made of polycrystalline transparent material. It does not shatter under high temperatures and can tolerate rapid temperature changes. This type of glass was initially produced to be integrated into the mirror mounts of astronomical telescopes [24], and it is used domestically on cooker hobs. The ceramic glass is also compatible with graphene materials. Both have a strong negative thermal expansion coefficient [13,25], can attain a transparency level comparable to low-iron glass, and have the potential for further improvement [26,27]. Graphene has a superior thermal capacity and thermal conductivity, allowing a higher temperature to accumulate on the glass surface beyond low-iron glass's safe operating temperature limits. Consequently, being a highly thermally conductive material, graphene films can be projected as a viable economic option for efficient heat dissipation materials suitable for mass production.

4. Conclusions

The extended thermal analysis has shown various aspects of the GC and its influences on the temperature gradient of the glass sample and its corresponding electrical output through the cell efficiency. Using low-iron glass as a base for graphene material to form the ND filter is not a durable solution. We have concluded that low-iron glass is not suitable for integrating with the GC through further thermal analysis in this work. This is confirmed through the breakage of glass samples with a more extended time of solar concentration exposure.

Author Contributions: Writing—original draft preparation, visualization, investigation process, M.M.A.; critical review, discussion, conceptualisation, A.R.; pre-publication review, supervision, S.S.; resources, conceptualisation, and supervision, T.K.M. All authors have read and agreed to the published version of the manuscript.

Funding: M.A. would like to duly acknowledge the Saudi Arabia Culture Bureau's financial support in the UK. A.R. and S.S. acknowledge the Agri-Tech Cornwall and the Isles of Scilly project (Award Number: 05R16P00366). The funders have no role in study design, data collection or preparation of the manuscript.

Institutional Review Board Statement: Not applicable.

Informed Consent Statement: Not applicable.

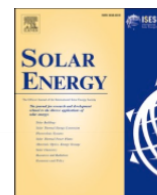
Conflicts of Interest: The authors declare no conflict of interest.

References

- Alzahrani, M.; Shanks, K.; Mallick, T.K. Advances and limitations of increasing solar irradiance for concentrating photovoltaics thermal system. *Renew. Sustain. Energy Rev.* **2021**, *138*, 110517. [[CrossRef](#)]
- Micheli, L.; Sarmah, N.; Luo, X.; Reddy, K.; Mallick, T.K. Opportunities and challenges in micro- and nano-technologies for concentrating photovoltaic cooling: A review. *Renew. Sustain. Energy Rev.* **2013**, *20*, 595–610. [[CrossRef](#)]
- Alzahrani, M.; Baig, H.; Shanks, K.; Mallick, T. Estimation of the performance limits of a concentrator solar cell coupled with a micro heat sink based on a finite element simulation. *Appl. Therm. Eng.* **2020**, *176*, 115315. [[CrossRef](#)]
- Barrutia, L.; Algora, C.; Rey-Stolle, I. *Optimization Pathways to Improve GaInP/GaInAs/Ge Triple Junction Solar Cells for CPV Applications*; Universidad Politécnica de Madrid: Madrid, Spain, 2017.
- Ingersoll, J.G. Simplified Calculation of Solar Cell Temperatures in Terrestrial Photovoltaic Arrays. *J. Sol. Energy Eng.* **1986**, *108*, 95–101. [[CrossRef](#)]
- Davis, M.W.; Fanney, A.H.; Dougherty, B.P. Prediction of Building Integrated Photovoltaic Cell Temperatures. *J. Sol. Energy Eng.* **2001**, *123*, 200–210. [[CrossRef](#)]
- Scheiman, D.A.; Landis, G.A.; Weizer, V.G. High-bandgap solar cells for near-sun missions. In Proceedings of the AIP Conference Proceedings, Pasadena, CA, USA, 12–16 July 1999; AIP: University Park, MA, USA, 1999; pp. 616–620.
- Vaillon, R.; Parola, S.; Lamnatou, C.; Chemisana, D. Solar Cells Operating under Thermal Stress. *Cell Rep. Phys. Sci.* **2020**, *1*, 100267. [[CrossRef](#)]
- Novoselov, K.S.; Geim, A.K.; Morozov, S.V.; Jiang, D.; Zhang, Y.; Dubonos, S.V.; Grigorieva, I.V.; Firsov, A.A. Electric field effect in atomically thin carbon films. *Science* **2004**, *306*, 666–669. [[CrossRef](#)] [[PubMed](#)]
- Zhang, Y.; Tan, Y.-W.; Stormer, H.L.; Kim, P. Experimental observation of the quantum Hall effect and Berry's phase in graphene. *Nature* **2005**, *438*, 201–204. [[CrossRef](#)] [[PubMed](#)]
- Novoselov, K.S.; Geim, A.K.; Morozov, S.V.; Jiang, D.; Katsnelson, M.I.; Grigorieva, I.V.; Dubonos, S.V.; Firsov, A.A. Two-dimensional gas of massless Dirac fermions in graphene. *Nature* **2005**, *438*, 197–200. [[CrossRef](#)] [[PubMed](#)]
- Roy, A.; Ghosh, A.; Benson, D.; Mallick, T.K.; Sundaram, S. Emplacement of screen-printed graphene oxide coating for building thermal comfort discernment. *Sci. Rep.* **2020**, *10*, 1–13. [[CrossRef](#)] [[PubMed](#)]
- Geim, A.K. Graphene: Status and Prospects. *Science* **2009**, *324*, 1530–1534. [[CrossRef](#)] [[PubMed](#)]
- Ye, F.; Lee, J.; Feng, P.X.-L. Electrothermally Tunable Graphene Resonators Operating at Very High Temperature up to 1200 K. *Nano Lett.* **2018**, *18*, 1678–1685. [[CrossRef](#)] [[PubMed](#)]
- Nan, H.Y.; Ni, Z.H.; Wang, J.; Zafar, Z.; Shi, Z.X.; Wang, Y.Y. The thermal stability of graphene in air investigated by Raman spectroscopy. *J. Raman Spectrosc.* **2013**, *44*, 1018–1021. [[CrossRef](#)]
- Liu, F.; Wang, M.; Chen, Y.; Gao, J. Thermal stability of graphene in inert atmosphere at high temperature. *J. Solid State Chem.* **2019**, *276*, 100–103. [[CrossRef](#)]
- Wehenkel, D.J.; Bointon, T.H.; Booth, T.; Bøggild, P.; Craciun, M.F.; Russo, S. Unforeseen high temperature and humidity stability of FeCl₃ intercalated few layer graphene. *Sci. Rep.* **2015**, *5*, 7609. [[CrossRef](#)] [[PubMed](#)]

18. Alzahrani, M.; Roy, A.; Shanks, K.; Sundaram, S.; Mallick, T.K. Graphene as a pre-illumination cooling approach for a concentrator photovoltaic (CPV) system. *Sol. Energy Mater. Sol. Cells* **2021**, *222*, 110922. [CrossRef]
19. Ahmed, A.; Alzahrani, M.; Shanks, K.; Sundaram, S.; Mallick, T.K. Effect of using an infrared filter on the performance of a silicon solar cell for an ultra-high concentrator photovoltaic system. *Mater. Lett.* **2020**, *277*, 128332. [CrossRef]
20. Wang, H.; Hu, S.; Takahashi, K.; Zhang, X.; Takamatsu, H.; Chen, J. Experimental study of thermal rectification in suspended monolayer graphene. *Nat. Commun.* **2017**, *8*, 15843. [CrossRef] [PubMed]
21. One Day Glass. Available online: <https://www.onedayglass.com/types-of-tempered-glass/heat-resistant-glass/> (accessed on 25 February 2021).
22. Shenzhen Ygy Tempered Glass Co., Ltd. Available online: <http://www.dantomchoeur.com/sale-3700446-safety-low-iron-tempered-glass-heat-strengthened-glass-sheets.html> (accessed on 25 February 2021).
23. Chelsea Bussell What's The Difference between Tempered and Ceramic Glass? Available online: <https://www.fireplacedoorsonline.com/whats-the-difference-between-tempered-and-ceramic-glass.html> (accessed on 25 February 2021).
24. El-Meliegy, E.; Noort, R. *Van Glasses and Glass Ceramics for Medical Applications*; Springer: Berlin/Heidelberg, Germany, 2012; Volume 9781461412, ISBN 9781461412281.
25. Hummel, F.A. Thermal Expansion Properties of Some Synthetic Lithia Minerals. *J. Am. Ceram. Soc.* **1951**, *34*, 235–239. [CrossRef]
26. Du Merac, M.R.; Bram, M.; Malzbender, J.; Ziegner, M.; Rasinski, M.; Guillon, O. Increasing Fracture Toughness and Transmittance of Transparent Ceramics using Functional Low-Thermal Expansion Coatings. *Sci. Rep.* **2018**, *8*, 15644. [CrossRef] [PubMed]
27. Transparent Ceramics. Available online: http://www.coorstek.co.jp/eng/rd/detail_04.html#:~:text=Polycrystallineceramicsgenerallyconsistof,glassorsinglecrystalsapphire (accessed on 25 February 2021).

Article 6. M. Alzahrani, A. Ahmed, K. Shanks, S. Sundaram, T. Mallick, "Optical component analysis for ultrahigh concentrated photovoltaic system (UHCPV)." Solar Energy, 227 (2021), [10.1016/j.solener.2021.09.019](https://doi.org/10.1016/j.solener.2021.09.019).



Optical component analysis for ultrahigh concentrated photovoltaic system (UHCPV)

Mussad Alzahrani^{a,b,*}, Asmaa Ahmed^{a,c}, Katie Shanks^a, Senthilarasu Sundaram^a, Tapas Mallick^a

^a Environmental and Sustainability Institute, University of Exeter, Penryn TR10 9FE, UK

^b Mechanical and Energy Engineering Department, Imam Abdulrahman Bin Faisal University, Dammam 34212, Saudi Arabia

^c Mechanical Power Engineering Department, Port Said University, Port Said 42523, Egypt

ARTICLE INFO

Keywords:

Fresnel lens
Multi-junction solar cell
UHCPV
Optical efficiency
Solar concentrator

ABSTRACT

This article investigates the discrepancy between the theoretical and the experimental optical characterisation results of a Fresnel Lens - silicon on glass (SOG), as a primary optical component toward UHCPV of >3000 suns design (Shanks et al., 2018). All the equations were elaborated for single- and multi-junction solar cells, emphasising the performance when the focal spot area is larger or lesser than the solar cell area. This simple prediction approach of optical characterisation has shown a strong agreement between the theoretical and experimental results of the multi-junction solar cell with a discrepancy of 2% at 7.7 W (77 suns) and 6% on the average cross a solar irradiance on the cell from 3.1 W to 7.7 W corresponding to 31 suns – 77 suns in concentration ratio. A theoretical analysis of the optical performance for a 1/4 of the system grouping three optical interfaces is performed to estimate the optical loss and its influence on the optical efficiency and optical concentration ratio.

1. Introduction

The need for solar energy and its application is growing; however, the current solar PV technology is limited by its cost-effectiveness and power density due to space limitations (M. Alzahrani et al., 2021b). There is also a growing concern about the environmental impact of the materials utilised for solar PV (Tawalbeh et al., 2021). To overcome these drawbacks, the concentrated photovoltaic system (CPV) intends to replace the usage of a large number of PV panels with inexpensive optics to intensify sun rays into smaller solar cells. Ultrahigh concentrator photovoltaic (UHCPV) has a high potential to increase the power output and minimise the solar cell size, which lowers the cell cost and upsurges the competitiveness of the CPV system. The ultrahigh concentration ratio is achieved by integrating multiple optics in one system. The succession of optics in the CPV system is designed to concentrate the incoming sun rays where the quality and shape of an optical surface strongly influence the optical losses. To achieve the ultrahigh level, the sunlight divergence should be abated to intensify the solar irradiance within a relatively small acceptance angle, considering the limitation by the angular size of the sun and submits to the law of etendue

conservation. The concentrator optics performance evenly relies on the manufacturing criteria, such as optics thickness and surface smoothness. The ultrahigh CPV system required a super-accurate tracking system to ensure minimal light divergence. The weight of optics and overall system components need to be carefully evaluated and interlinked with the payload design condition of a tracking system to ensure excellent solar monitoring and avoid tracking errors and dynamic load impact. An excellent optical tolerance allows room for relatively small misalignment during the stage of manufacturing and operation (Daneshazarian et al., 2018; Sharaf and Orhan, 2015). There is continually an unavoidable correlation among acceptance angle, optical efficiency and irradiance distribution but options were given to enhance those criteria (Shanks et al., 2016). Optics, such as light funnels and homogenisers, have been applied to relatively uniform the solar irradiance on the receiver area and to enlarge the acceptance angle (Canavarro et al., 2013; Fu et al., 2010; Gordon et al., 2008; Tang and Liu, 2011; Tang and Wang, 2013; Winston et al., 2005). Also, the reflective secondary optical stage has been introduced into the CPV system to enhance the solar flux distribution. However, incorporating those optics within the CPV system can decrease the optical efficiency and hence the concentration ratio due to their optical performance. Out of these, the attention to the elevated

* Corresponding author at: Environmental and Sustainability Institute, University of Exeter, Penryn TR10 9FE, UK.
E-mail address: ma778@exeter.ac.uk (M. Alzahrani).

<https://doi.org/10.1016/j.solener.2021.09.019>

Received 17 January 2021; Received in revised form 31 July 2021; Accepted 7 September 2021

Available online 16 September 2021

0038-092X/© 2021 International Solar Energy Society. Published by Elsevier Ltd. All rights reserved.

| Nomenclature | | | |
|----------------------|-----------------------------------|----------------------|--------------------------------|
| J | Radiant Flux ($\frac{W}{m^2}$). | eff | Effective |
| C | Concentration Ratio (Sun) | Si | Silicon |
| A | Area (m^2) | oc | Open circuit |
| %T | Total transmittance (%) | sc | Short circuit |
| %C | Fractional Loss (%) | exp | Experimental |
| I | Current (mA) | T | Top |
| V | Voltage (mV) | M | Middle |
| <i>Greek Symbols</i> | | <i>Abbreviations</i> | |
| η | Efficiency (%) | UHCPV | Ultra-high concentration ratio |
| <i>Subscript</i> | | CPV | Concentrated photovoltaic |
| g | Geometrical | MJ | Multi-junction |
| th | Theoretical | 1 J | Single – junction |
| Opt | Optical | FF | Fill factor |
| Fresnel | Fresnel lens | UV | Ultraviolet |
| Receiver | Receiver area of the solar cell | SOG | Silicon on Glass |
| | | CCD | charged-coupled device |

temperature on the subsequent optics after the primary optic and the receiver is most considered to avoid any thermo-mechanical stresses as a result of intensified solar irradiance. The solar cells should be maintained below 80 °C to act electrically within its safe operating conditions (Alzahrani et al., 2020). Thus, the optical tolerance in UHCPV required an investigation for all possible alignment uncertainty and losses, and that is unachievable without compromising with optical efficiency, concentration ratio, irradiance distribution, and the solar cell electrical performance.

Based on the concentration factor (sun), the CPV system is classified as either a low concentrated photovoltaic system (LCPV) (suns < 10), as a medium concentrated photovoltaic system (MCPV) (10 < suns < 100), as a high concentrated photovoltaic system (HCPV) (100 < suns < 2000), and as an ultrahigh concentrated photovoltaic system (UHCPV) (suns > 2000) (M. Alzahrani et al., 2021b; Shanks et al., 2016). As moving toward a higher concentration factor, the subsequent optics to the primary optic is exposed to a relatively higher temperature range to reach its maximum concentration and hence temperature on the solar cell.

The process of thermal extrication in a CPV system depends on the concept of either a pre-illumination cooling mechanism based on spectral decomposition or a post-illumination cooling mechanism based on heat transfer fluid (HTF). Post-illumination cooling is a common technique and well developed through either passive or active mechanisms. The active cooling mechanism proved its capability in maintaining the solar cell temperature; however, there is a parasitic load proportional correlation with increasing the concentration ratio where more fluid is needed to be pumped or fanned through the heat dissipation domain. Interestingly, two papers discussed a passive flat-plate heatsink's performance (AlFalah et al., 2020; Valera et al., 2019) and different microscale pin–fin configurations for a concentration ratio of up to 10,000 suns. The last study found that the linking of a microscale pin–fin with a flat-plate heatsink can operate the solar cell safely to 12,000 suns but only with the solar cell size not exceeding $1 \times 1 \text{ mm}^2$. Although the achieved level of concentration ratio is promising, such a cell size will certainly impede the system alignments and tracking accuracy.

The pre-illumination cooling mechanism directs the matchable spectral wavelength band to the solar cell and rejects or redirects the unutilised wavelength band to a thermal receiver. The difficulties in matching the optical properties with either the optical decomposition filter or HTF reflects the less maturation of the pre-illumination cooling mechanisms. The optical filter transmits a selective segment of the optical wavelength while eliminating other wavelength segments through

multiple optical filtering techniques. Recently, one of these optical techniques, termed a “neutral density filter (ND)”, was adopted as a pre-illumination cooling mechanism based on graphene material to attenuate the intensity of the solar irradiance for a CPV system (M. Alzahrani et al., 2021a, 2021c).

Increasing the concentration ratio results in inducing the temperature to a level at which the electrical performance is degraded. The state-of-the-art multi-junction solar cells exhibit a drop in cell efficiency for concentrations above a specific value due to their resistive losses. As a result, cooling arrangements is crucial in CPV system for consistent solar efficiency performance. A future solar cell architecture has been investigated for energy harvesting in the ultrahigh concentration range. Fernández et al. (Suns et al., 2019) developed a Vertical-tunnel-junction (VTJ) solar cell that showed no degradation in cell efficiency of 28.4 % with a concentration ratio of up to 15,000 suns. El-Gahouchi et al. (El-Gahouchi et al., 2020) fabricated duplicated junction solar cell architectures that can produce electrical energy with 33% of cell efficiency at 3,500 suns and 28% of cell efficiency beyond 10,000 suns.

Cassegrain-based and Fresnel-based focal point designs have been developed to reach ultrahigh concentration ratio design with high performance. For Cassegrain-based, Ferrer-rodríguez et al. (Ferrer-Rodríguez et al., 2016) designed an optical configuration of 4-off-axis Cassegrain ultrahigh concentrator photovoltaic module where it has a geometrical concentration ratio of 2304x. For this design, the effective optical efficiency, as the proportion between the power concentrated on the solar cell to the incoming module power, is 73% resulting in an effective optical concentration ratio of 1682 suns. Dreger et al. (Dreger et al., 2014) configured a mini-Cassegrain mirror optics concentrators to achieved a geometrical concentration ratio of 1037x. Still, due to the primary and secondary optics shape deviations, the effective optical efficiency is 77% resulting in the effective concentration ratio of 800 suns. In any case, paraboloid-hyperboloid pairs of optics have high surface roughness, and the polishing for the conical-shaped would alter the curvature and introduce optical inaccuracies in directing and redirecting of sun rays. Thus, for Fresnel-based, Miñano et al. (Miñano et al., 2013) has investigated the Fresnel lens theoretically toward the ultrahigh concentration ratio level. Dome-shaped Fresnel lens has been configured with four entrances into an optical receiver. This design has a geometrical concentration ratio of 2300x. Still, due to imperfection in the reflective and refractive optics and front metalised area on the secondary optics, the optical efficiency is 82% resulting in the optical concentration ratio of 1897suns. The manufacturability of the domed Fresnel lens is difficult and expensive due to the need for a unique

casting mould. Thus, Shanks et al. (Shanks et al., 2018) investigated an ultrahigh Fresnel lenses design based on 4- flat Fresnel Lens (SOG) concentrating into one central receive with the existence of redirecting optical materials has shown a geometrical and optical concentration ratio of 5831x and 4373 suns, respectively. In this design, a flat mirror as a secondary optics were selected instead of conically shaped due to its low surface roughness. Also, the favorability of the flat mirror is due to easy manufacturability and employability of reflective film (~97%) at a relatively low cost.

Fresnel lens is a refractive optical component that converges input solar rays into a focal spot. The focal length is idealised based on the intercept radius by readjusting the Fresnel lens position for its optimum energy output. Fresnel lens is one of the common primary concentrators in concentrator photovoltaic (CPV) system for its cost-effective, lightweight, relatively high acceptance angle and optical efficiency. However, the standard Fresnel lens is limited in concentration ratio to about 1000 suns due to the alteration of its refractive index materials with temperature (chromatic aberration). Thus, achromatic Fresnel doublets show a minimised chromatic aberration, increasing the concentration factor (González Montes et al., 2014; Shanks et al., 2016). Experimentally, a flat achromatic fresnel doublet showed a concentration factor of up to 2000x but is still not commercially available (Languy et al., 2013). Silicon-on-glass (SOG) Fresnel lens is manufactured by applying a thin layer of liquid silicon into a glass. The stamping and curing process is performed to form the Fresnel structure. However, the thin silicon layer leads to strong dependence between the ambient temperature and optical efficiency at which the thermal expansion coefficient of the silicon to glass magnitude is different. Thus, the temperature effect hinders the optical efficiency for the Fresnel lens and the solar cell efficiency due to different focal lengths and focal spot sizes (Hornung et al., 2011).

Optical characterisation of a Fresnel lens was found in the literature, mostly analysing the irradiance distribution of the focal spot for energy and optical efficiency with demanding approaches. Chemisana et al. (Chemisana et al., 2011) established an experimental practice on the performance of the Lambertian source (opal diffuser) is conducted to optically characterised Fresnel lenses. This practice relies on CCD Camera to capture the concentrated solar irradiance profile over the opal diffuser. Optical characteristics components such as optical efficiency and concentration ratio in the concentrated area on the receiver have been acquired for linear- and point-focus Fresnel lens.

Sansoni et al. (Sansoni et al., 2007) examined different patterns of the prismatic lens with different materials on the basis of the optical project. This adopted approach aims to prove the resemblance between the collector's theoretical design and the prismatic lens's performance. To do so, four different mask shapes, a collimator mirror, and concentrator mirror, photodetector, and integrated sphere are needed to attain optical characteristics through testing for the total collection efficiency, for the energy distribution evaluation, and the uniformity estimation.

Martinez Antón et al. (Martínez Antón et al., 2011) conducted another method to characterise the Fresnel lens flux transfer performance. This method depends on suiting the camera's entrance focus at the focal spot at which the camera image gives detailed performance maps of the variety of Fresnel lenses for different acceptance angles. The captured maps allow an estimation of the overall optical efficiency and demonstrate the error and defects of the refractive concentrator. This characterisation method is challenged by increasing the working area of the Fresnel lens, where the flux performance deteriorates significantly.

Victoria et al. (Victoria et al., 2016) showed a characterisation method anticipated by the IES-UPM to measure the optical efficiency and irradiance distribution generated by silicon-on-glass (SOG) and PMMA Fresnel lens. This method required a solar cell of a large area (for optical efficiency measurements) and a CCD camera with a low- or high-pass filter plus a diffuser (for irradiance distribution and focal spot size). A top and middle subcells were used for the optical efficiency measurements at which the short-circuit current (I_{sc}) is determined for each subcell of the multi-junction solar cell.

Further, Wang et al. (Wang et al., 2018) studied the optical performance of a Fresnel lens based on the polar-axis tracking system. The results show that the maximum optical efficiency loss experimentally is 1.87%. The maximum possible tracking error is 1° , where 1.5° of tracking error results in an optical efficiency loss of 17.42%. Wiesenfarth et al. (Wiesenfarth et al., 2014) considered the influence of the solar spectrum and the solar cell spectral response in optical characterisation but not for an ultrahigh concentration ratio and similar size Fresnel lens.

In this study, we show that simple measurements and geometrical calculations can be used to give a close prediction of the optical efficiency and concentration ratio instead of using complicated and time-consuming ray trace analysis. To experimentally measure the optical products (optical efficiency and concentration ratio), a single-junction solar cell of $10 \times 10 \text{mm}^2$ and $5.1 \times 5.1 \text{cm}^2$ and a multi-junction solar cell of $10 \times 10 \text{mm}^2$ are examined to compare with the theoretical analysis taking into consideration the geometrical calculations for the discrepancy determinations. This is an advantageous way to characterise the primary optic performance and move onto the more challenging secondary and tertiary optic characterisations for ultrahigh concentration. Hence, outlines for the equations' details of the theoretical optical efficiency and concentration ratio and of the effective optical efficiency and concentration ratio with the fractional concentration loss and its influence on the optical characterisation are explicitly illustrated. In addition, a full theoretical analysis of the UHCPV system is considered for different receiver sizes, dissimilar coatings materials on the reflective mirrors-secondary optic stage, and the tertiary optic.

2. Primary optic assessment/analysis – Fresnel lens

2.1. Theoretical optical characterisation

Two single junctions Polycrystalline silicon solar cell; one of $10 \times 10 \text{mm}^2$ surface area and the another of $5.1 \times 5.1 \text{cm}^2$ surface area, manufactured by SUNYIMA and one $10 \times 10 \text{mm}^2$ multi-junction solar cell with base material of GaInP/GaInAs/Ge on Ge substrates manufactured by AzurSpace (Azur Space Solar Power GmbH, 2014) are electrically investigated with and without a Fresnel lens as a refractive optical concentrator whilst maintaining the temperature of the back surface with a cooling mount base. The solar simulator manufactured by WACOM [Model no. WXS-210S-20] incorporates Xenon short-arc lamp and UV filter and AM 1.5G filter to emulate a solar irradiance approximating AM 1.5G (Wacom Electric Ltd, 2021). This solar simulator is rated as class AAA and has a spatial non-uniformity of solar irradiance within $\pm 2\%$. The used solar simulator coincides significantly with the AM 1.5G solar spectrum at 1000W/m^2 , as in Fig. 1. We have tested the cells under AM 1.5G spectrum with a beam divergence of 1.43° , which is not the standard test condition for the multi-junction solar cells, but this helps indicates the worst-case scenario values for the system before moving for outdoor testing.

The External Quantum efficiency (EQE) (%) was measured for the multi-junction solar cells and the polycrystalline Si solar cells to define the number of electrons out per incident photon. EQE was calculated for a wavelength compatible with the cells using Bentham PVE300 PV characterisation setup under standard AM 1.5 solar spectrum, as in Fig. 2.

Silicon on glass (SOG) Fresnel lens of aperture area of 529cm^2 ($23 \text{cm} \times 23 \text{cm}$) manufactured by ORAFOL based on untempered low-iron float glass has been introduced under the solar simulator and adjusted in height for the optimum focal spot and length where the highest concentration ratio is achieved. The irradiance output from a Fresnel lens is typically Gaussian distribution in contour (Jing et al., 2012). However, this Fresnel lens has an excellent relatively uniformed output over at least 1 cm in the centre. The solar cells have been placed within the focal spot and aligned for maximum electrical generation. However, within the focal spot, temperature raises significantly due to

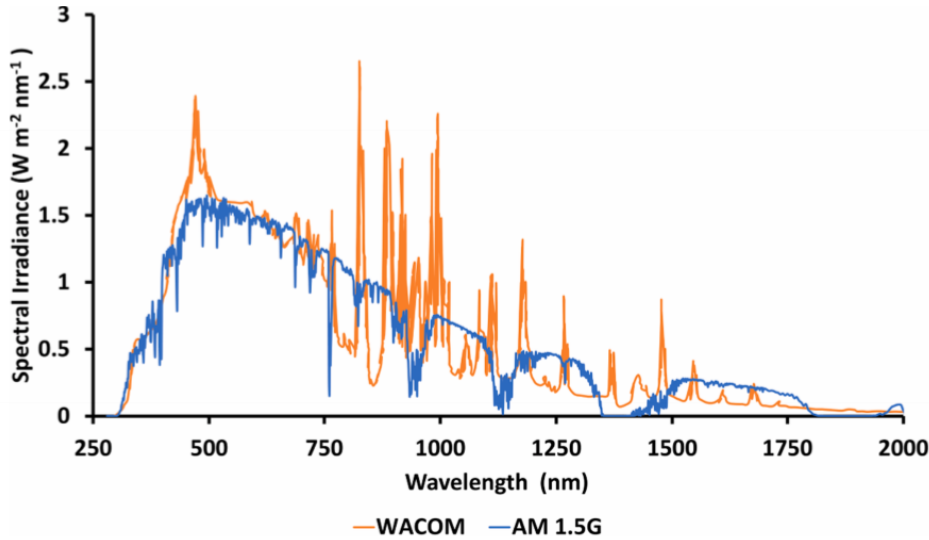


Fig. 1. The solar spectrum profile for the used WACOM solar simulator with AM 1.5G.

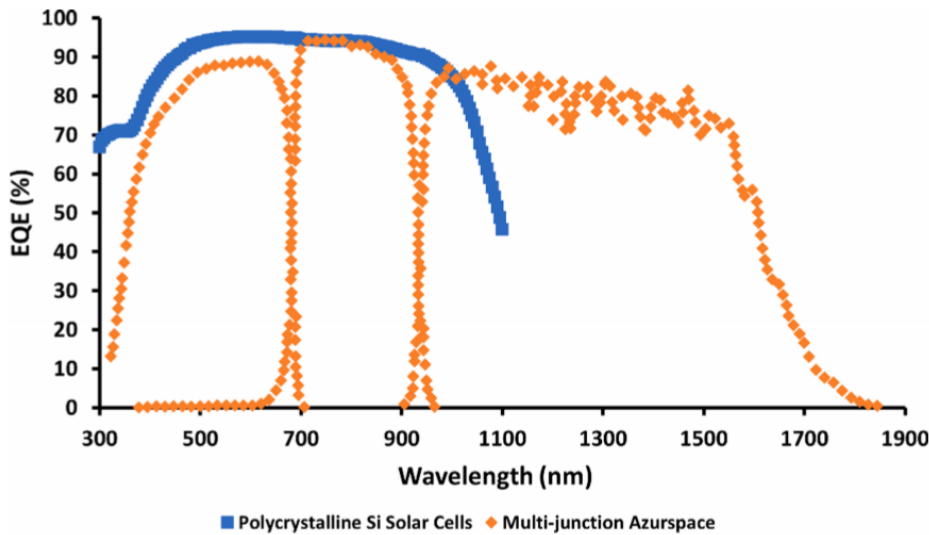


Fig. 2. EQE (%) measurements for the multi-junction solar cells and the polycrystalline Si solar cells.

the high concentration ratio. So, to avoid any thermomechanical defects to the solar cell and to assure a good fill factor (FF), a cooling mount setup is introduced at 25 °C, as in Fig. 3. Temperature is observed during the experiment utilising a thermocouple meter (Datalogger SDL200 - EXTECH INSTRUMENTS) to establish safe operating conditions.

A spectrophotometer device (PerkinElmer) is used to measure the total transmittance of the Fresnel lens (SOG) to allow accurate analysis for the optical efficiency and concentration ratio over the multi-junction and single-junction solar cells wavelength response range between 400 and 1800 nm and 350 – 1200 nm, respectively. The measured total transmittance will help to find out the optical efficiency and the concentration ratio of the Fresnel lens, which is intended to be 1 of 4 primary lenses in the ultrahigh CPV version of the system (Shanks et al., 2018).

To theoretically characterise the optical efficiency ($\eta_{opt,th}$) and the concentration ratio (C_{th}), we incorporate the average total transmittance (%T), the geometrical concentration ratio (C_g), and the fractional concentration loss (%C) with radiant flux (J) on the receiver area ($A_{receiver}$), and then divided with the radiant flux on the concentrator area ($A_{Fresnel}$), as in Eq. (1). For the multi-junction solar cell, the influence of incident spectrum irradiance on the short-circuit current (I_{sc}) to determine the

photocurrent generation ratio of the top subcell over the middle subcell (I_T/I_M) should be accountable for in the calculation of the optical efficiency (Fernández et al., 2017; Muñoz-Cerón et al., 2012). I_T/I_M terms in Eq. (1) is only to express that the optical efficiency for the case of a multi-junction cell is driven by the photocurrent generation ratio.

$$\eta_{opt,th} = \frac{(J \times A_{receiver}) \times \%T \times C_g \times \%C}{(J \times A_{Fresnel})} \times \frac{I_T}{I_M} \tag{1}$$

Hence, the theoretical concentration ratio can be given by Eq. (2)

$$C_{th} = \eta_{opt,th} \times C_g \tag{2}$$

The adjustment of the Fresnel lens under the solar simulator at 1000 W/m² shows an optimum focal length and a focal spot of 42cm and 2.8cm, respectively. Fig. 4 shows the experimental setup under the solar simulator and the tested solar cells.

The optical efficiency and optical concentration ratio after the Fresnel lens and with fractional concentration loss in preliminary setup are given with the wavelength range as well as two theoretical scenarios of optical efficiency, standard at 55% and state-of-art at 75% as in (Shanks et al., 2018) and in Fig. 5. The two scenarios demonstrate a further understanding of the optical efficiency and concentration ratio

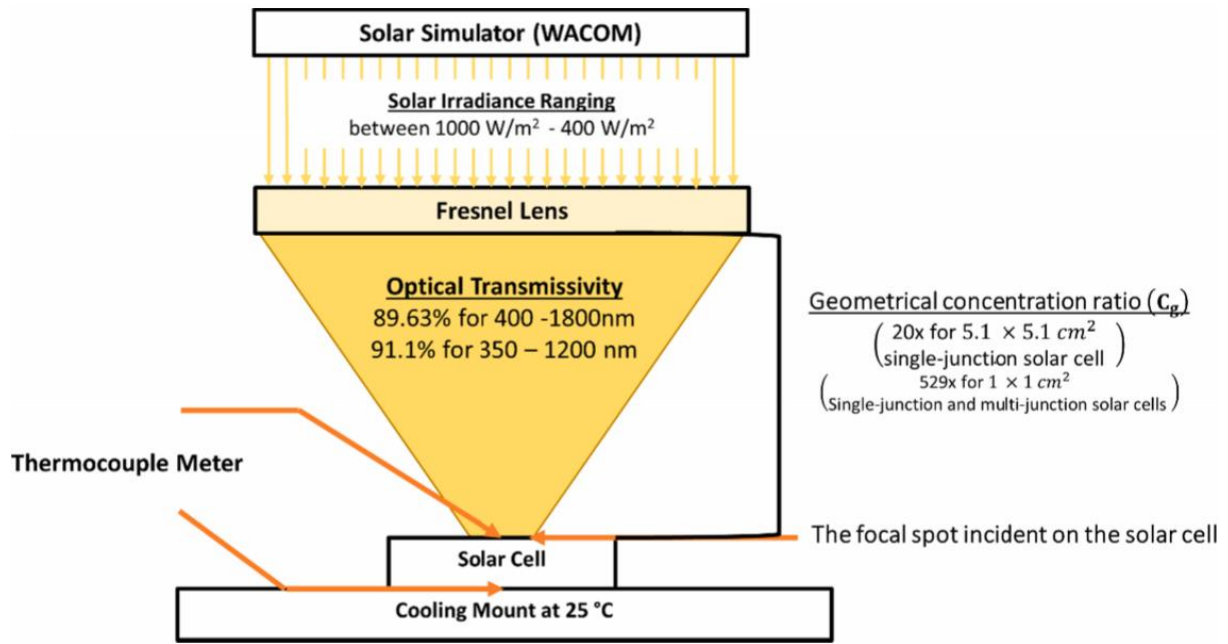


Fig. 3. Schematic diagram describing the experimental setup where AM 1.5G was simulated by WACOM solar simulator manufacturers (“WACOM ELECTRIC LTD,” 2021).

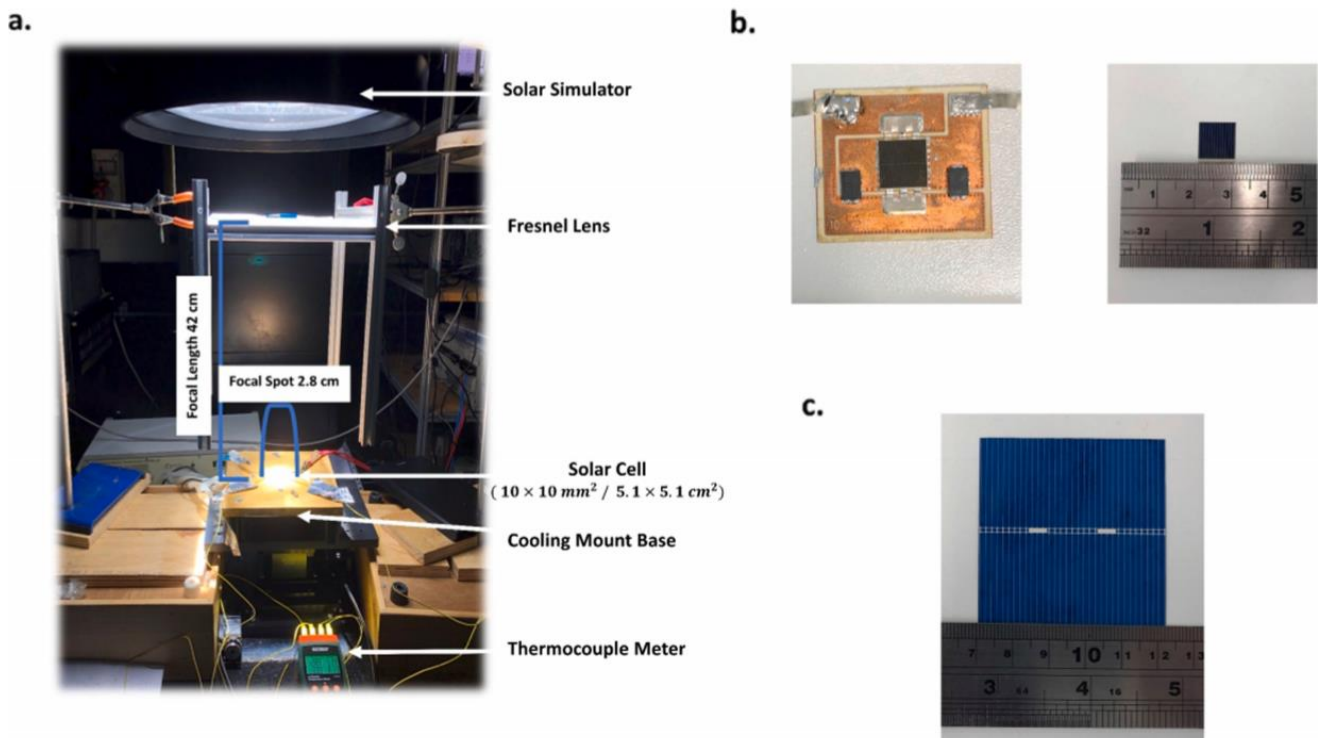


Fig. 4. a. Lab experimental setup for the primary optical components. b. Azur Space 3C44A ($10 \times 10 \text{ mm}^2$) and Si polycrystalline single junction ($10 \times 10 \text{ mm}^2$). c. Si polycrystalline single-junction ($5.1 \times 5.1 \text{ cm}^2$).

losses by incorporating multiple optical interfaces or optics with poor performance.

Clearly, the theoretical optical concentration ratio has shown a drop-in comparison to the geometrical concentration ratio on average by 10% for after the Fresnel lens. Also, the theoretical concentration ratio has shown a drop in contrast to after the Fresnel lens on average to be 25%, 45% and 84% for 75% state of the art optics, 55% standard optics and fractional concentration loss in preliminary setup, respectively. The

theoretical concentration ratio considering the fractional loss was found to be 77 suns on average.

The theoretical effective concentration ratio ($C_{eff,th}$) is calculated as the actual solar irradiance on the solar cell surface area after transmitting and concentrating through the Fresnel lens at different solar irradiance in the range of $400\text{--}1000 \text{ W/m}^2$ given the theoretical optical efficiency, as in Eq. (3):

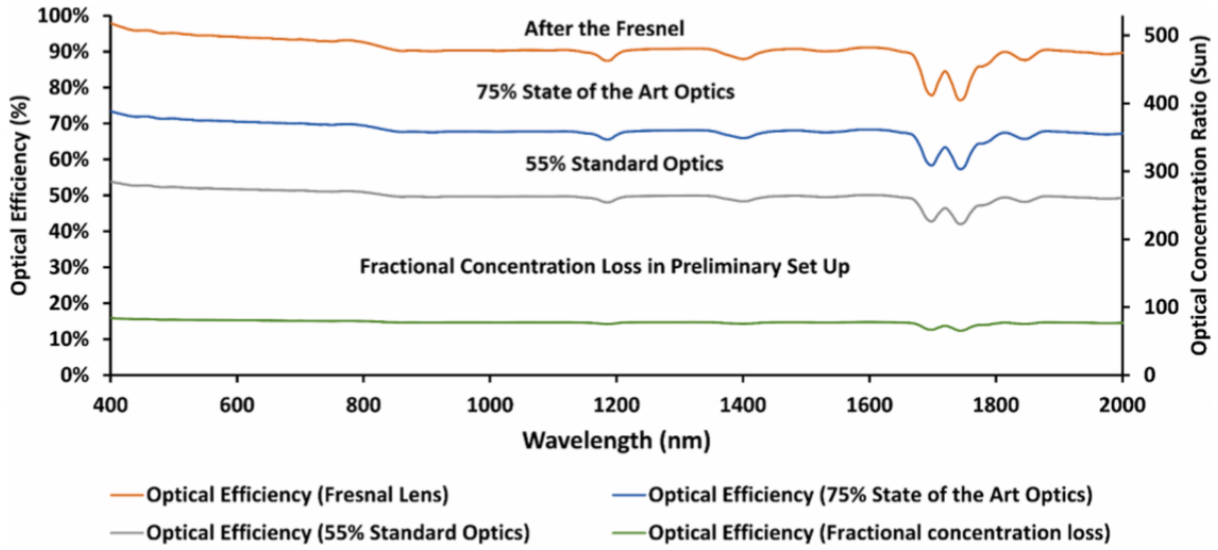


Fig. 5. Theoretical optical efficiency and optical concentration ratio with wavelength (computed relying on a solar cell area of $10 \times 10 \text{ mm}^2$ as a final stage).

$$C_{eff,th} = \frac{J \times C_g \times \eta_{opt,th}}{1000} = \frac{J \times A_{Fresnel} \times \%T}{A_{receiver} \times 1000} \quad (3)$$

2.2. Experimental optical characterisation

The optical characterisation of the Fresnel lens is experimentally achievable through the electrical characterisation of a solar cell. Indoor, we can control the solar intensity of the lamp (helicon value) at which electrical characterisation for different solar irradiance (concentration ratio after the Fresnel) is realistic. We simulate the solar irradiance from $400 - 1000 \text{ W/m}^2$ in the interval of 100 W/m^2 to measure the solar cell electrical products (I_{sc} , V_{oc} , FF). The I-V and power curves for the multi-junction solar cell (Azur Space 3C44A $10 \times 10 \text{ mm}^2$), for Si polycrystalline single-junction ($10 \times 10 \text{ mm}^2$), and Si polycrystalline single-junction ($5.1 \times 5.1 \text{ cm}^2$) are measured to determine the electrical limits with and without the Fresnel lens. The optimum arrangement of the Fresnel lens results in focal spot utilisation by the solar cell of $10 \times 10 \text{ mm}^2$ of only 16.24%, which is the actual portion of light falling on the cell, resulting in optical efficiency of 14.6% (Fractional concentration efficiency of $16.24\% \times$ average Fresnel lens transmittance of 89.6%) and concentration ratio of 77 suns, as illustrated in Fig. 6.a. In a solar cell of $5.1 \times 5.1 \text{ cm}^2$, the solar cell area is more significant than the focal spot area; hence the geometrical concentration ratio (the Fresnel lens area divided by the solar cell area) is not quite appropriate and instead the

Fresnel input aperture area divided by the illuminated cell area would give a more useful indication of concentration ratio. In Fig. 6.b, the theoretical optical efficiency was found to be 91.1% (simply the Fresnel transmittance), resulting in a theoretical concentration ratio of 18 suns.

2.2.1. Focal spot size > Solar cell area (Multi-junction /single-junction)

As known, the objective of the Fresnel lens is to concentrate solar irradiance onto a small solar cell area. Two types of solar cells are used to characterise the preliminary setup optic toward the ultrahigh system optically. Multi-junction (Azur Space 3C44A $10 \times 10 \text{ mm}^2$) and single-junction polycrystalline solar cell are electrically measured. Fig. 7. a and b show the electrical limits of multi-junction and single-junction solar cells in terms of I-V and power curves, respectively. At 1000 W/m^2 , the introduction of the Fresnel Lens shows an increase in P_{max} by about 167 times and in I_{sc} by about 78 times for the multi-junction solar cell, as in Fig. 7. a, whereas the growth in P_{max} and I_{sc} for the single-junction solar cell is by about 9 times and 34 times, respectively, as in Fig. 7. b. The multi-junction solar cell is designed to perform optimally at 500 suns, where its efficiency, I_{sc} , V_{oc} , and FF 41.4%, 7.49A, 3.11A, and 89.6% (Azur Space Solar Power GMBH, 2014), respectively. The multi-junction solar cell's performance improves from where the primary optical component (Fresnel lens) at 77 suns and gradually increase to get closer to the optimum design condition. Hence, the multi-junction solar cell's V_{oc} increases significantly comparably with the single-junction solar

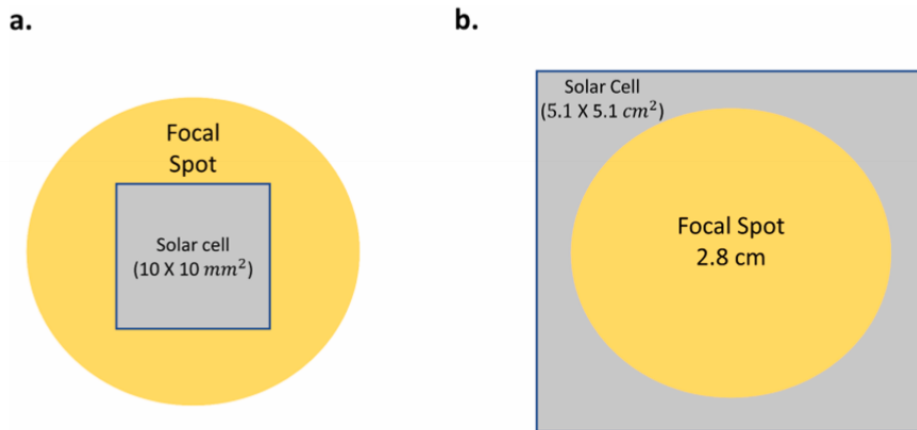


Fig. 6. a schematic diagram of a. fractional concentration loss (solar cell to focal spot area) ($10 \times 10 \text{ mm}^2$), and b. solar cell area larger than the focal spot area ($5.1 \times 5.1 \text{ cm}^2$).

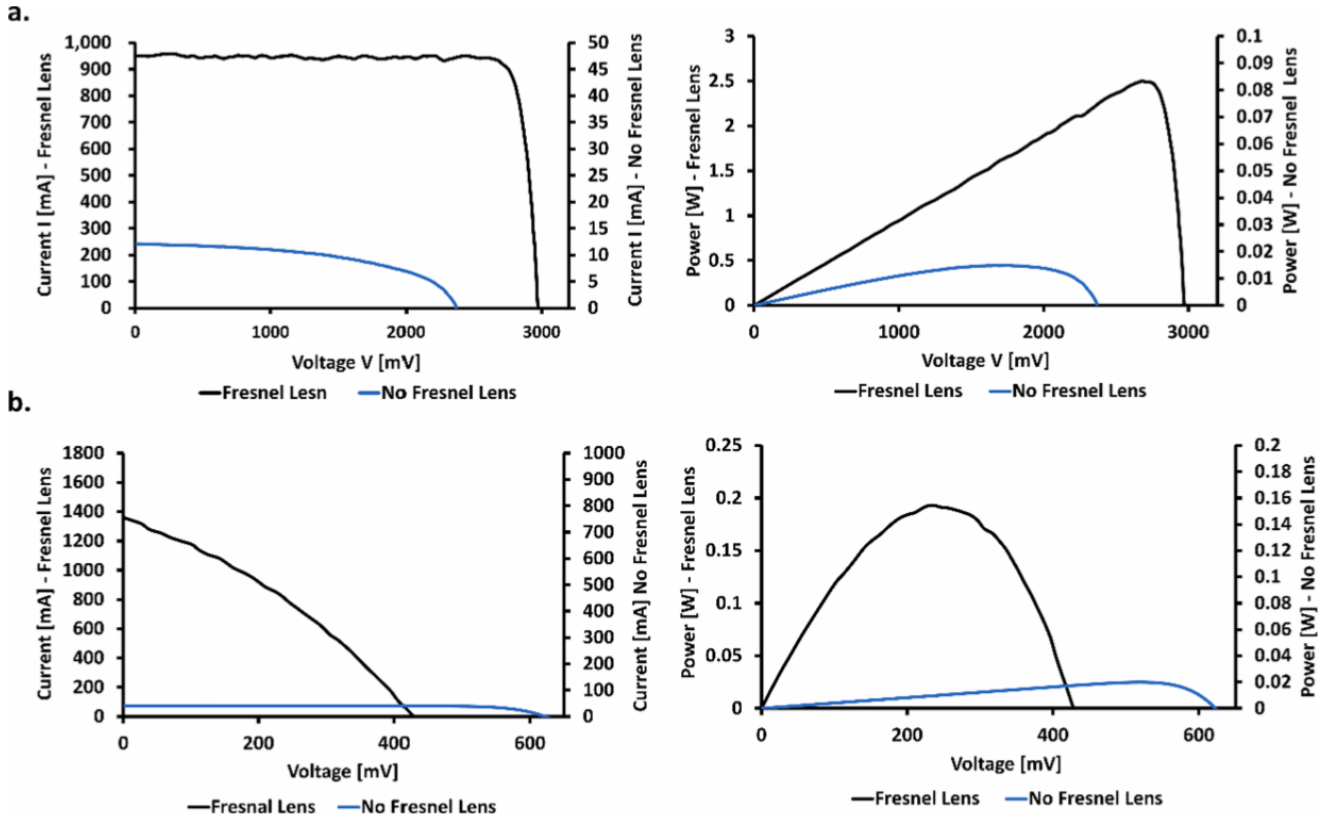


Fig. 7. I-V and power curves limits with/ without Fresnel lens at 1000 W/m² of a. Azur Space multi-junction solar cell of 10 × 10 mm² and b. the single-junction solar cell of 10 × 10 mm².

cell.

The limitation of the single-junction solar cell, as not being design for concentration system, is the high series-resistance reflected on the drop of V_{oc} and power output compared with the multi-junction solar cell. The multi-junction solar cell can absorb many photons energy due to its wider bandgap energy (monolithic stack configuration), where less intrinsic losses occur, such as thermalisation loss, resulting in high cell efficiency.

Experimentally, the effective concentration ratio ($C_{eff,exp}$) can be characterised considering the measured I_{sc} with/without the Fresnel, as in Eq. (4).

$$C_{eff,exp} = \frac{I_{sc,concentrated}}{I_{sc,notconcentrated}} \quad (4)$$

As in Fig. 5, the theoretical effective optical concentration ratio was found to be 77 suns after the Fresnel, where the experimental effective concentration ratio was found to be 78 suns, which is agreeable with the theoretical effective concentration ratio by 98%. In anticipation of the optical concentration ratio, the geometrical concentration ratio could be approached either by considering only the Fresnel lens area (0.0529m²) to the focal spot area ($A_{focalspot}$) (0.0006157m²) or by considering the area of the Fresnel to the area of the solar cell and then apply the fractional concentration loss of 16.24%, as in Eq.(5). The fractional concentration ratio only requires to be accounted for when the focal spot area is bigger than the solar cell, whilst the focal spot area matches the solar cell (usually due to another funnel optic receiver) or is smaller than the solar cell (like in the case of 5.1 cm × 5.1 cm cell) then there is no fractional concentration loss.

$$C_g = \frac{A_{Fresnel}}{A_{focalspot}} = \frac{A_{Fresnel}}{A_{receiver}} \times \%C \quad (5)$$

Fig. 8 shows the different value of effective irradiance incident on the

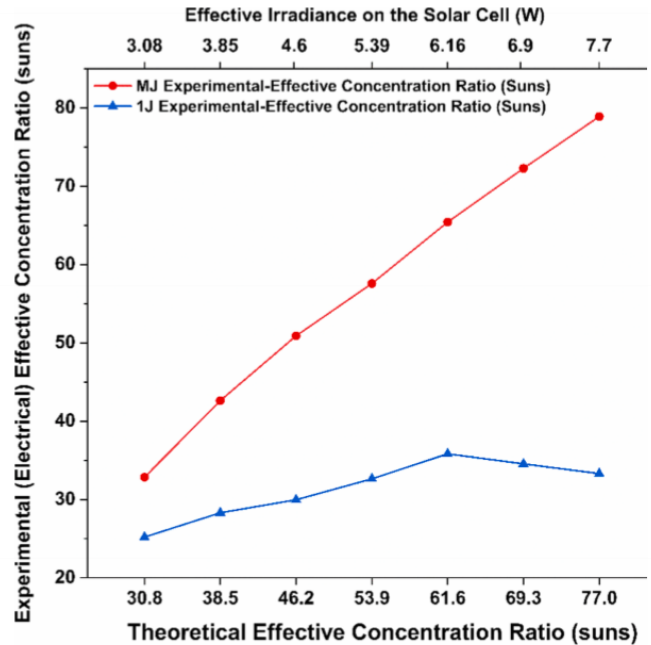


Fig. 8. Theoretical and experimental effective concentration ratio for single- (1 J) and multi-junction (MJ) solar cells where the experimental effective concentration ratio is calculated from the short circuit current increase of the cells.

solar cell (W) as secondary x-axis, the theoretical effective concentration ratio of the multi-junction and single-junction solar cell, as primary x-axis, and experimental effective concentration ratio of the multi-junction and single-junction solar cell, as the primary y-axis. A strong

linear correlation exists between the theoretical and experimental effective concentration ratio for the multi-junction solar cell. The experimental results have shown higher results by 6% on average. This discrepancy may be due to the calibration of the helicon value to simulate the solar irradiance values. On the other hand, the single-junction solar cell could not compete with the multi-junction solar cell due to its design condition at 1 sun. Although at concentrated solar irradiance of 3.1 W (31 suns), the single-junction solar cell has shown the lowest difference by about 17%, this difference kept increasing gradually with a widening gap up to 6.2 W (62 suns), which could be elaborated as a bottleneck after the experimental effective concentration ratio decreased. On average, the difference between the theoretical and experimental effective concentration ratio is 39%. The single-junction solar cell's short circuit current can be used to indicate concentration ratio but the interest from these results is the scale of the overall power losses on the single-junction cell due to the out of working range concentration ratios. The ultimate aim is to test concentrator multi-junction cells at increasingly high and ultrahigh concentration ratios, beyond their designed operation. Hence, as a starting point, understanding the performance of the single-junction cell beyond its working concentration is a low-risk investigation. With increases in concentration ratio comes an increase in temperature of the cell, which when significantly higher than its recommended range (especially possible if there are hot spots due to concentrated irradiance distribution), can cause breakages. The single-junction cell would hence likely not cope with ultrahigh concentration ratios to aid the testing of the optics (via the short circuit current) but is a useful stepping stone in these preliminary investigations.

2.2.2. Focal spot size < Solar cell area (single-junction)

This section introduces the experimental optical characterisation for solar cell bigger than the produced focal spot size by the selected Fresnel lens. We have utilised Si polycrystalline single-junction (5.1 × 5.1 cm²) solar cell. Fig. 9 shows the I-V and power curves limits for with and without Fresnel lens. At 1000 W/m², the introduction of the Fresnel lens

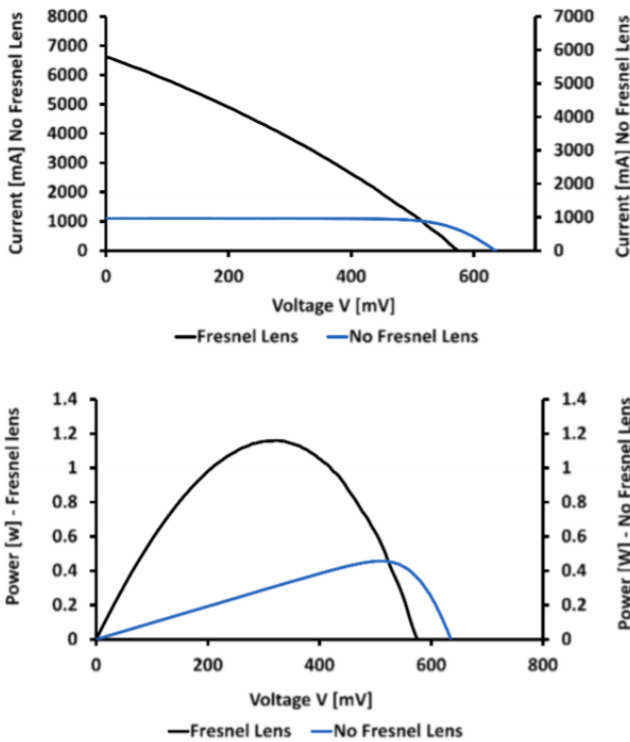


Fig. 9. I-V and power curves limits with/ without Fresnel lens at 1000 W/m² of the single-junction solar cell of 5.1 × 5.1 cm²

shows an increase in P_{max} by about four times and in I_{sc} by about 7 times. As highlighted in the previous section, this low performance is due to the high concentration ratio subjected to the solar cell surface inducing by that temperature.

Both Eqs. (3) and (4) were adopted to figure out the theoretical and effective concentration ratio. As known, the geometrical concentration ratio is the area of the Fresnel lens (0.0529m²) to the area of the solar cell (0.002601m²) resulting in 20 suns, as in Eq. (6).

$$C_g = \frac{A_{Fresnel}}{A_{receiver}} \tag{6}$$

Fig. 10 shows the difference between the theoretical and experimental effective concentration ratio. We can observe that the experimental effective concentration ratio performs as a positive slope with the less difference at 19 W and after the difference is growing with increasing the solar irradiance on the cell. This logarithmic difference is noticeable where the curve is then flattened after 28.5 W. On average, the discrepancy between the experimental and the theoretical effective concentration ratio is by about 50%.

2.3. Effective optical efficiency approach

To find out the effective optical efficiency ($\eta_{opt,eff}$), the electrical characterisation of the solar cell at different solar irradiance has been incorporated in Eq. (7) to predict the effective optical efficiency considering the Fresnel lens efficiency (Module efficiency - η_{module}) concerning solar cell efficiency (η_{cell}). I_T/I_M terms in both Eqs. (1) and (7) is only to express the subcell limits for the multi-junction cell.

$$\eta_{opt,eff} = \frac{\eta_{module}}{\eta_{cell}} \times \frac{I_T}{I_M} \tag{7}$$

The module efficiency is the maximum electrical power output from the solar cell to the power input for the Fresnel lens, as in Eq. (8):

$$\eta_{module} = \frac{Power_{max}(V_{oc}, I_{sc}, F, F), concentrated}{J \times A_{Fresnel}} \tag{8}$$

The theoretical module efficiency can be calculated by multiplying the optical efficiency of each component within the module and including any other forms of “stray light loss” such as the fractional loss discussed previously. This however must also take into account the

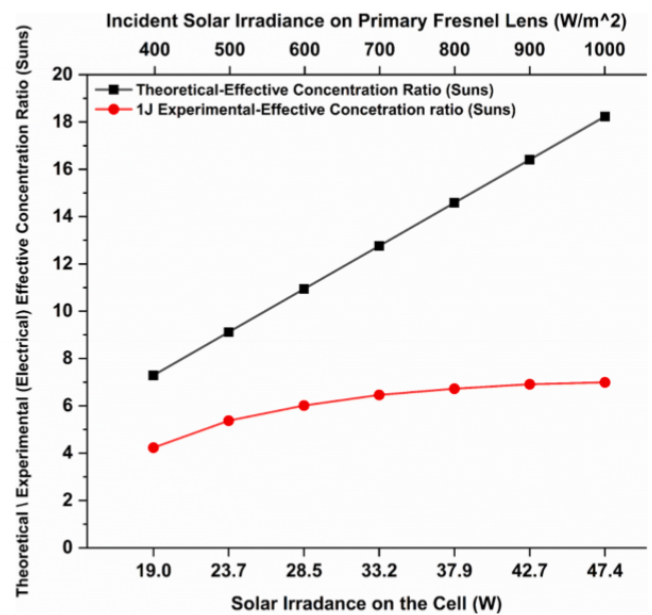


Fig. 10. Theoretical and experimental effective concentration ratio for single-junction (1 J) solar cells calculated from cell power output.

intended wavelength range of the solar cell. The Fresnel lens optical transmissivity was measured to be an average of 89.63% for a spectral band compatible with a multi-junction solar cell of 400–1800 nm and in module efficiency of 91.1% for a spectral band matching up with single-junction solar cell of 350 – 1200 nm. As discussed, when this is multiplied by 16.24% (area of focal spot incident on cell) this becomes 14.6%. This optical efficiency (transmittance of Fresnel lens) would be the theoretical module efficiency if all of the light focused from the Fresnel lens fell incident within the cell area and the cell was designed as such to have a good fill factor under the effective concentration ratio. For the intended ultrahigh system, both of these factors will be significantly improved though substantial losses for each are anticipated due to alignment challenges (entendue challenges) and current available concentrator cells. Comparing the current setup with the ultrahigh setup will confirm experimentally the gain in such a complex ultrahigh system. However, the module efficiency was experimentally found to be 5% on average for the multi-junction solar cell and found to be 0.7% on average for the single-junction solar cell both of $10 \times 10\text{mm}^2$ surface area. The module efficiency for the multi-junction solar cell shows excellent stability within varying the DNI from $1000 \frac{\text{W}}{\text{m}^2}$ to $400 \frac{\text{W}}{\text{m}^2}$ in an interval of $100 \frac{\text{W}}{\text{m}^2}$. On the other hand, the module efficiency for the single-junction solar cell was increased gradually from 0.364% at $1000 \frac{\text{W}}{\text{m}^2}$ to 1.17% at $400 \frac{\text{W}}{\text{m}^2}$. For the case of $5.1 \times 5.1\text{cm}^2$ single-junction solar cell, the module efficiency was found to be 2.19% at $1000 \frac{\text{W}}{\text{m}^2}$ and increased gradually to reach 5.36% at $400 \frac{\text{W}}{\text{m}^2}$, resulting in average module efficiency of 3.28%.

The cell efficiency is the electrical output to the power input of the cell with concentration, which is driven from an Eq. (9):

$$\eta_{\text{cell}} = \frac{\text{Power}_{\max}(V_{oc}, I_{sc}, F.F.)_{\text{concentrated}}}{\text{Radiant flux on the target area}((J \times A_{\text{Fresnel}}) \times \%T \times \%C)} \quad (9)$$

Experimentally, the power output for both single-junction and multi-junction solar cells was measured to compute the cell efficiency. As a result, the cell efficiency of $10 \times 10\text{mm}^2$ multi-junction solar cell was found to be 33.5% on average, with excellent consistency with altering the DNI input value. In contrast, the single-junction solar cell of $10 \times 10\text{mm}^2$ surface area showed a cell efficiency increasing progressively from 2.5% at a solar simulator irradiance of $1000 \frac{\text{W}}{\text{m}^2}$ to 8% at a solar simulator irradiance of $400 \frac{\text{W}}{\text{m}^2}$. Also, the single-junction solar cell of $5.1 \times 5.1\text{cm}^2$ surface area represented a cell efficiency increasing steadily from 2.4% at $1000 \frac{\text{W}}{\text{m}^2}$ to 5.88% at $400 \frac{\text{W}}{\text{m}^2}$.

As in Eq. (1), the theoretical optical efficiency of both $10 \times 10\text{mm}^2$ single- and multi-junction solar cell is found to be 14.6% due to accounting for the concentration fractional loss. Experimentally, the effective optical efficiency of both $10 \times 10\text{mm}^2$ single- and multi-junction solar cell leads to an exact similar result with the theoretical one, as in Eq.7. With varying the DNI value, the multi-junction solar cell showed consistency in both cell and module efficiencies resulting in a constant optical efficiency. On the other hand, the single-junction solar cell showed a gradual increase in both cells in module efficiencies, causing a continuous optical efficiency with changing the DNI value. In

the case of $5.1 \times 5.1\text{cm}^2$ single-junction solar cell, the theoretical and experimental optical efficiency is found to be 91.1% as the fractional loss discarded. Both cell and module efficiencies raised steadily, resulting in a continuous optical efficiency altering the DNI value. Compared to the experimental one, the high theoretical effective optical efficiency is because the single-junction solar cell is designed to cope with 1 sun. The overall study parameters and results are summarised in Table 1.

Although the concentration ratio value is far from the ultrahigh concentration limits, these results are an important step towards carrying out the full ultrahigh concentration setup experiment. This paper is focused on evaluating the optical components (Fresnel lens) individually, and the performance of the concentrator multi-junction cell in these poorer conditions to have a concrete reference performance for the full ultrahigh system.

Table 2 is listing all the detailed equations previously in three sections geometrical concentration, theoretical calculation, and experimental calculation. The number of equations in the table is correspondent to the number of equations in the paper.

3. Theoretical perspective toward ultrahigh CPV system

As a primary optical component toward the full UHCPV system as in (Shanks et al., 2018), the refractive optic (Fresnel lens) is characterised theoretically and experimentally. This Fresnel lens is 1 of 4 primary Fresnel lens optics exactly the same, which would make up the entry aperture (primary optic) for an ultrahigh CPV system of concentration ratio > 3000 suns. In this section, the subsequent optics, which are flat reflective mirror and tertiary optics on the top of the solar cell, are theoretically discussed, accounting only for three optical stages starting with the Fresnel lens to the flat plain reflective optical mirror ending with the tertiary optic. Due to the fractional concentration loss, significant loss occurs in the optical performance when compromised electrically, as systematically explained in the previous section. Incorporating more than one optic in the CPV system results in increasing the concentration ratio through minimised sunrays divergence. There will likely still be some loss and hence the optical efficiency of 14.6% due to the fractional loss is considered as the worst-case scenario through which the UHCPV system will be theoretically analysed and discussed. Certainly, the fractional loss would increase with increasing the concentration ratio. Checking the irradiance distribution of the Fresnel lens would reflect an increase in the fractional loss If the short-circuit current given here gave a concentration value significantly higher than the fractional loss indicated then the majority of the irradiance was actually focused on the inner area of the focal spot – where the 1 cm cells are placed, which would be important to know for the ultrahigh system. Still, the ultrahigh system is strongly influenced by alignment, manufactured optical materials, the temperature of optics and incidence source light (divergence angle).

In the ultrahigh CPV system design, four or three optical interfaces will be incorporated to accomplish an ultrahigh concentration ratio configuration. In the case of four optical stages, the sunrays will be

Table 1

Summarise the geometric concentration, theoretical/experimental optical concentration ratio, and the optical efficiency in every testing scenario at $1000 \frac{\text{W}}{\text{m}^2}$.

| Solar Cells | Geometrical concentration ratio (x) (Cg) | Theoretical Optical Concentration ratio (suns) (C_{th} and $C_{eff,th}$) | Experimental Optical Concentration ratio (suns) ($C_{eff,exp}$) | Theoretical Optical Efficiency (%) ($\eta_{opt,th}$) | Effective Optical Efficiency (%) ($\eta_{opt,eff}$) |
|-----------------------------------|--|--|---|--|---|
| $1 \times 1\text{cm}^2$ (1 J) | 529 | 77 | 33 | 14.6 | 14.6 |
| $5.1 \times 5.1\text{cm}^2$ (1 J) | 20 | 18 | 7 | 91.1 | 91.1 |
| $1 \times 1\text{cm}^2$ (MJ) | 529 | 77 | 79 | 14.6 | 14.6 |

Table 2
Summary for the used equations to solve for the optical concentration ratio and optical efficiency theoretically and experimentally.

| Number of Equation | Name of Equation (unit) | Equation |
|----------------------------------|---|---|
| Geometrical Concentration | | |
| 5 | Geometrical concentration for focal spot larger than the cell (x) | $C_g = \frac{A_{Fresnel}}{A_{focalspot}} = \frac{A_{Fresnel}}{A_{receiver}} \times \%C$ |
| 6 | Geometrical concentration ratio for solar cell larger than the focal spot (x) | $C_g = \frac{A_{Fresnel}}{A_{receiver}}$ |
| Theoretical Calculations | | |
| 1 | Theoretical Optical Efficiency (%) | $\eta_{opt,th} = \frac{(J \times A_{receiver}) \times \%T \times C_g \times \%C}{(J \times A_{Fresnel})} \times \frac{I_T}{I_M}$ |
| 2 | Theoretical Optical Concentration ratio (suns) | $C_{th} = \eta_{opt,th} \times C_g$ |
| 3 | Theoretical effective concentration ratio (suns) | $C_{eff,th} = \frac{J \times C_g \times \eta_{opt,th}}{1000} = \frac{J \times A_{Fresnel} \times \%T}{A_{receiver} \times 1000}$ |
| Experimental Calculations | | |
| 4 | Effective concentration ratio (suns) | $C_{eff,exp} = \frac{I_{sc,concentrated}}{I_{sc,notconcentrated}}$ |
| 7 | Effective optical efficiency (%) | $\eta_{opt,eff} = \frac{\eta_{module} \times I_T}{I_M}$ |
| 8 | Module efficiency (%) | $\eta_{module} = \frac{\eta_{cell}}{Power_{max}(V_{oc}, I_{sc}, F.F.)_{concentrated}}$ |
| 9 | Cell efficiency (%) | $\eta_{cell} = \frac{J \times A_{Fresnel} \times Power_{max}(V_{oc}, I_{sc}, F.F.)_{concentrated}}{Radiant\ flux\ on\ the\ target\ area((J \times A_{Fresnel}) \times \%T \times \%C)}$ |

refracted from the Fresnel lens into the flat reflective secondary mirror, which reflects concentrated sun rays into the third stage flat central mirror. Afterwards, the third stage flat central mirror will reflect the concentrated rays into the low refractive tertiary optic as a final optical stage. Although this number of optics in one system will add to the complexity of the fabrication and challenge the accuracy and alignment of the system, 1 of these optical stages is a flat mirror which should have minimum light divergence effects if of high quality. These optical stages will aid the system at which the convergence angle is minimised (less fractional concentration loss), resulting in increased concentration ratio. Inherently, a minimum light divergence (the maximum angle from the furthest incident rays from the normal axis to arrive at the focal spot) has a smaller acceptance angle, adding to the tracking system load and accuracy. In the UHCPV system, the concentrated rays would still not converge enough into the solar cell area, resulting in a reduction in the optical efficiency and hence in the optical concentration ratio. Although the UHCPV system aims to incorporate smaller multi-junction solar cells for higher geometrical concentration ratio, less heat generation, and

higher cell efficiency, the CPV system is challenged in design and alignment accuracy. Refractive tertiary optics is suggested and implemented on the top surface of the solar cell. Although tertiary optics would decrease the optical efficiency also, tertiary optics improve the acceptance angle and the uniformity of irradiance distribution

3.1. Theoretical review of secondary mirror coatings

The UHCPV system consists of Fresnel lens, as primary refractive optic, reflective mirror, as a secondary optic, and a tertiary centre optic, as final refractive optic attached on the solar cell. The secondary reflective mirror will be interpolated for four different metallic coatings: UV aluminium mirror, enhanced aluminium mirror, silver mirror, and gold mirror. These secondary mirrors optical efficiency (Reflectance %) are retrieved from the NEWPORT Corporation (Newport Corporation, n. d.) for broadband metallic mirrors (Borofloat 33), which operates well over a very wide-ranging of spectral wavelength with relatively insensitive to angle of polarisation and incident. Regarding tertiary centre

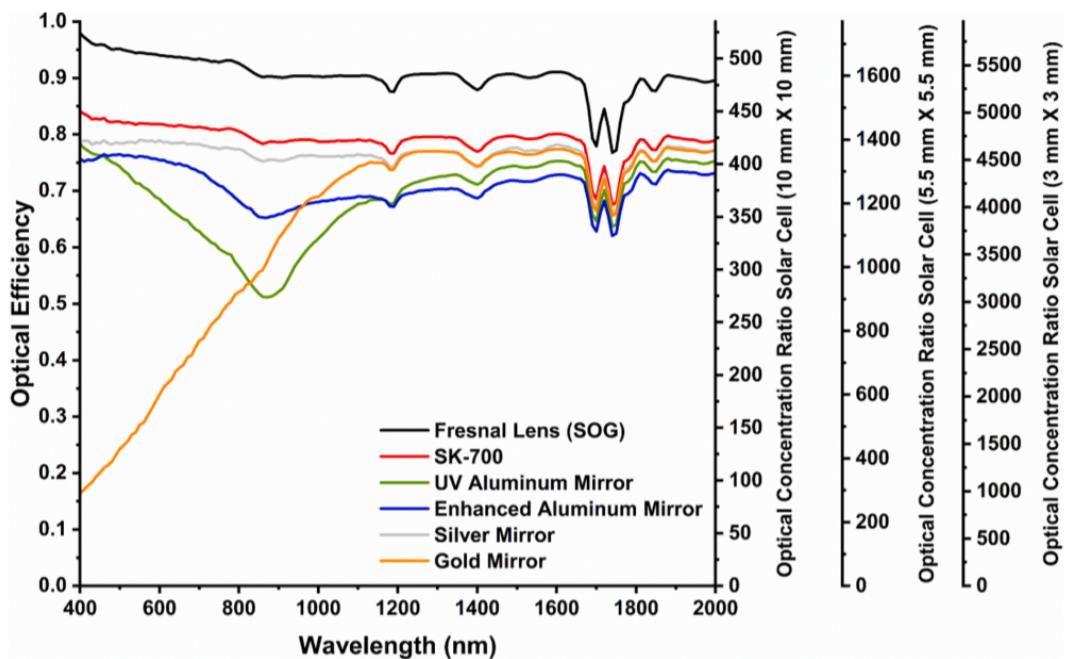


Fig. 11. Theoretical optical efficiency with wavelength (400 – 2000 nm) for four different reflective mirrors as a secondary optical stage associated with both the Fresnel lens and the SK-700. The optical concentration ratio computed relying on a solar cell area of 10 × 10 mm², 5.5 × 5.5mm², and 3 × 3mm² as a final stage and no fractional losses.

optic, the transmittance (%) performance of SK-700 material was retrieved from (Leem and Yu, 2012)(Shanks et al., 2018). The retrieved data will be integrated as a consecutive optic to the Fresnel lens to theoretically evaluate the optical efficiency and optical concentration ratio for a quarter of the system. The integration of the tertiary centre has dropped the optical efficiency due to the scattering losses at the top surface of the tertiary in the absence of the antireflective coating(Bruns et al., 2016) and the absorbance properties of the tertiary itself..

Fig. 11 shows the optical performance, optical efficiency as a primary y-axis of the Fresnel lens (SOG) itself, of SK-700 dependent on the performance of the Fresnel lens, and the four types of metallic coating dependent on the performance of both Fresnel lens and SK-700, as in Eq. (10).

$$\eta_{opt,th} = \eta_{Fresnellens} \times \eta_{metalliccoating(UV\ aluminum, Enhanced\ Aluminum, Silver, and\ Gold)} \times \eta_{SK-700} \tag{10}$$

The optical efficiency, in Fig. 10, is showing the losses for three optical stages, first the Fresnel lens material absorption and scattering, second the mirror’s coatings reflectivity, and third the tertiary optics absorption and scattering. Hence, the three stages’ performance would produce the final optical efficiency and concentration ratio for only ¼ of the system, when all 4 lenses and mirrors are in place the concentration would be × 4 (as all focal spots from each of the 4 Fresnel lenses are redirected via flat mirrors towards the centre (Shanks et al., 2018). Achieving high optical efficiency for 3 mm × 3 mm cell and optics setup as its maximum geometrical concentration ratio would become 23,511x, which it seems unlikely to be reached in real-life testing conditions within the current available optics and manufacturing. Given the fractional loss optical efficiency of 14.6%, the system optical efficiency would be 3433x, which is still within the target of the design of > 3000 suns. However, such an analysis is given to illustrate how considerable the effect of the final receiver size on the concentration ratio.

On average, the optical efficiency of the Fresnel lens and SK-700 extrapolated from Fig. 11 to be 79%. Also, the optical efficiency has been 69%, 71%, 77%, and 63% for UV aluminium mirror, enhanced aluminium mirror, silver mirror, and gold mirror incorporated with Fresnel lenses and SK-700, respectively. The highest optical efficiency is for silver coating mirror (>96% from 480 to 1100 nm; >98.5 for > 1.1 nm), which is better suited to multi-junction solar cell (350 nm – 1600 nm). However, the silver coating deteriorates when exposed to extreme metrological conditions, especially under concentrated sunrays. NEW-PORT Corporation utilises silver film of low emissivity, which is entirely encapsulated by a dielectric stack of multilayer to avoid oxidisation. The silver coating exhibited an excellent reflectivity performance on IR wavelength range while maintaining a proper performance in both visible and near IR. The most inferior performance is for gold mirror (>96% from 650 to 1700 nm; > 98% for > 1.7 nm) because its ideal for application requiring reflectance near IR and for the onward IR, an overcoat of a multilayer dielectric provides preservation to the gold from the outside weather conditions. In the case of the enhanced aluminium mirror, the average reflectivity is > 93% from 450 to 700 nm, and a dielectric stack of the multilayer is applied over the aluminium surface to increase reflectivity and enhance durability. An enhanced aluminium mirror is very suitable for the application required spectral band for visible and near-infrared. UV enhanced mirror has an average reflectivity of 90% from 250 to 600 nm. Also, UV enhanced mirror is proper for most applications due to its durability, which is enhanced by applying dielectric overcoating to avoid oxidisation of the metal.

Fig. 11 shows the optical concentration ratio for a quarter of the system a secondary y-axis for where the first secondary y-axis, second secondary y-axis, and third secondary y-axis is based on a geometrical concentration ratio for solar cell area of (10 × 10mm²), (5.5 × 5.5mm²), and (3 × 3mm²), respectively. On average, the optical concentration ratio has been computed for a spectral band from 400 to 2000 nm, as in Table 3 and as plotted in Fig. 12.

Table 3

The data extrapolated from Fig. 10 for four different types of metallic coatings on average across a wavelength range of 400 – 2000 nm for a quarter of the system.

| Solar cell Area (mm) | The optical concentration ratio (suns) | | | |
|----------------------|--|--------------------------|---------------|-------------|
| | UV Aluminum Mirror | Enhanced Aluminum Mirror | Silver Mirror | Gold Mirror |
| 10 × 10 | 364 | 376 | 405 | 333 |
| 5.5 × 5.5 | 1202 | 1239 | 1334 | 1100 |
| 3 × 3 | 4040 | 4166 | 4500 | 3699 |

For the entire system and given the geometrical concentration ratio for the selected primary optical stage, ultrahigh concentration ratio > 3000 suns is not achievable for a receiver area of 10 × 10mm² since the optimum theoretical concentration ratio for the silver mirror compared to others is 1620 suns. Indeed, the solar cell area of 5.5 × 5.5mm² and 3 × 3mm² is capable of attaining the ultrahigh concentration ratio. The optical losses are more likely to occur due to further transmittance and reflectiveness loss. Also, the amount of the accumulated heat at the focal spot due to the ultrahigh concentration ratio might induce other losses when compromising the optical performance electrically as the electrical performance deteriorates if no suitable cooling mechanism is in place. The secondary reflective mirror function is to minimise the light divergence, and the tertiary optics role is to funnel as much of the focal point light and concentrate it further to the cell size, hence minimising the geometrical fractional loss. The tertiary optic only reduces fractional loss but add some absorption/scattering to the concentrated light. So, the added dashed line in Fig. 12 gives a theoretical estimate of the minimum concentration ratio for the system. The aim is to build a prototype that falls within the solid lines and the dashed lines. Given the limits of ultrahigh concentration ratio of > 3000 suns and the calculated theoretical concentration ratio based on the selected optical mirror, the range of optical losses differ depending on the optical stages and their optical performance for solar cell area of 5.5 × 5.5mm² and 3 × 3mm² wherein our case and based on the selected optics. The detailed losses based on the performance of the coated reflective mirror have listed in Table 4.

4. Conclusions

The indoor optical characterisation is adopted to characterise the optical performance of the Fresnel lens theoretically and effectively. This approach allows simple measurements to estimate the effective optical efficiency and effective concentration ratio, especially in a concentrated photovoltaic system (CPV). From this optical characterisation, we can extract that the optical performance decay significantly due to the fractional concentration loss and the designing conditions of single-junction solar cells. Also, the multi-junction solar cell has shown minimal inconsistency in the experimental optical characterisation compared to the single-junction solar cells, resulting in a discrepancy of 2% at 7.7 W and 6% on the average cross a concentrated solar irradiance on the cell from 3.1 to 7.7 W. The theoretical analysis of the overall optical components in the UHCPV emphasised the optical losses and aspects that challenge the system to reach a concentration ratio > 3000 suns. Four different metallic coatings for the reflective secondary mirror have been analysed considering the range of optical losses to still achieve the ultrahigh concentration ratio and balance that with the correlation between the solar cell size and the primary optic size (geometrical concentration ratio).

Declaration of Competing Interest

The authors declare that they have no known competing financial interests or personal relationships that could have appeared to influence

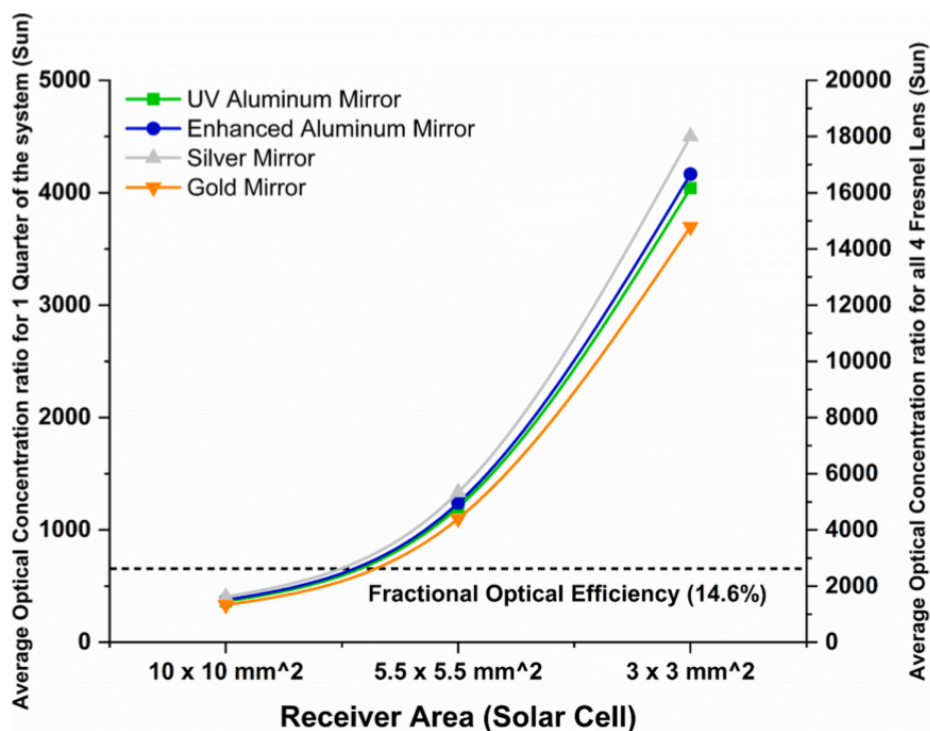


Fig. 12. Optical concentration ratio plotted from Table 3 for three sizes of the final receiver (solar cell) and for four types of metallic coatings associated with the tertiary optic (SK-700) and the Fresnel lens.

Table 4

The room of optical concentration ratio loss based on the selected optics and the metallic coating typed for the secondary reflective mirror and solar cell area of $5.5 \times 5.5 \text{ mm}^2$ and $3 \times 3 \text{ mm}^2$

| Solar cell Area (mm) | The range of optical concentration ratio losses (%) | | | |
|----------------------|---|---------------------------|---------------|-------------|
| | UV Aluminium Mirror | Enhanced Aluminium Mirror | Silver Mirror | Gold Mirror |
| 5.5×5.5 | 37.6% | 39.4% | 43.8% | 31.8% |
| 3×3 | 81.4% | 81.9% | 83.3% | 79.7% |

the work reported in this paper.

Acknowledgement

M.A would like to duly acknowledge the financial support from the Saudi Arabia Culture Bureau in the U.K. As well, the Ph.D. scholarship of A.A funded by Newton-Mosharafa Fund (UK-Egypt partnership) is acknowledged. The funders have no role in study design data collection, or preparation of the manuscript.

References

AlFalal, G., Maatallah, T.S., Alzahrani, M., Al-Amri, F.G., 2020. Optimisation and feasibility analysis of a microscale pin-fins heat sink of an ultrahigh concentrating photovoltaic system. *International Journal of Energy Research* 44, 11852–11871. <https://doi.org/10.1002/er.5826>.

Alzahrani, M., Baig, H., Shanks, K., Mallick, T., 2020. Estimation of the performance limits of a concentrator solar cell coupled with a micro heat sink based on a finite element simulation. *Applied Thermal Engineering* 115315. <https://doi.org/10.1016/j.applthermaleng.2020.115315>.

Alzahrani, M., Roy, A., Shanks, K., Sundaram, S., Mallick, T.K., 2021a. Graphene as a pre-illumination cooling approach for a concentrator photovoltaic (CPV) system. *Solar Energy Materials and Solar Cells* 222, 110922. <https://doi.org/10.1016/j.solmat.2020.110922>.

Alzahrani, M., Shanks, K., Mallick, T.K., 2021b. Advances and limitations of increasing solar irradiance for concentrating photovoltaics thermal system. *Renewable and Sustainable Energy Reviews* 138, 110517. <https://doi.org/10.1016/j.rser.2020.110517>.

Alzahrani, M.M., Roy, A., Sundaram, S., Mallick, T.K., 2021c. Investigation of Thermal Stress Arising in a Graphene Neutral Density Filter for Concentrated Photovoltaic System. *Energies* 14, 3515. <https://doi.org/10.3390/en14123515>.

Azur Space Solar Power GMBH, 2014. Enhanced Fresnel Assembly - EFA Type: 3C42A – with 10x10mm² CPV TJ Solar Cell Application: Concentrating Photovoltaic (CPV) Modules 0–4.

Bruns, S., Vergöhl, M., Zickenrott, T., Bräuer, G., 2016. Deposition of abrasion resistant single films and antireflective coatings on sapphire. *Surface and Coatings Technology* 290, 10–15. <https://doi.org/10.1016/j.surfcoat.2015.11.011>.

Canavarro, D., Chaves, J., Collares-Pereira, M., 2013. New second-stage concentrators (XX SMS) for parabolic primaries; Comparison with conventional parabolic trough concentrators. *Solar Energy* 92, 98–105. <https://doi.org/10.1016/j.solener.2013.02.011>.

Chemisana, D., Vossier, A., Pujol, L., Perona, A., Dollet, A., 2011. Characterisation of Fresnel lens optical performances using an opal diffuser. *Energy Conversion and Management* 52, 658–663. <https://doi.org/10.1016/j.enconman.2010.07.044>.

Daneshzarian, R., Cuce, E., Cuce, P.M., Sher, F., 2018. Concentrating photovoltaic thermal (CPVT) collectors and systems: Theory, performance assessment and applications. *Renewable and Sustainable Energy Reviews* 81, 473–492. <https://doi.org/10.1016/j.rser.2017.08.013>.

Dreger, M., Wiesenfarth, M., Kisser, A., Schmid, T., Bett, A.W., 2014. Development and investigation of a CPV module with cassegrain mirror optics. *AIP Conference Proceedings* 1616, 177–182. <https://doi.org/10.1063/1.4897055>.

El-Gahouchi, M., Aziziyan, M.R., Arès, R., Boucherif, A., 2020. Optimised duplicated-junction solar cells: An innovative approach for energy harvesting at ultra-high concentrations. p. 020003. [10.1063/5.0032136](https://doi.org/10.1063/5.0032136).

Fernández, E.F., Almonacid, F., Rodrigo, P.M., Pérez-Higueras, P., 2017. *CPV Systems. McEvoy's Handbook Photovoltaic* 931–985.

Ferrer-Rodríguez, J.P., Fernández, E.F., Almonacid, F., Pérez-Higueras, P., 2016. Optical design of a 4-off-axis-unit Cassegrain ultra-high concentrator photovoltaics module with a central receiver. *Optics Letters* 41, 1985. <https://doi.org/10.1364/ol.41.001985>.

Fu, L., Leutz, R., Annen, H.P., 2010. Secondary optics for Fresnel lens solar concentrators, in: Winston, R., Gordon, J.M. (Eds.), *International Society for Optics and Photonics*. p. 778509. [10.1117/12.860438](https://doi.org/10.1117/12.860438).

Gordon, J.M., Feuermann, D., Young, P., 2008. Unfolded aplanats for high-concentration photovoltaics. *Optics Letters* 33, 1114. <https://doi.org/10.1364/OL.33.001114>.

Hornung, T., Steiner, M., Nitz, P., 2011. Estimation of the influence of Fresnel lens temperature on energy generation of a concentrator photovoltaic system. *AIP Conference Proceedings* 1407, 97–100. <https://doi.org/10.1063/1.3658303>.

Jing, L., Liu, H., Zhao, H., Lu, Z., Wu, H., Wang, H., Xu, J., 2012. Design of novel compound fresnel lens for high-performance photovoltaic concentrator. *International Journal of Photoenergy* 2012. <https://doi.org/10.1155/2012/630692>.

Leem, J.W., Yu, J.S., 2012. Superhydrophilic Sapphires for High- Performance Optics. *Optics Express* 20, 769–773.

Martínez Antón, J.C., Vázquez Moliní, D., Muñoz de Luna, J., Gómez Pedrero, J.A., Fernández-Balbuena, A.Á., 2011. Method for the characterization of Fresnel lens flux

- transfer performance. *Optical Fabrication, Testing, and Metrology IV* 8169, 81690E. <https://doi.org/10.1117/12.896870>.
- Miñano, J.C., Benítez, P., Zamora, P., Buljan, M., Moledano, R., Santamaría, A., 2013. Free-form optics for Fresnel-lens-based photovoltaic concentrators. *Optics Express* 21, A494. <https://doi.org/10.1364/oe.21.00a494>.
- Muñoz-Cerón, E., Miñano, J.C., Benítez, P., Almonacid, G., Buljan, M., 2012. On-site measurement of limiting subcell in multijunction solar devices. pp. 157–160. 10.1063/1.4753857.
- Newport Corporation, n.d. Neutral Density Filter Selection Guide [WWW Document]. URL <https://www.newport.com/g/neutral-density-filter-selection-guide> (accessed 3.1.20).
- Sansoni, P., Francini, F., Fontani, D., 2007. Optical characterisation of solar concentrator. *Optics and Lasers in Engineering* 45, 351–359. <https://doi.org/10.1016/j.optlaseng.2005.02.009>.
- Shanks, K., Ferrer-rodriguez, J.P., Fernández, E.F., Almonacid, F., 2018. A > 3000 suns high concentrator photovoltaic design based on multiple Fresnel lens primaries focusing to one central solar cell. *Solar Energy* 169, 457–467. <https://doi.org/10.1016/j.solener.2018.05.016>.
- Shanks, K., Senthilarasu, S., Mallick, T.K., 2016. Optics for concentrating photovoltaics: Trends, limits and opportunities for materials and design. *Renewable and Sustainable Energy Reviews* 60, 394–407. <https://doi.org/10.1016/j.rser.2016.01.089>.
- Sharaf, O.Z., Orhan, M.F., 2015. Concentrated photovoltaic thermal (CPVT) solar collector systems: Part I – Fundamentals, design considerations and current technologies. *Renewable and Sustainable Energy Reviews* 50, 1500–1565. <https://doi.org/10.1016/j.rser.2015.05.036>.
- Suns, U.L.C., Fernández, E.F., Seoane, N., Almonacid, F., García-loureiro, A.J., 2019. Vertical-Tunnel-Junction (VTJ) Solar Cell for 40, 2018–2021.
- Tang, R., Liu, X., 2011. Optical performance and design optimisation of V-trough concentrators for photovoltaic applications. *Solar Energy* 85, 2154–2166. <https://doi.org/10.1016/j.solener.2011.06.001>.
- Tang, R., Wang, J., 2013. A note on multiple reflections of radiation within CPCs and its effect on calculations of energy collection. *Renewable Energy* 57, 490–496. <https://doi.org/10.1016/j.renene.2013.02.010>.
- Tawalbeh, M., Al-Othman, A., Kafiah, F., Abdelsalam, E., Almomani, F., Alkasrawi, M., 2021. Environmental impacts of solar photovoltaic systems: A critical review of recent progress and future outlook. *Science of The Total Environment* 759, 143528. <https://doi.org/10.1016/j.scitotenv.2020.143528>.
- Valera, A., Fernández, E.F., Rodrigo, P.M., Almonacid, F., 2019. Feasibility of flat-plate heat-sinks using microscale solar cells up to 10,000 suns concentrations. *Solar Energy* 181, 361–371. <https://doi.org/10.1016/j.solener.2019.02.013>.
- Victoria, M., Askins, S., Herrero, R., Domínguez, C., Nuñez, R., Antón, I., Sala, G., 2016. Measuring primary lens efficiency: A proposal for standardisation. *AIP Conference Proceedings* 1766. <https://doi.org/10.1063/1.4962123>.
- Wang, H., Huang, J., Song, M., Hu, Y., Wang, Y., Lu, Z., 2018. Simulation and experimental study on the optical performance of a fixed-focus Fresnel lens solar concentrator using polar-axis tracking. *Energies* 11. <https://doi.org/10.3390/en11040887>.
- Wiesenfarth, M., Steiner, M., Wolf, J., Schmidt, T., Bett, A.W., 2014. Investigation of different fresnel lens designs and methods to determine the optical efficiency. *AIP Conference Proceedings* 1616, 97–101. <https://doi.org/10.1063/1.4897037>.
- Winston, R., Miñano, J.C., Benítez, P., 2005. APPLICATIONS TO SOLAR ENERGY CONCENTRATION, in: *Nonimaging Optics*. Elsevier 317–394. <https://doi.org/10.1016/B978-012759751-5/50013-0>.
- Wacom Electric Ltd , 2021. URL <https://wacom-ele.co.jp/en/> (accessed 7.1.21).

Prepared for Submission

Article 7. M. Alzahrani, W. Cameron, K. Shanks, S. Sundaram, T. Mallick,
"Experimentally validating the thermal performance of a Fresnel lens
in concentrator photovoltaic system." International Journal of Energy
Research.

Experimentally Validating the Thermal Performance of a Fresnel Lens in Concentrator Photovoltaic System

Prepared for

International Journal of Energy Research

Mussad M. Alzahrani ^{1,2}, William J. Cameron¹, Katie Shanks¹, Senthilarasu Sundaram¹, Tapas K. Mallick ^{1*}

¹Environmental and Sustainability Institute, University of Exeter, Penryn Campus, Cornwall TR10 9FE, UK.

²Mechanical and Energy Engineering Department, Imam Abdulrahman Bin Faisal University, Dammam, 34212, Saudi Arabia

*Corresponding author: Tapas K. Mallick

Tel: 01326 259465

Email: t.k.mallick@exeter.ac.uk

Abstract

A three-dimensional numerical model was established to investigate the optical and hence the thermal performance of a concentrated photovoltaic system based on a single Fresnel Lens design. This study is a preliminary study toward the more complicated full ultrahigh concentrated photovoltaics system based on 4- Fresnel lenses with two or three stages of subsequent optics [1]. This study meant to use the ray-tracing algorithm in COMSOL Multiphysics software for examining the concentrated photovoltaic system. The ray optical module results were validated theoretically/experimentally and the thermal model was validated experimentally. Optically, the results have shown a strong agreement between the theoretical optical efficiency and the simulative optical efficiency and between the effective optical concentration ratio and the simulative optical concentration ratio with a discrepancy of only 1% and 0.3%, respectively. Thermally, the difference between the simulative maximum temperature and the experimental maximum temperature in the focal spot results is only 2.18%. It has been ascertained that the conducted approach is reliable, and we can utilize to investigate other systems such as ultrahigh concentrated photovoltaic system [1], which require significant optical and thermal understanding before full-scale experimental testing. This conducted method indicated the expected working range temperature for the material/components in the prototype ultrahigh concentrated photovoltaic system, where mirror components need to be $\sim 52\text{ }^{\circ}\text{C}$, and the receiver should not exceed $130\text{ }^{\circ}\text{C}$.

Keywords: CPV, Optical, Thermal, COMSOL, Modelling Validation.

1 Introduction

Concentrated optics aims to increase solar irradiance intensity on a solar cell area for higher power output. The combination of achromatic Fresnel lens – Silicon on Glass (SOG) of 95% optical efficiency (Transmissivity) and 46% of four-junction solar cell allowed the concentrated photovoltaic (CPV) system to achieve 43% of solar cell conversion efficiency [2]. Fresnel lens's high optical efficiency and affordability make it a preferable selection in CPV systems [3]. However, increasing the concentration ratio results in inducing the temperature to a level at which the electrical performance is degraded. The state-of-the-art multi-junction solar cells exhibit a drop in cell efficiency for concentrations above

a value due to resistive losses. As a result, cooling arrangements are necessary for the CPV system for consistent solar efficiency performance. A future solar cell structural design has been examined for energy-yielding in the ultrahigh concentration range. Fernández et al. [4] developed a Vertical-tunnel-junction (VTJ) solar cell that showed a decline in cell efficiency by 28.4% with a concentration ratio reaching 15,000 suns. El-Gahouchi et al. [5] manufactured duplicated junction solar cell architectures that can deliver electrical power with 33% of cell efficiency at 3,500 suns and 28% of cell efficiency out with 10,000 suns.

As a post-illumination heat extraction technique, the thermal performance in a CPV system and the arrangements of cooling mechanisms (passive or active,) accordingly with the concentration ratio have been investigated in multiple studies [6–9]. Thermal models were developed to study the limits of the cell temperature with no heatsink for a $3 \times 3 \text{ mm}^2$ multijunction solar cell (MJSC) [10]. Further studies investigated the concentration ratio limits of passive cooling mechanisms for different sizes of solar cells [10,11]. Two papers recently studied a different configuration of passive cooling mechanism for concentration ratio up to 10,000 suns and more [12,13]. These studies showed that the passive cooling mechanism still can maintain the operating temperature for the solar cell in a safe range. The active cooling mechanism has proven its competence in solar cell thermal management. All the conducted studies using COMSOL Multiphysics software define the generated heat on the solar cell due to the concentration ratio as a “boundary heat source” terms in the heat transfer balance equation [14–19] instead of ray optics model derived from Geometrical Optics physics module.

In this study, an optical and thermal numerical model is established using COMSOL Multiphysics software and carried out using a bidirectional coupled ray-tracing study approach. The optical model was established to operate a concentrated photovoltaic system based on a Fresnel lens as primary optical components toward multiple optics in one CPV system to achieve an ultrahigh concentration ratio [1]. Then, the generated heat on the receiver area as an output from the optical model will be interlinked with the heat transfer in the solid model as a heat boundary source term. The direct normal irradiance (DNI) in the range of $400 - 1000 \frac{\text{W}}{\text{m}^2}$ has been investigated optically, and its effective concentration influence thermally. The optical model results have been validated

theoretically and experimentally, where the thermal model results have been validated experimentally to ensure that conducted numerical approach is reliable.

2 CPV Design Aspects

Before experimentation, a numerical understanding of a CPV system is necessary to determine the type and size of the used solar cell based on the generated focal spot or line area. The ray-tracing analysis meant to examine the optical path based on the succession of optics within a CPV system and determine the focal area and its irradiance distribution. In addition, ray tracing helps to figure out both optical efficiency and optical concentration ratio. The heat transfer analysis determines the temperature operating range on the solar cell surface area and the optics. The temperature level helps to design and plan for the deployed cooling mechanism for the safe operating temperature of the solar cell below 80°C [20]. In the numerical study, the temperature operating range is influenced by the geographical location in terms of DNI and climate conditions.

3 Numerical Model

3.1 Optical Model

The optical model is calculated by the analogous to the Hamiltonian formulation in classical mechanics [21], which is a set of differential equations describing the trajectories of rays in terms of ray position $q(t)(m)$ and wave vector $k(t)(\frac{rad}{m})$. The angular frequency $(\omega) (\frac{rad}{s})$ substitute a place usually taken by the Hamiltonian (H) in the right-hand side of the Equations (1) and (2), which is the gradient of the angular frequency with respect to the vectors $q(t)$ and $k(t)$.

$$\frac{dq}{dt} = \frac{\partial \omega}{\partial k} \quad (1)$$

$$\frac{dk}{dt} = - \frac{\partial \omega}{\partial q} \quad (2)$$

In the isotropic medium, when the refractive index is homogenous, the Hamiltonian formulation as in Equation (1) and (2) is rewritten to only account for the constant speed and ray direction of light as in Equations (3) and (4).

$$\frac{dq}{dt} = \frac{c k}{n |k|} \quad (3)$$

$$\frac{dk}{dt} = 0 \quad (4)$$

where c is the speed of light ($c = 2.99792458 \times 10^8 \frac{m}{s}$), and n (dimensionless) is the refractive index.

When the inhomogeneous refractive index at the optical interface is accounted for, the direction of the refracted ray is calculated relying on Snell's law, as in Equation (5).

$$n_1 \sin(\theta_1) = n_2 \sin(\theta_2) \quad (5)$$

Where θ_1 and θ_2 denotes the angle of incidence and refraction, respectively.

The optical model performed Snell's law and the law of reflection between different optical interfaces based on the deterministic ray splitting approach.

The deposited ray power sub-node calculates the energy of concentrated rays that arrives on a surface relying on the incident ray's power based on Equation (6).

$$Q_s = \frac{1}{A_i} \sum Q_j \quad (6)$$

Where Q_s is the boundary heat flux ($\frac{W}{m^2}$), A_i is the receiver surface area (m^2), $\sum Q_j$ is the sum of rays depositing power into the receiver (W).

3.2 Thermal Model

In the thermal model, the heat transfer rate on the receiver area is governed based on the energy conservation equation for the steady-state condition, as in Equation (7). The heat source term (Q_s) is based on Equation (6) calculated in the optical model.

$$Q_s + Q_{conv.} + Q_{rad.} = Q_{cond.} \quad (7)$$

$Q_{cond.}$, $Q_{conv.}$, and $Q_{rad.}$ is the conduction heat transfer, the convection heat transfer, and the radiation heat transfer, respectively.

The amount of Q_{cond} through a domain is based on Fourier's law, where the conduction is proportional to the temperature gradient (ΔT) ($^{\circ}\text{C}$) relying on the thermal conductivity (k) ($\frac{\text{W}}{\text{m.K}}$) and the geometry thickness L (m), as in Equation 8.

$$Q_{\text{cond.}} = \nabla \left(-\frac{L}{k} \nabla T \right) \quad (8)$$

The operator (∇) identifies the conduction heat transfer in three dimensions (x, y, z). The material thermal resistance ($\frac{L}{k}$) affect the heat transfer rate with inverse correlation with the thermal conductivity.

The convective heat transfer $Q_{\text{conv.}}$ is influenced by both the wind speeds and the ambient temperature. Newton's law of cooling computes the $Q_{\text{conv.}}$ considering both the ambient temperature (T_a) and convective heat transfer coefficient (h), as in Equation (9).

$$Q_{\text{conv.}} = \nabla (h \nabla T) \quad (9)$$

Where the ΔT is between the receiver surface temperature and T_a .

Due to the concentrated solar flux on the receiver surface area, the temperature level stimulates the heat transfer in the process of electromagnetic waves. $Q_{\text{rad.}}$ is computed by Stefan-Boltzmann's law and is firmly proportional to the temperature of the emitting domain, as in Equation (10).

$$Q_{\text{rad.}} = \varepsilon \sigma (T_s^4 - T_{\text{sur.}}^4) \quad (10)$$

Where σ is the Stefan-Boltzmann constant ($5.67 \times 10^{-8} \frac{\text{W}}{\text{m}^2.\text{K}^4}$), ε is the receiver emissivity, T_s is the receiver surface temperature, and $T_{\text{sur.}}$ is the surrounding temperature.

4 Boundary Conditions

The numerical model was carried out using the "Geometrical Optic" and the "Heat Transfer in Solid" models to compute the system optically and hance thermally based on the "bidirectional coupled ray tracing".

Optically, the Fresnel lens was applied as an illuminated surface with a transmittance of 90%, and the copper plate was set up as a freezing surface with a "Ray Deposited Power" sub-node. The optical dispersion of the system surrounding domain held constant at 20 °C. The Fresnel lens design is build using SOLIDWORKS software to produce a focal length of 42 cm as in [22]. Thermally, all domains are subjected to a convective heat transfer coefficient of $10 \frac{W}{m^2.K}$ and ambient temperature of 20 °C. The thermal emissivity considered as 0.9 for the copper plate. The copper plate was also assigned as a boundary heat source relying on the "Ray Deposited Power" sub-node, which is calculated in the "Geometrical Optic" model. In the optical model, the optical dispersion for the SOG Fresnel lens and the chromatic aberration assumed to be negligible. The defined position for the Fresnel and the copper sheet with its geometry is shown in Figure 1a, where the optical and thermal boundary conditions are illustrated in Figure 1b.

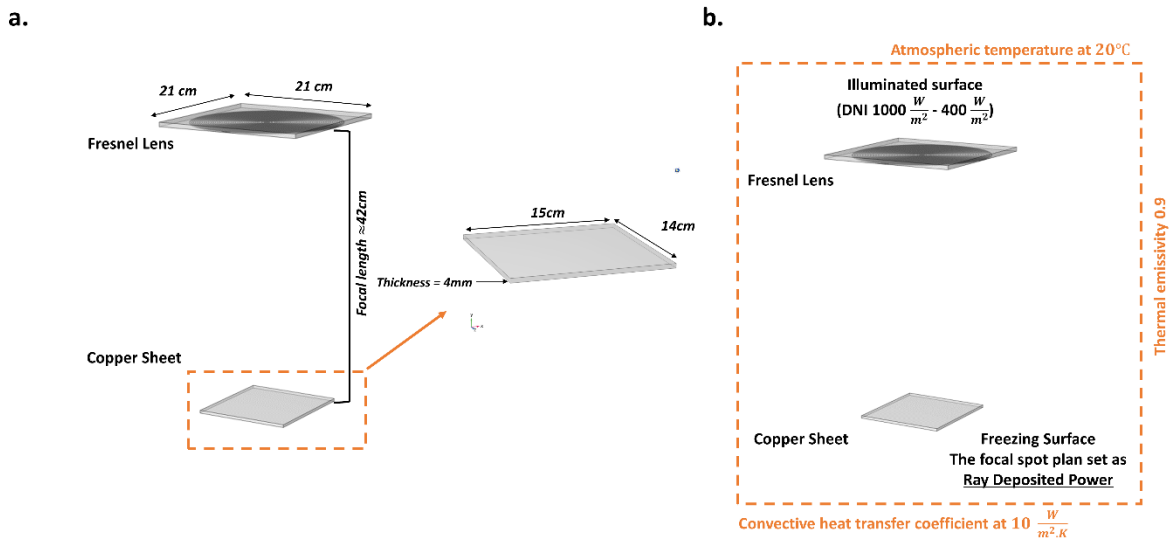


Figure 1 The asymmetric view for only the primary optic with the copper plate as a receiver where a. is the detailed geometry and b. is the optical and thermal boundary conditions.

5 Modelling Results

The ray tracing in COMSOL Multiphysics software is an approximate solution based on the finite element mesh. Consequently, the reliability of the solution depends on the mesh refinement. All boundaries that refract/reflect the rays must have a boundary mesh partitioned into small units to minimise the

discretisation errors. As a result, the receiver was analysed using finite element modelling to confirm accuracy in the results.

The results of the ray tracing can be exhibited as ray trajectories which show the ray in 3d initiated from the illuminated surface and absorbed at the freezing surface within 1.34×10^{-8} s. The modelled Fresnel lens resulted in an optical path (focal length of 42 cm), as in Figure 2.

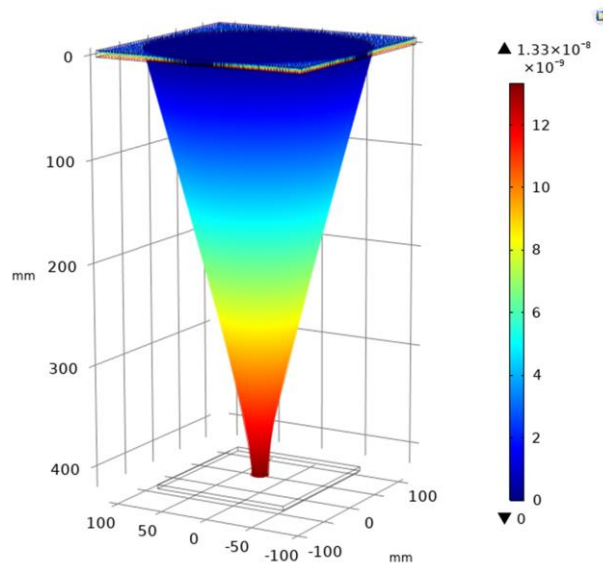


Figure 2 The ray trajectory plot for a focal length of 42 cm.

The established model predicted the maximum boundary heat source (simulative optical concentration ratio($C_{opt,sim}$)) on the copper plate with DNI ranging from $400 \frac{W}{m^2}$ to $1000 \frac{W}{m^2}$ in an interval of $100 \frac{W}{m^2}$. At $1000 \frac{W}{m^2}$, the result showed that the boundary heat source found to be $0.6 \frac{W}{mm^2}$, which is equivalent to 600 suns assuming 1 sun is $1000 \frac{W}{m^2}$. At $400 \frac{W}{m^2}$, the result showed that the boundary heat source found to be $0.24 \frac{W}{mm^2}$ (equivalent to 240 suns). The change in the DNI from $1000 \frac{W}{m^2}$ to $400 \frac{W}{m^2}$ showed a drop in the simulative optical concentration ratio by 60% (359 suns). The optical model resulted in a focal spot that is relatively uniformed with a diameter of 10 mm. The rest of the predicted results are shown for the produced focal spot on the copper surface for the simulative optical concentration ratio, as in Figure 3.

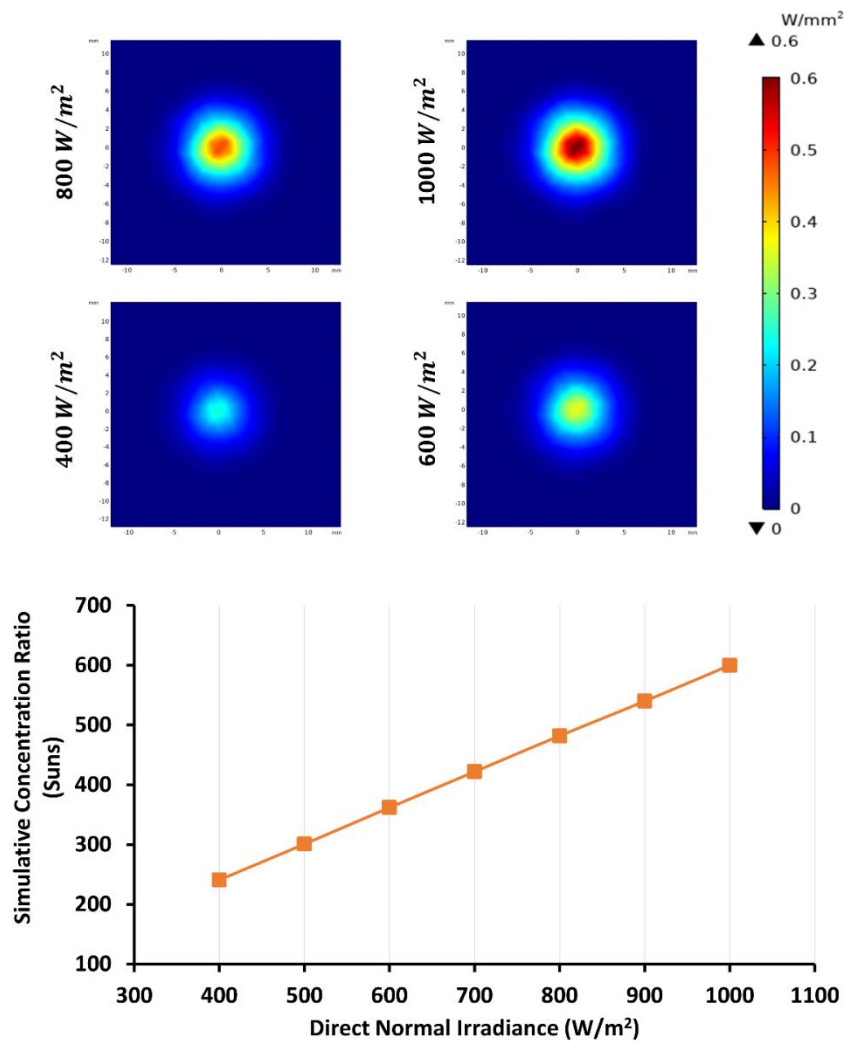


Figure 3 Shows the simulative optical concentration with DNI ranging from $400 \frac{W}{m^2}$ to $1000 \frac{W}{m^2}$ with four screenshots for the optical model generated from COMSOL to show also the optical irradiance distribution across the focal spot area at $400 \frac{W}{m^2}$, $600 \frac{W}{m^2}$, $800 \frac{W}{m^2}$, and $1000 \frac{W}{m^2}$.

Based on the bidirectionally coupled ray-tracing study approach, the thermal model calculated to predict the maximum temperature in the focal spot for DNI ranging from $400 \frac{W}{m^2}$ to $1000 \frac{W}{m^2}$ in an interval of $100 \frac{W}{m^2}$. The heat transfer in solid model predicted the temperature to be $61.7^\circ C$ and $37.2^\circ C$ at DNI of $1000 \frac{W}{m^2}$ and $400 \frac{W}{m^2}$, respectively. The temperature decreased with DNI from $1000 \frac{W}{m^2}$ to $400 \frac{W}{m^2}$ by 40% ($24.5^\circ C$). The screenshot for the temperature shows a homogeneous distribution across the focal spot, as in Figure 4.

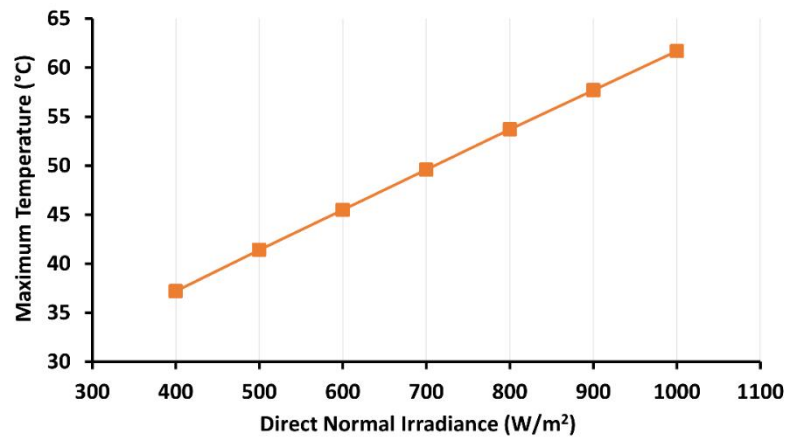
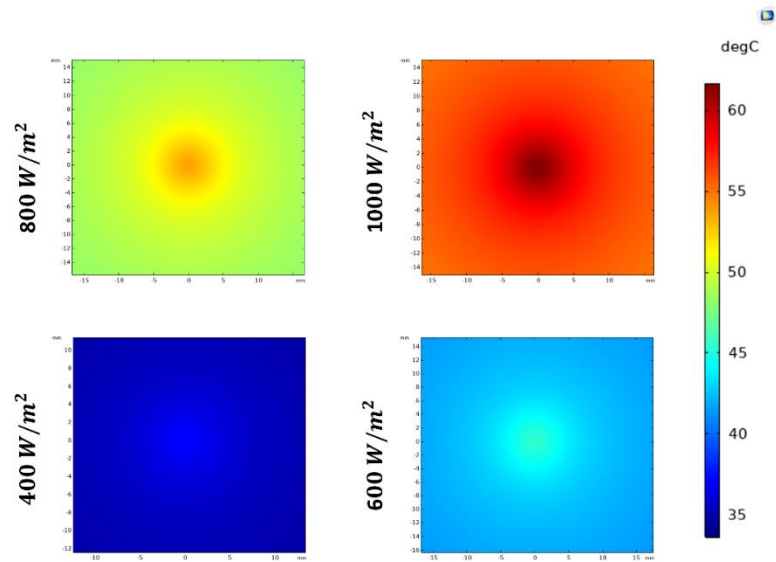


Figure 4 Shows the maximum temperature with DNI ranging from $400 \frac{W}{m^2}$ to $1000 \frac{W}{m^2}$ with four screenshots for the temperature in the focal spot area generated from COMSOL to show also the temperature distribution across the focal spot area at $400 \frac{W}{m^2}$, $600 \frac{W}{m^2}$, $800 \frac{W}{m^2}$, and $1000 \frac{W}{m^2}$.

6 Validation for the Optical and Thermal Model

To verify the reliability of the computational analysis model estimating the optical and thermal performance of the Fresnel Lens, two approaches were carried out for validation; one is a combined theoretical/experimental validation for the optical model results, and the other is experimental for the thermal model results.

An experimental thermal setup was established based on refractive optic [SOG- Fresnel lens] of 441 cm^2 aperture area, which is exposed to a constant solar irradiance of $1000 \frac{\text{W}}{\text{m}^2}$. A WACOM AAA rating and 2% spatial non-uniformity solar simulator combined both the Xenon short-arc lamp and an optical filter to reproduce a continuous solar irradiance at AM1.5 was utilized [23]. The refractive optic was vertically adjusted normal to the collimator lens of the solar simulator to perform the optimum focal length of 42 cm. At this focal length, the optimum focal spot of $\approx 1.5 \text{ cm}$ in diameter is generated on 210 cm^2 ($14 \text{ cm} \times 15 \text{ cm}$) copper surface area at which the maximum concentration ratio is achieved. The copper plate was adjusted to centre the focal spot on its plain. The temperature is measured and acquired utilizing a Datalogger SDL200 - EXTECH INSTRUMENTS. Three thermocouples were placed in the focal spot domain to gather the maximum measured temperatures and then average them for the measurement certainties, as illustrated in Figure 5.

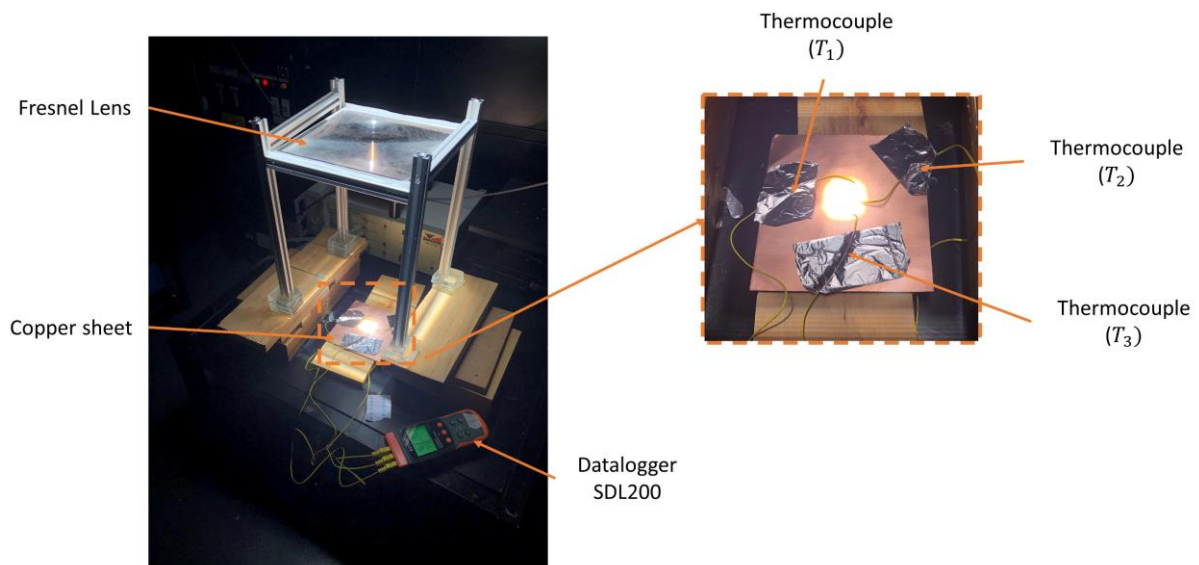


Figure 5 The experimental setup with a magnified copper plate to illustrate the thermocouple positions.

6.1 Theoretical/Experimental Optical Validation

To theoretically characterize the performance of a CPV system based on a Fresnel Lens design, we need to solve for the theoretical optical efficiency at different DNI ranging from $400 \frac{W}{m^2}$ – $1000 \frac{W}{m^2}$ in an interval of $100 \frac{W}{m^2}$. To do so, we need to consider the focal spot area that is generated from the optical model, which is 65.47 mm^2 , to find the geometrical concentration ratio (C_{geo}). C_{geo} being the area of the Fresnel lens ($A_{\text{Fresnel}} = 0.0441 \text{ m}^2$) to the area of the focal spot (A_{focal}). The optical efficiency of the Fresnel lens (transmissivity)(η_{Fresnel}) of $\sim 90\%$ (transmittance spectra measured via spectrophotometry) needs to be associated in the calculation [22]. Therefore, the theoretical optical efficiency ($\eta_{\text{opt,theo}}$) is calculated as in Equation (11)

$$\eta_{\text{opt,theo}} = \frac{(\text{DNI} \times A_{\text{Focal}}) \times \eta_{\text{Fresnel}} \times C_{\text{geo}}}{(\text{DNI} \times A_{\text{Fresnel}})} \quad (11)$$

Afterwards, the theoretical optical concentration ratio ($C_{\text{opt,theo}}$) is found in Equation (12).

$$C_{\text{opt,theo}} = \frac{\eta_{\text{opt,theo}} \times C_{\text{geo}} \times \text{DNI}}{1000} \quad (12)$$

As a result, $\eta_{\text{opt,theo}}$ is found to be 89.64% where $\eta_{\text{opt,sim}}$ is found to be 89.08% with a discrepancy of 1%. The $C_{\text{opt,theo}}$ showed a result of 604 suns, 543 suns, 483 suns, 423 suns, 362 suns, 301 suns, and 242 suns for DNI ranging from $1000 \frac{W}{m^2}$ to $400 \frac{W}{m^2}$ in an interval of $100 \frac{W}{m^2}$. The results of $C_{\text{opt,theo}}$ and $C_{\text{opt,sim}}$ per the input power to the Fresnel Lens is shown in Figure 6 for comparison. The discrepancy of optical concentration between $C_{\text{opt,theo}}$ and $C_{\text{opt,sim}}$ is only 0.3% on average, reflecting a strong agreement in the results.

As an example, a $10 \times 10 \text{ mm}^2$ multi-junction solar cell with base material of GaInP/GaInAs/Ge on Ge substrates manufactured by Azurspace was unitized to understand the electrical performance optically [24]. The multi-junction solar cell was placed in the focal spot zone and maintained in temperature at $25 \text{ }^\circ\text{C}$ using a cooling mount, similar to the conducted experimental approach in [25]. To figure out the effective concentration ratio ($C_{\text{opt,eff}}$) (suns), the impact of the solar intensity on MJSC in terms of short circuit current ($I_{\text{sc,conc.}}$) to the short circuit

current ($I_{sc,1\ sun}$) value at the reference intensity of 1 sun equivalent to $1000 \frac{W}{m^2}$ of solar irradiance, as in Equation (13).

$$C_{opt,eff} = \frac{I_{sc,conc}}{I_{sc,1\ sun}} \quad (13)$$

To validate the $C_{opt,sim}$ to the $C_{opt,eff}$, the simulation results must consider the collimating angle of irradiance for the WACOM solar simulator, which is 1.43° , and then account for the measured cell efficiency (η_{cell}) under the concentrated sun rays, which is found to be 33.5% on average.

The divergence of optical concentration between $C_{opt,eff}$ and $C_{opt,sim}$ is found to be 1.1% on average at 1.43° convergence angle, indicating a stable matching between the simulation and the experimental measurements. However, we can observe a drop in the optical concentration ratio at a convergence angle of 1.43° in comparison to the one at 0.27° because the large collimating angle results in a wider focal spot than the solar cell area where longer sun rays are lost.

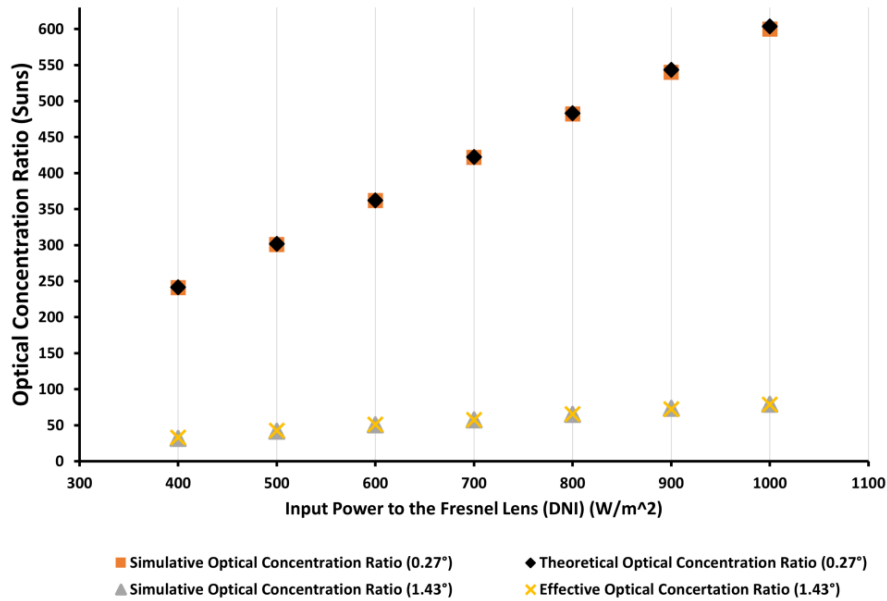


Figure 6 Shows the discrepancy between the simulative and theoretical optical concentration ratio with DNI arranging from 400 W/m^2 to 1000 W/m^2 in accordance with the input power to the Fresnel lens.

6.2 Experimental Validation for the Thermal Model

To measure the maximum temperature, the solar simulator illuminates the Fresnel lens, which concentrates solar irradiance to produce a focal spot on a copper plate. The focal spot temperature achieves saturation - witnessing no build-up in temperature - within a short time of 20 s. The temperature on the copper plate starts fluctuating with a minimized range around its saturation level. After the temperature reaches its saturation level, the temperature measurement is logged for a time interval of 5 minutes. Then, the logged data is averaged among the thermocouples (T_1 , T_2 , and T_3) and over the time (t) of 5 minutes, as in Equation 13.

$$T_{\text{max,average}} = \frac{\sum \left[\frac{T_1 + T_2 + T_3}{3} \right]}{\frac{\text{No. of logged data}}{t}} \quad (13)$$

The simulated maximum temperature using COMSOL Multiphysics software and measured maximum temperature are in good agreement with an average discrepancy of 2.18%, as in Figure 7.

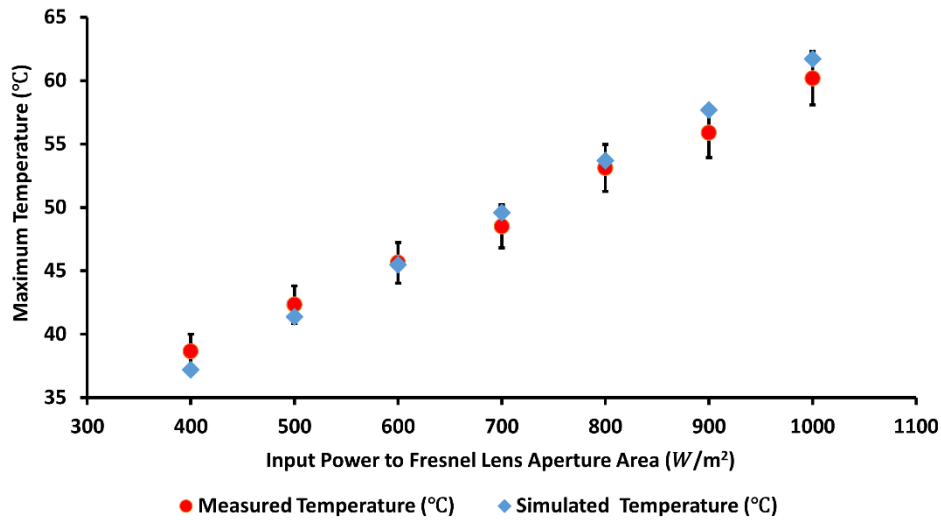


Figure 7 Validation for the predicted maximum temperature to the measured maximum temperature

6.3 The potential Temperature for $\frac{1}{4}$ of the Ultrahigh Concentrated Photovoltaic System

To prepare for the ultrahigh concentrated photovoltaic (UHCPV) system design, the temperature needs to be predicted to plan for the selected optical materials and sizing/configuring the associated cooling mechanism. The accumulation of temperature in the ultrahigh concentration range is harmful and could not only damage the receiver solar cells and their materials but any secondary or tertiary optics in between. Thus, the investigated model has been extended to account for the angular secondary mirror reflecting light into a flat central mirror and then into the final stage, which is the receiver to predicate the temperature on the optical stages and then on the final central receiver [1]. All the consecutive optics to the Fresnel lens has been selected as an aluminium material with keeping the same boundary condition as before. This section shows only the preliminary temperature level at an ambient temperature of 50°C and 20°C with keeping the convective heat transfer coefficient at 10 W/m².K where the detailed numerical investigation will follow up in a separate paper for the full UHCPV system. Figure 8 shows the temperature stratification on the consecutive optical surfaces for a $\frac{1}{4}$ of the system at an ambient temperature of a. 50 °C and b. 20 °C. Also, the temperature distribution is influenced by the angular orientation of the secondary optical stage, and that can be observed through the focal spot image reflective optics and the final receiver stages.

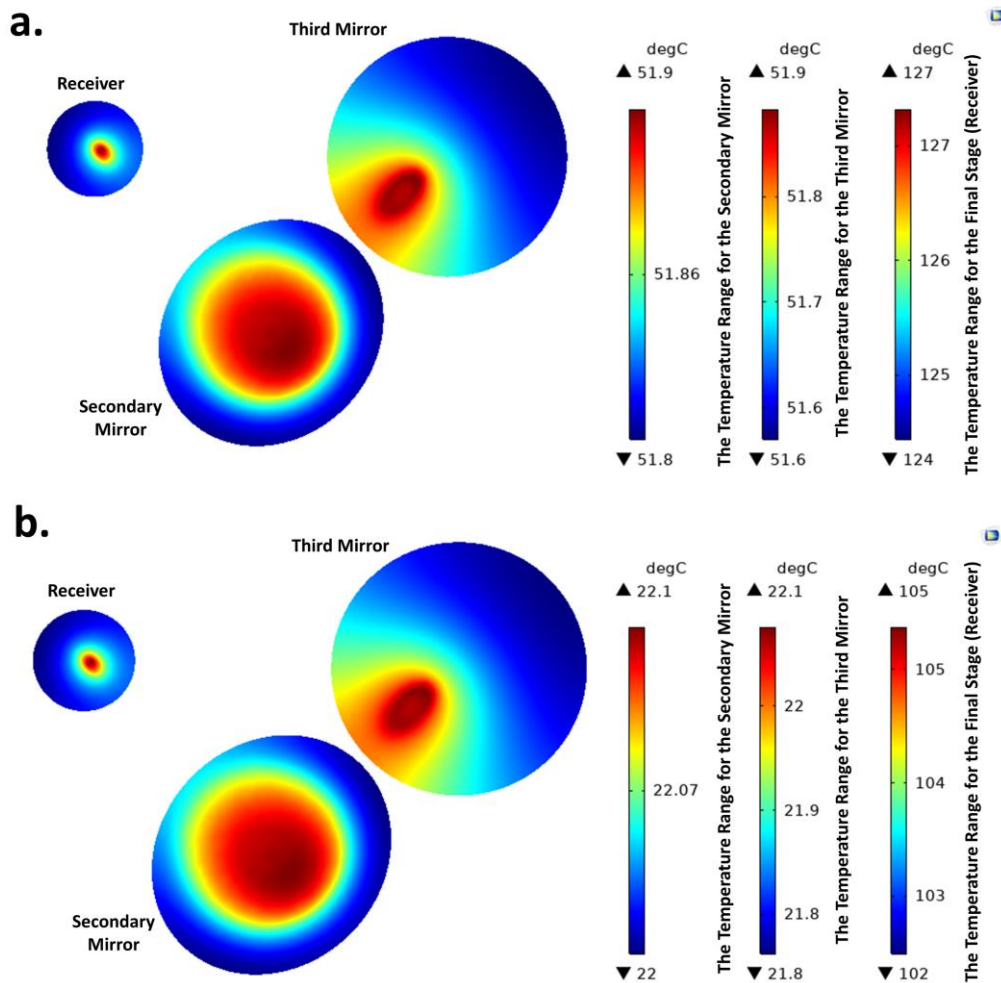


Figure 8 The temperature distribution on the reflective optics and the receiver at a. 50 °C and b. 20 °C and convective heat transfer coefficient of 10 W/m². K.

Figure 8 shows that the maximum estimated temperature conditions for the secondary mirror, third mirror and receiver are ~52, 52 and 130 °C. Hence for the experimental set-up of the full ultrahigh system, the materials chosen for these components should be stable within these temperatures ranges. If they are below these temperatures but above that presented in Figure 8 b then perhaps ambient temperature control will allow safe experimental testing if needed.

7 Performance Analogues and Discussion

The common approach to predicate the thermal performance numerically of a solar system either in flat PV panel or CPV system is through “Heat Transfer in Solids” physics in COMSOL Multiphysics software. In this approach, the heat source term in the heat transfer balance equation is defined as a physical node called “Boundary Heat Source” for a surface area or “heat source” for volume area. The heat source terms need to be interlinked into a domain within the solar

assembly where photogeneration is induced (semiconductor layer). Simply, all the photon energy within the bandgap energy of the semiconductor materials will be absorbed, and the rest generates thermal energy losses (thermalization intrinsic loss). The boundary heat source is generally calculated in unit (W/m^2) based on Equation (14) [11,26,27].

$$Q_s = \text{DNI} \times \eta_{\text{optical}} \times C_{\text{geo}} (1 - \eta_{\text{cell}}) \quad (14)$$

Where η_{optical} stands for the optical efficiency and η_{cell} stands for the electrical efficiency of the solar cell.

Performing a thermal numerical study based on this approach is less complicated and requires less time computational to predict the performance. However, this approach assumes completely uniform irradiance distribution over the cell surface area, which is not the case, especially for the fixed flat PV panel or CPV system for either point or focal line concentration. To overcome this issue, the ray-tracing model is computed in optical-based software (such as Zmax, ASPA, and APEX) and then imported into COMSOL Multiphysics software as an interpolation function to be incorporated with Equation (14).

This hassle can be easily avoided by using the ray optics model in COMSOL Multiphysics software, where its result can be interlinked with the heat transfer model to predict the thermal performance. Through the ray optics model, the optical concentration ratio is computed relying on the geometrical optics (system design). The instantaneous ray trajectory computation exhibits the solar irradiance distribution on a receiver surface area where helps to define the needed size of a solar cell. In contrast, the numerical study based only on the heat transfer on solid model assumed that the area of the focal spot is similar to the area of the solar cell and the heat distribution is homogenous across the solar cell area. This approach is still challenged by the selection of the mesh node size, where the optical result is significantly influenced. The computational time is another challenge only when the optical model is coupled with the thermal model to predict the performance optically and thermally.

8 Conclusion

A numerical model was built to investigate a CPV system based on a Fresnel Lens design optically and hence thermally. The model resulted in optical

efficiency of 89.08%, an optical concentration ratio ranging from 600 suns to 240 suns and a maximum focal spot temperature ranging from 61.7 °C and 37.2 °C corresponding to DNI ranging from $1000 \frac{W}{m^2}$ to $400 \frac{W}{m^2}$. This modelling result validated experimentally in both the optical and the thermal model. Theoretically, the optical analysis showed an effective concentration ratio ranging from 604 suns to 242 suns, where experimentally an effective concentration ratio was ranging between 79 suns to 32 suns in accordance with DNI $1000 \frac{W}{m^2}$ to $400 \frac{W}{m^2}$. Thermally, the experimental results showed a maximum temperature in the focal spot ranging from 60.2 °C and 38.67 °C corresponding to DNI ranging from $1000 \frac{W}{m^2}$ to $400 \frac{W}{m^2}$. The validation shows a strong agreement in the modelling results. The reliability of COMOSL software to numerically investigate a much-complicated CPV system or a UHCPV with multiple optical stages has been ascertained. This COMSOL Multiphysics software method signified the working temperature range for the UHCPV system, which is needed for material/components selection.

Acknowledgement

Mr Mussad Alzahrani would like to duly acknowledge the financial support from the Saudi Arabia Culture Bureau in the United Kingdom.

References

- [1] Shanks K, Ferrer-rodriguez JP, Fernández EF, Almonacid F. A > 3000 suns high concentrator photovoltaic design based on multiple Fresnel lens primaries focusing to one central solar cell. *Solar Energy* 2018;169:457–67. <https://doi.org/10.1016/j.solener.2018.05.016>.
- [2] Steiner M, Siefer G, Schmidt T, Wiesenfarth M, Dimroth F, Bett AW. 43% Sunlight to Electricity Conversion Efficiency Using CPV. *IEEE Journal of Photovoltaics* 2016;6:1020–4. <https://doi.org/10.1109/JPHOTOV.2016.2551460>.
- [3] Wiesenfarth M, Steiner M, Wolf J, Schmidt T, Bett AW. Investigation of different fresnel lens designs and methods to determine the optical efficiency. *AIP Conference Proceedings* 2014;1616:97–101. <https://doi.org/10.1063/1.4897037>.
- [4] Suns ULC, Fernández EF, Seoane N, Almonacid F, García-loureiro AJ. Vertical-Tunnel-Junction (VTJ) Solar Cell for 2019;40:2018–21.
- [5] El-Gahouchi M, Aziziyani MR, Arès R, Boucherif A. Optimized duplicated-junction solar cells: An innovative approach for energy harvesting at ultra-high concentrations, 2020, p. 020003. <https://doi.org/10.1063/5.0032136>.
- [6] Abo-Zahhad EM, Ookawara S, Radwan A, El-Shazly AH, El-Kady MF, Esmail MFC. Performance, limits, and thermal stress analysis of high concentrator multijunction solar cell under passive cooling conditions. *Applied Thermal Engineering* 2020;164:114497. <https://doi.org/10.1016/j.applthermaleng.2019.114497>.
- [7] Hu H, Yuan D, Wang T, Jiang Y. Dynamic performance of high concentration photovoltaic/thermal system with air temperature and humidity regulation system (HCPVTH). *Applied Thermal Engineering* 2019;146:577–87. <https://doi.org/10.1016/j.applthermaleng.2018.10.028>.
- [8] Dwivedi P, Sudhakar K, Soni A, Solomin E, Kirpichnikova I. Advanced cooling techniques of P.V. modules: A state of art. *Case Studies in Thermal Engineering* 2020;21:100674. <https://doi.org/10.1016/j.csite.2020.100674>.
- [9] Ali HM. Recent advancements in PV cooling and efficiency enhancement integrating phase change materials based systems – A comprehensive review. *Solar Energy* 2020;197:163–98. <https://doi.org/10.1016/j.solener.2019.11.075>.
- [10] Min C, Nuofu C, Xiaoli Y, Yu W, Yiming B, Xingwang Z. Thermal analysis and test for single concentrator solar cells. *Journal of Semiconductors* 2009;30:044011. <https://doi.org/10.1088/1674-4926/30/4/044011>.
- [11] Alzahrani M, Baig H, Shanks K, Mallick T. Estimation of the performance limits of a concentrator solar cell coupled with a micro heat sink based on a finite element simulation. *Applied Thermal Engineering* 2020;176:115315. <https://doi.org/10.1016/j.applthermaleng.2020.115315>.
- [12] AlFalah G, Maatallah TS, Alzahrani M, Al-Amri FG. Optimization and feasibility analysis of a microscale pin-fins heat sink of an <scp>ultrahigh</scp> concentrating photovoltaic system. *International*

Journal of Energy Research 2020;44:11852–71.
<https://doi.org/10.1002/er.5826>.

- [13] Valera A, Fernández EF, Rodrigo PM, Almonacid F. Feasibility of flat-plate heat-sinks using microscale solar cells up to 10,000 suns concentrations. *Solar Energy* 2019;181:361–71.
<https://doi.org/10.1016/j.solener.2019.02.013>.
- [14] Micheli L, Sarmah N, Luo X, Reddy KS, Mallick TK. Design of a 16-cell densely-packed receiver for high concentrating photovoltaic applications. *Energy Procedia* 2014;54:185–98.
<https://doi.org/10.1016/j.egypro.2014.07.262>.
- [15] Micheli L, Reddy KS, Mallick TK. Plate micro-fins in natural convection: An opportunity for passive concentrating photovoltaic cooling. *Energy Procedia* 2015;82:301–8. <https://doi.org/10.1016/j.egypro.2015.12.037>.
- [16] Micheli L, Sarmah N, Fernandez EF, Reddy KS, Mallick TK. Technical issues and challenges in the fabrication of a 144-Cell 500x Concentrating Photovoltaic receiver. 2014 IEEE 40th Photovoltaic Specialist Conference, PVSC 2014 2014:2921–5.
<https://doi.org/10.1109/PVSC.2014.6925543>.
- [17] Micheli L, Senthilarasu S, Reddy KS, Mallick TK. Applicability of silicon micro-finned heat sinks for 500x concentrating photovoltaics systems. *Journal of Materials Science* 2015;50:5378–88.
<https://doi.org/10.1007/s10853-015-9065-2>.
- [18] Micheli L, Fernandez EF, Almonacid F, Reddy KS, Mallick TK. Enhancing ultra-high CPV passive cooling using least-material finned heat sinks. *AIP Conference Proceedings* 2015;1679. <https://doi.org/10.1063/1.4931563>.
- [19] Ahmed A, Zhang G, Shanks K, Sundaram S, Ding Y, Mallick T. Performance evaluation of single multi-junction solar cell for high concentrator photovoltaics using minichannel heat sink with nanofluids. *Applied Thermal Engineering* 2021;182:115868.
<https://doi.org/10.1016/j.applthermaleng.2020.115868>.
- [20] Alzahrani M, Roy A, Shanks K, Sundaram S, Mallick TK. Graphene as a pre-illumination cooling approach for a concentrator photovoltaic (CPV) system. *Solar Energy Materials and Solar Cells* 2021;222:110922.
<https://doi.org/10.1016/j.solmat.2020.110922>.
- [21] Tawalbeh M, Al-Othman A, Kafiah F, Abdelsalam E, Almomani F, Alkasrawi M. Environmental impacts of solar photovoltaic systems: A critical review of recent progress and future outlook. *Science of The Total Environment* 2021;759:143528.
<https://doi.org/10.1016/j.scitotenv.2020.143528>.
- [22] Alzahrani M, Ahmed A, Shanks K, Sundaram S, Mallick T. Optical losses and durability of flawed Fresnel lenses for concentrated photovoltaic application. *Materials Letters* 2020;275:128145.
<https://doi.org/10.1016/j.matlet.2020.128145>.
- [23] WACOM ELECTRIC LTD 2021. <https://wacom-ele.co.jp/en/> (accessed July 1, 2021).

- [24] Azur Space Solar Power GMBH. Enhanced Fresnel Assembly - EFA Type: 3C42A – with 10x10mm² CPV TJ Solar Cell Application: Concentrating Photovoltaic (CPV) Modules 2014:0–4.
- [25] Alzahrani M, Ahmed A, Shanks K, Sundaram S, Mallick T. Optical component analysis for ultrahigh concentrated photovoltaic system (UHCPV). *Solar Energy* 2021;227:321–33. <https://doi.org/10.1016/j.solener.2021.09.019>.
- [26] Ahmed A, Shanks K, Sundaram S, Mallick T. Energy and exergy analyses of new cooling schemes based on a serpentine configuration for a high concentrator photovoltaic system. *Applied Thermal Engineering* 2021;199:117528. <https://doi.org/10.1016/j.applthermaleng.2021.117528>.
- [27] Y.M. Ali A, M. Abo-Zahhad E, Elqady HI, Rabie M, Elkady MF, Ookawara S, et al. Thermal analysis of high concentrator photovoltaic module using convergent-divergent microchannel heat sink design. *Applied Thermal Engineering* 2021;183:116201. <https://doi.org/10.1016/j.applthermaleng.2020.116201>.

Article 8. M. Alzahrani, W. Cameron, K. Shanks, S. Sundaram, T. Mallick,
"Optothermal Numerical Investigation on an Ultrahigh Concentrated
Photovoltaics System (UHCPV)." Prepared to be submitted for Solar
Energy Journal.

Optothermal Numerical Investigation on an Ultrahigh Concentrated Photovoltaics System (UHCPV)

Prepared for

Solar Energy Journal

Mussad M. Alzahrani^{1,2}, William J. Cameron¹, Katie Shanks¹, Senthilarasu Sundaram¹, Tapas K. Mallick^{1*}

¹Environmental and Sustainability Institute, University of Exeter, Penryn Campus, Cornwall TR10 9FE, UK.

²Mechanical and Energy Engineering Department, Imam Abdulrahman Bin Faisal University, Dammam, 34212, Saudi Arabia

*Corresponding author: Tapas K. Mallick

Tel: 01326 259465

Email: t.k.mallick@exeter.ac.uk

Abstract

The progression of research in fabricating a concentrated photovoltaic system endeavour needs to align closely with the advancement of solar cell production aiming to achieve a higher solar cell conversion efficiency. A small number of attempts to develop an ultrahigh concentrator photovoltaic system have been conducted experimentally. But to date, none of these systems are Fresnel lens based or combined with detailed thermal simulation. To bring more optical theoretical design study in [1] closer to the experimental phase, a numerical model was established using COMSOL Multiphysics software to evaluate simultaneously the thermal and optical performance of an ultrahigh concentrator photovoltaic system. Investigation of multi-interface ultrahigh concentrated photovoltaic systems with highly accurate optical and thermal modelling in COMSOL Multiphysics software is a clear absence in the literature. Therefore, in the COMSOL Multiphysics software, the system was analysed under DNI ranging from $400 \frac{W}{m^2}$ to $1000 \frac{W}{m^2}$ in an interval of $100 \frac{W}{m^2}$. The complete system was later optically examined and showed a simulative optical efficiency of approximately 93% and a simulative concentration ratio of 1361 suns. In addition, the thermal model was interlinked with the optical model to generate the results accordingly. A range of ambient temperature between 20 °C and 50 °C and a range of natural convective heat transfer coefficient between $4 \frac{W}{m^2.K}$ and $22 \frac{W}{m^2.K}$ were considered in the thermal model. The maximum temperature on the secondary and the tertiary reflective optical stages operate in a safe temperature range below 54 °C, whereas the final stage receiver shows a maximum temperature ranging between 157.4 °C and 78.5 °C. It is clear that a cooling mechanism arrangement is required for safe operating conditions and to ensure high cell conversion efficiency.

Keywords

UHCPV, Simulation, Optical, Thermal, Concentration Ratio, Optical Efficiency.

1 Introduction

Concentrated photovoltaic systems (CPV) are currently under the focus of research as they are able to accomplish the highest cell efficiency amongst all photovoltaics (PV) technologies. Combining achromatic silicon-on glass (SOG)

Fresnel lens of 95% transparency and the four-junctions solar cell of 46% efficiency has allowed the CPV system to achieve 43% of electricity conversion efficiency [2]. SOG Fresnel lenses are used in CPV system designs due to their affordability and high optical efficiency, ranging between 80-90% [3]. The curing process of silicon is achieved through the injection process of uncured optical silicon to a rigid glass and curing at a certain temperature level. This process of injecting silicon is proven to be affordable and highly scalable, permitting large dimension lenses. SOG Fresnel lens efficiency depends on the materials they are composed of, where silicon offers high precision and minimizes the inactive area amongst facets due to draft angles.

However, SOG Fresnel lenses suffer optically from the geometrical defects of the silicon grooves and edges during the manufacturing injection process. The refractive index of silicon materials depends on the lens temperature as a higher temperature elongates the focal distance and maximizes the focal spot size compared to its optimum size. Further, the attainable maximum concentration ratio for SOG is challenged by the sun divergence angle of $\pm 0.27^\circ$ and the chromatic aberration resulting in a wider focal spot. Two materials have been integrated to fabricate a Fresnel lens named Achromatic Doublet on Glass (ADG) to overcome the chromatic aberration effect, resulting in maximizing the concentration ratio theoretically concerning an identical SOG [4]. However, ADG design is currently not commercially available. As a result, the practice of using a mirror as a secondary reflective stage is an alternative approach to achieve an ultrahigh (UH) concentration ratio which also overcomes the limits of achromatic aberration beyond 1000 suns incorporated with the SOG Fresnel lens [5][6].

Multiple optical interfaces need to be incorporated into a singular system; however, the optical performance of every optical interface besides the errors in the manufacturing and alignment considerably influence the overall optical output. Therefore, the system design should aim for a higher geometrical concentration ratio design anticipating high optical losses. Karp et al.[7] proposed a method based on a planer micro-optic solar collector to concentrate solar irradiance up to 2500 suns, assuming an optical efficiency of no less than 80%. Coughenour et al. [8] presented a high concentration dish coupled with Kohler optics offering a concentration ratio of 1000 suns with an optical efficiency of 80%.

Dreger et al. [9] designed a mini-Cassegrain CPV system to concentrate sun rays by a geometrical concentration ratio of 1037 suns into a receiver size of 1 mm^2 , achieving an effective concentration ratio of 800 suns with an optical efficiency of 80%. Ferrer-Rodriguez et al. [10] designed Cassegrain-Koehler UHCPV with a geometrical concentration ratio of up to 6000 suns and optical efficiency of 80% employing ray-tracing simulation. In this study, a one-cell prototype with a geometrical concentration ratio of 3015 suns was characterized indoors to achieve effectively 938 suns corresponding with an optical efficiency of 31%. Shanks et al. [1] designed a ultrahigh concentrator photovoltaic system with a geometrical concentration ratio of 5800 suns based on 4 Fresnel lenses as a primary optical interface that concentrates sun rays into a single central solar cell. Two simulation approaches were conducted, one with ADG grouped with $\sim 97\%$ reflective mirror and another with a standard SOG Fresnel lens and reflective mirror. This resulted simulatively in optical efficiency between 75 – 55%, which translates to an optical concentration ratio of no less than 3000 suns. This last study is promising due to the use of commercially available SOG Fresnel lens primaries and flat reflector secondaries, but further studies are required to authenticate the UHCPV system. These should include the mechanical design and manufacturing aspects, opto-thermal numerical simulations to observe UHCPV system capacity and limitation, and indoor and outdoor testing to validate the ultrahigh system design experimentally.

Increasing the concentration ratio on the surface of the multijunction solar cell tends to increase the solar cell conversion efficiency, reduce the necessary size of the solar cell, and reduce the cost share of the photovoltaics to the whole system cost. However, an affordable low-efficiency solar cell is still preferred over the CPV regardless of their higher efficiency and lower utilisation of space [11]. This increase in cell conversion efficiency for the multijunction solar cell is challenged by the level of the concentration ratio and its temperature output. Some multijunction solar cell exhibit an increase in the cell efficiency up to 1000 suns at which the cell efficiency drops significantly as resistive loss dominates [12]. The temperature impact is substantial at UH concentrations, a high performing cooling mechanism is necessary. For instance, the multijunction Azur Space assembly for Enhanced Fresnel Assembly (EFA) - (Model 3C44A – $5.5 \times 5.5 \text{ mm}^2$) presents the lowest cell conversation efficiency of about 39.5%

at 1500 suns with the requirement of not having an operating temperature exceeding 110 °C on the cell junction and a maximum temperature not exceeding 175 °C on the multijunction assembly [13]. A variety of attempts have been made to design and investigate different passive cooling configurations to maintain the temperature of the solar cell but with the limitation to preserve the cell at the safe operating temperature at a particular concentration factor [14–17]. Recently, two papers discussed a flat-plate heatsink's performance [18] and different microscale pin-fin configurations for an ultrahigh concentration ratio up to 10,000 suns. The last study found that the coupling of a microscale pin-fin with a flat-plate heatsink can allow the cell to operate safely at a concentration ratio of up to 12,000 suns but only with the solar cell size not exceeding $1 \times 1 \text{ mm}^2$. Although the achieved level of concentration is promising, such a cell size will surely challenge the system's alignments and tracking accuracy.

In this paper, an opto-thermal numerical investigation is performed to evaluate the system's performance and anticipate the temperature limits in correlation with optical input power and concentration ratio. Different levels of direct normal irradiance (DNI) ranging from 400 W/m^2 to 1000 W/m^2 in an interval of 100 W/m^2 is investigated. In the thermal model, wind effect by varying the natural convective heat transfer coefficient between $4 \left[\frac{\text{W}}{\text{m}^2 \cdot \text{K}} \right]$ and $22 \left[\frac{\text{W}}{\text{m}^2 \cdot \text{K}} \right]$ and the outdoor temperature between 20 °C and 50 °C is also investigated.

2 Optical and Thermal Modelling for UHCPV System

The design of the UHCPV system needs to be investigated numerically to estimate the performance optically and thermally. The modelling results can build a clear understanding of the achieved level of concentration ratio in comparison to the geometrical level and the resultant temperature profile over each optical interface. The modelling can help further to interpret the system under an expected range of the environmental condition given the optical dimensions and configurations within the system design and material properties. An opto-thermal numerical model was established using COMSOL Multiphysics software. The study was carried out using a bidirectionally coupled ray tracing. This type of study required the rays to be traced first and then heat transfer in a solid model can be calculated. The amount of deposited ray power in a domain can generate

enough heat to considerably influence the geometry usually according to the level of temperature.

3 Material Geometry and Thermo-Physics Properties

The optical and thermal performance of an UHCPV system is reliant on the selected material and its surface formation and dimensions. In this study, ray tracing models were built based on three optical interfaces subsequent to the primary refractive optic (Silicon-on-Glass (SOG) Fresnel lens). The Fresnel lens was designed in SOLIDWORKS software taking into consideration an actual plain active area of 21 cm × 21 cm and its produced focal length of ≈ 42 cm. This focal length was identified experimentally under WACOM AAA rated solar simulator capable of a constant solar irradiance of 1000 W/m² at AM1.5 spectrum coincidence. The identification of the focal length helps to define the position of every optical stage simulatively for the optimum optical and thermal output. The simulative positioning for the incorporated optics in the UHCPV system will be applied experimentally especially during the stage of optics adjustment and alignment. Although the scope of this work is not to design the Fresnel lens, the Fresnel lens geometry details are provided in Table 1.

Table 1 the geometry details for the Fresnel lens design.

| Material | Silicon Diameter (Active area) | Focal length | Fresnel lens prism spacing | Fresnel lens prism per length | Fresnel prism height increase | Fresnel constant angle |
|------------------------|--------------------------------|--------------|----------------------------|-------------------------------|-------------------------------|------------------------|
| Silicon-on-Glass (SOG) | 21 cm × 21 cm | 420 mm | 0.01mm | 4mm | 0.04mm | 0.55° |

The secondary, the tertiary, and the receiver stage materials were modelled as circular aluminium flat plates. Figure 1 shows the detailed dimensions of optics, location, and the ray paths. In addition, the successful movement of the rays between the optics also depends on the focal length produced from the Fresnel lens which sets the longest path for the rays. As rays reflect from one optical stage to another the concentration ratio increases with relatively homogeneous flux and the divergence angle diminishes [19].

Determining the distance between optics and moving optics by a millimetre or an angle has considerable influence on the results. Repeated alignment adjustments were carried out until the model revealed the maximum optical simulative concentration ratio at which the distances between optics were ascertained. It should be noted that alignment such as this, for ultrahigh concentration levels, is very time consuming and future manufacturing will need to incorporate accurate placement and testing technology. The optimum distance was found to be 24 cm between the Fresnel lens and the secondary optic, 16 cm between the third central reflective optic and the Fresnel lens, and a gap of 2.5 cm between the third central mirror and the central receiver. The defined positioning of the optics was used to carry out both the optical and thermal analysis, as in Figure 1.

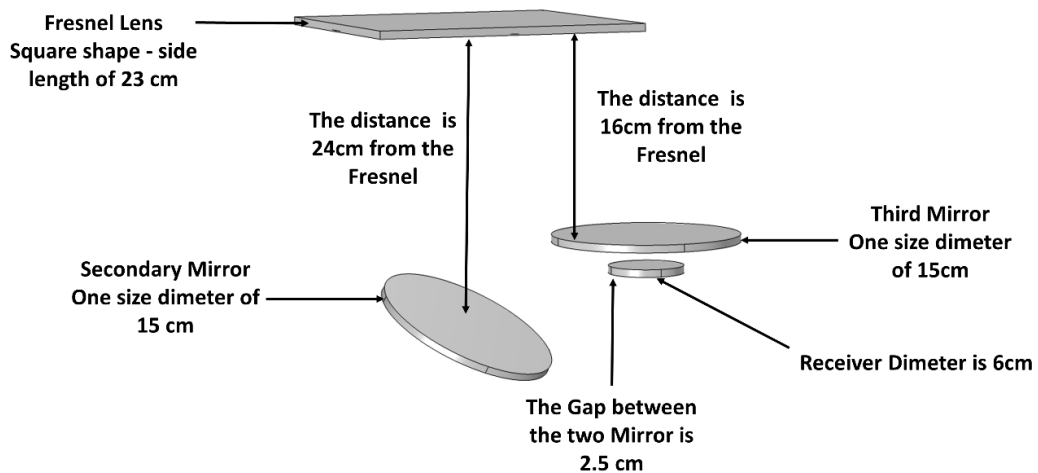


Figure 1 Asymmetric view of $\frac{1}{4}$ of UHCPV system with geometrical illustration and optimum position for the highest optical performance.

The system materials were added from the optical material library in COMSOL Multiphysics software. The selected material for the optics utilizes an optical dispersion model specified by the producer to identify the refractive index. Once the optics materials are assigned, the optical dispersion model coefficients are automatically loaded. The Fresnel lens was selected as silica glass material and subsequent optics were selected to be aluminium.

The thermal properties for the materials assigned to domains are listed in Table 2, which is a necessity to find a solution for the heat transfer in solid model.

Table 2 The thermal properties for the optics to solve the Heat transfer in solid model.

| Optical and thermal properties | Silica Glass | Aluminium |
|--|-------------------------|------------------|
| Reflective index, real part [dimensionless] | 1.45 | - |
| Thermal conductivity [W/(m. K)] | 1.38 | 238 |
| Density [kg/m³] | 2203 | 2700 |
| Heat Capacity [J/(kg. K)] | 703 | 900 |

4 The Governing Equations

To model the sun ray's concentration and then the temperature level on the optics, the model needs to solve first the geometrical optics interface to compute the ray trajectories. Afterwards, the output of the geometrical optics model as boundary heat source will be used to solve the heat transfer in the solid model to compute the temperature level on the lenses.

4.1 Optical Model

The ray optics model derived from the electromagnetic module under geometrical optics physics, the ray trajectories are simulated. A first-order ordinary differential equations are solved, as in Equation (1) and (2).

$$\frac{dq}{dt} = \frac{\partial \omega}{\partial k} \quad (1)$$

$$\frac{dk}{dt} = -\frac{\partial \omega}{\partial q} \quad (2)$$

Where q (m) is the ray spot, k (rad/m) is the wave-vector, ω (rad/s) is the angular frequency, and t (s) is time. In the isotropic medium, the k and ω are further correlated by Equation (3).

$$\omega = \frac{c |k|}{n(q)} \quad (3)$$

where c is the speed of light ($c = 2.99792458 \times 10^8 \frac{m}{s}$), and n (dimensionless) is the refractive index.

The geometrical optics interface controls reflection and refraction for the concentrated rays between different media using a deterministic ray splitting approach. The refracted ray propagation is based on the reflective index of the material applying Snell's law, as in Equation (4). If the concentrated rays undergo total internal reflection, then no refracted rays are generated and no secondary rays need to be discharged.

$$n_1 \sin (\theta_1) = n_2 \sin (\theta_2) \quad (4)$$

Where θ_1 and θ_2 denotes the angle of incidence and refraction, respectively.

The deposited ray power sub-node computes the total concentrated energy flux on a surface relying on the incident ray's power, which is assigned for all the subsequent optics to the Fresnel lens, as in Equation (5).

$$Q_s = \frac{1}{A_i} \sum Q_j \quad (5)$$

Where Q_s is the heat source ($\frac{W}{m^2}$), A_i is the surface area (m^2) subjected to the concentrated rays, Q_j is the sum of ray amount transferring power (W) into a surface area.

4.2 Thermal Model

In this model, the heat transfer rate on every optical stage is governed based on the energy conservation equation for the steady-state condition, as in Equation (6). The heat source term (Q_s) is based on Equation (5) solved in the optical model for the subsequent optics to the Fresnel lens.

$$Q_s = Q_{\text{cond.}} - Q_{\text{conv.}} - Q_{\text{rad.}} \quad (6)$$

$Q_{\text{cond.}}$ is the conduction heat transfer, $Q_{\text{conv.}}$ is the convection heat transfer, and $Q_{\text{rad.}}$ is the radiation heat transfer.

The amount of $Q_{\text{cond.}}$ through a domain is processed based on Fourier's law, where the conduction is proportional to the temperature gradient (ΔT) ($^{\circ}\text{C}$). The proportionality coefficient is the thermal conductivity (k) ($\frac{W}{m.K}$), as in Equation (7).

$$Q_{\text{cond.}} = \nabla \left(-\frac{L}{k} \nabla T \right) \quad (7)$$

Where L (m) is the domain thickness and ∇ identifies a solution for the conduction heat transfer in three dimensions (x, y, z). The heat transfer rate is influenced by the product of $\left(\frac{L}{k}\right)$, which is the material thermal resistance. Clearly, the thermal conductivity and the thermal resistance are inversely correlated.

The wind speeds and the ambient temperature considerably affect the amount of $Q_{\text{conv.}}$. Newton's law of cooling solves the rate of $Q_{\text{conv.}}$ considering both the ambient temperature (T_a) and convective heat transfer coefficient (h), which is dependent on the wind speed, as in Equation (8).

$$Q_{\text{conv.}} = \nabla (h \nabla T) \quad (8)$$

Where the ΔT is between the domain surface temperature and T_a .

The level of temperature due to the concentrated solar irradiance encourages the transfer of energy in the process of electromagnetic waves. $Q_{\text{rad.}}$ is governed by Stefan-Boltzmann's law and is strongly correlated to the temperature of the emitting domain, as in Equation (9).

$$Q_{\text{rad.}} = \varepsilon \sigma (T_s^4 - T_{\text{sur.}}^4) \quad (9)$$

Where σ is the Stefan-Boltzmann constant $\left(5.67 \times 10^{-8} \frac{\text{W}}{\text{m}^2 \cdot \text{K}^4}\right)$, ε is the emissivity product, T_s is the surface temperature, and $T_{\text{sur.}}$ is the surrounding temperature.

5 The optical and Thermal Model Boundary Conditions

5.1 Optical Model Description

The Fresnel lens domain is selected as an illuminated surface for direct normal irradiance (DNI) ranging between 1000-400 $\frac{\text{W}}{\text{m}^2}$ assuming that the released rays are reflected from an exterior radiation source. The Fresnel lens established with a transmissivity of 95% and illuminated with 30,000 rays. Both secondary and tertiary reflective optics are established as specular reflection wall of 95% meaning the incident angle is equal to the reflection angle. The model was set up to compute both the intensity and power of the concentrated rays on the optics interfering with the concentrated rays. The heat source calculation is carried out in the secondary and tertiary reflective optical stage and the receiver using the ray deposited power function. The receiver is established as a freezing

domain. The freezing domain identifies that the ray's position and vector wave are fixed at the point of immediate contact to the domain, where the ray intensity is normally recovered. The optical dispersion for the external domain is kept at the initial temperature of 20 °C. The optical model assumes that there is no chromatic aberration effect and the optical dispersion of the SOG Fresnel lens is negligible. Figure 2 details the boundary condition for the optical model.

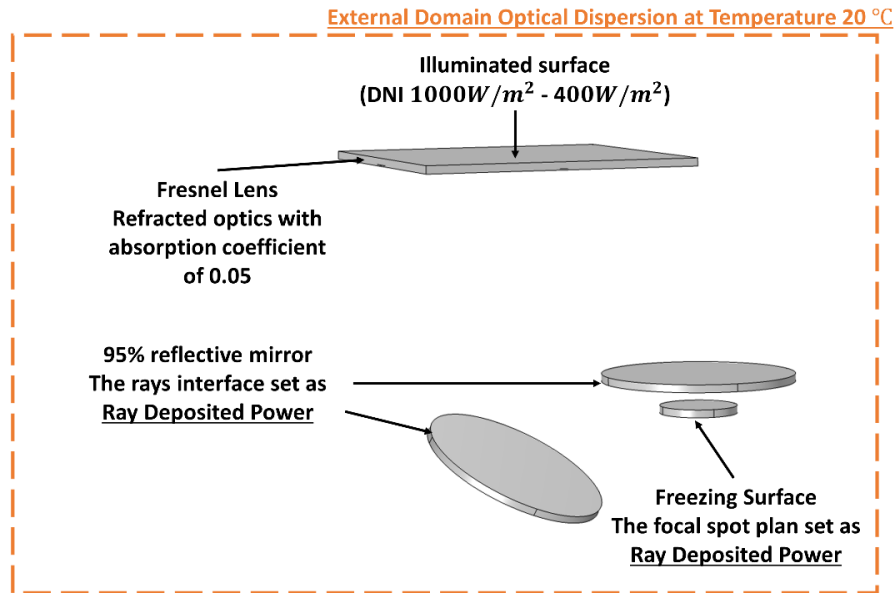


Figure 2 The optical boundary condition as in COMSOL software for a 1/4 of UHCPV system.

5.2 Thermal Model Description

To establish the boundary condition for the heat transfer in the solid model, all optics were assigned for heat flux ($Q_{conv.}$) and surface-to-ambient radiation ($Q_{rad.}$). Within heat flux, the model was investigated with a parametric sweep for the ambient temperature at 20 °C and 50 °C and convective heat transfer coefficient at $4 \frac{W}{m^2.K}$ and $22 \frac{W}{m^2.K}$. This parametric sweep study aimed to observe the thermal model in relatively excellent weather conditions for the combination of (20 °C and $22 \frac{W}{m^2.K}$) and for extreme weather conditions for the combination of (50 °C and $4 \frac{W}{m^2.K}$). The radiation heat transfer model has an emissivity product of 0.82 for the aluminium surfaces [20]. Boundary heat source nodes were selected for all optics successive to the Fresnel lens. Through these nodes, the calculated ray deposited power in the optical model was interlinked with the boundary heat source in the thermal model to find a solution. The thermal

model has no thermal insulation selections. Figure 3 illustrates the boundary condition for the thermal model.

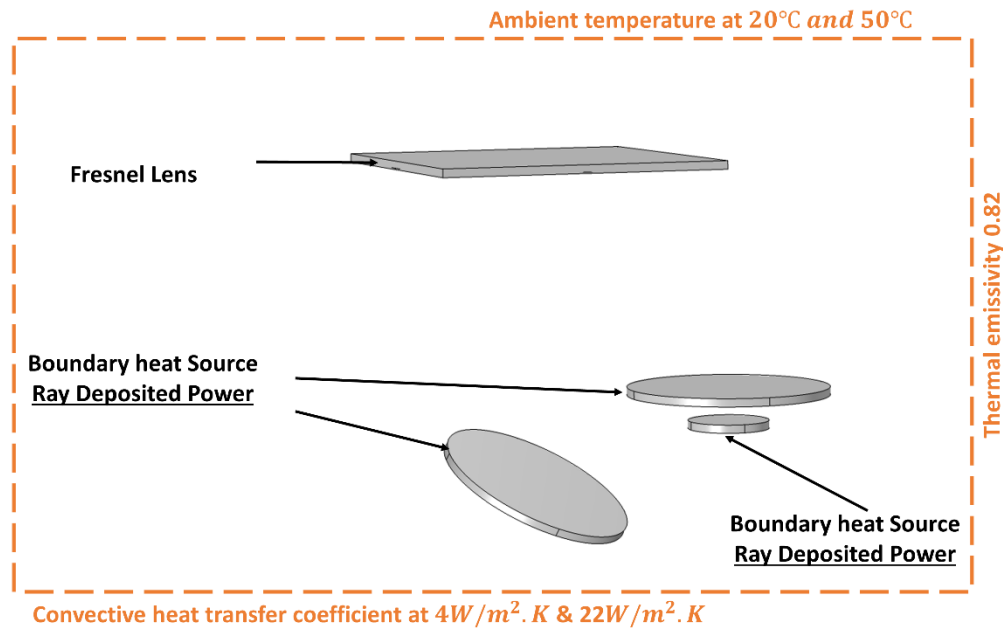


Figure 3 The thermal boundary condition as in COMSOL software for a 1/4 of UHCPV system.

6 Validation

The numerical model was customized to account only for the Fresnel lens and a Azur Space 3C44A 10 × 10 mm² multijunction solar cell (MJSC). Afterward, the model carried out the same numerical approach through solving the model optically and thermally. The boundary heat source results are clearly influenced by the counterbalance between the mesh size and the number of rays. Therefore, the analysis was carried out to check the meshing resolution was sufficient to avoid inaccuracy.

The model was validated thermally with Aldossary et al. [21] and Alamri et al. [22] utilizing a Fresnel lens of 441 ×, ambient temperature of 25 °C, and solar intensity of 1000 W/m². Figure 4 shows the result where a. is the ray trajectory results in ns, and b. is 3D thermal distribution highlighting the maximum temperature results.

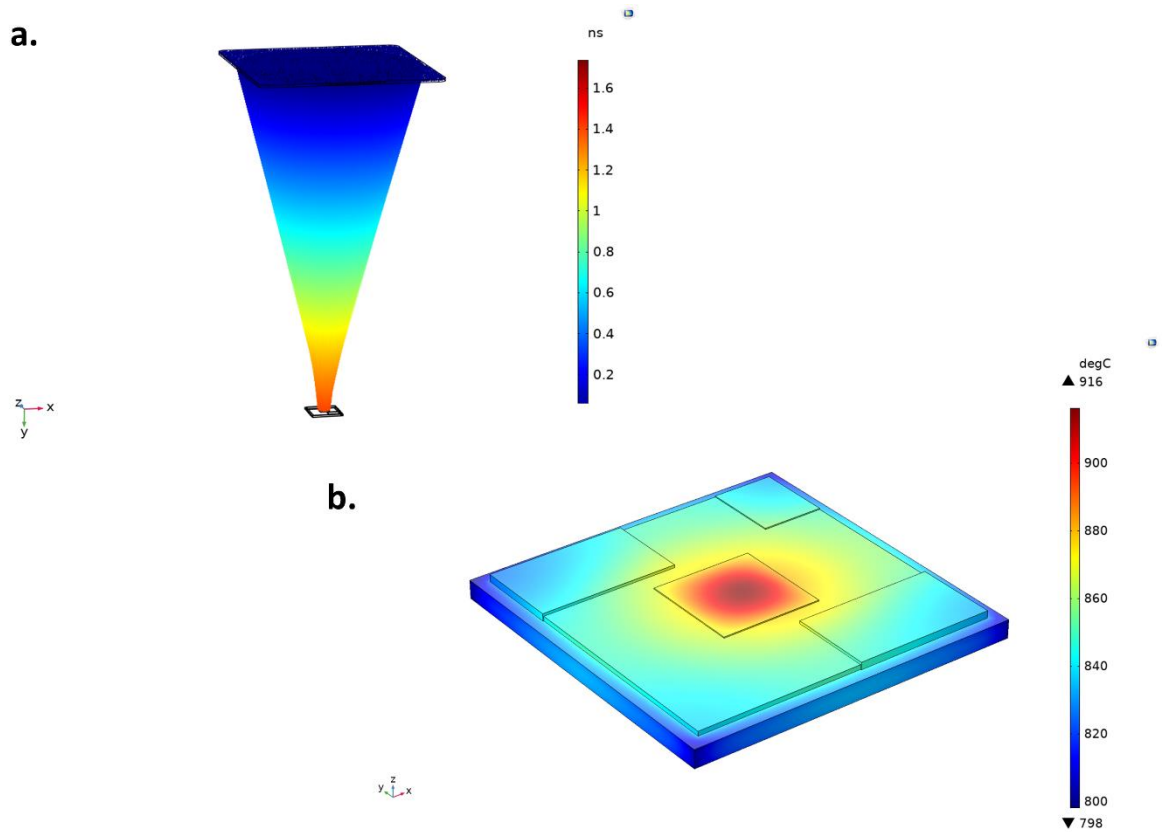


Figure 4 The modelling results for only the Fresnel lens and a $10 \times 10 \text{ mm}^2$ solar cell where a. is the ray trajectory result and b. is the 3D thermal profile with highlighting the maximum temperature.

The validation shows an excellent agreement between the current study and Aldossary et al. [21] and the current study and Alamri et al. [22] with a maximum discrepancy of 0.65% and 0.11%, respectively, as presented in Figure 5.

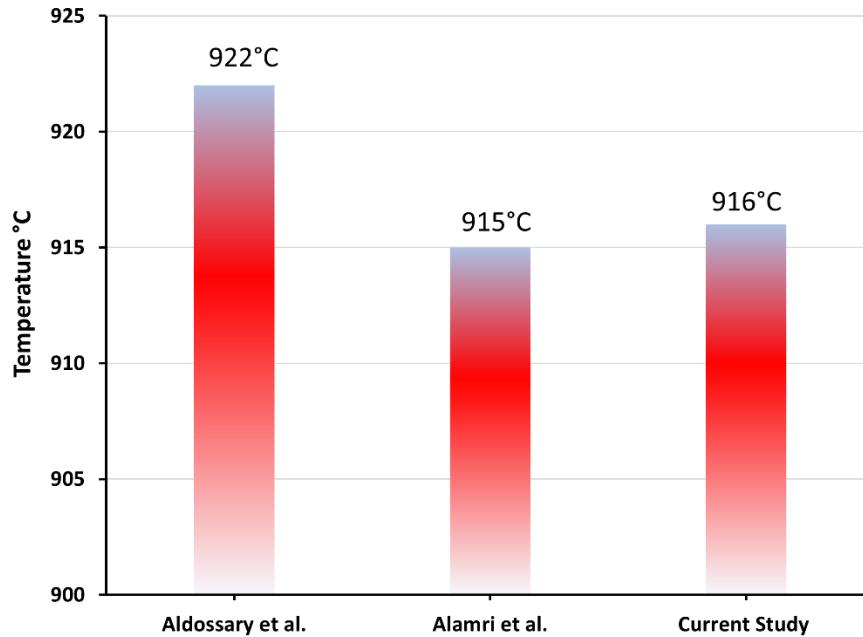


Figure 5 The numerical model validation.

7 Results and Discussion

In this model, the influence of direct normal irradiance, which is the main driver for the optical and thermal output, was established to test the UHCPV system in a representative range of solar irradiance in actual conditions from $1000 \frac{W}{m^2}$ to $400 \frac{W}{m^2}$. The UHCPV system was exposed to worst-case and optimistic conditions, assuming the typical temperature range of Saudi Arabia/India and some European countries, respectively. The respective convective heat transfer coefficients are $4 \frac{W}{m^2.K}$ and $22 \frac{W}{m^2.K}$, while the T_a for each case is $50 \text{ }^\circ\text{C}$ and $20 \text{ }^\circ\text{C}$. These ranges of temperature and natural convective heat transfer establish the limits of system operation thermally.

7.1 $\frac{1}{4}$ UHCPV System Optical

Since the design of the UHCPV system is based on 4-asymmetric quadrants, only a $\frac{1}{4}$ of the UHCPV system is simulated. The ray trajectories show the concentrated solar irradiance being refractive from the primary optic and then reflected from the secondary optics all the way to the receiver with 1.67 nano-second (ns), as in Figure 6.

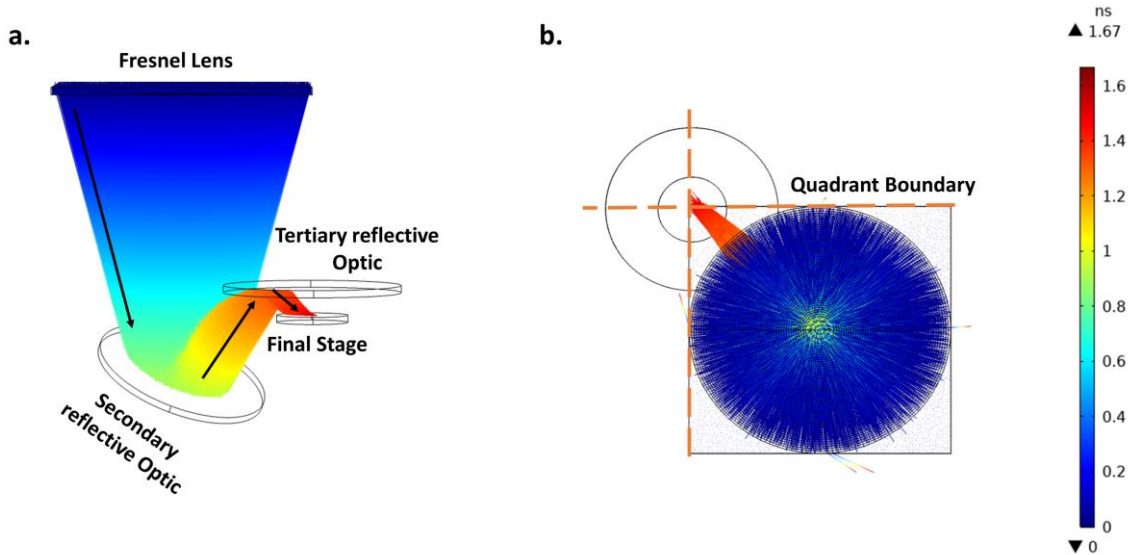


Figure 6 The ray trajectories for a 1/4 of UHCPV system where a. is ray trajectory in a side-view and b. is the ray trajectories in top-view.

The optical performance can be evaluated through the optical concentration ratio and the optical efficiency, where the optical efficiency of the UHCPV system is related to the attainable simulative concentration ratio (C_{sim}) out of the designed geometrical concentration ratio ($C_g = \frac{Area_{concentrator}}{A_{receiver}}$), as in Equation 10. The geometrical concentration ratio for $\frac{1}{4}$ of the UHCPV system is found to be 1458 suns for a solar cell area of $5.5 \text{ mm} \times 5.5 \text{ mm}$.

$$\eta_{\text{simulative optical}} = \frac{C_{sim}}{C_g} \quad (10)$$

The deposited ray power was assessed on every optical stage subsequent to the Fresnel lens. Knowing the boundary heat source on the optics prior to the receiver illustrates the losses in the boundary source power of concentrated rays. At DNI of $1000 \frac{W}{m^2}$, the boundary heat source on the optical interfaces was found to be $1.28 \times 10^3 \frac{W}{m^2}$ (1 sun), $10 \times 10^3 \frac{W}{m^2}$ (10 suns), and $1.361 \times 10^6 \frac{W}{m^2}$ (1361 suns) on the surface of the secondary mirror, tertiary mirror, and the receiver, respectively. The boundary heat source on the final receiver resulted in simulative optical efficiency ($\eta_{\text{simulative optical}} = 93\%$). The irradiance distribution on the optics influenced by the angular reflection of concentrated rays is given in Figure 7a and the magnified irradiance distribution on the receiver is given in Figure 7b.

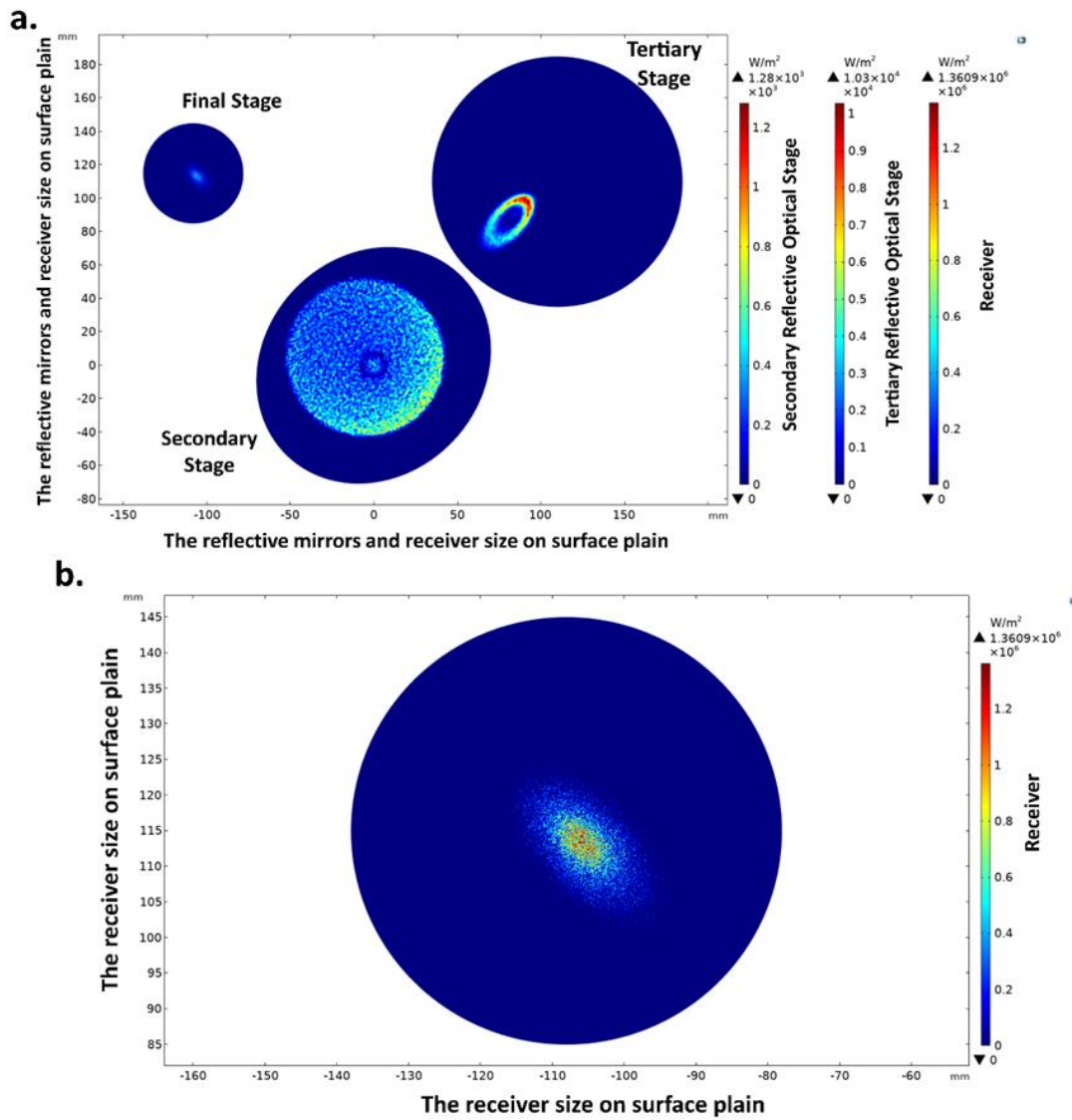


Figure 7 Irradiance distribution at $1000 \frac{W}{m^2}$ a. on the optical interfaces and b. on the receiver magnified.

At a range of DNI from $1000 \frac{W}{m^2} - 400 \frac{W}{m^2}$, the boundary heat source was predicted to be in the range of $1.28 \times 10^3 \frac{W}{m^2} - 5.12 \times 10^2 \frac{W}{m^2}$ for the secondary reflective mirror, in a range of $1.03 \times 10^4 \frac{W}{m^2} - 4.11 \times 10^3 \frac{W}{m^2}$ for the tertiary reflective mirror, and in the range of $1.361 \times 10^6 \frac{W}{m^2} - 5.44 \times 10^5 \frac{W}{m^2}$ for the receiver correspondent to simulative concentration ratio of 1361 suns- 544 suns. The correlation between the boundary heat source and the input power (DNI) is strongly linear, as expected and shown in Figure 8.

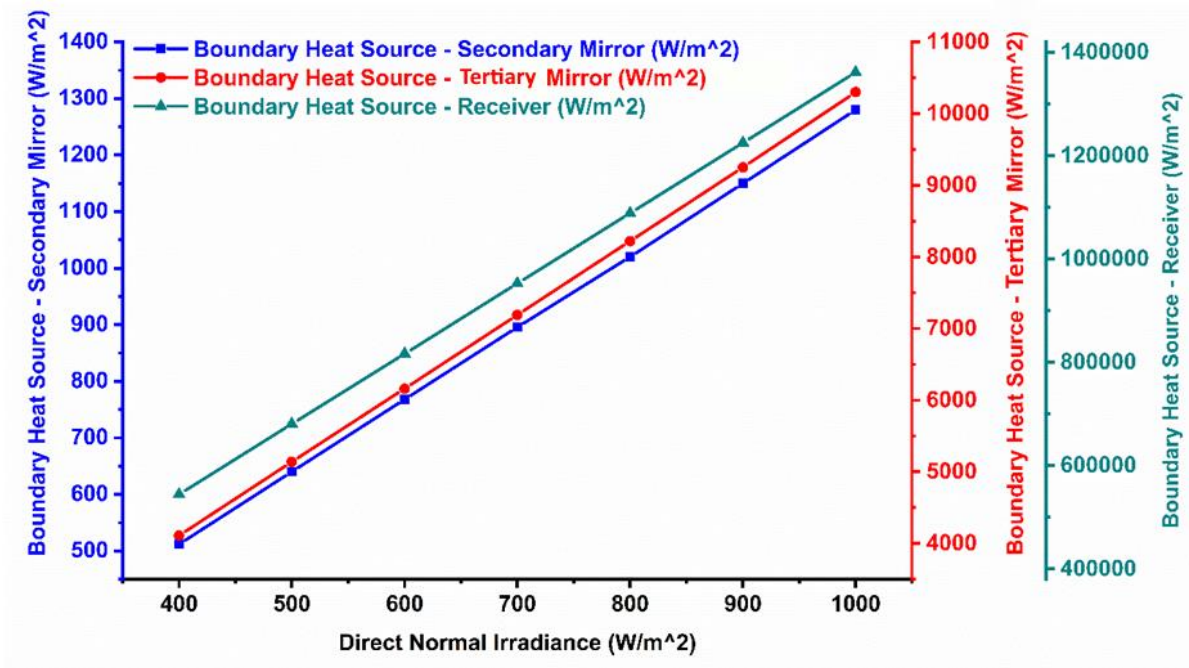


Figure 8 The boundary heat source correlated with the input power on the secondary optic, tertiary optic, and receiver.

7.1.1 Solar Divergence Angle

To establish light cones at the points of sun rays, the sun divergence angle of 4.65 mrad (0.27°) is considered which is the approximation of the solar disc size when observed from earth. The solar radiation from the solar disc centre has a tendency to be greater in solar intensity than solar radiation from the edges of the sun disc which is known as the limb darkening phenomenon. There is a strong inverse correlation between the divergence angle and the concentration ratio. The attained simulative concentration ratio is limited to 1361 suns due to the sun angular size of 0.27°, as in Figure 9a. To account for a relatively wider optical tolerance when tracking the sun, a sun angular size of 1° resulted in a wider focal spot and hence a concentration ratio of 610 suns ($\eta_{\text{simulative optical}} = 42\%$), as in Figure 9b. This shows the sensitivity of the system to scattering from the optical stages.

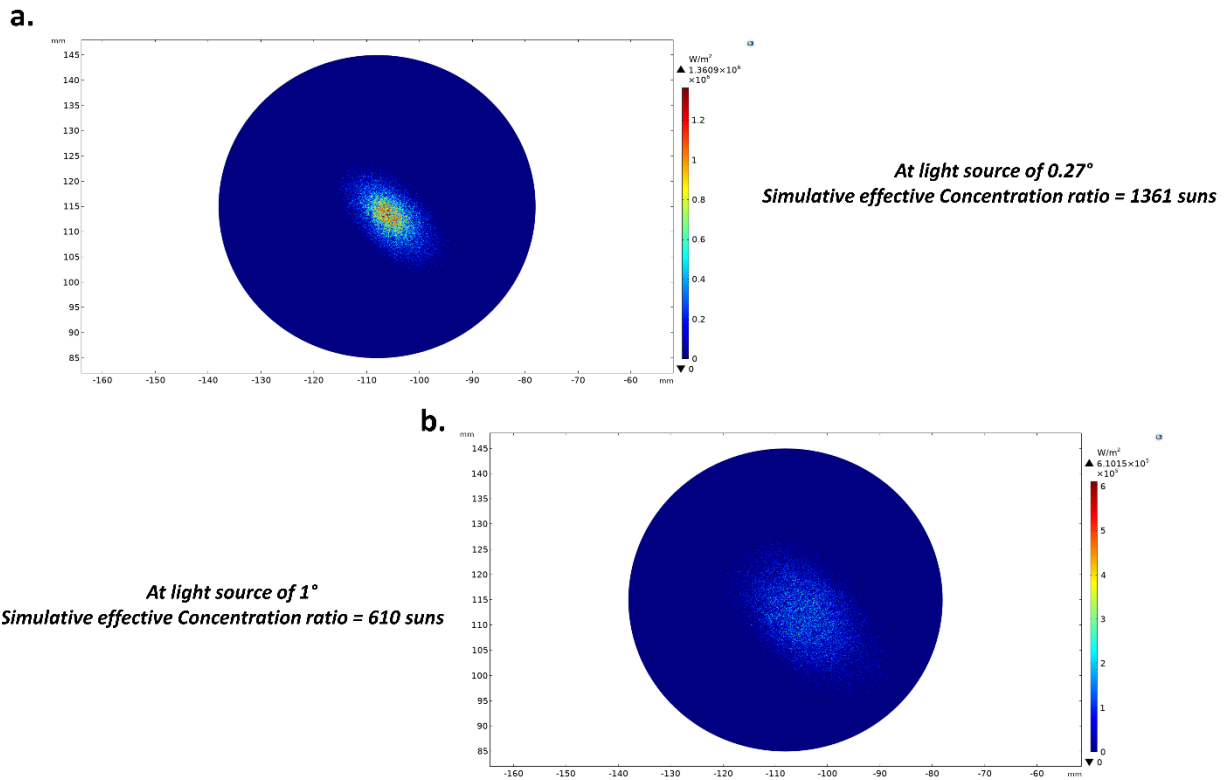


Figure 9 Focal spot size at divergence angle of a. 0.27° and b. 1°.

7.2 ¼ UHCPV System Thermal

The deposited power density in the optical model was coupled to solve the heat transfer in the solid model. As a result, the maximum surface temperature at an ambient temperature in a range between 20°C and 50 °C with convective heat transfer of $4 \frac{W}{m^2.K}$ was found for the combination for (50 °C and $4 \frac{W}{m^2.K}$). Certainly, the maximum temperature (worst operating) was exhibited on the receiver with a magnitude of 157.4 °C. Figure 10 and Figure 11 shows the temperature distribution profile at a different DNI with an interval of $200 \frac{W}{m^2}$ for (20 °C and $4 \frac{W}{m^2.K}$) and (50 °C and $22 \frac{W}{m^2.K}$), respectively.

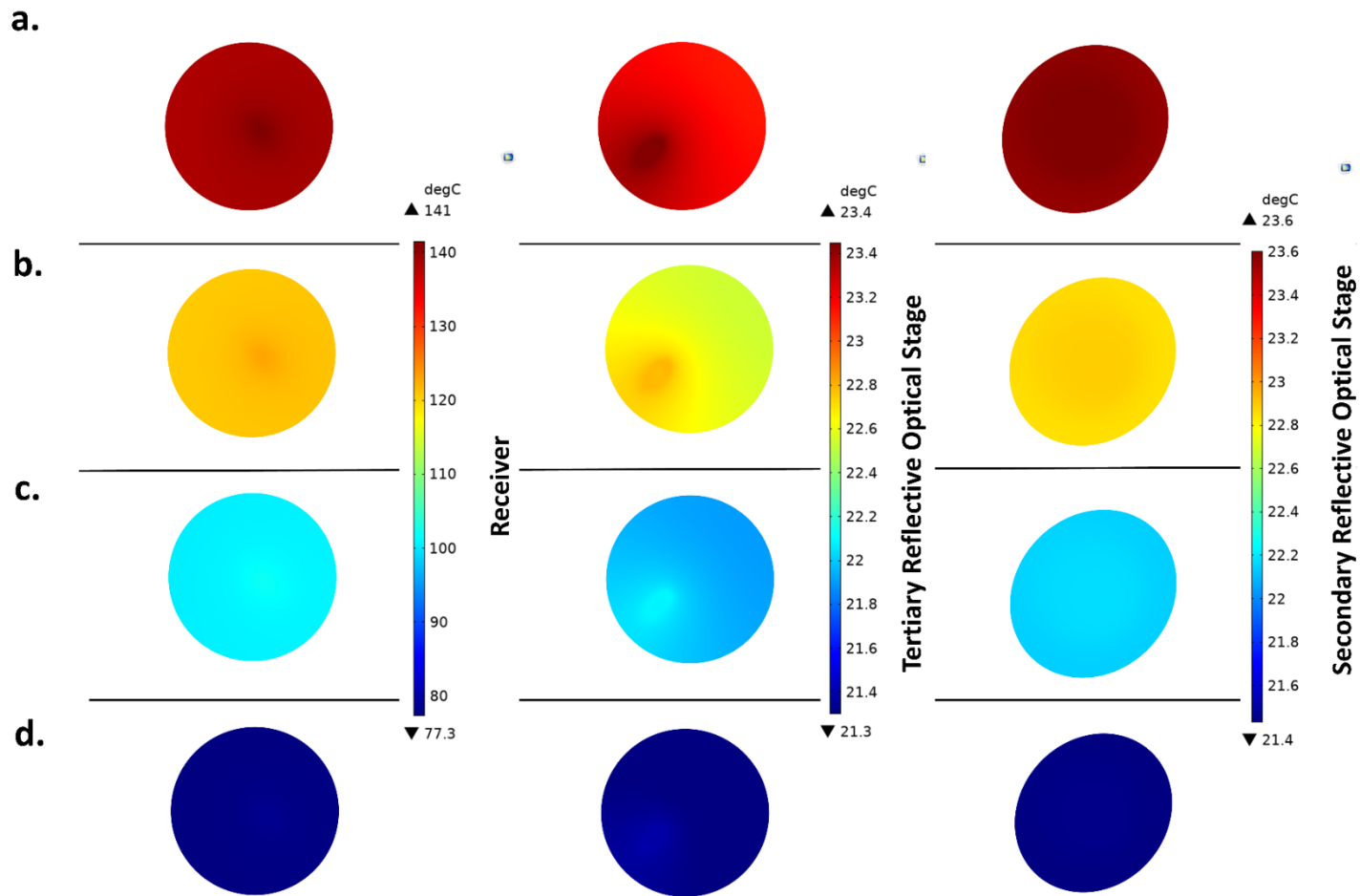


Figure 10 Shows the temperature stratification of plain surface at ambient temperature of 20 °C and convective heat transfer coefficient of $4 \frac{W}{m^2.K}$, where a. at 1000 $\frac{W}{m^2}$, b. at 800 $\frac{W}{m^2}$, c. at 600 $\frac{W}{m^2}$, and d. at 400 $\frac{W}{m^2}$.

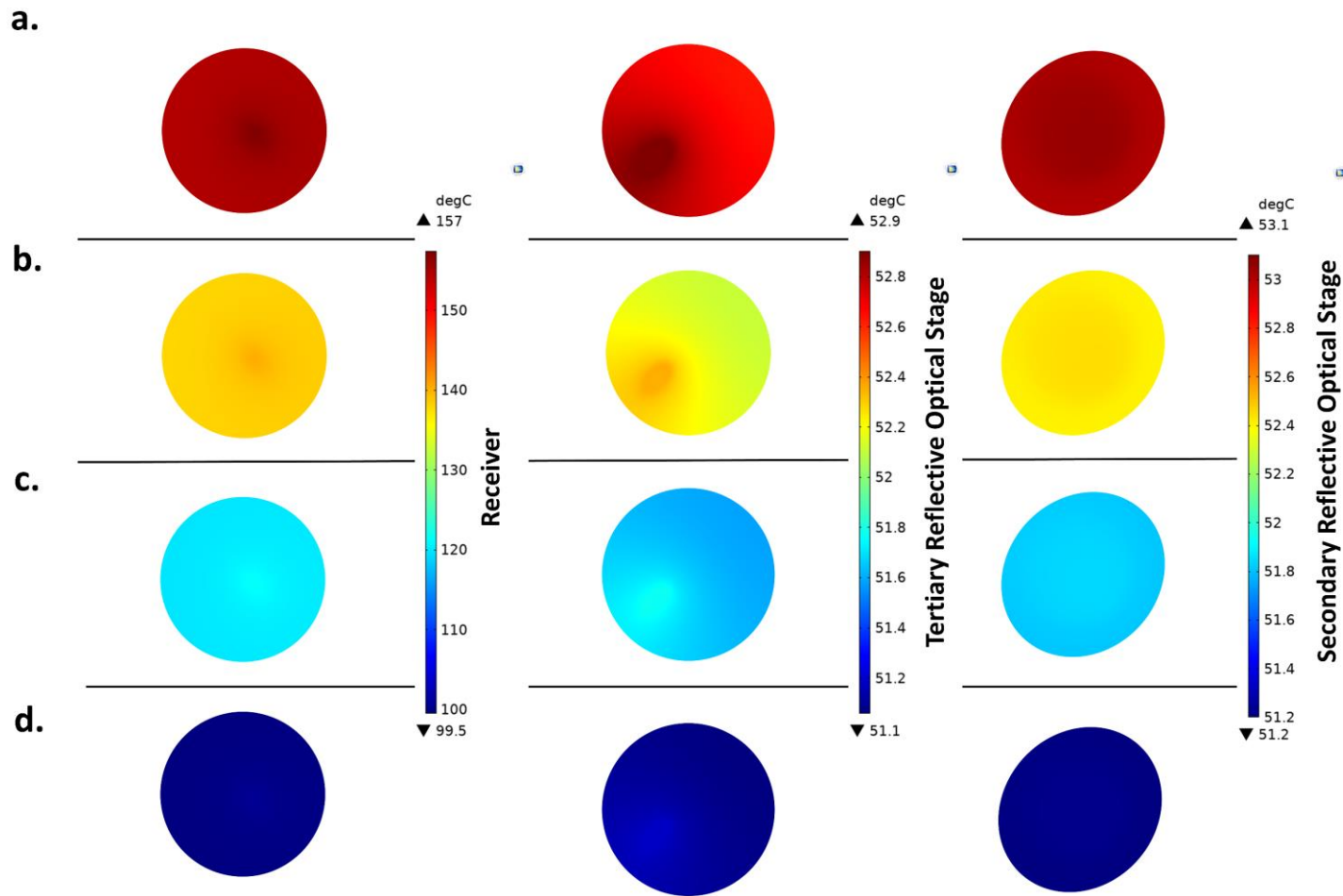


Figure 11 Shows the temperature stratification of plain surface at an ambient temperature of 50 °C and convective heat transfer coefficient of $4 \frac{W}{m^2.K}$, where a. at 1000 $\frac{W}{m^2}$, b. at 800 $\frac{W}{m^2}$, c. at 600 $\frac{W}{m^2}$, and d. at 400 $\frac{W}{m^2}$.

The results of Figure 10 and Figure 11 were combined into one linear graph (Figure 12) to exhibit the linear correlation with shading pattern to observe the working range within the selected ambient temperature in accordance with the convective heat transfer coefficient. An obvious discrepancy between model with ambient temperature of 20 °C and 50 °C at $4 \frac{W}{m^2.K}$ shows on average value of 18% , 56.9%, and 56.7% for receiver, secondary mirror and tertiary mirror, respectively. Figure 12 shows a strong linear correlation between the output power (effective concentration) and maximum temperature on the optics.

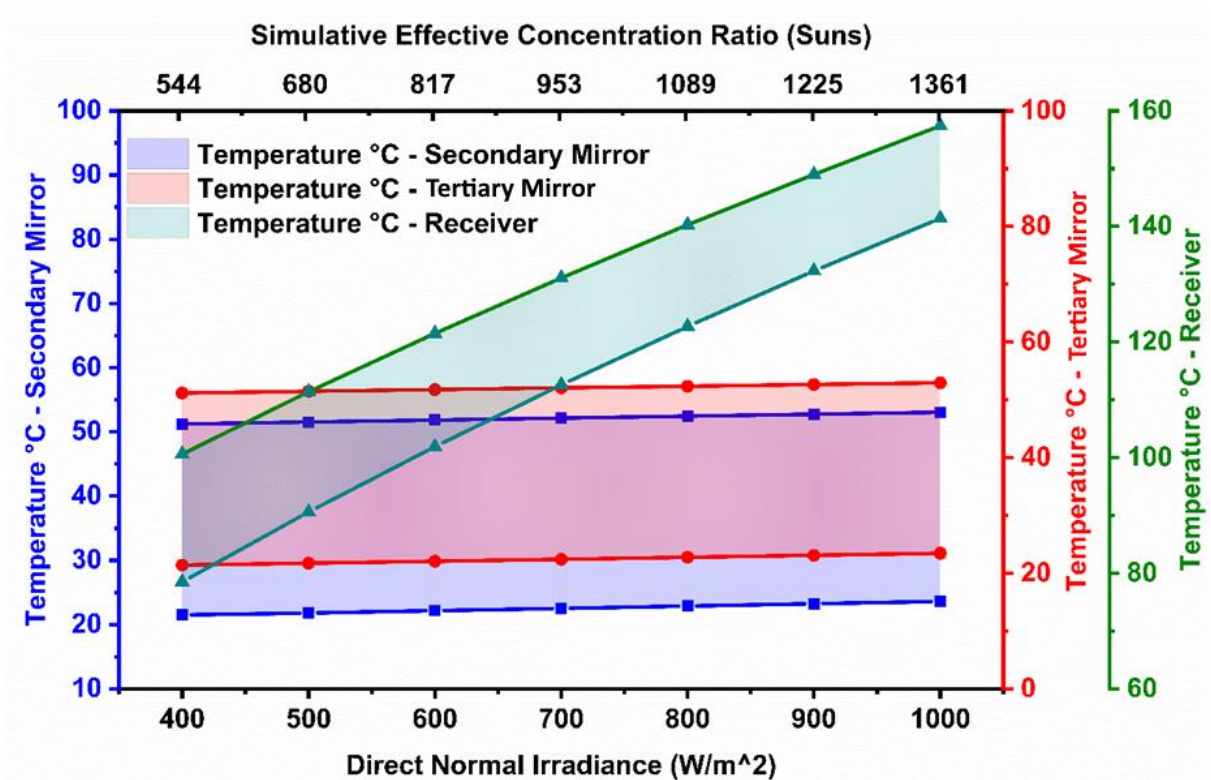


Figure 12 Shows the linear correlation between the concentration ratio and the temperature at an ambient temperature in a range between 50 °C and 20 °C and convective heat transfer coefficient of $4 \frac{W}{m^2.K}$.

At an ambient temperature of 20°C and 50 °C and convective heat transfer of $22 \frac{W}{m^2.K}$, the maximum surface temperature was found on the receiver with a value of 101.8 °C. Both Figure 16 and Figure 17 shows the temperature stratification on a plane surface with DNI of an interval of $200 \frac{W}{m^2}$. The lowest temperature (safe operating) is at weather condition of 20 °C and $22 \frac{W}{m^2.K}$ showing a maximum temperature of 74.9 °C.

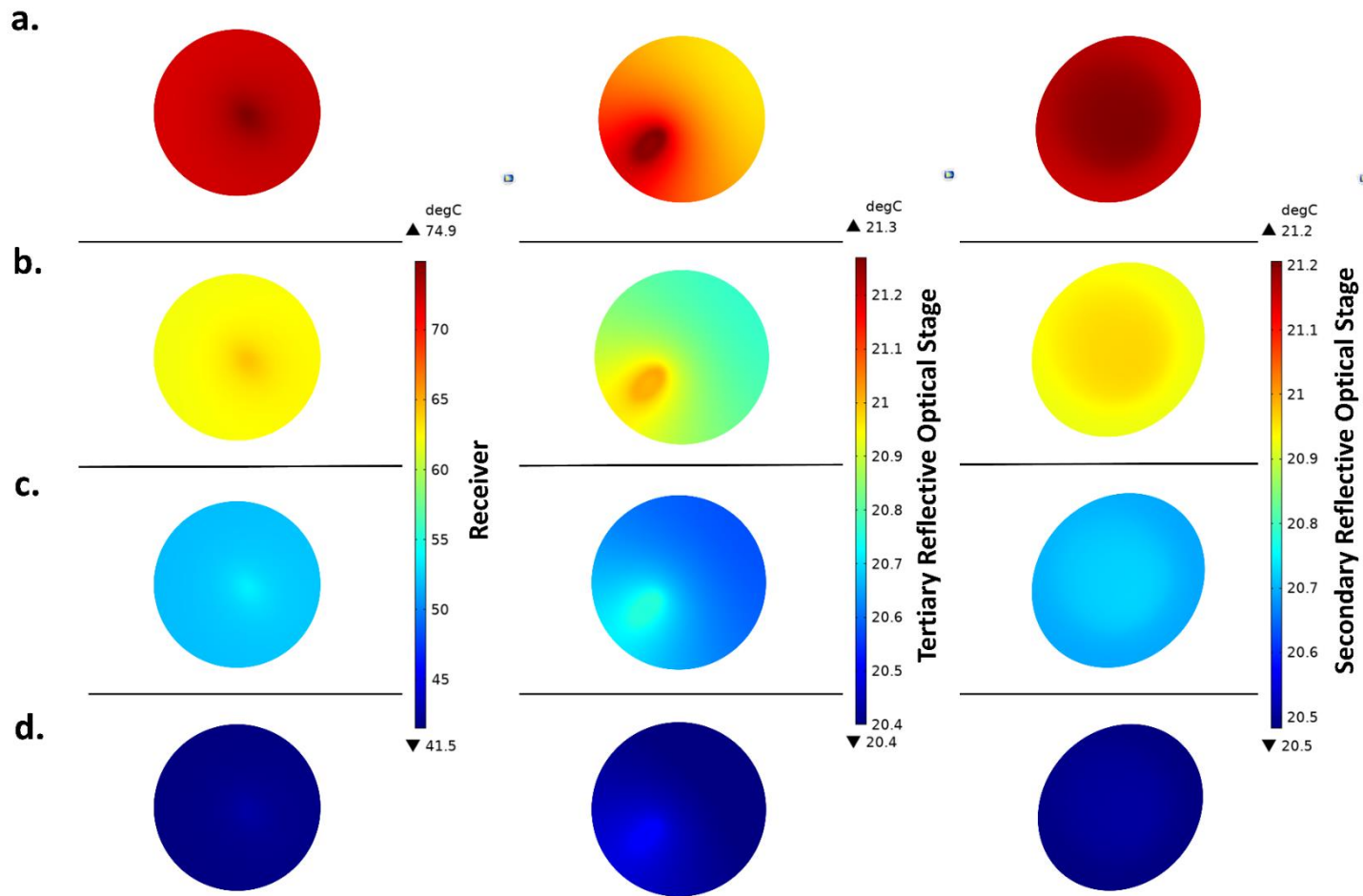


Figure 13 Shows the temperature stratification of plain surface at an ambient temperature of 20 °C and convective heat transfer coefficient of 22 $\frac{W}{m^2.K}$, where a. at 1000 $\frac{W}{m^2}$, b. at 800 $\frac{W}{m^2}$, c. at 600 $\frac{W}{m^2}$, and d. at 400 $\frac{W}{m^2}$.

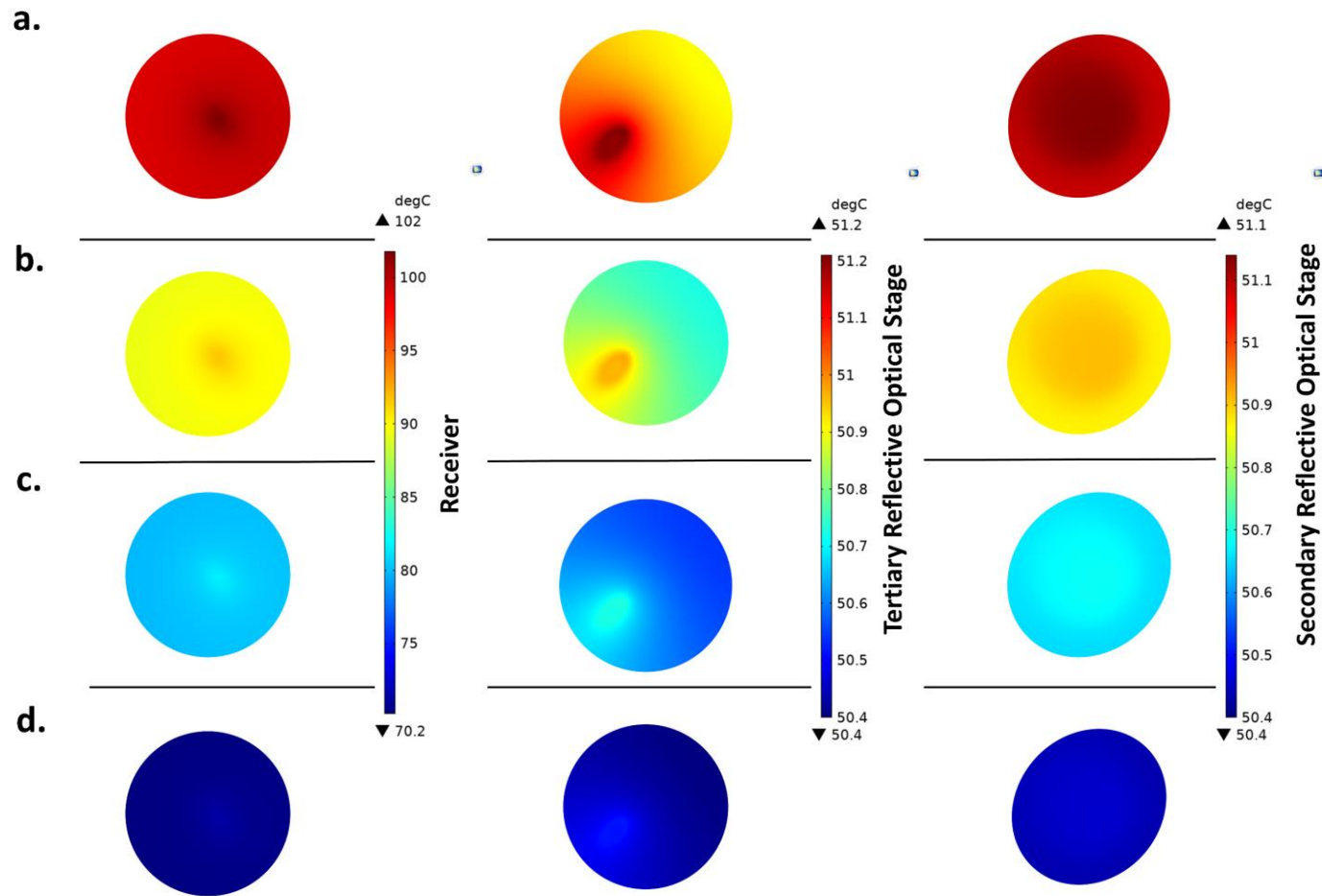


Figure 14 Shows the temperature stratification of plain surface at an ambient temperature of 50 °C and convective heat transfer coefficient of 22 $\frac{W}{m^2.K}$, where a. at 1000 $\frac{W}{m^2}$, b. at 800 $\frac{W}{m^2}$, c. at 600 $\frac{W}{m^2}$, and d. at 400 $\frac{W}{m^2}$.

The results of Figure 13 and Figure 14 were gathered into one graph (Figure 15) to demonstrate the strong linear correlation with shading pattern to observe the working range within the selected ambient temperature in accordance with the convective heat transfer coefficient. A clear discrepancy between model with ambient temperature of 20 °C and 50 °C at $22 \frac{W}{m^2.K}$ shows on average value of 49%, 58.9%, and 59% for receiver, secondary mirror and tertiary mirror, respectively. Figure 15 represents a strong linear correlation between the output power (effective concentration) and maximum temperature on the optics.

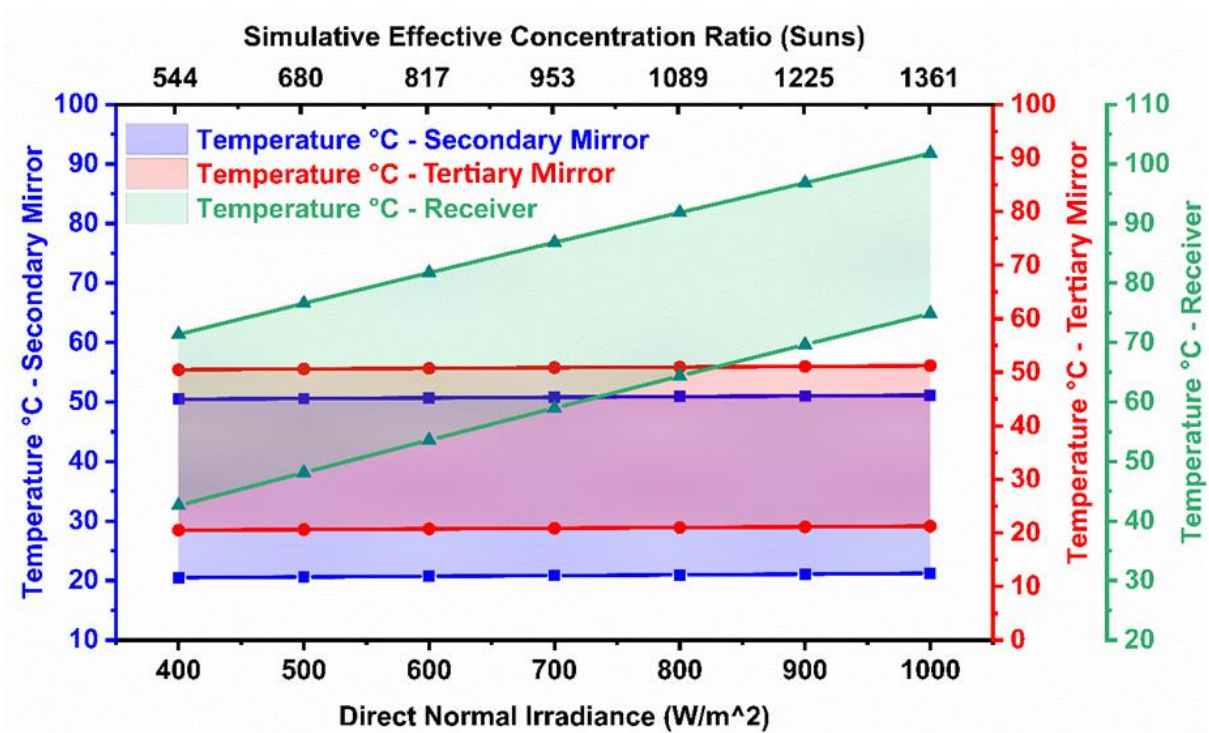


Figure 15 Shows the linear correlation between the concentration ratio and the temperature at an ambient temperature in a range between 50 °C and 20 °C and convective heat transfer coefficient of $22 \frac{W}{m^2.K}$.

The temperature changes contribute to thermal expansion on the optics surfaces. This thermal deformation and the changes in the optical reflectivity influence the overall system performance as high accuracy is needed to achieve the ultrahigh concentration ratio. In addition to this, the thermal expansion might cause permanent surface structural deformation hindering the system's reliability. Therefore, the prediction of temperature aims to expose the system model to a wide range of environmental conditions to assure safe operation in practical

applications. It is clear the temperature of the optics is reliant on the thermal properties of the material and the optical geometries.

8 Conclusion

Clearly, analyzing the UHCPV system is very demanding simulatively for full system coherence. In this study, the COMSOL Multiphysics software was utilized to evaluate the UHCPV system optically and thermally. DNI was investigated in a range between $400 \frac{W}{m^2}$ – $1000 \frac{W}{m^2}$ assuming different geographical locations, which helps to evaluate the optical performance in terms of simulative optical concentration ratio. In addition, a range of ambient temperatures and convective heat transfer coefficients was studied assuming a wide range of meteorological conditions considering both the worst-case scenario and the best-case scenario in order to realize the maximum achievable temperature on the optics and finally on the receiver. This informs the design for a suitable cooling mechanism arrangement. The temperature range on the secondary and tertiary reflective optics are safe enough to not cause substantial thermal stress whereas the receiver subjected to the maximum working temperature operating between $157\text{ }^{\circ}\text{C}$ and $74.8\text{ }^{\circ}\text{C}$ in accordance with the DNI. It is ascertained that a heat extraction mechanism is a necessity at the receiver stage to ensure a safe operating condition when a solar cell is integrated.

Appendix

Meshing

The ray tracing algorithm recognizes ray-boundary connection using the underlying finite element mesh. To compute the ray's power and density, a finer mesh is necessary due to the piecewise discontinuous of the density over the deposited ray power boundary. There is a trade-off between the mesh size and the number of rays. Extremely fine mesh might result in some rays being unaccounted for; therefore, the solution is to increase the number of rays to eliminate the "hole" in the deposited ray power domain. Although increasing the number of rays overcomes the missed node in the meshed boundary, the machine is challenged by the excessively long computational time and the required computer memory. The boundary heat source stratification on 2D domain is clearly influenced by the counterbalance between the mesh size and the number of rays.

References

1. Shanks, K.; Ferrer-rodriguez, J.P.; Fernández, E.F.; Almonacid, F. A > 3000 suns high concentrator photovoltaic design based on multiple Fresnel lens primaries focusing to one central solar cell. *Solar Energy* **2018**, *169*, 457–467, doi:10.1016/j.solener.2018.05.016.
2. Steiner, M.; Siefer, G.; Schmidt, T.; Wiesenfarth, M.; Dimroth, F.; Bett, A.W. 43% Sunlight to Electricity Conversion Efficiency Using CPV. *IEEE Journal of Photovoltaics* **2016**, *6*, 1020–1024, doi:10.1109/JPHOTOV.2016.2551460.
3. Wiesenfarth, M.; Steiner, M.; Wolf, J.; Schmidt, T.; Bett, A.W. Investigation of different fresnel lens designs and methods to determine the optical efficiency. *AIP Conference Proceedings* **2014**, *1616*, 97–101, doi:10.1063/1.4897037.
4. Vallerotto, G.; Victoria, M.; Askins, S.; Herrero, R.; Domínguez, C.; Antón, I.; Sala, G. Design and modeling of a cost-effective achromatic Fresnel lens for concentrating photovoltaics. *Optics Express* **2016**, *24*, A1245, doi:10.1364/OE.24.0A1245.
5. Shanks, K.; Senthilarasu, S.; Mallick, T.K. High-Concentration Optics for Photovoltaic Applications. In; 2015; pp. 85–113.
6. Vallerotto, G.; Askins, S.; Victoria, M.; Antón, I.; Sala, G. A novel achromatic Fresnel lens for high concentrating photovoltaic systems. *AIP Conference Proceedings* **2016**, *1766*, doi:10.1063/1.4962089.
7. Karp, J.H.; Tremblay, E.J.; Hallas, J.M.; Ford, J.E. Orthogonal and secondary concentration in planar micro-optic solar collectors. *Optics Express* **2011**, *19*, A673, doi:10.1364/oe.19.00a673.
8. Coughenour, B.M.; Stalcup, T.; Wheelwright, B.; Geary, A.; Hammer, K.; Angel, R. Dish-based high concentration PV system with Köhler optics. *Optics Express* **2014**, *22*, A211, doi:10.1364/OE.22.00A211.
9. Dreger, M.; Wiesenfarth, M.; Kisser, A.; Schmid, T.; Bett, A.W. Development and investigation of a CPV module with Cassegrain mirror optics.; 2014; pp. 177–182.
10. Ferrer-Rodríguez, J.P.; Saura, J.M.; Fernández, E.F.; Almonacid, F.; Talavera, D.L.; Pérez-Higueras, P. Exploring ultra-high concentrator photovoltaic Cassegrain-Koehler-based designs up to 6000x. *Optics Express* **2020**, *28*, 6609, doi:10.1364/OE.382236.
11. Alzahrani, M.; Shanks, K.; Mallick, T.K. Advances and limitations of increasing solar irradiance for concentrating photovoltaics thermal system. *Renewable and Sustainable Energy Reviews* **2021**, *138*, 110517, doi:10.1016/j.rser.2020.110517.
12. Sharaf, O.Z.; Orhan, M.F. Concentrated photovoltaic thermal (CPVT) solar collector systems: Part I – Fundamentals, design considerations and current technologies. *Renewable and Sustainable Energy Reviews* **2015**, *50*, 1500–1565, doi:10.1016/j.rser.2015.05.036.
13. Azur Space Solar Power GMBH Enhanced Fresnel Assembly - EFA Type: 3C42A – with 10x10mm² CPV TJ Solar Cell Application:

Concentrating Photovoltaic (CPV) Modules. **2014**, 0–4.

14. Micheli, L.; Sarmah, N.; Fernandez, E.F.; Reddy, K.S.; Mallick, T.K. Technical issues and challenges in the fabrication of a 144-Cell 500× Concentrating Photovoltaic receiver. In Proceedings of the 2014 IEEE 40th Photovoltaic Specialist Conference (PVSC); IEEE, 2014; pp. 2921–2925.
15. Abo-Zahhad, E.M.; Ookawara, S.; Radwan, A.; El-Shazly, A.H.; Elkady, M.F. Numerical analyses of hybrid jet impingement/microchannel cooling device for thermal management of high concentrator triple-junction solar cell. *Applied Energy* **2019**, *253*, 113538, doi:10.1016/j.apenergy.2019.113538.
16. Abo-Zahhad, E.M.; Ookawara, S.; Radwan, A.; El-Shazly, A.H.; El-Kady, M.F.; Esmail, M.F.C. Performance, limits, and thermal stress analysis of high concentrator multijunction solar cell under passive cooling conditions. *Applied Thermal Engineering* **2020**, *164*, 114497, doi:10.1016/j.applthermaleng.2019.114497.
17. Alzahrani, M.; Baig, H.; Shanks, K.; Mallick, T. Estimation of the performance limits of a concentrator solar cell coupled with a micro heat sink based on a finite element simulation. *Applied Thermal Engineering* **2020**, *176*, 115315, doi:10.1016/j.applthermaleng.2020.115315.
18. Valera, A.; Fernández, E.F.; Rodrigo, P.M.; Almonacid, F. Feasibility of flat-plate heat-sinks using microscale solar cells up to 10,000 suns concentrations. *Solar Energy* **2019**, *181*, 361–371, doi:10.1016/j.solener.2019.02.013.
19. Zhang, Y.; Xiao, G.; Luo, Z.; Ni, M.; Yang, T.; Xu, W. Comparison of different types of secondary mirrors for solar application. *Optik* **2014**, *125*, 1106–1112, doi:10.1016/j.ijleo.2013.07.113.
20. Shurtz, R.C. Total Hemispherical Emissivity of Metals Applicable to Radiant Heat Testing.
21. Aldossary, A.; Mahmoud, S.; Al-dadah, R. Technical feasibility study of passive and active cooling for concentrator PV in harsh environment. *Applied Thermal Engineering* **2016**, *100*, 490–500, doi:10.1016/j.applthermaleng.2016.02.023.
22. Alamri, Y.A.; Albaik, I.; Mahmoud, S.; Al-Dadah, R.; Ismail, M.A. Integration of concentrated multi-junction solar cells with small-scale organic rankine cycle. *Energy Conversion and Management* **2021**, *239*, 114235, doi:10.1016/j.enconman.2021.114235.

Article 9. M. Alzahrani, W. Cameron, K. Shanks, S. Sundaram, T. Mallick,
"Mechanical Design Aspects for Ultrahigh Concentrated
Photovoltaics System (UHCPV)." Prepared to be submitted for Solar
Energy Journal.

Mechanical Design Aspects for Ultrahigh Concentrated Photovoltaics System (UHCPV)

Prepared for

Solar Energy Journal

Mussad M. Alzahrani ^{1,2}, William J. Cameron¹, Katie Shanks¹, Senthilarasu Sundaram¹, Tapas K. Mallick ^{1*}

¹Environmental and Sustainability Institute, University of Exeter, Penryn Campus, Cornwall TR10 9FE, UK.

²Mechanical and Energy Engineering Department, Imam Abdulrahman Bin Faisal University, Dammam, 34212, Saudi Arabia

*Corresponding author: Tapas K. Mallick

Tel: 01326 259465

Email: t.k.mallick@exeter.ac.uk

Abstract

The progression of research in fabricating a concentrated photovoltaic system endeavoured to align similarly with the advancement of fabricated solar cells aiming to achieve a higher conversion efficiency solar cells. Few attempts toward the ultrahigh concentration ratio have been conducted experimentally but not based on Fresnel lens design. To bring the optical theoretical design study in [1,2] into the experimental phase, a mechanical design for the ultrahigh concentrated photovoltaic system has been established based on SOLIDWORKS software detailing the ultrahigh concentrated photovoltaic design aspect and the design boundary condition. The system design features a significant degree of freedom, giving each optical stage multiple linear and angular room for adjustments. Hence, the system required an accurate 3-dimensional sun tracker. The selection of the sun tracker and its specification approach is detailed. Incorporating the ultrahigh concentrated photovoltaic system with the sun tracker required counterbalance design and load analysis, which has been illustrated. Most of the material's types and manufacturers were listed with geometry. The windage analysis is also conducted to know the torque to assure a safe operating condition for the entire setup.

Keywords

UHCPV, Optics, Sun Tracker, Counterbalance, Simulation, SOLIDWORKS.

1 Introduction

In recent years, concentrated photovoltaic (CPV) systems have been well studied and investigated for energy production. Common concentrates are based on either curved surface, such as a parabolic dish or parabolic trough, or Fresnel flat mirror. CPV systems are fabricated to a certain extent to achieve a required optical concentration ratio (C_R) classified as low ($C_R < 10$ suns), medium ($10 \text{ suns} < C_R < 100 \text{ suns}$), high ($100 \text{ suns} < C_R < 2000 \text{ suns}$), and ultrahigh ($C_R > 2000 \text{ suns}$) [3]. Moving toward a design aiming to achieve a high to ultrahigh concentration ratio required either a parabolic dish with a maximised surface area [4,5] or a compact design based on either a Cassegrain design [6,7] or Fresnel design [1,2,8]. However, maximising the primary optic for a parabolic dish challenges the design by adding weight, the required tracking accuracy and energy load, the minimised acceptance angle, and the optical performance

surface relying on the surface smoothness flatness [9]. Although the concentrating compact design reduces the load on the tracking system, the compact design is challenged by the low optical efficiency, complex system tolerance and alignment, and the impact of high thermal stress.

To attain the highest optical concentration, solar irradiance, and solar cell efficiency, a sun tracking instrument with high accuracy is crucial to operating a CPV system based on either point-or line- focal system. Although the sun tracker is a solution to increase the power production when the sun is not within the range of the system acceptance angle, the parasitic energy losses of the sun tracker need to be carefully considered along with the sun tracker payload capacity. The sun tracker payload capacity, which is the total weight of the CPV system and the counterbalance, plus the pointing accuracy are two important factors that must be counted in the CPV system design if the plan is to purchase an off-shelf sun tracker. Several methods of tracking systems are thoroughly discussed in the literature through manufacturing all the way to control strategies for different solar systems [10,11]. As a result, there is a directly proportional correlation between the level of concentration ratio and required accuracy for the sun tracker systems.

This paper describes the mechanical compact design and manufacturing process of the first prototype for an ultrahigh concentrated photovoltaic system (UHCPV) in Penryn Campus- University of Exeter. A detailed description of the selected sun tracker is presented. Also, the interlink mechanical structure (beam structure), designed and built to mount on the sun tracker and host the compact UHCPV system from one side and the counterbalance weight for another side, is analysed numerically. SOLIDWORKS software is utilised to analyse the beam structure's static load and the windage load impact on the whole design setup.

2 Mechanical Design Condition and Overview

The UHCPV design is based on a rigorous principle and carefully considered the interlink among the main system components: UHCPV mechanical structure, sun tracker, and interlink mechanical structure. Boundary design conditions were assigned first to guide the mechanical structure and facilitate components' employability to process the design. The following conditions were given

1. The system is based on four pieces of Fresnel lens – Silicon on Glass (SOG).

2. Fresnel lenses are fixed in place.
3. The system is based on one central third stage and/ or receiver.
4. The system can operate either with three and/ or four optical interfaces.
5. The rest of the optical interfaces are adjustable with a large degree of freedom.
6. The system is designed to host a reflective mirror in secondary and third stages for different diameter sizes ranging from 10, 15, and 20 cm with thickness ranging between 4 – 6 mm.
7. The designed UHCPV system can be experimented with by utilising a sun tracker with excellent weight compatibility to host the UHCPV system.

The system has been established first as a diamond shape in the middle with four triangles attached to the side of the diamond. The idea of the central diamond is to clear the centre from any mechanical obstacle that will interfere with the concentrated light path. The complete UHCPV system is shown in asymmetric view and plane view, where Figure 1 a and b shows the SOLIDWORKS screenshot and Figure 1 c and d show the actual system photo, respectively. The mechanical structure has been built using aluminium sturt profiles 20 × 20 mm with a 6 mm slot, lightweight and minimal beam deflection. Eight vertical aluminium sturt profiles have a length of 500 mm/piece, 12 horizontal aluminium sturt profiles framing the base of every tringle with a size of 210 mm/piece, and two horizontal aluminium sturt profiles, one linked to the third optical stage and another to the receiver, both with a size of 324 mm/piece. The design/actual system photos are exhibited for the UHCPV system in Figure 1.

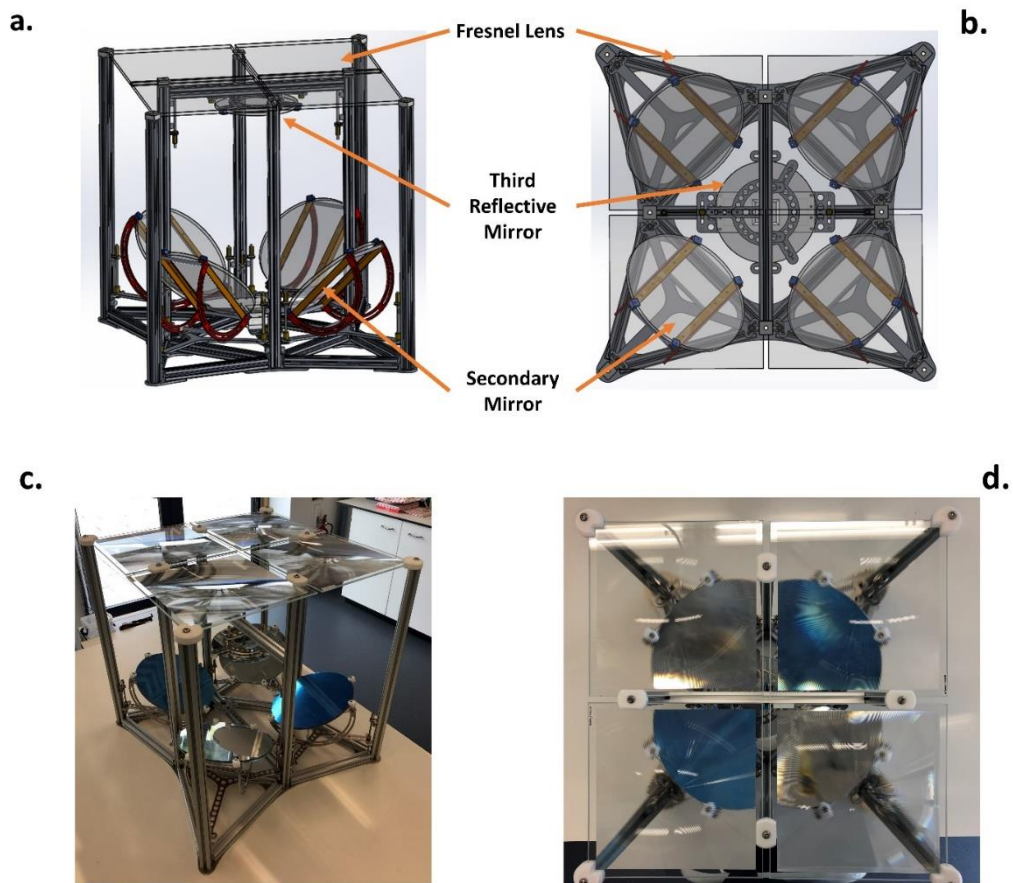


Figure 1 SOLIDWORKS screenshot for the complete designed UHCPV system a. asymmetric view and b. Top view and actual design of UHCPV system c. asymmetric view and d. top view.

3 Optical

Concentrating light into ultrahigh factor required a system with a high degree of freedom to allow correctness and high accuracy of directing and redirecting concentrated light – focal length. The focal spot intends to contract from one optical stage to another until arriving at the receiver, which is eventually challenged by the divergence angle of the sun.

3.1 Secondary Optical Stage

The secondary mirror frame has been constructed to reflect the concentrated light from the Fresnel lens to the third central reflective mirror. Three degrees of freedom is adopted in the design. First, the secondary mirror is adjustable vertically from the centre of the mirror to the centre of the Fresnel lens, which can travel as close as 10 cm to the Fresnel and as far as 35 cm. Second, it can be adjusted angularly between 0-70°. Last, the entire frame base has a yaw angle of

$\pm 5^\circ$. The secondary mirror frame is equipped with three thumb nuts, an intermediate between the aluminium sturt and the secondary mirror mount, travelling along the vertical sturt utilising two inside brackets 6 mm per thumb nut. Every $\frac{1}{4}$ of the system is built on one apex node and two twin-apex nodes to be linked with neighbouring quarters.

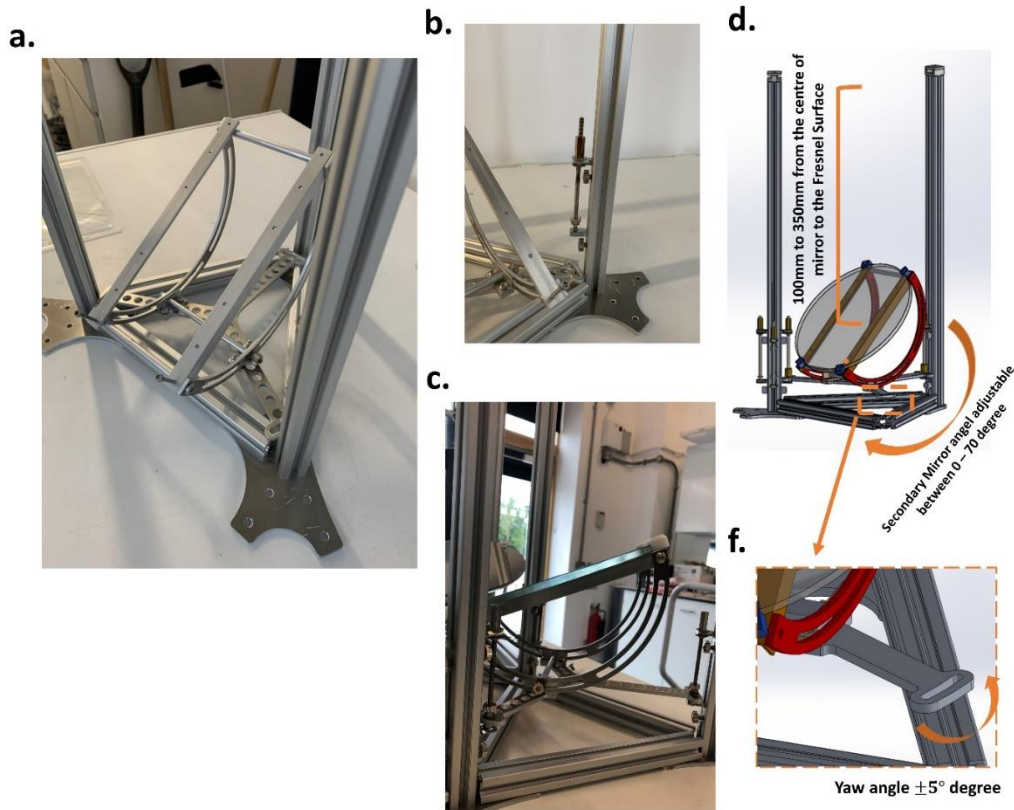


Figure 2 The actual design for $\frac{1}{4}$ of the system at 45° position, where a. is the secondary mirror frame, b. is the designed thumb nut to allow the secondary mirror to be adjusted vertically with locking feature and c. the entire secondary mirror stage including the mirror. The SOLIDWORKS design for $\frac{1}{4}$ of the system at 45° position, where d. the full secondary mirror frame with the reflective mirror at 35 cm focal length with the degree of freedom illustrations and f. the visualisation of the yaw angle of the secondary mirror frame.

3.2 Third Optical Stage

The third reflective stage is a central mirror that receives concentrated light from four secondary reflective mirrors, where this stage demands a high degree of adjustment. The mirror is placed on a mounting frame linked into a horizontal sturt profile firmed and adjusted vertically utilising two thumb nuts. This stage is designed to adopt five degrees of freedom. The third stage can transfer vertically

with a similar range as the secondary stage, as in Figure 3a, and horizontally in latitude and longitude distances between ± 40 mm and ± 15 mm from its centre, respectively, as in Figure 3b. As well, the base of the third reflective mirror has roll and pitch angular tunings by $\pm 5^\circ$ from its centre, as in Figure 3c and d. Figure 3f shows the actual outcome for the SOLIDWORKS design in Figure 3b. The third stage could be terminated as a reflective optical stage and turned into a final receiver stage. This option was given in the design in case achieving the ultrahigh level through four interfaces is problematic due to this first prototype's optical and mechanical limitations.

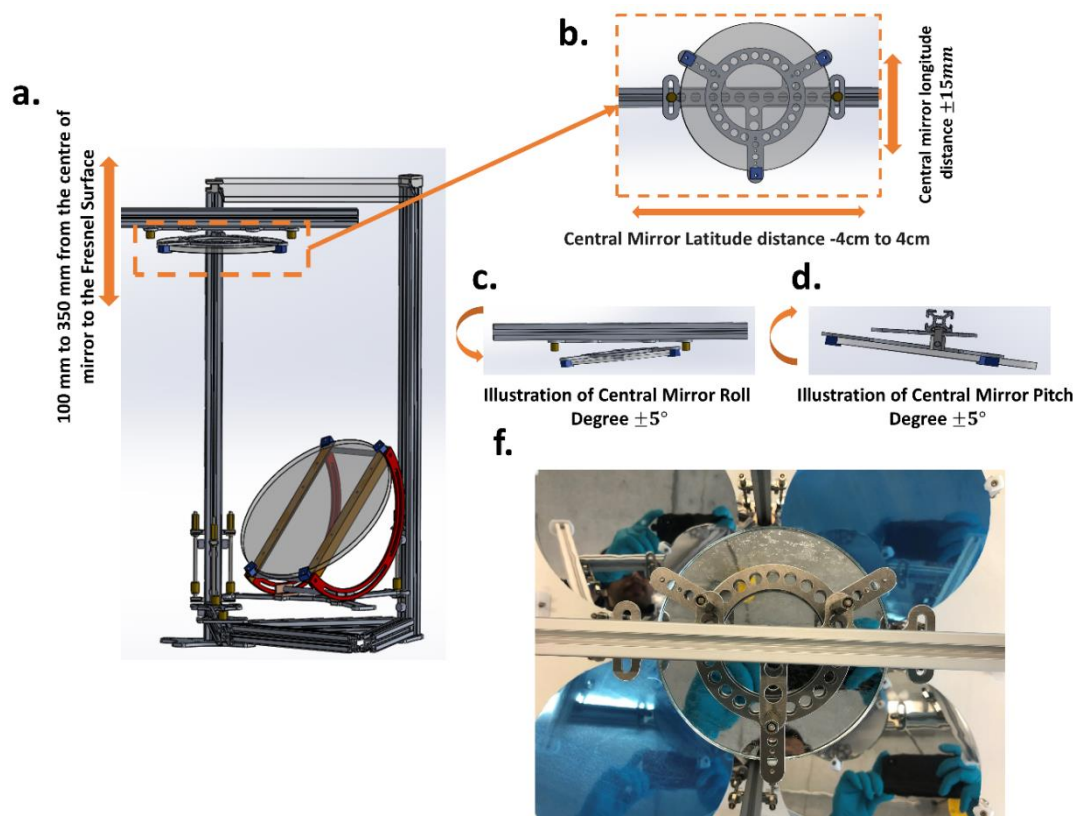


Figure 3 SOLIDWORKS drawings for 1/4 of the UHCPV where a. is the vertical movement for the third stage, b. is the latitude and longitude movement, c. is the roll angular freedom, and d. is the pitch angular freedom, where f. is showing the actual system photographed for the third stage frame with the mirror.

3.3 Receiver Stage

Finally, the receiver stage is parallel to the third stage and implements three degrees of freedom. Two of which is similar to the latitude and longitude movements in the third stage, as in Figure 4b (SOLIDWORKS screenshot) and

4c (actual design), and the last one is a vertical transfer to become close to 7.5 cm to the third stage and far as 44 cm, as in Figure 4a (SOLIDWORKS design) and 4f (actual configuration). The mounting plate for the receiver can accompany different sizes of post-illumination cooling mechanisms allowing the scaling of the thermal receiver to the concentration range. A heat shield was incorporated in the design to protect the adjacent mechanical components in case of misalignment for the focal spot, which burns out the system. The heat shield has an open window to allow only concentrated rays impinging the solar cell surface area, as in Figure 4d.

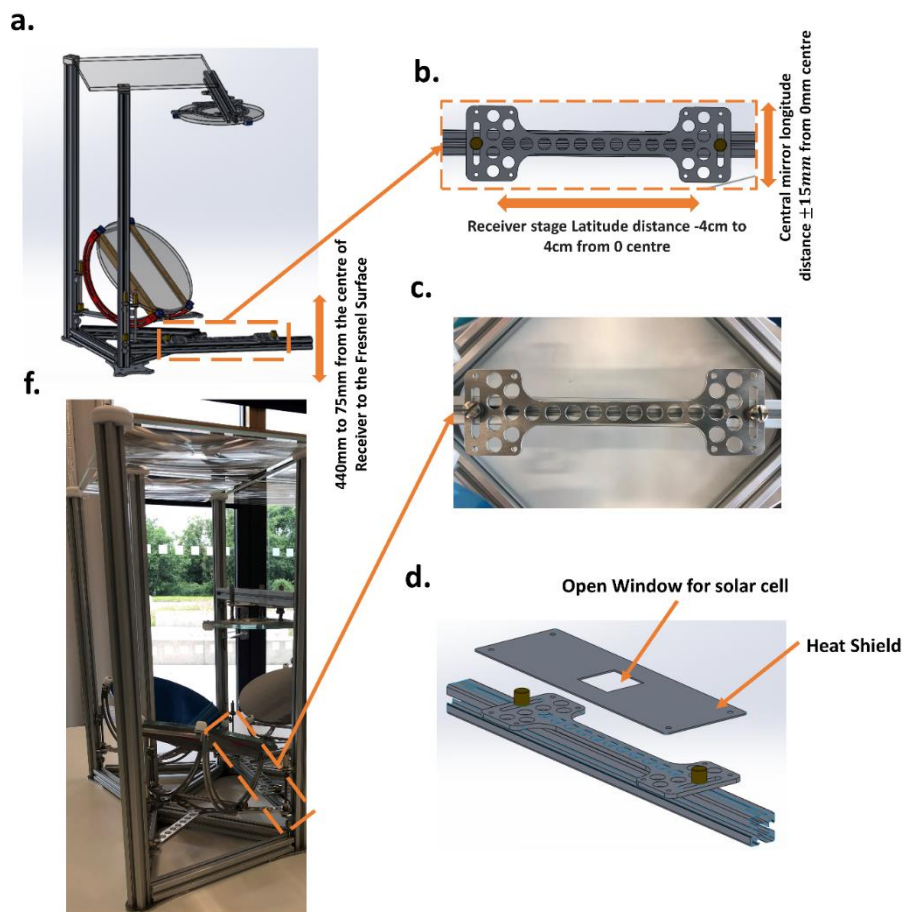


Figure 4 The SOLIDWORKS drawings for $\frac{1}{4}$ of the UHCPV system where a. shows the vertical transfer for the receiver base, b. shows the latitude and longitude transfer for the receiver base, c. shows the actual design for the receiver base, d. shows the heat shield, and f. shows the exact receiver position with the whole UHCPV system.

4 Materials selection

All the inside brackets 6 mm are made of Zinc plated steel. Both Aluminium strut profiles 20 × 20 mm and inside brackets are bought off the shelf from KJN Aluminium Profiles company [12]. The heat shield, central mirror frame, central mirror mount plate, secondary mirror segment, apex node, twin-apex node, and secondary mirror mount were all made of Aluminium (AL5083) and outsourced for the laser cutting process in Laser Precision Cutting Company [13]. All fasteners and fixings mechanical elements are purchased from RS Components Ltd [14]. Corrosion inhibitors (ULTRA Tef-Gel), primarily for stainless-steel screws to aluminium threads, was applied as the system will be operated outdoors where this gel offers waterproof lubricant with anti-corrosion and anti-seize properties and does not break down in salt water or detergents.

The primary optical components, SOG - Fresnel lens, were manufactured by Orafol Fresnel Optics [15]. The Fresnel lens is made of un-tempered low-iron glass of working distance ≈ 45 cm, clear aperture of $21 \times 21 \text{ cm}^2$, and glass plate dimensions of 23 cm × 23 cm × 4.0 mm. For the secondary and third stage optics, tempered low-iron glass and Pilkington mirror were manufactured and prepared by Cornwall Glass Company [16]. The manufactured glass was a circular mirror of 5 cm, 10 cm, and 15 cm in diameter with a thickness of 6 mm. The tempered low iron glass for the secondary and third stage mirrors is ordered to be filmed with high reflective efficiency.

5 Sun Tracker: Aspects and limitations

The ultrahigh concentration ratio level requires a high accuracy tracking system where slight light divergence (acceptance angle) is needed to attain the ultrahigh level. The optical tolerance of an ultrahigh system relies on many factors, one of which is the tracking system accuracy. The sunlight divergence angle of $\pm 0.265^\circ$ infers a slight acceptance angle where a sun tracker with a similar angular accuracy range should capture all the solar radiation emitted from the sun. However, other factors influence the accuracy where a relatively wider acceptance angle than the sun divergence angle is needed to challenge the optical tolerance and quality.

Two products of sun trackers manufactured by KIPP & ZONEN were investigated to incorporate the UHCPV system for continuous three-dimensional

tracking. At first, SOLYS2 sun tracker was selected for this study where SOLYS2 is a versatile solution allowing a wide range of radiometers to be mounted, as in Figure 5a. SOLYS2 sun tracker has both wire and Ethernet ports for communication and data acquisition feature with remote access for locating the sun position (zenith and azimuth angles). However, the SOLYS2 sun tracker was confronted due to its payload of only 20 kg, where UHCPV system can only be 10 kg, and a counterbalance weight of 10 kg must be applied to offer system stability and tracking precision. Therefore, the SOLYES Gear Drive (GD) was selected instead of the SOLYS2. SOLYES (GD) is ideal as it has all the features of SOLYS2 plus more of the payload of 80 kg, torque of 60 N.m, pointing accurately to the sun on higher windage and extreme weather conditions. The SOLYS GD can be installed on the same cast Aluminum SOLYS2 tripod. However, if the total weight of the tracker and the associated UHCPV system and radiometers is over 50 kg and/or there is a large windage, a heavy-duty tripod floor stand fitted with a height extension tube is suggested by the manufacturer to be used, as in Figure 5b. Table 1 summarises the specification comparisons between the two sun trackers.

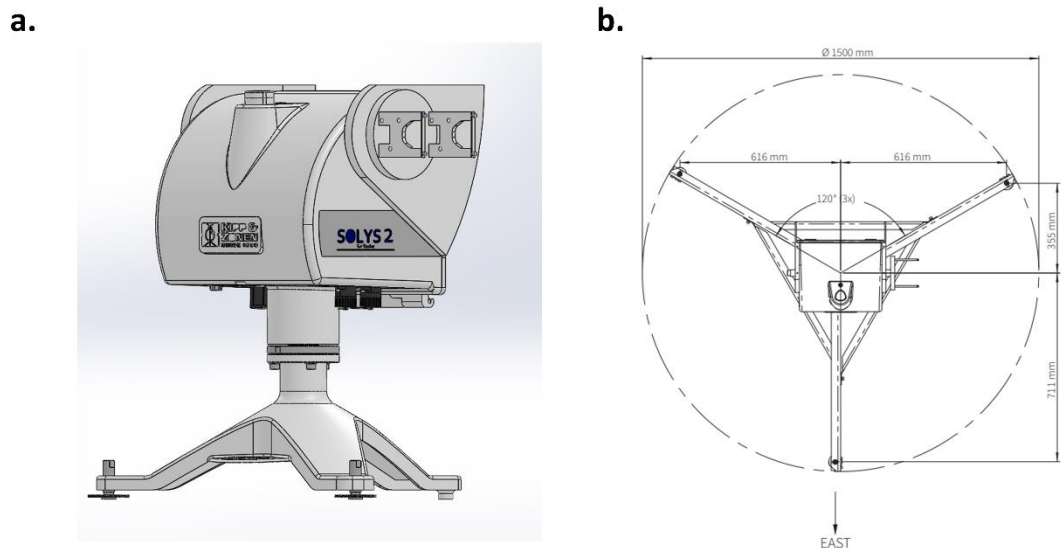


Figure 5 a. the SOLIDWORKS drawing for the SOLYS2 sun tracker with tripod and b. the top view screenshot for the heavy-duty floor stand [17].

Table 12 The sun trackers specifications comparison [18].

| Sun tracker Model | SOLYS2 | SOLYS Gear Drive (GD) |
|------------------------------|--|---|
| Pointing / Tracking Accuracy | < 0.1 ° (passive) < 0.02 ° (active) | < 0.1 ° (passive) < 0.02 ° (active) |
| Torque | 20Nm | 60Nm |
| Payload (Counterbalance) | 20kg | 80kg |
| System Weight | 28kg (sun tracker with tripod) | 26kg (only sun tracker) |
| Tripod | Included | Not included (Tripod of SOLYS2 can be used with limit (No more than 50 kg)) |
| Transmission System | Inverted tooth belts | High precision reduction gear |

6 Interlink Mechanical Structure – Beam Analysis

To link the UHCPV design to the sun tracker, two tube beams are needed to carry weights on both sides. Those weights are the UHCPV system and the counterbalance. The selected arms are a hollow square tube of 20 mm × 20 mm × 1.5 mm made of stainless-steel grade 316. The first design was made to be just a straight tube beam for simplification, and then a static load analysis using SOLIDWORKS software was conducted to assure the tube beam was suitable for the design. The static load study is meant to make sure the resulted in stress distribution after applying the system weight, and the counterbalance weight is below the yielding value. Not only this, but most importantly, the resulting deformation is below 0.01 mm for alignment and system accuracy. The tube geometry is illustrated in Figure 6a, where the scaled-up stress distribution and deformation distribution results are shown in Figure 6b and c, respectively. The principle of moments is applied to counterbalance the counterbalance weight and the UHCPV system weight. This helped to define the arm length with the correspondent applied mass. Both maximum stress and deformation are presented for an applied mass of 6.5 kg on both sides. The applied mass is simulated only for one beam.

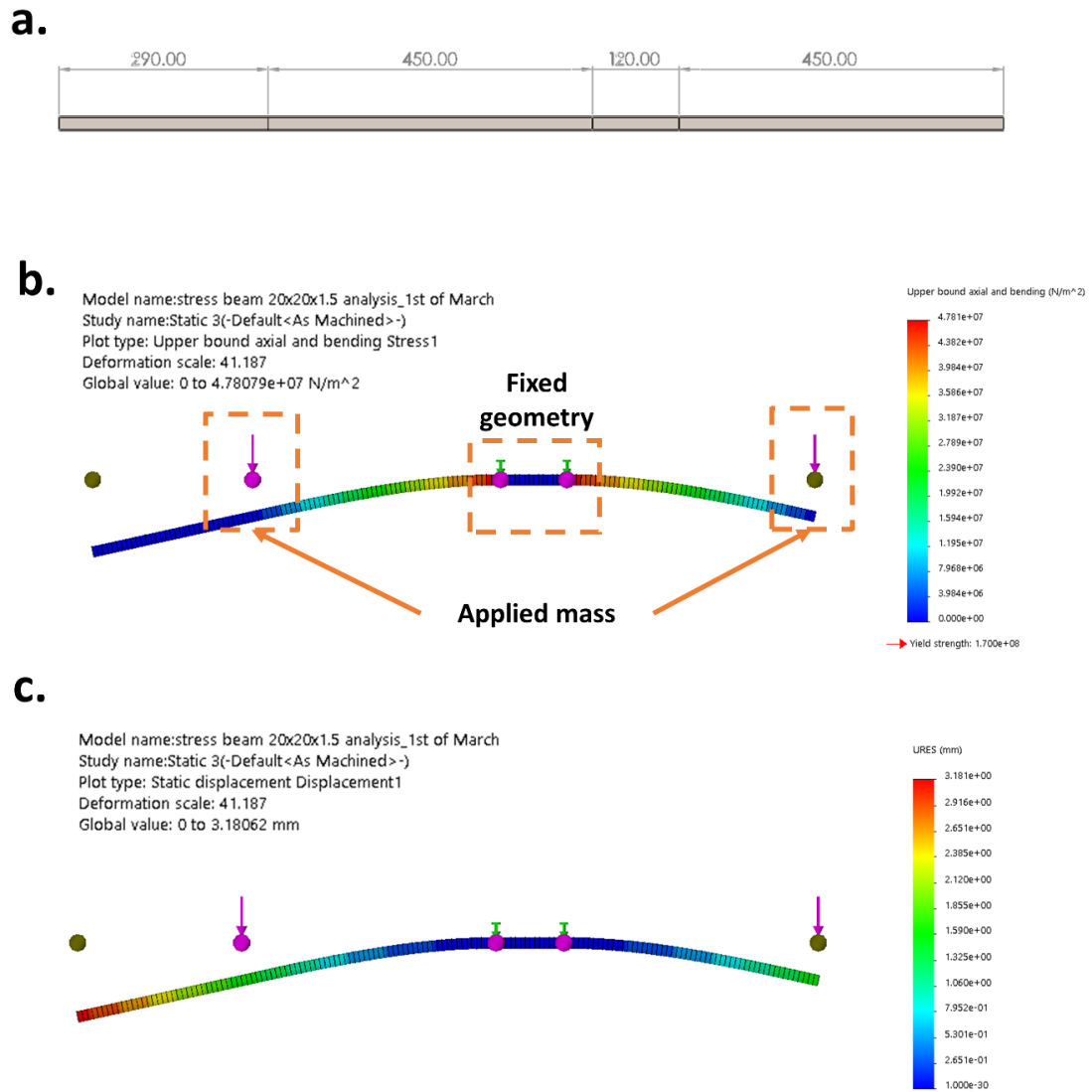


Figure 6 Shows the SOLIDWORKS screenshot where a. is the tube dimension, b. is the stress distribution results, and c. is the deformation distribution results.

The tube beam was examined for applied mass ranging from 0.5 kg to 10 kg in an increment of 0.5 kg. The read crossline shows the values at the applied mass. The applied mass resulted in a maximum deformation value ranging between 0.2 to 4.9 mm. The maximum stress value ranges between $3.7 \frac{\text{MN}}{\text{m}^2}$ to $73 \frac{\text{MN}}{\text{m}^2}$. The results are fully illustrated in Figure 7.

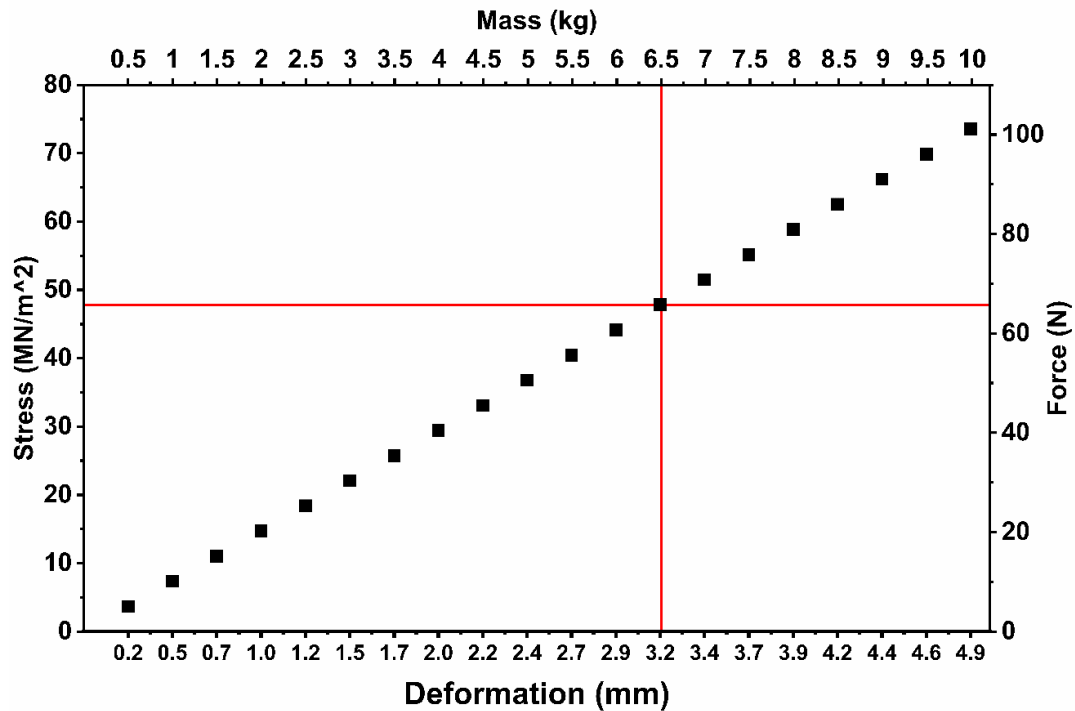


Figure 7 Shows the stress, force, and deformation at applied masses. The crossline shows the values at the actual applied system mass and counterbalance of (6.5 kg/ each side).

Obviously, the previous design is falling by producing a deformation of 3.2 mm, which will result in extreme off-alignment. Therefore, the configuration was revisited to reinforce the tube beam. The reinforcement is employed by adding a tube beam in a triangular shape to strengthen the design. The geometry dimension is given in Figure 8a. The static load analysis using SOLIDWORKS software is conducted again with a new design applying the same masses. Figures 8b and c show the stress and deformation distribution, respectively.

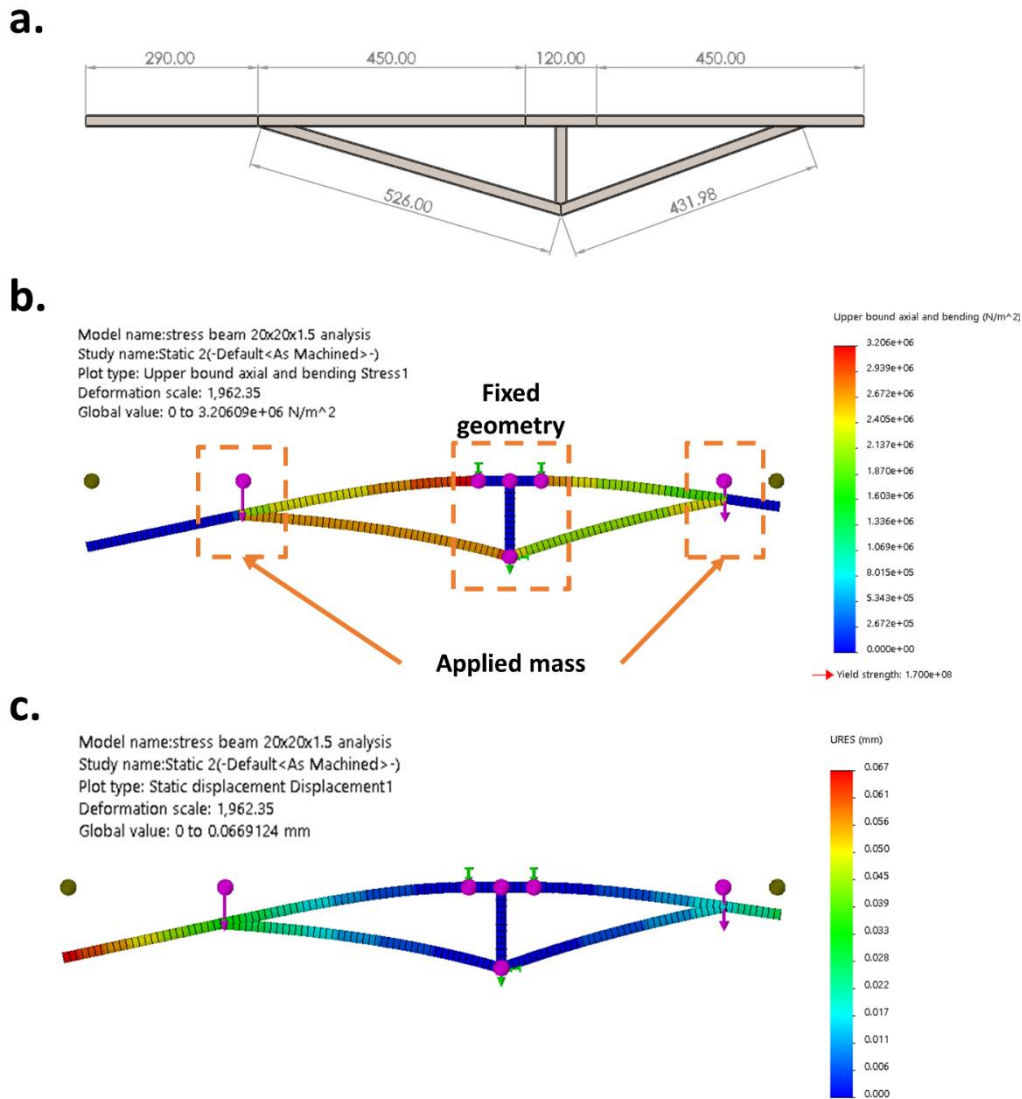


Figure 8 Shows the SOLIDWORKS screenshot where a. is the reinforced design dimension, b. is the stress distribution results, and c. is the deformation distribution results.

The reinforced tube beam was again assessed for applied mass ranging from 0.5 kg to 10 kg in an increment of 0.5 kg. The read crossline indicates the values at the applied mass. The applied mass resulted in a maximum deformation value ranging between 0.005 mm to 0.1004 mm. The maximum stress value varies between $0.25 \frac{\text{MN}}{\text{m}^2}$ to $5.04 \frac{\text{MN}}{\text{m}^2}$. The findings are fully illustrated in Figure 8. The reinforced design shows an excellent deformation result where a large weight can still be applied up to 10 kg with a deformation not exceeding 0.1 mm.

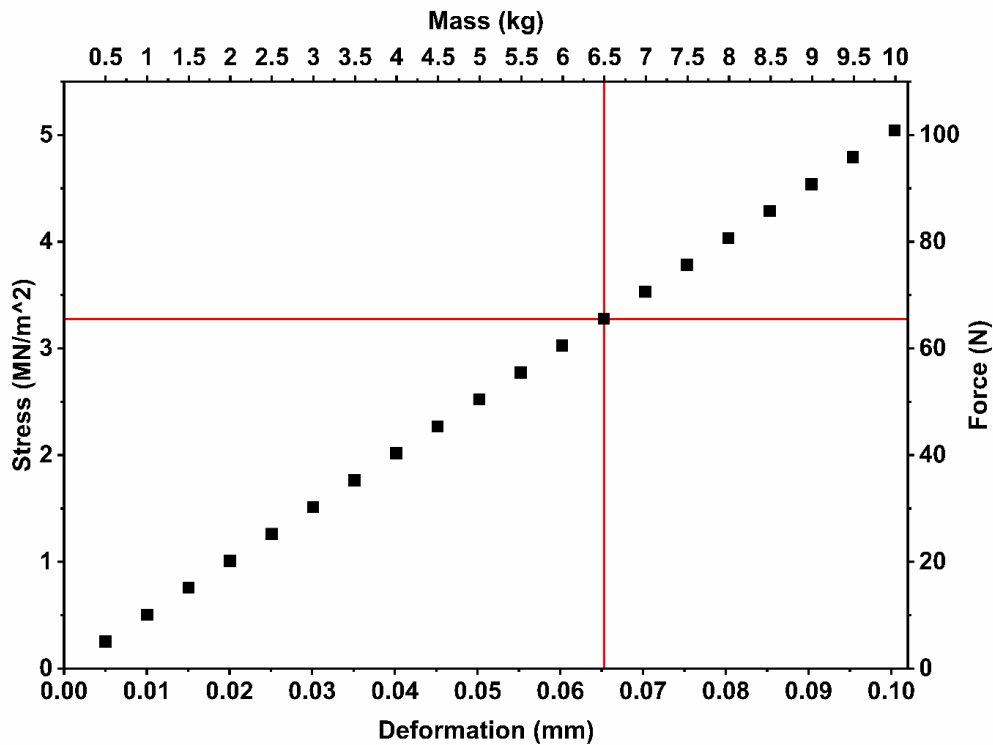
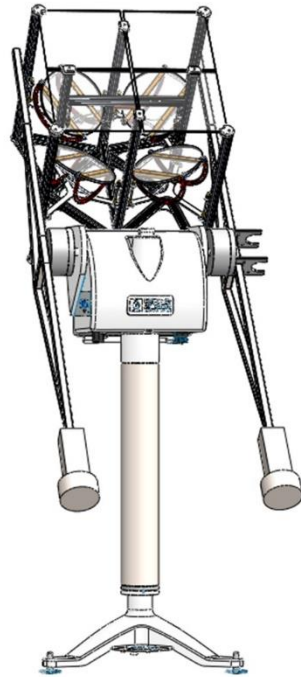


Figure 9 Shows the stress, force, and deformation at applied masses for the reinforced design. The crossline shows the values at the actual applied system mass and counterbalance of (6.5 kg/ each side).

7 System Component Integration and Spatial Consideration

The UHCPV system, counterbalance arm, and weight were integrated with the sun tracker and plotted in SOLIDWORKS. This integration is meant to perform system spatial analysis for the minimum required operating area and have an excellent visualisation for the overall system considering both azimuth angle and sun elevation, as in Figure 10a and b. The sun tracker rotates a lap when it is powered up, starting with 270° to the left and then another 270° to the right to take off from a home position. To perform the rotation lap, a minimum of 2-meter in diameter (width length) and a height of 2-meter are required to allow the UHCPV system plus the sun tracker to move freely. The required space area exists on the north light roof of the Environmental and Sustainability Institute (ESI) - Penryn Campus, University of Exeter. The UHCPV system is interlinked with the reinforced tube beam and parallel to the centre of mass for the UHCPV system, which is 250 mm to the top surface of the Fresnel lens.

a.



b.



Figure 10 The integration of counterbalance arm, counterbalance weight, and UHCPV system to the sun tracker, where a. is the SOLIDWORKS design and b. is the full actual system outdoor ready for testing. The drawings in Figure 10a includes the extended tube but not the heavy-duty floor stand tripod, where Figure b shows the real heavy-duty floor stand tripod.

8 Impact of Wind Load

The impact of wind load is an essential factor in ensuring no extra loads occur on the system. The associated loads will affect the sun tracker by either turning over the entire setup or applying an excessive torque higher than the system torque capacity of 60 N.m. The setup is mechanically fixed, and the infrastructure is made to assure system stability. As a result, the turning over is not a concern. On the other hand, the torque needs to be investigated in all directions (x, y, z) and with changing the setup angle ($100^\circ, 145^\circ, 185^\circ$). According to the World Weather Online database [19], the maximum wind speed by the record occurred in Penryn campus was 54 kmph (15 m/s) in December 2015. Thus, we will analyse the torque results at all dimensions and comply with the one reached first as an operating limit, either the sun tracker torque limit or the maximum wind speed. In this section, the UHCPV system was built as a solid block to worsen the impact of wind, at which safe operating conditions will always be in place.

The flow simulation study was accomplished in SOLIDWORKS software in three dimensions. Wind speed was applied from a minimum value of 3 m/s to an extreme level of 22 m/s (this level is characterised as a tropical storm) in an interval of 3 units. The right-hand rule is applied to determine the torque direction, where wind speed (Force) in x-direction applies torque in the z-direction, y-direction wind speed (Force) applies torque in the z-direction, and wind speed (Force) in z-direction applies torque in the x-direction. Figure 11a, b, and c shows the results of the complete system setup oriented at 100°, 145°, and 185°. In all figures, the sun tracker torque limit and the wind speed limit were plotted as a crossline generating a recommended outdoor operating condition as in the shaded area. Although this study is essential for a temporary sited outdoor system, this experimental setup will be operated outdoor only on clear sunny days to comply with Penryn Campus – University of Exeter safety regulations.

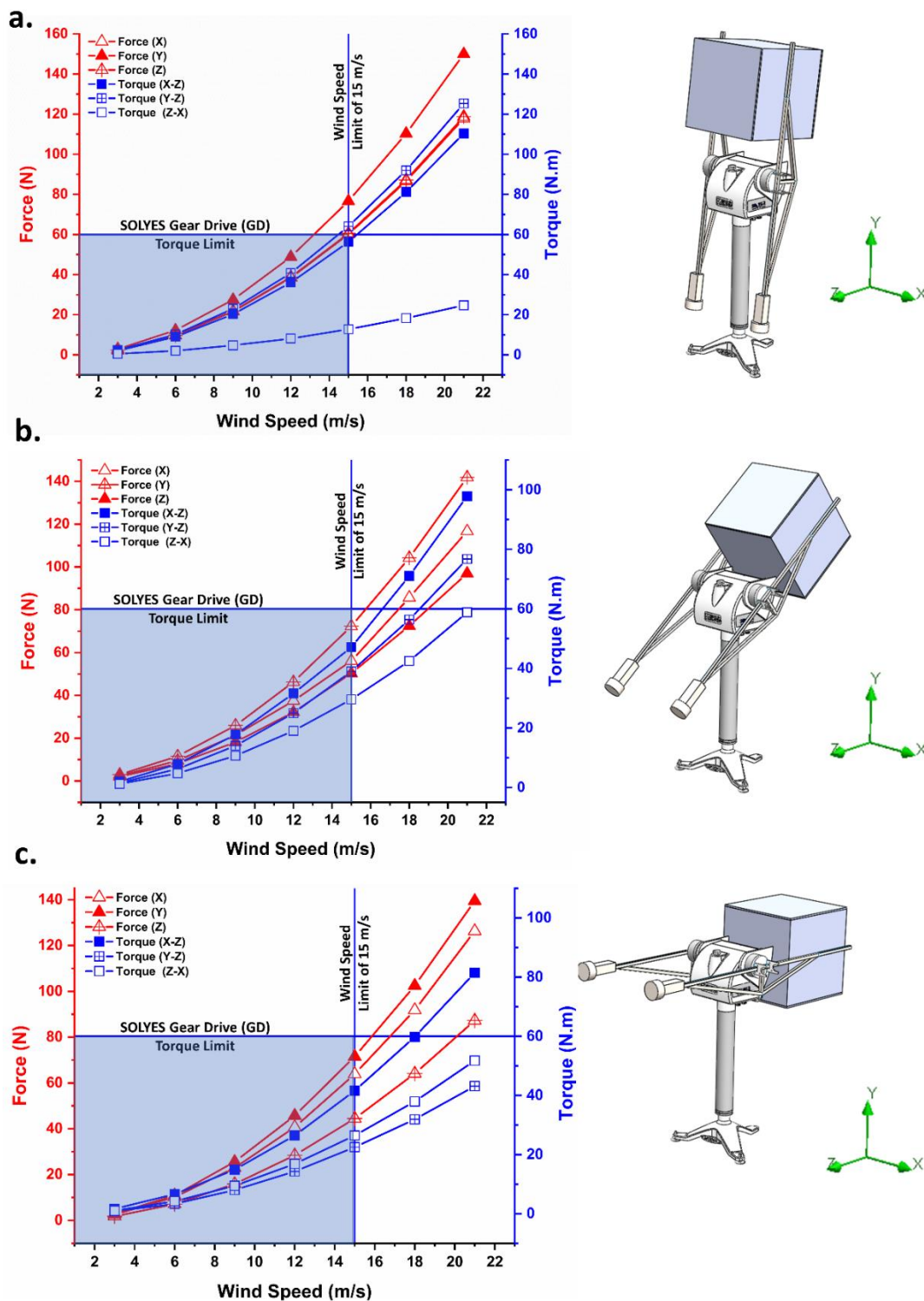


Figure 11 Shows the applied wind speed and the resulted force and torque values with SOLIDWORKS screenshots for the complete setup at an oriented angle, where a. sited at 100°, b. sited at 145°, and c sited at 185°.

9 Conclusion

This mechanical study showed the sited boundary condition for the design through which the system was built. All the system design and numerical analysis were performed using SOLIDWORKS software. The main mechanical items were

detailed in the manuscript and further illustrated in photographs based on the optical stage order. Most of the design items were outsourced and assembled in the workshop of the Solar Energy Group in Penryn Campus - University of Exeter. The selected sun tracker to host the UHCPV system were discussed, pointing out its specification and capacity. Two interlink mechanical beam structure designs were presented to exhibit both the stress and deformation distribution. The entire setup integration for spatial and windage analyses was performed.

Acknowledgement

M.A would like to duly acknowledge the financial support from the Saudi Arabia Culture Bureau in the U.K. The funder has no role in study design data collection or manuscript preparation.

Reference:

- [1] K. Shanks, J.P. Ferrer-rodriguez, E.F. Fernández, F. Almonacid, A > 3000 suns high concentrator photovoltaic design based on multiple Fresnel lens primaries focusing to one central solar cell, *Solar Energy*. 169 (2018) 457–467. doi:10.1016/j.solener.2018.05.016.
- [2] M. Alzahrani, A. Ahmed, K. Shanks, S. Sundaram, T. Mallick, Optical component analysis for ultrahigh concentrated photovoltaic system (UHCPV), *Solar Energy*. 227 (2021) 321–333. doi:10.1016/j.solener.2021.09.019.
- [3] K. Shanks, S. Senthilarasu, T.K. Mallick, Optics for concentrating photovoltaics: Trends, limits and opportunities for materials and design, *Renewable and Sustainable Energy Reviews*. 60 (2016) 394–407. doi:10.1016/j.rser.2016.01.089.
- [4] K. Lovegrove, G. Burgess, J. Pye, A new 500 m² paraboloidal dish solar concentrator, *Solar Energy*. 85 (2011) 620–626. doi:10.1016/j.solener.2010.01.009.
- [5] M. Schmitz, N. Wiik, G. Ambrosetti, A. Pedretti, S. Paredes, P. Ruch, B. Michel, A. Steinfeld, A 6-focus high-concentration photovoltaic-thermal dish system, *Solar Energy*. 155 (2017) 445–463. doi:10.1016/j.solener.2017.05.087.
- [6] J.P. Ferrer-Rodríguez, J.M. Saura, E.F. Fernández, F. Almonacid, D.L. Talavera, P. Pérez-Higueras, Exploring ultra-high concentrator photovoltaic Cassegrain-Koehler-based designs up to 6000×, *Optics Express*. 28 (2020) 6609. doi:10.1364/OE.382236.
- [7] J.P. Ferrer-Rodríguez, E.F. Fernández, F. Almonacid, P. Pérez-Higueras, Optical design of a 4-off-axis-unit Cassegrain ultra-high concentrator photovoltaics module with a central receiver, *Optics Letters*. 41 (2016) 1985. doi:10.1364/OL.41.001985.
- [8] M. Alzahrani, A. Ahmed, K. Shanks, S. Sundaram, T. Mallick, Optical losses and durability of flawed Fresnel lenses for concentrated photovoltaic application, *Materials Letters*. 275 (2020) 128145. doi:10.1016/j.matlet.2020.128145.
- [9] M. Alzahrani, K. Shanks, T.K. Mallick, Advances and limitations of increasing solar irradiance for concentrating photovoltaics thermal system, *Renewable and Sustainable Energy Reviews*. 138 (2021) 110517. doi:10.1016/j.rser.2020.110517.
- [10] A. Awasthi, A. Kumar, M.M.S. R, Review on sun tracking technology in solar PV system, *Energy Reports*. 6 (2020) 392–405. doi:10.1016/j.egyr.2020.02.004.
- [11] R. Singh, S. Kumar, A. Gehlot, R. Pachauri, An imperative role of sun trackers in photovoltaic technology : A review, *Renewable and Sustainable Energy Reviews*. 82 (2018) 3263–3278. doi:10.1016/j.rser.2017.10.018.
- [12] KJN Aluminium Profiles, (n.d.). <https://www.aluminium-profile.co.uk/> (accessed April 6, 2021).

- [13] Laser Precision Cutting Company, (n.d.). <https://www.laser.co.uk/> (accessed April 10, 2021).
- [14] RS Components Ltd, (n.d.). <https://uk.rs-online.com/web/>.
- [15] ORAFOL Fresnel Optics GmbH, (n.d.). <https://www.orafol.com/en/> (accessed March 10, 2022).
- [16] Cornwall Glass Comapny_Penryn, (n.d.). <https://cornwallglass.co.uk/your-branch/penryn/> (accessed March 10, 2022).
- [17] Kipp & ZONEN, Instruction Manual : SOLYS2 & SOLYS Gear Drive, 2003.
- [18] KIPP & ZONEN, (n.d.). <https://www.kippzonen.com/> (accessed April 11, 2021).
- [19] World Weather Online, (n.d.). <https://www.worldweatheronline.com> (accessed February 2, 2022).

Article 10. M. Alzahrani, K. Shanks, Y. Chanchangi, W. Cameron, S. Sundaram, T. Mallick, "Record High Solar Concentration for PV: Experimental Validation Achieving > 1200 effective sun.' Prepared to be Submitted to Nature Energy Journal.

**Record High Solar Concentration for PV: Experimental Validation
Achieving > 1200 effective sun**

In preparation for

Nature Energy Journal

Mussad M. Alzahrani^{1,2}, Katie Shanks¹, Yusuf Chanchangi¹, William J. Cameron¹, Senthilarasu Sundaram¹, Tapas K. Mallick^{1*}

¹Environmental and Sustainability Institute, University of Exeter, Penryn Campus, Cornwall TR10 9FE, UK.

²Mechanical and Energy Engineering Department, Imam Abdulrahman Bin Faisal University, Dammam, 34212, Saudi Arabia

*Corresponding author: Tapas K. Mallick

Tel: 01326 259465

Email: t.k.mallick@exeter.ac.uk

In this paper, we demonstrated the performance of ultrahigh concentrator photovoltaics system design with a geometrical concentration ratio up to $5831 \times$. The system is fabricated to allowed stepped concentration level testing and characterised outdoors, achieving the highest effective concentration ratio of 1291 suns and an estimated 1880 suns if sufficient cooling is deployed. Three types of secondary mirrors were investigated: Aluminium reflective and ReflecTech® Polymer films and Pilkington Optimirror (mirror). Continuous sun tracked measurement for a $\frac{1}{4}$ UHCPV system and a 4-domed territory optical element is carried out. To the best of the authors' knowledge, this compact ultrahigh concentrator photovoltaics system represented the highest geometrical concentration ratio and the highest effective concentration ratio.

A concentrated photovoltaic system (CPVs) can illuminate smaller solar cell where their cost is counterbalanced by the inexpensive optics resulting in an economically feasible technology. However, the flat plate solar PV module is cheaper than that of the concentrated optical component, regardless of CPV being higher efficiency and area-efficient successfully achieved. Now, ultrahigh concentrator photovoltaics (UHCPV) with concentration ratios > 1000 suns¹² have a high potential in increasing the power output and being more cost-effective despite the poorer efficiencies of the cells. The ongoing research of multijunction solar cells (MJSC) have pushed the envelope of efficiency records to 47.1%; thus, a similar progressive in concentrator optical designs is in demand to comply³. Few studies of Cassegrain-based and Fresnel-based focal point configurations in the literature report an optical system capable of achieving ultrahigh (UH) factor theoretically with high performance⁴.

For Cassegrain-based, two studies have investigated the paraboloid-hyperboloid pairs of optics into one central receiver. One of those designs is an optical configuration of a 4-off-axis Cassegrain UH concentrator photovoltaic module of a $2304 \times$ geometrical concentration resulting in an optical concentration ratio of 1682 suns, respectively⁵. This design has been further developed theoretically to reach a geometrical concentration ratio of $6000 \times$. Only a CPV module of a $3015 \times$ geometrical concentration one-cell compact prototype was constructed and characterised indoor to result in 938 suns effectively⁶. Another one is the mini-Cassegrain mirror optics concentrators of the $1037 \times$

geometrical concentration prototype, where it has attained an optical concentration ratio of 800 suns, respectively⁷. However, paraboloid-hyperboloid pairs of optics have high surface roughness. The polishing for the conical shaped would alter the curvature and introduce optical inaccuracies in directing and redirecting sun rays.

Two studies have investigated the Fresnel Lens theoretically toward the UH concentration ratio level for Fresnel-based. A dome-shaped Fresnel Lens has been configured with four entrances into an optical receiver for a $2300 \times$ geometrical concentration ratio resulting in an optical concentration ratio of 1897 suns, respectively⁸. However, the manufacturability of this optic is difficult and expensive due to the need for a particular casting mould. A design of a $4096 \times$ based on four symmetric optics with an optical guide was proposed theoretically. Preliminary indoor experimentation of this design was conducted for only a $2400 \times$ of geometrical concentration resulting only in 556 suns of effective concentration ratio. A > 3000 suns based on 4-flat Fresnel Lens (SOG) concentrating into one central receive with the existence of redirecting optical materials have shown a geometrical and optical concentration ratio of 5831 suns and 4373 suns, respectively⁹. This system is configured based on a 4-fresnel lens due to the fabrication limits and the high cost of a large Fresnel Lens. This design selected a flat mirror as a secondary optics instead of conically shaped due to its low surface roughness. Also, the favourability of flat mirror is due to easy manufacturability and employability of reflective film ($\sim 97\%$) at a relatively low cost. All the tested systems were not yet able to reach the UH (> 1000 suns), and did not even successfully break through an effective concentration ratio of 1000 suns. Also, none of these studies were tested outdoors in actual weather conditions, which is clearly absent in the literature.

Here, we report a prototype of a UHCPV design⁹ based on 4 Fresnel lenses concentrating into a $5.5 \times 5.5 \text{ mm}^2$ MJSC to validate the system capacity of achieving the UH concentration range. The total geometrical concentration ratio of this optical technology is $5831 \times$, as in Figure 1a . The optical system was interlinked with a high pointing accuracy SOLYS GEAR Drive sun tracker of $< 0.02^\circ$ to trace the direct solar irradiance in outdoor real weather conditions¹⁰. Because of how complex UH system alignment and testing can be, we have:

- 1st: tested the optical efficiency of each component on it own to understand their individual losses.
- 2nd: then the combination of the primary Fresnel Lenses plus secondary mirrors only and done this for 1/4 , 2/4, 3/4, and 4/4 outdoors with only passive solar cell cooling, as in Figure 1b.
- 3rd: finally, we included the final optic which significantly increases concentration, but testing is currently limited to only ¼ of the system due to high solar cell temperatures, as in Figure 1c.

The tested system generates 27% more effective concentration to the latest level in the literature by far⁶ (1291 suns instead of 938 suns). This study represents the proof of concept for a tested UHCPV compact system design, which shows an essential step toward achieving a UH concentration ratio for actual outdoor power generation.

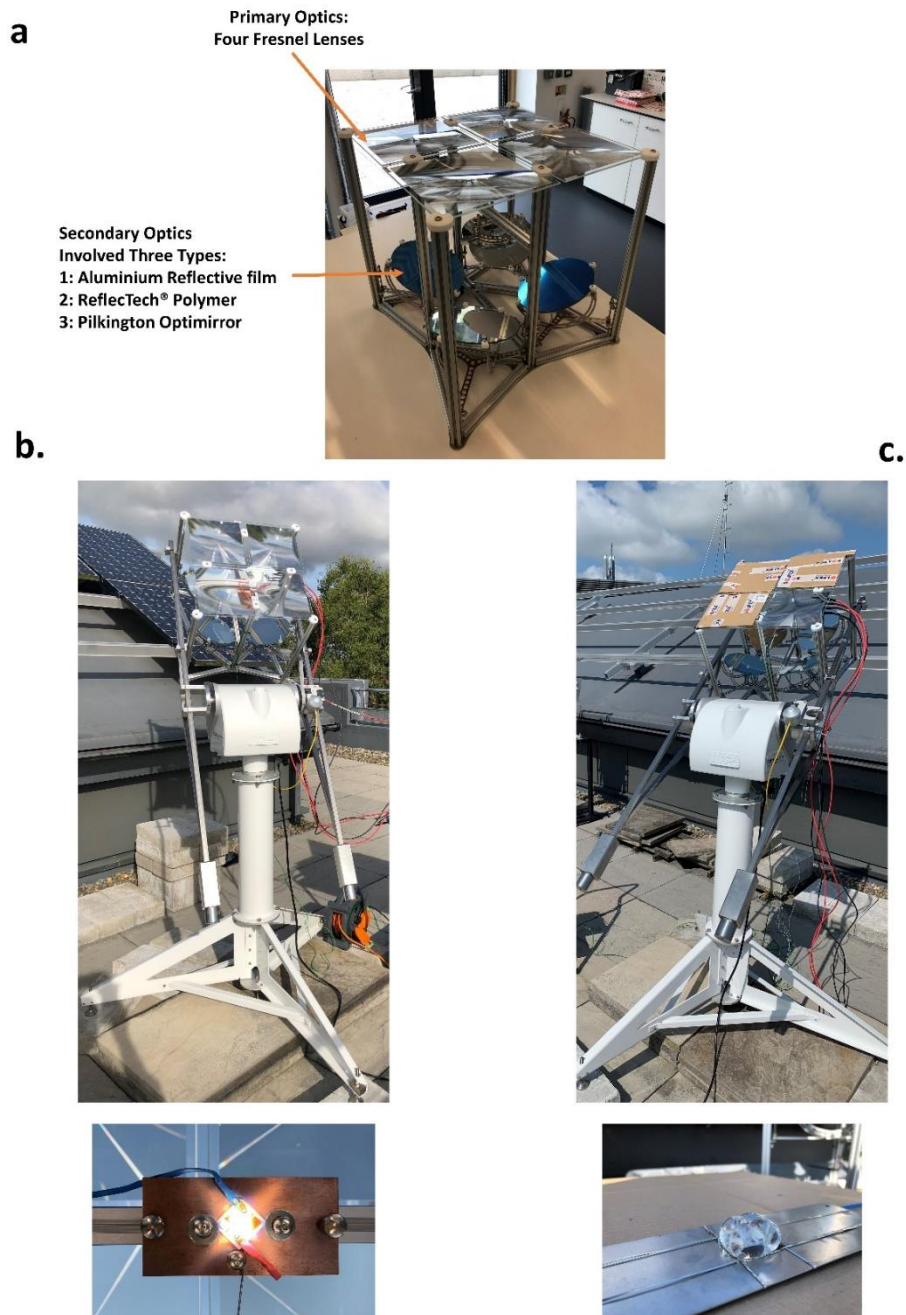


Figure 1 Images for a. the built UHCPV system with highlighting the primary and secondary optical stages. b. shows the full UHCPV system setup testing the bare cell where c. shows the $\frac{1}{4}$ UHCPV system setup testing the TOE with the cell.

UHCPV System Design

The UHCPV one-cell model is designed and fabricated to result in a geometrical concentration ratio of $5831 \times$. To consistently target concentration ratios above 1000 suns a high tolerance design is required. The UHCPV design is meant to be simplified for viability and hence employs a wide degree of freedom at every optical stage. Enhanced Fresnel Assembly - EFA (3C44A) - $5.5 \times 5.5 \text{ mm}^2$ MJSC is incorporated in the system for evaluating the optical performance electrically. A 4-domed optic was manufactured based on Silygard-184 material (Figure 2a) in-house and directly attached to the cell (Figure 2b). Three types of reflective optic were implemented in the secondary optical stage. Two of which involved applying high reflective films to flat metallic substrates, and the other is a coated glass type flat mirror. The reflective films are Aluminium Reflective film (Figure 2c) and ReflecTech® Polymer¹¹ (Figure 2e), whereas the flat mirror is Pilkington Optimirror (Figure 2d).

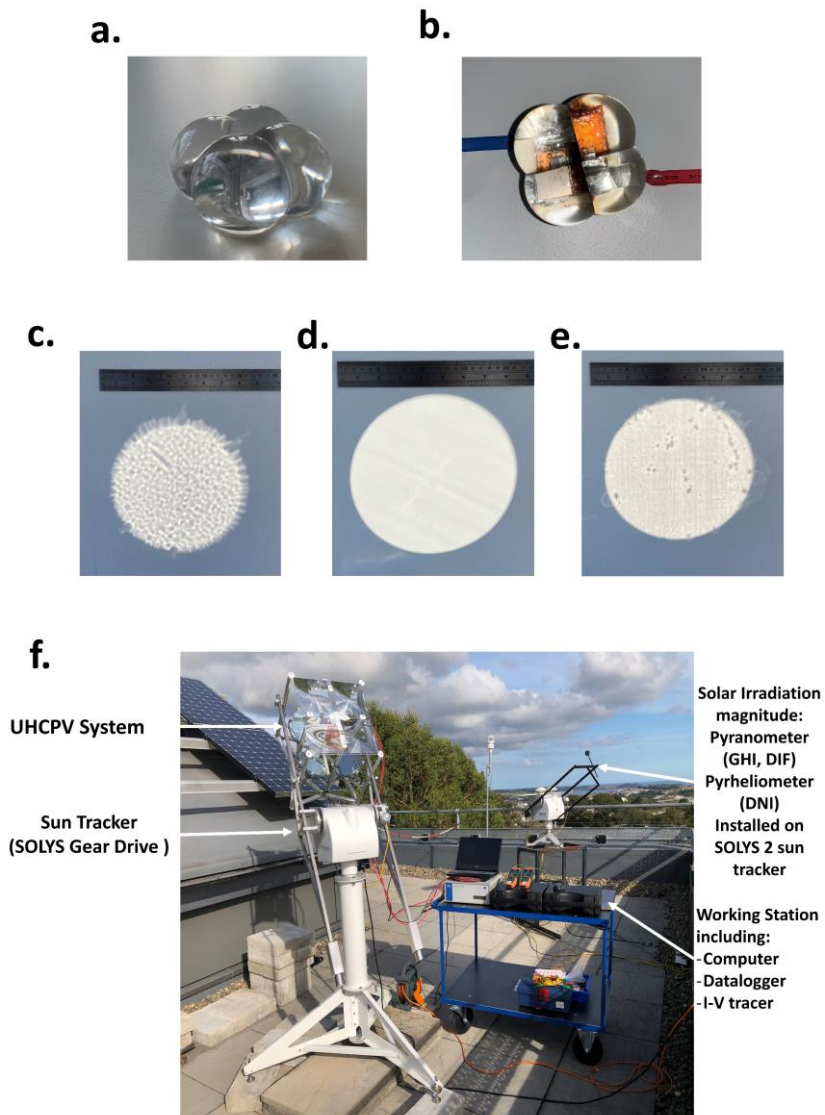


Figure 2 Images for a. Tertiary Optical Element (TOE), b. Tertiary Optical Element (TOE) bonded to the cell. c. shows the reflective image for the coated Aluminium film on low-iron glass simulated on a flat surface. The imperfection of the coated film is apparent in the reflected image as a bubble surface (challenging to observe on the coated film), resulting in an optical dispersion. d. shows the reflective image of the mirror with a clear reflective image. e. shows the reflective mirror of the ReflecTech® Polymer. The reflected image of the ReflecTech® Polymer is slight less dispersion than the Aluminium film. f. shows the full outdoor experimental setup.

CPV System Testing

Optical

All the associated optics were optically characterised for SOG - Fresnel Lens and the secondary optics before the outdoor testing. The illustrated images in Figure 2c, d, and e raised attention to the losses due to optical dispersion for the secondary coated films and mirrors. Thus, UV/Vis/NIR spectrophotometers were utilised to measure the reflectivity of prepared secondary optic and the transmissivity of both the TOE and the SOG - Fresnel lens. Figure 3a spectral response (SR) calculation as a result of the EQE (external quantum efficiency) measurements implies the generated currents to the power incident on the solar cell in subcell categories⁶. The fabricated TOE based on a Sylgard-184 material presented an excellent optical performance of $> 90\%$ for wavelength $400 < \lambda < 1100$ nm in visible and near infrared range, after which there are clear drops in performance, as in Figure 3a. The secondary optics show relatively excellent optical performance with the highest results for the ReflecTech® Polymer and the lowest for the mirror due to the drop in wavelength range $500 < \lambda < 1600$ nm. The reflectivity was $\approx 91.3\%$ for Aluminium Reflective film, $\approx 96.8\%$ for ReflecTech® Polymer, and $\approx 85.8\%$ for the mirror. The SOG Fresnel lens showed a transmittance of 93.8% in the same wavelength range. All the reflectivity is based on the averaged measurements for wavelength between $400 < \lambda < 2000$ nm, as in Figure 3b. All the incorporated mirrors in the secondary stage are influenced by the optical performance of the SOG Fresnel lens at the first.

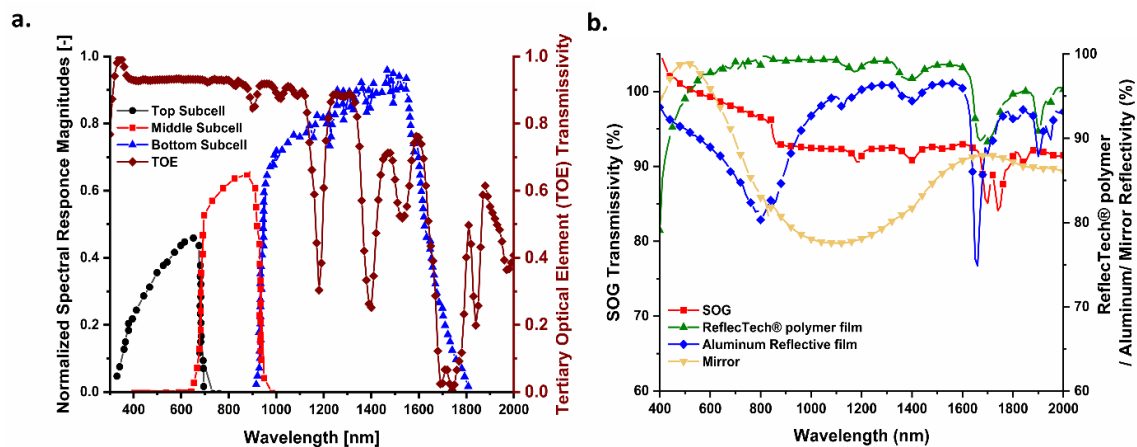


Figure 3 The optical characterisation results for a. the TOE and the solar cell SR and b. the secondary optics.

Electrically

The UHCPV system was assessed on 1/4 base (1/4 of the aperture area - 1 Fresnel lens), 2/4 (2 Fresnel lenses), 3/4 (3 Fresnel lenses), and 4/4 (complete system - 4 Fresnel lenses) to observe the solar cell electrical performance. The aperture area is kept covered to ensure a focal spot capable of burning out system components is not produced. Therefore, the Fresnel lens was exposed for only 3 seconds with instantaneous measurements on a 1/4 basis, relying on the I-V tracer instrument to evaluate electrical components. All the measurements in this section were conducted on the 23rd of August 2021. The electrical characterisation of the full UHCPV one-cell at outdoor condition yielded the following electrical values: for the Aluminium reflective film $I_{sc} = 4.3$ A, (open-circuit voltage (V_{oc})) $V_{oc} = 2.2$ V, (fill factor (FF)) $FF = 0.68$, (maximum power(P_{max})) $P_{max} = 6.75$ W, the mirror $I_{sc} = 5.4$ A, $V_{oc} = 2.8$ V, $FF = 0.53$, $P_{max} = 7.87$ W, and ReflecTech® Polymer $I_{sc} = 5.6$ A, $V_{oc} = 2.1$ V, $FF = 0.58$, $P_{max} = 7.09$ W. The rest of the measured data is exhibited in Figure 4, where a. is the Aluminium reflective film, b. is the mirror, and c. is ReflecTech® Polymer. The proportional correlation is apparent in all Figure 4a through the increase in I_{sc} and the reduction in the V_{oc} with increasing concentration ratio. The electrical output components have shown an excellent electrical measurement through the relatively squared shape of the I-V curve and curvature of power. The power curve shows a quenching in power generation with concentration ratio, especially with 3/4 and 4/4 Fresnel lenses in Aluminium reflective film, where the power curve for ReflecTech® Polymer shows relatively similar results of both 3/4 and 4/4 Fresnel lens.

Due to the reflectance levels at > 1600 nm, the mirror has the highest power output regardless of being not the highest I_{sc} . The ReflecTech® Polymer has the highest overall average reflectance and hence has the highest I_{sc} , which relates directly to the concentration of the solar irradiance. Also, the results indicate that the best overall performance is not correlated only to the maximum I_{sc} but most importantly to the optical device. Therefore, the unwanted wavelengths that contribute significantly to heat are high, and the results suggest prioritising decreasing the heat through utilizing a secondary optic with relatively lower average reflectance.

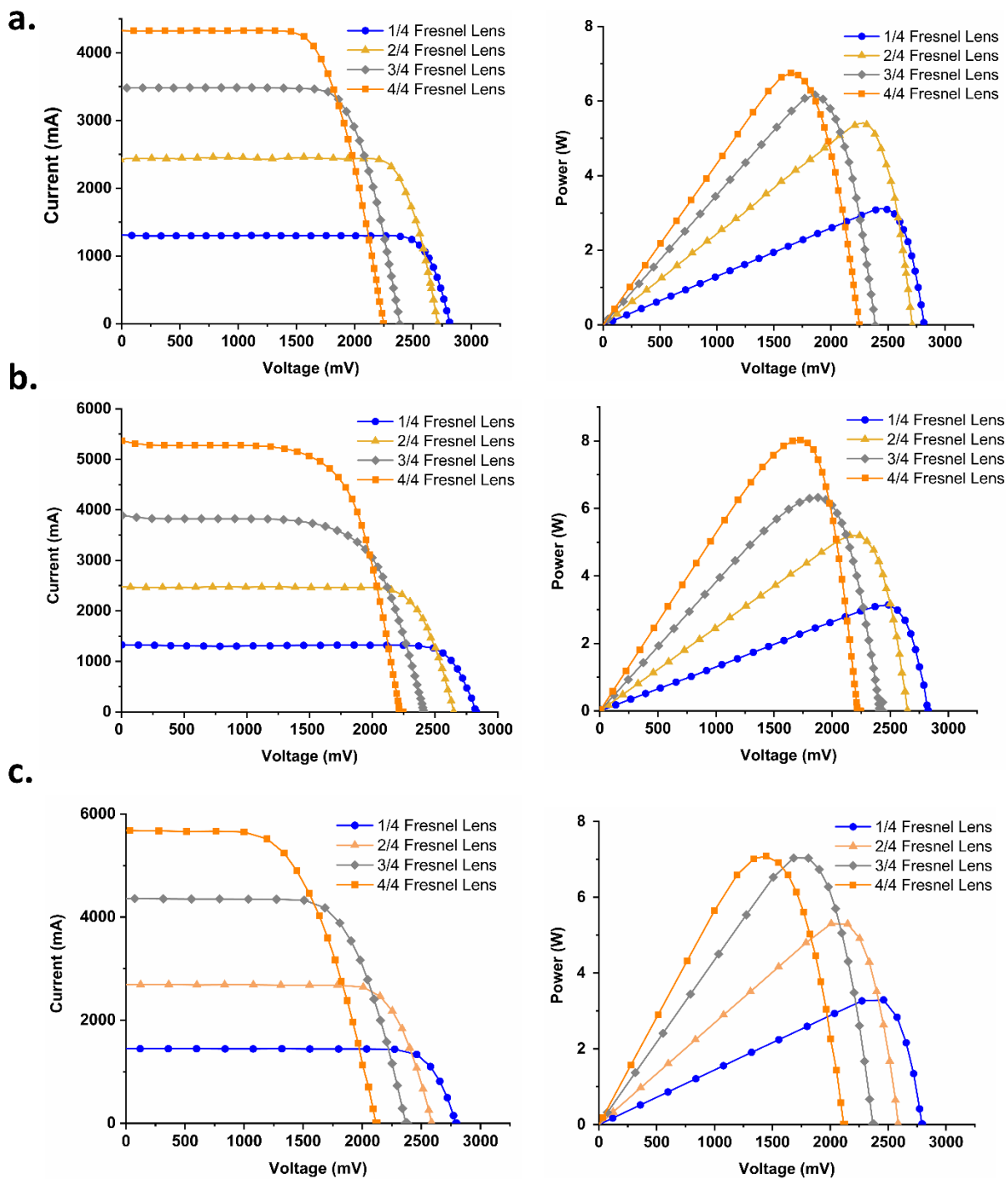


Figure 4 Shows the measured I-V and power curves for a. Aluminium reflective film, b. mirror, and c. ReflecTech® Polymer.

The electrical components help to complete the optical performance of the UHCPV system. To establish the effective concentration correlation, the solar cell electrical performance was measured under the illumination of 1 sun resulting in I_{SC} of 4.4 mA. Therefore, the effective concentration (C_{eff}) is solved based on the

fraction of $I_{sc,conc}$ under concentration to the I_{sc} , with no concentration ($C_{eff} = I_{sc,conc}/I_{sc}$). The optical efficiency is related to C_{eff} to the geometrical concentration (C_{geo}). Figure 5a display both the effective concentration ratio and optical efficiency, where the maximum results (complete system operation – 4 Fresnel lenses) shows C_{eff} of 984 suns, 1220 suns, and 1291 suns and η_{opt} on average 18.5%, 20.25%, and 22% for Aluminium reflective film, Pilkington Optimirror, and ReflecTech® Polymer, respectively. Although the optical efficiency is low for this UHCPV system design, the achieved level of effective concentration ratio for both mirror and ReflecTech® Polymer has never been accomplished for a compact design. Figure 5b and c show the effective concentration ratio with FF and cell efficiency (η_{cell}). At full system performance, the FF shows a value of 0.68, 0.53, and 0.49, and the cell efficiency shows a result of 15.5%, 18.8%, and 16.4% for Aluminium reflective film, Pilkington Optimirror, and ReflecTech® Polymer, respectively, as in Figure 5b and c. The drop in FF indicates the impact of concentration, in terms of generated heat on the solar cell surface, where the drop in the η_{cell} with increasing C_{eff} attests to undesirable loss in both FF and V_{oc} . Figure 5d illustrates power to η_{cell} with increasing C_{eff} . The power boosted linearly for mirror with increasing system working aperture area from 3.2 W to 7.9 W, where the power increased in a logarithmic curve for Aluminium reflective film in a range between 3.1 W and 6.7 W. Interestingly, the power production for the ReflecTech® Polymer reached its maximum limit when the system was operating with 3/4 and 4/4 Fresnel lens showing a result fluctuating between 7.069 W and 7.092 W.

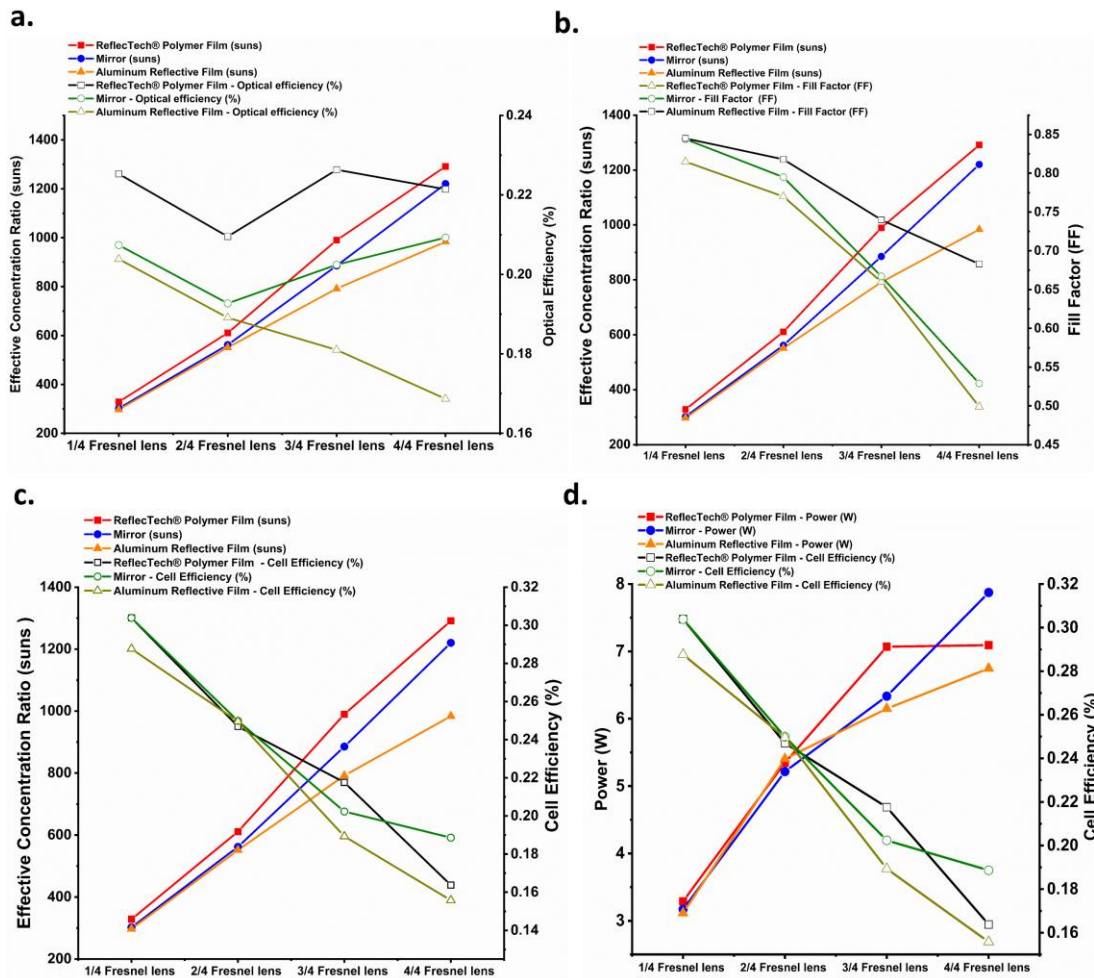


Figure 5 The electrical to optical correlations where a. is C_{eff} to the η_{opt} , b. is the C_{eff} to the FF, c. is the C_{eff} to the η_{cell} , and d. is the power to η_{cell} .

Continuous Measurements for 1/4 of the UHCPV System

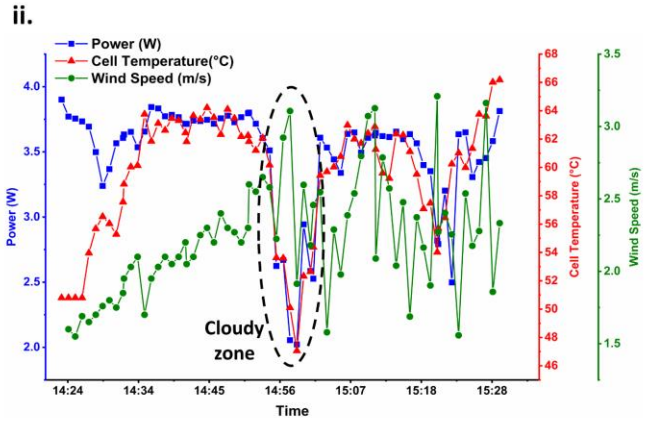
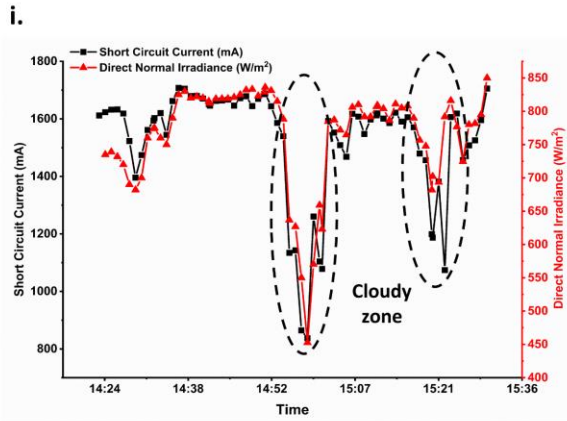
In this section, a detailed breakdown of the radiation component measurements is used to evaluate the power production hourly for a quarter of the system utilising Aluminium film, ReflecTech® Polymer, and mirror run conducted on 25th of August 2021. The emphasis here is to see the solar cell performance in power and I_{sc} in accordance with wind load and cell temperature. For the Aluminium film mirror, the results show a strong correlation between the I_{sc} and the direct normal irradiance (DNI) (W/m^2), where I_{sc} ranged between 1.7 – 0.85 A, as in Figure 6a i. The temperature was measured on the back side of the solar cell and presented a variation between 47 – 66 °C. The wind speed was ranged between 1.5 – 3.4 m/s and showed its impact through the drop in cell temperature. Also, we can observe a cell temperature fluctuating slightly with wind speed. The power fluctuated between 3.8 W and 2 W under DNI, ranging

between 450 – 850 W/m^2 , as in Figure 6a ii. Also, wind speed benefits the system by, to some extent dropping the cell temperature, but also peaks of winds might relatively push the UHCPV system out of its alignment, resulting in a drop in power output.

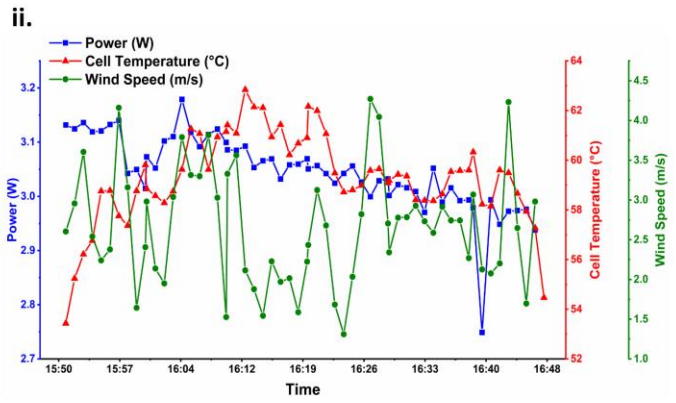
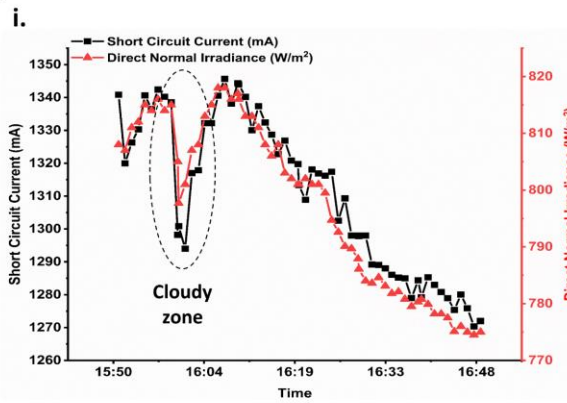
For Pilkington Optimirror, the I_{sc} oscillated in a range between 1.34 A to 1.27 A corresponding with DNI ranging between 815 - 775 W/m^2 , as in Figure 6b i. The linear drop in the DNI is associated with the sun latitude angle leaning gradually for the sunset. The wind speed, power, and cell temperature vary between the 1.25 – 4.2 m/s , 2.75 – 3.15 W, and 53 – 63 °C, as in Figure 6b ii, respectively. Inverse correlation is evident between the wind speeds and cell temperatures, where identical data trend is accruing between the I_{sc} and DNI.

For ReflecTech® Polymer, the continuous measurements were carried out following the Pilkington Optimirror. The I_{sc} was between 1.23 A and 1.08 A in accordance with DNI ranging between 670 – 750 W/m^2 , as in Figure 6c i. The reduction is clear in I_{sc} and that is due to the DNI drop as the sun is far west and with a low elevation angle. The power, cell temperature, and wind speed measured to be in a range of 2.55 – 3 W/m^2 , 52 – 62 °C, and 1 - 3.2 m/s , as in Figure 6c ii, respectively.

a.



b.



c.

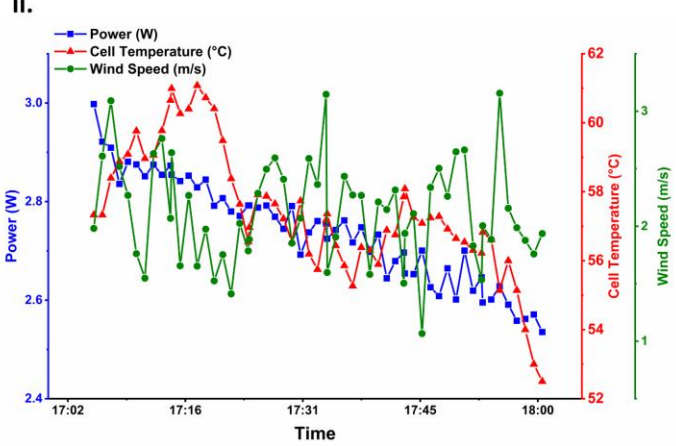
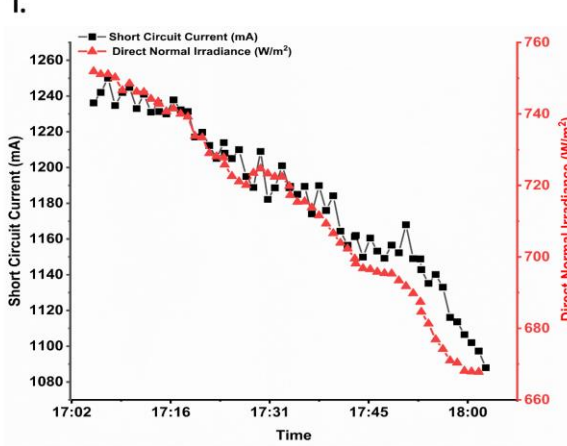


Figure 6 1-hour continuous measurements for 1/4 of UHCPV system using a. Aluminium film, b. mirror, and c. ReflecTech® Polymer where i. shows I_{sc} to DNI and ii. shows power, cell temperature, and wind speed correlations with times.

TOE addition into UHCPV System

The built 4-domed TOE in-house is bonded into the solar cell and then used in the system. Sylgard-184 is an excellent optical material with relatively high heat resistance. The Sylgard-184 offers a reflective index of about ~ 1.5 . The result here is only for $\frac{1}{4}$ of the system and compared with $\frac{1}{4}$ achieved results with a bare cell for Aluminium film, Pilkington Optimirror, and ReflecTech® Polymer secondary optics.

TOE has improved optical efficiency by offering a wider acceptance, compensating for any slight misalignment in performing the system. TOE utilisation improves optical efficiency and enhances effective concentration ratio by 32% in all secondary optic types, as in Figure 7a and b. The effective concentration ratio and optical efficiency increased for TOE $\frac{1}{4}$ UHCPV system to be 440 suns, 448 suns, and 485 suns, and 30%, 31%, and 33% for Aluminium film, mirror, and ReflecTech® Polymer, respectively.

The amount of generated heat is excessive and reaches 155 °C within the instantaneous measurements of 3 seconds for $\frac{1}{4}$ UHCPV system with TOE. This is not the maximum temperature of the cell, and the evidence is clear through $\frac{1}{4}$ UHCPV continuous measurements where it reached 66 °C. The absence of a proper cooling mechanism scaled up with the resulting effective concentration ratio limited the ability to examine the whole system with TOE. Therefore, relying on the typical temperature coefficient to predict the electrical product utilising the initial measurements of the AZUR SPACE 3C44- 5.5x5.5 mm² MJSC with $\frac{1}{4}$ of the UHCPV and TOE. The typical temperature coefficients with temperature ranging (25 – 80 °C), assuming the availability of an excellent cooling mechanism, are $(\frac{\Delta I_{sc}}{I_{sc(25^\circ C)}})/\Delta T = 0.080\%/K$, $(\frac{\Delta V_{oc}}{V_{oc(25^\circ C)}})/\Delta T = -0.135\%/K$, $(\frac{\Delta P_{mpp}}{P_{mpp(25^\circ C)}})/\Delta T = -0.106\%/K$, and $(\Delta \eta / \eta_{(25^\circ C)})/\Delta T = -0.106\%/K$. These coefficients resulted in an effective concentration ratio of 1705 suns, 1740 suns, and 1879 suns, a cell efficiency of 7.51%, 7.97%, and 7.73%, and an optical efficiency of 29%, 30%, and 32% for Aluminium film, mirror, and ReflecTech® Polymer, respectively as in Figure 7c. These results are the highest by far for all concentrator systems.

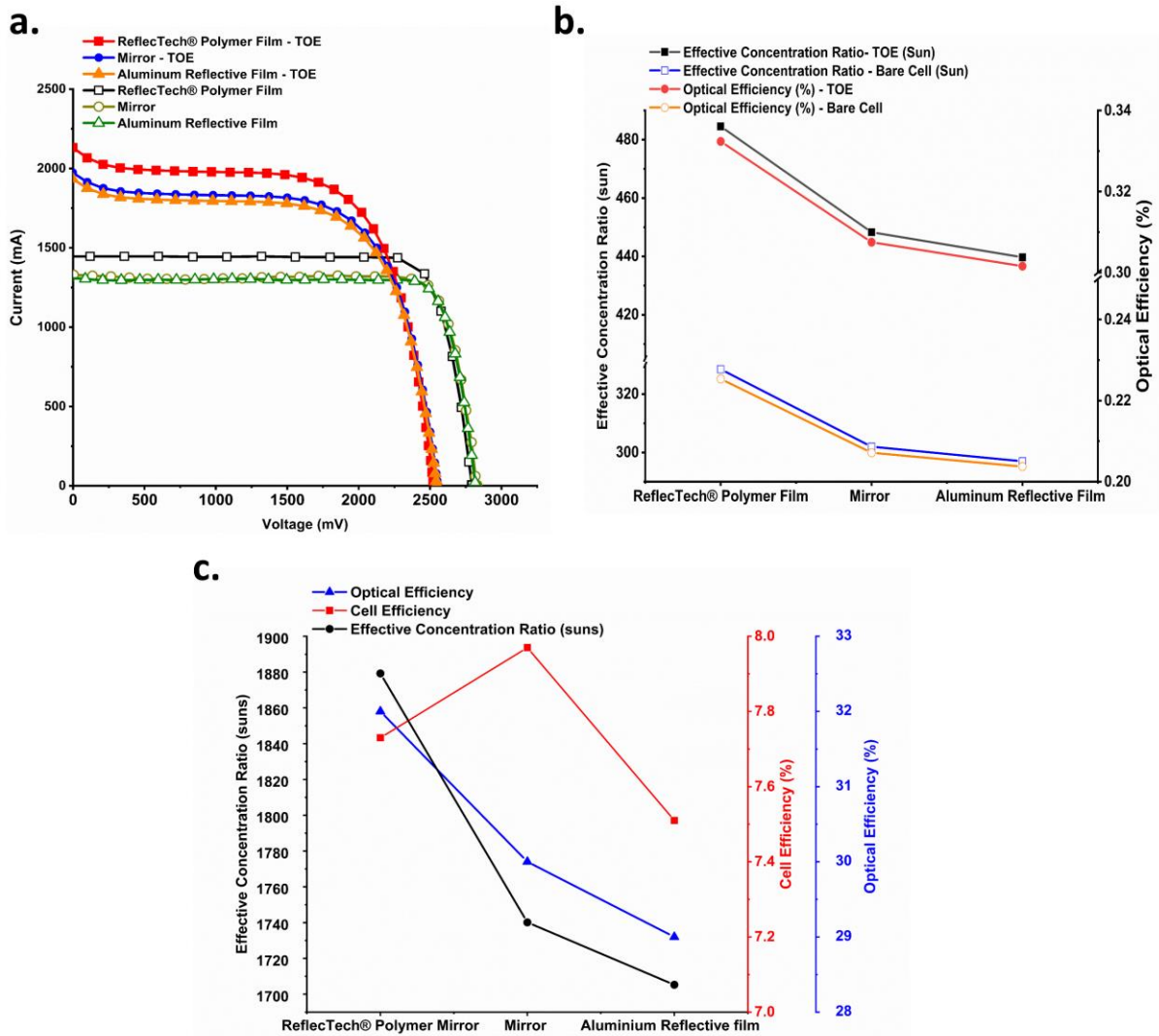


Figure 7 Displays $\frac{1}{4}$ UHCPV system with and without TOE performance for Aluminium film, mirror, and ReflecTech® Polymer where a. shows I-V curve and b. shows effective concentration ratio and optical efficiency results for $\frac{1}{4}$ UHCPV system. C displays the predicted results for the entire UHCPV system with TOE.

Discussion

UHCPV system design is limited to a low optical efficiency in general, which is very clear in this prototype. All tested optics are based on standard optical materials. Therefore, state of the art optics is highly recommended for the next step for better optical performance. The system design was approached and conducted by prioritising the employment of mechanical components and assembly more than the optical efficiency. The lack of a proper cooling mechanism has limited the complete system's continuous outdoor experimentations and testing the entire system with TOE. Even though the

system is designed for use with a solar cell, it is expected that thermal application would also be of great significance under this level of concentration. Consequently, the design of cooling mechanisms established in a serpentine configuration is ongoing to be incorporated in the system for thermal generation capacity¹². The literature review was thoroughly conducted to ensure that this outdoor experimental work is the highest in both the geometrical concentration ratio and its resulting effective concentration ratio. This design achieved more elevation than the limit of > 1000 suns, so the results of the UHCPV compact design is the highest in both geometrical and effective results, as in Figure 8.

The proof of the system design concept was successfully approved by achieving a new record of effective concentration ratio of 1220 suns for mirror and then 1291 suns for ReflecTech® Polymer. However, it is important to highlight that the mirror type gave the highest power output (highest cell efficiency) likely due to the reduced average reflectance < 1600 nm. This implies that the UHCPV system will benefit from wavelength filtering – even if it means compromising the optical efficiency of the useful wavelengths between 400-1600nm.

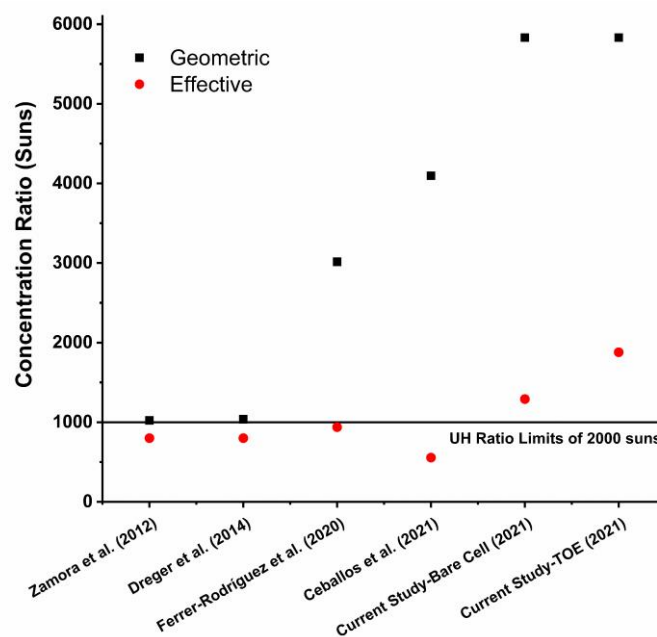


Figure 8 Literature review for comparative studies highlighting the geometrical and effective concentration ratios values.

Conclusion

In summary, we report the outdoor experimental validation for UHCPV compact design that accomplish an effective concentration ratio of 984 suns, 1220 suns, and 1291 suns and optical efficiency on average of 18.5%, 20.25%, and 22% for Aluminium reflective film, Pilkington Optimirror, and ReflecTech® Polymer, respectively. Due to the lack of proper active heatsink design, just ¼ UHCPV system was tested with 4-domed TOE and in one-hour continuous measurement. Still, losses regarding the FF and V_{oc} are present due to the existing heat due to the exciting heat, which can be avoided by scaling up an appropriate cooling mechanism not only for better electrical performance but also to evaluate the waste heat captured of the system. However, an effective concentration ratio of 1705 suns, 1740 suns, and 1879 suns and an optical efficiency of 29%, 30%, and 32% for Aluminium film, mirror, and ReflecTech® Polymer, respectively, were found which is the highest results in literature by far.

Method

System Fabrication

The UHCPV system mechanical items were designed and assembled based on SOLIDWORKS software. All the used mechanical items were made of Aluminium and produced by laser cutting process, except fasteners and fixings which are stainless steel. The primary optics-Fresnel lenses were manufactured by Orafol Fresnel optics company to generate a focal length of 45 cm through an aperture area of $21 \times 21 \text{ cm}^2$. The secondary optical stage incorporates a low-iron glass made by Cornwall Glass Company covered by either Aluminium film or ReflecTech® Polymer or a mirror (Pilkington Optimirror)¹⁵.

Outdoor Experimental Testing

The full experimental setup was assembled in the Environmental and Sustainability Institute (ESI) – Penryn Campus of the University of Exeter site. The system was measured during the peak hour of solar radiation in the site between 11 am and 2 pm. The optics contained by the UHCPV system was aligned and adjusted preliminary relying on the resulted configuration in the numerical model. Afterwards, the system was connected to the sun tracker and tested every quarter of it with minimal adjustment to assure the maximum output of short circuit current (I_{sc}). Consequently, the distance from the centre of the

Fresnel lens to the centre of the secondary mirror was established to be 24 cm, and the secondary mirror was tilted with an angle of 32°. The distance for the aperture area to the central solar cell is 13.5 cm. The system is susceptible to misalignment where minimal changes cause a significant drop in the electrical performance.

The UHCPV system was coupled with a sun tracker to concentrate the direct normal irradiance (DNI). The sun tracker is SOLYS Gear Drive (GD) with an extended tube and heavy-duty tripod. The sun tracker model offers an angular accuracy of $< 0.02^\circ$, an allowable payload and torque of 80 kg and 60 nm, respectively, as in Figure 2f. The counterbalance weight was made to stabilise the sun tracker with a weight equivalent to the UHCPV system of 13 kg¹⁶.

Current-voltage data acquire using EKO Instruments (I-V curve tracer: MP-160) measuring unit for outdoor measurements using 4-point connections to reduce the impact of series resistive losses¹⁷. The UHCPV system was initialised by turning on the sun tracker and uncovering the aperture area (4 Fresnel lenses) one by one. Temperature is detected during the experiment utilising a thermocouple meter sitting in the solar cell's back side (Datalogger SDL200 - EXTECH INSTRUMENTS) to ascertain safe operating conditions within the instantaneous measurements of only 3 seconds.

The complete weather station measures solar irradiation magnitude using a pyranometer (Global Horizontal Irradiation (GHI) and Diffuse Horizontal Irradiation (DIF)), and pyrhelimeter (Direct Normal Irradiance (DNI)) is established on a SOLYES2 sun tracker for accurate measurements, as in Figure 2f.

Acknowledgement

M.A would like to duly acknowledge the financial support from the Saudi Arabia Culture Bureau in the U.K. The funder has no role in study design data collection or manuscript preparation.

References

1. Algora, C. & Rey-Stolle, I. *Chapter 2 The Interest and Potential of Ultra-High Concentration. Next Generation of Photovoltaics: New Concept. Journal of Chemical Information and Modeling* **165**, (Springer Berlin Heidelberg, 2012).
2. Mohammad, M. E., Aziziyan, R., Fafard, S., Boucherif, A. & Arès, R. Cost-effective energy harvesting at ultra-high concentration with duplicated concentrated photovoltaic solar cells. 2760–2770 (2020). doi:10.1002/ese3.692
3. Gordon, J. M., Katz, E. A., Feuermann, D. & Huleihil, M. Toward ultrahigh-flux photovoltaic concentration. *Applied Physics Letters* **84**, 3642–3644 (2004).
4. Ferrer-Rodríguez, J. P., Fernández, E. F., Almonacid, F. & Pérez-Higueras, P. Optical design of a 4-off-axis-unit Cassegrain ultra-high concentrator photovoltaics module with a central receiver. *Optics Letters* **41**, 1985 (2016).
5. Optical design of a 4-off-axis-unit Cassegrain ultra-high concentrator photovoltaics module with a central receiver. **41**, 3–6 (2016).
6. Ferrer-Rodríguez, J. P. *et al.* Exploring ultra-high concentrator photovoltaic Cassegrain-Koehler-based designs up to 6000x. *Optics Express* **28**, 6609 (2020).
7. Wiesenfarth, M., Kisser, A., Schmid, T. & Bett, A. W. Development and investigation of a CPV module with Cassegrain mirror optics. (2014). doi:10.1063/1.4897055
8. Miñano, J. C. *et al.* Free-form optics for Fresnel-lens-based photovoltaic concentrators. **21**, 494–502 (2013).
9. Shanks, K., Ferrer-rodriguez, J. P., Fernández, E. F. & Almonacid, F. A > 3000 suns high concentrator photovoltaic design based on multiple Fresnel lens primaries focusing to one central solar cell. *Solar Energy* **169**, 457–467 (2018).
10. Kipp & Zonen. Instruction Manual SOLYS2 Sun Tracker SOLYS Gear Drive Sun Tracker. *Instruction Manual* **001**, 1–112 (2017).
11. Digrazia, M. & Jorgensen, G. REFLECTECH MIRROR FILM : DESIGN FLEXIBILITY AND DURABILITY IN REFLECTING SOLAR APPLICATIONS.
12. Ahmed, A., Shanks, K., Sundaram, S. & Mallick, T. Energy and exergy analyses of new cooling schemes based on a serpentine configuration for a high concentrator photovoltaic system. *Applied Thermal Engineering* **199**, 117528 (2021).
13. COMSOL. Ray Optics Module. (2018).
14. Azur Space Solar Power GMBH. Enhanced Fresnel Assembly - EFA Type: 3C42A – with 5.5x5.5 mm² CPV TJ Solar Cell Application: Concentrating Photovoltaic (CPV) Modules. 0–4 (2014).

15. Cornwall Glass Comapny_Penryn. Available at: <https://cornwallglass.co.uk/your-branch/penryn/>. (Accessed: 10th March 2022)
16. Kipp & ZONEN. *Instruction Manual : SOLYS2 & SOLYS Gear Drive. International Business* (2003).
17. EKO Instruments (I-V curve tracer: MP-160). Available at: <https://eko-eu.com/>. (Accessed: 20th March 2022).